UNIVERSITY OF SOUTHAMPTON

FACULTY OF ENGINEERING AND THE ENVIRONMENT

Aerodynamics and Flight Mechanics

Digital-filter and forward-stepwise method-based synthetic inflow turbulence generation: Applications to horizontal axis turbines

by

Kutalmis Bercin

Thesis for the degree of Doctor of Philosophy

September 2018

UNIVERSITY OF SOUTHAMPTON

ABSTRACT

FACULTY OF ENGINEERING AND THE ENVIRONMENT

Aerodynamics and Flight Mechanics

Doctor of Philosophy

DIGITAL-FILTER AND FORWARD-STEPWISE METHOD-BASED SYNTHETIC INFLOW TURBULENCE GENERATION: APPLICATIONS TO HORIZONTAL AXIS TURBINES

by Kutalmis Bercin

The main aim of this study is to create an easy-to-reproduce knowledge unit wherein the digital-filter method-based (DFM) and forward-stepwise method-based (FSM) synthetic inflow generator classes are conceptualised, explored, and improved for large eddy simulation applications (LES). To this end, the following novelties were introduced: [i] both classes were abstracted and documented into four non-CFD and five CFD model stages, [ii] two new DFM variants were derived, [iii] with these two, four preexisting DFM-FSM variants were code implemented, [iv] a new analytic function that can transform the skewness-kurtosis of synthetic inflow to target values without changing existing statistics was derived and verified, [v] two other skewness-kurtosis transformation approaches were derived and proved ineffectual, [vi] five easy-to-code computational speedup techniques for DFM-FSM were introduced and quantified, [vii] two new methods to enable DFM-FSM to be computed on nonuniformly-discretized arbitrary boundary geometries were developed, [$viii$] a preliminary method to ensure the divergence freeness in DFM-FSM was studied, [ix] each DFM-FSM model stage was evaluated by controlled studies of extensive-than-the-literature range of input variables and output statistics within non-CFD and LES environments through decaying homogeneous isotropic turbulence, homogeneous shear turbulence and smooth-wall plane channel flow, [x] five LES post-solution verification approaches were reviewed and compared via these building-block flows. In addition, horizontal axis wind and marine turbine flows were explored by various means including DFM-FSM: [xi] for these explorations, in-house codes were written and verified for the blade element momentum theory (BEMT), the time-accurate Euler-Bernoulli beam theory, a BEMT-CFD coupling through the actuator disk method, and the actuator line method, [xii] hydrodynamics of a marine turbine under decaying homogeneous isotropic turbulence with four different turbulence intensities were investigated by wall-modelled & actuator-line modelled LES computations, and twelve analytical wake models, [$xiii$] the arbitrary mesh interface technique under turbulent inflows was quantitatively assessed, and lastly, [xiv] considerable amount of for-the-first-time observations and remarks were quantified and reported.

Contents

Declaration of Authorship

I, Kutalmis Bercin , declare that the thesis entitled *Digital-filter and forward-stepwise method-based synthetic inflow turbulence generation: Applications to horizontal axis turbines* and the work presented in the thesis are both my own, and have been generated by me as the result of my own original research. I confirm that:

- This work was done wholly or mainly while in candidature for a research degree at this University;
- Where any part of this thesis has previously been submitted for a degree or any other qualification at this University or any other institution, this has been clearly stated;
- Where I have consulted the published work of others, this is always clearly attributed;
- Where I have quoted from the work of others, the source is always given. With the exception of such quotations, this thesis is entirely my own work;
- I have acknowledged all main sources of help;
- Where the thesis is based on work done by myself jointly with others, I have made clear exactly what was done by others and what I have contributed myself;
- Parts of this work have been published as:
  - Bercin et al., *EWTEC* (2013) Aalborg, Denmark.
  - Bercin et al., *OpenFOAM Workshop* (2017) Exeter, the United Kingdom.
  - Bercin et al., *ETC* (2017) Stockholm, Sweden.
  - Bercin et al., *Computers & Fluids* 172 (2018) 443-466.

Signed:.....

Date:.....

Acknowledgements

Throughout my life, like most *Homo sapiens* have been doing, I have been voraciously searching for a meaning of life. If I had not been accepted to this PhD programme, if I had not been being in such a transformative experience so far, very likely, I would have already judged life is not worth living, and I would have been a thing of the past now. For this reason, first of all, I would like to gratefully thank my supervisors, Dr. Zheng-Tong Xie and Prof. Stephen R. Turnock for changing my entire life for good by offering this opportunity; for their excellent research skills; for teaching me how to 'think'; and for their patience despite all drawbacks. Many thanks. I also gratefully thank to my father, Mustafa Berçin, for respecting my decision not to continue the family business, which would have made me much wealthier, and for his rigorous support in every aspect of my life. I am using his initial 'M' in my publications although it is not my name. *İyi ki varsın, Babam.* I am also grateful to my sister, Dilara Sakallı, for her deep love; the best friend, the best carer, the best person, and the most hot tempered. *İyi ki varsın, Dilişim.* I am absolutely indebted to my lovely mother, Ayşe Berçin, for her subjective support, her unbalanced deep love, and unique-funny character, and her more love. *İyi ki varsın, Annecim.* I am also indebted to Dr. Yusik Kim, Dr. Stefan C. Schlanderer, Matteo Magherini, and also, even though our acquaintance was a bit late, Geoffroy Claisse, for their curious, novel, entertaining and supportive characters, their life changing moral support and technical help without expecting any return, thank you very much. I am also so glad to have Dr. Eda Doğan, Dr. Halil Yetgin, Dr. Recep Kahraman; many thanks for being you. I would like to acknowledge and thank Dr. Robert Bleischwitz, Dr. Thomas Lloyd and Dr. Steven Daniels for their help and friendship. My dear close friends from Turkey: Recep Gürün, A. Muzaffer Arslan, Merve Türker, Elçin Özden, Nihan Çetin, Akın Ateş, İnal Sinanoğlu, Yiğitcan Tuğlu, Ahmet T. Kucur, Mustafa Kamçi, thank you very much for your support without expecting any return. I would like to acknowledge and thank Dr. S. Schreck and Dr. I. Afgan for providing me the raw data from the NREL Phase VI experiment and their journal papers, respectively. I would like to thank 'StackExchange' and 'Wikipedia' communities as well as Google LLC for their immense help. And last but not least, I would like to gratefully thank Albert Camus, literally for saving my life via *the Outsider, the Plague, the Fall, the Myth of Sisyphus, the Rebel,* and *Meursault.* I know now that life has no meaning, we are just 'spinning senselessly on a tiny rock in a corner of an indifferent universe'. I also know that my 'efforts will be largely futile, our lives soon forgotten, and our species irredeemably corrupt'. 'And yet! I will endure, nevertheless'. I have judged life is worth living, and I will do my very best to '*create* (*meanings* into the life) in the very midst of this desert', and will live.[1]

[1] I have used the quoted sentences from the YouTube channel, *the School of Life* since my English skills were not adequate to express some of my thoughts.

To unipolar and bipolar disorder patients...

Chapter 1

Introduction

1.1 Motivation

The primary objective of low carbon/renewable energy technologies on the basis of public reason is to reduce mainly CO_2 emissions from energy sectors in order to contribute to meet the Kyoto Protocol obligations [31]. To date, the largest source of CO_2 emissions among energy subsectors is the electricity generation sector [13, p. 2] and this forms (with heat generation) almost 42% of global CO_2 emissions [15, p. 10, Fig. 10]. Moreover, with the current policies in use, CO_2 emissions stemming from the energy sectors were projected to increase by nearly 84% from 2009 through 2050 [14, p. 7]. It is therefore argued that the compliance of the Kyoto commitments could not be fulfilled without low carbon/renewable energy technologies.

As a "good news story", the last two decades have seen a noticeable development and proliferation of utility-scale wind energy, which also underlay marine energy technologies.[1] The average levelised cost of (onshore) utility-scale wind power plants reduced more than three times from 1980s to the early 2000s [19, p. iv, Fig. ES-1], to that of conventional/advanced coal and nuclear power plants [32, Table 1-2]. In parallel, the utility-scale power conversion from wind was increased by a factor of more than 45 at approximately 22% per year from 1990s to 2010 in the world [12, p. 7], and 2.5% of the global electricity demand was provided by wind power plants within the year of 2013 [14, p. 5]. In addition to its increased competitive capacity, the future role of wind energy within the energy sector gained further importance due to its weak correlation between electricity costs and fossil fuel price variations, its more secure energy supply, and its

[1] Dynamics and prospectives of horizontal axis wind and marine turbines are in general deemed to share similarities. For instance, a technical challenge in one of them may also be observed in the other, or a numerical methodology being used in analyses for either of them may be utilised for the other. Therefore, in this section, the motivational line of reasoning and relevant examples were limited to wind turbines, and their applicability on marine turbines was presumed.

potential contributions to emission reductions (no direct greenhouse gas/pollutant emission). As a result, the International Energy Agency [14, p. 5] predicted that 12% the global electricity supply will be provided by wind energy by 2050, yet five years later, the rising trend led to a revision in this prediction as 15-18%.

Research and development studies (R&D) has been the primary instrument in tackling technical challenges in wind turbines to date [12, p. 2]. Also, a further decrement of 25-45% in current costs of wind energy is projected solely based on R&D by 2050 [14, p. 5]. The estimated period of time for resolving non-technological issues related to policies, finance and public acceptance is anticipated to be considerably short, and to be completed by 2020 among many International Energy Agency member countries [14]. However, the estimated time-frame for technical challenges extends to 2030-2050 [14, 12]. It is therefore put forth in this study that wind energy technologies should be further developed as a matter of priority to reach the aforementioned targets whilst non-technological challenges are deemed to be of secondary importance.

Inflow through the rotor plane of a turbine is almost always spatiotemporal-variant due to the atmospheric boundary layer, surrounding terrain, vegetation, wake ingestion from neighbouring turbines, to name but a few. This poses significant technical challenges particularly to the development of rotating components of utility-scale wind turbines [5, p. 1072]. Also, the importance of dealing with these challenges manifests itself in records of downtime events. For example, [23, p. 1] reported based on analyses of downtime durations of wind turbines in Germany from 2003 to 2007 that the most frequently failed first three turbine components respectively were gearbox, generator, and blades, which are all rotating elements. Additionally, failures of these components are considered the most unfavourable since they are at the centre of energy conversion processes and system dynamics. As an example, [23, p. 1] maintained from the above downtime analyses that the maintenance, and if need be, replacement of gearboxes shared nearly 40% costs of an entire turbine system.

A positive correlation between the number of malfunctions in wind turbines and turbulent wind conditions was noted by [3, p. 644] through analyses of wind turbine field data from Germany and Denmark. Furthermore, [24, p. 191] postulated that uneven loads caused by turbulence may be the primary reason for gearbox failures. Turbulence may also cause undesired oscillations in mechanical element, load imbalances, exceedances of the rated power, amplifications of bending moments, hence increments in fatigue loads [29, p. 14], and swift-substantial power fluctuations considering typical response rate of mechanical circuits is order of milliseconds [21, p. 2249]. Moreover, turbulence was quantified as the second most influential parameter to power after mean wind speed and before wind shear by [6] analysing roughly two thousand computations from a standard industrial turbine design tool. Even more significantly, [10, p. 255] asserted that encountering turbulence likely plays a role in the decision processes that the wind turbine industry avoids a number of wind turbine designs, which still has been studied in

the academia, e.g. variable speed stall/active stall controlled turbines. Consequently, assuming these deductions reflect the actuality, turbulence may be more costly than assumed for wind turbines.

According to [12, p. 2-4], there are 46 technical issues which need to be addressed in priority over the rest of the issues. As far as inflow-blade interactions are concerned, two of these issues were highlighted as driving forces of future cost reductions: *i*. concepts of rotor, i.e. blades and hub, and *ii*. time-accurate incoming wind assessment [19, p. vii].

Regarding the first driving mechanism, there is a trend towards taller and larger-in-diameter rotors to increase the amount and rate of wind energy conversion. One of the largest rotors today is 164[m] in diameter with 80[m]-long rotor blades [36]. Such a size is approximately more than ten times larger in comparison to turbines from mid-1980s [7, p. 30]. Although this trend may level off or even reverse itself in the future (e.g. 127[m] with 7.5[MW] rated power turbine [38] was erected, yet larger-yet-less-powerful turbines could be found such as 154[m]-7.0[MW] turbine [26]), it is argued that a typical utility-scale turbine's rotor diameter will remain above 100[m] considering upscaling rotors up to 250[m] was found technically feasible [8, p. 12], and examples of relevant studies/projects such as 141[m]-10[MW] design [9], [30, p. 12] were present. However, larger rotors result in increments in blade flexibility. In addition to this, the emergent need for lighter materials/structures to alleviate rotor weight increases due to diameter enlargements further augments the blade flexibility. As a consequence, blades may become more prone to adverse effects of incoming flow conditions such as turbulence.

With regard to the second driving mechanism, the research trend is towards developments for non-intrusive measurement techniques [14, p. 28] and numerical modelling for the *spatiotemporal-varying nature* of incoming flow. Nevertheless, spatiotemporal characterisation of inflow is not possible to high extents with the contemporary wind measurement devices (e.g. cup anemometers) [22, p. 33], or the inflow models given in the IEC Standard 61400-1 [28].

In principle, the direct numerical simulation technique can be utilised to characterise and evaluate inflow full-scale scenarios. However, to date, no adequate computational resources exist to explore such high Reynolds number flows involving complex inflow-turbine interactions.

A trending compromise between fidelity and computational costs to investigate inflow-turbine interactions has been the large eddy simulation technique, which offered first principles to industry and academia with low-cost scalability. Advancements, however, brought new challenges, especially for spatiotemporal-variant inflow boundary condition modelling of convection-dominant flows. As a consequence of chaotic turbulence dynamics, stochastic and/or statistical characterisation of such boundary conditions was found to be arduous, yet rewarding. Therefore, various inflow turbulence generation methods were put forth to date.

Two important generator classes among diverse inflow turbulence generation methods are the *digital-filter method-based* [18] and *forward-stepwise method-based* [39] synthetic inflow turbulence generators, on both of which there is a growing body of literature that recognises their promising capabilities.

Relative to their various alternatives, both methods are easier-to-code, cheaper-to-run, and able to generate spatiotemporal-variant turbulence-like time-series that contains first- and second-order statistics. Moreover, unlike many other alternatives, both classes do not require a computational fluid dynamics (CFD) setup, which make their computations in non-CFD design tools possible. On top of these, the inner tools constituting these classes are shared by various disciplines such as turbulence modelling community, signal processing, statistics and finance, to name a few. Being subject to research studies for further developments from many angles gives another advantage to the two classes to make advances through knowledge transfers. Nonetheless, as elaborated throughout the thesis, there are still many aspects to be explored and improved.

Accordingly, with explorations of inflow-turbine interactions also in mind, this study has set its aim to create an easy-to-reproduce knowledge unit wherein the digital-filter method-based and forward-stepwise method-based synthetic inflow generator classes are conceptualised, explored, and improved for large eddy simulation applications, particularly of involving horizontal axis wind and marine turbines.

1.2 Outline

This thesis is designed as a three-paper thesis, and is composed of seven chapters including the Introduction. In the pages that follow, the remaining of the thesis is structured as follows:

In Chapter 2, the fundamental governing equations of incompressible single-phase fluid dynamics are briefly derived, and presented.

In Chapter 3, the three paper-structured research studies are summarised.

From Chapter 4 to 6, the three paper-structured research studies are presented. The titles of these papers respectively are:

- Paper-I: *Exploration of digital-filter and forward-stepwise synthetic turbulence generators and an improvement for their skewness-kurtosis*
- Paper-II: *Evaluation of digital-filter and forward-stepwise synthetic turbulence generators with large eddy simulation of three canonical flows, and various model enhancements*

- Paper-III: *Large eddy simulation and analytical wake model investigations on hydrodynamics of a marine turbine under decaying homogeneous isotropic turbulence: Freestream turbulence intensity effects*

In Chapter 7, i.e. Appendix, one peer-reviewed conference paper, and two accepted conference abstracts are presented. The titles of these papers respectively are:

- (Presented) *Efficient method for analysing fluid-structure interaction of horizontal axis tidal turbine blades*
- (Presented) *OpenFOAM-Exploration of digital-filter-based synthetic turbulence generation methods and an improvement to their non-Gaussian capabilities*
- (Presented) *An evaluation of digital-filter based synthetic turbulence generation methods and improvements to their quantified deficiencies*

Chapter 2

Governing equations

2.1 Reynolds transport theorem

As noted by [27, p. 98], the original forms of the physical laws relevant to incompressible fluid mechanics, namely *i*. the conservation of mass and *ii*. Newton's second law of motion[1], were formalized for *isolated system*s through which neither energy nor mass is allowed to pass.

The *Reynolds transport theorem* adapts these forms of the physical laws to arbitrarily-deformable and -moving *open system*s through which either energy or mass can pass, so that the laws could be applied to practical problems of fluid mechanics. The reader is referred to [25] for the theorem's derivation and its mathematical insight. The final form of the theorem can be expressed as follows [25]:

$$\underbrace{\frac{d\,\mathrm{F}(t)}{dt}}_{1} = \underbrace{\int\limits_{\Omega(t)} \frac{\partial}{\partial t}\, f(\mathbf{x},t)\, d\Omega}_{2} + \underbrace{\int\limits_{\partial\Omega(t)} f(\mathbf{x},t)\,(\mathbf{u}\cdot\mathbf{n})\; d\,(\partial\Omega)}_{3} \tag{2.1}$$

where $\Omega(t)$ is the time-variant material volume, $\partial\Omega(t)$ the time-variant boundary of the material volume, $\mathbf{n}$ the boundary-normal unit vector, $\mathbf{u}$ the velocity of the boundary elements, $f(\mathbf{x},t)$ is an arbitrary quantity with an intensive property which could be a zeroth-, first-, or second-order tensor, and $\mathrm{F}(t)$ the volume integration of $f(\mathbf{x},t)$ such that $\mathrm{F}(t) = \int_{\Omega(t)} f(\mathbf{x},t)\, d\Omega$, an extensive property. The first term expresses the net rate of change of $\mathrm{F}(t)$ within the material volume, the second term the rate of change of creation/destruction of $\mathrm{F}(t)$ due to sources/sinks within the volume, and the third term the rate of inflow/outflow flux of $\mathrm{F}(t)$ through the boundaries.

[1] More precisely, Euler's second law of motion which extended Newton's second law of motion to make it applicable to rigid bodies instead of idealized point masses [17].

Let $\mathbb{G}(f(\mathbf{x},t))$ be a mathematical operator that performs the entire Reynolds transport theorem onto the arbitrary quantity $f(\mathbf{x},t)$. The conservation of mass and (linear) momentum equations can then be obtained by replacing the argument of the operator $\mathbb{G}$ with m and $m\mathbf{u}$, respectively:

$$\mathbb{G}(f(\mathbf{x},t)) = \begin{cases} \text{conservation of mass} & \text{if } f = m \\ \text{conservation of momentum} & \text{if } f = m\mathbf{u} \end{cases} \tag{2.2}$$

Two further simplifications can be made: First, the third term of Eq. 2.1 can be transformed into a volume integral by means of the *divergence theorem*. Second, the volume integration can be entirely removed to obtain a differential form of the theorem by the *Leibniz's integral rule* through assuming time-invariant $\Omega(t) = \Omega$, and collecting all the terms on the left-hand side with a proper sign convention. Both steps are shown as follows:

$$\frac{d\,\mathrm{F}(t)}{dt} = \int\limits_{\Omega(t)} \frac{\partial}{\partial t} f(\mathbf{x},t)\, d\Omega + \int\limits_{\Omega(t)} \nabla \cdot (f(\mathbf{x},t)\mathbf{u})\; d\Omega \tag{2.3}$$

$$\frac{\partial f(\mathbf{x},t)}{\partial t} + \nabla \cdot (f(\mathbf{x},t)\,\mathbf{u}) + \mathbf{b} = 0 \tag{2.4}$$

where the second term of Eq. 2.1 is assumed to be the net source within the material volume. This form is called *differential* or *strong* form of the equation. Moreover, the equation is in the *conservative* form. The *non-conservative* form can be obtained if the divergence term is expanded into its components and then the continuity constraint is applied. Their difference is often significant due to peculiar implications of numerical implementations since their discrete forms are not the same.

2.2 The equation of the conservation of mass

The conservation of mass equation can be obtained by means of replacing $f(\mathbf{x},t)$ in Eq. 2.4 with mass $m(\mathbf{x},t)$. Assuming $\mathbf{b} = 0$:

$$\frac{\partial m(\mathbf{x},t)}{\partial t} + \nabla \cdot (m(\mathbf{x},t)\mathbf{u}) = 0 \tag{2.5}$$

$m(\mathbf{x},t)$ can be expressed as $m(\mathbf{x},t) = \rho(\mathbf{x},t)\delta x\delta y\delta z$ where $\rho(\mathbf{x},t)$ is the volumetric mass density, and $\delta x\delta y\delta z$ the dimensions of the time-invariant volume Ω. Eq. 2.5 can therefore be:

$$\underbrace{\frac{\partial \rho(\mathbf{x},t)}{\partial t}}_{1} + \underbrace{\nabla \cdot (\rho(\mathbf{x},t)\mathbf{u})}_{2} = 0 \tag{2.6}$$

where the constants $\delta x \delta y \delta z$ in both terms are cancelled out. The first term represents the local rate of change of volumetric mass density $\rho(\mathbf{x}, t) = \rho$, and the second term the convective rate of change of mass flux[2], $\rho\mathbf{u}$.

The second term of Eq. 2.6, the divergence of a scalar-multiplied vector, can be expanded as in the following:

$$\nabla \cdot (\rho\mathbf{u}) = (\nabla\rho) \cdot \mathbf{u} + \rho\,(\nabla \cdot \mathbf{u}) \tag{2.7}$$

Two assumptions are made. First, the *Boussinesq approximation for density* which results in the omission of density variations within flow. Therefore, $(\nabla\rho) \cdot \mathbf{u} = 0$ since $(\nabla\rho)$, that is variations of the volumetric mass density within the field of interest at an instant, is null [4].

The second is the assumption of the *incompressibility* of the flow, which implies $\partial\rho/\partial t = 0$. Accordingly, Eq. 2.7 evolves into the following since $\rho \neq 0$:

$$\nabla \cdot \mathbf{u} = 0 \tag{2.8}$$

The applicability of the incompressible flow assumption to wind turbine flows

In wind turbine aerodynamics, the incompressible flow assumption is the norm. One reason is that the blade-tip maximum-Mach number is a priori constrained to 0.3 in nearly all designs in order to protect blades from the effects of compressibility at the blade-tip [33]. Further increase in the tip speed will reduce blade solidity as well as increase the chances that peculiar flow events occur; hence, a blade may become more prone to various damages. For example, one of the largest wind turbines, V164-8.0MW [35], was designed with the tip-nominal-Mach number 0.26. Another reason is, as noted by [11], the low-Mach number flow around the blade-root, i.e. as low as 0.01, which makes solving the equations of compressible flow arduous in this flow regime.

2.3 The equation of the conservation of (linear) momentum

The conservation of (linear) momentum equation can be obtained by means of replacing $f(\mathbf{x}, t)$ in Eq. 2.4 with $m(\mathbf{x}, t)\mathbf{u}(\mathbf{x}, t)$, or equivalently for the current scope, $\rho(\mathbf{x}, t)\mathbf{u}(\mathbf{x}, t) = \rho\mathbf{u}$. With $\mathbf{b} \neq 0$:

$$\frac{\partial(\rho\mathbf{u})}{\partial t} + \nabla \cdot (\rho\mathbf{u}\mathbf{u}) = \mathbf{b} \tag{2.9}$$

[2]Note that the units of flux and flow rate are $\mathrm{m^{-2}s^{-1}}$, and $\mathrm{s^{-1}}$, respectively. e.g. The units of mass flow rate is then $\mathrm{kg\,s^{-1}}$.

A number of manipulations is made in order to simplify Eq. 2.9 as follows. First, the local derivative term is decomposed:

$$\rho\frac{\partial \mathbf{u}}{\partial t} + \mathbf{u}\frac{\partial \rho}{\partial t} + \nabla \cdot (\rho \mathbf{u}\mathbf{u}) = \mathbf{b} \tag{2.10}$$

Further, the divergence term of the product of the scalar volumetric mass density ρ, and the dyadic velocity tensor $\mathbf{uu}$ are decomposed:

$$\rho\frac{\partial \mathbf{u}}{\partial t} + \mathbf{u}\frac{\partial \rho}{\partial t} + (\nabla\rho) \cdot (\mathbf{u}\mathbf{u}) + \rho\nabla \cdot (\mathbf{u}\mathbf{u}) = \mathbf{b} \tag{2.11}$$

The dot product of the vector $\nabla\rho$ and the dyadic tensor $(\mathbf{uu})$, and the divergence of the dyadic tensor $\nabla \cdot (\mathbf{uu})$, can also be further decomposed:

$$\rho\frac{\partial \mathbf{u}}{\partial t} + \mathbf{u}\frac{\partial \rho}{\partial t} + (\nabla\rho \cdot \mathbf{u})\,\mathbf{u} + \rho\,(\mathbf{u} \cdot \nabla\mathbf{u}) + \rho\,(\mathbf{u}\,(\nabla \cdot \mathbf{u})) = \mathbf{b} \tag{2.12}$$

Rearranging this equation by the distributive law yields:

$$\rho\left\{\frac{\partial \mathbf{u}}{\partial t} + \mathbf{u} \cdot \nabla\mathbf{u}\right\} + \mathbf{u}\left\{\frac{\partial \rho}{\partial t} + \nabla\rho \cdot \mathbf{u} + \rho\,(\nabla \cdot \mathbf{u})\right\} = \mathbf{b} \tag{2.13}$$

The second term on the left-hand side of the above equation reduces to zero due to the Boussinesq approximation for density and the conservation of mass:

$$\mathbf{u}\left\{\frac{\partial \rho}{\partial t} + \nabla\rho \cdot \mathbf{u} + \rho\,(\nabla \cdot \mathbf{u})\right\} = \mathbf{u}\left\{\frac{\partial \rho}{\partial t} + \nabla \cdot (\rho\mathbf{u})\right\} = 0 \tag{2.14}$$

Therefore, the final equation of the conservation of (linear) momentum is:

$$\underbrace{\rho\frac{\partial \mathbf{u}}{\partial t}}_{1} + \underbrace{\rho\,\mathbf{u} \cdot \nabla\mathbf{u}}_{2} = \rho\frac{\mathrm{D}\mathbf{u}}{\mathrm{D}t} = \mathbf{b} \tag{2.15}$$

where the first term represents the rate of change of momentum within the volume, the second term the net inflow rate of momentum through the boundaries of the volume, $\mathbf{b}$ the momentum source, and $\mathrm{D}(.)/\mathrm{D}t \equiv \partial(.)/\partial t + \mathbf{u} \cdot \nabla(.)$ the material derivative operator.

Navier-Stokes equations

Cauchy broke down the right-hand side of Eq. 2.15 into the terms due to *i.* surface forces, and *ii.* body forces [2]. The difference is that body forces act across a given body whereas surface forces act solely on the bounding surface of the body. This resulted in the so-called *Cauchy momentum equation*:

$$\rho\frac{\mathrm{D}\mathbf{u}}{\mathrm{D}t} = \mathbf{b}_{\text{surface}} + \mathbf{b}_{\text{body}} = \nabla \cdot \boldsymbol{\sigma} + \mathbf{b}_{\text{body}} \tag{2.16}$$

where $\boldsymbol{\sigma}$ is the second-order Cauchy stress tensor.

$\mathbf{b}_{\text{surface}}$ can be further compartmentalized with regard to the direction of the surface forces, and this can be represented within the Cauchy stress tensor:

$$\mathbf{b}_{\text{surface}} = \mathbf{b}_{\text{pressure}} + \mathbf{b}_{\text{viscous shear}} + \mathbf{b}_{\text{viscous normal}} \tag{2.17}$$

where pressure forces are normal to the bounding surface in a compressive way, viscous normal forces normal to the surface in a tensile way, and viscous shear forces parallel to the bounding surface.

Accordingly, the elements of Cauchy stress tensor can be expressed as:

$$\boldsymbol{\sigma} = \begin{bmatrix} \tau_{xx} - p & \tau_{xy} & \tau_{xz} \\ \tau_{yx} & \tau_{yy} - p & \tau_{yz} \\ \tau_{zx} & \tau_{zy} & \tau_{zz} - p \end{bmatrix} \tag{2.18}$$

A common rearrangement to Cauchy stress tensor is to express the elements of pressure and viscous terms in two separate tensors, mostly due to their distinctive effects. Additionally, viscous term vanishes if no velocity gradient exists (fluid at rest) [16]; therefore, pressure can be examined by itself.

$$\boldsymbol{\sigma} = \begin{bmatrix} -p & 0 & 0 \\ 0 & -p & 0 \\ 0 & 0 & -p \end{bmatrix} + \begin{bmatrix} \tau_{xx} & \tau_{xy} & \tau_{xz} \\ \tau_{yx} & \tau_{yy} & \tau_{yz} \\ \tau_{zx} & \tau_{zy} & \tau_{zz} \end{bmatrix} = -p\mathbf{I} + \mathbf{T} \tag{2.19}$$

where $\mathbf{I}$ is the unit tensor, and $\mathbf{T}$ viscous (deviatoric) stress tensor, which is the difference between the total (Cauchy) and mean (hydrostatic) stresses [16].

Taking the divergence of Eq. 2.19 in order to substitute it into Eq. 2.16 yields:

$$\begin{aligned} \nabla \cdot \boldsymbol{\sigma} &= \nabla \cdot (-p\mathbf{I} + \mathbf{T}) = \nabla \cdot (-p\mathbf{I}) + \nabla \cdot \mathbf{T} \\ &= -(\nabla p) \cdot \mathbf{I} + (\nabla \cdot \mathbf{I})\, p + \nabla \cdot \mathbf{T} \end{aligned} \tag{2.20}$$

where $-(\nabla p) \cdot \mathbf{I}$ is equal to $-\nabla p$, and $\nabla \cdot \mathbf{I} = 0$. Substituting the simplified expressions into Eq. 2.16 produces:

$$\rho \frac{\mathrm{D}\mathbf{u}}{\mathrm{D}t} = -\nabla p + \nabla \cdot \mathbf{T} + \mathbf{b}_{\text{body}} \tag{2.21}$$

Cauchy momentum equation is valid for all mediums (e.g. liquid and gas). The difference stems from the dissimilar *constituent* relations between "known" $\mathbf{u}$ and unknown $\boldsymbol{\tau}$, which are required due to the less number of equations than that of unknowns in Eq. 2.21. It is stated that [34] the viscous stress terms can be modelled as a function of corresponding strain rates, hence velocity gradients.

In order to establish such a viscous stress tensor-velocity gradient tensor relationship, a number of criteria, named *Stokes' axioms*, need to be fulfilled [1]: *i*. no shear stresses are generated (i.e. $\nabla \cdot \mathbf{T} = 0$) when the fluid is at a standstill, *ii*. viscous stresses and

corresponding velocity gradients are linearly correlated, thus a Newtonian fluid, and *iii*. $\mathbf{T}$ is the same in all orientations (i.e. isotropy).

An explicit expression for this relation can be obtained by analysing the velocity gradient term. While any tensor can be separated into its symmetric and anti-symmetric components, the velocity gradient term can also be split into its parts:

$$\nabla \mathbf{u} = \mathbf{S} + \mathbf{\Omega} \tag{2.22}$$

where $\mathbf{S}$ is the second-order strain rate tensor (symmetric) and $\mathbf{\Omega}$ the second-order rotation rate tensor (anti-symmetric). It is *assumed* [1] that viscous stresses are produced solely by the local rate of deformation (i.e. $\mathbf{S}$) and $\mathbf{\Omega}$ is responsible for only orientation changes of bodies in question. In detail, $\mathbf{S}$ is expressed in terms of the velocity gradient tensor as follows:

$$\mathbf{S} = \frac{1}{2}\left(\nabla \mathbf{u} + \nabla \mathbf{u}^{\intercal}\right) \tag{2.23}$$

The final expressions of the constitutive relations are shown for normal- and viscous shear stresses in Einstein notation, respectively:

$$\tau_{ii} = 2\mu \frac{\partial u_i}{\partial x_i} + \lambda \frac{\partial u_k}{\partial x_k} \tag{2.24}$$

where $\mu = \mu(T)$ is the first proportionality coefficient of viscosity, and $\lambda = \lambda(T)$ the second coefficient of viscosity both of which are functions of temperature T. The former relates the linear deformation to the viscous stresses, and the latter relates the volumetric deformation (i.e. $\partial u_k / \partial x_k = \nabla \cdot \mathbf{u}$) to the viscous stresses [34].

$$\tau_{ij} = \tau_{ji} = \mu \left(\frac{\partial u_i}{\partial x_j} + \frac{\partial u_j}{\partial x_i} \right) = 2\mu S_{ij} \tag{2.25}$$

The viscous stress tensor, $\mathbf{T}$, therefore, can be expressed in terms of the strain rate tensor as follows:

$$\mathbf{T} = \begin{pmatrix} 2\mu S_{xx} + \lambda \nabla \cdot \mathbf{u} & 2\mu S_{xy} & 2\mu S_{xz} \\ 2\mu S_{yx} & 2\mu S_{yy} + \lambda \nabla \cdot \mathbf{u} & 2\mu S_{yz} \\ 2\mu S_{zx} & 2\mu S_{zy} & 2\mu S_{zz} + \lambda \nabla \cdot \mathbf{u} \end{pmatrix} \tag{2.26}$$

Eq. 2.26 is the compressible flow, Newtonian fluid Navier-Stokes equations. In order to impose the incompressible flow assumption, two further assumptions are made: *i*. The total volume of the body in question is preserved (i.e. $\nabla \cdot \mathbf{u} = 0$), and *ii*. temperature is constant, hence the constant first coefficient of viscosity, μ. Moreover, the second coefficient of viscosity λ automatically goes to zero since it is inherently related to volume changes, which are assumed to be null through the first assumption above.

Expansion of $\nabla \cdot \mathbf{T}$ in each direction reveals a term of divergence of velocity, which is null. As an example, the rearrangement of the z-direction component of $\nabla \cdot \mathbf{T}$ is shown

below:

$$
\begin{aligned}
(\nabla \cdot \mathrm{T})_z &= \frac{\partial}{\partial x}\left(2\mu S_{zx}\right) + \frac{\partial}{\partial y}\left(2\mu S_{zy}\right) + \frac{\partial}{\partial z}\left(2\mu S_{zz} + \cancelto{0}{\lambda \nabla \cdot \mathbf{u}}\right) \\
&= \frac{\partial}{\partial x}\left\{2\mu \frac{1}{2}\left(\frac{\partial u}{\partial z} + \frac{\partial w}{\partial x}\right)\right\} + \frac{\partial}{\partial y}\left\{2\mu \frac{1}{2}\left(\frac{\partial v}{\partial z} + \frac{\partial w}{\partial y}\right)\right\} + \frac{\partial}{\partial z}\left\{2\mu \frac{1}{2}\left(\frac{\partial w}{\partial z} + \frac{\partial w}{\partial z}\right)\right\} \\
&= \frac{\partial}{\partial x}\left\{\mu\left(\frac{\partial u}{\partial z} + \frac{\partial w}{\partial x}\right)\right\} + \frac{\partial}{\partial y}\left\{\mu\left(\frac{\partial v}{\partial z} + \frac{\partial w}{\partial y}\right)\right\} + \frac{\partial}{\partial z}\left\{\mu\left(2\frac{\partial w}{\partial z}\right)\right\} \\
&= \mu\frac{\partial^2 u}{\partial x \partial z} + \mu\frac{\partial^2 w}{\partial x^2} + \mu\frac{\partial^2 v}{\partial y \partial z} + \mu\frac{\partial^2 w}{\partial y^2} + 2\mu\frac{\partial^2 w}{\partial z^2} \\
&= \mu\frac{\partial}{\partial z}\cancelto{0}{\left\{\frac{\partial u}{\partial x} + \frac{\partial v}{\partial y} + \frac{\partial w}{\partial z}\right\}} + \mu\frac{\partial^2 w}{\partial x^2} + \mu\frac{\partial^2 w}{\partial y^2} + \mu\frac{\partial^2 w}{\partial z^2} \\
&= \mu\nabla^2 w
\end{aligned}
\tag{2.27}
$$

As a result, $\nabla \cdot \mathbf{T}$ reduces to $\mu\nabla^2\mathbf{u} \equiv \nabla \cdot (\mu\nabla\mathbf{u})$.

Finally, the differential form of incompressible flow, Newtonian fluid, single-phase Navier-Stokes equations can be expressed as follows:

$$
\rho\frac{\mathrm{D}\mathbf{u}}{\mathrm{D}t} = -\nabla p + \mu\nabla^2\mathbf{u} + \mathbf{F}_{\text{body}} \tag{2.28}
$$

Space-filtered Navier-Stokes equations

Reynolds decomposition

Let $\phi(\mathbf{x}, t)$ is defined in a spatial domain $\Omega \subseteq \mathbb{R}^i$ where $i = 1, 2, 3$ and in a temporal domain $t \in [0, t_{final}]$. *Reynolds decomposition* is a signal decomposition method in which the original signal ϕ is separated into a term on which a chosen "averaging" operator is applied, $\overline{\phi}$, and the rest, ϕ'. Although "time-averaging" is mostly utilised as the operator, other types of averaging are also eligible for the *Reynolds decomposition* [37, p. 529]. For instance, with an arbitrary linear filter $\overline{(\cdot)}$, ϕ can be expressed as a summation of an over-filter component $\overline{\phi}$, and a sub-filter (fluctuation) component ϕ' around this filtering:

$$
\phi(\mathbf{x}, t) = \overline{\phi(\mathbf{x}, t)} + \phi'(\mathbf{x}, t) \tag{2.29}
$$

The properties of Reynolds conditions

Any averaging operator utilised for *Reynolds decomposition* needs to fulfil a number of requirements known as "the Reynolds conditions" [20, p. 207] shown in the following:

$$
\overline{\phi\,\overline{\varphi}} = \overline{\phi}\,\overline{\varphi} \tag{2.30}
$$

Linearity:

$$\overline{\phi + \varphi} = \overline{\phi} + \overline{\varphi} \tag{2.31}$$

$$\overline{c\phi} = c\overline{\phi} \quad \& \quad \overline{c} = c \rightarrow c = \text{constant} \tag{2.32}$$

Commutativity:

$$\overline{\frac{\partial \phi}{\partial s}} = \frac{\partial \overline{\phi}}{\partial s} \quad s = (x, y, z, t) \tag{2.33}$$

Furthermore, $\overline{\phi' \varphi'} \neq 0$. Yet this assertion is true *if and only if* a correlation exists between ϕ' and φ' [34, p. 64].

The set of space-filtered governing equations

Considering the aforementioned remarks, the application of a linear space filter on Eq. 2.28 and the expansion of the first term[3] of Eq. 2.28 result in the following:

$$\rho \left\{ \frac{\partial \overline{\mathbf{u}}}{\partial t} + \nabla \cdot (\overline{\mathbf{u}}\overline{\mathbf{u}}) \right\} = -\nabla \overline{p} + \mu \nabla^2 \overline{\mathbf{u}} \tag{2.34}$$

whose further modelling was elaborated in the following papers.

[3] In intermediate steps of an actual computation of this term, the continuity constraint remains non-zero; therefore, $\nabla \cdot (\mathbf{uu})$ was not reduced to $(\mathbf{u} \cdot \nabla)\mathbf{u}$ by the incompressibility assumption in practice.

Chapter 3

Summary

Paper-I

The performance of four synthetic turbulence generators that represent the majority of capabilities of *i*. digital-filter-based (DFM) and *ii*. forward-stepwise-based (FSM) generator categories is evaluated prior to transferring generator outputs into computational fluid dynamics simulations. In addition, a cheap-to-run and easy-to-code piecewise closed-form function that transforms one-spatial-point skewness-kurtosis of a synthetic time-series to a target value is derived and presented. The two main purposes of the study are to support model users in their decision process for choosing the most convenient type and their understanding of the models through a systematic exploration of model variables and modelling stages, and to extend the Gaussian nature of these models at a spatial point into non-Gaussianity for the first time. The evaluation test-bed contains three benchmarks, each of which focuses on an isolated aspect of turbulent flows: *i*. decaying homogeneous isotropic turbulence, *ii*. homogeneous shear turbulence and *iii*. plane channel flow with smooth walls. Results obtained reveal that: (i) the original DFM provides the highest level of reconstruction for input one-spatial-point second-order correlation tensors and two-spatial/temporal-point correlation functions; (ii) FSM yields the best trade-off between the computational cost and the level of reconstruction; (iii) the use of exponential-form correlation functions as a model approximation is more advisable than that of Gaussian-form, as the former removes the premature, sharp, flow-type-independent drop in power spectra observed for the latter; (iv) the proposed non-Gaussian functionality reconstructs the target one-spatial-point skewness-kurtosis pairs of the test-bed flows virtually without altering their already-embedded statistics; (v) the Lund transformation changes existing statistics only in statistically inhomogeneous lateral directions of a flow when anisotropic Reynolds stresses are present; and (vi) a spatial variation of correlation functions on turbulence generation plane improves the overall reconstruction fidelity in terms of correlation functions and power spectra.

Paper-II

Digital-filter-based (DFM) and forward-stepwise-based (FSM) turbulence-like time-series generator classes were conceptualised into five model stages within computational fluid dynamics set-ups. In addition, two new methods enabling DFM-FSM to be seamlessly computed on nonuniformly-discretized boundaries were proposed alongside a new mass-flux correction technique, and two new code practices for computational speedup. Through four DFM-FSM variants representing the majority of capabilities of the classes, each DFM-FSM model stage was explored by controlled studies of extensive-than-the-literature range of input variables and output statistics with large eddy simulation (LES) computations of decaying homogeneous isotropic turbulence, homogeneous shear turbulence and smooth-wall plane channel flow. Moreover, five LES post-solution verification metrics were reviewed and compared via these building-block flows. Among sixty-two observations, the prominent findings were that: [*i*] The traditional 80% turbulent kinetic energy resolution was quantified to be more robust than the modern LES post-verification metrics considered. [*ii*] In the first three nodes, input Reynolds stresses were consistently suppressed, particularly in shear components and lateral directions. Divergence-freeness enforcement was quantified to be the driving factor. [*iii*] Input autocorrelations were suppressed to a more limited extent. Navier-Stokes equation algorithms was deemed to be the cause. [*iv*] Streamwise evolution of Reynolds stresses followed an asymmetric quadratic pattern rather than a monotonic pattern. [*v*] The first DFM almost always produced the highest amplitude resemblances and the shortest adaptation lengths for Reynolds stresses and wall shear stresses. [*vi*] Amplifying input shear stresses reduced amplitude distortions downstream, and shortened adaptation lengths. [*vii*] A parabolic relation was found between input length scale sizes and amplitude/adaptation lengths of Reynolds stresses/wall shear stresses. [*viii*] Seamless nonuniform DFM-FSM and using multiple input length-scale sets did not affect flow to an important extent. [*ix*] Mass-influx corrections significantly improved pressure predictions and reduced computational costs, albeit no impact on velocity-based statistics.

Paper-III

A rigid model-scale experimental horizontal-axis marine turbine (so-called the *Southampton turbine*) was numerically investigated under decaying homogeneous isotropic turbulence in absence of its tower. Twelve controlled computations were carried out through wall-modelled and actuator-line-modelled large eddy simulations where the three-dimensional turbulence intensity, $I_{\mathbf{u}'_{\mathrm{rms}}}$, was the control variable. The first four computations excluded the blades, and examined the flow prediction effects of the *arbitrary mesh interface technique* while *i*. stationary and *ii*. rotating, and *iii*. the presence of the turbine nacelle. The last eight computations explored the ways how three-dimensional turbulence intensity affects the turbine and its surrounding flow fields. Four turbulence intensities were tested, $I_{\mathbf{u}'_{\mathrm{rms}}}=\{0, 10, 20, 40\}[\%]$. In addition, twelve analytical wake models from the wind and marine turbine literature were reviewed and assessed with respect to the wall-modelled computations under the same range of $I_{\mathbf{u}'_{\mathrm{rms}}}$. Among many, the prominent outcomes were as follows: [*i*] The *arbitrary mesh interface technique* adversely affected amplitude-based statistics while the AMI-region was in rotation by causing discontinuities on the AMI-region boundaries, and differences between the inside and outside of the AMI-region. The effects were increased outwards from the AMI-region centre. [*ii*] However, the rotating AMI did not affect time-based statistics. [*iii*] The stationary AMI did not affect flow fields. Furthermore, irrespective of freestream $I_{\mathbf{u}'_{\mathrm{rms}}}$: [*iv*] Longitudinal mean speed fields (U-fields) began to be affected by the presence of the turbine nearly 4 rotor radii upstream of the turbine; [*v*] maxima of changes in U-fields occurred at around 2 rotor radii downstream of the turbine; [*vi*] U-fields became virtually indistinguishable commencing around 6 to 10 rotor radii downstream within the alignment of the turbine; however, were kept turbine signature by remaining different from U-freestream despite turbulence entrainment; [*vii*] wake recovery rates as a function of downstream distance followed a half-Gaussian-form. [*viii*] No significant deviations between the wall-modelled and actuator-line modelled computations occurred in terms of the statistics quantified. [*ix*] The coefficient of variation, skewness, kurtosis and maxima of longitudinal forces/moments were increasing functions of $I_{\mathbf{u}'_{\mathrm{rms}}}$ whilst the mean and minima were inversely varying with $I_{\mathbf{u}'_{\mathrm{rms}}}$. [*x*] An analytical model that was derived and calibrated specifically for a similar marine turbine was quantified to be superior to the other models in terms of wake profile and speed predictions, highlighting the importance of the similarity level between turbine-flow particulars at hand, and analytical model's derivation particulars.

References

[1] Allen, M. B., Herrera, I., and Pinder, G. F. *Numerical modeling in science and engineering*. John Wiley & Sons, Inc., Hoboken, NJ, USA, 1987. ISBN 9781118207239. doi: 10.1002/9781118207239. (page 11, 12)

[2] Biswas, G. *Introduction to fluid mechanics & fluid machines*. Tata McGraw-Hill Publishing Company Limited, New Delhi, India, 2nd edition, 2007. ISBN 0-07-049497-5. URL http://bit.ly/2cLCmU8. (page 10)

[3] Byon, E., Ntaimo, L., Singh, C., and Ding, Y. Wind energy facility reliability and maintenance. In Pardalos, P. M., Rebennack, S., Pereira, M. V. F., Iliadis, N. A., and Pappu, V., editors, *Handbook of Wind Power Systems*, pages 639–673. Springer-Verlag Berlin Heidelberg, 2013. doi: 10.1007/978-3-642-41080-2. (page 2)

[4] Castro, I. P. Turbulence I: Physics & Measurement, Lecture notes, University of Southampton, 2012. (page 9)

[5] Chattot, J. J. Helicoidal vortex model for wind turbine aeroelastic simulation. *Computers and Structures*, 85(11-14):1072–1079, 2007. doi: 10.1016/j.compstruc.2006.11.013. (page 2)

[6] Clifton, A., Fleming, P., Kilcher, L., and Lundquist, J. K. Effects of changing atmospheric conditions on wind turbine performance. In *American Geophysical Union Fall Meeting 3-7 December 2012*, San Francisco, CA, 2012. (page 2)

[7] European Wind Energy Association. Wind energy factsheets. Technical report, European Wind Energy Association, 2010. URL http://bit.ly/1ee9Seg. (page 3)

[8] European Wind Energy Association. UpWind: Design limits and solutions for very large wind turbines. Technical report, 2011. URL http://bit.ly/2cVFcd2. (page 3)

[9] Frøyd, L. and Dahlhaug, O. G. Rotor design for a 10 MW offshore wind turbine. In *Proceedings of the Twenty-first (2011) International Offshore and Polar Engineering Conference*, Maui, Hawaii, United States, 2011. The International Society of Offshore and Polar Engineers (ISOPE). URL http://bit.ly/13pLjeA. (page 3)

[10] Hansen, A. D., Iov, F., Blaabjerg, F., and Hansen, L. H. Review of contemporary wind turbine concepts and their market penetration. *Wind Engineering*, 28(3):247–263, 2009. doi: 10.1260/0309524041590099. (page 2)

[11] Hansen, M. O. L., Sørensen, J. N., Voutsinas, S., Sørensen, N., and Madsen, H. A. State of the art in wind turbine aerodynamics and aeroelasticity. *Progress in Aerospace Sciences*, 42(4):285–330, 2006. doi: 10.1016/j.paerosci.2006.10.002. (page 9)

[12] International Energy Agency. Long-term research and development needs for wind energy for the time-frame 2012 to 2030. Technical report, The International Energy Agency Wind Agreement, 2013. URL http://bit.ly/2caVYUy. (page 1, 2, 3)

[13] International Energy Agency. Electricity in a climate constrained-world: Data and analyses. Technical report, The International Energy Agency, 2013. URL http://bit.ly/1mgco93. (page 1)

[14] International Energy Agency. Technology roadmap: Wind energy. Technical report, The International Energy Agency, 2013. URL http://bit.ly/2cPaker. (page 1, 2, 3)

[15] International Energy Agency. CO2 Emissions from fuel combustion highlights 2015 edition. Technical report, The International Energy Agency, 2015. URL http://bit.ly/2cBilAh. (page 1)

[16] Johnson, R. W. *The handbook of fluid dynamics*. CRC Press and Springer-Verlag, 1998. ISBN 9780849325090. (page 11)

[17] Kasdin, N. J. and Paley, D. A. *Engineering dynamics: A comprehensive introduction*. Princeton University Press, 2011. ISBN 9780691135373. (page 7)

[18] Klein, M., Sadiki, A., and Janicka, J. A digital filter based generation of inflow data for spatially developing direct numerical or large eddy simulations. *Journal of Computational Physics*, 186(2):652–665, 2003. ISSN 00219991. doi: 10.1016/S0021-9991(03)00090-1. (page 4)

[19] Lantz, E., Wiser, R., and Hand, M. IEA Wind Task 26: The past and future cost of wind energy. Technical report, National Renewable Energy Laboratory, 2012. URL http://bit.ly/2cEFG5O. (page 1, 3)

[20] Monin, A. S. *Statistical fluid mechanics: The mechanics of turbulence*, volume 45. Cambridge University Press, Cambridge, MA, United States, 1977. doi: 10.1119/1.10870. (page 13)

[21] Muller, S., Deicke, M., and De Doncker, R. W. Adjustable speed generators for wind turbines based on doubly-fed induction machines and 4-quadrant IGBT converters linked to the rotor. In *Conference Record of the 2000 IEEE Industry Applications Conference. Thirty-Fifth IAS Annual Meeting and World Conference on Industrial Applications of Electrical Energy (Cat. No.00CH37129)*, volume 4, pages 2249–2254. IEEE, 2000. ISBN 0-7803-6401-5. doi: 10.1109/IAS.2000.883138. (page 2)

[22] National Renewable Energy Laboratory. U.S. Department of Energy workshop report: Research needs for wind resource characterization. Technical report, Broomfield, Colorado, USA, 2008. URL http://bit.ly/2cnH5dz. (page 3)

[23] Oyague, F. Gearbox modeling and load simulation of a baseline 750-kW wind turbine using state-of-the-art simulation codes. Technical report, National Renewable Energy Laboratory, Golden, Colorado, USA, 2009. (page 2)

[24] Ragheb, A. M. and Ragheb, M. Wind turbine gearbox technologies. In Carriveau, R., editor, *Fundamental and Advanced Topics in Wind Power*, chapter 8. InTech, 2011. ISBN 978-953-307-508-2. doi: 10.5772/18717. URL http://bit.ly/2cn3vek. (page 2)

[25] Schobeiri, M. T. *Fluid mechanics for engineers: A graduate textbook*. Springer Berlin Heidelberg, Berlin, Heidelberg, 2010. ISBN 9783642115936. doi: 10.1007/978-3-642-11594-3. (page 7)

[26] Siemens Energy. Wind turbine SWT-6.0-154, 2013. URL http://sie.ag/12z5Cin. (page 3)

[27] Stickel, J. J. and Powell, R. L. *Fluid mechanics and rheology of dense suspensions*, volume 37. Cambridge University Press, Cambridge, 2005. ISBN 978-0-8243-0737-0. doi: 10.1146/annurev.fluid.36.050802.122132. (page 7)

[28] The British Standards Institution. Wind turbines Part 1: Design requirements, 2010. (page 3)

[29] Tong, W. Fundamentals of wind energy. In Tong, W., editor, *Wind Power Generation and Wind Turbine Design*, volume 48, pages 3–42. WIT Press, 2010. ISBN 9781845642051. (page 2)

[30] TPWind Secretariat. Wind European industrial initiative team EWI 2013-2015 implementation plan. Technical report, 2013. URL http://bit.ly/1lEfJl8. (page 3)

[31] United Nations Climate Change Secretariat. Kyoto Protocol, 1997. URL http://bit.ly/1mkvESN. (page 1)

[32] U.S. Energy Information Administration. Levelized cost and levelized avoided cost of new generation resources in the annual energy outlook 2016, 2016. URL http://1.usa.gov/1gEihMR. (page 1)

[33] Velázquez, M. T., Carmen, M. V. D., Francis, J. A., Pacheco, L. A. M., and Eslava, G. T. Design and experimentation of a 1 MW horizontal axis wind turbine. *Journal of Power and Energy Engineering*, pages 9–16, 2014. doi: 10.4236/jpee.2014.21002. (page 9)

[34] Versteeg, H. K. and Malalasekera, W. *An introduction to computational fluid dynamics:*

The finite volume method. Pearson Education Ltd, 2nd edition, 2007. ISBN 978-0-13-127498-3. (page 11, 12, 14)

[35] Vestas Wind Systems A/S. V164 8.0 MW, 2011. URL http://bit.ly/XxTNPi. (page 9)

[36] Vestas Wind Systems A/S. V164-8.0 MW at a glance, 2014. URL http://bit.ly/OeJuKohttp://bit.ly/2cVFsZu. (page 3)

[37] Wegner, B., Maltsev, A., Schneider, C., Sadiki, A., Dreizler, A., and Janicka, J. Assessment of unsteady RANS in predicting swirl flow instability based on LES and experiments. *International Journal of Heat and Fluid Flow*, 25(3):528–536, 2004. doi: 10.1016/j.ijheatfluidflow.2004.02.019. (page 13)

[38] Windpower Monthly. The 10 biggest turbines in the world, 2014. URL http://bit.ly/ZE9RKq. (page 3)

[39] Xie, Z.-T. and Castro, I. P. Efficient generation of inflow conditions for large eddy simulation of street-scale flows. *Flow, Turbulence and Combustion*, 81(3):449–470, 2008. ISSN 13866184. doi: 10.1007/s10494-008-9151-5. (page 4)

Paper - I

EXPLORATION OF DIGITAL-FILTER AND FORWARD-STEPWISE SYNTHETIC TURBULENCE GENERATORS AND AN IMPROVEMENT FOR THEIR SKEWNESS-KURTOSIS

Computers and Fluids 172 (2018) 443–466

Contents lists available at ScienceDirect

Computers and Fluids

journal homepage: www.elsevier.com/locate/compfluid

Exploration of digital-filter and forward-stepwise synthetic turbulence generators and an improvement for their skewness-kurtosis

Kutalmis M. Bercin, Zheng-Tong Xie*, Stephen R. Turnock

Faculty of Engineering and the Environment, University of Southampton, Southampton SO17 1BJ, UK

ARTICLE INFO

Article history:
Received 5 October 2017
Revised 15 February 2018
Accepted 28 March 2018
Available online 29 March 2018

Keywords:
Inflow turbulence
Synthetic turbulence
Inlet conditions
Random flow generation
Synthetic wind
Non-Gaussian turbulence
Non-Gaussian wind

ABSTRACT

The performance of four synthetic turbulence generators that represent the majority of capabilities of *i.* digital-filter-based (DFM) and *ii.* forward-stepwise-based (FSM) generator categories is evaluated prior to transferring generator outputs into computational fluid dynamics simulations. In addition, a cheap-to-run and easy-to-code piecewise closed-form function that transforms one-spatial-point skewness-kurtosis of a synthetic time-series to a target value is derived and presented. The two main purposes of the study are to support model users in their decision process for choosing the most convenient type and their understanding of the models through a systematic exploration of model variables and modeling stages, and to extend the Gaussian nature of these models at a spatial point into non-Gaussianity for the first time. The evaluation test-bed contains three benchmarks, each of which focuses on an isolated aspect of turbulent flows: *i.* decaying homogeneous isotropic turbulence, *ii.* homogeneous shear turbulence and *iii.* plane channel flow with smooth walls. Results obtained reveal that: (i) the original DFM provides the highest level of reconstruction for input one-spatial-point second-order correlation tensors and two-spatial/temporal-point correlation functions; (ii) FSM yields the best trade-off between the computational cost and the level of reconstruction; (iii) the use of exponential-form correlation functions as a model approximation is more advisable than that of Gaussian-form, as the former removes the premature, sharp, flow-type-independent drop in power spectra observed for the latter; (iv) the proposed non-Gaussian functionality reconstructs the target one-spatial-point skewness-kurtosis pairs of the test-bed flows virtually without altering their already-embedded statistics; (v) the Lund transformation changes existing statistics only in statistically inhomogeneous lateral directions of a flow when anisotropic Reynolds stresses are present; and (vi) a spatial variation of correlation functions on turbulence generation plane improves the overall reconstruction fidelity in terms of correlation functions and power spectra.

1. Background to inflow turbulence generation

Turbulent flow regimes are the norm in nature. Hence, it is important that engineering applications represent turbulent effects with reasonable fidelity. At many levels of industry and academia, the contemporary trend in turbulence modeling is away from semi-/empiricism towards first principles with minimal cost increase. This trend, however, poses substantial ongoing challenges, particularly for inflow boundary conditions of convective flows. In theoretical and numerical means, spatiotemporal delineation of these conditions, stochastically and statistically, is proved to be challenging mainly due to the chaotic dynamics of turbulence and various requirements on the fidelity.

For computational fluid dynamics (CFD), most of the inflow turbulence generation approaches aim to satisfy all or a part of the prescribed conditions, i.e. up to 2nd order statistics, integral length scales and Gaussian distribution of turbulent fluctuations. Some of them are also able to produce reasonable autocorrelation and spectrum. Only a very few synthetic turbulence generation approaches spend efforts on the 3rd order (skewness) and 4th order (kurtosis) statistics [1,2]. Lack of high order statistics modeling for turbulence generation may significantly impact the modeling accuracy for some applications, such as wind loading [3,4]. A rigorous assessment of the abilities of current synthetic turbulence generation approaches, and a simple and efficient model to generate non-Gaussian turbulence are of great interest.

Most of the inflow turbulence generation methods were classified into four main categories by Dhamankar et al. [5]: *i.* library-based, *ii.* recycling-based, *iii.* transition inducement-based, and *iv.* synthetic methods.[1] The last category may further be divided into six subcategories on the basis of their methodology: *i.* linearised

* Corresponding author.
E-mail address: Z.Xie@soton.ac.uk (Z.-T. Xie).

[1] [6, p. 553] and [7], however, regarded the first two as a single category.

https://doi.org/10.1016/j.compfluid.2018.03.070
0045-7930/

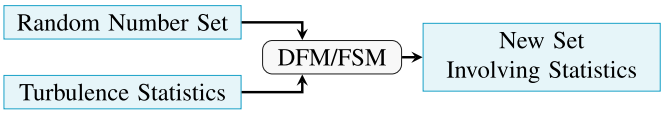

Fig. 1. A diagram showing synthetic turbulence generation with DFM/FSM. A color-blind proof and print-standard-friendly color scheme produced by Cameron [79] was used in this study.

turbulence model-based [8], *ii*. Fourier-based [9,10], *iii*. proper orthogonal decomposition-based [11], *iv*. synthetic-eddy-based [12], *v*. digital filter-based [13], and *vi*. forward stepwise-based [14]. In this study, the scope is limited to the last two subcategories, namely the digital filter-based methods (hereafter, DFM) and forward stepwise-based methods (hereafter, FSM), whilst the two arguably demand the simplest code implementation, yet provide high model fidelity with relatively low computational costs. The reader is, therefore, referred to [5–7] for the other categories.

Fig. 1 shows that DFM or FSM transforms a given random number set to a spatiotemporally new set involving a group of *target* statistical measures.[2] A chain of arithmetic operations is performed for the transformation. Within the chain, the target statistics arrange the properties and order of the operations, so that the *realized* statistics of the new sets could match the *target*.

Although Borgman [15] earlier elaborated on a method in which synthetic ocean wave processes are generated through digital filtering of a group of statistics and white-noise time-series[3], the contemporary DFM was introduced by Klein et al. [13], based on preliminaries from [16]. The authors developed a three-consecutive-stage framework: (*i*.) random number set generation, (*ii*.) embedding of arbitrary two-spatial-point autocorrelation functions through digital filters, and (*iii*.) incorporation of one-spatial-point second-order correlation tensor by a tensor transformation [17] (hereafter, the Lund transformation). In addition, the authors simplified the second-stage by restricting autocorrelation functions to Gaussian-form, so that filter coefficients can be explicitly evaluated, whose evaluation requires a root-finding algorithm otherwise. The function-form choice was justified with the same form observed in the viscous-dissipation stage of homogeneous isotropic turbulence.

In this initial DFM, five principal limitations exist, which subsequent studies attempted to alleviate: output (*i*.) contains no physical information beyond input statistics, (*ii*.) can only be generated on Cartesian grids,[4](*iii*.) is not divergence-free, (*iv*.) is statistically stationary, and (*v*.) obeys Gaussian probability density function (PDF) at a spatial point.

For the first limitation, di Mare et al. [18] investigated the possibility and practical viability of inserting arbitrary-form autocorrelation functions into the second model-stage. They proposed a new algorithm in which standard linear algebra tools are used to numerically solve a designed 'bilinear difference equation' to obtain digital-filter coefficients corresponding to the given autocorrelation function. The authors held the view that Klein et al.'s [13, p. 658] simplification is decent for free-shear flows whereas their more-information-carrying algorithm appears advisable for wall-bounded flows [18, p. 10]. Afterwards, di Mare and Jones [19, p.687] put forward another algorithm, which was presented as computationally cheaper, more competent and robust in comparison to their previous algorithm. Further, Fathali et al. [20, p. 96] claimed that the third model-stage distorts the resultant statistics from the second model-stage for highly anisotropic flow fields. On this basis, the authors put forth a two-stage-unified framework, which aimed to remove distortions and embed two-spatial-point cross-correlations. Subsequently, Xie and Castro [14] argued that the exponential-form functions are more appropriate simplification than Klein et al.'s [13] Gaussian-form, specifically for turbulent shear flows. Furthermore, the authors derived FSM which was quantified equivalent-in-effect to, and yet cheaper-to-compute than more complex digital filters. Then, the second model-stage of DFM in the streamwise direction was substituted with FSM; thus, resulting in a hybrid DFM-FSM.

The second limitation was, on the other hand, not shared by FSM, with which synthetic time-series generation on non-uniform grids is possible. For DFM, however, Kempf et al. [21] replaced the second model-stage with a diffusion process deemed equivalent to digital filtering, so that synthetic time-series can be seamlessly generated on non-uniformly spaced grids or on arbitrary boundary geometries. In addition, Fru et al. [22, p. 328] purported that a hybrid of the methods from [13] and [21] was developed, which is allegedly immune to this limitation. The authors, however, failed to clearly describe what the new method is. Lastly, Dhamankar et al. [23] enabled DFM to be used in curvilinear structured grids without interpolations through generating time-series on a Cartesian grid which is inherently a one-to-one-mapped corresponding curvilinear grid. Although the approach worked round interpolation errors, new drawbacks of their own arose [23, p. 11].

The third limitation reportedly causes erroneous pressure fluctuations [24, p. 1089], which was quantified by Kim et al. [25, Fig. 11] for incompressible plane channel flows wherein several orders of magnitude over-predicted pressure fluctuations persistent across the computational domain were observed. In contrast, negligible alterations due to non-divergence were expected and reported for velocity fluctuations [21, p. 76], [25, Fig. 11]. In general, therefore, it seems that non-divergence can be anticipated influential solely on computations where pressure is the principal field of interest. Considering these implications, divergence-freeness was first imposed into DFM for homogeneous isotropic turbulence by Ewert [26, p. 5] through devising solenoidal digital filters. For non-homogeneous anisotropic turbulence, on the other hand, [26, p. 7] was contented with a suggestion to use Smirnov et al.'s [27, p. 3–5] transformation method. Similarly, Klein et al. [13, p. 659] and Kempf et al. [21, p. 76] suggested a projection method from [10] in order to divergence-free transition synthetic time-series. None of the two suggestions were, however, tested to date. From another viewpoint, Kim et al. [25] rendered the hybrid DFM-FSM divergence-free by directly embedding synthetic time-series into the momentum predictor equation in a pressure-velocity coupling algorithm, in which case any non-solenoidal velocity field could be transformed without additional costs.

Regarding the fifth limitation, which was not studied in the DFM/FSM literature to date, evidence suggests that the frequency of occurrence of various turbulence characteristics tends to follow non-Gaussian distributions at a single spatial point. For instance, Jiménez [28] reviewed the literature that the one-spatial-point Pearsonian coefficient of kurtosis is approximately 2.85 (rather than 3.00) for velocity fluctuations in homogeneous isotropic turbulence. Even more pronouncedly, Moser et al. [29] reported for Re=395 plane channel flow that the one-spatial-point Pearsonian coefficient of skewness and kurtosis of velocity fluctuations vary across from −0.8 to 0.4, and from 2.1 to 38.0, respectively.[5]

[2] Measures predominantly consist of *i*. one-spatial-point second-order correlation tensor (i.e. Reynolds stress tensor) and *ii*. two-spatial/temporal-point autocorrelation functions.

[3] *White-noise* refers to a uniform power distribution across a frequency spectrum. By contrast, herein, the *Gaussianity* of a time-series will only refer to the probability distribution of amplitude

[4] A *Cartesian* grid herein refers to a grid wherein cells are unit squares/cubes.

[5] *Skewness* and *kurtosis* quantify the extent of PDF asymmetry and tail shape deviating from the normal distribution, respectively. Qualitatively, the former shows

Apart from the above, eight more studies offered major changes in various topics. For instance, Touber and Sandham [30, p. 104–105] systematically extended the hybrid DFM-FSM to compressible flows by generating thermodynamic fluctuations with synthetic velocity fluctuations via 'the strong Reynolds analogy'. Furthermore, Breuer and Schmidt [31, p. 677] expanded DFM to be utilised on interfaces of a hybrid LES-URANS methodology by formulating a modeled kinetic energy equation as a function of synthetic velocity fluctuations. Moreover, Anupindi and Sandberg [32, p. 703] seamlessly coupled, stricter than the aforementioned, the hybrid DFM-FSM into another LES-RANS methodology, wherein flow quantities at RANS-side of an interface are time-accurately sampled to create synthetic time-series at LES-side. Additionally, Okaze and Mochida [33, p. 25] modified the Lund transformation of the hybrid DFM-FSM to include scalar fluctuations and their complete correlations with flow variables although previously [34, p. 1313] utilised DFM to prescribe spatiotemporally-variant scalars by omitting their flow-cross-correlations. The hybrid DFM-FSM of [14] was extended by Kim et al. [35] with replacing DFM in all directions; hence, leading to "pure" FSM. Last but not least, Schmidt and Breuer [36] designated an approach where synthetic time-series are introduced into a computational domain via source terms in the momentum equation in order to freely determine the boundary location.

In DFM/FSM theory, arguably, no fundamental development was followed. Nevertheless, transferable performance improvements were put forth for the two DFM/FSM steps which are the costliest: (*i.*) digital filtering, and (*ii.*) generation of Gaussian random number sets. For the former, Veloudis et al. [37, p. 9] advanced filtering in frequency domain, which may reduce floating-point operations per time-step (FLOPT) from $\mathcal{O}(n^i)_{\{n\in\mathbb{N};\, i\in\{1,2,3\}\}}$ to $\mathcal{O}(n\log_i n)$. Additionally, Veloudis et al. [37, p. 10] assessed the potentiality of time-step reductions of synthetic time-series generation within a more restrictive environment (e.g. LES) without deteriorating temporal accuracy. Alternatively, Kempf et al. [38] propounded filtering via the separable convolution summation method' [39, p. 404] where convolution summations are consecutively performed on number sets along each coordinate. As a result, a speed-up of FLOPT from $\mathcal{O}(n^i)_{\{i=3\}}$ to $i\mathcal{O}(n)_{\{i=3\}}$ may be observed. Furthermore, the authors devised a parallelization procedure with zero-inter-communication by seeding pseudo-random number generators with constant pairs of integers and corresponding grid node indices. For the latter cost source, Xie and Castro [14] manipulated $\mathcal{O}$ (10) uniformly-distributed random number sets into normal samples through the central limit theorem. By contrast, Touber and Sandham [30, p. 104–105] asserted that the Box–Muller's theorem can reduce the number of these sets to two.

Besides the known limitations, previous studies failed to fill knowledge gaps in three main areas. First, although a number of independent and consecutive model stages form DFM/FSM, no investigation was made on to which extent each stage performs its task in isolation and interacts with the others. Second, all the research to date quantified DFM/FSM as a whole with CFD whereas the both are separate entities, and the latter causes metamorphosis of time-series produced by the former. Therefore, the performance of DFM/FSM *itself*, without the impact of CFD, remains unquantified. Third, most existing accounts either did not consider 'buildding-block' flows to evaluate DFM/FSM (e.g. no homogeneous isotropic/shear turbulence study was performed with [14].) or did not contain the complete set of *fundamental* assessment measures (e.g. [13] did not provide any results of power spectral density function.).

the dominant sign of the deviations from the mean turbulence quantities, and the latter the frequency of occurrence of extreme events in turbulence.

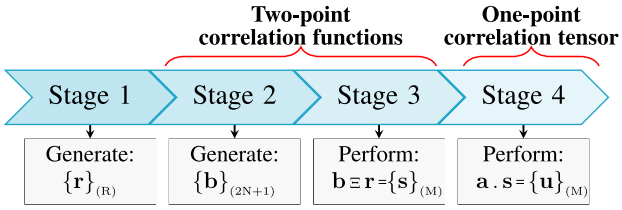

Fig. 2. A general view of DFM/FSM model stages for a one-dimensional field of discrete points.

The lack of structured knowledge in the three areas, however, hinders any attempts for theoretical capability-oriented improvements in DFM/FSM, for conveying their benefits to a wider audience, as well as for decision-making of the most appropriate variant to the problem at hand. The aims of this study are therefore *i.* to advance our understanding of the aforementioned knowledge gaps with the help of systematic explorations of model parameters and stages, and *ii.* to improve DFM/FSM capability portfolio through implementing a non-parametric one-spatial-point skewness-kurtosis transformation functionality.

To this end, a brief description of four synthetic turbulence generators including DFM and FSM is presented in Section 2, and the new one-spatial-point non-Gaussian functionality is described in Section 3. Section 4 presents three benchmark flows for tests and the statistical measures used. The obtained results including the assessment of the four synthetic turbulence generators and the new functionality are illustrated in Section 5. Clear-cut conclusions alongside a discussion on remaining challenges are listed in Section 6.

2. A brief description of four synthetic turbulence generators

2.1. Digital-filter-based and forward-stepwise-based synthetic turbulence generators

DFM and FSM construct spatiotemporal-variant Reynolds-decomposed fluctuation velocity (or scalar) fields, $\left\{u_i'(\mathbf{x},t)\in\mathbb{Q}\right\}_{\{i\in\mathbb{N}\,:\,i\in[1,3];\,t>0\}}$. Both generators may be abstracted into four consecutive and independent model stages as shown in Fig. 2 for a one-dimensional field of discrete points.

The first stage is the generation of a set of random numbers, $\{\mathrm{r}\}_{\{|\mathrm{r}|=\mathrm{R};\ \mathrm{k,j}\in\mathbb{N}\,:\,1\le\mathrm{k+j}\le\mathrm{R}\}}$, obeying the PDF of zero-mean ($\mathrm{R}^{-1}\sum_{\mathrm{k}=1}^{\mathrm{R}}\mathrm{r_k}=0$), unit-variance ($\mathrm{R}^{-1}\sum_{\mathrm{k}=1}^{\mathrm{R}}\mathrm{r_k^2}=1$), independent ($\mathrm{R}^{-1}\sum_{\mathrm{k}=1}^{\mathrm{R}}\mathrm{r_k r_j}=0$ for $\mathrm{k}\neq\mathrm{j}$) Gaussian white-noise.

In the second stage, a set of numbers 'calibrated' to two-spatial/temporal-point correlation functions, {b}, is generated. With DFM, the set is computed by Klein et al.'s [13, p. 657] relation between {b} and an autocorrelation function, ρ:

$$\rho(\mathrm{q},\mathrm{p})=\underbrace{\frac{\overline{u_\mathrm{p}'u_{\mathrm{p+q}}'}}{\overline{u_\mathrm{p}'u_\mathrm{p}'}}}_{\text{known}}=\underbrace{\frac{\sum_{\mathrm{j=-N+q}}^{\mathrm{N}}\mathrm{b_j b_{j-q}}}{\sum_{\mathrm{j=-N}}^{\mathrm{N}}\mathrm{b_j^2}}}_{\text{unknown}}\tag{1}$$

where $\mathrm{q}_{\{\mathrm{q}\in\mathbb{N}\,:\,\mathrm{q}\ge0\}}$ is the lag number, p the maximum lag number, $\{\mathrm{b}\}_{\{|\mathrm{b}|=2\mathrm{N}+1\,:\,\mathrm{b}\in\mathbb{Q}\}}$ a set of filter coefficients, and $\{\mathrm{N}\}_{\{|\mathrm{N}|\in\mathbb{N}\,:\,\mathrm{N}>0\}}$ the support of a filter. The diversity in DFM mainly arises from the different expressions proposed to invert Eq. (1). In contrast, in FSM, {b} is redefined by a group of integral length-scales weighted with empirical constants and limits of integration.

In the third stage, {b} is embed into {r} via a mathematical operation, so that a new set, {*s*}, is constructed with a new spatiotemporal stochastic pattern and yet consisting of correlation

function statistics. While FSM simply uses element-wise multiplication, DFM utilises convolution summation as follows:

$$s_k \equiv F_N(k) = \sum_{j=-N}^{N} b_j r_{k+j} \tag{2}$$

where $\{s\}_{\{|s|=M\,:\,s\in\mathbb{Q}\}}$ is a set of digital-filtered numbers, and F_N a linear, non-recursive, discrete filter operator performing a convolution summation on two finite sequences. In F_N, the two sets must completely overlap; thus, producing only a subset of the conventional *full* convolution summation. Accordingly, the size of the sets is related as: R−(2N+1)+1=M.

In the last stage, the one-spatial-point correlation tensor is incorporated into $\{s\}$ through the Lund transformation [17, p. 255]: $u_i'(\mathbf{x},t) = a_{ij}(\mathbf{x})\, s^i(\mathbf{x},t)$ where a_{ij}, a spatial-variant amplitude tensor of second-order, is shown below:

$$a_{ij} = \begin{bmatrix} (R_{11})^{0.5} & 0 & 0 \\ R_{21}/a_{11} & (R_{22}-a_{21}^2)^{0.5} & 0 \\ R_{31}/a_{11} & (R_{32}-a_{21}a_{31})/a_{22} & (R_{33}-a_{31}^2-a_{32}^2)^{0.5} \end{bmatrix} \tag{3}$$

where R_{ij} is the (known) one-spatial-point correlation tensor in units of variance. It should be noted that a_{ij} is conventionally spatial-variant and temporal-invariant whereas there is no theoretical objection to its temporal variation.

2.1.1. Klein et al.'s method – DFM

Klein et al. [13, p. 657–658] approximated the right-hand side of Eq. (1) as a Gaussian-form function of integral length-scales, so that {b} can be explicitly evaluated. The proposition was justified with the fact that autocorrelation functions of late-stage homogeneous turbulence have Gaussian-form. For a computational grid of cubic cells with $\{\Delta_i\}_{\{i\in[1,\,3]\}}$, constant grid size in a specific direction, the approximation to Eq. (1) in its discrete-form is shown below:

$$\rho \approx \exp\left(-\frac{\pi}{4}\frac{(m_i\,\Delta_i)^2}{(n_i\,\Delta_i)^2}\right) = \exp\left(-\frac{\pi}{4}\frac{m_i^2}{n_i^2}\right) \tag{4}$$

where m is the rectilinear distance of the node in question to the zero-lag correlation node, and n the length-scale size. Both are in grid spacing units. Correspondingly, Klein et al. [13, p.658] derived a closed-form expression for {b}:

$$\{b\}_i \approx \widetilde{\{b\}}_i \Big/ \left(\sum_{j=-N}^{N} \tilde{b}_j^2\right)^{0.5} \quad \text{as} \quad \widetilde{\{b\}}_i = \exp\left(-\frac{\pi}{2}\frac{m_i^2}{n_i^2}\right) \tag{5}$$

The validity of the approximation was shown to have two constraints: *i.* the length-scale size is limited to the range $2 \le n_i \le 100$, and *ii.* the support of the filter must at least be two times the scale size, $N_i \ge 2n_i$.

2.1.2. A customized method in spirit of di Mare et al.'s method – DFM

The possibility of the direct inversion of Eq. (1) was investigated by di Mare et al. [18] through an iterative root-finder algorithm of Newton's method, so that arbitrary-form of correlation functions could be used in DFM. The main disadvantage of this method is arguably deemed to be its difficult code implementation. In this study, for this reason, a new approach with the *spirit* of [18] was invented as follows. First, a given arbitrary-form correlation dataset is curve fit to a chosen-form of a continuous function. Then, the direct inversion of Eq. (1) is conducted on this curve-fit function. Accordingly, for the study's set of benchmarks, the following expression was devised as the most proper form of the function:

$$\{b\} = \mathscr{R}[\rho] = \mathscr{R}[\mathscr{C}\{a\exp(-bx) + c\exp(-dx)\}] \tag{6}$$

where $\mathscr{R}$ denotes the chosen root-finder algorithm, $\mathscr{C}$ the curve-fit algorithm, and $\{a,b,c,d\}_{\{\forall\in\mathbb{Q}\}}$ are the curve-fit parameters. Herein, filter supports are sized to the point where correlation functions drop below few percent of their zero-lag value.

2.1.3. Xie and Castro's method – hybrid DFM-FSM

In contrast to Klein et al. [13], Xie and Castro [14, p. 454] modeled the right-hand side of Eq. (1) as an exponential-form function, which was deemed more valid for turbulent shear flows:

$$\rho \approx \exp\left(-c\,\frac{\pi}{2}\,\frac{|m_i|}{n_i}\right) \quad \text{resulting in} \quad \widetilde{\{b\}}_i \approx \exp\left(-c\,\pi\,\frac{|m_i|}{n_i}\right) \tag{7}$$

where c=1 is a constant. Furthermore, to reduce computational costs, the streamwise convolution summation in DFM was replaced by a simpler and a quantitatively justified equivalent procedure, named FSM [14, p. 456]. Therein, streamwise integral length-scales are input through temporal-correlation of two planes of $\{s^i\}$, which are generated at successive time-steps:

$$s^{i\Psi}(y,z,t{+}\Delta_t) = s^{i\Psi}(y,z,t)\exp\left(-c\,\frac{\pi}{2}\,\frac{\Delta_t}{T}\right) + s^{i\psi}(y,z,t{+}\Delta_t)\left\{1-\exp\left(-c\,\pi\,\frac{\Delta_t}{T}\right)\right\}^{0.5} \tag{8}$$

where $\{s^{i\Psi}\}$ is a temporal slice of $\{s^i\}$ including transverse length-scales $\{L_\alpha\}_{\{\alpha\in\{y,\,z\}\}}$ at time t, $\{s^{i\psi}\}$ an auxiliary temporal slice generated with a new set of random numbers in the same way with $\{s^{i\Psi}\}$, T streamwise Lagrangian time-scale computed with Taylor's frozen turbulence hypothesis [40].[6]

In their discussion of the default value of c=1, Kim et al. [25, p. 57] put forth c=0.5 is more apt to use for their plane channel flow CFD simulations. In view of this statement, herein, three values of c=$\{1, 0.5, 0.25\}$ were tested via the three benchmark flows without CFD (Section 4.1). For the majority of the scenarios, c=0.5 yielded the highest level of similarity to the benchmarks in terms of correlation functions and power spectra (not reported). Therefore, Kim et al's. [25] preference was used throughout the study as the default model constant instead of the original value of c. It should be stressed that c=0.5 is not universal, yet a solution of model calibration to the flows in question. One may thereby seek other values of c for other types of flows.

2.1.4. Kim et al.'s method – FSM

Xie and Castro's [14] one-direction of FSM was extended to all directions by Kim et al. [35, p. 135]; hence, leading to the use of convolution summations of DFM being abolished. FSM is subsequently applied to each direction in an arbitrary order to yield $\{s^i\}$ as follows:

$$s_y^i(t,\,j{+}1,\,k) = s_y^i(t,\,j,\,k)\exp\left(-\frac{c_y}{n_y}\right) + r(t,\,j,\,k)\left\{1-\exp\left(-\frac{2c_y}{n_y}\right)\right\}^{0.5} \tag{9a}$$

$$s_{yz}^i(t,\,j,\,k{+}1) = s_{yz}^i(t,\,j,\,k)\exp\left(-\frac{c_z}{n_z}\right) + s_y^i(t,\,j,\,k)\left\{1-\exp\left(-\frac{2c_z}{n_z}\right)\right\}^{0.5} \tag{9b}$$

$$s_{yzx}^i(t{+}1,\,j,\,k) = s_{yzx}^i(t,\,j,\,k)\exp\left(-\frac{c_x}{n_x}\right) + s_{yz}^i(t,\,j,\,k)\left\{1-\exp\left(-\frac{2c_x}{n_x}\right)\right\}^{0.5} \tag{9c}$$

where $\{c_i(\mathbf{x})\}_{\{i\in\{x,y,z\}\}}$ is a set of constants to scale $\{n_i\}$, and {r} a planar set of random numbers.

[6] According to the hypothesis: L_x=U_xT, where L_x is a streamwise integral length-scale, U_x, mean flow speed in the same direction, and T streamwise Lagrangian time-scale.

3. Development of the one-spatial-point non-Gaussian functionality

Transformation of skewness-kurtosis pairs of DFM/FSM at a spatial point was studied by means of three new approaches: *i.* non-Gaussian random number set input-based approach, *ii.* deterministic deconvolution-based approach, and *iii.* PDF transformation-based approach. The tests showed that the first two proposed approaches were proved to be ineffective, and the third approach to be promising, which is accordingly introduced in the following. It is however still deemed to present what the first two *sound* methods are for the reader's examination; thus, presented in Section SA.1-2.

3.1. PDF transformation-based approach

The approach is based on a transformation function. It is introduced as a new model stage between the 3rd and 4th stages illustrated in Fig. 2. The function is a piecewise closed-form function shown in Eq. (11), which was derived by means of two concepts: *i.* the memoryless nonlinear transformation method (MNT; also known as the *zero-memory non-linear transformation*) [41,42], and *ii.* the Johnson system of PDFs [43].

$$\text{IO}'_i(\mathbf{x},t)=\begin{cases}\dfrac{1}{\sigma_U}\left\{\sinh\left(\dfrac{u'_i(\mathbf{x},t)-\gamma}{\delta}\right)-\mu_U\right\}, & \text{for } S_U \text{ - Unbounded}\\ \exp\left\{u'_i(\mathbf{x},t)\right\}, & \text{for } S_L \text{ - Log-Normal}\\ \dfrac{1}{\sigma_B}\left[\left\{1+\exp\left(\dfrac{\gamma-u'_i(\mathbf{x},t)}{\delta}\right)\right\}^{-1}-\mu_B\right], & \text{for } S_B \text{ - Bounded}\end{cases} \tag{11}$$

MNT is the core concept of the current family of non-Gaussian process generation methodologies. Its main formulation was proposed by Grigoriu [42, p. 611] as:

$$\text{IO}'_i(\mathbf{x},t)=g_i\{u'_i(\mathbf{x},t)\}=F^{-1}_{\text{IO}'_i}\left\{\phi_{u'_i}\{u'_i(\mathbf{x},t)\}\right\} \tag{10}$$

where u'_i is a process (known input) obeying a source PDF, IO'_i corresponding transformed process (unknown output) obeying a target PDF, $\phi_{u'_i}$ the source cumulative distribution function (CDF), and $F^{-1}_{\text{IO}'_i}$ the target inverse CDF. The condition of the existence of the relation is satisfied if $g_i\{\cdot\}=F^{-1}_{\text{IO}'_i}\{\phi_{u_i}\{\cdot\}\}$ is a monotonic function. Through the concept, a given u'_i, obeying a Gaussian CDF $\phi_{u'_i}$, could be transformed into a new process, IO'_i, obeying a target non-Gaussian CDF $F_{\text{IO}'_i}$.

The first potential drawback associated with the use of sole MNT is that Eq. (10) may modify spectral contents of u'_i towards IO'_i [44, p. 19] due to the non-linearity of the function [45, p. 1196]. Whereas, as a rare counter-argument, Smallwood [46, p. 3] claimed that no substantial change should be expected in the spectral content of u'_i, because this is mostly determined by zero-crossings, which are not significantly altered by Eq. (10). The second drawback is the high computational cost of interpolations to execute Eq. (10) for each spatial-temporal point of random processes obeying arbitrary-form PDFs.

For a process, arbitrary-form non-Gaussianity implies infinite combinations of infinite-order non-standard moments; hence, has a broad meaning. In the context of turbulence, however, non-Gaussianity may be restricted to non-standard skewness and kurtosis only due to the fading physical interpretation of the ever-increasing level of abstraction in higher moments and their diminishing distinguishable impact on the physicality of turbulent flow developments.

With this constraint, identification of a unique and closely-approximated non-Gaussian distribution that can be customized to any valid combination of the first four central moments may be achieved through the Johnson system of distributions [43]. This system includes all valid skewness-kurtosis pairs (illustrated in [47, Fig. 1]) through its three members: *i.* S_U unbounded, *ii.* S_L log–normal (a transition line from *i* to *iii*) and *iii.* S_B bounded families [43, p. 156]. The readers are referred to [47] for the basic characteristics of the system.

More importantly, the substitution of the Johnson system into Eq. (10) yields a piecewise closed-form expression for IO'_i, which is easy-to-code and cheap-to-execute, as follows (for derivation details, refer to Section A.3.1):

where $\gamma(\beta_1,\ \beta_2)$ and $\delta(\beta_1,\beta_2)_{\{\delta>0\}}$ are the shape parameters of the Johnson system, $\mu_{U/B}(\gamma,\delta)-\sigma_{U/B}(\gamma,\delta)$ the first two *theoretical* normalized moments of the corresponding families, $\beta_1^{0.5}=\mu_3/\sigma^3$ and $\beta_2=\mu_4/\sigma^4$ the Pearson's moment coefficient of skewness and kurtosis, μ_3 and μ_4 the third and fourth central moments, and σ the standard deviation. The expression leads to two further questions: for a $(\beta_1,\ \beta_2)$-pair, *i.* how to choose the appropriate family, and *ii.* how to compute γ-δ.

The criteria to choose one of the families rely on the relative position of the target skewness-kurtosis pair values with respect to the Cullen and Frey graph's log–normal curve [47, Fig. 1]. The curve was obtained by a parametric system of equations in [43, Eq. (14)]. The set of equations, however, does not lend itself to a direct relation between skewness and kurtosis; thus, resulting in difficulties in the selection. Such functional relation, $g(\beta_2)\sim\beta_1$, was then derived by Tuenter [48], and summarized in Eqs. (A.46)–(A.50). Accordingly, the following conditionals determine the family member: S_U, if $g(\beta_2)>\beta_1$; S_L, if $g(\beta_2)=\beta_1$ and S_B, if $g(\beta_2)<\beta_1$. In addition, the region wherein pairs cannot exist was defined as: $\beta_2-\beta_1-1<0$ [43, Fig. 2].

After finding the family that the pair belongs to, γ-δ can be computed through a *moment-matching technique*, where the family's theoretical expressions of skewness-kurtosis are solved for γ-δ with the help of root-finding algorithms. Parameterizations which considerably reduced the complexity of the root-finding problem were proposed by Tuenter [48, p. 310] for S_U, and [49, p. 746–748] for S_B. Herein, these set of equations were manipulated in compliance with the requirements of the study and reported in Eqs. (A.12)–(A.17) for S_U and Eqs. (A.18)–(A.45) for S_B.

Table 2 compares the typical number of computational operations performed by Eqs. (10) and (11). As shown, the new method eliminated all algorithms and reduced the number of elementary

function operations. Moreover, the data preprocessing demand is less for the new method. For instance, the pairing between γ–δ and β_1–β_2 is a bijection; therefore, for each β_1–β_2 pair, γ–δ is computed only *once and for all* whereas, for the same β_1–β_2 pair, Eq. (10) needs to store an interpolation table of $F^{-1}_{\mathrm{IO}'_i}$ values that also need to be computed by numerical integrations. Spatial-variation of β_1–β_2 across inflow plane, on the other hand, exponentially amplifies this contrast.

4. Methodology

4.1. Benchmarks and numerical settings

The four methods and the non-Gaussian approach were implemented into OpenFOAMv1612+ [50], and tested through a test-bed of three benchmark flows. The methods sorted by descending theoretical FLOPT are labeled as: *i*. Custom [18], *ii*. Klein et al. [13], *iii*. Xie–Castro [14], and *iv*. Kim et al. [35]. The chosen methods represent the majority of DFM/FSM capabilities and varieties. The test-bed involves three 'building-block' flows: *i*. decaying homogeneous isotropic turbulence (HIT; the case of M=0.0508) [51], *ii*. homogeneous shear turbulence (HST; the case of h=0.305) [52], and *iii*. plane channel flow with smooth walls (PCF; the case of Re_τ=395) [29], each of which focuses on an isolated aspect of turbulent flows. In this study, the finite-volume method and Navier-Stokes equation models were turned off in order to prevent any hard-to-measure distortions in output statistics of the methods. The details of the benchmarks and numerical set-ups are given in the following.

4.1.1. Common numerical settings

Each benchmark reports measurements for several test sections. For each benchmark, one of these sections was chosen, and corresponding time-variant planar flow field was approximately reconstructed by the methods. Then, the level of reconstruction was evaluated through a set of statistical measures shown in Table 1.

The dimensions of the planar physical sections were replicated in the numerical models. A Cartesian coordinate system in an inertial frame of reference, $\mathscr{I}=(\mathcal{O}, \mathbf{e}_x, \mathbf{e}_y, \mathbf{e}_z)$, was defined by $(x, y, z)_{\mathscr{I}} \equiv (1, 2, 3)_{\mathscr{I}}$ wherein x is the longitudinal (mean flow direction), y the vertical, z the transversal axis (statistically homogeneous direction for HST and PCF), and $\mathcal{O}$ the origin at the left-bottom corner of the planar numerical domain.

Three grids with the refinement ratio of 2.0 were generated for each benchmark. The planar domains were uniformly discretized into squares whose centroids store synthetic turbulence fields. Estimations for the upper- and lower-limits of the spatial resolutions were made in accordance with large eddy simulation (LES) requirements. An upper limit may be deemed as the minimum spatial resolution required for a conservative direct numerical simulation: $\Delta \lessapprox 2(\nu^3 \mathrm{L} \mathrm{U_c}^{-3})^{0.25}$ where Δ is the isotropic grid spacing, ν the kinematic viscosity of flow, L isotropic integral length-scale, and $\mathrm{U_c}$ the characteristic flow speed.[7] A lower limit, as proposed by Baggett et al. [54, p. 62], may be set $\Delta \approx 0.1\mathrm{L}_\epsilon$, where L_ϵ is an integral dissipation scale, and order of L [54, p. 53]. The spatial-compatible temporal resolution, Δ_t, was then computed considering the constraint of the theoretical pressure-velocity coupling algorithm of PISO [55]: $\Delta_t < \mathrm{U_c}^{-1}\Delta$.

In order to make plausible inferences about the statistical population of interest, the minimum sample size required at a 98% confidence level, n_{min}, was estimated as 13, 000 elements via the following expression [56, Section 7.2.2.2.]: $n_{min}=(z_{1-\alpha/2}+z_{1-\beta})^2\sigma^2_{est}/\mathrm{CI}^2$ where z is the standard score in a normal distribution, α–β the type I-II error rates, σ_{est}=1 the forecasted standard deviation of the sample, and CI the confidence interval. Moreover, statistical convergence was qualitatively assessed through the time-series of the first four sample moments whereas no constraint, such an iterative linear solver requires, exists on the convergence.

4.1.2. Decaying homogeneous isotropic turbulence – HIT

HIT may be considered as the initial step in any turbulence model benchmarking whilst, in particular, any cross-correlation in its statistics is ideally zero. Through HIT, therefore, the isolated role of each model stage on the final output is expected to be revealed without cross interactions.

As a benchmark, from [51], the stationary-grid experiment of approximately isotropic decaying turbulent flow was used. The utilized experimental scenario belongs to the measurements at 42M downstream the turbulence generation grid, where M=0.0508[m] is the grid mesh size. At 42M, the mean longitudinal flow speed is $\mathrm{U_c}$=12.7[ms^{-1}], and Reynolds number based upon Taylor micro-scale, λ, is Re_λ=71.6. For the non-Gaussianities in HIT, Jiménez et al. [57, p. 71] numerically and Jiménez [28, p. 146] theoretically demonstrated that $\widehat{\beta}_2 \approx 2.85$, which is independent of Re [57, p. 70].[8] The set of input statistics is comprised of one-spatial-point normal-anisotropic correlations, and longitudinal and transverse integral length-scales, which respectively are: $\{\overline{(u'_{ii})^2}\}_{\{i\in(1,2,3)\}}$=0.049284[$\mathrm{m}^2\mathrm{s}^{-2}$], $\{\overline{(u'_{ij})^2}\}_{\{i\neq j\}}$=0.00, $\mathrm{L_{long}}$=0.024[m] and $\mathrm{L_{trans}}$=0.0127 [51, p. 299].

The dimensions of the planar numerical domain were specified as (y=10M, z=10M $\approx 20\mathrm{L_{long}}$) in order to resemble Dietzel et al.'s [59, p. 119] 10M preference for their HIT tests. The spatial and temporal resolutions of the domains, respectively, were {64, 128, 256}$_{\mathrm{HIT}}$ node per domain edge, and {(0.1, 0.05, 0.025)[$t^\star$]}$_{\mathrm{HIT}}$, where $t^\star=\mathrm{U_c}\mathrm{M}^{-1}\Delta_t$. The duration of the tests was 10.32[s]$\approx$20 pass-through in which each sample contained more than 15, 000 elements.

4.1.3. Homogeneous shear turbulence – HST

Towards real-world turbulence, HST could be considered as a transition step wherein large-scale anisotropy is partially incorporated into HIT; nonetheless, the statistical uniformity in space and homogeneity in spanwise direction reduces the sophistication of the flow. By means of HST, isolated effects of *a single* one-spatial-point anisotropic stress and cross-integral length-scale were sought.

The benchmark was the experiment of virtually transverse homogeneous and uniform shear turbulent flow from [60]. The chosen scenario was based on the experimental flow field at a downstream plane of x_1/h=11.0, where h=0.305[m] is the height of the shear-turbulence generator at the experiment inlet, and x_1 the horizontal distance to the generator. At the plane, the mean shear is $\mathrm{d}U_1/\mathrm{d}x_2$=46.8[$\mathrm{s}^{-1}$] and the mean longitudinal flow speed at the plane centerline equals to $\mathrm{U_c}$=12.4[s^{-1}]. Furthermore, Tavoularis and Corrsin [60, p. 321] experimentally found that $\widehat{\beta}_{1x}=-0.22^2$, $\widehat{\beta}_{1y}=0.16^2$, $\widehat{\beta}_{1z}=0.00$, $\widehat{\beta}_{2x}=0.10$, $\widehat{\beta}_{2y}=0.20$ and $\widehat{\beta}_{2z}=0.30$. The random error ranges were $\widehat{\beta}_1 \pm 0.03^2$ and $\widehat{\beta}_2 \pm 0.05$. The input set of stresses and scales contains: $\overline{(u'_1)^2}$=0.475[$\mathrm{m}^2\mathrm{s}^{-2}$], $\overline{(u'_2)^2}$=0.165, $\overline{(u'_3)^2}$=0.248 and $\overline{u'_1 u'_2}$=–0.126; $\mathrm{L}_{11,1}$=0.057[m], $\mathrm{L}_{22,1}$=0.01311, $\mathrm{L}_{33,1}$=0.01938, $\mathrm{L}_{11,2}$=0.01881, $\mathrm{L}_{11,3}$=0.01425, $\mathrm{L}_{22,2}=\mathrm{L}_{22,3}$=0.006555

[7] For the smallest resolved structure of size Δ, the maximum grid spacing could be 0.5Δ due to the Nyquist theorem [53, p. 10]. Assuming $\Delta \sim \eta$, where $\eta = (\nu^3/\epsilon)^{0.25}$ is the Kolmogorov length-scale and $\epsilon \sim \mathrm{U_c^3/L}$, then the maximum spacing roughly becomes $2(\nu^3 \mathrm{L} \mathrm{U_c}^{-3})^{0.25}$.

[8] For HIT, $\widehat{\beta}_1$ was assumed zero as a consequence of a lack of thoroughly examined data (despite some reports such as $\widehat{\beta}_1 = 0.051$ in [58, p. 310]).

and $L_{33,2}$=$L_{33,3}$=0.00969[9] [60, p. 320, 329, 334]. The values of the last four scales were derived by employing the isotropy assumption, e.g. $0.5L_{22,1}$=$L_{22,2}$.

The dimensions of the domains replicated those of the experiment as $(y{=}h, z{=}h \approx 7L_{11,1})$. The spatial resolution of the three grids were: $\{64, 128, 256\}_{HST}$ node per domain edge, and the corresponding temporal resolutions: $\{(15.6248, 7.8124, 3.9062)[t^\star]\}_{HST}$, where $t^\star_{HST}$=$1000U_c h^{-1}\Delta_t$. The test duration was 7.6864[s], and the samples included at least 40, 000 elements.

4.1.4. Plane channel flow with smooth walls – PCF

The majority of real-world turbulent flows is bounded by at least one solid surface. Therefore, a fundamental wall-bounded flow, PCF, was utilised to evaluate the capability of the methods in relation to wall effects on flow statistics. In addition, the reconstruction of spatial-variant integral length-scales across flow plane was examined with the aid of PCF.

The benchmark was hinged upon [29] direct numericual simulation of statistically stationary, pressure-gradient driven, fully developed plane channel flow with smooth walls, wherein the friction velocity, u_τ, and channel half-width, δ, based Reynolds number is Re_τ=$u_\tau \delta/\nu$=395 [29, p. 943]. The input set, including $\widehat{\beta}_1$ and $\widehat{\beta}_2$, is large to show in full herein; for this reason, it can be fetched from the web page of [61] as text files.

The dimensions of the domains were: $(y{=}2\delta, z{=}\pi\delta)$. The spatial and temporal resolutions of the grids were in turn: {(64, 100), (128, 201), (256, 402)}$_{PCF}$ and $\{(8, 4, 2)[t^\star]\}_{PCF}$, where $t^\star_{PCF}$=$100U_c\delta^{-1}\Delta_t$ with the test duration of 25[s] containing at least 200, 000 elements.

4.2. Statistical measures

The tests were conceptualized into two main branches: *i.* precision tests, wherein the model stages were investigated whether they perform their assigned tasks when they are in isolation, and when they interact each other; and *ii.* accuracy tests, wherein the CFD-free performance of the models in terms of the level of flow reconstruction fidelity was quantified and compared to the test-bed. In Section 2.1, the model stages were elaborated. For the following plots, the stages were labeled as follows: the incorporation of two-spatial/temporal-point correlation functions: *3rd stage*, incorporation of one-spatial-point correlations: *4th stage*, and PDF transformation-based skewness-kurtosis transformation approach: *NG stage*.

The flow reconstructions were explored mainly via six statistical measures: *i.* statistical weak stationarity, *ii.* statistical weak ergodicity, *iii.* first four standardized central moments, *iv.* one-spatial-point correlation tensor of second-order,[10] *v.* two-spatial/temporal-point correlation functions, and *vi.* one-dimensional one-sided power spectral density functions. The exact expressions of the measures are summarized in Table 1. In a simulation, each numerical domain node accommodates a time-series of velocity vector. After computing sample statistical measures for the time-series, the measure averages were performed in statistically homogeneous directions. Moreover, whenever suitable, statistics obtained from the test-bed flows and method outcomes were quantitatively compared each other with the help of *discrete Fréchet distance* [62–64], which is a metric that quantifies the level of similarity between two arbitrary curves. A code from [65–67] was utilised to compute the metric, which is briefly explained in Section A.4.

4.3. Code practices

In terms of computational cost of DFM/FSM, two model units are the most expensive: *i.* Gaussian random number generation, and *ii.* convolution summation.

The former ideally demands *i.* high computational speed, and samples that are *ii.* statistically independent, and *iii.* fast-convergent to the normal distribution. To that end, in literature, Xie and Castro[14] used the central limit theorem wherein $\mathcal{O}(10)$ of uniformly-distributed random number sets are first generated, and then manipulated into Gaussian samples. Later, Touber and Sandham [30, p. 104–105] pointed out that two uniformly-distributed sets are adequate for this purpose if the Box–Muller's theorem is used instead. However, Thomas et al. [68] quantified that the both approaches (and a number of other Gaussian random number generators) could not fulfil the three aforementioned properties satisfactorily and proportionately. The Ziggurat algorithm [69], on the other hand, came to the forefront in their comparisons as the optimum generator [68, p. 5]. Accordingly, in this study, Eddelbuettel's [70] C++ implementation of a modified Ziggurat algorithm [71] was utilised to generate Gaussian random number sets.

The conventional convolution summation requires FLOPT of $\mathcal{O}\{\left[(\Pi_{m=1}^{i} R_m)(\Pi_{m=1}^{i} N_m)\right]_{\{i\in(2,3)\}}\}$.[11] In order to decrease this cost, Veloudis et al. [37, p. 9] reminded first that convolution in the frequency domain is only an element-wise multiplication, thereby the computational time complexity may be reduced by $\mathcal{O}\{\Pi_{m=1}^{i} N_m / \log\{\Pi_{m=1}^{i} R_m\}\}$. The following was then proposed for Eq. (2): $\{s\}$=$\mathscr{F}^{-1}\{\mathscr{F}\{b\}\mathscr{F}\{r\}\}$ where $\mathscr{F}$ is a discrete fast Fourier transform operator and $\mathscr{F}^{-1}$ its inverse. Note that $\{b\}$ is Fourier-transformed only once per simulation. Apart from this proposition, the separable convolution summation method [39, p. 404] was suggested by Kempf et al. [38] to evaluate Eq. (2):

$$\begin{aligned}\{s\} &= \sum_{k=-N_p}^{N_p}\sum_{j=-N_q}^{N_q}\sum_{i=-N_l}^{N_l} b_{ijk}\, r_{m+i,\, n+j,\, o+k} \\ &= \sum_{k=-N_p}^{N_p}\sum_{j=-N_q}^{N_q}\sum_{i=-N_l}^{N_l} l_i q_j p_k\, r_{m+i,\, n+j,\, o+k} \\ &= \sum_{k=-N_p}^{N_p} p_k \left\{ \sum_{j=-N_q}^{N_q} q_j \left[\sum_{i=-N_l}^{N_l} l_i\, r_{m+i,\, n+j,\, o+k} \right] \right\} \end{aligned} \tag{12}$$

In virtue of this method, the theoretical speed-up becomes in the order of $\mathcal{O}\{\Pi_{m=1}^{i} N_m / \Sigma_{m=1}^{i} N_m\}$.[12] The complexity ratio between the Fourier and separable convolutions then turns out to be $\mathcal{O}\{\Sigma_{m=1}^{i} N_m / \log\{\Pi_{m=1}^{i} R_m\}\}$. Considering $R \gg N$ in DFM, the Fourier convolution is *theoretically* expected to be $\mathcal{O}(1)$–$\mathcal{O}(10)$ faster than the separable convolution. Yet the tests in this study have suggested that the two may deliver considerable and comparable performance gains, likely due to the implementation-algorithm dependent effects.

5. Results and discussion

In order to avoid duplications, the computation results from all test-bed scenarios were grouped in terms of their common and distinct characteristics. The premises supporting the same argument were presented through representative evidences from one of

[9] For $L_{ij,\,k}$, ij denote the directions of two velocity components of interest, and k the measurement direction.

[10] The term can also be expressed as *Reynolds stress tensor* when scaled by the density.

[11] For instance, R_2 denotes the size of random set in the 2nd-direction, and N_3 that of the filter coefficient set in the 3rd-direction.

[12] Another method, which has not been utilised in DFM, is the helix transformed [72] convolution, where multi-dimensions are regressed to one-dimension. In tests, however, its cost reduction was observed to be inconsiderable.

the benchmarks, and were denoted with a phrase 'representative-to-all' to make clear when the concluding remarks are valid for all scenarios. Furthermore, the spatio-temporally grid independent results were reported, which belong to the following numerical domains: $\{64\}_{HIT}$, $\{64\}_{HST}$ and $\{64, 100\}_{PCF}$ node per domain edge.

5.1. The first four one-spatial-point statistical moments

The 4th model stage requires that the sets of the 3rd stage output, $\{s\}$ of Eq. (2), has zero-mean and unit-variance [13, p. 656]. The majority of the literature presumes that the requirement is automatically fulfilled. Veloudis et al. [37, p. 8–9], however, held an opposite view that the 3rd stage generally alters the zero-mean unit-variance of the random number sets. Therefore, they proposed a renormalization of $\{s\}$ to ensure the requirement is fulfilled.[13] The authors nevertheless did not present any quantification to support this objection.

To assess the view, the sample mean and sample standard deviation of each node-time-series were computed at each stage of the models. Further, the arithmetic average and variance of all these sample pairs were calculated. Table 3 presents a *representative-to-all* HIT results for this quantification. Data in the table shows that the order of magnitude of changes in zero-mean and unit-variance due to the 3rd stage is around 0.001 with a variance of around 0.0001. The effect of the non-Gaussian stage is, on the other hand, several decades lower than that of the 3rd stage. Moreover, the observation is consistent across DFM/FSM methods. Contrary to Veloudis et al.'s [37] argument, the study did not find a significant effect of the 3rd (as well as the non-Gaussian) stage on the zero-mean and unit-variance. In addition, the low variance indicated the level of effect is almost the same across stochastically and statistically different node-time-series. The renormalization requires operations of an addition, a summation, an exponentiation and a square-root per grid-node at each time-step. More importantly, the time-series throughout the duration of a computation needs to be known a priori, because time averages should be performed for the normalization. This may demand large data storage and complicate on-the-fly computations. It is thus suggested that the renormalization is redundant in terms of its effects, and its omission is advisable to avoid extra cost and complications.

Following the first two moments, the skewness-kurtosis pairs of the benchmarks were reconstructed through the new PDF transformation-based approach, Eq. (11). Figs. 3 and 4 illustrate *representative-to-all* PCF skewness and kurtosis results, respectively.

In the both figures, the 3rd stage's skewness-kurtosis pairs closely follow the values of (0–3). This confirms that the pairs produced by the original DFM/FSM is Gaussian. This also corroborates the presumption that the input set of statistics as it stands does not automatically develop higher-order moments during the flow reconstruction. By contrast, as shown in the figures, the new non-Gaussian stage helped DFM/FSM to closely reconstruct the skewness-kurtosis pairs of the benchmark in terms of magnitude and patterns despite their spatial variation across a considerable range of pair combinations. Additionally, in the non-Gaussian stage, no appreciable differences were observed among DFM/FSM methods. This finding implies that the different 3rd stages of the methods do not affect the subsequent non-Gaussian stage outcomes.

The 4th stage needs a closer look, because [20, p. 96] put forward the idea without quantification that this stage, Eq. (3), alters the statistics constructed in the previous stages. The reasons and extent of the alterations were however not examined therein as well as in the literature. Fig. 3 and 4 may provide some insights into the argument.

[13] As an example, [38, p. 59] used the renormalization.

In fact, the v-component skewness-kurtosis pairs were observed distorted by the 4th stage. The maximum change due to the 4th stage in skewness was around 10% and in kurtosis 5%.[14] The level of distortion was gradually increased with the distance to the Gaussian values; nevertheless, the overall benchmark pattern was preserved in the numerical results. What's more, the asymmetry of the distortion for the same v-skewness magnitudes at different channel heights implied that the magnitude of skewness-kurtosis pairs and Reynolds stress tensor components determine the distortion level in a nonlinear interrelation.

On the contrary, no 4th stage effect was found on the skewness-kurtosis of u-,w-components. This discrepancy stems from Eq. (3). In the 4th stage, the amplitude of $\{s^u\}$-sets is solely multiplied element-wise by time-invariant a_{11} whereas the operation adopted for $\{s^v\}$-sets includes a multiplication and an addition: i.e. $v=s^u a_{21}+s^v a_{22}$. In the former, the sole multiplication causes the same scaling at two separate points of $\{s^u\}$-sets in space and time, thereby the two-point correlation functions as well as one-point moments of the sets remain unchanged. In the latter, however, the addition of a stochastic $\{s^u\}$-set distorts the amplitude proportionality between any two-spatial/temporal points within a $\{s^v\}$-set; hence, distortion in embedded statistics. This disruption should also be detected for w-component while its 4th stage consists of three multiplication and two additions: i.e. $w=s^u a_{31}+s^v a_{32}+s^w a_{33}$. The disruption was however absent for PCF because the additions vanish due to the statistical homogeneity in the w-direction: $a_{31}=a_{32}=0$.

Furthermore, the same patterns were observed for HST as can be seen from Table 5 wherein only v-component skewness-kurtosis differed in nearly (18–2)% compared to the previous stage. Considering this explanation, the 4th stage should have no effect on the pre-embedded statistics for HIT, because the absence of any one-point cross-correlation component should eliminate all the addition operations. Indeed, Table 4 confirms this expectation as all the skewness-kurtosis pairs remained the *same* at the end of the 4th stage.

These findings suggest that the 4th stage, namely the Lund transformation, to some extent distorts the pre-existing statistics only in the statistically inhomogeneous lateral directions. On the other hand, the same findings indicate that the streamwise and statistically homogeneous lateral direction statistics are not prone to such distortion.

5.2. One-spatial-point second-order correlation tensor

The reconstruction of the one-spatial-point second-order correlation tensor of fluctuations (hereafter, the tensor) is fundamental to the synthetic turbulence generation, because the evolution of turbulence mostly depends upon energy transfer processes shaped by the tensor. The gradients of the mean velocity components work done on the deviatoric part of the tensor. This part then energizes the isotropic part of the tensor (whose half trace is the turbulent kinetic energy) which redistributes and dissipates the energy. As a result, the mean velocity field loses its convective momentum to the fluctuating velocity field. A realistic turbulence development therefore demands successful reconstruction of the tensor.

Fig. 5 presents the *representative-to-all* PCF results for the six tensor components[15] reconstructed by the 4th model stage. Due to the antisymmetry of the deviatoric tensor around the channel half-height, the results across the entire section were shown. As a consequence of inadequate spatial resolution adjacent to the walls,

[14] Percentage difference$=(x_r-x_n)/x_r \cdot 100\%$, where x_r is the magnitude of the relevant parameter for the reference, and x_n that for the numerical study.

[15] The tensor is symmetric.

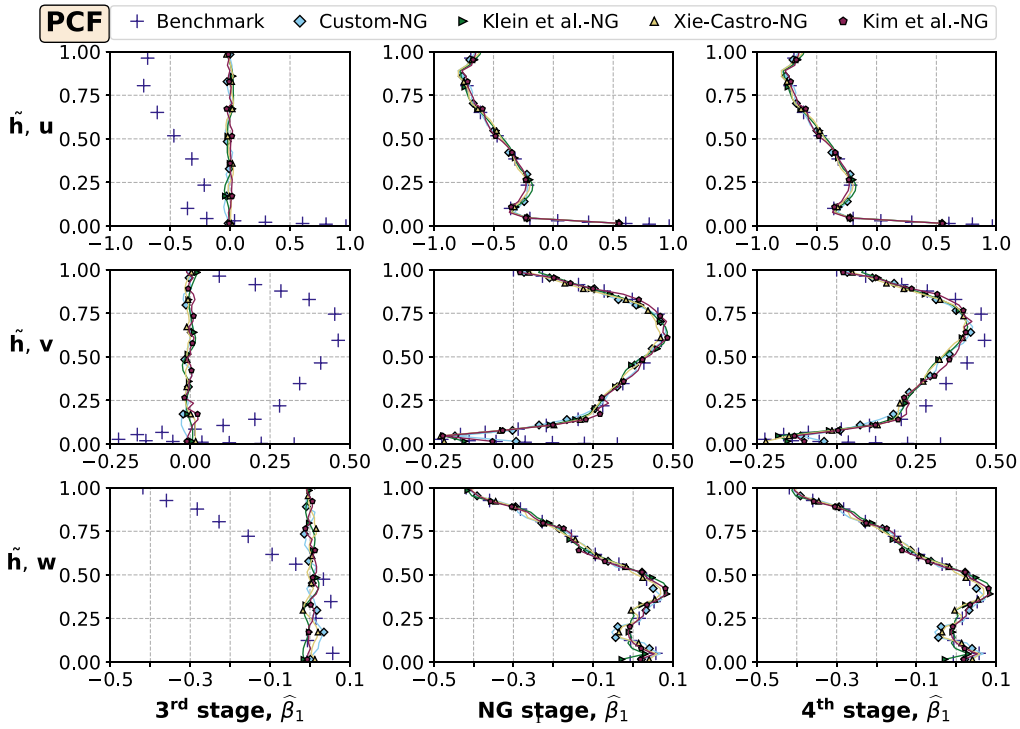

Fig. 3. The Pearson's moment coefficient of sample skewness results, $\widehat{\beta}_1$, from DFM/FSM computations of the plane channel flow with smooth walls (PCF) [29]. From left to right, the 3rd, non-Gaussian (NG) and 4th model stages and from top to bottom, velocity components, (u, v, w), are depicted. Of a subplot, the vertical axis denotes the normalized channel half-height, $\tilde{h}$=h/δ where h and δ are the half-height of the computational and benchmark domains, respectively. PCF is statistically symmetric along the channel centerline; hence, only the results belong to the half-height are shown. The horizontal axis stands for skewness, which was computed for each node-time-series and arithmetic averaged in the statistically homogeneous direction of the flow.

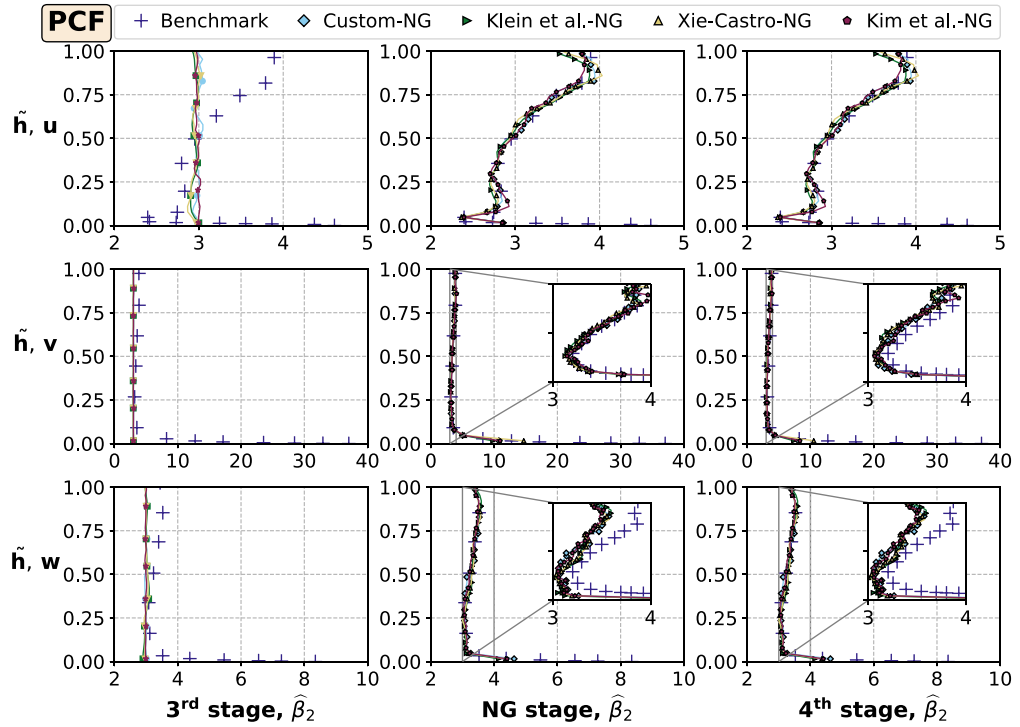

Fig. 4. The Pearson's moment coefficient of sample kurtosis results, $\widehat{\beta}_2$, from DFM/FSM computations of the smooth-wall plane channel flow (PCF). The figure descriptions are as in Fig. 3.

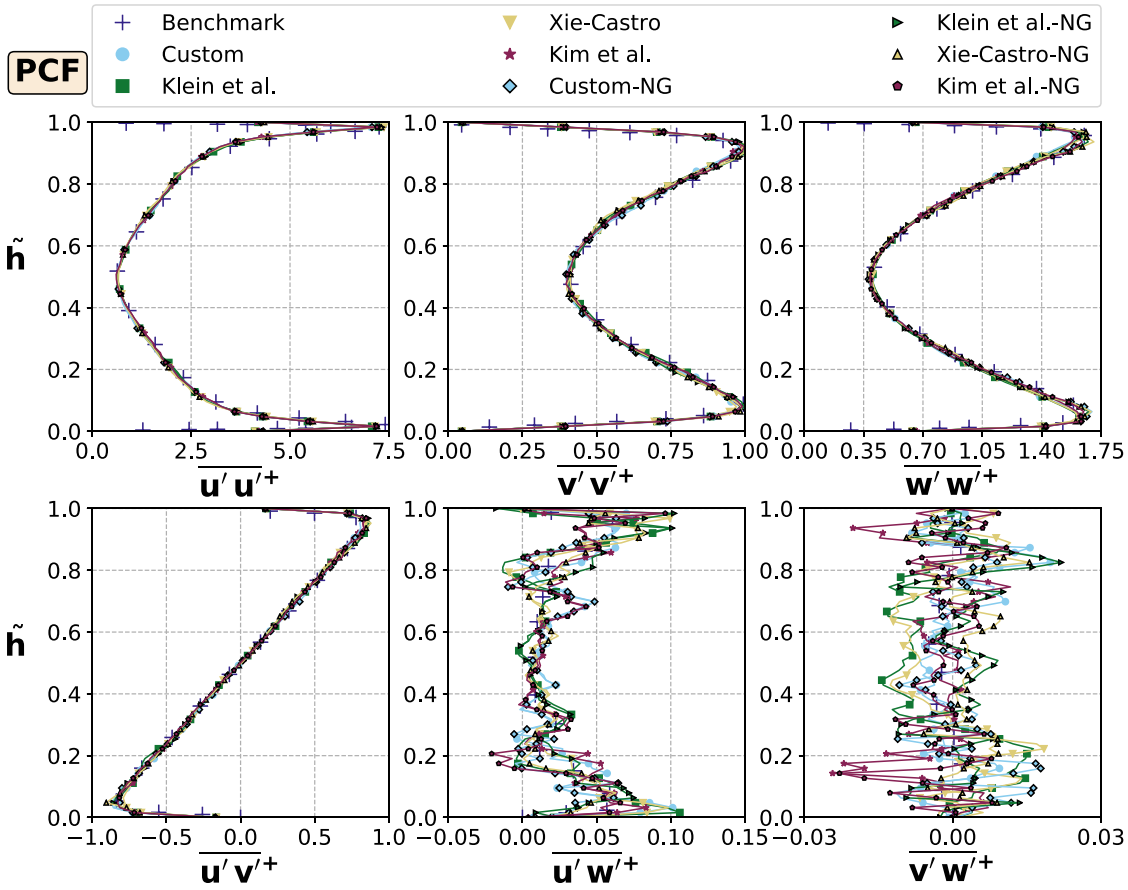

Fig. 5. The results from DFM/FSM computations of the plane channel flow with smooth walls (PCF) [29] for one-spatial-point second-order correlation tensor of discrete fluctuating velocities, $\{u_i'(n\Delta, m\Delta_t)\, u_j'(n\Delta, m\Delta_t) \in \mathbb{Q}\}_{\{i,j,n,m\in\mathbb{N};\, i,j\in[1,3];\, n,m,\Delta_t>0\}}$. The vertical axis of a subplot stands for the normalized channel full-height, $\tilde{h}=h/(2\delta)$ where h and δ are the full-height of the computational domain and the half-height of the benchmark domain, respectively. The dependencies of the tensor components on space and time were reduced by arithmetic average in time and the statistically homogeneous direction of the flow; hence, $\overline{u_i' u_j'}^{+}$. $\{\bar{\cdot}\}$ denotes combined time and spanwise space average, and $\{\cdot\}^+=\{\cdot\}/u_\tau^2$ a normalization operator, where u_τ is the estimated friction velocity. The corresponding expression used in the computations is shown in Table 1.

Table 1
List of statistical measures used in the study.

	Measure	Tool for quantifications
i.	Statistical weak stationarity	Augmented Dickey–Fuller unit-root test [75].
ii.	Statistical weak ergodicity	Wald–Wolfowitz test [76].
iii.a.	Unbiased estimation of mean	$\widehat{\mu}_1 = \bar{x} = n^{-1}\sum_{i=1}^{n} x_i$.
iii.b.	Unbiased estimation of variance	$\widehat{\mu}_2 = (n-1)^{-1}\sum_{i=1}^{n}(x_i-\widehat{\mu}_1)^2$.
iii.c.	Pearsonian coefficient of sample skewness	$\sqrt{\widehat{\beta}_1} = \frac{\widehat{\mu}_3^2}{\widehat{\mu}_2^3} = \frac{n^{-1}\sum_{i=1}^{n}(x_i-\widehat{\mu}_1)^3}{\widehat{\mu}_2^3}$.
iii.d.	Pearsonian coefficient of sample kurtosis	$\widehat{\beta}_2 = \frac{\widehat{\mu}_4}{\widehat{\mu}_2^2} = \frac{n^{-1}\sum_{i=1}^{n}(x_i-\widehat{\mu}_1)^4}{\widehat{\mu}_2^2}$.
iv.	One-point correlation tensor	$R_{xy} = z^{-1}\sum_{k=1}^{z}\left\{\mathrm{T}^{-1}\sum_{i=\Delta_t}^{n\Delta_t}(x_{ki}-\widehat{\mu}_{1_{x_k}})(y_{ki}-\widehat{\mu}_{1_{y_k}})\right\}$.
v.	Unbiased estimation of correlation functions	$\widehat{\rho}_{XY} = \frac{\widehat{R}_{XY}}{\widehat{\mu}_{2_X}\widehat{\mu}_{2_Y}}$; $\widehat{R}_{XY} = (\mathrm{N}-a)^{-1}\sum_{i=\Delta_t}^{(\mathrm{N}-a)\Delta_t} x_i\, y_{i+a\Delta_t}$.
vi.	One-sided power spectral density function	Welch's method [78], window: Hanning, overlap: 50%.

n denotes the size of a discrete sample x, $\widehat{\cdot}$ the estimation operator, z the number of nodes along the statistically homogeneous direction, T the sample duration, Δ_t the time-step size, a the lag (time-offset) number, and N the maximum lag number.

numerical results for a few benchmark points were not available in the figure.

The results demonstrate that spatial-variant fields of the reconstructed tensor components were virtually the same with the benchmark. For instance, the maximum deviation among all scenarios was observed 3.8% away from the benchmark, which belongs to Kim et al.'s construction of $\overline{w'w'}^{+}$ near the top wall. In comparison to the rest of the results, however, this deviation could be considered an outlier whilst the majority of all deviations was found to be below 1%. Furthermore, apart from minor differences because of the stochastic nature of model outcomes, no significant difference among models, including non-Gaussian counterparts, was identified. The most likely reason of this is that each model used the same Lund transformation for the 4th stage, and

Table 2
Approximate number of calls for the computational operations that are required by Eqs. (10) and (11) during the transformation of a standard normal skewness-kurtosis pair to a target one. For brevity, operations needed for a single velocity component per time-step are shown.

Operations		S_U	S_L	S_B	Eq. (10) with arbitrary $F_{IO_i'}^{-1}$	Eq. (10) with Gaussian $F_{IO_i'}^{-1}$
Arithmetic functions	Addition	–	–	1	2	1
	Subtraction	3	–	2	3	2
	Multiplication	–	–	–	3	5
	Division	3	–	3	1	1
Elementary functions	$\exp(\cdot)$	2	1	1	–	–
Non-elementary functions/algorithms		–	–	–	1 $\mathrm{erf}(\cdot)$ 1 Search algorithm	1 $\mathrm{erf}(\cdot)$ 1 $\mathrm{erf}^{-1}(\cdot)$

Table 3
The arithmetic average, $\overline{(\cdot)}$, and variance, $Var(\cdot)$, of the sample pairs from all nodes. A pair contains the sample mean, $\widehat{\mu}_1$, and sample standard deviation, $\sqrt{\widehat{\mu}_2}$, of a node-time-series. S-3, S-NG, and S-4 denote the 3rd, non-Gaussian, and 4th model stages, respectively. Each cell, $(\cdot|\cdot)$, represents values of $(\overline{(\cdot)}|Var(\cdot))$ rounded to two decimal places in the scientific notation.

	Custom			Klein et al.		
	S-3	S-NG	S-4	S-3	S-NG	S-4
$\widehat{\mu}_1$ $(10^{-3}\|10^{-4})$	−1.19|3.88	−1.19|3.88	−0.26|0.18	0.16|3.53	0.16|3.53	0.04|0.161 × 10^{-2}
$\sqrt{\widehat{\mu}_2}$ $(1\|10^{-4})$	1.00|0.94	1.00|0.86	0.22|0.04	1.00|1.25	1.00|1.14	0.22|0.06
	Xie–Castro			**Kim** et al.		
	S-3	S-NG	S-4	S-3	S-NG	S-4
$\widehat{\mu}_1$ $(10^{-3}\|10^{-4})$	−0.61|4.58	−0.62|4.58	−0.14|0.22	0.95|5.43	0.95|5.43	0.21|0.26
$\sqrt{\widehat{\mu}_2}$ $(1\|10^{-4})$	1.00|1.14	1.00|1.06	0.22|0.05	1.00|1.37	1.00|1.28	0.22|0.06

Table 4
The Pearson's moment coefficient of sample skewness, $\widehat{\beta}_1$, and sample kurtosis, $\widehat{\beta}_2$, obtained from Klein et al.'s method [13] computations of the decaying homogeneous isotropic turbulence (HIT) [51]. The other three methods produced results which were entirely in line with the table content. The benchmark skewness-kurtosis is $(\widehat{\beta}_1\text{-}\widehat{\beta}_2)$=(0.00–2.85) Section 4.1.2. S-3, S-NG, and S-4 denote the 3rd, non-Gaussian, and 4th model stages, respectively. Each cell value was computed as follows: first, sample skewness-kurtosis of each node-time-series were found, second the median of all values was calculated and then results were rounded to two decimal places.

			S-3	S-NG	S-4			S-3	S-NG	S-4
HIT	$\widehat{\beta}_1$ (10^{-3})	u	0.16	4.11	4.11	$\widehat{\beta}_2$	u	2.99	2.85	2.85
		v	−1.40	3.04	3.04		v	3.00	2.85	2.85
		w	0.49	4.85	4.85		w	3.00	2.85	2.85

Table 5
The Pearson's moment coefficient of sample skewness, $\widehat{\beta}_1$, and sample kurtosis, $\widehat{\beta}_2$, obtained from Klein et a.'s method [13] computations of the homogeneous shear turbulence (HST) [52]. The other three methods produced results which were entirely in line with the table content. The benchmark values can be found in Section 4.1.3. S-3, S-NG, and S-4 denote the 3rd, non-Gaussian, and 4th model stages, respectively. Each cell value was computed as follows: first, sample skewness-kurtosis of each node-time-series were found, second the median of all values was calculated and then results were rounded to two decimal places.

			S-3	S-NG	S-4			S-3	S-NG	S-4
HST	$\widehat{\beta}_1$ (10^{-3})	u	−4.75	-0.21×10^{3}	-0.21×10^{-3}	$\widehat{\beta}_2$	u	2.98	3.07	3.07
		v	1.34	0.16×10^{3}	0.13×10^{3}		v	2.99	3.19	3.12
		w	0.77	1.37	1.37		w	3.00	3.29	3.29

this stage was followed by no other model stage. Another implication of this indifference is that the previous model stages do not have any appreciable effect on the 4th stage output. Lastly, $\overline{u'w'}^{+}$ and $\overline{v'w'}^{+}$ subplots in Fig. 5 illustrate an evidence for the presumption that the level of reconstruction of DFM/FSM is restricted by the input statistics while no input was provided for the both components due to the statistical homogeneity in the spanwise direction of the flow, and indeed, the both correlations remained random.

5.3. Two-spatial/temporal-point correlation functions

In this section, *representative-to-all* results of the variance-normalized two-spatial/temporal-point sample autocorrelation functions (hereafter, autocorrelation) are presented with three figures in order to examine primarily patterns and similarities. First, Figs. 6 and 7 show the results obtained from HIT and HST computations. The two includes two longitudinal, $\widehat{\rho}_{\mathbf{xu}}$ and $\widehat{\rho}_{\mathbf{yv}}$, and one lateral autocorrelation, $\widehat{\rho}_{\mathbf{xv}}$, in order to additionally discuss the DFM/FSM model stage effects on the autocorrelation. Second, Fig. 8 exemplifies a complete autocorrelation tensor from HST computations to fill the gap that the majority of studies in the literature contended with in reporting longitudinal autocorrelations only, e.g. $\widehat{\rho}_{\mathbf{xx}}$ or $\widehat{\rho}_{\mathbf{yy}}$.

To begin with, no noticeable alterations due to the non-Gaussian stage were found. The remark is exemplified in Figs. 6 and 7 where the non-Gaussian stage outcome bears a marked resemblance to the previous 3rd stage. This is also valid for

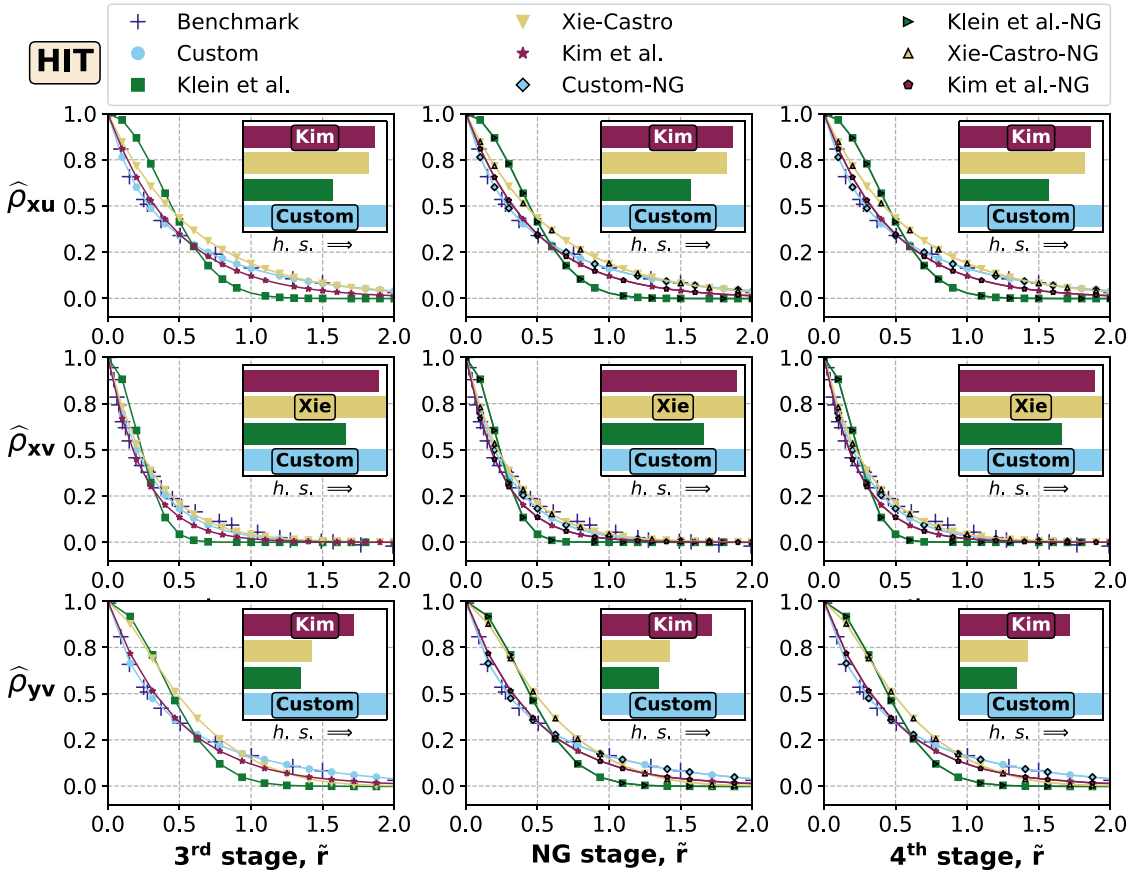

Fig. 6. The two-spatial/temporal-point sample autocorrelation function results, $\widehat{\rho}_{mn}$, from the decaying homogeneous isotropic turbulence computations (HIT) [51]. In $\widehat{\rho}_{mn}$, '*m*' stands for the measurement direction, and '*n*' for the measured velocity component. $\widehat{\rho}_{mn}$s were computed for each node-time-series, and their arithmetic average was performed in the statistically homogeneous directions. From left to right, the 3rd, non-Gaussian (NG) and 4th model stages are shown. From top to bottom, two longitudinal, $\widehat{\rho}_{xu}$ and $\widehat{\rho}_{yv}$, and one lateral, $\widehat{\rho}_{xv}$, autocorrelation functions are demonstrated. The horizontal axes denote the spatial lag, $\tilde{\mathbf{r}}$, normalized by the characteristic length M=0.0508 [m]. The horizontal bar chart illustrates the Fréchet distance of each model curve to the benchmark. Each bar is normalized by the most-similar-to-the-benchmark model curve. The maximum height of a bar is the unity, and '*h.s.*' with the arrow means the direction of *higher similarity*.

PCF computations wherein the skewness-kurtosis pairs are highly varying, and is supported by Section 5.2 observations. Secondly, as can be deduced from Fig. 6, no change due to the 4th stage took place in HIT whereas Fig. 7 reveals that the Lund transformation caused a rise nearly 10% of the zero-lag in the most $\widehat{\rho}_{\mathbf{xv}}$ and $\widehat{\rho}_{\mathbf{yv}}$ of HST. On the other hand, $\widehat{\rho}_{\mathbf{xu}}$ of HST was found to be unaltered. These results are in agreement with those obtained in Section 5.1, which further support the aforementioned three remarks: *i.* in the absence of anisotropic Reynolds stresses, the 4th stage does not adversely affect the previous stage statistics, *ii.* in the presence of anisotropic Reynolds stresses, the 4th stage remains neutral to the pre-existing statistics in the streamwise and statistically homogeneous lateral directions; however, *iii.* the 4th stage amplifies those statistics in the statistically inhomogeneous lateral direction, which almost certainly leads to an uninvited increase of output turbulence scales in this direction.

On the question of similarities, the following observations were made. According to the Fréchet distance in the horizontal bar charts of the figures, the closest and farthest overall proximity to the reference autocorrelation tensor components were yielded by the Custom and Klein et al.'s methods, respectively, with no counter-examples. In addition, Kim et al.'s method nearly always produced the second best approximations, which also closely followed the Custom's high fidelity reproductions. Xie–Castro's method mostly ranked number three; nevertheless, occasionally reached Kim et al.'s fidelity. With respect to the patterns in the output autocorrelations, five patterns were observed. *i.* One finding is that Klein et al.'s method produced Gaussian-shaped autocorrelations although the rest of the models as well as the benchmarks yielded exponential forms. This confirms the anticipation that the filter kernel casts whatever its shape onto the output autocorrelations. Another implication of the finding is that the Gaussian-form is not an appropriate choice for the benchmark flows considered, and very probably also, not for the other turbulent flows which share similarities with these three benchmarks. The remaining four patterns are *maximal* generalizations about the performance of the models, because they were observed consistently across different flow scenarios: *ii.* Klein et al.'s method overpredicted the references by $\sim$20–25 $\pm$ 5% up to $\sim$20–25% of the zero-lag, and then underpredicted them by $\sim$10%. *iii.* By contrast, the Custom method generally reconstructed the references with less than $\sim$1% difference. Yet its 4th stage resulted in $\mathcal{O}(1)$% increase in autocorrelations of the statistically inhomogeneous lateral direction, e.g. $\widehat{\rho}_{\mathbf{xv}}$ of HST. *iv.* Similarly, Kim et al.'s method reproduced the references in close resemblance up to $\sim$20% of the zero-lag, and then slightly underpredicted them with few exceptions, e.g. $\widehat{\rho}_{\mathbf{zu}}$ of HST. *v.* Lastly, Xie–Castro's method usually resulted in $\sim$5–10% overpredictions along the most part of the benchmark autocorrelations. In some of the cases, however, the method made a higher overprediction around $\sim$20–25% till $\sim$15–20% of the zero-lag, which was followed by an underprediction, as can be seen in $\widehat{\rho}_{\mathbf{zw}}$ of HST. Considering these results, the overprediction tendency could conceivably be hypothesised that DFM/FSM as is often greatens input scales to some extent.

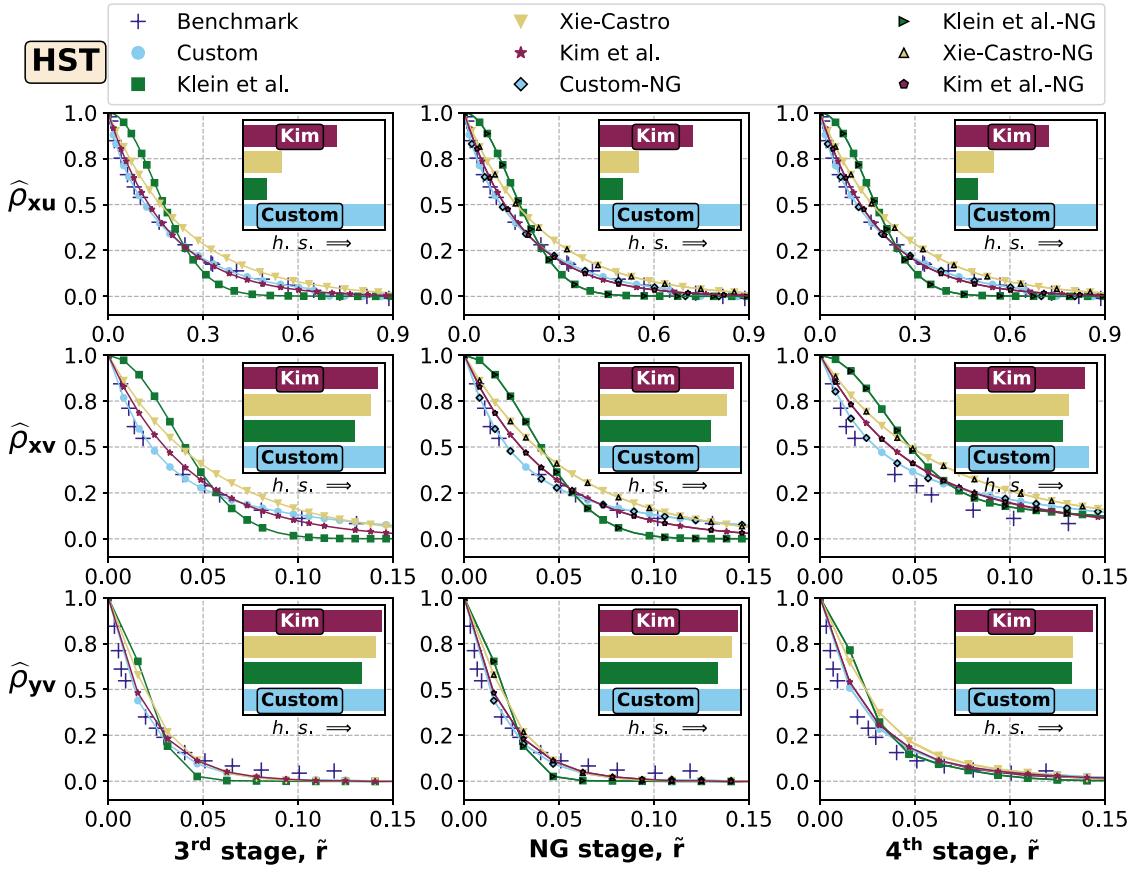

Fig. 7. The two-spatial/temporal-point sample autocorrelation function results from the homogeneous shear turbulence computations (HST) [52]. The figure descriptions are the same with Fig. 6.

Another subtle finding was about the streamwise autocorrelations of PCF, which do not level off zero, yet a positive constant value. It was observed that DFM/FSM could not construct such tail behavior, because their theoretical equations decay *certainly* and asymptotically to zero at a certain decorrelation distance.

5.4. Power spectral density functions

This section presents *representative-to-all* results of the sample one-dimensional one-sided power spectral density functions as a function of spatial wavenumbers (hereafter, power spectrum) in order to investigate the model stage effects and performance of the models within inertial and energy containing ranges of the spectrum. Representative evidence of the following remarks are illustrated in Figs. 9 and 10, respectively, for HIT and HST.

What stands out in the both figures is a premature and flow-type-independent drop with a non-linear slope in the power spectra created by Klein et al.'s method towards the outset of inertial range wavenumbers. Klein et al. [13] did not report any result for power spectra; however, Dietzel et al. [59, p. 122] identified a similar drop for this method in HIT. The most likely cause of the drop is the method's Gaussian-form of the filter function. Consider the Fourier transform of the Gaussian autocorrelation function, Eq. (4), whose derivation and parametrization are given in A.5.1 [73]:

$$\mathscr{F}_x\left\{\exp\left[-\frac{\pi}{4}\frac{x^2}{L^2}\right]\right\}(\kappa) = 2\,L\,\exp\left[-4\pi L^2\kappa^2\right] \tag{13}$$

which is also another Gaussian function, where $\mathscr{F}_x$ is the Fourier transform operator on the spatial variable $\{x\}_{\{x>0\}}$, $L\,[m(2\pi)^{-1}]$ an integral length-scale, and $\kappa\,[(2\pi)m^{-1}]$ the spatial wavenumber. Eq. (13) in Figs. 9 and 10 illustrates that Klein et al.'s method theoretically produces the drop. Herewith the model, towards the inertial range, the power spectrum declines considerably more rapidly than $\kappa^{-5/3}$. Consequently the net spectral energy flux in the inertial range also steeply decreases; thus, leading to a spurious preservation of the energy in large scales along time.

In contrast, two different observations were noted in Figs. 9 and 10 for all the other methods' inertial range reconstructions: first, the aforementioned drop disappeared and the inertial range slope was more closely followed; and second, an upward transient spike occurred at the high-wavenumber tail. As regards the power spike, temporal aliasing can be attributed as the main contributor to this excess power, which typically results from the sampling process rather than the models. Therefore, no further explanation was sought for the second observation.

One of the major differences between Klein et al.'s method and the rest is that the autocorrelation function of the latter has an exponential-form. The *Gaussian-exponential* distinction might be the key factor in the power drop formation. In order to examine this postulation, a Fourier analysis likewise above was performed for the exponential function. In addition, Klein et al.'s Gaussian-form was converted into an exponential one, and several tests were carried out. The Fourier transform of the exponential autocorrelation function, Eq. (7), can be shown as follows ((A.5.2) [74]):

$$\mathscr{F}_x\left\{\exp\left[-\frac{\pi}{4}\frac{x}{L}\right]\right\}(\kappa) = \frac{8L\pi^{-1}}{(8L\kappa)^2+1} \tag{14}$$

which is a Lorentzian function that theoretically possesses a linear decay slope of κ^{-2} after a corner wavenumber, κ_c. Accordingly, Eq. (14) was also plotted in Figs. 9 and 10.

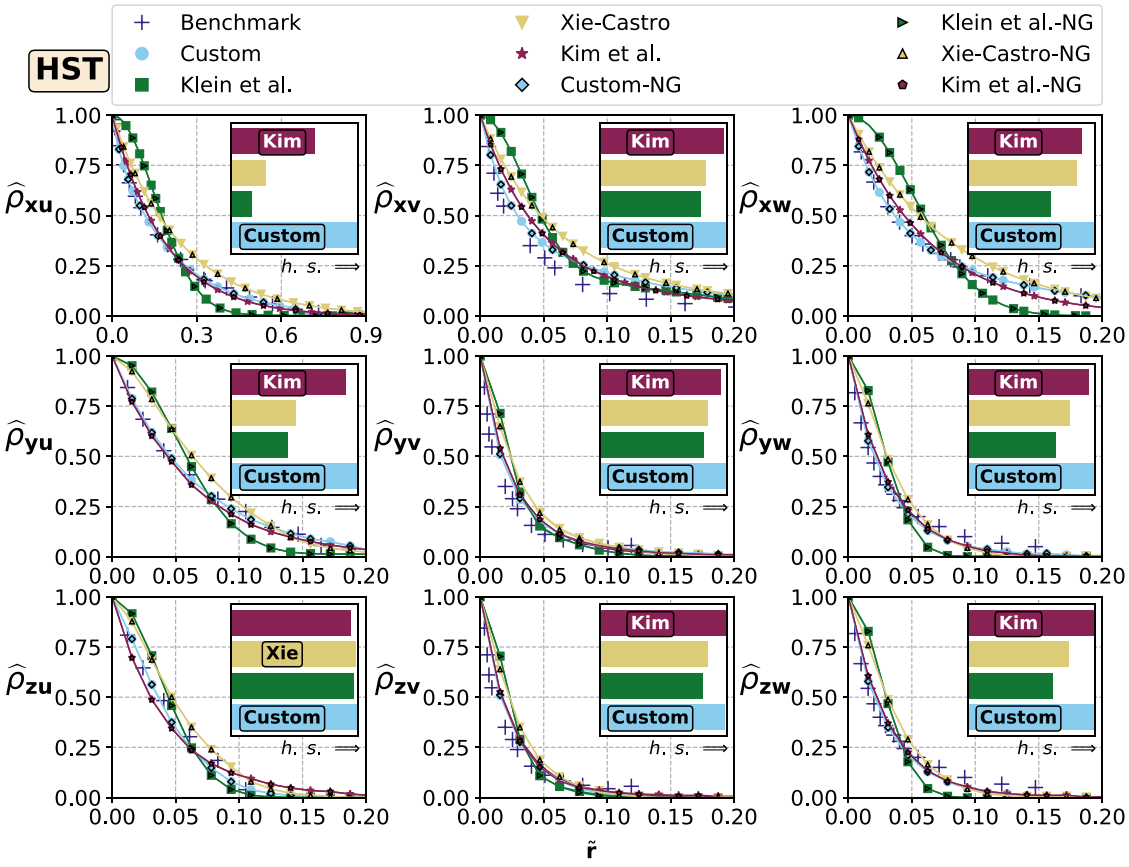

Fig. 8. The two-spatial/temporal-point sample autocorrelation function results from the homogeneous shear turbulence computations (HST) [52]. Herein, all nine components of the correlation tensor are demonstrated. The figure descriptions are the same with Fig. 6.

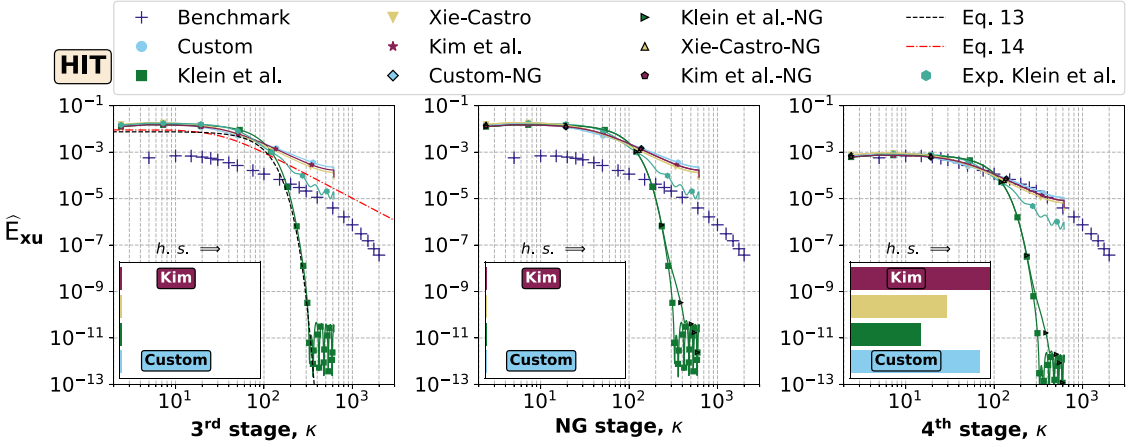

Fig. 9. The sample one-dimensional power spectral density function results, $\widehat{E}_{\mathbf{xu}}$ [$m^3 s^{-2}$], as a function of spatial wavenumber, κ [m^{-1}], from the decaying homogeneous isotropic turbulence computations (HIT) [51]. In $\widehat{E}_{\mathbf{xu}}$, '**x**' stands for the measurement direction, and '**u**' for the measured velocity component in this direction. 'Exp. Klein et al.' denotes Klein et al.'s method using the exponential-form filter function. $\widehat{E}_{\mathbf{xu}}$s were computed for time-series of each node, and their arithmetic average was performed in the statistically homogeneous directions. From left to right, the 3rd, non-Gaussian (NG) and 4th model stages are shown. The horizontal bar chart illustrates the Fréchet distance of each model curve to the benchmark. Each bar is normalized by the model curve which is the most similar to the benchmark. The maximum height of a bar is the unity, and '*h.s.*' with the arrow means the direction of *higher similarity*.

Inspection of the two figures reveals a number of characteristics. First, the Fréchet distances of the 4th stage and qualitative examination indicate that the Custom, Kim et al. and Xie–Castro's methods performed alike in overall spectra estimation unlike both Klein et al.'s methods. Yet the energy-containing range patterns were adequately estimated by all the methods, both Gaussian- and exponential-form; thus, no superiority of one form on the other in this respect. Another observation comparing the 3rd and 4th stages is that the overall shape of the power spectra is established by the 3rd stage only whilst the 4th stage seems responsible in rescaling the power level to the target. In addition to this, the non-Gaussian stages shown in Figs. 9 and 10 assert that the skewness-kurtosis transformation did not modify the power spectra previously constructed in the 3rd stage.

A closer look into the inertial subrange of the both figures' 3rd stages discloses that the inertial subrange slopes created by the

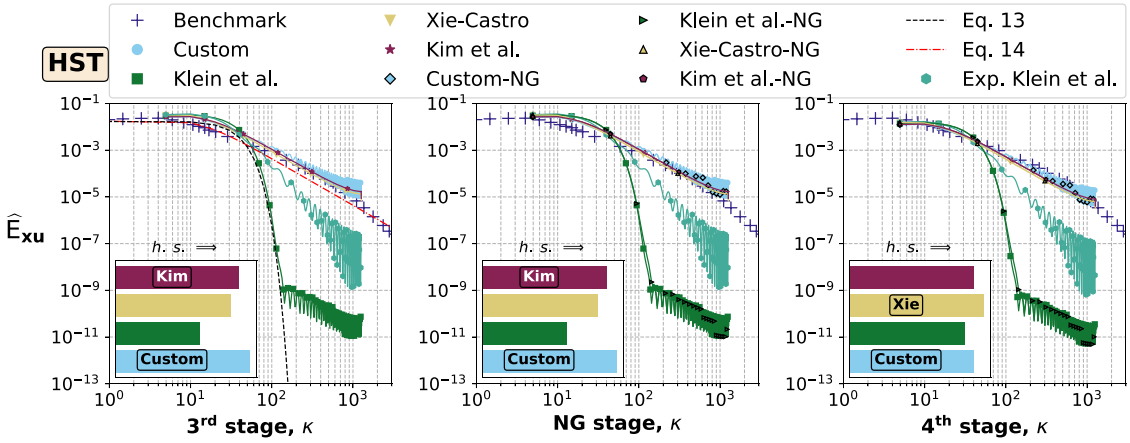

Fig. 10. The sample one-dimensional power spectral density function results, $\widehat{E}_{xu}$ [$m^3 s^{-2}$], as a function of spatial wavenumber, κ [m^{-1}], from the homogeneous shear turbulence computations (HST) [52]. The figure descriptions are as in Fig. 9.

exponential-form methods (except the exponential Klein et al.'s method) and the corresponding Lorentzian functions are virtually the same. The power amplitude of these methods are, however, generally $\sim \mathcal{O}(1)$ order of magnitude higher than that of the Lorentzian functions.

The implications of these findings are threefold. First of all, the exponential-form methods seem to yield the inertial subrange slope of κ^{-2}=$\kappa^{-6/3}$ rather than $\kappa^{-5/3}$. The former's slope is still steeper than that of the latter albeit to a significantly lesser extent than by Eq. (13). Because of this, the above-mentioned decrease of the net spectral energy flux generated by the Gaussian-form methods continues its existence, yet with a significantly reduced dissimilarity to what $\kappa^{-5/3}$ may produce. Further quantifications may however be needed whether this level of difference between κ^{-2} and $\kappa^{-5/3}$ is negligible from the perspective of turbulence development. Second, the use of Eq. (14) as well as (13), which were parametrized for DFM/FSM herein for the first time, could be useful in order for predicting power spectra of a prospective simulation before actually completing the entire simulation.

Thirdly, the exponentiality incorporated into Klein et al.'s method eliminated the Gaussian power drop *to a large extent*; however, a slight decline persisted in the order of $\sim \mathcal{O}(1)$-$\mathcal{O}(10)$ with respect to the other exponential-form methods. Furthermore, the method's slope was found considerably flatter than those of Gaussian-form methods, yet mildly steeper than κ^{-2}. This outcome is somewhat counterintuitive, because the implementation of the exponential-form was expected to transform Klein et al.'s method into an exponential-form method in all aspects. Accordingly, the results imply that the omission of Gaussian-form correlation function, per se, is the key to avoid the aforementioned spurious power drop whereas another unnamed mechanism within Klein et al.'s method also seems to contribute the drop.

It should be highlighted that similar observations were also deduced for PCF and different spectra, e.g. $\widehat{E}_{vv}$. In summary, these deductions support the notion that exponential-form of correlations is more apt than Gaussian-form for the synthetic turbulence generation.

5.5. Miscellaneous

5.5.1. Statistical weak stationarity and ergodicity

The initial presumption of the model development for DFM/FSM is the *statistical weak stationarity* of time-series generated by each model stage. The augmented Dickey-Fuller unit-root test [75], which searches stochastic trends in a time-series, was used to quantify the stationarity. As a result, *all* velocity-component time-series from each stage of each benchmark, including skewness-kurtosis computations, were found to be statistically weak stationary at a 1% statistical significance level.

The second presumption is the *statistical weak ergodicity* of the time-series. The Walf–Wolfowitz test [76] was utilised to assess the ergodicity. The test requires two samples of the same size from the same method, e.g. containing $n \times m$ elements. The first sample is generated with a single random seed which initializes the pseudorandom number generator. The second sample is then generated as a combination of n subsamples containing m elements, where each subsample is created with a new random seed. For a given moment of order k, the test conducts comparisons for whether the invariance of the kth moment's statistics is preserved in spite of the stochastic differences in the samples. Grazzini [76, p. 7] suggests n=100 and m=1000 for a decent estimation. With this suggestion, the test was performed for all the 36 benchmark/model scenarios up to the first four central moments of each velocity component. At a 5% statistical significance level, 9 out of 144 cases were estimated non-ergodic. No clear pattern was observed among the non-ergodic cases; however, 4 of them belonged to kurtosis. Owing to the high portion of the ergodic cases, it can be concluded that DFM/FSM is almost always *weakly ergodic* up to the fourth moment. In consequence, a stationary sample from DFM/FSM almost certainly includes the true moments of the population.

5.5.2. The use of different correlation functions at inlet spatial zones

In the literature, DFM/FSM has almost always been utilised by using a single set of integral length- or time-scales as an input for an entire synthetic turbulence generation plane. Two deficiencies may arise from this practice. First, in reality, length- and time-scales may spatiotemporally vary across a typical cross-section of a flow. Second, the usage of a single set of time-scales inherently causes a spatial variation in particularly streamwise length-scales due to the Taylor's frozen turbulence hypothesis [40] unless cross-sectional mean flow speed is uniform. For example, two pockets of fluctuation generated with the same time-scale and at two different spatial positions will convect downstream proportional to the convective mean longitudinal flow speed at these two points. If these flow speeds differ from those considered in the time-scale computation, the corresponding length-scales will be different to each other. Moreover, the literature preference for the single set usage seems due to the lack of not only available data but also quantifications regarding the merits and costs of using more-than-one sets as an input.

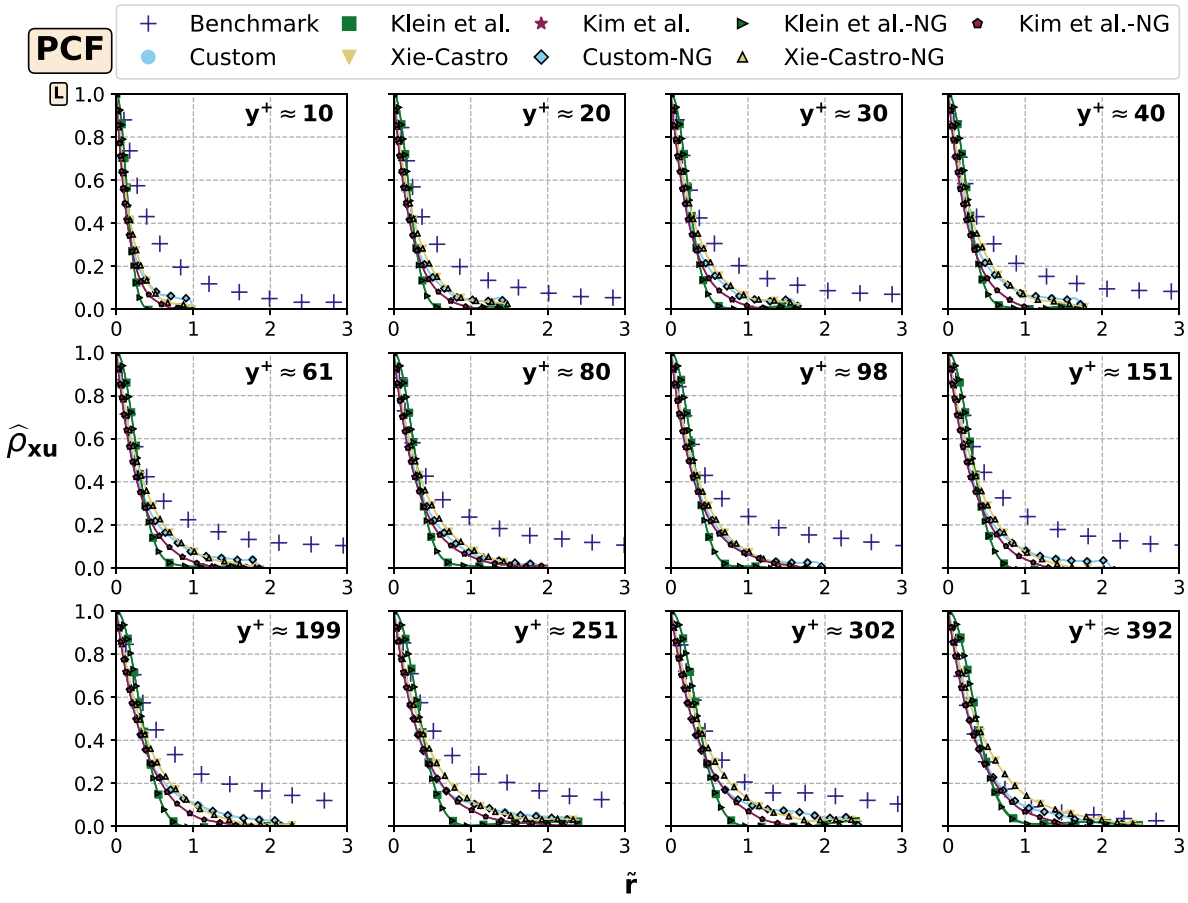

Fig. 11. The two-spatial/temporal-point sample autocorrelation function results, $\widehat{\rho}_{xu}$, from the smooth-wall plane channel flow computations (PCF) [29] wherein a single set of correlation tensor, **L**, was input. $\mathbf{y}^{+}$=$u_\tau\, y/\nu$ is the dimensionless wall distance, u_τ the friction velocity, ν the kinematic viscosity of the fluid, x the measurement direction, u the measured velocity component, and $\tilde{\mathbf{r}}$, the spatial lag normalized by the channel half-height, δ=1.0 [m]. The channel cross-section was segmented into 12 sections in the wall-normal direction, where the center of a section is at the specified y^{+}. The same input correlation tensor was used for all sections. Only the channel half-height from the top wall is shown due to the statistical symmetry along the half-height. $\widehat{\rho}_{xu}$s were computed for each node-time-series, and their arithmetic average was performed in the statistically homogeneous spanwise direction and each section height.

In this part, therefore, effects of the spatial variation in turbulence scales are investigated. To this end, PCF was reconstructed by using a single and then twelve sets of integral length-scales (tagged by **1L** and **12L** in the figures, respectively). Comparisons for correlations and power spectra were made, and *representative-to-all* results were presented. For the **12L** case, the synthetic turbulence generation plane was geometrically divided into twelve zones in the wall-normal direction. The zonal dimensions and associated correlation functions were provided by the benchmark. The integral length-scales were computed through the integration of these correlation functions, where the upper bound of the integration was set to 10% of the zero-lag.[16] Each input set of each zone contained nine integral length-scales belonging to each velocity component–direction pair, $(u, v, w) - (x, y, z)$. For the **1L** case, the length-scales reported for the channel half-height, y^{+}=392, were input uniformly across the generation plane.

Figs. 11 and 12 show the *representative-to-all* results of the variance-normalized sample autocorrelation function, $\widehat{\rho}_{\mathbf{xu}}$, as a function of spatial lag for **1L** and **12L**, in turn. Each figure includes twelve subplots related to a zone whose center is at a vertical distance of y^{+} from the wall.

In Fig. 11, the first observation is that the use of **1L** produced a variation in streamwise length-scales across the channel cross-section, increasing from the wall to the channel centerline. This is due to the fact that the **1L** length-scales was converted to Lagrangian time-scales based upon the mean flow speed at the height of y^{+}=392 through the Taylor's hypothesis. In a constant time-step computation, however, inputting the same Lagrangian time-scales across the channel cross-section automatically caused variations of length-scales because of the spatial varying mean flow speed across the same section. Consequently, this gave rise to uncontrolled generation of different scales. In addition, the following patterns were deduced from Fig. 11. Underpredictions occurred in all y^{+} zones and for all methods after a certain percentage of the zero-lag. In y^{+}=10 zone, the common underprediction started at $\sim$ 90% zero-lag. Towards higher y^{+} zones, this starting point then reduced till $\sim$ 40–70% zero-lag with gradually decreasing slope. Typically, Klein et al.'s method yielded maximum $\sim$ 20–30% underpredicted correlations whereas this ratio remained around $\sim$ 5–15% for the other methods. On the other hand, in y^{+}=392 zone

[16] The integral length-scale, L, is defined here as follows: $\mathrm{L}=\mathscr{L}_0^{\infty}(\widehat{\rho}(\Delta)) \approx \mathscr{L}_0^{a}(\widehat{\rho}(\Delta))$, where $\mathscr{L}_b^{a}(\cdot)$ is an operator applying a numerical integration method over the interval $[a, b]$. Despite its precise definition, the upper bound of the integral, i.e. b, is open to debate. Arguably, the main reason of the doubt is the different interpretations of the tail of the correlation functions on whether their tails mean something physical or spurious. O'Neill et al. [77, p. 3] implied based upon several tests that selecting the upper bound when the first zero-crossing happens is the most convenient option. This was, however, found inappropriate for the PCF while particularly the streamwise correlations do not level off zero.

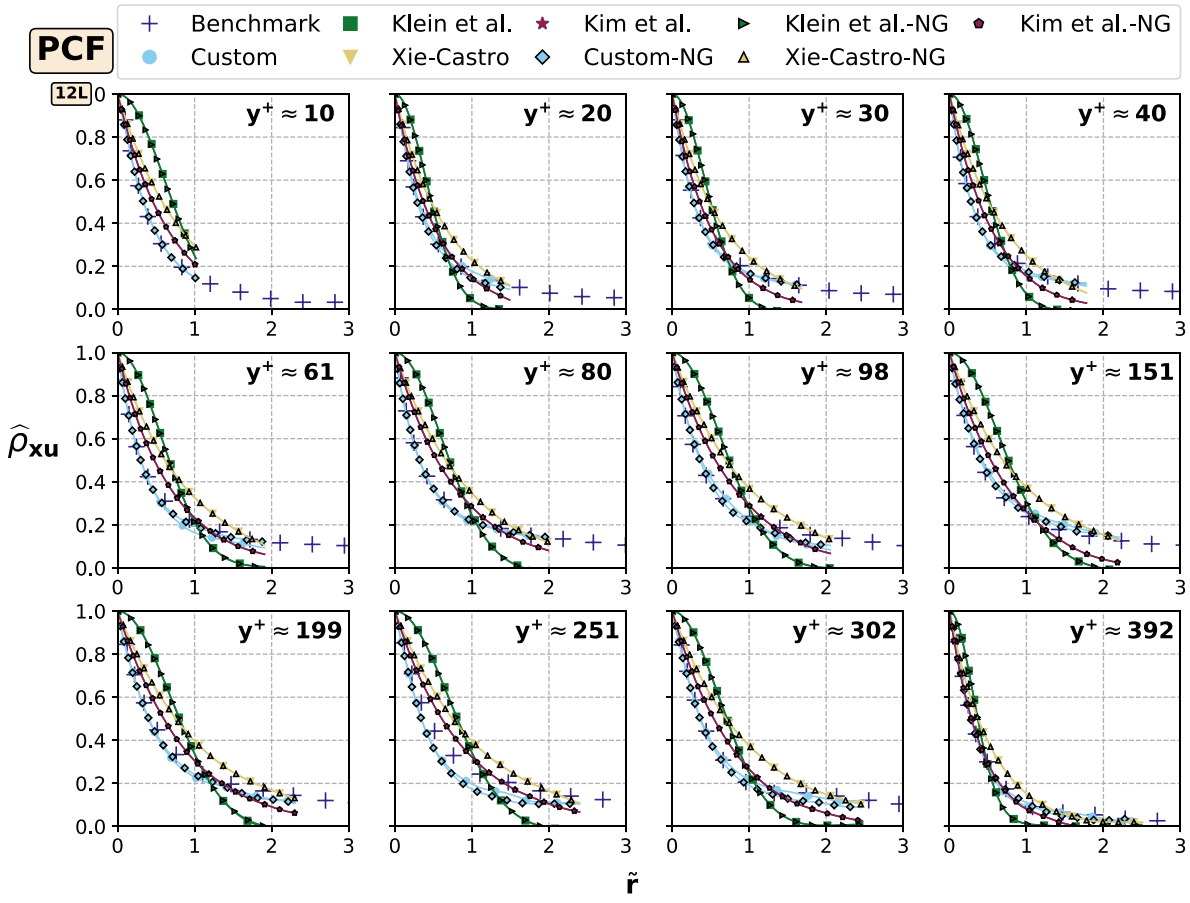

Fig. 12. The two-spatial/temporal-point sample autocorrelation function results, $\widehat{\rho}_{xu}$, from the smooth-wall plane channel flow computations (PCF) [29] wherein twelve correlation tensors, **12L**, were input. The figure descriptions are the same with Fig. 11.

where the input **1L** belongs to, the method performance findings in Section 5.3 were reobserved.

In Fig. 12, the observations similar to in Section 5.3 spread out the other y^+ zones by virtue of the spatial variation. On the whole, as maxima, Klein et al.'s method made $\sim$ 20–40% overpredictions until $\sim$ 20% zero-lag and afterwards $\sim$ 20% underpredictions. Xie–Castro's method overpredicted the benchmark in the level of $\sim$ 5–20% without exception. Custom and Kim et al.'s methods followed the benchmark in high proximity except in the y^+=251 zone,[17] yet the latter deviated for $\sim$ 5–10% underpredictions after $\sim$ 20% zero-lag.

Figs. 13 and 14 compared the power spectra for the **1L** and **12L** cases. As Fig. 13 shows, Klein et al.'s method yielded the aforementioned power drop except for the y^+=10 zone where the model outcome seems comparable to the benchmark. The rest of the methods performed in a common trend wherein the level of similarity to the benchmark was improved till y^+=61, then stayed roughly the same until y^+=151, and fell off. In detail, these methods had $\sim\mathcal{O}(10^3\text{–}10^4)$ higher power with respect to the spectrum tail at the y^+=10 zone. The difference steadily reduced to $\sim\mathcal{O}(10^2)$ by the y^+=61 zone and remained almost unchanged until y^+=151. Subsequently, it rose back to $\sim\mathcal{O}(10^3)$ towards the channel centerline.

As illustrated in Fig. 14, the performance trend of the models in Fig. 13 was repeated yet with a reduced degree of differences to the benchmark overall. Unlike the y^+=10 zone resemblance of Klein et al.'s method in the **1L** case, the likeness disappeared in the **12L** case with the refined length-scale input therein. That resemblance therefore may seem now to be a mere coincidence. The degree of the power difference, with respect to the spectra tails, overpredicted by the rest of the models was $\sim\mathcal{O}(10^2\text{–}10^3)$, $\sim\mathcal{O}(10^1\text{–}10^2)$ and $\sim\mathcal{O}(10^2\text{–}10^3)$ for the sectors between y^+=10–61, y^+=61–151 and y^+=151–392, respectively.

Taken together, the results of this section indicate that the spatial variation of scales often improves the overall statistical fidelity till the natural boundaries of fidelity that a model provides. In a single set of scales case, in contrast, somewhat arbitrary and hard-to-control statistics form in terms of magnitude and patterns for the majority of regions of a flow.

The spatial variation of scales brings along some theoretical and practical shortcomings, nevertheless, which are distinct for DFM and FSM. Klein et al. [13, p. 658] discouraged the use of the spatial variation of length-scales in DFM. The authors foresaw that such practice almost surely causes two issues: *i.* the Gaussian-form of Eq. (4) is distorted, and *ii.* an essential building-block assumption for the derivation of Eq. (1) is violated. Klein et al. [13], however, saw the spatial variation from another angle. The authors expected the acquisition of the variation occurs through calibrating filter coefficients within a single filter in accordance to given spatial-variant length-scales, namely via a *spatially varying filter*, and filtering an *undivided* synthetic turbulence generation plane with this filter. This, in fact, violates the essential model assumption wherein the filter coefficients were assumed spatially constant.

In the current DFM approach, however, the generation plane is separated into zones, and different *spatially-invariant* filters are put to use at different zones. Accordingly, each zone independently

[17] It should be mentioned that the main reason why the discrepancy from the Custom method at the y^+=251 zone occurred could not be spotted and explained.

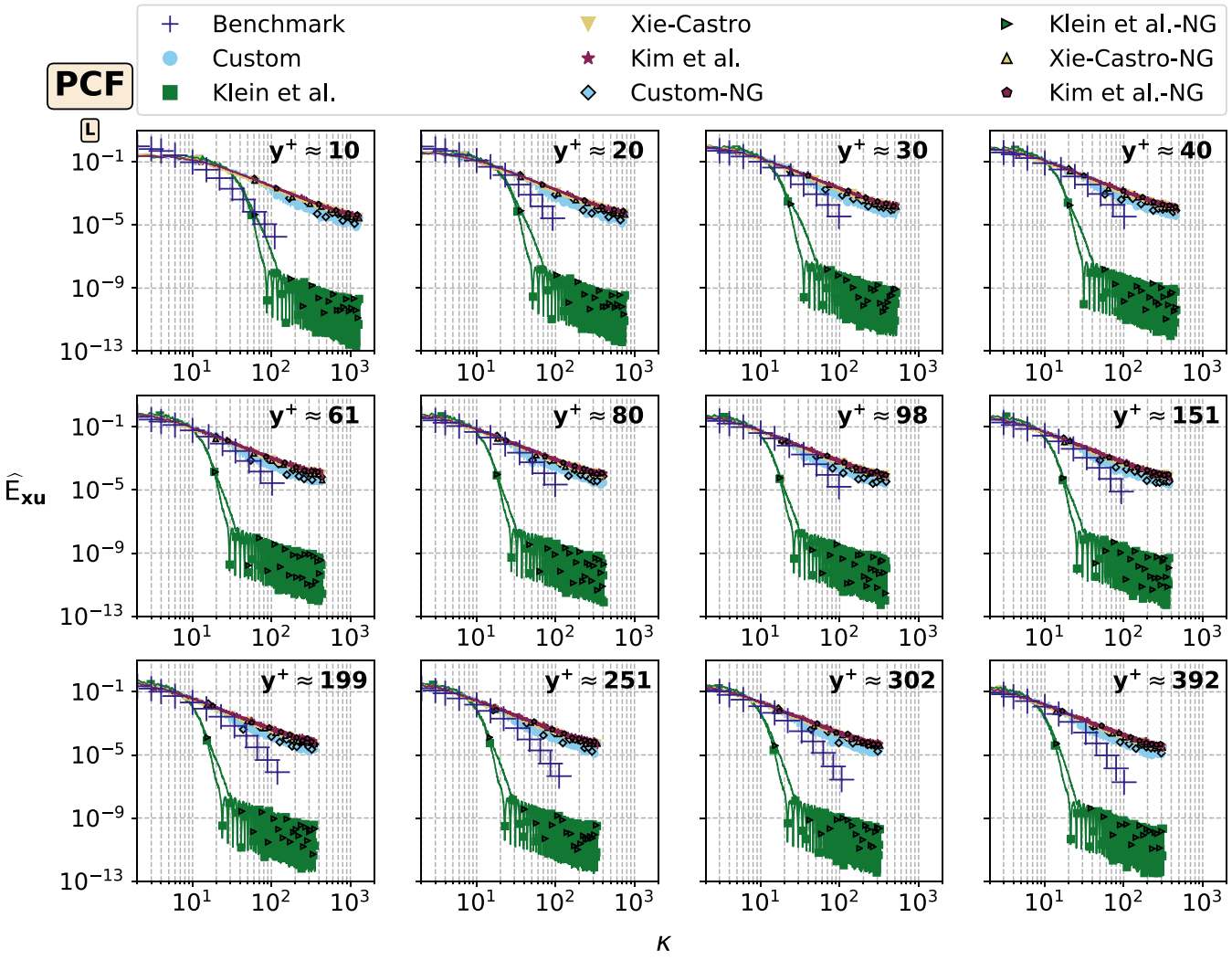

Fig. 13. The sample one-dimensional one-sided power spectral density function results, $\widehat{E}_{\mathbf{xu}}$ [$m^3 s^{-2}$], as a function of spatial wavenumber, κ [m^{-1}], from the smooth-wall plane channel flow computations (PCF) [29] wherein a single set of correlation tensor, **L**, was input. $\mathbf{y}^+ = u_\tau\, y/\nu$ is the dimensionless wall distance, u_τ the friction velocity, ν the kinematic viscosity of the fluid, x the measurement direction, u the measured velocity component, and $\tilde{\mathbf{r}}$, the spatial lag normalized by the channel half-height, δ=1.0 [m]. The channel cross-section was segmented into 12 sections in the wall-normal direction, where the center of a section is at the specified y^+. The same input correlation tensor was used for all sections. Only the channel half-height from the top wall is shown due to the statistical symmetry along the half-height. $\widehat{\rho}_{xu}$s were computed for each node-time-series, and their arithmetic average was performed in the statistically homogeneous spanwise direction and each section height.

possesses associated scales without breaching the two above-mentioned issues. Although the zone-separation discards these two theoretical issues, this approach suffers from two new practical weaknesses. Firstly, statistical discontinuities emerge between zone boundaries. In particular, the statistics in the zone-separation direction are more prone to such discontinuities. As an example, the size of a zonal scale may far exceed the dimension of its zone. While non-CFD applications might not be adversely affected as zones remain independent of each other, CFD applications could be profoundly influenced by unforeseen impacts on turbulence evolution due to the nonlinear mixing of discontinuities downstream.

In the limit of infinite grid nodes and zones, prospective discontinuities may disappear. The second weakness, however, arose as a limiting factor is the extra computational cost. Veloudis et al. [37, p. 9] stated without an explanation or quantification that a modest increase in the number of zones results in a 'substantial' cost increase for the same number of nodes. The reason why the cost increases is two-fold: *i.* new $\sim k(x\text{–}1)(\text{N}\text{–}1)$ random numbers required to be generated per time-step, where k is the number of scales input into a zone, x the number of zones, and N the filter support for a scale (A.6), and *ii.* these new numbers increase the size of sets which need to be convolved each time-step. Taking into these account, the additional computational cost is estimated by $\mathcal{O}(1)$ times the current cost.

The above remarks are pertinent to only DFM. FSM is immune to such cost impact. The zone-separation is not demanded by FSM, and the spatial variation is achieved through *solely* a spatial-variant arrangement of the input scale set. In this regard, a possible problem for FSM *may* be that the derivation of Eq. (8) for the spatial variation of scales was not engaged with by the literature, to date.

Notwithstanding these concerns, the results obtained in practice arguably weigh the merits of the spatial variation of scales more against additional costs. As an outcome, such implementation is advisable for non-CFD applications, particularly for FSM because of the fact that it poses considerably less trouble to beneficiaries.

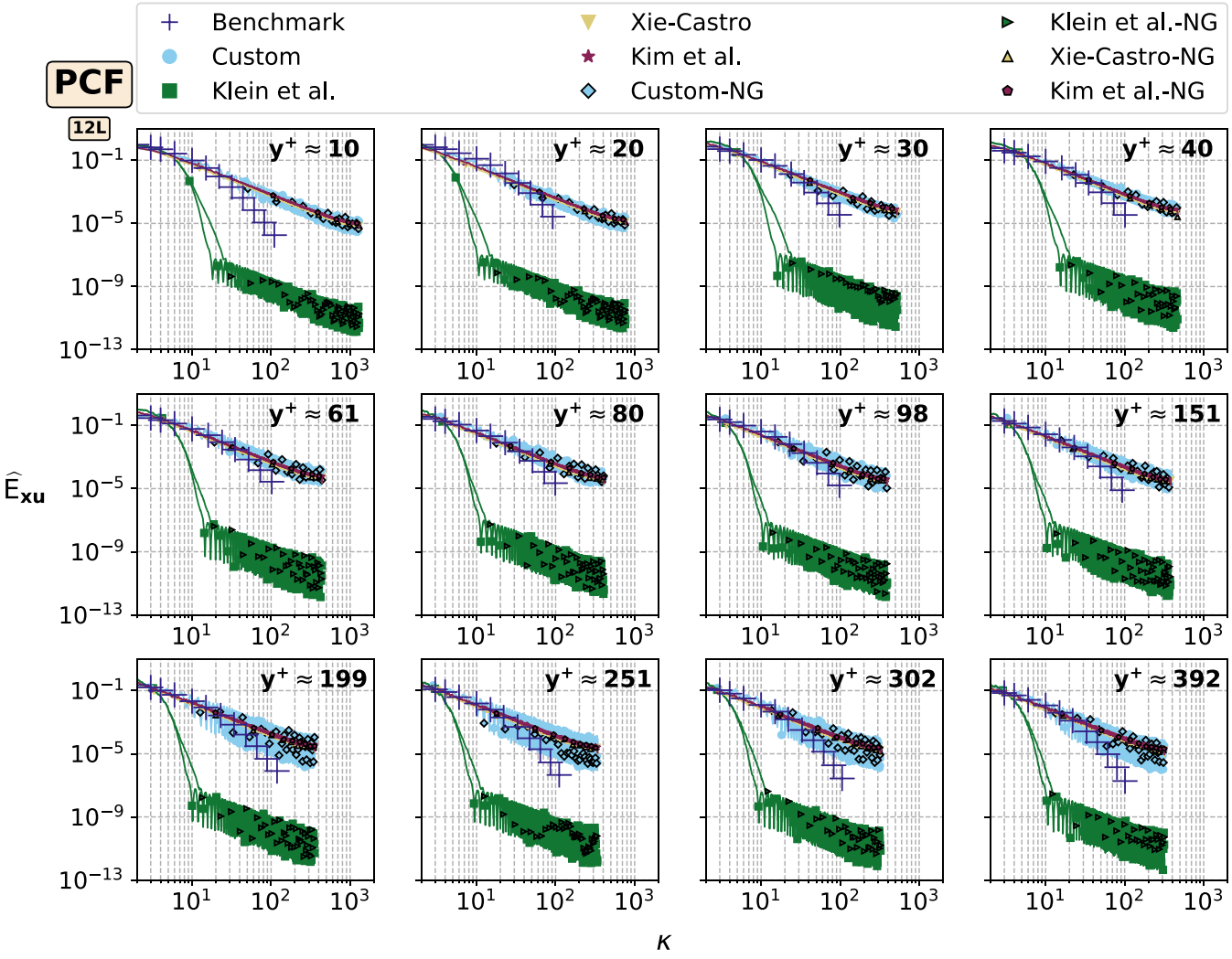

Fig. 14. The sample one-dimensional one-sided power spectral density function results, $\widehat{E}_{xu}$ [$m^3 s^{-2}$], as a function of spatial wavenumber, κ [m^{-1}], from the smooth-wall plane channel flow computations (PCF) [29] wherein twelve correlation tensors, **12L**, were input. The figure descriptions are as in Fig. 13.

6. Conclusions

The main aim of this study was to provide beneficiaries quantitative insights regarding the working mechanisms and performance of digital-filter-based (DFM) and forward-stepwise-based (FSM) synthetic turbulence generation methods. Another aim of the study was to add them a capability wherein one-spatial-point skewness and kurtosis values can be changed to target values.

To this end, four synthetic turbulence generation methods that belong to Kim et al. [35] (FSM), Xie and Castro [14] (Hybrid DFM-FSM), Klein et al. [13] (DFM), and a new method (DFM) were implemented into OpenFOAMv1612+. The novel applications within the methods were twofold: First, the new method, named *Custom*, was developed as a more efficient version of di Mare et al.'s concept [18]. Second, Kim et al.'s method was formalized and put through its first major tests. In addition to these, a new, cheap-to-run and easy-to-code piecewise closed-form function that transforms one-spatial-point Gaussian skewness-kurtosis of a given time-series to a non-Gaussian pair was derived from a combination of the memoryless nonlinear transformation method and the Johnson system of probability distribution functions. All the methods were abstracted into four modeling stages. Prior to transfer the model outputs into CFD simulations, the methods were explored in isolation via a test-bed containing decaying homogeneous isotropic turbulence, homogeneous shear turbulence and smooth-wall plane channel flow by means of various statistical measures and aspects.

In conclusion, apart from minor findings stated within the text, the study provided six primary insights: (*i*). the new non-Gaussian functionality successfully embeds target one-spatial-point skewness-kurtosis pairs into synthetic turbulence time-series, and does not alter the other types of existing statistics within the series. (*ii*). Moreover, the Lund transformation does not alter previous model stage statistics when anisotropic Reynolds stresses are absent. However, on the condition that anisotropic stresses are present, the Lund transformation amplifies the existing statistics *only* in statistically inhomogeneous lateral directions. The amplification generally manifests itself as a maximum $\sim$10% increase in autocorrelation functions. Statistics in the streamwise and statistically homogeneous lateral directions are, on the other hand, not affected by the transformation in contrast to the presumption in the literature. (*iii*). The level of reconstruction fidelity in terms of autocorrelation functions and power spectra was obtained by the methods of, which are sorted from the highest to the lowest level: Custom, Kim et al., Xie and Castro and Klein et al.. (*iv*). Kim et al.'s method provides the best trade-off between the reconstruction fidelity and computational cost. (*v*). Correlation functions determine overall shape of their power spectra. In detail, all methods reconstruct energy-containing region of the spectra in high fidelity. Yet

Klein et al.'s method theoretically and numerically produces a premature and flow-type-independent Gaussian drop in power spectra towards wavenumbers higher than those of energy-containing region, predominantly due to its Gaussian-form of correlation functions. In contrast, the rest of the methods, which uses exponential-form correlation functions, yields $\sim\kappa^{-2}$-slope drop by theoretical and numerical means. (*vi*). The spatial variation of correlation functions at a turbulence generation plane through zones was found to increase the overall fidelity of autocorrelation functions and power spectra. Its merits weigh more than its accompanied costs, particularly for FSM.

Last but not least, further research is required to determine whether the findings of the study differ within CFD simulations. For this purpose, the transfer and evolution of DFM/FSM output inside CFD simulations need to be quantified systematically.

Acknowledgement

The authors acknowledge the use of the IRIDIS High Performance Computing Facility, associated support services at the University of Southampton, in the completion of this work. Bercin also acknowledges the Overseas Rayleigh Studentship from the Faculty of Engineering and the Environment at the University of Southampton.

Appendix A. Appendix

A1. Non-Gaussian random number set input-based approach

The method is a heuristic approach rather than a rigorous model. Withinside, the probability mass function (*pmf*) of generated random number sets is changed from the standard normal distribution to a prescribed non-Gaussian one. The basic assumption of the approach is that the *pmf* of the random number sets proportionately yields a similar *pmf* for the digital-filtered sets at the end of the filtering. Thus, such adjustment may suffice to designate the *pmf* of the outcome.

A2. Deterministic deconvolution-based approach

In contrast to the first approach, the fundamental presumption of this approach is that the *pmf* of the first-stage random number sets is not similar to that of the last-stage digital-filtered sets; however, the former with a *particular pmf* may determine the *desired pmf* of the latter.

Recall that the basic mathematical operation in DFM is convolution (Eq. (2)), which may be recast into a simplified form as: $\mathbf{s} = \mathbf{b} \star \mathbf{r}$, where $\star$ is the convolution operator. Herein, $\mathbf{b}$ and $\mathbf{r}$ are known sets; and, $\mathbf{s}$ is unknown.

Let $\mathbf{b}$ and $\mathbf{s}$ are known, and $\mathbf{r}$ is unknown in the same convolution relation. In principle, $\star$ may be reversed in order to obtain $\mathbf{r}$. This process is called *deconvolution*, which can be expressed as:

$$\mathbf{s} \boxed{*} \mathbf{b} = \mathbf{r}^* \approx \mathbf{r} \tag{A.1}$$

where $\boxed{*}$ is the deconvolution operator, and $\mathbf{r} = \mathbf{r}^* + \epsilon$ with ϵ an element-wise error field.

The second basic assumption is that the *particular pmf* of $\mathbf{r}$ may be found through the deconvolution: Consider a *desired pmf* $\mathbf{h}_{\mathbf{s}'}$, and let n random sets $\{\mathbf{s}'_m\}_{\{m\in[1,n]\,\&\,\mathbf{s}'_m\neq\mathbf{s}'_q \text{ if } m\neq q\}}$ are generated according to $\mathbf{h}_{\mathbf{s}'}$. Then, $\mathbf{r}^*_m \approx \mathbf{r}_m$ may be computed through the deconvolution for known and constant $\mathbf{b}$. Denoting each *pmf* of $\{\mathbf{r}_m\}$ as h_i, a generic *pmf* for $\mathbf{r}$ might be approximated by the arithmetic average of h_i: i.e. $n^{-1}\sum_{i=1}^{n} h_i = \mathbf{h}_\mathbf{r}$ when $n \gg 1$. Finally, a new random number set $\mathbf{r}$ obeying the *pmf* of $\mathbf{h}_\mathbf{r}$ could be convolved with $\mathbf{b}$ to yield a digital-filtered random set $\mathbf{s}'$ which follows the desired $\mathbf{h}_{\mathbf{s}'}$.

In practice, arguably, no standard form of deconvolution exists, and its form depends upon various characteristics of its operands. Whilst $\mathbf{b}$ is always precisely known, the optimal choice for this study is the deterministic deconvolution [80], which may be defined as an arithmetic division of Fourier transformed operands in the frequency domain:

$$\mathbf{r} \approx \mathbf{r}^* = \mathscr{F}^{-1}\left\{\frac{\mathscr{F}\{\mathbf{s}\}}{\mathscr{F}\{\mathbf{b}\}}\right\} \tag{A.2}$$

where $\mathscr{F}\{\cdot\}$ the discrete fast Fourier transform operation, and $\mathscr{F}^{-1}\{\cdot\}$ its inverse.

Two challenges, however, exist in respect to the formulation. The first is that Eq. (A.2) does not guarantee a definition of a solution due to the possibility of the presence of zero in the denominator term. The second challenge is the arithmetic division by a small number, which may cause spurious spikes in the output Claerbout et al. [81, p. 86], therefore, proposed the following modification to Eq. (A.2) in order to alleviate the aforementioned challenges:

$$\mathbf{r} \approx \mathbf{r}^* = \mathscr{F}^{-1}\left\{\frac{\mathscr{F}\{\mathbf{s}\}\mathscr{F}\{\mathbf{b}\}^*}{\mathscr{F}\{\mathbf{b}\}\mathscr{F}\{\mathbf{b}\}^* + \epsilon^2}\right\} \tag{A.3}$$

where $\mathscr{F}\{\mathbf{b}\}^*$ is the complex conjugate of $\mathscr{F}\{\mathbf{b}\}$, and ϵ a small real number proportional to the arithmetic average of $\mathscr{F}\{\mathbf{b}\}\mathscr{F}\{\mathbf{b}\}^*$ such $\epsilon = \lambda\{\overline{\mathscr{F}\{\mathbf{b}\}\mathscr{F}\{\mathbf{b}\}^*}\}^2$ with a constant λ. For an illustrative example, [81, p. 87] set $\lambda = 0.03$; however, no range of values was particularly suggested.

A3. PDF transformation-based approach

A3.1. Derivations

The standard Gaussian CDF is:

$$\phi_\mathrm{N}(x) = \frac{1}{2} + \frac{1}{2}\mathrm{erf}\left(\frac{x}{\sqrt{2}}\right) \tag{A.4}$$

The standard Gaussian quantile function is:

$$\phi_\mathrm{N}^{-1}(x) = \sqrt{2}\mathrm{erf}^{-1}(2x-1) \tag{A.5}$$

S_U unbounded family

The quantile function of Johnson S_U family:

$$F_\mathrm{SU}^{-1}(q;a,b) = \sinh\left[\frac{\phi^{-1}(q)-a}{b}\right] \tag{A.6}$$

The substitution of Eq. (A.5) into Eq. (A.6) yields the following:

$$\begin{aligned} F_\mathrm{SU}^{-1}(q;a,b) &= \sinh\left[\frac{\sqrt{2}\mathrm{erf}^{-1}(2q-1)-a}{b}\right] \\ &= \sinh\left[\frac{\sqrt{2}\mathrm{erf}^{-1}\left[2\left(\frac{1}{2}+\frac{1}{2}\mathrm{erf}\left(\frac{x}{\sqrt{2}}\right)\right)-1\right]-a}{b}\right] \quad q=\phi_\mathrm{N}(x) \Rightarrow \\ &= \sinh\left[\frac{\sqrt{2}\mathrm{erf}^{-1}\left[\mathrm{erf}\left(\frac{x}{\sqrt{2}}\right)\right]-a}{b}\right] \quad \mathrm{erf}^{-1}(\mathrm{erf}(x/\sqrt{2}))=x/\sqrt{2} \Rightarrow \\ &= \sinh\left[\frac{x-a}{b}\right] \end{aligned} \tag{A.7}$$

S_L Log–Normal family

The quantile function of Johnson S_L family:

$$F_\mathrm{SL}^{-1}(q;\sigma) = \exp\left[\sigma\phi^{-1}(q)\right] \tag{A.8}$$

The substitution of Eq. (A.5) into Eq. (A.8) yields the following:

$$F_{SL}^{-1}(q;\sigma) = \exp[\sigma x] \tag{A.9}$$

S_B bounded family

The quantile function of Johnson S_B family:

$$F_{SB}^{-1}(q;a,b) = \frac{1}{1+\exp\left[\frac{-1}{b}\left\{\phi_N^{-1}(q)-a\right\}\right]} \tag{A.10}$$

The substitution of Eq. (A.5) into Eq. (A.10) yields the following:

$$\begin{aligned} &F_{SB}^{-1}(q;a,b) \\ &= \frac{1}{1+\exp\left[\frac{-1}{b}\left\{\phi_N^{-1}(q)-a\right\}\right]} \\ &= \frac{1}{1+\exp\left[\frac{-1}{b}\left\{\sqrt{2}\mathrm{erf}^{-1}(2q-1)-a\right\}\right]} \qquad q=\phi_N(x) \Rightarrow \\ &= \frac{1}{1+\exp\left[\frac{-1}{b}\left\{\sqrt{2}\mathrm{erf}^{-1}\left(2\left[\frac{1}{2}+\frac{1}{2}\mathrm{erf}\left(\frac{x}{\sqrt{2}}\right)\right]-1\right)-a\right\}\right]} \\ &= \frac{1}{1+\exp\left[\frac{-1}{b}\left\{\sqrt{2}\mathrm{erf}^{-1}\left(\mathrm{erf}\left(\frac{x}{\sqrt{2}}\right)\right)-a\right\}\right]} \qquad \mathrm{erf}^{-1}(\mathrm{erf}(x/\sqrt{2}))=x/\sqrt{2} \Rightarrow \\ &= \frac{1}{1+\exp\left[\frac{a-x}{b}\right]} \end{aligned} \tag{A.11}$$

A3.2. S_U unbounded family [48]

$$\beta_1 = \left(\omega+1-\sqrt{4+2\left[\omega^2-\frac{\beta_2+3}{\omega^2+2\omega+3}\right]}\right) \times \left(\omega+1+\frac{1}{2}\sqrt{4+2\left[\omega^2-\frac{\beta_2+3}{\omega^2+2\omega+3}\right]}\right)^2 \tag{A.12}$$

$$m=-2+\sqrt{4+2\left[\omega^2-\frac{\beta_2+3}{\omega^2+2\omega+3}\right]} \tag{A.13}$$

$$\mu_U=\mathrm{sign}(\beta_1^2)\sqrt{\frac{\omega+1}{2}\left(\frac{\omega-1}{m}-1\right)} \tag{A.14}$$

$$\sigma_U=(\omega-1)\sqrt{\frac{\omega+1}{2m}} \tag{A.15}$$

$$\delta=\frac{1}{\sqrt{\log(\omega)}} \tag{A.16}$$

$$\gamma=\frac{-\mathrm{sign}(\beta_1^2)\sinh^{-1}\left(\sqrt{\frac{\omega+1}{2\omega}\left(\frac{\omega-1}{m}-1\right)}\right)}{\sqrt{\ln\omega}} \tag{A.17}$$

A3.3. S_B bounded family

$$\beta_1^2=\left(\frac{2\mu^3-3\mu\mu_2+\mu_3}{\sigma^3}\right)^2 \tag{A.18}$$

$$\beta_2=\frac{-3\mu^4+6\mu^2\mu_2-4\mu\mu_3+\mu_4}{\sigma^4} \tag{A.19}$$

$$\mu=\frac{A-B}{CD} \tag{A.20}$$

$$\mu_2=\mu(1-\delta\gamma)+\frac{\delta}{CD}\left(A_\gamma-B_\gamma-\mu C_\gamma D\right) \tag{A.21}$$

$$\mu_3=\mu+1.5\delta\mu_\gamma+0.5\delta^2\mu_{\gamma^2} \tag{A.22}$$

$$\mu_4=\mu+\frac{11}{6}\delta\mu_\gamma+\delta^2\mu_{\gamma^2}+\frac{1}{6}\delta^3\mu_{\gamma^3} \tag{A.23}$$

$$A=\frac{1}{2\delta}+\frac{1}{\delta}\sum_{n=1}^{\infty}\left\{\exp\left(\frac{-n^2}{2\delta^2}\right)\cosh\left(\frac{n(1-2\delta\gamma)}{2\delta^2}\right)\mathrm{sech}\left(\frac{n}{2\delta^2}\right)\right\} \tag{A.24}$$

$$A_\gamma=-\frac{1}{\delta^2}\sum_{n=1}^{\infty}\left\{n\exp\left(\frac{-n^2}{2\delta^2}\right)\sinh\left(\frac{n(1-2\delta\gamma)}{2\delta^2}\right)\mathrm{sech}\left(\frac{n}{2\delta^2}\right)\right\} \tag{A.25}$$

$$A_{\gamma^2}=\frac{1}{\delta^3}\sum_{n=1}^{\infty}\left\{n^2\exp\left(\frac{-n^2}{2\delta^2}\right)\cosh\left(\frac{n(1-2\delta\gamma)}{2\delta^2}\right)\mathrm{sech}\left(\frac{n}{2\delta^2}\right)\right\} \tag{A.26}$$

$$A_{\gamma^3}=-\frac{1}{\delta^4}\sum_{n=1}^{\infty}\left\{n^3\exp\left(\frac{-n^2}{2\delta^2}\right)\sinh\left(\frac{n(1-2\delta\gamma)}{2\delta^2}\right)\mathrm{sech}\left(\frac{n}{2\delta^2}\right)\right\} \tag{A.27}$$

$$B=2\pi\delta\sum_{n=1}^{\infty}\left\{\exp\left(-\frac{1}{2}(2n-1)^2\pi^2\delta^2\right)\sin\left((2n-1)\pi\delta\gamma\right) \times \mathrm{cosech}\left((2n-1)\pi^2\delta^2\right)\right\} \tag{A.28}$$

$$B_\gamma=2(\pi\delta)^2\sum_{n=1}^{\infty}\left\{(2n-1)\exp\left(-\frac{1}{2}(2n-1)^2\pi^2\delta^2\right) \times \cos\left((2n-1)\pi\delta\gamma\right)\mathrm{cosech}\left((2n-1)\pi^2\delta^2\right)\right\} \tag{A.29}$$

$$B_{\gamma^2}=-2(\pi\delta)^3\sum_{n=1}^{\infty}\left\{-(2n-1)^2\exp\left(-\frac{1}{2}(2n-1)^2\pi^2\delta^2\right) \times \sin\left((2n-1)\pi\delta\gamma\right)\mathrm{cosech}\left((2n-1)\pi^2\delta^2\right)\right\} \tag{A.30}$$

$$B_{\gamma^3}=-2(\pi\delta)^4\sum_{n=1}^{\infty}\left\{-(2n-1)^3\exp\left(-\frac{1}{2}(2n-1)^2\pi^2\delta^2\right) \times \cos\left((2n-1)\pi\delta\gamma\right)\mathrm{cosech}\left((2n-1)\pi^2\delta^2\right)\right\} \tag{A.31}$$

$$C=1+2\sum_{n=1}^{\infty}\left\{\exp\left(-2n^2\pi^2\delta^2\right)\cos\left(2n\pi\delta\gamma\right)\right\} \tag{A.32}$$

$$C_\gamma=-4\pi\delta\sum_{n=1}^{\infty}\left\{n\exp\left(-2n^2\pi^2\delta^2\right)\sin\left(2n\pi\delta\gamma\right)\right\} \tag{A.33}$$

$$C_{\gamma^2}=-8(\pi\delta)^2\sum_{n=1}^{\infty}\left\{n^2\exp\left(-2n^2\pi^2\delta^2\right)\cos\left(2n\pi\delta\gamma\right)\right\} \tag{A.34}$$

$$C_{\gamma^3} = 16(\pi\delta)^3 \sum_{n=1}^{\infty} \left\{ n^3 \exp\left(-2n^2\pi^2\delta^2\right) \sin\left(2n\pi\delta\gamma\right) \right\} \tag{A.35}$$

$$D = \sqrt{2\pi} \exp\left(\frac{\gamma^2}{2}\right) \tag{A.36}$$

$$D_{\gamma} = \gamma D \tag{A.37}$$

$$D_{\gamma^2} = (\gamma^2 + 1)D \tag{A.38}$$

$$D_{\gamma^3} = (\gamma^3 + 3\gamma)D \tag{A.39}$$

$$\mu_{\gamma} = \frac{A_{\gamma}}{CD} - \frac{ADC_{\gamma}}{(CD)^2} - \frac{ACD_{\gamma}}{(CD)^2} - \left(\frac{B_{\gamma}}{CD} - \frac{BDC_{\gamma}}{(CD)^2} - \frac{BCD_{\gamma}}{(CD)^2} \right) \tag{A.40}$$

$$\begin{aligned}
\mu_{\gamma^2} = {} & \frac{A_{\gamma}}{CD} - \frac{A_{\gamma}C_{\gamma}}{C^2D} - \frac{A_{\gamma}D_{\gamma}}{CD^2} \\
& - \frac{A_{\gamma}C_{\gamma}}{C^2D} - \frac{-2AC_{\gamma}^2}{C^3D} - \frac{-AC_{\gamma}D_{\gamma}}{C^2D^2} - \frac{AC_{\gamma^2}}{C^2D} \\
& - \frac{A_{\gamma}D_{\gamma}}{CD^2} - \frac{-AC_{\gamma}D_{\gamma}}{C^2D^2} - \frac{-2AD_{\gamma}^2}{CD^3} - \frac{AD_{\gamma^2}}{CD^2} \\
& - \frac{B_{\gamma}}{CD} + \frac{B_{\gamma}C_{\gamma}}{C^2D} + \frac{B_{\gamma}D_{\gamma}}{CD^2} \\
& + \frac{B_{\gamma}C_{\gamma}}{C^2D} + \frac{-2BC_{\gamma}^2}{C^3D} + \frac{-BC_{\gamma}D_{\gamma}}{C^2D^2} + \frac{BC_{\gamma^2}}{C^2D} \\
& + \frac{B_{\gamma}D_{\gamma}}{CD^2} + \frac{-BC_{\gamma}D_{\gamma}}{C^2D^2} + \frac{-2BD_{\gamma}^2}{CD^3} + \frac{BD_{\gamma^2}}{CD^2}
\end{aligned} \tag{A.41}$$

$$\begin{aligned}
\mu_{\gamma^3}(x) = {} & \frac{-x_{\gamma^2}C_{\gamma}}{C^2D} + \frac{-x_{\gamma^2}D_{\gamma}}{CD^2} + \frac{x_{\gamma^3}}{CD} \\
& - \frac{-2x_{\gamma}(C_{\gamma})^2}{C^3D} - \frac{-x_{\gamma}C_{\gamma}D_{\gamma}}{C^2D^2} - \frac{x_{\gamma^2}C_{\gamma}}{C^2D} - \frac{x_{\gamma}C_{\gamma^2}}{C^2D} \\
& - \frac{-x_{\gamma}C_{\gamma}D_{\gamma}}{C^2D^2} - \frac{-2x_{\gamma}(D_{\gamma})^2}{CD^3} - \frac{(x_{\gamma})^2D}{CD^2} - \frac{x(D_{\gamma})^2}{CD^2} \\
& - \frac{-2x_{\gamma}(C_{\gamma})^2}{C^3D} - \frac{-x_{\gamma}C_{\gamma}D_{\gamma}}{C^2D^2} - \frac{x_{\gamma^2}C_{\gamma}}{C^2D} - \frac{x_{\gamma}C_{\gamma^2}}{C^2D} \\
& - \frac{-2x_{\gamma}(C_{\gamma})^2}{C^3D} - \frac{2(C_{\gamma})^2D_{\gamma}}{D^2C^3} - \frac{6x(C_{\gamma})^3}{C^4D} - \frac{-4xC_{\gamma}C_{\gamma^2}}{C^3D} \\
& - \frac{-x_{\gamma}C_{\gamma}D_{\gamma}}{C^2D^2} - \frac{2(C_{\gamma})^2D_{\gamma}}{C^3D^2} - \frac{2C_{\gamma}(D_{\gamma})^2}{C^2D^3} - \frac{-xD_{\gamma^2}C_{\gamma}}{C^2D^2} \\
& - \frac{-xC_{\gamma^2}D_{\gamma}}{C^2D^2} \\
& - \frac{x_{\gamma}C_{\gamma^2}}{C^2D} - \frac{-2xC_{\gamma}C_{\gamma^2}}{C^3D} - \frac{-xC_{\gamma^2}D_{\gamma}}{C^2D^2} - \frac{xC_{\gamma^3}}{C^2D} \\
& - \frac{-x_{\gamma}C_{\gamma}D_{\gamma}}{C^2D^2} - \frac{-2x_{\gamma}(D_{\gamma})^2}{CD^3} - \frac{x_{\gamma^2}D_{\gamma}}{CD^2} - \frac{x_{\gamma}D_{\gamma^2}}{CD^2} \\
& - \frac{-x_{\gamma}C_{\gamma}D_{\gamma}}{C^2D^2} - \frac{2x(D_{\gamma})^2C_{\gamma}}{C^2D^3} - \frac{-xC_{\gamma}D_{\gamma^2}}{C^2D^2} - \frac{2x(C_{\gamma})^2D_{\gamma}}{C^3D^2} \\
& - \frac{-xC_{\gamma^2}D_{\gamma}}{C^2D^2} \\
& - \frac{-2x_{\gamma}(D_{\gamma})^2}{CD^3} - \frac{2xC_{\gamma}(D_{\gamma})^2}{C^2D^3} - \frac{-4xD_{\gamma}D_{\gamma^2}}{CD^3} - \frac{6x(D_{\gamma})^3}{CD^4} \\
& - \frac{x_{\gamma}D_{\gamma^2}}{CD^2} - \frac{-xC_{\gamma}D_{\gamma^2}}{C^2D^2} - \frac{-2xD_{\gamma}D_{\gamma^2}}{CD^3} - \frac{xD_{\gamma^3}}{CD^2}
\end{aligned} \tag{A.42}$$

$$\mu_{\gamma^3} = \mu_{\gamma^3}(A) + \mu_{\gamma^3}(B) \tag{A.43}$$

$$\mu_B = \mu \tag{A.44}$$

$$\sigma_B = \text{sign}(\beta_1)\sqrt{\mu_2 - \mu^2} \tag{A.45}$$

A3.4. Criterion

$$g(\beta_2) = (\omega_1 - 1)(\omega_2 + 2)^2 \sim \beta_1 \tag{A.46}$$

$$\omega_1 = \frac{1}{2}\left(-1 + \sqrt{d} + \sqrt{\frac{4}{\sqrt{d}} - d - 3}\right) \tag{A.47}$$

$$\omega_2 = \sqrt{-1 + \sqrt{2(\beta_2 - 1)}} \tag{A.48}$$

$$d = -1 + \sqrt[3]{7 + 2\beta_2 + 2\sqrt{D}} - \sqrt[3]{2\sqrt{D} - 7 - 2\beta_2} \tag{A.49}$$

$$D = \frac{(3 + \beta_2)(16\beta_2^2 + 87\beta_2 + 171)}{27} \tag{A.50}$$

A4. Discrete Fréchet distance metric [63, p. 2]

Let $\{\mathbf{P}_{\Delta_t}\}_{\{0\le\Delta_t\le T;\ 1\le t\le p;\ t\in\mathbb{Z}^+\}}=\{P_{\Delta_1},\ldots,P_{\Delta_p}\}$, and similarly $\{\mathbf{Q}_{\Delta_t}\}=\{Q_{\Delta_1},\ldots,Q_{\Delta_q}\}$, be two the-same-size discrete time-series, where Δ_t is an arbitrary instant, and t an index of a set member. Let further consider a set $\{\mathbf{L}\}$ that contains of all possible member pairs between $\{\mathbf{P}_{\Delta_t}\}$ and $\{\mathbf{Q}_{\Delta_t}\}$ such that $\{\mathbf{L}\}=\{(P_{a_1},Q_{b_1}),\ldots,(P_{a_m},Q_{b_m})\}_{\{\{\Delta_1\le a_i\le\Delta_p\};\ \{\Delta_1\le b_i\le\Delta_q\};\ \{1\le i\le m-1\}\}}$. Then, the *discrete Fréchet distance*, δ_{dF}, whose value depends on the values (position) and order of the set members, is defined as follows:

$$\delta_{dF}(\mathbf{P}_{\Delta_t},\mathbf{Q}_{\Delta_t}) = \min_{\mathbf{L}}\left(\max_{i=1,\ldots,m}|P_{a_i} - Q_{b_i}|\right) \tag{A.51}$$

For identical sets δ_{dF}=0 whilst a rise in δ_{dF} indicates an increase in dissimilarities. In addition, it should be noted that the discrete Fréchet distance is an approximation to the Fréchet distance to allow easier code implementation and lower computational costs.

A5. Fourier transformation of some filter kernels

A5.1. Gaussian-form autocorrelation function

The Fourier transform of a Gaussian function can be derived as follows [73]:

$$\mathscr{F}_x\left\{\exp\left[-\frac{\pi}{c}\frac{x^2}{L^2}\right]\right\}(\kappa) = \mathscr{F}_x\left\{\exp\left[-ax^2\right]\right\}(\kappa) \qquad a \leftrightarrow \pi c^{-1}L^{-2} \tag{A.52a}$$

$$= \int_{-\infty}^{\infty} \exp\left[-ax^2\right] \exp\left[-2\pi i\kappa x\right] dx \tag{A.52b}$$

$$= \int_{-\infty}^{\infty} \exp\left[-ax^2\right] \left[\cos(2\pi\kappa x) - i\sin(2\pi\kappa x)\right] dx \tag{A.52c}$$

$$= \int_{-\infty}^{\infty} \exp\left[-ax^2\right] \cos(2\pi\kappa x)\, dx \; - i \int_{-\infty}^{\infty} \exp\left[-ax^2\right] \sin(2\pi\kappa x)\, dx \tag{A.52d}$$

$$= \sqrt{\pi\, a^{-1}} \exp\left[-\frac{\pi^2\kappa^2}{a}\right] \tag{A.52e}$$

$$= \sqrt{c}\, L \exp\left[-c\pi L^2\kappa^2\right] \qquad a \leftrightarrow \pi c^{-1}L^{-2} \tag{A.52f}$$

where $\mathscr{F}_x$ is the Fourier transform operator on the variable x, $\mathrm{L}[m(2\pi)^{-1}]$ the integral length-scale, $\kappa\,[(2\pi)m^{-1}]$ the spatial wavenumber, and c a model constant, for instance in Eq. (4) c=4. The first term of Eq. (A.52d) reduces to Eq. (A.52e) [73], and its second term goes to zero due to the symmetrical integration of the odd function [73].

A5.2. Exponential-form autocorrelation function

The Fourier transform of an exponential function is derived as follows [74]:

$$\mathscr{F}_x\left\{\exp\left[-\frac{\pi}{c}\frac{x}{\mathrm{L}}\right]\right\}(\kappa)=\mathscr{F}_x\{\exp[-ax]\}(\kappa)\qquad a\leftrightarrow\pi c^{-1}\mathrm{L}\quad\text{(A.53a)}$$

$$=\int_{-\infty}^{\infty}\exp[-ax]\exp[-2\pi i\kappa x]dx\quad\text{(A.53b)}$$

$$=\int_{-\infty}^{0}\exp[-2\pi i\kappa x]\exp[2\pi ax]dx+\int_{0}^{\infty}\exp[-2\pi i\kappa x]\exp[-2\pi ax]dx\quad\text{(A.53c)}$$

$$=\int_{-\infty}^{0}[\cos(2\pi\kappa x)-i\sin(2\pi\kappa x)]\exp[2\pi ax]dx+\int_{0}^{\infty}[\cos(2\pi\kappa x)-i\sin(2\pi\kappa x)]\exp[-2\pi ax]dx\quad\text{(A.53d)}$$

$$(-x\leftrightarrow u;\,-dx\leftrightarrow du)$$

$$=\int_{0}^{\infty}[\cos(2\pi\kappa u)+i\sin(2\pi\kappa u)]\exp[-2\pi au]du+\int_{0}^{\infty}[\cos(2\pi\kappa u)-i\sin(2\pi\kappa u)]\exp[-2\pi au]du\quad\text{(A.53e)}$$

$$=2\int_{0}^{\infty}\cos(2\pi\kappa u)\exp[-2\pi au]du\quad\rightarrow\int_{0}^{\infty}\cos(\kappa u)\exp[-bu]du=\frac{b}{b^2+\kappa^2}\quad\text{(A.53f)}$$

$$=\quad\cdots\quad\text{(A.53g)}$$

$$=\frac{2c\mathrm{L}\pi^{-1}}{(2c\mathrm{L}\kappa)^2+1}\qquad a\leftrightarrow\pi c^{-1}\mathrm{L}\quad\text{(A.53h)}$$

where $\mathscr{F}_x$ is the Fourier transform operator on the variable $\{x\}_{\{x>0\}}$, $\mathrm{L}[m(2\pi)^{-1}]$ the integral length-scale, $\kappa\,[(2\pi)m^{-1}]$ the spatial wavenumber, and c a model constant, for instance in Eq. (7) c=2.

A6. Size of extra random numbers due to the spatial variation of scales

Consider a planar synthetic turbulence generation grid that has n nodes. Let the grid is divided into x zones which are assumed having the same number of nodes, n/x. Also assume that a scale set, which contains k number of scales, is input for each zone. The following relations then can be presented among the size of random number set required for "*valid*" type of convolution summations on an undivided grid, M_1, and on a zone, M_2, and the filter support of the scale N_1:

$$\begin{aligned}n&=\mathrm{M}_1-\mathrm{N}_1+1\\ \mathrm{M}_2-\mathrm{N}_1+1&=\frac{\mathrm{M}_1-\mathrm{N}_1+1}{x}\qquad\text{for a zone}\\ x\mathrm{M}_2-x\mathrm{N}_1+x&=\mathrm{M}_1-\mathrm{N}_1+1\\ x\mathrm{M}_2-\mathrm{M}_1&=(x-1)(\mathrm{N}_1-1)\end{aligned}\quad\text{(A.54)}$$

where $x\mathrm{M}_2-\mathrm{M}_1$ is the size of new random sets that needs to be generated for the whole grid for a single scale per time-step.

References

[1] Rosales C, Meneveau C. Anomalous scaling and intermittency in three-dimensional synthetic turbulence. Phys Rev E 2008;78(1):016313. doi:10.1103/PhysRevE.78.016313.

[2] AL-Bairmani S, Li Y, Rosales C, Xie Z-T. Subgrid-scale stresses and scalar fluxes constructed by the multi-scale turnover lagrangian map. Phys Fluids 2017;29(4):045103. doi:10.1063/1.4979719.

[3] Gong K, Chen X. Influence of non-Gaussian wind characteristics on wind turbine extreme response. Eng Struct 2014;59:727–44. doi:10.1016/j.engstruct.2013.11.029.

[4] Berg J, Natarajan A, Mann J, Patton EG. Gaussian vs non-Gaussian turbulence: impact on wind turbine loads. Wind Energy 2016;19(11):1975–89. doi:10.1002/we.1963.

[5] Dhamankar NS, Blaisdell GA, Lyrintzis AS. Overview of turbulent inflow boundary conditions for large-eddy simulations. AIAA J 2017:1–18. doi:10.2514/1.J055528.

[6] Tabor GR, Baba-Ahmadi MH. Inlet conditions for large eddy simulation: a review. Comput Fluids 2010;39(4):553–67. doi:10.1016/j.compfluid.2009.10.007.

[7] Wu X. Inflow turbulence generation methods. Annu Rev Fluid Mech 2017;49(1):23–49. doi:10.1146/annurev-fluid-010816-060322.

[8] Mann J. Spectral velocity tensor in moderately complex terrain. J Wind Eng Ind Aerodyn 2000;88(2–3):153–69. doi:10.1016/S0167-6105(00)00046-5.

[9] Kraichnan RH. Diffusion by a random velocity field. Phys Fluids 1970;13(1):22. doi:10.1063/1.1692799.

[10] Lee S, Lele SK, Moin P. Simulation of spatially evolving turbulence and the applicability of Taylor's hypothesis in compressible flow. Phys Fluids A 1992;4(7):1521–30. doi:10.1063/1.858425.

[11] Druault P, Lardeau S, Bonnet J-P, Coiffet F, Delville J, Lamballais E, et al. Generation of three-dimensional turbulent inlet conditions for large-eddy simulation. AIAA J 2004;42(3):447–56. doi:10.2514/1.3946.

[12] Jarrin N, Benhamadouche S, Laurence D, Prosser R. A synthetic-eddy-method for generating inflow conditions for large-eddy simulations. Int J Heat Fluid Flow 2006;27(4):585–93. doi:10.1016/j.ijheatfluidflow.2006.02.006.

[13] Klein M, Sadiki A, Janicka J. A digital filter based generation of inflow data for spatially developing direct numerical or large eddy simulations. J Comput Phys 2003;186(2):652–65. doi:10.1016/S0021-9991(03)00090-1.

[14] Xie ZT, Castro IP. Efficient generation of inflow conditions for large eddy simulation of street-scale flows. Flow Turbul Combust 2008;81(3):449–70. doi:10.1007/s10494-008-9151-5.

[15] Borgman LE. Ocean wave simulation for engineering design. Technical report. Berkeley, California: Hydraulic Engineering Laboratory; 1967.

[16] Nobach H. Verarbeitung stochastisch abgetasteter signale, Germany: University of Rostock; 1997. Ph.d. thesis.

[17] Lund TS, Wu X, Squires KD. Generation of turbulent inflow data for spatially-developing boundary layer simulations. J Comput Phys 1998;140(2):233–58. doi:10.1006/jcph.1998.5882.

[18] di Mare L, Klein M, Jones WP, Janicka J. Synthetic turbulence inflow conditions for large-eddy simulation. Phys Fluids 2006;18(2):025107. doi:10.1063/1.2130744.

[19] di Mare L, Jones WP. Algebraic and operator methods for generation of inflow data for LES and DNS. In: Proceedings of the fourth international symposium on turbulence and shear flow phenomena (TSFP4). Williamsburg, Virginia; 2005. p. 687–92.

[20] Fathali M, Klein M, Broeckhoven T, Lacor C, Baelmans M. Generation of turbulent inflow and initial conditions based on multi-correlated random fields. Int J Numer Methods Fluids 2008;57(1):93–117. doi:10.1002/fld.1627.

[21] Kempf A, Klein M, Janicka J. Efficient generation of initial- and inflow-conditions for transient turbulent flows in arbitrary geometries. Flow Turbul Combust 2005;74(1):67–84. doi:10.1007/s10494-005-3140-8.

[22] Fru G, Janiga G, Thévenin D. Direct numerical simulation of highly turbulent premixed flames burning methane. In: Kuerten H, editor. ERCOFTAC Series, 15. Eindhoven, The Netherlands: Springer-Verlag; 2011. p. 327–32. ISBN 9789400724815. doi:10.1007/978-94-007-2482-2_52.

[23] Dhamankar NS, Martha CS, Situ Y, Aikens KM, Blaisdell GA, Lyrintzis AS, et al. Digital filter-based turbulent inflow generation for jet aeroacoustics on non-uniform structured grids. In: Proceedings of the 52nd aerospace sciences meeting. Reston, Virginia, USA: American Institute of Aeronautics and Astronautics; 2014. p. 1–35. ISBN 978-1-62410-256-1. doi:10.2514/6.2014-1401.

[24] Allegrini J, Carmeliet J. Evaluation of the filtered noise turbulent inflow generation method. Flow Turbul Combust 2017;98(4):1087–115. doi:10.1007/s10494-016-9798-2.

[25] Kim Y, Castro IP, Xie ZT. Divergence-free turbulence inflow conditions for large-eddy simulations with incompressible flow solvers. Comput Fluids 2013;84:56–68. doi:10.1016/j.compfluid.2013.06.001.

[26] Ewert R. The simulation of slat noise applying stochastic sound sources based on solenoidal digital filters (SDF). In: Proceedings of the Euromech colloquium 467: turbulent flow and noise generation, July 18–20, 2005. Reston, Virigina: American Institute of Aeronautics and Astronautics; 2005. ISBN 978-1-62410-052-9. https://doi.org/10.2514/6.2005-2862.

[27] Smirnov A, Shi S, Celik I. Random flow generation technique for large eddy simulations and particle-dynamics modeling. J Fluids Eng 2001;123(2):359. doi:10.1115/1.1369598.

[28] Jiménez J. Turbulent velocity fluctuations need not be gaussian. J Fluid Mech 1998;376. doi:10.1017/S0022112098002432.

[29] Moser RD, Kim J, Mansour NN. Direct numerical simulation of turbulent channel flow up to reτ=590. Phys Fluids 1999;11(4):943–5. doi:10.1063/1.869966.

[30] Touber E, Sandham ND. Large-eddy simulation of low-frequency unsteadiness in a turbulent shock-induced separation bubble. Theor Comput Fluid Dyn 2009;23(2):79–107. doi:10.1007/s00162-009-0103-z.

[31] Breuer S, Schmidt M. Extended synthetic turbulence inflow generator within a hybrid LES-URANS methodology for the prediction of non-equilibrium wall-bounded flows. Flow Turbul Combust 2015;95(4):669–707. doi:10.1007/s10494-015-9639-8.

[32] Anupindi K, Sandberg RD. Implementation and evaluation of an embedded LES-RANS solver. Flow Turbul Combust 2017;98(3):697–724. doi:10.1007/s10494-016-9787-5.

[33] Okaze T, Mochida A. Cholesky decomposition-based generation of artificial inflow turbulence including scalar fluctuation. Comput Fluids 2017;159:23–32. doi:10.1016/j.compfluid.2017.09.005.

[34] Ihme M, See YC. LES Flamelet modeling of a three-stream MILD combustor: analysis of flame sensitivity to scalar inflow conditions. Proc Combust Inst 2011;33(1):1309–17. doi:10.1016/j.proci.2010.05.019.

[35] Kim Y, Xie ZT, Castro IP. A forward stepwise method of inflow generation for LES. In: AIP conference proceedings, 1376. American Institute of Physics; 2011. p. 134–6. ISBN 9780735409361. doi:10.1063/1.3651856.

[36] Schmidt S, Breuer M. Source term based synthetic turbulence inflow generator for eddy-resolving predictions of an airfoil flow including a laminar separation bubble. Comput Fluids 2017;146:1–22. doi:10.1016/j.compfluid.2016.12.023.

[37] Veloudis I, Yang Z, McGuirk JJ, Page GJ, Spencer A. Novel implementation and assessment of a digital filter based approach for the generation of les inlet conditions. Flow Turbul Combust 2007;79(1):1–24. doi:10.1007/s10494-006-9058-y.

[38] Kempf AM, Wysocki S, Pettit M. An efficient, parallel low-storage implementation of Klein's turbulence generator for LES and DNS. Comput Fluids 2012;60:58–60. doi:10.1016/j.compfluid.2012.02.027.

[39] Smith SW. The scientist & engineer's guide to digital signal processing. California Technical Pub; 1999. ISBN 0-9660176-6-8.

[40] Taylor GI. The spectrum of turbulence. Proc R Soc A: Math Phys Eng Sci 1938;164(919):476–90. doi:10.1098/rspa.1938.0032.

[41] Booton RC. Nonlinear control systems with random inputs. IRE Trans Circuit Theory 1954;1(1):9–18. doi:10.1109/TCT.1954.6373354.

[42] Grigoriu M. Crossings of non-Gaussian translation processes. J Eng Mech 1984;110(4):610–20. doi:10.1061/(ASCE)0733-9399(1984)110:4(610).

[43] Johnson NL. Systems of frequency curves generated by methods of translation. Biometrika 1949;36(1–2):149–76. doi:10.1093/biomet/36.1-2.149.

[44] Gurley KR, Tognarelli MA, Kareem A. Analysis and simulation tools for wind engineering. Probab Eng Mech 1997;12(1):9–31. doi:10.1016/S0266-8920(96)00010-0.

[45] Yamazaki F, Shinozuka M. Digital generation of non-Gaussian stochastic fields. J Eng Mech 1988;114(7):1183–97. doi:10.1061/(ASCE)0733-9399(1988)114:7(1183).

[46] Smallwood DO. Generation of partially coherent stationary time histories with non-Gaussian distributions. Shock and vibration symposium. Monterey, CA, USA: U.S. Department of Energy, Office of Scientific and Technical Information; 1996 http://bit.ly/2bSgqbr.

[47] Bowman KO, Shenton LR. Johnson's system of distributions. In: Encyclopedia of statistical sciences, 4. Hoboken, NJ, USA: John Wiley & Sons, Inc.; 1982. p. 303–14. doi:10.1002/0471667196.ess1309.pub2.

[48] Tuenter HJH. An algorithm to determine the parameters of SU-curves in the Johnson system of probabillity distributions by moment matching. J Stat Comput Simul 2001;70(4):325–47. doi:10.1080/00949650108812126.

[49] Flynn MR. On the moments of the 4-parameter lognormal distribution. Commun Stat – Theory and Methods 2005;34(4):745–51. doi:10.1081/STA-200054397.

[50] OpenFOAM user guide. The open source CFD toolbox. OpenCFD Ltd (ESI Group). 2017. URL http://www.openfoam.com/.

[51] Comte-Bellot G, Corrsin S. Simple eulerian time correlation of full-and narrow-band velocity signals in grid-generated, isotropic turbulence. J Fluid Mech 1971;48(2):273–337. doi:10.1017/S0022112071001599.

[52] Tavoularis S, Corrsin S. Experiments in nearly homogeneous turbulent shear flow with a uniform mean temperature gradient. Part 2. The fine structure. J Fluid Mech 1981;104:349–67. doi:10.1017/S0022112081002942.

[53] Sagaut P. Large eddy simulation for incompressible flows: an introduction. 3rd. Berlin, Heidelberg: Springer; 2006. ISBN 978-3-540-26344-9. doi:10.1007/b137536.

[54] Baggett JS, Jiménez J, Kravchenko AG. Resolution requirements in large-eddy simulation of shear flows. In: Annual research briefs – 1997. Stanford, CA, USA: Stanford University; 1997. p. 51–66.

[55] Issa RI. Solution of the implicitly discretised fluid flow equations by operator-splitting. J Comput Phys 1986;62(1):40–65. doi:10.1016/0021-9991(86)90099-9.

[56] NIST-SEMATECH. NIST/SEMATECH E-handbook of statistical methods. National Institute of Standards and Technology; 2003.

[57] Jiménez J, Wray AA, Saffman PG, Rogallo RS. The structure of intense vorticity in isotropic turbulence. J Fluid Mech 1993;255:65–90. doi:10.1017/S0022112093003393.

[58] Farge M, Schneider K. CVS decomposition of 3D homogeneous turbulence using orthogonal wavelets. Center for turbulence research; 2000. p. 305–17.

[59] Dietzel D, Messig D, Piscaglia F, Montorfano A, Olenik G, Stein OT, et al. Evaluation of scale resolving turbulence generation methods for large eddy simulation of turbulent flows. Comput Fluids 2014;93:116–28. doi:10.1016/j.compfluid.2014.01.013.

[60] Tavoularis S, Corrsin S. Experiments in nearly homogenous turbulent shear flow with a uniform mean temperature gradient. Part 1. J Fluid Mech 1981;104(EM6):311–47. doi:10.1017/S0022112081002930.

[61] Moser R.D.. DNS data for turbulent channel flow. 2007. URL http://bit.ly/2rJeQ3u.

[62] Fréchet MM. Sur quelques points du calcul fonctionnel. Rend Circolo Mat Palermo 1906;22(1):1–72. doi:10.1007/BF03018603.

[63] Eiter T, Mannila H. Computing discrete Fréchet distance. Technical report. Wien: Technische Universität Wien; 1994. doi: 10.1.1.90.937

[64] Eiter T, Mannila H. Distance measures for point sets and their computation. Acta Inform 1997;34(2):109–33. doi:10.1007/s002360050075.

[65] Michaud-Agrawal N, Denning EJ, Woolf TB, Beckstein O. MDAnalysis: a toolkit for the analysis of molecular dynamics simulations. J Comput Chem 2011;32(10):2319–27. doi:10.1002/jcc.21787.

[66] Gowers RJ, Linke M, Barnoud J, Reddy TJE, Melo MN, Seyler SL, et al. MDAnalysis: a Python package for the rapid analysis of molecular dynamics simulations. In: Benthall S, Rostrup S, editors. Proceedings of the 15th Python in science conference; 2016. p. 98–105.

[67] Seyler SL, Kumar A, Thorpe MF, Beckstein O. Path similarity analysis: a method for quantifying macromolecular pathways. PLoS Comput Biol 2015;11(10). doi:10.1371/journal.pcbi.1004568.

[68] Thomas DB, Luk W, Leong PHW, Villasenor JD. Gaussian random number generators. ACM Comput Surv 2007;39(4). doi:10.1145/1287620.1287622.

[69] Marsaglia G, Tsang WW. The ziggurat method for generating random variables. J Geol Soc Lond 2000;5(8):1–7. doi:10.18637/jss.v005.i08.

[70] Eddelbuettel D.. RcppZiggurat: 'Rcpp' integration of different "Ziggurat" normal RNG implementations. 2015.

[71] Leong PHW, Zhang G, Lee D-U, Luk W, Villasenor JD. A comment on the implementation of the ziggurat method. J Stat Softw 2005;12(7):1–4. doi:10.1007/978-1-60327-198-1_26.

[72] Claerbout JF. Multidimensional recursive filters via a helix. Geophysics 1998;63(5):1532–41. doi:10.1190/1.1444449.

[73] Weisstein E.W. Fourier Transform–Gaussian. From *MathWorld–A* Wolfram Web Resource. http://mathworld.wolfram.com/FourierTransformGaussian.html.

[74] Weisstein E.W. Fourier Transform–Exponential Function. From *MathWorld–A* Wolfram Web Resource. http://mathworld.wolfram.com/FourierTransformExponentialFunction.html.

[75] Dickey DA, Fuller WA. Distribution of the estimators for autoregressive time series with a unit root. J Am Stat Assoc 1979;74(366):427. doi:10.2307/2286348.

[76] Grazzini J. Analysis of the emergent properties: stationarity and ergodicity. Jasss 2012;15(2). doi:10.18564/jasss.1929.

[77] O'Neill PL, Nicolaides D, Honnery DR, Soria J. Autocorrelation functions and the determination of integral length with reference to experimental and numerical data. In: Proceedings of the 15th Australasian fluid mechanics conference, 1. Sydney, Australia: The University of Sydney; 2004. p. 1–4.

[78] Welch PD. The use of fast fourier transform for the estimation of power spectra: a method based on time averaging over short, modified periodograms. IEEE Trans Audio Electroacoust 1967;15(2):70–3. doi:10.1109/TAU.1967.1161901.

[79] Cameron PJ. Colour schemes. Technical Note. SRON Netherlands Institute for Space Research; 1982. doi:10.1016/S0304-0208(08)73255-9.

[80] Neidell NS. Deterministic deconvolution operators – 3 point or 4 point? Geophysics 1972;37(6):1039–42. doi:10.1190/1.1440312.

[81] Claerbout JF, Karrenbach M, Balog O. Earth soundings analysis: processing versus inversion; 1992. ISBN 978--0865422100..

Paper - II

EVALUATION OF DIGITAL-FILTER AND FORWARD-STEPWISE SYNTHETIC TURBULENCE GENERATORS WITH LARGE EDDY SIMULATION OF THREE CANONICAL FLOWS, AND VARIOUS MODEL ENHANCEMENTS

Evaluation of digital-filter and forward-stepwise synthetic turbulence generators with large eddy simulation of three canonical flows, and various model enhancements

Kutalmis M. Bercin*, Zheng-Tong Xie, Stephen R. Turnock

Faculty of Engineering and the Environment, University of Southampton, SO17 1BJ, Southampton, the UK

Abstract

Digital-filter-based (DFM) and forward-stepwise-based (FSM) synthetic (turbulence-like) time-series generator classes were conceptualised into five model stages within computational fluid dynamics set-ups. In addition, two new methods enabling DFM-FSM to be seamlessly computed on nonuniformly-discretized boundaries were proposed alongside a new mass-flux correction technique, and two new code practices for computational speedup. Through four DFM-FSM variants representing the majority of capabilities of the classes, each DFM-FSM model stage was explored by controlled studies of extensive-than-the-literature range of input variables and output statistics with large eddy simulation (LES) computations of decaying homogeneous isotropic turbulence, homogeneous shear turbulence and smooth-wall plane channel flow. Moreover, five LES post-solution verification metrics were reviewed and compared via these building-block flows. Among sixty-two observations, the prominent findings were that: [*i*] The traditional 80% turbulent kinetic energy resolution was quantified to be more robust than the modern LES post-verification metrics considered. [*ii*] In the first three nodes, input Reynolds stresses were consistently suppressed, particularly in shear components and lateral directions. Divergence-freeness enforcement was quantified to be the driving factor. [*iii*] Input autocorrelations were suppressed to a more limited extent. Navier-Stokes equation algorithms was deemed to be the cause. [*iv*] Streamwise evolution of Reynolds stresses followed an asymmetric quadratic pattern rather than a monotonic pattern. [*v*] The first DFM almost always produced the highest amplitude resemblances and the shortest adaptation lengths for Reynolds stresses and wall shear stresses. [*vi*] Amplifying input shear stresses reduced amplitude distortions downstream, and shortened adaptation lengths. [*vii*] A parabolic relation was found

* Corresponding author
Email address: kbercin@gmail.com (Kutalmis M. Bercin*)

between input length scale sizes and amplitude/adaptation lengths of Reynolds stresses/wall shear stresses. [*viii*] Seamless nonuniform DFM-FSM and using multiple input length-scale sets did not improve flow to an important extent. [*ix*] Mass-influx corrections significantly improved pressure predictions and reduced computational costs, albeit no impact on velocity-based statistics.

Keywords: inflow turbulence, synthetic turbulence, inlet conditions

1. Introduction

In nature, turbulent flows are ubiquitous; hence, turbulence modelling is essential in industrial and academic engineering applications. Today, the trend in turbulence modelling is towards higher fidelity in tandem with low-cost scalability. Advancements, however, brought new challenges, especially for spatiotemporal-variant inflow boundary condition modelling of convection-dominant flows. As a consequence of chaotic turbulence dynamics, stochastic and/or statistical characterisation of such boundary conditions was found to be arduous, yet rewarding. Therefore, various inflow turbulence generation methods were put forth to date. In this study, the scope is limited from the outset to two groups of *synthetic turbulence generators*: digital filter-based [1], and forward-stepwise-based [2] methods (abbr. DFM and FSM). Thus, the reader is referred to [3, 4, 5] for the categorisation and description of other methods.

Fig. 1 shows an input-output diagram of DFM/FSM. Therein, a random number set and a group of statistics are fused into a new number set by a chain of mathematical operations whose characteristics are determined by the statistics.

The modern DFM was introduced by [1] although earlier similar ideas/methods can be noted in [6, 7]. The authors proposed a three-step frame: [*i*] generating random number sets from the standard Gaussian probability distribution, [*ii*] incorporating arbitrary two-point[1] autocorrelation functions by means of *digital filter*s, and [*iii*] imbedding one-point second-order correlation tensor via a tensor transformation [8] (abbr. the *Lund transformation*). Furthermore, the arbitrary-form autocorrelations in the [*ii*]-step were modelled in Gaussian-form to eliminate the requirement of a root-finding algorithm to obtain filter coefficients in favour of explicit evaluations.

One of the limitations of DFM is that its output (i.e. synthetic time-series) does not include any physical information apart from input statistics. Six studies sought to improve the physical content

[1] In this paper, *number*-point signifies the *number* of *spatial* points utilised in the computation of a statistic.

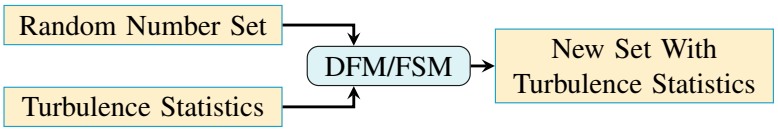

Figure 1: An input-output diagram illustrating the working principle of DFM/FSM. Modified from [9, Fig. 1].

of the output therefrom: [10] studied the viability of arbitrary-form autocorrelation functions in the [*ii*]-step. A linear algebra algorithm was put forward to compute digital-filter coefficients from an autocorrelation function, and the authors [10, p. 10] suggested the algorithm for wall-bounded flows. In a follow-up study, the algorithm was updated to provide computationally cheaper, more robust and capable solution processes [11, p. 687]. In addition, [12, p. 96] unified the [*ii*] and [*iii*] steps to prevent possible distortions of the [*ii*]-step statistics due to the [*iii*]-step, and to input two-point cross-correlations. Later, [2] questioned the use of the Gaussian-form simplification as the most appropriate option for turbulent shear flows, and replaced it with an exponential-form. Also, FSM was derived in the same study as a cheaper equivalent of DFM, and was substituted into the [*ii*]-step's longitudinal direction, hence the first hybrid DFM-FSM. Using this hybrid method, [13] associated [*ii*]-step with a *finite impulse response filter* to make function forms possessing analytical inverse and forward Fourier transforms usable in DFM, e.g. two-sided exponential-form. Lastly, [9] propounded an approach to overcome the impracticability of [10] (e.g. its intricate code implementation) wherein an arbitrary-form correlation function is first curve fitted to a chosen-form continuous function (e.g. a sum of two exponential functions), and then digital-filter coefficients are computed from the curve fit in a similar idea that [10] follows.

Another limitation is that DFM output can only be created on unit-square/cube grids. As the first attempt to generate synthetic time-series on non-uniformly-discretised grids on arbitrary-shaped boundaries, [14] modelled the [*ii*]-step as a digital-filter equivalent diffusion process. Subsequently, a combined method of [14] and [1] was introduced by [15, p. 328] claiming the output generation on non-uniform grids; however, no tangible description of the method was conveyed. DFM on curvilinear grids was enabled by [16] through the use of a one-to-one-mapping between Cartesian and curvilinear grids. Nevertheless, the generation still requires to be performed on Cartesian grids; therefore, the method could not be qualified as a seamless generator of time-series on non-uniform grids. For FSM, on the other hand, the time-series generation on non-uniform grids is possible in theory. To the authors' knowledge, however, no study was utilised or investigated

FSM regarding this.

The third limitation is that DFM/FSM is not divergence free, and their mass flux is not conserved. The consequence of non-solenoidality is reportedly spurious pressure fluctuations [13, p. 1089]. For instance, [17, Fig. 11] observed pressure fluctuations three to six orders of magnitude higher than the benchmark in an incompressible plane channel flow computation. By contrast, the impact of non-solenoidality on velocity fluctuations was reported negligible [14, p. 76], [17, Fig. 11]. To remedy this issue, [18, p. 5] enforced solenoidality upon DFM via a solenoidal digital filter in case for homogeneous isotropic turbulence time-series. Nonetheless, [18, p. 7] made a mere suggestion to utilise [19, p. 3-5]'s transformation method for non-homogeneous anisotropic turbulence without providing its repeatable application on DFM. Likewise, the possibility of using a projection method [20] was merely mentioned by [1, p. 659] and [14, p. 76]. Adopting another perspective, [17] devised a work-around applicable to DFM/FSM that the momentum predictor equation of a pressure-velocity coupling algorithm (i.e. cell nodes) receives time-series instead of inflow boundary conditions of the system of algebraic equations (i.e. boundary face centres), so that solenoidality is enforced. Yet this method did not render DFM/FSM divergence-free in themselves. Regarding mass flux conservation, previous studies did not systematically address its effects. As a rare counter-example, [17, p. 61] maintained that the violation of mass flux conservation causes spurious pressure fluctuations similar to the lack of divergence-freeness, and the authors [17, p. 57] advanced a heuristic correction ensuring time-variant mass flux remains constant.

Eight more studies put forth major developments in a variety of topics: Single-direction contribution of FSM within the hybrid DFM-FSM of [2] was extended to the remaining directions by [21], hence the straight FSM. Compressible flow computations with the hybrid DFM-FSM were systematically enabled by [22, p. 104-105]. In addition, DFM was expanded by [23, p. 677] to be used in hybrid LES-URANS interfaces through a new kinetic energy equation accepting synthetic time-series as its argument. Another hybrid LES-URANS methodology coupled the hybrid DFM-FSM was proposed by [24, p. 703] where RANS-side instantaneous flow quantities are utilised to generate synthetic time-series on LES-side. For spatial-temporal-variant scalar fluctuations without flow-cross-correlations, DFM was first-time used by [25, p. 1313]. Flow-scalar cross-correlations were, however, rendered possible for DFM/FSM by [26, p. 25] who methodically upgraded the $[iii]$-step of DFM. Regarding non-Gaussian statistics, [9] presented a functionality that can reconstruct given one-point spatial-variant skewness-kurtosis pairs into synthetic time-series without changing

its preexisting statistics whereas the method thus far was not tested in CFD. Last but not least, on the *qualitative* grounds that synthetic time-series go through a series of statistical metamorphoses downstream within a CFD domain, [27] described a monotonic optimisation method adjusting input statistics on the fly to carry target statistics to fields of interest downstream.

Arguably, much of the remaining research on DFM/FSM were performance and application improvements transferable across the above-mentioned fundamental studies. For a short list of such studies, the reader is referred to [9, p. 445], and on top of this list, two recent studies can be added: First, [28] designed synthetic time-series as source terms to be able to position DFM/FSM boundaries inside a domain with an arbitrarily oriented fashion. Second, [9, p. 449] offered the *Ziggurat algorithm* as the optimum pseudo-random number sampling approach over the *Box-Muller transform* and *Marsaglia polar method*.

Despite the aforementioned studies, there is a lack of extensive research in five topics that hampers theoretical/practical advancement of DFM/FSM in CFD. First, although stochastic/statistical metamorphoses are *qualitatively* expected in input synthetic time-series that enter and convect through a computational domain, much uncertainty exists as to the extent and causes of these metamorphoses. One implication of the uncertainty is a state that statistics in the field of interest could be different from input statistics at an unknown level. Very little is currently known in the literature due to the lack of abstractions of DFM/FSM phases, isolation of model parameters and *quantification* of their effects and interactions. Therefore, conceptualisation of DFM/FSM phases, and thereafter, controlled tests quantifying and clarifying DFM/FSM uncertainties need to be conducted to build a systematic understanding of how x affects/contributes to y in DFM/FSM.

Second, the existing accounts failed to invent an approach generating synthetic time-series on arbitrarily-discretized arbitrary boundary geometries. Currently, the conventional practices are to perform nearest-neighbour projection [2] or linear interpolation using two-dimensional Delaunay triangulation [13] from unit-square virtual grids, whereon synthetic time-series are created, onto corresponding boundaries. Yet information distortion is not decisively prevented via these practices during the information transfer through non-conformal interfaces. Therein, interpolation errors are somewhat expected to increase overall modelling uncertainties. Moreover, the same accounts did not quantify isolated effects of information transfer processes on synthetic time-series although almost any non-conformity should cause information distortion to a certain extent.

Third, no studies have been found which compare DFM/FSM variants to each other in CFD[2] whereas eight studies examined single variant of DFM or FSM against variants from other turbulence generation method categories: [29, 30, 31, 32, 33, 34, 35, 13, 36] whose assertions will be referred in the following sections accordingly.

In addition, systematic 'building-block' flow explorations of DFM/FSM are lacking (e.g. no DHIT/HST study exists with [2]), which may complicate to identify isolated effects of major turbulence concepts, such as pure shear.

Lastly, research on the subject has been mostly restricted to low-order statistics in their comparative evaluations, and has not touched upon higher-order statistics (e.g. enstrophy) in spite of the fact that theoretical, experimental and computational high-fidelity datasets are adequately available for benchmark flows.

The absence of structured knowledge in these five subjects hinders attempts for theory/practice-oriented improvements within DFM/FSM, decision-makings as to the most apt DFM/FSM variant to the CFD problem in hand, and conveying DFM/FSM benefits to a wider audience. Therefore, the aims of this study are to minimise the aforementioned knowledge gaps through systematic explorations of DFM/FSM via building-block flows with statistics including previously-not-considered measures, and to expand DFM/FSM functionality portfolio in various aspects, e.g. a capability wherein synthetic time-series can be seamlessly generated on nonuniformly-spaced structured boundary grids. To this end, the theory behind DFM/FSM, large eddy simulation, and proposed new capabilities are briefly explained in §2, the methodology is presented in §3, relevant results are shown and discussed in §4, and clear-cut conclusions alongside remaining challenges are given in §5.

2. Theory

2.1. Flow modelling

2.1.1. Physical phenomena

In this study, the scope of physical phenomena is limited to Newtonian single-phase incompressible fluid flows, excluding any thermal, chemical, electromagnetic, and scalar interactions. In this

[2] A comparative non-CFD investigation amongst DFM/FSM variants was performed by [9].

scope, the set of governing equations is the following pointwise conservation equations of mass and momentum in an inertial frame of reference within an external conservative force field [37]:

$$\overline{\nabla \cdot \mathbf{u}} = 0, \qquad \text{in} \quad \Omega \times (0, \mathrm{T}) \tag{1a}$$

$$\overline{\mathbf{u}_t} + \overline{\nabla \cdot (\mathbf{uu})} = -\overline{\nabla \tilde{p}} + \overline{\nu \nabla^2 \mathbf{u}}, \qquad \text{in} \quad \Omega \times (0, \mathrm{T}) \tag{1b}$$

where $\overline{(.)}$ is a linear operator, $\mathbf{u}(\mathbf{x}, t)$ a vector field of velocity [ms^{-1}], $\mathbf{uu}$ a dyadic field of velocity [$\mathrm{m}^2\mathrm{s}^{-2}$], ν the constant kinematic viscosity of the fluid [$\mathrm{m}^2\mathrm{s}^{-1}$], $\tilde{p}(\mathbf{x}, t)$ a scalar field of modified pressure [$\mathrm{m}^2\mathrm{s}^{-2}$], Ω a finite-size fixed-in-space volume [m^3] with bounding surface $\partial\Omega$ [m^2], T an arbitrary instant of time [s], and $\mathbf{u}_t \equiv \partial\mathbf{u}/\partial t$ [ms^{-2}]. The external field term, say $\mathbf{f}$, complements the pressure gradient term when $\mathbf{f}$ is conservative (i.e. $\mathbf{f} = -\nabla f$, f a potential function); thus, the manipulation of $(-\nabla p + \mathbf{f})/\rho = (-\nabla p - \nabla f)/\rho = -\nabla \tilde{p}$ was performed, where ρ is the uniform fluid density [kgm^{-3}]. In intermediate steps of an actual computation of Eq. 1b, the continuity constraint remains non-zero; therefore, $\nabla \cdot (\mathbf{uu})$ was not reduced to $(\mathbf{u} \cdot \nabla)\mathbf{u}$ by the incompressibility assumption [38]. The computations of Eq. 1 were carried out via OpenFOAM®v1712 [39] software, where *finite volume method* discretisations are performed on the integral form of Eq. 1. In what follows, the majority of the reported model equations was reverse engineered from the software.

2.1.2. Turbulence modelling

In this study, large eddy simulation (LES) was chosen as the mathematical approach to compute Eq. 1 in order to trade off computational costs for desired-fidelity flow modelling. In LES, a time/frequency-domain low-pass filter is applied onto Eq. 1 as a whole in order to derive a filtered set of equations, so that a quantity larger than the filter cutoff (i.e. over-filter scales) is explicitly computed, and smaller quantities (i.e. sub-filter scales) are treated in another cheaper-to-run way (modelling or ignoring). Conventionally, the operator $\overline{(.)}$ in Eq. 1 is a linear, homogeneous, time-invariant, spatial filter, which inherently produces a temporal filtering effect on Eq. 1 due to the natural associations between temporal and spatial scales [40, p. 13, 261]. This results in spatially-filtered Eq. 1 wherein $\overline{\mathbf{uu}}$ is unknown.

Furthermore, the *implicitly filtered* variant of LES was used [41, p. 381] (abbr. IFLES).[3] IFLES

[3] It should be noted that IFLES is not 'implicit LES' (ILES) wherein sub-filter scales are not modelled, and their effects are expected to happen solely due to discretisations. In IFLES, however, a sub-filter scale model is in use alongside implicit filtering. The use of a model may be questionable. Numerical dissipation due to certain

aims to prevent computational (e.g. extra filtering) and theoretical complexities (e.g. boundary commutation issues due to the use of an explicit filter) associated with LES [43, p. 476-477]. To this end, over-filter and sub-filter scales are not separated by means of an explicit filter, but implicit actions. The rationale of IFLES is justified by two notions: (*i*) wavenumbers higher than the grid Nyquist wavenumber[4] cannot be captured and become indistinguishable from lower wavenumbers [44, p. 88], and (*ii*) discretisations introduce errors, mainly on resolved high wavenumbers, similar in size and effect to dissipative actions of sub-filter scale models [40, p. 331]. Both automatically determines the highest resolvable wavenumbers. For this reason, an explicit filter is presumed to be replaced by this existing elimination mechanism.

Although it is a widely held view in the *finite volume method* literature that an equivalence between a volume-average of a variable (i.e. implicit filtering) and a top-hat kernel convolution of the same variable (i.e. explicit filtering) exists (e.g. [45, p. 1308], [41, p. 381]), few such as [46, p. 3849] [47, p. 1] argued that the relation is actually an ill-defined approximation. In contrary, three layers form an effective filter [40, p. 331]: discretisations of (*i*) domain, and (*ii*) equations, and (*iii*) a closure model, each of which filters out certain scales. In view of hard-to-measure contributions from each layer, the effective filter cut-off scale dissociates from the grid size and becomes ambiguous for a priori identification. In addition, discretisation errors and sub-filter scale modelling uncertainty become functions of the grid size, and further, interact each other [48, p. 131]. As an implication, these notions preclude grid-independency in IFLES[5]; hence, the quality quantifications of IFLES computations need to be carried out *a posteriori* by other means as shown in §2.2.

The closure of Eq. 1 is delivered as follows. First, the unknown $\overline{\mathbf{u}\mathbf{u}}$ is re-expressed in a more modellable form by the Reynolds decomposition, i.e. $\mathbf{u}\equiv\overline{\mathbf{u}}+\mathbf{u}'$, and [49]'s triple decomposition, which ensures no second filtering is required unlike the double decomposition [40, p. 49-50]:

$$\overline{\mathbf{u}\mathbf{u}} = \underbrace{\overline{\mathbf{u}'\,\overline{\mathbf{u}}} + \overline{\overline{\mathbf{u}}\,\mathbf{u}'}}_{1} + \underbrace{\overline{\mathbf{u}'\mathbf{u}'}}_{2} + \underbrace{\left(\overline{\overline{\mathbf{u}}\,\overline{\mathbf{u}}} - \overline{\mathbf{u}}\,\overline{\mathbf{u}}\right)}_{3} + \overline{\mathbf{u}}\,\overline{\mathbf{u}} \qquad \text{with} \quad \overline{\mathbf{u}'\,\overline{\mathbf{u}}} \neq \overline{\overline{\mathbf{u}}\,\mathbf{u}'} \tag{2}$$

algorithms was observed that they can shape flow development to a similar level that a sub-filter scale model of explicit LES can do [42, p. 24]. Therefore, a model's augmentation of dissipation may be redundant. In this study, however, no exclusive algorithms were utilised, and it was assumed that the use of a sub-filter scale model could be acceptable as long as an IFLES computation is thoroughly verified or validated.

[4] For the smallest resolved one-dimensional structure of size Δ, the maximum grid spacing could be 0.5Δ due to the Nyquist theorem [40, p. 10].

[5] Several cases were reported where grid refinement even deteriorated computation outcomes [47, p. 1].

where the under-braced terms are tensors of cross-stress, Reynolds decomposed sub-filter scale stress, and Leonard stress, respectively. The first and third terms are not Galilean-invariant [50, p. 64], thereby yielding different results for the same terms in different inertial frames [51, p. 61].[6] As a consequence, the two terms are often omitted. The modelling practice is ultimately designated on: $(\overline{\mathbf{u}}\,\overline{\mathbf{u}}\text{-}\overline{\mathbf{u}}\,\overline{\mathbf{u}})\approx\overline{\mathbf{u}'\mathbf{u}'}$.

Second, inter-scale interactions between over- and sub-filter scales are deemed to be *functional* rather than *structural*. The former concept purports that inter-scale energy transfer is an adequate ground to model inter-scale interactions and over-filter scale evolution [40, p. 104]. For this purpose, a modelled energy sink is applied to over-filter scales by leaving the dynamic characteristics of sub-filter undefined. Here, this was achieved by adopting the *Boussinesq eddy-viscosity hypothesis*: $\overline{\mathbf{u}'\mathbf{u}'}\approx\underline{\underline{\mathbf{B}}}\equiv 0.\dot{6}\,k_{\mathrm{sfs}}\,\underline{\underline{\mathbf{I}}}\text{-}\nu_t\underline{\underline{\mathbf{S}}}_d$, where $\underline{\underline{\mathbf{B}}}$ is a symmetric tensor field [$\mathrm{m^2s^{-2}}$], k_{sfs} the modelled sub-filter scale kinetic energy field per unit mass [$\mathrm{m^2s^{-2}}$], $\underline{\underline{\mathbf{I}}}$ an identity tensor field [-], $\underline{\underline{\mathbf{S}}}_d=\{\underline{\underline{\mathbf{S}}}_t\text{-}3^{-1}\,\mathrm{Tr}(\underline{\underline{\mathbf{S}}}_t)\underline{\underline{\mathbf{I}}}\}$ [$\mathrm{s^{-1}}$] the deviatoric part of the twice strain rate tensor field, i.e. $\underline{\underline{\mathbf{S}}}_t=2\underline{\underline{\mathbf{S}}}=2\{0.5(\nabla\mathbf{u}+(\nabla\mathbf{u})^{\intercal})\}$ [$\mathrm{s^{-1}}$], $\mathrm{Tr}(\cdot)\equiv\sum_{i=1}^{n}(\cdot)_{ii}$ the trace of a tensor, and $\{\nu_t\}_{\{\nu_t\geq 0\}}$ the modelled eddy-viscosity scalar field [$\mathrm{m^2s^{-1}}$]. In this work, k_{sfs} and ν_t were modelled by using the *Smagorinsky model* [53] equipped either with the *van Driest wall-damping function* [54] or a Lagrangian-averaging dynamic procedure [55], depending on the case in question.

The *Smagorinsky model* evaluates ν_t and k_{sfs} as shown below:

$$\nu_t = C_k\,\Delta\,k_{\mathrm{sfs}}^{0.5} \qquad\qquad k_{\mathrm{sfs}} = \left\{\left(\text{-}b+(b^2+4ac)^{0.5}\right)(2a)^{\text{-}1}\right\}^2 \tag{3}$$

where C_k is a model constant [-], $\{\Delta\}_{\{|\Delta|=\mathrm{N}\}}=m\sqrt[3]{V}$ a scalar field of the domain-layer component of the effective (first) filter [m], m a heuristic coefficient with a default value of 1 [-], $\{V\}_{\{V\geq 0\}}$ the corresponding scalar field of the time-invariant computational cell volume [$\mathrm{m^3}$], N the number of cells in the computational domain [-], $a\equiv C_e\,\Delta^{\text{-}1}$ a quadratic coefficient field [-], C_e another model constant [-], $b\equiv 0.\dot{6}\,\mathrm{Tr}(\underline{\underline{\mathbf{S}}})$ a linear coefficient field [-], $c\equiv 2C_k\Delta(\mathrm{dev}(\underline{\underline{\mathbf{S}}}):\underline{\underline{\mathbf{S}}})$ a free term field [-], and $\{:\}$ the double inner two-tensor product operator, i.e. $\{\underline{\underline{\mathbf{A}}}:\underline{\underline{\mathbf{B}}}\}\equiv\sum_{i=1}^{n}\sum_{j=1}^{m}A_{ij}B_{ij}$.

The *van Driest function* was applied onto Δ in order to limit ν_t towards walls, so that eddy-formation-preventing dissipation and solver instability can be avoided [37, p. 78]. The main reason

[6] For instance, Härtel and Kleiser (1997) [52, p. 103] demonstrated that filter-independent sub-filter scale energy transfer is not possible with Galilean-variance.

of its usage herein is, however, to ensure consistent comparisons with the literature while a number of development proposals were available, such as in [56, p. 26]. Its formulation with a minimum switch that was introduced by [50, p. 124, 260] reads:

$$\Delta = \min\left(\Delta,\, \kappa C_s^{-1}\,|\mathbf{d}_{nw}|\left\{(1+\epsilon) - \exp[\,|\mathbf{d}_{nw}|\,(y^*\mathrm{A}^+)^{-1}]\right\}\right) \tag{4a}$$

$$y^* = \nu_w\left\{(\nu_w + \nu_{\mathrm{sfs,w}})\,|\mathbf{n}_f \cdot (\nabla \mathbf{u}_w)_f| + \epsilon_s\right\}^{-0.5} \tag{4b}$$

where κ=0.41 is the von Kármán constant, C_s the Smagorinsky constant, $|\mathbf{d}_{nw}|$ the node-wall-normal distance within y^+<500 [m], ϵ the machine epsilon [-], y^*=ϵ^{-1} a scalar field with its boundary condition defined in Eq. 4b [m], A^+=26.0 a model coefficient [-], $\{\cdot\}_w$ wall boundary fields, $\mathbf{n}_f$ surface normal vector, and ϵ_s the minimum machine floating point number.

With the Lagrangian-averaging dynamic procedure, the forms of ν_t and k_{sfs} become:

$$\nu_t = \mathfrak{J}_{\mathrm{LM}}(\mathfrak{J}_{\mathrm{MM}})^{-1}\Delta^2(\underline{\underline{\mathbf{S}}}_d{:}\underline{\underline{\mathbf{S}}}_d)^{0.5} \qquad\qquad k_{\mathrm{sfs}}{=}(2\,\mathfrak{J}_{\mathrm{LM}}\,\mathfrak{J}_{\mathrm{MM}}^{-1})^{2/3}\,C_a^{-2/3}\,\Delta^2\,|\underline{\underline{\mathbf{S}}}_d|^2 \tag{5}$$

where C_a is a model constant [-], $\mathfrak{J}_{\mathrm{LM}}$ with $\mathfrak{J}_{\mathrm{MM}}$ scalar fields [$\mathrm{m^4s^{-4}}$] defining $C_s^2\,(\mathbf{x},t){=}\mathfrak{J}_{\mathrm{LM}}\mathfrak{J}_{\mathrm{MM}}^{-1}$ [55, Eq. 3.5] and being solved from the two transport equations shown below [55, Eq. 3.8-3.9]:

$$\partial_t\mathfrak{J}_{\mathrm{LM}} + \nabla\cdot(\mathbf{u}\,\mathfrak{J}_{\mathrm{LM}}) = \mathrm{T}^{-1}((\underline{\underline{\mathbf{L}}}{:}\underline{\underline{\mathbf{M}}}) - \mathfrak{J}_{\mathrm{LM}}) \tag{6a}$$

$$\partial_t\mathfrak{J}_{\mathrm{MM}} + \nabla\cdot(\mathbf{u}\,\mathfrak{J}_{\mathrm{MM}}) = \mathrm{T}^{-1}((\underline{\underline{\mathbf{M}}}{:}\underline{\underline{\mathbf{M}}}) - \mathfrak{J}_{\mathrm{MM}}) \tag{6b}$$

where $\partial_t\{\cdot\}$ is a partial temporal derivative operator [$\mathrm{s^{-1}}$], $\mathrm{T}{=}(\theta\Delta)^{-1}(\mathfrak{J}_{\mathrm{LM}}\mathfrak{J}_{\mathrm{MM}})^{-0.125}$ a Lagrangian averaging time scale [s], θ a heuristic coefficient [$\mathrm{m^{-2}}$] with a suggested value of 1.5 [55, p. 363] that ensures a time-lag for Lagrangian autocorrelation functions of $(\underline{\underline{\mathbf{L}}}{:}\underline{\underline{\mathbf{M}}})$ and $(\underline{\underline{\mathbf{M}}}{:}\underline{\underline{\mathbf{M}}})$ reducing below e^{-1}-lag, $\underline{\underline{\mathbf{L}}}{=}\{\underline{\underline{\mathbf{Q}}}{-}3^{-1}\,\mathrm{Tr}(\underline{\underline{\mathbf{Q}}})\underline{\underline{\mathbf{I}}}\}$ a symmetric tensor field with $\underline{\underline{\mathbf{Q}}}{=}\{\mathfrak{F}[\mathbf{u}^2]{-}(\mathfrak{F}[\mathbf{u}])^2\}$ [$\mathrm{m^2s^{-2}}$], $\underline{\underline{\mathbf{M}}}{=}\,2\,\Delta^2\,\{\mathfrak{F}[(\underline{\underline{\mathbf{S}}}_d{:}\underline{\underline{\mathbf{S}}}_d)\underline{\underline{\mathbf{S}}}_d]{-}4\,(\underline{\underline{\mathbf{S}}}_{\mathfrak{f}d}{:}\underline{\underline{\mathbf{S}}}_{\mathfrak{f}d})\underline{\underline{\mathbf{S}}}_{\mathfrak{f}d}\}$ another symmetric tensor field [$\mathrm{m^2s^{-2}}$], $\underline{\underline{\mathbf{S}}}_{\mathfrak{f}d}$ an equivalent of $\underline{\underline{\mathbf{S}}}_d$ applied on $\mathfrak{F}[\mathbf{u}]$ instead of $\mathbf{u}$, and $\mathfrak{F}[\cdot]$ the second (explicit) filter operator whose formulation is:

$$\mathfrak{F}[\phi] = \left(\sum\nolimits_f \phi_f A_f\right)\left(\sum\nolimits_f A_f\right)^{-1} \tag{7}$$

where f stands for a cell face, ϕ an arbitrary field, ϕ_f the corresponding field interpolated from the cell centre to one of its faces, A_f face area [$\mathrm{m^2}$], and $\mathfrak{F}[\phi]$ the top-hat filtered field. It should be

highlighted that although the aforestated derivations in the dynamic procedure were hinged upon the cut-off scale size of 2Δ in the second filter [55, p. 354], the filter radius of Eq. 7 is smaller than 2Δ in the software to some extent. The difference in theory and practice was, however, presumed to be ineffective on outcomes by the academic community, and the opposite premise was not investigated to date.

2.1.3. Inflow modelling

2.1.3.1. Digital-filter-based and forward-stepwise-based synthetic time-series generators[7]

DFM and FSM create spatiotemporal-variant fields of Reynolds-decomposed velocity (or scalar) fluctuations, $\{u_i'(\mathbf{x},t)\in\mathbb{Q}\}_{\{i\in\mathbb{N}:\,i\in[1,3];\,t>0\}}$, which do not directly stem from governing equations of fluid motion. As illustrated in Fig. 2, both methods can be conceptualized four independent stages.

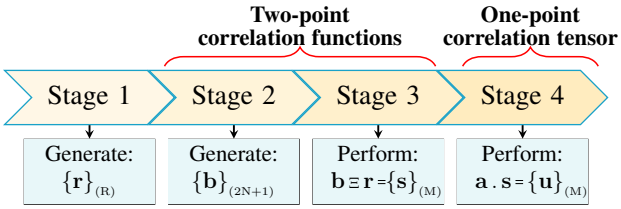

Figure 2: An illustration of DFM/FSM stages in case of a one-dimensional field. Modified from [9, Fig. 2].

In the first stage, a set of random numbers are generated: $\{\mathrm{r}\}_{\{|\mathrm{r}|=\mathrm{R};\ \mathrm{k},\mathrm{j}\in\mathbb{N}:\,1\le\mathrm{k}+\mathrm{j}\le\mathrm{R}\}}$, which follows the probability density function of zero-mean ($\mathrm{R}^{-1}\sum_{\mathrm{k}=1}^{\mathrm{R}}\mathrm{r_k}=0$), unit-variance ($\mathrm{R}^{-1}\sum_{\mathrm{k}=1}^{\mathrm{R}}\mathrm{r_k^2}=1$), independent ($\mathrm{R}^{-1}\sum_{\mathrm{k}=1}^{\mathrm{R}}\mathrm{r_k r_j}=0$ for $\mathrm{k}\neq\mathrm{j}$) Gaussian white-noise.[8]

The second stage is the generation of a number set, {b}, representing two-point correlation functions. In DFM, the set is evaluated through the following relation between {b} and an arbitrary autocorrelation function, ρ [1, p. 657]:

$$\rho(\mathrm{q},\mathrm{p})=\underbrace{\frac{\overline{u_\mathrm{p}'u_{\mathrm{p+q}}'}}{\overline{u_\mathrm{p}'u_\mathrm{p}'}}}_{\text{known}}=\underbrace{\frac{\sum_{\mathrm{j}=-\mathrm{N}+\mathrm{q}}^{\mathrm{N}}\mathrm{b_j b_{j-q}}}{\sum_{\mathrm{j}=-\mathrm{N}}^{\mathrm{N}}\mathrm{b_j^2}}}_{\text{unknown}}\tag{8}$$

[7] This section is an extended paraphrasing of [9, §2].

[8] *Mersenne Twister* pseudo-random number generator [57] and *Marsaglia polar method* [58] for Gaussian PDF sampling were used.

where $\{\mathrm{N}\}_{\{|\mathrm{N}|\in\mathbb{N}:\mathrm{N}>0\}}$ is the support of a filter, $\{\mathrm{b}\}_{\{|\mathrm{b}|=2\mathrm{N}+1:\mathrm{b}\in\mathbb{Q}\}}$ a set of the filter coefficients, $\mathrm{q}_{\{\mathrm{q}\in\mathbb{N}:\mathrm{q}\geq 0\}}$ the lag number, and p the maximum lag number. The different variants of DFM are largely due to alternative propositions to invert Eq. 8. In FSM, on the other hand, {b} is defined as a set of integral length-scales adjusted by some empirical constants and integration limits.

Within the third stage, {b} is inserted into {r}. To this purpose, FSM utilises element-wise multiplication whilst DFM convolution summation as noted below:

$$s_{\mathrm{k}} \equiv \mathrm{F_N}\left(\mathrm{k}\right) = \sum_{\mathrm{j}=-\mathrm{N}}^{\mathrm{N}} \mathrm{b_j r_{k+j}} \tag{9}$$

where $\{s\}_{\{|s|=\mathrm{M}:s\in\mathbb{Q}\}}$ is a set of digital-filtered numbers, and $\mathrm{F_N}$ a non-recursive, linear, discrete filter operator carrying out a convolution summation on two finite sequences. For $\mathrm{F_N}$, the two sets should completely overlap; thus, yielding a subset of the conventional *full* convolution summation. The size of the sets can be linked as: R-(2N+1)+1=M.

In the fourth stage, a given one-point correlation tensor is embed into $\{s\}$ by the *Lund transformation* [8, p. 255], $u_i'\left(\mathbf{x},t\right) = a_{ij}(\mathbf{x})\ s^i(\mathbf{x},t)$ where a_{ij} is a second-order amplitude tensor:

$$a_{ij} = \begin{bmatrix} (R_{11})^{0.5} & 0 & 0 \\ R_{21}/a_{11} & (R_{22}-a_{21}^2)^{0.5} & 0 \\ R_{31}/a_{11} & (R_{32}-a_{21}a_{31})/a_{22} & (R_{33}-a_{31}^2-a_{32}^2)^{0.5} \end{bmatrix} \tag{10}$$

where R_{ij} is a known one-point correlation tensor in units of variance. It should be noted that a_{ij} is conventionally spatial-variant and temporal-invariant whereas there is no theoretical objection to its temporal variation. Moreover, the members of a_{ij} need to be constrained in three ways to avoid domain errors: *(i)* R_{11}>0, *(ii)* $R_{11}R_{22}$-R_{21}^2>0, and *(iii)* R_{33}-$R_{31}^2R_{11}^{-1}$-(R_{32}-$R_{21}R_{31}\{R_{11}(R_{11}R_{22}$ -$R_{21}^2)\}^{-1}$)$^2\geq$0.

Klein et al.'s method - DFM

In this variant, the right-hand side of Eq. 8 is presumed to be a Gaussian-form function of integral length-scales [1, p. 657-658]. For a computational grid of cubic cells with constant grid size in all

directions, $\{\Delta_i\}_{\{i\in[1,3]\}}$, the approximation to Eq. 8 can be written in its discrete-form as follows:

$$\rho \approx \exp\left(-\frac{\pi}{4}\,\frac{(m_i\,\Delta_i)^2}{(n_i\,\Delta_i)^2}\right) = \exp\left(-\frac{\pi}{4}\,\frac{m_i^2}{n_i^2}\right) \tag{11}$$

where m is the rectilinear distance of a node to the zero-lag correlation node, and n the length-scale size, which of both are in grid spacing units. Correspondingly, a closed-form expression for $\{\mathrm{b}\}$ was derived by [1, p. 658]:

$$\{\mathrm{b}\}_i \approx \widetilde{\{\mathrm{b}\}}_i \left(\sum_{\mathrm{j}\,=\,-\mathrm{N}}^{\mathrm{N}} \widetilde{\mathrm{b}}_{\mathrm{j}}^2\right)^{-0.5} \quad \text{as} \quad \widetilde{\{\mathrm{b}\}}_i = \exp\left(-\frac{\pi}{2}\,\frac{m_i^2}{n_i^2}\right) \tag{12}$$

Two constraints to the approximation validity were stated: (i) the range of length-scales is limited to $2{\leq}n_i{\leq}100$, and (ii) the minimum size of a filter support is two times a given scale size, $\mathrm{N}_i \geq 2n_i$.

Custom method - DFM

Within this variant [9], firstly, a given arbitrary-form correlation function is curve fitted to a more generic yet similar continuous function. In subsequent, Eq. 8 is numerically inverted based upon the obtained curve-fit function. For the set of benchmark flows in this study, the following expression was put forth as the most suitable function form:

$$\{\mathrm{b}\} = \mathscr{R}\,[\rho] = \mathscr{R}\,\left[\mathscr{C}\,\{a\exp(-b\,x) + c\exp(-d\,x)\}\right] \tag{13}$$

where $\mathscr{R}$ denotes a root-finding algorithm, $\mathscr{C}$ a curve-fit algorithm, and $\{a, b, c, d\}_{\{\forall\in\mathbb{Q}\}}$ are curve-fit parameters. In this study, filter supports were sized to the point where correlation functions drop below few percent of their zero-lag value.

Xie and Castro's method - Hybrid DFM-FSM

For DFM part of this variant, the right-hand side of Eq. 8 is an exponential-form function [2, p. 454]:

$$\rho \approx \exp\left(-c\,\frac{\pi}{2}\,\frac{|m_i|}{n_i}\right) \quad \text{leading to} \quad \widetilde{\{\mathrm{b}\}}_i \approx \exp\left(-c\,\pi\,\frac{|m_i|}{n_i}\right) \tag{14}$$

where c is a constant which is tuned to 0.5 for the current benchmark flows [9, p. 446]. For FSM part [2, p. 456], streamwise integral length-scales are embedded, as shown below, through a

temporal-correlation of two planes of $\{s^i\}$, which are created at subsequent time-steps:

$$s^{i\Psi}\left(y,z,t{+}\Delta_t\right) = s^{i\Psi}\left(y,z,t\right)\exp\left(\text{-}c\,\frac{\pi}{2}\,\frac{\Delta_t}{\mathrm{T}}\right) + s^{i\psi}(y,z,t{+}\Delta_t)\left\{1\text{-}\exp\left(\text{-}c\,\pi\,\frac{\Delta_t}{\mathrm{T}}\right)\right\}^{0.5} \tag{15}$$

where $\{s^{i\Psi}\}$ is a temporal slice of $\{s^i\}$ comprising of transverse length-scales $\{\mathrm{L}_\alpha\}_{\{\alpha\in\{y,z\}\}}$ at
240 an instant t, $\{s^{i\psi}\}$ an auxiliary temporal slice created by a new set of random numbers in the same manner to $\{s^{i\Psi}\}$, T streamwise Lagrangian time-scale evaluated by means of *Taylor's frozen turbulence hypothesis* [59].[9]

Kim et al.'s method - FSM

In this method, the use of convolution summations from DFM are entirely discarded [21, p. 135]. Accordingly, the following set of equations, which can be computed in any order, depicts the method:

$$s^i_y\left(t,j{+}1,k\right) = s^i_y\left(t,j,k\right)\exp\left(\text{-}\frac{c_y}{n_y}\right) + \mathrm{r}\left(t,j,k\right)\left\{1\text{-}\exp\left(\text{-}\frac{2c_y}{n_y}\right)\right\}^{0.5} \tag{16a}$$

$$s^i_{yz}\left(t,j,k{+}1\right) = s^i_{yz}\left(t,j,k\right)\exp\left(\text{-}\frac{c_z}{n_z}\right) + s^i_y\left(t,j,k\right)\left\{1\text{-}\exp\left(\text{-}\frac{2c_z}{n_z}\right)\right\}^{0.5} \tag{16b}$$

$$s^i_{yzx}\left(t{+}1,j,k\right) = s^i_{yzx}\left(t,j,k\right)\exp\left(\text{-}\frac{c_x}{n_x}\right) + s^i_{yz}\left(t,j,k\right)\left\{1\text{-}\exp\left(\text{-}\frac{2c_x}{n_x}\right)\right\}^{0.5} \tag{16c}$$

where $\{\mathrm{r}\}$ is *a* random number set at time t, and $\{c_i(\mathbf{x})\}_{\{i\in\{x,y,z\}\}}$ a constant set to weigh $\{n_i\}$.

2.1.3.2. DFM on non-uniform grids

For DFM, the generation of synthetic time-series on non-uniform grids was attempted with the help of two concepts: (i) the Fourier transform of the discrete convolution and (ii) non-equispaced discrete Fourier transform (abbr. N-DFT), which is an arbitrary-node generalisation of DFT [60, p. 1]. In the proposed method, the frequency domain information obtained by the first concept on a uniform grid is converted into a spatial domain information on a non-uniform grid via the second concept. First, the convolution summation of Eq. 9 is expressed in the frequency domain [61, p. 39]:

$$\{s\} \equiv \mathscr{F}^{\text{-}1}[\![\mathscr{F}[\![\mathrm{b}]\!] \circ \mathscr{F}[\![\mathrm{r}]\!]]\!] \tag{17}$$

[9] *Taylor's frozen turbulence hypothesis* assumes that: $\mathrm{L}_x{=}\mathrm{U}_x\,\mathrm{T}_l$, where T_l is a streamwise Lagrangian time-scale, U_x mean flow speed in the same direction, and L_x the corresponding streamwise integral length-scale.

where $\mathscr{F}[\![\cdot]\!]$ is a DFT operator, $\mathscr{F}^{-1}[\![\cdot]\!]$ its inverse, and $\circ$ the Hadamard operator for complex number pairs (i.e. element-wise multiplication). Both Eq. 9 and 17 are, however, by definition delimited to uniform grids; thus, the output sets can only contain equally-spaced samples.

Second, $\mathscr{F}^{-1}[\![\cdot]\!]$ is switched to an N-DFT operator, $\mathscr{G}[\![\cdot]\!]$, so that Eq. 17 becomes [62, p. 5]:

$$\{\mathfrak{s}\} \equiv \mathscr{G}[\![\mathscr{F}[\![\mathrm{b}]\!] \circ \mathscr{F}[\![\mathrm{r}]\!]]\!] \qquad \text{with} \quad \mathscr{G}(\{\mathbf{x}\}_{\mathrm{j}})[\![\cdot]\!] \equiv \sum_{\boldsymbol{\kappa}\in\{I_{\boldsymbol{N}}\}} [\![\cdot]\!]_{\boldsymbol{\kappa}} \exp\left(-2\pi i \boldsymbol{\kappa}\{\mathbf{x}\}_{\mathrm{j}}\right) \tag{18}$$

where $\{\mathfrak{s}\}_{\{|\mathfrak{s}|=\mathrm{M}\,:\,\mathfrak{s}\in\mathbb{Q}\}}$ is a set digitally filtered on arbitrarily-positioned nodes, $\{\mathbf{x}\}_{\{\mathbf{x}\in\mathbb{R}^d\,:\,d\in[1,3];-0.5\leq x_d<0.5\}}$ the normalised-shifted positions of the nodes[10] in the d^{th}-direction [-], $\{\mathrm{j}\}_{\{\mathrm{j}\in\mathbb{N}^d\,:\,0\leq \mathrm{j}_d<|\{\mathbf{x}\}_d|\}}$ an index set, $\{I_{\boldsymbol{N}}\}_{\{\boldsymbol{\kappa}\in\mathbb{Z}^d\,:\,-0.5N_d\leq\kappa_d\leq 0.5N_d\}}$ a set of spatial frequencies $\boldsymbol{\kappa}$, and $\boldsymbol{N}_{\{N_d\in 2\mathbb{N}\}}$ the (always even) filter support sizes in each direction.

Further, the computational complexity of N-DFT is reduced through [60]'s non-equispaced fast Fourier transform (abbr. N-FFT) algorithm implemented into an open-software library, NFFT 3.0 [62]. N-FFT is the conventional FFT algorithm [63] wrapped with a window-function-based approximation scheme involving truncations in the spatial and frequency domains and oversampling. The approximation leads to a systematic error that can be controlled through three parameters: an oversampling factor, $\sigma_{\{\sigma\in\mathbb{Q}\,:\,\sigma>1.0\}}$, a window function truncation parameter, $m_{\{m\in\mathbb{N}\}}$, and the window function type which should be well localised both in the spatial and frequency domains. For fixed settings, the approximation error exponentially decays with m [60, p. 19], and can be reduced down to the order of machine precision [60, p. 3]. The complexity of FFT is, however, increased from $\mathcal{O}(\mathfrak{N}\log(\mathfrak{N}))$ to $\mathcal{O}(\mathfrak{n}+\log(\mathfrak{n})+m^d\mathrm{M})$, where $\mathfrak{N}=\Pi_{i=1}^{d}\mathrm{N}_i$ is the total FFT length, $\mathrm{N}_{i\{\mathrm{N}_i\in 2\mathbb{N}\}}$ the FFT length in the i^{th}-direction, $\mathfrak{n}=\Pi_{i=1}^{d}\mathrm{n}_i$ the total N-FFT length, $\mathrm{n}_i=\sigma\mathrm{N}_{i\{\mathrm{n}_i\in 2\mathbb{N}\}}$ the oversampled FFT length in the same direction, and $\mathrm{M}_{\{\mathrm{M}\in\mathbb{N}\}}$ the number of arbitrarily-positioned nodes.

For the usage of N-FFT, four points may need to be highlighted: (*i*) the forward N-FFT definition is the opposite of that of the forward FFT wherein transformations are from the spatial to frequency domain, (*ii*) the zero-frequency component of N-FFT output is centred in spectra, (*iii*) N-FFT output is not normalised; therefore, it should be scaled by the number of nodes, and (*iv*) the imaginary part of complex-valued N-FFT output is ultimately dropped while the phase information is random. Apart from the above, N-FFT is thoroughly explained in [60, p. 15-20]

[10] $\{x_d\}=\{\mathfrak{r}_d\}\mathfrak{X}_{\max}^{-1}-0.5$ where $\{x_d\}$ is a set of normalised-shifted node positions in the d^{th}-direction [-], $\{\mathfrak{r}_d\}$ a set of absolute node positions in the same direction [m], and $\mathfrak{X}_{\max}$ the maximum absolute position within all directions.

and [62, p. 6-10].

2.1.3.3. FSM on non-uniform grids

Although the published FSM formulations, i.e. [2, p. 456] and [21, p. 135], have not been described in consideration of non-uniform grids, FSM is inherently not limited to uniform grids. Therefore, no major change was necessary for its generalisation.

The new approach merely involves a modification within the arguments of the two exponential functions in Eq. 16. Therein, the parameters non-dimensionalised with a constant grid size were re-dimensionalised. As a result, the arguments became $\exp(\text{-}c_d\, l_{id}\, L_d^{\text{-}1})$ and $\exp(\text{-}2\, c_d\, l_{id}\, L_d^{\text{-}1})$, respectively, where $c_{d\{c_d\in\mathbb{Q}\}}$ is a weighting constant in the d^{th}-direction [-], $l_{id\{l_{id}\in\mathbb{Q}\}}$ the absolute distance between the i^{th} and $(i\text{-}1)^{\text{th}}$ nodes (or the one-dimensional grid-size belongs to the i^{th} node) in the same direction [m], and $L_{d\{L_d\in\mathbb{Q}\}}$ the corresponding integral length scale [m].

The verifications of Eq. 16, which were given in [2, Eq. 15], were repeated with the new arguments as follows:

$$\overline{\Psi_0\,\Psi_k} = \overline{\Psi_0\left\{\Psi_{k\text{-}1}\exp\left(\text{-}c\,\frac{l_k}{L}\right)+\psi_{k\text{-}1}\left[1\text{-}\exp\left(\text{-}c\frac{l_k}{L}\right)\right]^{0.5}\right\}} \tag{19a}$$

$$= \overline{\Psi_0\,\Psi_{k\text{-}1}\exp\left(\text{-}c\,\frac{l_k}{L}\right)+\Psi_0\,\psi_{k\text{-}1}\left[1\text{-}\exp\left(\text{-}c\frac{l_k}{L}\right)\right]^{0.5}} \tag{19b}$$

$$= \overline{\Psi_0\,\Psi_{k\text{-}1}}\,\exp\left(\text{-}c\,\frac{l_k}{L}\right) \qquad \text{as} \quad \Psi_0\,\psi_{k\text{-}1}\text{=}0 \tag{19c}$$

$$= \overline{\Psi_0\left\{\Psi_{k\text{-}2}\exp\left(\text{-}c\,\frac{l_{k\text{-}1}}{L}\right)+\psi_{k\text{-}2}\left[1\text{-}\exp\left(\text{-}c\frac{l_{k\text{-}1}}{L}\right)\right]^{0.5}\right\}}\exp\left(\text{-}c\,\frac{l_k}{L}\right) \tag{19d}$$

$$= \cdots \tag{19e}$$

$$= \overline{\Psi_0\,\Psi_0}\,\exp\left(\text{-}c\,\frac{\sum_{i=0}^{k} l_i}{L}\right)\text{=}\exp\left(\text{-}c\,\frac{\sum_{i=0}^{k} l_i}{L}\right) \qquad \text{as} \quad \Psi_0\,\Psi_0\text{=}1 \tag{19f}$$

where Ψ_0 denotes information at a point of an arbitrarily-spaced one-dimensional grid, Ψ_k information at the k^{th}-point which is some Δ_k distance away in the positive direction from the 0^{th}-point, and $\overline{\{\cdot\}}$ a time-averaging operator. In the light of $\Delta_k\text{=}\sum_{i=0}^{k} l_i$ and $\overline{\Psi_0\,\Psi_k}\text{=}\exp(\text{-}c\Delta_k L^{\text{-}1})$, Eq. 19

verifies the new approach with which non-uniformly spaced structured grid and varying time-step computations become possible.[11]

2.2. Solution post-verification approaches

Various LES-quality post-verification metrics that do not require experimental or direct numerical simulation (abbr. DNS) data were proposed in the literature. In order to circumvent consequences implied by the lack of grid-independency in IFLES, six metrics deemed optimum were used herein, and presented below in terms of the number of computations they required.

2.2.1. Single-grid metrics

The first metric, $\{\Gamma_{\text{Pope}}(\mathbf{x})\}_{\{0<\Gamma<1\}}$, is a criterion from [64, p. 560]. It asserts that an 'acceptable quality' LES resolves at least 80% of the total turbulent kinetic energy of a flow field. The metric formula reads: $\Gamma_{\text{Pope}}(\mathbf{x})=[k_{\text{ofs}}]_\mu\,[k_{\text{tot}}^{-1}]_\mu>0.8$ where $[x]_\mu=\text{T}^{-1}\sum_{i=\Delta_t}^{n\Delta_t} x_i$ is an unbiased time-mean estimator, n the size of a discrete sample x, T the sample duration, Δ_t the time-step size, $k_{\text{ofs}}(\mathbf{x},t)=0.5\sum_{i=1}^{3}\overline{u_i'u_i'}$ the over-filter scale, $k_{\text{tot}}(\mathbf{x},t)=(k_{\text{ofs}}+k_{\text{sfs}})$ the total, and $k_{\text{sfs}}(\mathbf{x},t)$ the modelled sub-filter scale turbulent kinetic energy fields per unit mass $[\text{m}^2\text{s}^{-2}]$. Outcomes of the metric need to be interpreted with caution due to three primary reasons: First, the derivation arguments are arguably heuristic rather than systematic, which do not fully explain why the metric variable is k and its threshold is 80%. Second, the true k_{sfs} is always approximated; thus, increasing Γ_{Pope}'s uncertainty and demanding its own assessment. Lastly, as demonstrated by [65, p. 957] and [48, p. 135] with k_{ofs} comparisons between an LES and a corresponding filtered DNS, $\Gamma_{\text{Pope}}>1$ is able to occur despite its non-physicality.

The second metric is an index, $\{\Gamma_{\text{Celik-I}}(\mathbf{x})\}_{\{0<\Gamma<1\}}$, that was derived by [65, Eq. 8a]: $\Gamma_{\text{Celik-I}}=\left\{1+\alpha_\nu\left([\nu_{\text{eff}}]_\mu\,\nu_{\text{lam}}^{-1}\right)^n\right\}^{-1}=\left\{1+\alpha_\nu\,(\Gamma_\nu)^n\right\}^{-1}$ where ν_{lam} is the kinematic viscosity of the fluid $[\text{m}^2\text{s}^{-1}]$, Γ_ν an underlying metric, $\nu_{\text{eff}}(\mathbf{x})=\nu_{\text{num}}+\nu_{\text{sfs}}+\nu_{\text{lam}}$ the effective viscosity, $\nu_{\text{num}}(\mathbf{x})\approx C_\nu h(C_n h^2\Delta^{-2}[\text{k}_{\text{sfs}}]_\mu)^{0.5}$ the estimated numerical viscosity with recommended values [66, p. 3, 5, Eq. 28]: $0.05<C_\nu<0.3$, $C_n\approx1$, $h\approx\Delta$, $n\approx0.53$, and $\alpha_\nu=0.05$. For 80% turbulent kinetic energy resolution, $\Gamma_{\text{Celik-I}}\approx0.8$ and $\Gamma_\nu=[\nu_{\text{eff}}]_\mu\nu_{\text{lam}}^{-1}\approx20$ are expected, whose decreasing value indicates an increase in quality.

[11] Unstructured/arbitrarily-discretized grids and local grid refinements were not considered.

2.2.2. Several-grid estimators

Another metric containing a pair of measures was put forward by [65, Eq. 15-16]: $\Gamma_{\text{Fine}}(\mathbf{x})=\{1+(1-[k_{\text{ofs},1}]_\mu\,[k_{\text{ofs},2}^{-1}]_\mu)(\alpha^p-1)^{-1}\}^{-1}$ and $\Gamma_{\text{Coarse}}(\mathbf{x})=\{1+([k_{\text{ofs},2}]_\mu\,[k_{\text{ofs},1}]_\mu^{-1}-1)\alpha^p(\alpha^p-1)^{-1}\}^{-1}$ where the subscripts 1 and 2 respectively indicate coarse and fine grids, $\Gamma_{\text{Coarse}}\equiv\Gamma_{\text{Celik-II}}$ the coarse-grid index, $\Gamma_{\text{Fine}}\equiv\Gamma_{\text{Celik-III}}$ the fine-grid index, $p=2$ the estimated order of numerical scheme accuracy in terms of Taylor series truncation error [66, p. 3], $\{\alpha(\mathbf{x})\}_{\{\alpha>1\}}=\Delta_{\text{ref},1}\,\Delta_{\text{ref},2}^{-1}$ the grid refinement parameter [65, p. 952], and $\Delta_{\text{ref}}(\mathbf{x})$ the local characteristic grid size. In some cases, higher kinetic energy can be observed in a coarser grid in comparison to finer grids or benchmarks [65, p. 952], thereby non-physically causing $\Gamma_{\text{Celik-II}}>\Gamma_{\text{Celik-III}}$ and even $\Gamma_{\text{Celik-II}}>1$. For such cases, the authors put forth a modified expression [65, Eq. 18] (simplified herein): $\Gamma_{\text{Celik-III}}(\mathbf{x})=1-\|a_k\|\,(a_k+[k_{\text{ofs},2}]_\mu)^{-1}$ with $a_k(\mathbf{x})=([k_{\text{ofs},2}]_\mu-[k_{\text{ofs},1}]_\mu)(\alpha^p-1)^{-1}$. Interpretation of $\Gamma_{\text{Celik-II}}$ and $\Gamma_{\text{Celik-III}}$ is the same with $\Gamma_{\text{Celik-I}}$ wherein $\Gamma\approx0.8$ implies 80% turbulent kinetic energy resolution.

The last metric is the *Lyapunov exponent* [67], which quantifies the level of resolution of time-accurate flow structures unlike the five statistical metrics above. Its evaluation is carried out for a statistically converged computation possessing $\mathbf{u}(\mathbf{x})$ at an instant t_o in five steps: Firstly, a new flow field $\mathbf{u}^*(\mathbf{x})$ is computed by perturbing $\mathbf{u}$ according to $\mathbf{u}^*=\mathbf{u}+\epsilon\|\mathbf{u}\|_2$ [67, Eq. 7] where $\|\cdot\|_2\equiv\left\{V_{\text{all}}^{-1}\sum_{i=1}^{n}(\cdot)^2V_i\right\}^{0.5}$, V_{all} the volume of the numerical domain containing n cells, V_i the i^{th} cell volume, and $\epsilon=10^{-8}$. Secondly, the computations of $\mathbf{u}^*$ and $\mathbf{u}$ are advanced from t_o to t_n, and $\|\delta\mathbf{u}(t)\|_2=\|\mathbf{u}^*(t)-\mathbf{u}(t)\|_2$ is evaluated for a reasonable amount of time-steps [67, Eq. 8]. The same pseudo-random number sets need to be fed into both computations for each time-step, and this is attainable by using the same seed for the pseudo-random number generator. Thirdly, the set of $\log_{10}(\|\delta\mathbf{u}(t)\|_2)$ is plotted as a function of time and linearly regressed. An expected-to-be-observed linear slope of the growth gives the *Lyapunov exponent*, λ, via $\lambda t=\ln(\|\delta\mathbf{u}(t)\|_2\,\|\delta\mathbf{u}(t_0)\|_2^{-1})$ [67, p. 5]. Finally, exponents are computed for each grid available, and inspected as a function of the characteristic grid size. The start of a level-off in plots indicates that almost all degrees of freedom shaping global chaotic dynamics are resolved [67, p. 11].

3. Methodology

3.1. Benchmarks & numerical settings

Four methods were implemented into OpenFOAM®v1712 [39]:[12] (*i*) Kim et al. [21], (*ii*) Xie-Castro [2], (*iii*) Klein et al. [1], and (*iv*) Custom [9]. The majority of DFM/FSM capabilities and varieties are represented by these methods. These methods were tested through a test-bed of three benchmark flows: (*i*) decaying homogeneous isotropic turbulence (DHIT; the case of M=0.0508) [68], (*ii*) homogeneous shear turbulence (HST; the case of h=0.305) [69], and (*iii*) plane channel flow with smooth walls (PCF; the case of Re_τ=395) [70], each of which concerns an isolated aspect of turbulent flows. The benchmarks and numerical set-ups were presented in the following.

3.1.1. Common numerical settings

3.1.1.1. Domain modelling

Numerical domain modelling involves: the determinations of (*i*) the domain shape, and (*ii*) the distance of the field of interest to domain boundaries. Although the domain shape may be influential to certain flow computations, e.g. [71, p. 11], unless dictated by the benchmark, rectangular prisms were deemed appropriate in this study. The distance to boundaries is then chiefly determined by (*i*) integral length scales, (*ii*) the level of boundary condition error propagation to the field of interest, (*iii*) cost, and (*iv*) blockage ratio (not applicable herein).

A domain side several times larger than corresponding integral length scales is advisable while a suppression on or a clip to a scale likely alter energy transfer mechanisms, hence an unrealistic flow development. Based upon systematic homogeneous isotropic turbulence computations, [72, p. 3] suggested that a domain side should at least be six-length-scale in size similar to [64, p. 346]'s eight-length-scale presumption, which was previously stated three-length-scale [73, p. 507].

Exact spatiotemporal dynamics of boundary conditions (abbr. BCs) are nearly always unknown, yet BCs must present to ensure a well-posed problem. As a result, BCs are approximated at a distance to the field of interest which can allow the flow developing to BCs' characteristics, so that BCs could not unrealistically force the surrounding flow to conform its specifications. Accordingly, parts of the computations deemed affected by nearby BCs were omitted in the reported results.

[12] The methods are ascending sorted in terms of their theoretical floating point operations per second.

For the domains, a Cartesian coordinate system in an inertial frame of reference, $\mathscr{I}$=$(\mathscr{O}, \mathbf{e}_x, \mathbf{e}_y, \mathbf{e}_z)$, whose origin, $\mathscr{O}$, is at the left-bottom corner of the inlet boundary, was designated with $(x, y, z)_{\mathscr{I}} \equiv (1, 2, 3)_{\mathscr{I}}$, i.e. the positive x is the longitudinal, y the vertical, z the right transversal directions.

3.1.1.2. Spatial domain discretisation

The spatial resolutions were estimated (and post-assessed §2.2) for free-shear and wall-bounded flow regions. The physical domains were then discretised into unstructured rectangular cuboid finite volumes without local grid refinement by the grid generator *blockMesh* of OpenFOAM® [74].

Arguably, no generic estimation is possible for free-shear regions [75, p. 8], [76, p. 262]. Nonetheless, [77, p. 4] stated that overall $\mathrm{N}_\Delta \propto \mathrm{Re}$, where N_Δ is total number of nodes. Locally, minimal recommendations from the literature project a view of approximately ten nodes per integral length scale, L. For example, in case of high-Reynolds-number homogeneous isotropic turbulence, [64, p. 577-578] analysed that $38\pi^{-1}\Delta_x \approx \mathrm{L}$ and $54\pi^{-1}\Delta_x \approx \mathrm{L}$ are needed to resolve 80%-k_{ofs} when utilising sharp spectral and Gaussian filters, respectively. Furthermore, [40, p. 102] reported that keeping Taylor and cut-off scales in the same order is an advisable criterion, i.e. $\mathcal{O}(\lambda) \sim \mathcal{O}(\Delta_x)$, thereby $15^{-0.5}(A\,\mathrm{Re_L})^{0.5}\Delta_x \approx \mathrm{L}$, where $A \sim \mathcal{O}(1)$ [78, p. 67]. Moreover, [79, p. 62] advised $10\Delta_x \approx \mathrm{L}_\epsilon$ to render sub-filter scale model ineffective for the bulk region of a channel flow, where the integral dissipation scale $\mathrm{L}_\epsilon \sim \mathrm{L}$ [79, p. 53]. Besides, from a heuristic perspective, [80, p. 40] recommended ≈15-20 nodes per shear layer thickness whilst [65, p. 951] and [81, p. 1024] advised $8\Delta_x \approx \mathrm{L}$.

Within wall-bounded regions, more concrete estimates were proposed. For medium $\mathrm{Re_L}$ flows (i.e. $\mathrm{Re_L}$<10^6 relevant to this study), [82, p. 1305] postulated $\mathrm{N}_\Delta \propto \mathrm{Re}^{9/5}$, $\Delta_x^+ \approx 100$, $\Delta_z^+ \approx 20$, $y^+ \sim 1$ and $n_y \approx 10$, of which last is the number of nodes stretched within the viscous wall region where momentum-transfer-dominant scales are order of viscous length scales.[13] A broader range of values from the literature was provided by [83, p. 3] as $\Delta_x^+ \approx$ 50-130, $\Delta_z^+ \approx$ 15-30 and $n_y \approx$ 10-30.

In general, flow scales differ in each direction. The above estimations should therefore yield anisotropic cells. The influence of anisotropy on LES was, however, claimed not to be fully comprehended [84, p. 2401], and correspondingly [75, p. 8] suggested isotropic cells depended upon physical and numerical justifications. For these reasons, isotropic cells were preferred wherever possible in this study. For wall-bounded regions, on the other hand, grid stretching was deployed in compliance

[13] $(.)^+ \equiv (.)\mathbf{u}_\tau \nu^{-1}$, where $\mathbf{u}_\tau$ is the friction velocity.

with the literature suggestions for maximum expansion ratios[14]: overall 1.3 [85, p. 7], and 1.25 [86, p. 379] [87, p. 10] along the wall-normal log-layer.

The grids were verified by the default mesh quality metrics defined in [88]. Notably, the maximum face non-orthogonality, face skewness, and cell aspect ratio for DHIT and HST grids were $(0, 0, 1)$, and for PCF $(0, 0, 13\text{-}22)$, where the ideal values are $(0, 0, 1)$.

3.1.1.3. Equation discretisation

OpenFOAM® computes Eq. 1 on a co-located grid arrangement, wherein cell centroids store flow quantities. Practical-level pressure-velocity decoupling due to the co-located arrangement is removed by a slightly modified [89, p. 71-75] *Rhie-Chow momentum interpolation method* [90]. The volume integrals of the terms in Eq. 1 involving spatial derivatives are transformed into the surface-of-the-volume integrals by means of the *Gauss-Ostrogradsky* theorem, and discretized. The terms without spatial derivatives are, on the other hand, discretized through presuming constant spatial quantities throughout the given volume. Therein, face-information required by surface integrals is interpolated from adjoining cell nodes to a single point on a face. Across a face, interpolated information is assumed constant and uniform; therefore, OpenFOAM® is spatially limited to the second-order accuracy in terms of Taylor series truncation error. In this study, numerical integration of all spatial derivatives-variables, and node-to-face interpolations were held by the *central difference scheme*.

3.1.1.4. Temporal domain discretisation

Temporal resolution, Δ_t, requires to consider three factors. The first is the numerical stability of the solution process. Settings ensuring stable solutions is generally quantified by the *Courant-Friedrichs-Lewy number* [91] defined for a single cell in OpenFOAM® as: Co=$\Delta_t \Lambda$, where Λ=$0.5V^{-1}$ $\sum_{\text{faces}} |\boldsymbol{\phi}_i|$ is a cell-flow frequency scale [s^{-1}], and $\boldsymbol{\phi}$ the volumetric face-flux vector [m^3s^{-1}]. The second is the derivation assumption imposed by the preferred theoretical-level pressure-velocity coupling algorithm, PISO [92]. It presumes that the linear velocity-pressure coupling dominates over the non-linear velocity-velocity coupling while Δ_t goes to zero [93, p. 52], hence viable pressure corrections within the same Δ_t. The third is the second-order backward difference temporal scheme which produces false diffusion in proportion to Δ_t because of its disregard for temporal

[14] The term 'expansion ratio' is defined as the width ratio between the expanded and initial cells in one direction.

Table 1: The boundary conditions employed for pressure, velocity and turbulent kinematic viscosity at each geometric boundary. The hyphenated sequences stand for DHIT–HST–PCF, and the single word the common boundary condition. N denotes zero-gradient Neumann, D fixed-zero Dirichlet, C cyclic, S symmetric, ND stepwise combined Neumann-Dirichlet, A convective and L calculated boundary conditions.

Boundaries ↓ Fields →	p	**u**	ν_t	$\mathfrak{J}_{\mathrm{LM}}$, $\mathfrak{J}_{\mathrm{MM}}$
Inlet	Neumann	Synthetic	D–D–L	Neumann
Outlet	Dirichlet	ND–ND–A	N–N–L	Neumann
Laterals	C–S–C	C–S–C	C–S–C	C–S
Top-Bottom	C–S–N	C–S–D	C–S–N	C–S

[a] A *boundary* is a topological element of a computational domain.
[b] A *boundary condition* is a set of mathematical operations computed at the boundary.

variations in 'face fluxes and derivatives' [50, p. 115]. All necessitate adequately small Δ_t, typically $\mathrm{Co}_{\max} \sim \mathcal{O}(\text{-}1)$. As an example, for free-shear and wall-bounded flow ILES, [94, p. 86] found $\mathrm{Co}_{\max}$=0.5 satisfactory whereas advised $\mathrm{Co}_{\max} \leq 0.2$. Moreover, in this study, constant time-stepping was adopted, and *second-order backward difference scheme* was used for numerical integration of temporal derivatives-variables.

3.1.1.5. Boundary condition types

The boundary conditions adopted for each field on geometric boundaries were illustrated in Table 1. Among them, a convective BC [95] was opted for to ensure resolved structures outflowing without affecting upstream significantly owing to the fact that [96, p. 31] quantified and [97, Fig. 8] visualised upstream-fluctuation-suppressing imprint of the conventional Neumann BC.

3.1.1.6. Solution algorithms and solvers

Term discretisations are followed by the construction of the linear equation system. At this point, however, the bandwidth of the coefficient matrix may be high. This means that values of the global indices for neighbouring nodes are far apart, whence lower performance of solver algorithms [98, p. 30]. Therefore, the bandwidth was narrowed by [99]'s scheme (i.e. *renumberMesh* in OpenFOAM®). Eq. 1 was recast into pressure and momentum equations to be solved sequentially by the theoretical-level pressure-velocity coupling algorithm PISO [92] with 4 momentum correctors. Finally, numerical solution of linearised explicit Eq. 1 was performed through linear solvers: *Geometric agglomerated algebraic multigrid solver* with the *Gauss-Seidel smoother* for pressure (tolerance=10^{-6}, relative tolerance=0-10^{-3}), and an iterative solver using the same smoother for

velocity and other fields (tolerance=10^{-8}, relative tolerance =0). In case some field computations require more stability, the *stable biconjugate gradient method* preconditioned with the *diagonal-based incomplete LU preconditioner* was put into use (tolerance=10^{-5}, relative tolerance =0). Grids and fields were decomposed by the *scotch* partitioning method [100] for parallel executions.

3.1.1.7. Initialisations and sampling

For each benchmark, the first-upstream-section measurements were used to construct synthetic time-series. IFLES initialisations were carried out, and their statistical convergence was qualitatively assessed via the first four sample moments of probed time-series whereas considerable number of pass-throughs were simulated to inherently ensure statistical weak stationarity.[15] Subsequent to computations, the evaluations were conducted according to a set of measures reported in §3.3. The minimum sample size needed to interpret statistics of the population of interest at a 98% confidence level was estimated as 1.3×10^4 elements [101, §7.2.2.2.], which was few orders smaller than the size of samples obtained.

3.1.2. Specific numerical settings

3.1.2.1. Decaying homogeneous isotropic turbulence - DHIT

The DHIT benchmark was a stationary-grid approximately-isotropic decaying turbulent flow experiment from [68]. Synthetic time-series were based upon the experimental measurements at $42M$ section, where M=0.0508[m] is the characteristic size. Thereon, the set of input included: the mean longitudinal flow speed U_c=12.7[ms^{-1}], the fluid kinematic viscosity ν_{lam}=1.4941×10^{-5}[m^{2}s^{-1}] (based on Re_M=3.4×10^4, and U_o=10[ms^{-1}]), one-point normal-anisotropic correlations $\{\overline{(u'_{ii})^2}\}_{\{i\in(1,2,3)\}}$ =4.9284×10^{-2}[m^{2}s^{-2}]-$\{\overline{(u'_{ij})^2}\}_{\{i\neq j\}}$=0.0, and longitudinal-transverse integral length-scales L_{long}=2.4×10^{-2}[m]-L_{trans}=1.27×10^{-2} [68, p. 299]. The rectangular prism computational domain possessed the dimensions of $(7.62, 1.524\times10^{-1}, 1.524\times10^{-1})_{\mathscr{I}}$[m]=$(300, 6, 6)_{\mathscr{I}}$[$\text{L}_{\text{long}}$]=$(600, 12, 12)_{\mathscr{I}}$[$\text{L}_{\text{trans}}$]. The spatial resolution involved cubic cells and 10 nodes per L_{long}; resulting in $(3000, 60, 60)_{\mathscr{I}}$ nodes, and the temporal resolution was Δ_t=5×10^{-5}[s]. The sub-filter scales were modelled by the *Smagorinsky model* using the *Lagrangian-averaging dynamic procedure* (§2.1.2). The computations were initialised and sampled for 20 mean-flow pass-through, i.e. 24[s] each.

[15] Methods quantifying statistical convergence of LES solutions may also be found, e.g. [13] using passive scalars.

3.1.2.2. Homogeneous shear turbulence - HST

The HST benchmark was [69]'s experiment of virtually transverse-homogeneous uniform-shear turbulent flow. The chosen scenario belonged to x_1/h=7.5 plane measurements, where h=0.305[m] is the shear-turbulence generator height, and x_1 the downstream distance to the generator. At the plane, the mean longitudinal centreline flow speed was U_c=12.4[s^{-1}], the mean longitudinal-shear dU_1/dx_2=46.8[s^{-1}], one-point correlations $\overline{(u_1')^2}$=2.80×10^{-1}[m^2s^{-2}], $\overline{(u_2')^2}$=1.00×10^{-1}, $\overline{(u_3')^2}$=1.56×10^{-1}, $\overline{u_1'u_2'}$=-4.50×10^{-1}, $\{\overline{(u_{ij}')^2}\}_{\{i\neq j, i\neq 1, j\neq 2\}}$=0.0, and integral scales $L_{11,1}$=4.4×10^{-2}[m], $L_{22,1}$=1.012×10^{-2}, $L_{33,1}$=1.496×10^{-2}, $L_{11,2}$=1.452×10^{-2}, $L_{11,3}$=1.1×10^{-2}, $L_{22,2}$=$L_{22,3}$=5.06×10^{-3} and $L_{33,2}$=$L_{33,3}$=7.48×10^{-3} [69, p. 320, 329, 334], where the last four scales were derived by the isotropy assumption: $0.5L_{22,1}$=$L_{22,2}$[16], and the fluid kinematic viscosity ν_{lam}=1.49778636445×10^{-5}[m^2s^{-1}]. The numerical domain was a rectangular prism replicating the experimental set-up, i.e. $(5.6425, 3.05\times10^{-1}, 3.05\times10^{-1})_{\mathscr{I}}$[m]≈$(128, 6.9, 6.9)_{\mathscr{I}}[L_{11,1}]$≈$(389, 21, 21)_{\mathscr{I}}[L_{11,2}]$. The spatial domain was discretised into $(1332, 72, 72)_{\mathscr{I}}$ cubic cells with ∼10.4 nodes per $L_{11,1}$, and the temporal resolution was Δ_t=1×10^{-4}[s]. Similar to DHIT, the sub-filter scales were modelled by the *Smagorinsky model* with *Lagrangian-averaging dynamic procedure* (§2.1.2). The initialisations and samplings lasted for ≈17 and 34 bottom-mean-flow pass-through, i.e. 18.2[s]-36.4[s], which was equivalent to 40-80 centreline-mean-flow pass-through.

3.1.2.3. Plane channel flow with smooth walls - PCF

The PCF benchmark was the wall-resolved DNS of statistically stationary, pressure-gradient driven, fully developed plane channel flow with smooth walls from [70], wherein Re_τ=$u_\tau\delta/\nu_{lam}$=395 with u_τ=1.0[ms^{-1}] the friction velocity, ν_{lam}=0.002531646[m^2s^{-1}] the fluid kinematic viscosity, and δ=1.0[m] the channel half-width [70, p. 943]. The large-to-present input datasets were fetched from the web page [102][17]. The numerical domain duplicating [17] was created in order to minimise uncertainties in model comparisons. The domain [17] had the following particulars: its dimensions were $(60.0, 2.0, \pi)_{\mathscr{I}}$[m]≈$(153.8, 5.1, 8.1)_{\mathscr{I}}[L_{11,1;y^+=392}]$[18], the number of nodes was $(600, 64, 70)_{\mathscr{I}}$ with Δ_x^+≈39.5, Δ_z^+≈17.7, y^+≈3.8×10^{-3}, and wall-normal cell-to-cell expansion ratio of 1.0795 (i.e. OpenFOAM® expansion ratio of 10.7028). Its temporal resolution was Δ_t=2×10^{-3}[s]. Follow-

[16] Within $L_{ij,k}$, ij signifies the directions of two velocity components in hand, and k measurement direction.

[17] Integral length-scales were defined here as: L=$\mathscr{L}_0^\infty(\widehat{\rho})$≈$\mathscr{L}_0^a(\widehat{\rho})$, where $\mathscr{L}_b^a(\cdot)$ is a numerical integration operator on a sample autocorrelation function, $\widehat{\rho}$, over $[a, b]$. The upper bound of the integral was accepted 10% zero-lag, similar to [17, p. 61], which was justified by that the streamwise correlations in [102] do not level off zero in general.

[18] In [17]'s domain, z=3.5[m]. Nevertheless, [70]'s original value of z=π[m] was followed in this study.

ing [17], the *Smagorinsky model* with the *van Driest wall-damping function* was utilised for the sub-filter scale modelling (§2.1.2). Its model coefficients were C_ϵ=1.048 and C_k=0.0265463553 resulting in C_s=0.065. The computations were initialised for 20 pass-through based on $U_{y^+=392}$=20.133 [ms^{-1}], and sampled for 40 pass-through.

3.2. New code practices

On top of [9, p. 449]'s quoted-from-the-literature and proposed recommendations to reduce theoretical computational costs of DFM/FSM, two new code practices were offered here.

The new DFM practice is the direct generation of Gaussian white-noise in the frequency domain. For DFM implementations in which FFT is in use, random number sets are typically generated in the time domain and Fourier-transformed every time-step to perform convolution. This transformation can be eliminated by generating real-valued Gaussian random samples directly inside a complex-valued set wherein the following arrangement is preset:

$$\mathfrak{H}_k = h_k + ih_{k+\mathrm{N}/2} \qquad k \in [0, \mathrm{N}/2\text{-}1] \tag{20a}$$

$$\mathfrak{H}_k = \mathfrak{H}^*_{\mathrm{N}\text{-}\mathrm{k}} \qquad k \in [\mathrm{N}/2, \mathrm{N}\text{-}1] \tag{20b}$$

where $\{h\}_{\{|h|=\mathrm{N};\, h_k\in\mathbb{Q}\}}$ is a real-valued Gaussian white-noise set, $\{\mathrm{N}\}_{\{\mathrm{N}\in\mathbb{N}\}}$ its size, and $\{\mathfrak{H}\}_{\{|\mathfrak{H}|=\mathrm{N};\, \mathfrak{H}_k\in\mathbb{C}\}}$ a complex-valued conjugate-symmetric set.

In FSM, a brute implementation requires 18 summation-subtraction, 45 multiplication-division, 9 square-root and 18 exponential function executions per node per time step for velocity correlations in each direction. By pre-computing the exponential terms in Eq. 15, this can be shrunk into 9 summation and 18 multiplication executions for stationary grid and constant time-step computations.

3.3. Investigation subjects & measures

DFM/FSM generates synthetic inflow time-series in four non-CFD model stages. This non-CFD model unit was explored in [9], and illustrated in Fig. 2 with its stages. Therefore, the scope of this study was limited to the subsequent unexplored CFD model unit.

The CFD unit can be abstracted into two main sub-units through which non-CFD time-series progress till the field of interest: (*i*) *transfer* sub-unit and (*ii*) *development* sub-unit whose constituents comprise several options to make. The conceptualisation was displayed in Fig. 3.

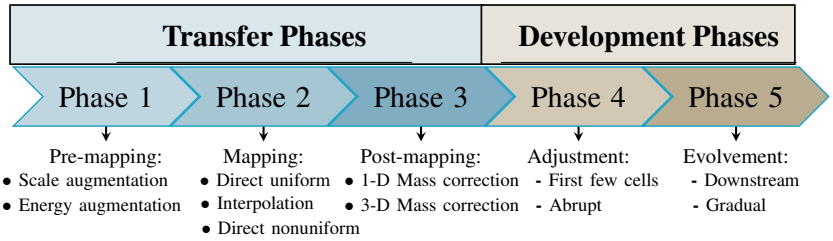

Figure 3: A sequential diagram of the phases transforming a DFM/FSM synthetic time-series towards the field of interest in a CFD domain. Terms of *transfer* and *development* stand for the phases wherein the Navier-Stokes equations are and are not involved, respectively.

The *transfer sub-unit* denotes a set of final preparation phases before the Navier-Stokes (abbr. N-S) equations become in effect. Therein, time-series are prepared for a given numerical set-up in three phases: (*i*) pre-mapping conditioning, (*ii*) mapping, and (*iii*) post-mapping conditioning. The *pre-mapping phase* implies the final conditioning operations independent of the CFD grid, such as skewness-kurtosis transformation [9], heuristic [17] or optimised [27] kinetic energy augmentations/diminutions. Secondly, the *mapping phase* refers to information transfer from the DFM/FSM virtual grid to the CFD grid, both of which may or may not conform, for example the nearest-neighbour projection [2]. Lastly, the *post-mapping phase* indicates any operation on time-series that is mapped onto the CFD grid, such as mass flux corrections [17, p. 57].

The successive *development sub-unit* signifies processes where synthetic time-series become a part of the system of algebraic equations. The sub-unit can be further abstracted into two phases: (*i*) *adjustment* and (*ii*) *evolvement*. The *adjustment phase* occurs in the first few cells neighbouring the inlet boundary. There, abrupt and considerable alterations are expected in the statistical and stochastic characteristics of time-series in view of the fact that DFM/FSM inherently does not use the N-S equations to produce series. In the *evolvement phase* along the rest of the domain, on the other hand, a typical downstream evolution of time-series is anticipated. Therein, in contrast to the *adjustment phase*, the signature of DFM/FSM gradually fades away, and other numerical settings dominate the flow development.

In the light of the above abstractions, the tests were designed in three suites. In the first suite, all the IFLES cases were assessed by various means including the six LES-quality post-verification metrics introduced in §2.2, and the metrics themselves were evaluated as well. In the second suite, DHIT, HST and PCF scenarios were computed with the four DFM/FSM variants (§2.1.3), and performance of each model along the *development sub-unit* was monitored with predetermined (default) *transfer sub-unit* options. The motivation behind the predetermination is to avoid the

possibility of numerous option combinations at the outset due to the *transfer sub-unit* (i.e. tens of combinations per model per flow), which may cause a loss of focus. Therefore, an option combination deemed as the most basic and common one was chosen for the *transfer sub-unit*: no *pre-mapping* and *post-mapping* manipulation and the simplest *mapping* method of nearest-neighbour projection.

In the third suite, viable options within the *transfer sub-unit* were investigated in terms of their effects on the *development sub-unit*. Therein, only Klein et al.'s (i.e. pure DFM) and Kim et al.'s (i.e. pure FSM) models alongside PCF were used to investigate the aforementioned options as the benchmark datasets in increasing fidelity were only available for PCF. For the *pre-mapping phase*, three particulars were isolated: the magnitude of shear stresses, the size of integral length scales, and the number of integral length scale sets. In the first, four scenarios were studied: the magnitude of shear stresses were zeroed, kept default, doubled, and the no-slip wall boundary condition was changed to slip condition alongside with default settings. In the second, three scenarios were studied: the size of integral length scales was halved, kept default and doubled. In the third, the use of different inlet spatial zones was examined with a single set of integral length scales covering the entire synthetic turbulence generation plane, and a duo set wherein an extra set of length scales was input at the 10% wall-normal zone. For the *mapping phase*, three mapping methods were tested: nearest-neighbour projection, bilinear interpolation, and seamless projection. Finally, for the *post-mapping phase*, three approaches were studied: null, longitudinal, and three-dimensional mass flux corrections. The effects were quantified through the statistics listed in Table 2, and compared with the corresponding default case. Due to the vast amount of data produced, the information as to the statistics that were almost unchanged relative to the half-precision machine epsilon was qualitatively conveyed. On the other hand, the changes in the statistics deemed significant were presented and discussed in the relevant sections.

Table 2: List of statistical metrics used in the study.

	Measure	Expression
i.	Unbiased sample arithmetic mean	$\widehat{\mu}_1 = n^{-1} \sum_{i=1}^{n} x_i$
ii.	Unbiased sample variance	$\widehat{\mu}_2 = (n-1)^{-1} \sum_{i=1}^{n} (x_i - \widehat{\mu}_1)^2$
iii.	Estimator of skewness	$\widehat{\gamma}_1 = \{n(n-1)\}^{0.5} (n-2)^{-1} \left\{ n^{-1} \sum_{i=1}^{n} (x_i - \widehat{\mu}_1)^3 \right\} \widehat{\mu}_2^{-1.5}$
iv.	Estimator of kurtosis excess	$\widehat{\gamma}_2 = \{(n-2)(n-3)\}^{-1} \left\{ (n^2-1) \left\{ n^{-1} \sum_{i=1}^{n} (x_i - \widehat{\mu}_1)^4 \right\} \widehat{\mu}_2^{-2} - 3(n-1)^2 \right\}$
v.	Sample one-point correlation tensor	$R_{xy} = z^{-1} \sum_{k=1}^{z} \left\{ \mathrm{T}^{-1} \sum_{i=\Delta_t}^{n\Delta_t} (x_{ki} - \widehat{\mu}_{1_{x_k}})(y_{ki} - \widehat{\mu}_{1_{y_k}}) \right\}$
vi.	Unbiased sample correlation functions	$\widehat{\rho}_{XY} = \frac{\widehat{\mathrm{R}}_{XY}}{\widehat{\mu}_{2_X} \widehat{\mu}_{2_Y}}; \widehat{\mathrm{R}}_{XY} = (\mathrm{N}-a)^{-1} \sum_{i=\Delta_t}^{(\mathrm{N}-a)\Delta_t} x_i \, y_{i+a\Delta_t}$
vii.	Sample one-sided power spectral density function	Welch's method [103], window: Hanning, overlap: 50%
viii.	Wall shear stress vector field	$\mathbf{u}_\tau = \{\mathbf{S}_f \, \|\mathbf{S}_f\|^{-1}\} \cdot \left\{ -\nu_{\mathrm{eff}} \{ \underline{\underline{\mathbf{S}}}_t - 3^{-1} \, \mathrm{Tr}(\underline{\underline{\mathbf{S}}}_t) \underline{\underline{\mathbf{I}}} \} \right\}$
ix.	Over-filter scale kinetic energy transport equation	$k_{\mathrm{Loc}} + k_{\mathrm{Conv}} = k_{\mathrm{TransU}} + k_{\mathrm{TransP}} + k_{\mathrm{Prod}} + k_{\mathrm{Diff}} + k_{\mathrm{Diss}}$
x.	Over-filter scale velocity derivative skewness and kurtosis fields	$\partial_x \widehat{\gamma}_1 = -(\nabla_x \overline{\mathbf{u}}_x)^3 \quad \text{and} \quad \partial_x \widehat{\gamma}_2 = (\nabla_x \overline{\mathbf{u}}_x)^4$
xi.	Enstrophy transport equation	$\mathfrak{E}_I + \mathfrak{E}_C = \mathfrak{E}_P + \mathfrak{E}_T + \mathfrak{E}_D + \mathfrak{E}_S + \mathfrak{E}_\epsilon$
xii.	Mean total strain transport equation	$\mathfrak{S}_I = \mathfrak{S}_{\mathrm{ProdS}} + \mathfrak{S}_{\mathrm{ProdE}} + \mathfrak{S}_{\mathrm{Diss}}$

n means the size of a discrete sample x, $\widehat{\{\cdot\}}$ an estimation operator, z the number of nodes along the statistically homogeneous direction, T a sample duration, Δ_t a time-step size, a the lag (time-offset) number, N the maximum lag number, $\{\cdot\}$ the inner product, $\mathbf{S}_f$ face area vector field [m^2], $\nu_{\mathrm{eff}} = \nu_{\mathrm{lam}} + \nu_{\mathrm{sfs}}$ the effective viscosity scalar field with ν_{lam} the kinematic viscosity of the fluid and ν_{sfs} the modelled eddy-viscosity scalar field [$\mathrm{m}^2\mathrm{s}^{-1}$], $\underline{\underline{\mathbf{S}}}_t = 2\{0.5(\nabla\mathbf{u} + (\nabla\mathbf{u})^\intercal)\}$ the twice strain rate tensor field $\underline{\underline{\mathbf{S}}}$ [s^{-1}], $\mathrm{Tr}(\cdot) \equiv \sum_{i=1}^{n} (\cdot)_{ii}$ the trace of a tensor, and $\underline{\underline{\mathbf{I}}}$ an identity tensor field [-]. For the transport equation of the over-filter scale kinetic energy, k_{ofs}: $k_{\mathrm{Loc}} = \partial_t k_{\mathrm{ofs}}$ is the local derivative of k_{ofs} [$\mathrm{m}^2\,\mathrm{s}^{-3}$], $k_{\mathrm{Conv}} = \mathrm{U}_{\mathrm{mean}} \cdot \nabla k_{\mathrm{ofs}}$ the convective derivative of k_{ofs}, $k_{\mathrm{TransU}} = -\nabla \cdot (\overline{\mathbf{u}}\, k_{\mathrm{ofs}})$ the transport of k_{ofs} via velocity fluctuations, $k_{\mathrm{TransP}} = -\nabla \cdot (\overline{\mathbf{u}}\, \overline{p})$ the transport of k_{ofs} via pressure fluctuations, $k_{\mathrm{Prod}} = -\{\overline{\mathbf{u}}^2\}_{\mathrm{mean}} : \nabla \mathrm{U}_{\mathrm{mean}}$ the production of k_{ofs}, $k_{\mathrm{Diff}} = \nu_{\mathrm{lam}} (\nabla \cdot (\overline{\mathbf{u}} \cdot \underline{\underline{\mathbf{S}}}_t))$ the viscous diffusion of k_{ofs}, $k_{\mathrm{Diss}} = -\nu_{\mathrm{lam}} (\underline{\underline{\mathbf{S}}}_t : \nabla \overline{\mathbf{u}})$ the viscous dissipation of k_{ofs}, k_{sfs} the modelled turbulent kinetic energy, and ϵ_{sfs} the modelled dissipation rate. $\partial_x \widehat{\gamma}_1$ and $\partial_x \widehat{\gamma}_2$ are the over-filter scale velocity derivative skewness and kurtosis respectively [s^{-3}]-[s^{-4}]. For the enstrophy transport equation, $\mathfrak{E}$ [s^{-2}]: $\mathfrak{E}_I = 0.5\, \partial_t (\overline{\boldsymbol{\omega}} \cdot \overline{\boldsymbol{\omega}})$ the scalar field of the increase rate of $\mathfrak{E}$ [s^{-3}], $\mathfrak{E}_C = 0.5\, \{\mathrm{U}_{\mathrm{mean}} \cdot \nabla (\overline{\boldsymbol{\omega}} \cdot \overline{\boldsymbol{\omega}})\}$ the convection of $\mathfrak{E}$, $\mathfrak{E}_P = -\{(\overline{\boldsymbol{\omega}} \cdot \overline{\mathbf{u}}) : \nabla \omega_{\mathrm{mean}}\}$ the production of $\mathfrak{E}$, $\mathfrak{E}_T = -0.5 \nabla \cdot (\overline{\mathbf{u}} (\overline{\boldsymbol{\omega}} \cdot \overline{\boldsymbol{\omega}}))$ the diffusion of $\mathfrak{E}$ by velocity fluctuations, $\mathfrak{E}_D = -0.5 \nu_{\mathrm{sfs}} \nabla^2 (\overline{\boldsymbol{\omega}} \cdot \overline{\boldsymbol{\omega}})$ the diffusion of $\mathfrak{E}$ by viscosity, $\mathfrak{E}_S = (\overline{\boldsymbol{\omega}}^2 : \underline{\underline{\mathbf{S}}}) + (\overline{\boldsymbol{\omega}}^2 : \underline{\underline{\mathbf{S}}}_{\mathrm{mean}}) + ((\overline{\boldsymbol{\omega}} \cdot \underline{\underline{\mathbf{S}}}) \cdot \omega_{\mathrm{mean}})$ the production of vorticity fluctuations via vortex stretching, $\mathfrak{E}_\epsilon = -\{\nu_{\mathrm{sfs}} (\nabla \overline{\boldsymbol{\omega}} : \nabla \overline{\boldsymbol{\omega}})\}$ the dissipation of $\mathfrak{E}$. $\overline{\boldsymbol{\omega}} = \nabla \times \overline{\mathbf{u}}$ the over-filter scale vorticity [s^{-1}], $\mathfrak{E}_P = \boldsymbol{\omega} \cdot \{\underline{\underline{\mathbf{S}}} \cdot \boldsymbol{\omega}\}$ the production of $\mathfrak{E}$ due to vortex stretching, $\mathfrak{E}_D = \nu_{\mathrm{sfs}} (\boldsymbol{\omega} \cdot \nabla^2 \boldsymbol{\omega})$ the dissipation of $\mathfrak{E}$. For the transport equation of mean total strain, $\mathfrak{S}$ [s^{-2}]: $\mathfrak{S}_I = 0.5 \partial_t (\underline{\underline{\mathbf{S}}} : \underline{\underline{\mathbf{S}}})$ the scalar field of the increase rate of $\mathfrak{S}$ [s^{-3}], $\mathfrak{S}_{\mathrm{ProdS}} = -(\underline{\underline{\mathbf{S}}} \cdot \underline{\underline{\mathbf{S}}}) : \underline{\underline{\mathbf{S}}}$ the production of $\mathfrak{S}$ by self-amplifications, $\mathfrak{S}_{\mathrm{ProdE}} = -0.25 \{(\boldsymbol{\omega} \cdot \boldsymbol{\omega}) : \underline{\underline{\mathbf{S}}}\}$ the production of $\mathfrak{S}$ by enstrophy effects, and $\mathfrak{S}_{\mathrm{Diss}} = \nu_{\mathrm{sfs}} \{\mathfrak{S}_{\mathrm{Diss}} : (\nabla^2 \mathfrak{S}_{\mathrm{Diss}})\}$ the viscous dissipation of $\mathfrak{S}$.

Within the suits, investigations were conducted in respect to *input* and *formed* statistical mea-

sures[19]. The input statistics included: (*i*) mean velocity profiles, (*ii*) one-point second-order correlation tensor,[20] (*iii*) two-point correlation functions, and (*iv*) one-dimensional one-sided power spectral density functions. The formed statistics comprised: (*i*) over-filter scale kinetic energy transport equation terms, (*ii*) over-filter scale enstrophy transport equation terms, (*iii*) mean flow total strain transport equation terms, (*iv*) one-point third and fourth statistical central moments and probability density functions, and (*v*) wall-shear stresses. The discrete expressions used to compute these measures were shown in Table 2.

Test suite results were obtained through numerical domain nodes and probes.[21] For spatially-variant flow field statistics, cumulative moving averaging was performed on time-accurate node values along time. For statistics that require the entire temporal dataset at once (e.g. power spectra), probe time-series were used in their computations. All the sample statistics were then spatially-arithmetic averaged in statistically homogeneous directions. In the results section, only the crucial premises were presented with essential evidence strictly representative to all cases and tagged as *representative-to-all*. Also, all these data manipulations were abbreviated by the tag *conditioned*.

Moreover, statistics from the benchmarks/methods and their relative changes were quantified through the *centineper* (i.e. the log percentage: $100 \log_e(x_{\text{data}}/x_{\text{benchmark}})$ [cNp] [106, p. 45]) which is additive and symmetric unlike the conventional percentage formula (hence less misleading) as well as the *discrete Fréchet distance* [107][22] when necessary. For brevity, the denotations *bench-diff* and *default-diff* were used below to indicate amplitude differences between the quantity of interest and corresponding benchmark/default computational case in units of the quantity. Furthermore, the term *adaptation length* is used to loosely describe a supposed distance at which a given statistic reaches its statistically stationary ergodic state within a turbulent flow.

In addition, to prevent other redundant word repetitions across the results sections, two more abbreviations were made: First, the *Big O notation* was redefined as an indicator of the digit place of the first significant figure in a given range of magnitudes (e.g. for a range between 0.14 and

[19] The terms *input* and *formed* were coined to distinguish the statistical information required by DFM/FSM, and generated by CFD, respectively.

[20] In case of scaling by fluid density, the term can be written as *Reynolds stress tensor*.

[21] Probe data were obtained by an inverse-distance-weighting linear interpolation of node information to the arbitrary location of the probe within the node's cell.

[22] A metric that quantifies the level of similarity between two arbitrary discrete datasets. A code from [108] was used to calculate the metric, which was shortly explained in [9, p. 464].

$0.52 \rightarrow \mathcal{O}(\text{-}1)$; between 25.1 and $88.3 \rightarrow \mathcal{O}(2)$ etc.) in contrast to its actual meaning for a function's limiting behaviour. Second, the model names were shortened to the first author, e.g. Klein model instead of Klein et al.'s model.

Finally, for each results section, the following line of questions were addressed in the order given: why was the statistic studied; what/how was the study carried out; what was observed in the *adjustment* and *evolvement phases* as a result; what did the results mean in theory and practice; what were the key benefits for the audience and what did remain unsolved [109, p. 134]. Having defined what the test framework is, the next chapter presents the *conditioned* results and remarks.

4. Results & Discussion

4.1. Confidence assessments

Prior to analyses, confidence assessments of each computation were carried out in four subjects: (*i*) spatial/temporal resolutions, (*ii*) numerical stability, (*iii*) statistical convergence of computational fields, and (*iv*) of probe samples. These assessments did not measure the accuracy of the computations; thus, they did not address validation. In contrast, verifications of the target computational settings were sought herein. Therefore, any qualification here only implies confirmation of the intended settings rather than the validity of the modelling.

(*i*) The spatiotemporal resolutions of the computations were post-assessed through five statistical metrics and one stochastic metric (§2.2). In addition, the capabilities of these metrics were compared, and their viability was discussed. For the statistical metrics, the first four one-point sample moments (i.e. $\widehat{\mu}_1$ and $\widehat{\mu}_2$; and to reveal more local trends, $\widehat{\gamma}_1$ and $\widehat{\gamma}_2$), minima, medians and maxima of the metric fields[23] were exhibited in a supplementary document, i.e. Suppl. Doc.-1. The sample means of the metric fields with their corresponding coefficients of variation were summarised in Table 3.

To start with, the analyses of the stochastic-metric *Lyapunov exponent* demonstrated that the exponent levelled off with resolution refinements in DHIT, HST and PCF (not reported). As a result of this, the majority of the degrees of freedom in contribution to the global dynamics of the computations were deemed to be resolved in compliance with the interpretations from [67, p. 11].

[23] Each metric produces a scalar per cell node.

Table 3: The sample means (i.e. $\widehat{\mu}_1$) and their corresponding coefficient of variation (i.e. $\{\bullet\}_{\text{CV}}$) of time-averaged spatial-variant fields of five IFLES-quality post-verification metrics (i.e. Γ_{Pope}, Γ_{ν}, $\Gamma_{\text{Celik-I}}$, $\Gamma_{\text{Celik-II}}$, and $\Gamma_{\text{Celik-III}}$ in §2.2). The fields were obtained from the computations of decaying homogeneous isotropic turbulence (DHIT), homogeneous shear turbulence (HST), and plane channel flow with smooth walls (PCF) (§3.1) using the four synthetic time-series generators (i.e. Custom, Klein et al., Xie-Castro, and Kim et al. in §2.1.3). The biased estimator of the coefficient of variation was defined as the ratio between the sample standard deviation and sample mean: $(\widehat{\mu}_2)^{\text{-}0.5}/\widehat{\mu}_1$.

Method ↓ $\widehat{\mu}_{1_{\text{CV}}}$ →		Γ_{Pope}	Γ_{ν}	$\Gamma_{\text{Celik-I}}$	$\Gamma_{\text{Celik-II}}$	$\Gamma_{\text{Celik-III}}$
DHIT	Custom	$0.977_{0.41}$	$1.764_{18.07}$	$0.937_{0.46}$	$0.937_{2.21}$	$0.936_{2.12}$
	Klein et al.	$0.980_{0.44}$	$1.822_{16.59}$	$0.936_{0.36}$	$0.939_{1.45}$	$0.939_{1.31}$
	Xie-Castro	$0.985_{0.30}$	$1.730_{36.99}$	$0.937_{0.30}$	$0.932_{1.43}$	$0.932_{1.22}$
	Kim et al.	$0.975_{0.48}$	$1.772_{26.89}$	$0.937_{0.50}$	$0.933_{2.83}$	$0.932_{2.63}$
HST	Custom	$0.947_{0.77}$	$7.306_{37.04}$	$0.875_{1.52}$	$1.089_{51.96}$	$0.878_{63.75}$
	Klein et al.	$0.953_{0.71}$	$8.003_{46.91}$	$0.870_{1.60}$	$1.050_{24.39}$	$0.904_{26.82}$
	Xie-Castro	$0.953_{0.66}$	$7.837_{22.04}$	$0.871_{1.57}$	$1.014_{21.98}$	$0.924_{22.72}$
	Kim et al.	$0.947_{0.87}$	$7.579_{111.34}$	$0.873_{1.40}$	$1.070_{89.28}$	$0.906_{105.22}$
PCF	Custom	$0.929_{8.67}$	$1.230_{10.70}$	$0.947_{0.29}$	-	-
	Klein et al.	$0.930_{8.66}$	$1.231_{10.87}$	$0.947_{0.29}$	-	-
	Xie-Castro	$0.930_{8.69}$	$1.230_{10.81}$	$0.947_{0.29}$	-	-
	Kim et al.	$0.928_{8.76}$	$1.229_{10.65}$	$0.947_{0.29}$	-	-

With regard to the first statistical-metric Γ_{Pope}, $\widehat{\mu}_1[\Gamma_{\text{Pope}}(\mathbf{x})]$ of all cases ranged from 0.928 to 0.985 ($\{\Gamma_{\text{Pope}}\}_{\text{advice}}$=0.800) as illustrated in Table 3. The influence of the inflow generators on $\widehat{\mu}_1[\Gamma_{\text{Pope}}]$ was, however, found to be indistinguishable up to two-decimal places. Similar to $\widehat{\mu}_1$, the coefficients of variation in Γ_{Pope} fields remained virtually the same within $\sim\mathcal{O}$(-1) as can be seen from the subscripts of Table 3. Also, the coefficients were observed to be an order of magnitude lower for DHIT/HST than those in PCF. This observation implies spatially-invariant Γ_{Pope} fields for DHIT/HST whereas spatial variations for PCF.

By contrast to the relatively global $\widehat{\mu}_1$-$\widehat{\mu}_2$, effects of the DFM/FSM variants began to appear with more local $\widehat{\gamma}_1$-$\widehat{\gamma}_2$: Klein et al./Xie-Castro models yielded positive $\widehat{\gamma}_1[\Gamma_{\text{Pope}}]$, and Custom/Kim et al. models negative $\widehat{\gamma}_1[\Gamma_{\text{Pope}}]$ with a degree of $\mathcal{O}(1)$ in DHIT and $\mathcal{O}$(-1) in HST. Nevertheless, $\widehat{\gamma}_1[\Gamma_{\text{Pope}}]$ was negative $\mathcal{O}(1)$ for all models in PCF cases (Suppl. Doc.-1, Table 2). The negativity indicated an asymmetry in the metric fields within which less-than-median outliers of Γ_{Pope} (i.e. lower quality according to the metric) occurred more frequently in PCF, and vice versa.

Furthermore, all cases were quantified to be leptokurtic (i.e. positive $\widehat{\gamma}_2[\Gamma_{\text{Pope}}]$) (Suppl. Doc.-1, Table 2). This positiveness signified that the source of local Γ_{Pope} variations was scattered to an extent directly proportional to $\widehat{\gamma}_2$; thus, transitions across different quality regions were mostly not smooth for relatively high $\widehat{\gamma}_2$. For example, qualitative inspections of the PCF-Γ_{Pope} field histograms revealed that multiple and separate aggregations existed. These groupings were layered

in a cascade of waning strength towards the walls with a quadratic trend as the lowest Γ_{Pope} was observed three layers away from the walls (not reported).

It was deduced that the above interpretations can also be applied to the results of the remaining statistical metrics. For this reason, the following presentation was confined to generic and specific remarks that encountered no counterexamples instead of re-expressing similar result-meaning pairs for each metric.

First, according to the metric guidelines in §2.2, all the mean values of the metrics shown in Table 3 qualified all the corresponding IFLES cases as statistically adequate. Nevertheless, the mean qualification is global; hence, spatiotemporally-accurate local structures may still not be resolved within a computation ascertained 'decent' by the grid metrics. Second, the metrics did not provide results completely consistent to each other. For instance, $\widehat{\mu}_1[\Gamma_{\text{Pope}}]$ led a ranking from the highest to lowest 'quality' as DHIT-HST-PCF whereas $\widehat{\mu}_1[\Gamma_\nu]$ and its derivative $\widehat{\mu}_1[\Gamma_{\text{Celik-I}}]$ resulted in a ranking of PCF-DHIT-HST. Consequently, the level of spatiotemporal resolution of a computation could be quantified notably different by the grid metrics. Third, the influence of DFM/FSM on the fidelity level of an IFLES computation seems to be limited to free-shear flows. This was exemplified by PCF in what all the metric results of the moments were observed to be almost the same up to two-three decimal places for any inflow generator, and this observation was absent for the free-shear flow cases. It might therefore be speculated that wall effects blur the imprints of the inflow models on the computational fidelity. The final general remark is that no inflow method was found to be superior or inferior to any other in regard to the estimated fidelity. An example of this was that Kim/Klein/Xie models in the same DHIT cases were predicted the lowest 'quality' model by different grid metrics.

In addition to the general deductions, distinct remarks pertain to each metric can be drawn: In Γ_ν (Suppl. Doc.-1, Table 3), no mechanism was identified which constrains the upper magnitude limit of Γ_ν, albeit its lower limit of zero. In consequence, unrealistic positive deviations of Γ_ν larger than the level of $\widehat{\mu}_1[\Gamma_\nu]$ could occur for maxima and higher moments. As an example of such deviations, the followings were measured from the DHIT cases: $\widehat{\gamma}_1[\Gamma_\nu]\sim\mathcal{O}(3)$-$\mathcal{O}(4)$, $\widehat{\gamma}_2[\Gamma_\nu]\sim\mathcal{O}(6)$-$\mathcal{O}(7)$, and $\max[\Gamma_\nu]\sim\mathcal{O}(3)$-$\mathcal{O}(4)$. It was ascertained that these high-amplitude occurrences stem from ν_{sfs} fields. However, the underlying reason can be further attributed to the dynamic sub-filter scale model which is anticipated to generate relatively large spatiotemporal variations in ν_{sfs} fields [55, p. 355]. This premise was further supported by the implication [66, p. 3] that Γ_ν was developed for

constant-coefficient eddy-viscosity sub-filter scale models, and by the PCF results[24] in which the high-amplitude variations disappeared from all the moments. Taken together, it has been identified that Γ_ν is very likely unable to cope with assessments of dynamic-procedure IFLES.

In the case of $\Gamma_{\text{Celik-I}}$ (Suppl. Doc.-1, Table 4), more robust predictions were observed as opposed to Γ_ν. Therein, maxima, higher-order moments, and coefficients of variation of Γ_ν were overall reduced by several orders of magnitude alongside few exceptions. Although $\Gamma_{\text{Celik-I}}$ is also a function of ν_{sfs} like Γ_ν and the root cause of the exceptions were again traced to ν_{sfs}, the overall amelioration of $\Gamma_{\text{Celik-I}}$ arose from the fact that ν_{sfs} was wrapped by five elementary functions [65, Eq. 8a] in $\Gamma_{\text{Celik-I}}$'s formulation, which softened the effects of ν_{sfs} outliers.

With respect to $\Gamma_{\text{Celik-II}}$ (Suppl. Doc.-1, Table 5), two abnormalities were noted: $\Gamma_{\text{Celik-II}}$ was globally or locally able to exceed unity (e.g. the DHIT maxima), and be able to become negative (e.g. the HST minima). Celik et al. [65, p. 952] also observed such exceedances, and attributed them to a state when coarse-grid $k_{\text{ofs},1}$ locally exceeds fine-grid $k_{\text{ofs},2}$. In fact, any local $k_{\text{ofs},1}>k_{\text{ofs},2}$ breaks down the metric locally with either of an exceedance or negativity even when $k_{\text{ofs},1}<k_{\text{ofs},2}$ globally. This susceptibility can be tracked down to the denominator of the formula [65, Eq. 15] wherein the exceedance occurs when $k_{\text{ofs},1}\, k_{\text{ofs},2}^{-1}>1$, and the negativity when $k_{\text{ofs},1}\, k_{\text{ofs},2}^{-1}>\alpha^p$ (§2.2.2). Celik et al. [65, p. 953] argued that some failures of $\Gamma_{\text{Celik-II}}$ are because of realistic oddities in physical or numerical processes (e.g. backscatter). On contrary, here, the attribution of failures was made to a generic incapability of the metric formulation on the grounds that $k_{\text{ofs},1}\, k_{\text{ofs},2}^{-1}>1$ can still locally happen even for monotonically convergent computations. For instance, a resolution increase may result in a spatial translation of a dynamic structure in a computation. Thus, at a certain point and its neighbourhood, a substantial redistribution of fine k_{ofs} fields may transpire. The metric fails to detect such incidents or rule out their effects, which may then propagate neighbouring points or dominate the metric globally.

As regards $\Gamma_{\text{Celik-III}}$ (Suppl. Doc.-1, Table 6), the two aforementioned deficiencies of $\Gamma_{\text{Celik-II}}$ were observed to persist locally in spite of the statement that $\Gamma_{\text{Celik-III}}$ was a remedy [65, p. 952] to $\Gamma_{\text{Celik-II}}$'s deficiencies. The reason of the persistence is the denominator of the new formula [65, Eq. 18] which remains as a function of $(k_{\text{ofs},2}\text{-}k_{\text{ofs},1})$. Thereby $\Gamma_{\text{Celik-III}}$ could still exceed the unity or be negative.

Γ_{Pope}, on the other hand, provided relatively robust outcomes which nearly always did not cross

[24] The constant-coefficient Smagorinsky sub-filter scale model was in use (§2.1.2).

any viable metric limits. As an example, neither negative Γ_{Pope} nor abrupt changes were observed in the moments. Besides, Γ_{Pope} was identified not to be prone to any metric calibration owing to the fact that all independent variables of Γ_{Pope} arise from the computation itself. Unlike Γ_{Pope}, however, Celik et al.'s metrics require several constants to tune, and moreover, they cannot be precisely tuned according to the settings available. This heuristic further complicates assessments to some degree. Taking all the aforementioned premises, the use of Γ_{ν} and $\Gamma_{\text{Celik-I, II, III}}$ in the IFLES framework seems questionable, and despite the counterarguments mentioned in §2.2.1, Γ_{Pope} is arguably preferable among all metrics considered as far as its results are interpreted cautiously.

(*ii*) The numerical stability and the fulfilment of PISO building-block assumption were evaluated through Co_{mean} and Co_{max} which were measured approximately 0.25-0.28, 0.30-0.50, and 0.40-1.00 for the DHIT, HST and PCF cases, respectively. The values roughly obeyed the recommendations discussed in §3.1.1.4. Therefore, the computations were deemed 'adequate' in temporal aspect as well. (*iii*) Prior to the statistical convergence assessments, the computations were postulated to be statistically weak stationary and ergodic based upon the affirmative tests conducted for the same models and benchmarks within a non-CFD environment by [9, p. 457]. In the light of qualitative assessments, velocity and pressure's first four sample moment time-series were found to steadily approach a limit (not reported). Accordingly, the statistical convergence of the computational fields was assumed occurred. (*iv*) Lastly, the probe sample sizes were kept several times more than the threshold calculated in §3.1.1.7 (i.e. 13,000) to ensure the sample statistics reflect the statistical population of interest. The probe sample sizes for DHIT, HST and PCF were: 480,000, 364,000, and 60,000 elements, respectively. Thereupon, the statistical convergence of the probe samples was assumed.

4.2. DFM/FSM with default settings

4.2.1. Mean velocity

Mean velocity field is essential to the initiation, distribution and maintenance of turbulence. According to the energy cascade theorem [110], all the kinetic energy of turbulence is initially channelled out from the mean velocity field with an amount of mechanical work done by the mean velocity spatial gradient fields[25] on the Reynolds stress tensor field. In detail, the strain gradients of mean velocity (i.e. $\partial_i U_i$) stretch parallel and anti-parallel vortex structures (i.e. *vortex stretching*

[25] From now on, the term *gradient* refers to the *spatial gradient*.

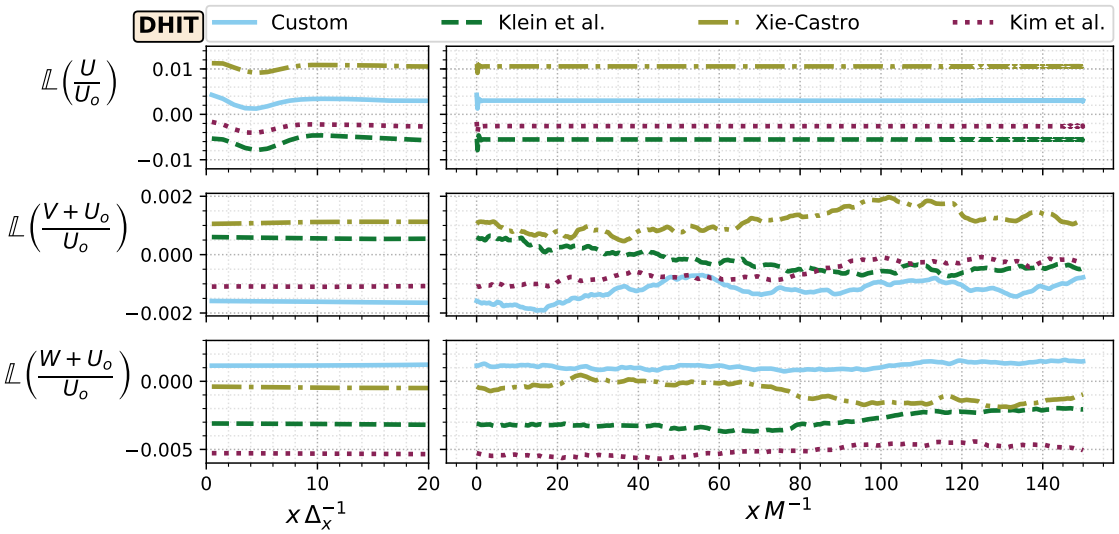

Figure 4: The mean velocity components from the decaying homogeneous isotropic turbulence computations (DHIT) [68]. The vertical axis of a subplot stands for the log percentage change of a component, i.e. $\mathbb{L}\equiv 100\log_e(x_{\text{data}}/x_{\text{bench}})$[cNp], with respect to the input longitudinal mean speed, U_o=12.7[ms^{-1}]. Of each component, $\mathbf{u}(\mathbf{x},t)\equiv(u,v,w)(\mathbf{x},t)$, the sample time-series were first time-averaged at each node, and then spatial-averaged in the statistically homogeneous lateral and vertical directions, hence $\mathbf{U}(x)\equiv(U,V,W)(x)$. The left- and right-block horizontal axes represent the *adjustment* and *evolvement* regions of the longitudinal distance of the computational domain, x, non-dimensionalised by the grid size, Δ_x, and the characteristic length M=0.0508[m], respectively. The V- and W-components were translated by U_o owing to the fact that the input V_o and W_o were zero.

minus *vortex squeezing*), whose diameters shrink to preserve their mass. Due to the conservation of angular momentum, the rotational speed of vortices increases with the reduced radius of rotation; thus, (de-)energising the surrounding velocity/vorticity field occurs at various scales. Moreover, the cross gradients of mean velocity (i.e. $\partial_j U_i$) bend and reorient the principal axes of right-angled vortices (i.e. *vortex tilting*), with which a portion of energy is transferred to the orthogonal vorticity fields. In view of these, any unintended alteration in the mean velocity gradient will eventually be reflected in the driving mechanisms of turbulence to a certain extent, e.g. mean velocity profiles in DFM were found to greatly affect LES results of planar turbulent jets by [1, p. 663][10, p. 10]. For this reason, the mean velocity information needs to be correctly conveyed into a computation.

In this section, *representative-to-all* remarks for the *conditioned* mean velocity component fields were presented with Figs. 4–6. In Fig. 4 (DHIT), the centineper *bench-diffs* of each mean velocity component were shown as a function of the downstream distance. In Figs. 5 and 6 (PCF), the vertical profiles of the velocity components were shown across the *adjustment* and *evolvement* *phases*, respectively.

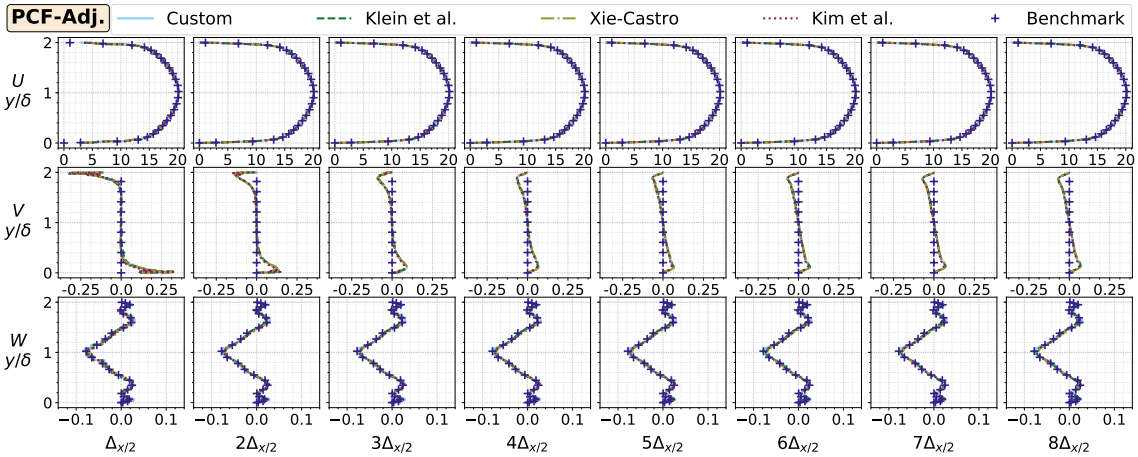

Figure 5: The along-channel-height profiles of the mean velocity components along the longitudinal *adjustment phase* (Adj.), i.e. the eight initial nodes from the inlet (left to right), from the computations of the smooth-wall plane channel flow (PCF) [70]. The vertical axes show the channel height, y, non-dimensionalised by the half channel height, δ. The horizontal axes illustrate the speed magnitudes in [ms^{-1}]. The time-averaged $\mathbf{U}(\mathbf{x})$ fields were arithmetic averaged in the statistically homogeneous direction, z, at the indexed longitudinal positions of the cell nodes, $\Delta_{x/2}$, thus $\mathbf{U}(x,y)\equiv(U,V,W)(x,y)$. It should be noted that the linear interpolation was turned off in the first-node results to avoid some code implementation issues, hence the stepwise appearance.

`[A.`i`]` As illustrated in the figures, at the first node next to the inlet, the maximum *bench-diffs* of all components were observed to be roughly $\mathcal{O}$(-2)/$\mathcal{O}$(-3)[cNp] for DHIT, HST and the bulk of PCF cross sections. Exceptions were identified in the vicinity of the PCF walls where the local *bench-diffs* were increased up to $\mathcal{O}$(2)[cNp]. `[A.`ii`]` Along the rest of the *adjustment phase*, the DHIT and HST *bench-diffs* of U initially declined by an amplitude of ≈0.004 & ≈0.01[cNp] until roughly their fourth node, and then recovered back to the input levels. `[A.`iii`]` In addition, in PCF, the *bench-diffs* of V nearby the walls were halved in the second node and then continued to gradually decrease. All the other *bench-diffs*, however, stayed roughly the same with the first node values along the *adjustment phase*. `[A.`iv`]` Throughout the *evolvement phase*, on the other hand, all the *bench-diffs* remained virtually at their input levels except HST-V which rose linearly in the negative direction, and PCF-W which contracted to an almost zero profile.

These findings have two implications: First, for each benchmark and component, the four model results were observed to follow look-alike trends and amplitude levels within few orders of magnitude smaller than the associated input. Therefore, it was ascertained that the different model mechanisms are ineffective on mean velocity field developments. Second, the models were found to be able to reconstruct input mean velocity profiles that can preserve themselves within a CFD domain or can

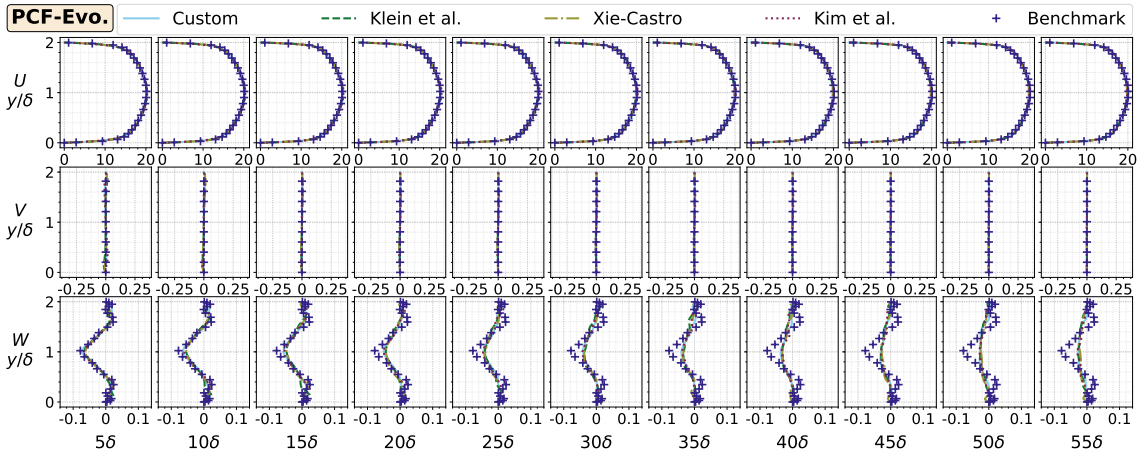

Figure 6: The along-channel-height profiles of the mean velocity components along the longitudinal *evolvement phase* (Evo.), i.e. 11 equidistant stations from 5δ to 55δ away the inlet (5δ-distance step), from the computations of the smooth-wall plane channel flow (PCF) [70]. The remaining figure particulars and axes limits are the same with Fig. 5.

appropriately develop downstream. The evidence was that the level of deviations was overall within $\mathcal{O}(-3)/\mathcal{O}(2)$[cNp] with respect to U magnitudes. Also, the deviations were similar irrespective of the presence of significant flow notions, such as shear stresses or walls. This postulation is in-line with [27, p. 45] who observed that the input length scales and Reynolds stress tensor do not affect the hybrid DFM-FSM's mean velocity profile developments. Nevertheless, these larger-than-machine-accuracy deviations were also expected due to the domain and equation discretisations, thus making assertion difficult whether the inflow models are the main contributors to these deviations.

These results suggest that no improvement is required for mean velocity capabilities of DFM/FSM in the level of traditional engineering accuracy requirements. This argument is in agreement with the DFM/FSM literature on various types of flows, [10, Fig. 3][2, Fig. 6, 11][17, Fig. 3] to name but a few.

4.2.2. One-spatial-point second-order correlation tensor

Within a flow, the one-point second-order symmetric correlation tensor of fluctuations (abbr. *the tensor*) shapes the energy transfer processes which are important determinants of mean and turbulent flow development. In simplified terms, as also mentioned in §4.2.1, the work done by the symmetric part of the mean velocity spatial gradient on the anisotropic part of *the tensor* [64, p. 126] channels out the energy of the mean velocity field into the fluctuating velocity field to be redistributed and dissipated. Therefore, the construction of *the tensor* is essential to the model

Table 4: The log percentage change, i.e. $100\log_e(x_{\text{data}}/x_{\text{bench}})$[cNp], of the Reynolds stress tensor components with respect to the corresponding benchmark data at four different stations, (i|ii|iii|iv). Within a table cell, the first two stations were in the *adjustment phase*: The station (i) is at the first node longitudinal-away from the inlet, and the (ii) is at the node approximately one length scale away from the inlet downstream, i.e. tenth, eleventh and fourth nodes for DHIT, HST, and PCF, respectively. The remaining two stations were in the *evolvement phase*: For DHIT, HST and PCF, the station (iii) is at $56M$, $2h$ and 5δ, and the station (iv) is at $129M$, $3.5h$ and 15δ, respectively, which corresponds to the benchmark data stations as shown in Figs. 7 and 10. In PCF results, the log percentage changes were computed by arithmetic averaging the absolute amplitude profiles to prevent any cancellation of negative and positive values. The reported results were rounded to one decimal places.

Case ↓	cNp →	Custom	Klein et al.	Xie-Castro	Kim et al.
DHIT	$u'u'$	-4.9|2.9|2.7|2.3	-0.1|9.0|24.4|9.9	-2.4|4.1|22.7|14.8	-2.8|3.7|-0.7|-3.9
	$v'v'$	-7.4|-18.2|-6.4|-0.2	-3.2|-7.3|20.7|14.5	-4.6|-11.4|15.9|16.7	-7.2|-15.6|-8.4|-4.1
	$w'w'$	-7.4|-18.1|-6.3|-0.0	-3.0|-7.2|20.7|14.6	-4.7|-11.4|16.1|16.8	-7.9|-16.9|-7.6|-3.6
HST	$u'u'$	-4.1|-2.8|-12.3|-16.4	0.3|6.0|0.6|-5.2	-2.1|0.7|-4.9|-9.0	-2.5|-1.8|-16.6|-22.9
	$v'v'$	-13.8|-21.1|-28.4|-25.7	-13.4|-14.1|-5.7|-3.2	-14.1|-17.4|-18.1|-14.6	-15.5|-21.3|-29.7|-30.0
	$w'w'$	-14.2|-28.4|-33.5|-28.9	-14.5|-22.8|-15.5|-10.8	-15.0|-26.1|-25.1|-19.4	-16.1|-29.6|-37.8|-34.9
	$u'v'$	-18.9|-69.1|-38.4|-36.7	-10.3|-51.6|-4.8|-5.6	-14.1|-61.8|-21.0|-18.9	-16.7|-63.7|-44.1|-46.8
PCF	$u'u'$	4.4|6.2|15.2|9.2	1.5|2.4|7.2|4.9	4.8|4.3|9.7|6.8	6.2|9.3|21.7|14.1
	$v'v'$	19.6|26.6|42.9|26.0	17.4|16.1|21.3|12.3	16.9|23.7|33.6|15.4	20.9|31.8|54.1|33.9
	$w'w'$	12.3|19.1|37.5|23.4	8.9|11.6|19.0|11.2	10.1|15.2|26.7|12.8	12.0|22.0|47.1|30.2
	$u'v'$	39.0|131.5|54.6|12.2	27.0|136.6|20.8|13.8	38.6|147.3|42.7|12.7	40.9|116.6|71.3|21.0

system of a turbulent flow, hence the synthetic time-series generation.

In this part, the *conditioned* results of *the tensor* were illustrated by Figs. 7–10 and Table 4, and *representative-to-all* remarks were discussed. In Fig. 7 (DHIT & HST), the longitudinal profiles of *the tensor* components were shown with a close-up of the *adjustment phase*. In Figs. 9 and 10 (PCF), the channel-height profiles of the components were demonstrated at a number of successive observation planes of the *adjustment* and *evolvement phases*. The corresponding centineper *bench-diffs* were given in Table 4. In the following, *the tensor* was more closely monitored and discussed in detail at four stations: two *adjustment phase* stations, i.e. the first node and the node at one-longitudinal integral scale distance downstream, and two *evolvement phase* stations for which benchmark measurements were available. *The tensor* components of $\overline{u'w'}$ and $\overline{v'w'}$ were left out from the presentation because of their pseudo-random dispositions at levels of $\mathcal{O}(\text{-}5)/\mathcal{O}(\text{-}8)[\text{m}^2\text{s}^{\text{-}2}]$.

At the first *adjustment-phase* node, the flow is dominated by effects of the inlet boundary condition (hence, DFM/FSM) owing to the considerably lower boundary area of the lateral boundary conditions therein. With this in mind, five generalised observations were made there. [B.i] First, the amplitude of all the input *tensor* components was reduced for all the benchmarks and models except Klein model in HST-$\overline{u'u'}$. As can be deduced from Table 4 and Figs. 7 and 9, the extent of amplitude reductions in terms of *bench-diffs* was between $\mathcal{O}(\text{-}1)/\mathcal{O}(2)$[cNp] within the DHIT-HST-PCF scenarios. [B.ii] Second, in terms of patterns across *the tensor* components, $\overline{u'u'}$ *bench-diffs*

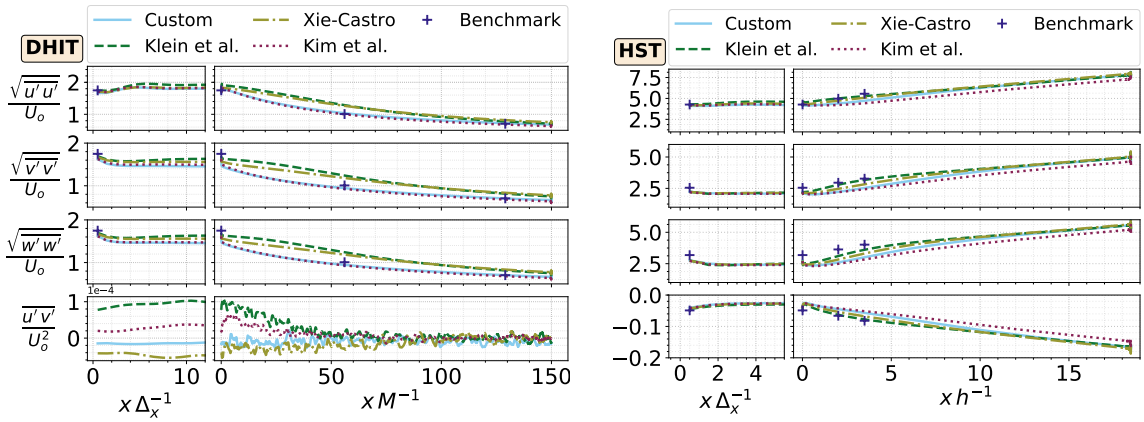

Figure 7: The longitudinal profiles of the one-point second-order symmetric correlation tensor of fluctuating velocity components from the decaying homogeneous isotropic turbulence (DHIT, the left subplot) [68] and homogeneous shear turbulence (HST, the right subplot) [69] computations. The sample fluctuating velocity field, $\mathbf{u}'\equiv(u',v',w')(\mathbf{x},t)$, was first cross-producted with itself at each spatial node, i.e. $(\mathbf{u}'\times\mathbf{u}')(\mathbf{x},t)$, and then cumulative moving time-averaged, thus $(\overline{\mathbf{u}'\times\mathbf{u}'})(\mathbf{x})$. The resulting fields were then arithmetic spatial-averaged in the statistically homogeneous lateral and vertical directions, hence $(\overline{\mathbf{u}'\times\mathbf{u}'})(x)$. Herein, $\overline{u'w'}$ and $\overline{v'w'}$ were excluded owing to their pseudo-random patterns. The vertical axes of the subplots represent the tensor components normalised by the input longitudinal mean speeds, $U_{o,\mathrm{DHIT}}$=12.7[ms^{-1}] & $U_{o,\mathrm{HST}}$=12.4, and multiplied by 100. The horizontal axes illustrate the longitudinal distance from the inlet, x, normalised by the uniform cell size, Δ_x, for the *adjustment phase* (the left sub-subplots) and the characteristic lengths M_{DHIT}=0.0508[m] and h_{HST}=0.305 for the *evolvement phase* (the right sub-subplots).

were found to be consistently lower than its orthogonal and shear neighbours in all scenarios. For instance, the DHIT *bench-diffs* of $\overline{v'v'}$ and $\overline{w'w'}$ were roughly twice those of $\overline{u'u'}$. [B.*iii*] Moreover, the level of *bench-diffs* of the spatial-variant shear component $\overline{u'v'}$ in PCF was observed to be several times higher than those of its normal components in contrast to HST wherein the order of spatial-invariant $\overline{u'v'}$ was similar to its lateral components. [B.*iv*] Looking for patterns across the models revealed two particulars: With the default settings of the models, Klein model produced the least *bench-diffs* throughout almost all the scenarios. Even in case of the exceptions, Klein model remained the closest to the least *bench-diff* models. For example, Klein model's *bench-diff* in HST-$\overline{w'w'}$ was -14.5[cNp] whilst the least *bench-diff* from Xie model was -14.2[cNp]. In opposition to Klein model, Custom and Kim models almost always yielded the highest *bench-diffs* for the same scenarios. [B.*v*] Lastly, the aforementioned remarks were unaffected by the progression of flow fidelity, i.e. the addition of shear stresses (from DHIT to HST), or of wall boundary conditions (from HST to PCF).

The direct causal role of DFM/FSM in the deviations observed above was ruled out by the evidence shown in [9, Fig. 5] which illustrated that the models in the same yet non-CFD setups

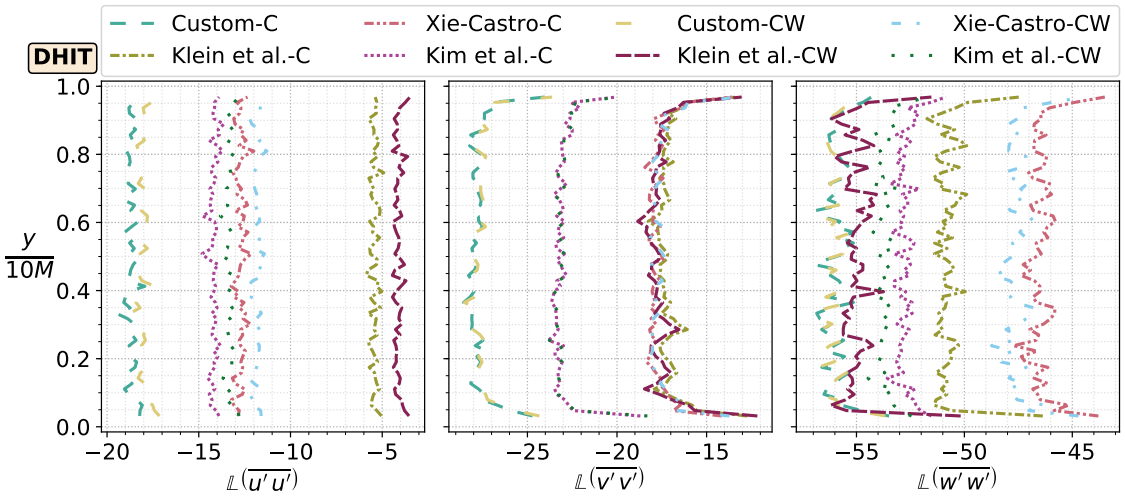

Figure 8: The inlet-height profiles of the diagonal components of the one-point second-order correlation tensor, i.e. $(\overline{\mathbf{u}'\times\mathbf{u}'})(y)$, obtained from a non-CFD decaying homogeneous isotropic turbulence (DHIT) computation on which divergence-freeness, i.e. $\nabla\cdot\mathbf{u}\approx 0$, was subsequently imposed. The same data reduction in Fig. 7 was applied onto $\mathbf{u}'(\mathbf{x},t)$ to obtain $(\overline{\mathbf{u}'\times\mathbf{u}'})(y)$ except that the arithmetic spatial-average was performed in the longitudinal x-, and lateral z-directions. The vertical axes show the domain inlet height, y, non-dimensionalised by ten times the characteristic length M=0.0508[m], and the horizontal axes the log percentage change of a component, i.e. $\mathbb{L}\equiv 100\log_e(x_{\text{data}}/x_{\text{bench}})$[cNp], with respect to the corresponding tensor results of the non-corrected non-CFD $\mathbf{u}(\mathbf{x},t)$ fields. In the legend, the affixes '-C' and '-CW' denote the *divergence correction scheme* [111] and the *weighted divergence scheme* using *generalized cross validation optimisation* [112], respectively, which were designed to zeroize the velocity field divergence of a volumetric particle image velocimetry dataset with aiming minimum alteration of the velocity field.

are able to reconstruct an input *tensor* almost exactly. It is postulated that three contributors are associated with the five remarks: (*i*) the first-time execution of the N-S equation algorithms on synthetic time-series, (*ii*) the first-time enforcement of the velocity solenoidality due to the incompressibility condition, and (*iii*) the *transfer phases* illustrated in Fig. 3. A pre-assessment indicated that only the *post-mapping phase* among the other *transfer phases* can be influential on the deviations (discussed in §4.5) since effects of the first two *transfer phase* were naturally absent in the DHIT-HST computations. On the other hand, the divergence-freeness enforcement on synthetic time-series entirely acts within the first node. However, a presumption that the solenoidal condition is the dominant contributor may still be speculative. Therefore, the divergence-freeness enforcement was isolated from the other N-S equation procedures, and investigated as follows.

Non-CFD DHIT computations using the current models and settings were performed, and the divergence of the resultant velocity fields was attempted to be locally removed with minimum stochastic and statistical distortion via two experimental tools: the *divergence correction scheme* from [111]

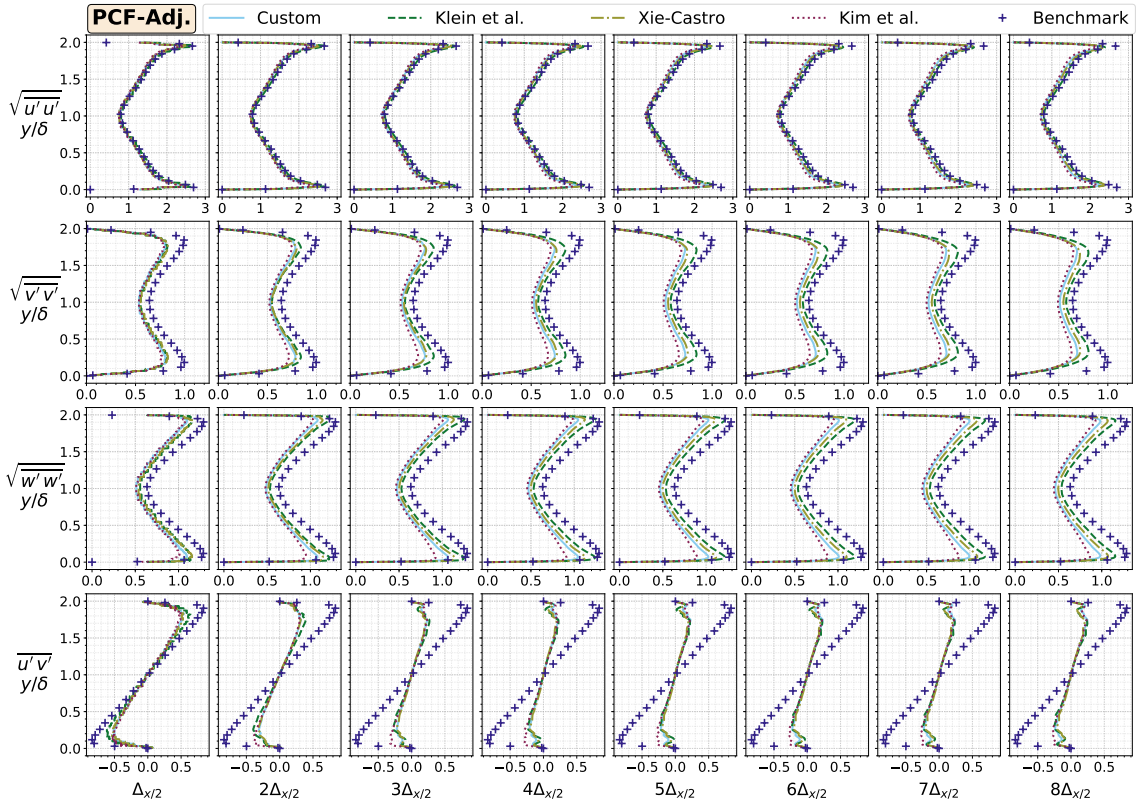

Figure 9: The along-channel-height profiles of the one-point second-order symmetric correlation tensor components along the longitudinal *adjustment phase* (Adj.), i.e. the eight initial nodes from the inlet (left to right), obtained from the smooth-wall plane channel flow (PCF) computations [70]. The vertical axes signify the channel height, y, normalised by the half channel height, δ, and the horizontal axes the magnitude of the tensor components row-wise.

and the *weighted divergence scheme* using *generalized cross validation optimisation* from [112].[26] Also, the level of divergence-freeness of synthetic time-series was quantified by Zhang et al.'s metric, δ_z [113, Eq. 25], where δ_z=1.0 means a complete non-solenoidal field, and δ_z=0.0 an exact solenoidality [113, p. 12]. The quantifications for each scenario showed that $\delta_z \approx 1.00$ and $\delta_z \approx 0.17$ before and after the corrections, respectively. Accordingly, the divergence-freeness of the corrected fields was assumed. *The tensor* was then computed for an inspection in Fig. 8.

From Fig. 8, the observation [B.*i*] and the isolated divergence-freeness enforcement appeared to be closely related since the amplitude of all *the tensor* components belonging to the corrected fields was also downscaled therein. Concerning the reason of the observation [B.*ii*], the evidence from Fig. 8 suggested a link to the divergence-freeness enforcement as well while the *bench-diffs* of

[26] In actuality, the two tools are in order for volumetric particle image velocimetry measurement corrections.

the new $\overline{u'u'}$ were also observed the lowest as against the lateral components. With this potential link, the mean flow speed in each direction was identified as the prominent difference amongst *the tensor* components: U was at least two orders of magnitude greater than V and W in the benchmarks. Based on this remark, the directional mean speeds were extracted from the non-CFD time-series on hand, and consecutively, the corrections were conducted in the same way. The results disclosed that when the mean speeds were removed, *the tensor* component amplitudes were equally reduced with the divergence-freeness enforcement (not reported). This disclosure highlighted the amplitude differences among mean speeds as a principal determining factor of the observation [B.*ii*]. For the greater-valued mean speed direction, the level of amplitude alterations due to divergence-freeness enforcement reduces in comparison to the other directions. On the question of the reason behind the observation [B.*iv*], the same ranking in terms of the resemblance level to the benchmark was found in Fig. 8. As an example, the *bench-diffs* of $\overline{u'u'}$ there were around -5[cNp] for Klein and -18[cNp] for Custom methods. However, the mainspring of Klein model's superiority in this regard could not be identified. Therefore, it was confined that an unidentified mechanism exists within Klein method which facilitates the divergence-freeness imposition, thus leading to less distortion in the input Reynolds stress tensor relative to the other methods. Nevertheless, it can also be pointed out that being DFM should not be the reason, because Custom yielded the highest *bench-diffs*.

The overall contribution of other boundary conditions to the flow development monotonically increases downstream. Therefore, DFM/FSM information effects gradually fade away. With that in mind, at the cross sections of one-longitudinal integral scale downstream, four observations were made. [C.*i*] Firstly, the *bench-diffs* were mostly increased at a level from less than one times (e.g. HST-$\overline{v'v'}$) to five times (e.g. PCF-$\overline{u'v'}$) in comparison with the first-node state. As demonstrated in Table 4, the increment occurred in 38 scenarios out of 44, wherein all models showed an increase in 7 component-wise cases, and at least three models produced an increment in all cases. [C.*ii*] Secondly, the observations [B.*i*] and [B.*ii*] persisted for the lateral components; however, $\overline{u'u'}$ mainly switched to an overprediction with no particular pattern in its *bench-diff* changes. Furthermore, the level of *bench-diffs* in $\overline{u'u'}$ departed from the observation [B.*iii*] levels several times. [C.*iii*] Thirdly, likewise to [B.*iv*], Klein and Custom/Kim models retained the lowest and highest *bench-diffs* in most cases, i.e. in 8 and 9 out of 11 component-wise cases, respectively. Sporadic counterexamples were also observed like in DHIT-$\overline{u'u'}$ where the ranking became the opposite way round. [C.*iv*] Finally, closer inspection of Figs. 7 and 9 qualitatively showed that the rate of changes in *the*

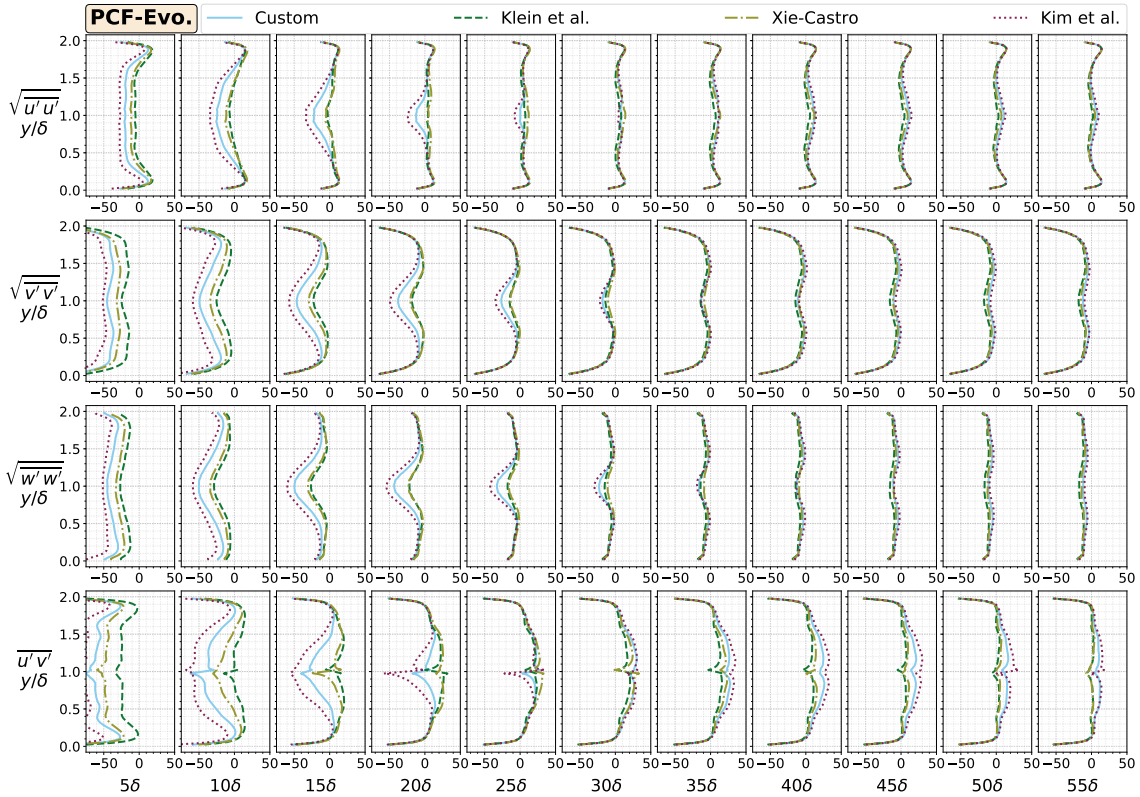

Figure 10: The along-channel-height profiles of the one-point second-order symmetric correlation tensor components along the longitudinal *evolvement phase* (Evo.), i.e. 11 equidistant stations from 5δ to 55δ away from the inlet in 5δ-distance steps, obtained from the smooth-wall plane channel flow (PCF) computations [70]. The results represent the log percentage changes with respect to the benchmark, i.e. $\mathbb{L}\equiv 100\log_e(\bullet)$ centineper [cNp]. The absolute amplitudes were given in Fig. A.24. The remaining figure particulars and axes limits are the same with Fig. 9.

tensor became virtually constant for DHIT, HST and PCF after the 4-6$^{\text{th}}$, 2$^{\text{nd}}$ and 3-8$^{\text{th}}$ nodes, respectively. This, however, does not imply fully developed turbulence, yet a starting point for its gradual evolvement, which may help downstream predictions for *the tensor*.

Further downstream, at two selected planes of the *evolvement phase*, three generic observations were noted. [D.i] To begin with, the underprediction trends previously noted in [B.i] and [C.i] continued to present in the *evolvement phase* at the level of $\mathcal{O}(1)/\mathcal{O}(2)$[cNp], albeit less frequently. In 28 scenarios of DHIT-HST combined, for instance, 20 of them retained the underprediction relative to the first-plane benchmark, and in the second plane, the number increased to 21. Some counterevidence to this premise, nonetheless, emerged from $\mathcal{O}(2)$-level [cNp] overpredictions made by Klein and Xie methods in DHIT for each component. [D.ii] Also, the relative levels between the *bench-*

diffs of *the tensor* components remained the same as in the observations [B.*ii*] and [C.*ii*]. [D.*iii*] In parallel to [B.*iv*] and [C.*iii*], the model ranking in terms of the *bench-diffs* also remained nearly unchanged along the *evolvement phase*. Klein and Kim models yielded the lowest and highest *bench-diffs* in turn in 8 out of 11 component-wise cases, and the exceptions arouse out of DHIT where this ranking was reversed. [D.*iv*] The *adaptation lengths* of *the tensor* were observed in different trends for free-shear and wall-bounded flows. On the assumption that the *adaptation length* criterion for free-shear flows is approximately reaching a linear rate of change in amplitude of the components as a function of the longitudinal distance, it was inferred from Fig. 7 that the *adaptation length* was reached within the *adjustment phase* irrespective of the models and components. For wall-bounded flows, another criterion deemed more appropriate was assumed: the first-time reduction of the maximum and absolute *bench-diff* below 15[cNp] across *the tensor* profile during a declining trend. On this basis, *bench-diff* analyses of Figs. 9 and 10 revealed that the *adaptation lengths* were exclusively reached within the *evolvement phase* for all models and components: The approximate *adaptation lengths* of $\{u'u', v'v', w'w', u'v'\}$-components in Klein, Xie, Custom and Kim models were $\{10\text{-}15, 20\text{-}25, 25\text{-}30, 5\text{-}10\}[\delta]$,$\{10\text{-}15, 20\text{-}25, 25\text{-}30, 10\text{-}15\}[\delta]$, $\{15\text{-}20, 30\text{-}35, 35\text{-}40, 15\text{-}20\}[\delta]$, and $\{20\text{-}25, 30\text{-}35, 35\text{-}40, 25\text{-}30\}[\delta]$. If the criterion is, however, relaxed for the close vicinity of the centreline of the channel, these *adaptation lengths* reduce to a considerable extent. Such relaxation may be viable since the overpredictions of *the tensor* components were also observed in various similar-resolution studies, e.g. [17, Fig. 3, p. 61].

In summary, four concluding remarks can be drawn from *the tensor* investigations: This study has identified a general tendency of $\mathcal{O}(1)/\mathcal{O}(2)$-level [cNp] amplitude reduction in the input *tensor* components within *adjustment-phase* and successive *evolvement-phase* nodes ([B.*i*] [C.*i*] [D.*i*]). The tendency is virtually independent of benchmarks, models and *tensor* components. The same tendency was also reported by [13, p. 1112] for the lateral components; however, the authors conceded that they could not offer an adequate explanation for the reduction. On the other hand, the quantifications of this study indicate that the divergence-freeness enforcement is the dominant factor in the *adjustment-phase* reductions, which observed shaping *evolvement-phase* trends as well, particularly for free-shear flows. The second major finding is that the longitudinal $\overline{u'u'}$ component nearly always deviates from the input less than the lateral and shear components irrespective of benchmarks and models ([B.*ii*] [C.*ii*] [D.*ii*]). The findings suggested that the underlying determinant may be the higher mean speed U, and its interactions with divergence-freeness enforcement. The research has

also shown that Klein model in general provided the lowest *bench-diffs* and shortest *adaptation lengths* for *the tensor* whereas Custom/Kim methods the opposite ([B.*iv*] [C.*iii*] [D.*iii*]). Although DFM/FSM used the same *Lund transformation* for *the tensor* reconstruction and [9, p. 450] demonstrated the same models yielded no *tensor* component differences in non-CFD setups, the models differently behaved in CFD. This rather inconsistent result is attributed to an unidentified factor within DFM/FSM stages prior to the *Lund transformation* that interacts with CFD in different ways, hence dissimilar *tensor* results among the models. Finally, as regards the longitudinal changes of *bench-diffs*, [27, p. 38] asserted that *the tensor* monotonically changes. However, the findings of this study disconfirm this overgeneralization, and suggest that the *bench-diffs* follow a pattern similar to an asymmetric quadratic function (i.e. initially increasing then decreasing) rather than a monotonic function. This quadratic pattern also implies that *the tensor* as an *adaptation length* indicator always needs to be interpreted with caution in contrast to the conventional practice in the literature. Nonetheless, the changes could be deemed monotonic if the *adjustment phase* is completely omitted.

4.2.3. Two-spatial/temporal-point correlation functions

Amplitude-based tools (e.g. Reynolds stress tensor) do not convey any information regarding the spatial-temporal structure of turbulence (e.g. *white noise*s and *triangular wave*s are indistinguishable through the amplitude-based tools although both possess disparate temporal structures [114, p. 2-5]). This deficit is covered by the two-spatial/temporal-point correlation function tensor (here, the tensor input was limited to its normal components, hence autocorrelations). The size and shape of tensor components affect turbulence development: Elementarily, the size determines the degree of influence of one-location/time fluctuations' amplitude on other location/time fluctuating quantities' amplitude. Also, through the size, the viscous energy dissipation rate is determined. The shape, on the other hand, characterizes the energy composition in the frequency domain.

In view of its importance, the *development phase* of the input two-point[27] autocorrelation functions (abbr. *acorr*) was investigated in this section. The *conditioned* results were displayed in Figs. 11–15. Fig. 11 (DHIT) compared the longitudinal *acorrs* from the first *adjustment-phase* node and corresponding non-CFD cases to find out the *adjustment phase* effects on input *acorrs*.

[27] *Two-point* meant spatial points in the lateral directions, and temporal points in the longitudinal direction via Taylor's frozen turbulence hypothesis [59].

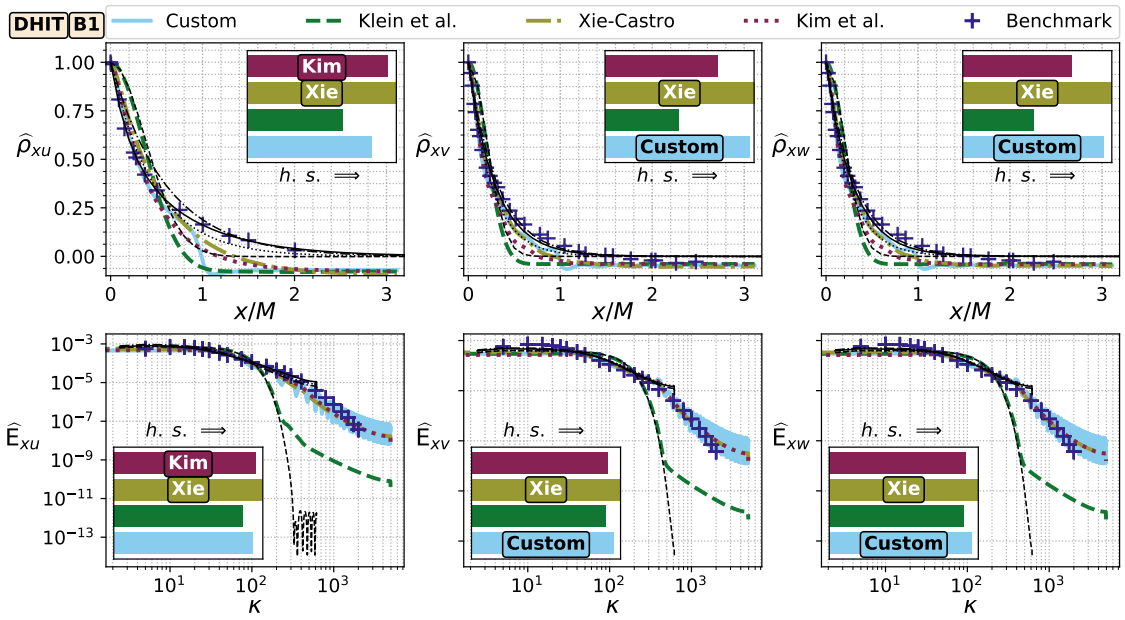

Figure 11: The two-temporal-point longitudinal sample autocorrelation function, $\widehat{\rho}_{mn}$[-], (the top subplots) and one-dimensional sample power spectral density function, $\widehat{\mathrm{E}}_{mn}$[m^{3}s^{-2}], (the bottom subplots) results obtained from the first block of nodes (B1) of the decaying homogeneous isotropic turbulence computations (DHIT) [68]. Along the vertical axis, the statistic magnitudes are given. 'mn' stands for the measurement direction 'm' and measured velocity component 'n', respectively. The horizontal axes of the top subplots represent the spatial lag, x, normalised by the characteristic length M=0.0508[m], and those of the bottom subplots the spatial wavenumber, κ[m^{-1}]. For each node time-series, the statistics were computed and then arithmetic spatial-averaged in the statistically homogeneous directions, i.e. (y, z). The inner horizontal bar charts show the Fréchet distance of the model curves to the benchmark. Each bar height was normalised by the most similar model's distance magnitude, thus the maximum height of a bar is the unity. '$h.s.$' with the arrow denotes the direction of higher similarity.

In Fig. 12 (DHIT), the metamorphosis of the same set of *acorrs* was tracked along the *evolvement phase*. Furthermore, through Figs. 13–15 (PCF), the level of *bench-diffs* formed within the *evolvement phase* was exemplified from a broader perspective by two *acorrs* and a two-point cross-correlation function (abbr. *ccorr*).

At the first *adjustment-phase* node, five premises were identified: [E.*i*] Throughout the benchmarks, models and *acorr* components, a maximum of $\mathcal{O}(1)$[cNp] decrement was detected in *acorr* levels in a form of gradual decrease after 0.2-0.4 characteristic length by contrast to their non-CFD counterparts. [E.*ii*] Further to this, with regard to patterns amongst *acorr* components, all predictions either went to negative or briefly fluctuated around zero after a certain lag onwards (at least a characteristic length or more), particularly for the u-component *acorr*. [E.*iii*] Notwithstanding this transfiguration, the shape of input *acorrs* was conserved, i.e. Klein model produced a Gaussian-

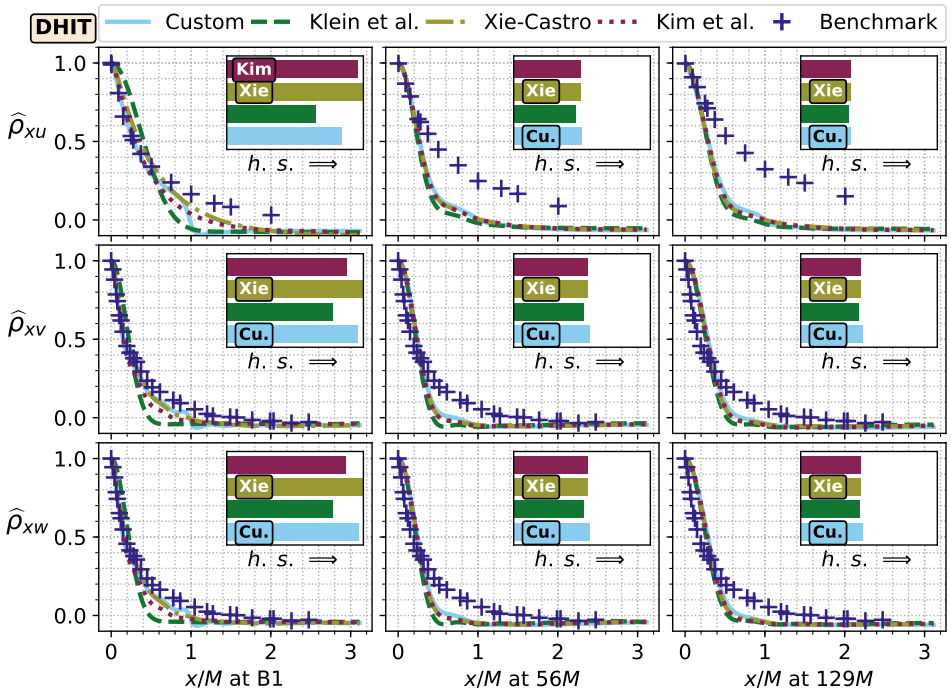

Figure 12: The two-temporal-point longitudinal sample autocorrelation function results from the decaying homogeneous isotropic turbulence computations (DHIT) [68] at three observation stations: the first block of nodes, i.e. B1 ($\approx 0M$), $56M$, and $129M$ longitudinally away from the inlet boundary, which correspond to $42M$, $98M$ and $171M$ benchmark stations in [68, p. 292]. The figure descriptors are the same with Fig. 11.

form, and the others an exponential-form. [E.*iv*] Additionally, observing model patterns across the same scope revealed that Klein model brought forth the highest *bench-diffs* in unit of Fréchet distance without any counterexample unlike its superiority in the Reynolds stress tensor predictions. By contrast, Xie, Custom and Kim models resulted in the lowest *bench-diffs* for 6, 2, and 1 cases within 9 component-wise cases, respectively, by closely following each other. The Gaussian-exponential form differentiation was in accord with the non-CFD observations [9, p. 453]. [E.*v*] On top of these, the correlation functions of the second and third nodes were also monitored (not shown), and compared to those of the preceding node to spot prospective patterns. However, almost no difference smaller than the half-precision machine epsilon was observed in amplitudes and shapes of the functions.

The causes of the observations [E.*i*] and [E.*ii*] have been a subject of further investigation. The *acorr* reduction represented that the *first-order successive difference* of fluctuation amplitudes at consecutive points is generally in increase along a direction, hence more 'jigsaw' appearance in

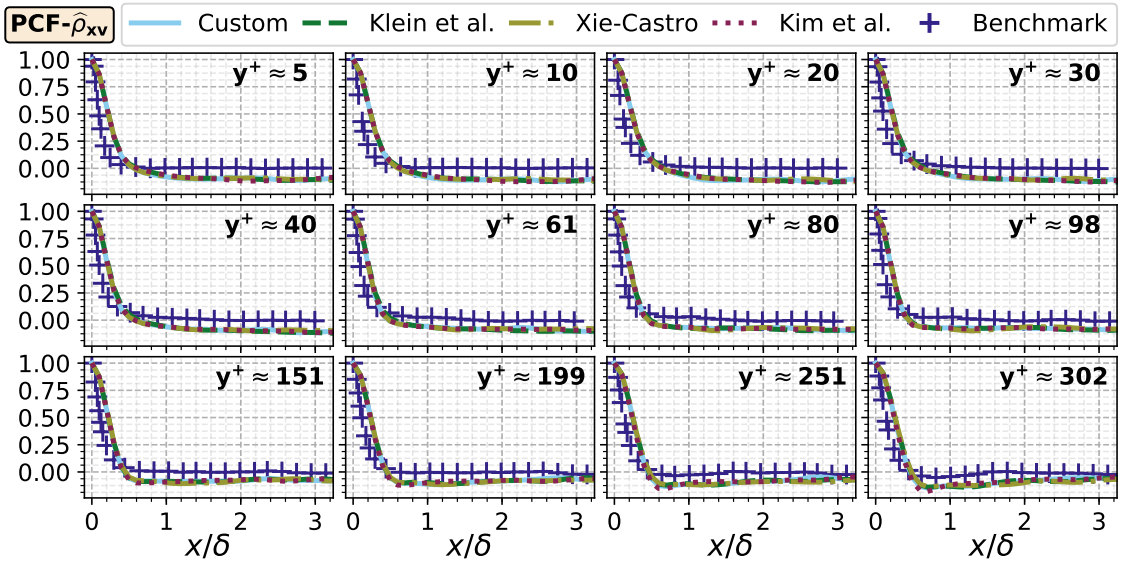

Figure 13: The two-point sample autocorrelation functions of $\widehat{\rho}_{\mathrm{xv}}$ obtained from the smooth-wall plane channel flow computations (PCF) [70]. The subplots illustrate the results at twelve wall-normal stations, y^+=$u_\tau\, y\, \nu^{-1}$, where y^+ is the dimensionless distance from the bottom wall, u_τ=1.0[ms^{-1}] the friction velocity, ν=0.002531646[m^{2}s^{-1}] the fluid kinematic viscosity that associates with Re_τ=395. The samples were obtained from the spatial-accurate points given by [70] along the longitudinal direction, x, starting from x_0=40[m], hence Taylor's frozen turbulence hypothesis was not used. The horizontal axis is non-dimensionalised by the channel half height, δ=1.0[m], and the other figure descriptors are the same with Fig. 11.

time-series. In the same vein, the negativity in *acorr* tails described an emerging anti temporal relationship between consecutive fluctuations. Therein, the probability of concurrent occurrence of opposite-amplitude fluctuations at lag-zero and lag-t was amplified. For this reason, the dominant sign of fluctuations show more frequent reversals as time progresses. Nonetheless, this reduction does not imply a homogeneous decrease/increase in amplitudes themselves. Therefore, a factor which is spatially/temporally less uniform in its effect is expected as dominantly responsible for this reduction. With this insight, similar to §4.2.2, the non-CFD divergence-freeness enforcement was carried out to isolate solenoidality effects on *acorrs*. However, no appreciable effect on *acorrs* within the single-precision machine accuracy was observed (not shown). Consequently, it is postulated that the divergence-freeness enforcement has spatially-uniform impact on synthetic time-series, and does not play a role in shaping *acorrs*. Instead, due to the inability for further isolation among three agents listed in §4.2.2, it has only been speculated that the N-S equation algorithms and domain/equation discretisations gave rise to this *acorr* reduction at the first *adjustment-phase* node.

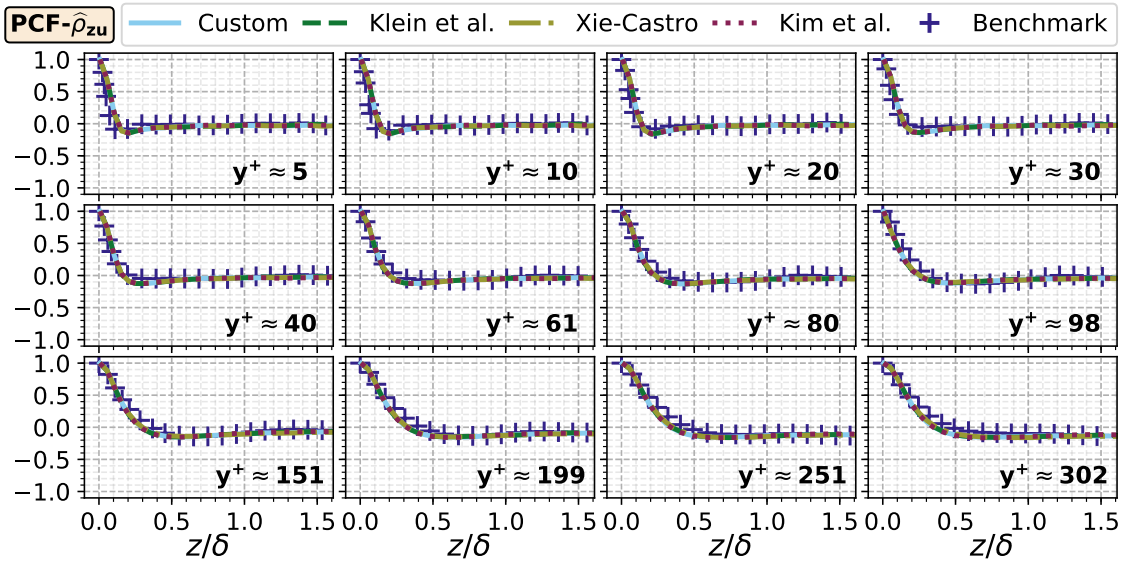

Figure 14: The two-point sample autocorrelation functions of $\widehat{\rho}_{\mathrm{zu}}$ obtained from the smooth-wall plane channel flow computations (PCF) [70]. The figure descriptions are the same with Fig. 13 except the following: The samples were obtained from the spatial-accurate points given by the benchmark along the lateral direction, z, at x_0=40 [m] and indicated y^+, hence no Taylor's frozen turbulence hypothesis.

With regard to the *evolvement phase*, five patterns were found: [F.*i*] What stands out in this phase throughout all benchmarks and models was the convergence of *acorrs* and *ccorrs* towards the same function, which qualitatively resembled with a Gaussian-form most of the time. As exemplified in Fig. 12, the model differences virtually disappeared according to the Fréchet distance. [F.*ii*] What can also be seen was that the wall-bounded flow led to shape trends closer to the benchmark and lower *bench-diffs* than the free-shear flows with the exclusion of longitudinal pressure correlations. From the data in Fig. 12, it can be seen that the model results in DHIT disunited the benchmark around 0.2 characteristic length up to a *bench-diff* of $\mathcal{O}(2)$[cNp], which deepened downstream while the benchmark *acorrs* were amplified. In spite of that, as illustrated in Fig. 13 for all channel height stations of PCF, the models made overpredictions till 0.4 characteristic length and then underpredictions in the level of $\mathcal{O}(1)$ *bench-diff* [cNp]. [F.*iii*] Furthermore, the converged model *acorrs* of the free-shear flow cases remained approximately the same along the *evolvement phase* despite the benchmark length scales were reported in increase, especially for *u-acorrs* [68, Fig. 5] [69, Fig. 18]. Also, the anti-correlation trend of the *adjustment phase* after around one characteristic length arguably persisted in most cases, albeit weaker. [F.*iv*] As far as the patterns among the

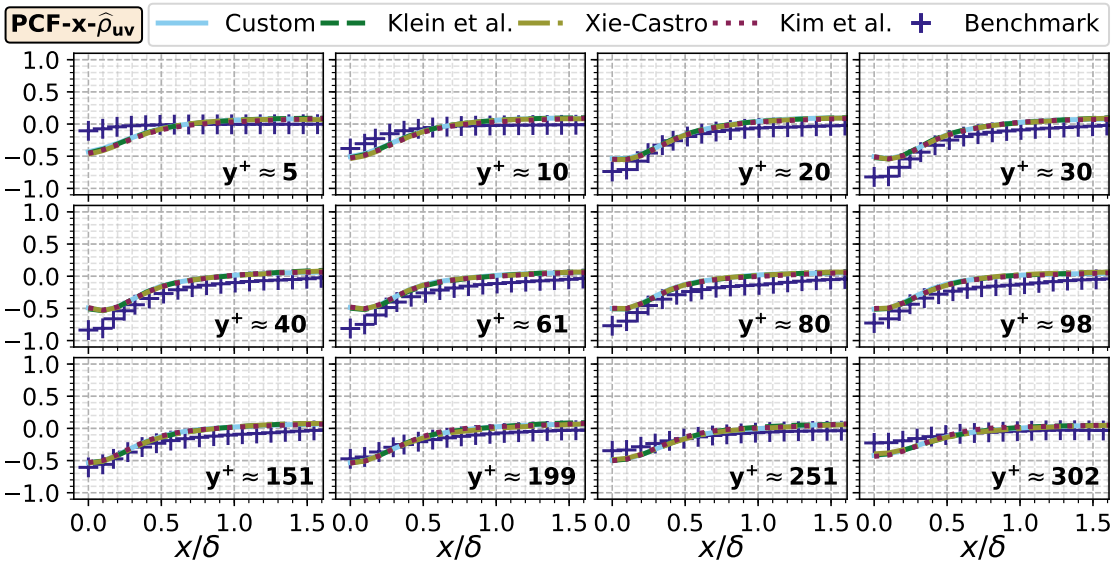

Figure 15: The two-spatial-point sample cross-correlation functions of $\widehat{\rho}_{\text{uv}}$ measured along the longitudinal direction, x, of the smooth-wall plane channel flow computations (PCF) [70]. The figure descriptions are the same with Fig. 13.

components are concerned, the lateral *acorrs* and *ccorrs* were frequently observed involving lower *bench-diffs* than the longitudinal correlations.[28] An illustration of this can be seen in Fig. 12 where the maximum *bench-diffs* of the longitudinal component were approximately twice those of the lateral components. [F.v] In addition to this, a PCF comparison between Fig. 13 and Fig. 14 qualitatively indicated that the *acorrs* across all channel height stations in the x-direction had lower level of resemblance with the benchmark in comparison to the z-direction in terms of amplitudes and trends. This postulation also seems valid for *ccorrs* (not shown).

The first of two reasons why the observation [F.i] occurred is claimed to be the domain/equation discretisations rather than the N-S equations due to the fact that the converged profiles overall did not resemble the benchmark profiles that are natural outcomes of the N-S equations. The second is the accumulating dominance of the lateral boundary conditions over the inlet. Because of these, the possibility of contributions from DFM/FSM in *acorr* degradations along the *evolvement phase* are ruled out. The most likely causes of the observations [F.ii] and [F.iii] could be sought in the main differences between the free-shear and wall-bounded flow cases. The first difference is that the free-shear cases had finer temporal and spatial resolutions, e.g. DHIT, HST, and PCF possessed

[28] These remarks are not relevant to HST since no downstream *acorr* benchmark was available.

≈10, ≈10.4 and ≈3.9 nodes per their longitudinal-u length scale. Another main difference is the Smagorinsky sub-filter scale model setup in which the free-shear cases used a dynamic procedure whereas the wall-bounded case calibrated model coefficients. The last dissimilarity is the turbulent kinetic energy production mechanism as illustrated in Figs. A.27 and A.28. The free-shear cases rely on internal spatial gradients of mean velocity whilst the wall-bounded case on the same quantity, yet highly agitated by the no-slip velocity boundary condition. Despite the favouring setup fidelity for the free-shear cases, the occurrence of high level of *bench-diffs* relative to the wall-bounded case eliminated the setup setting effects from possible reasons. This inconsistency may suggest that more difficulty in sustaining turbulence in a free-shear flow than wall-bounded flows is likely the main reason of the two observations. Lastly, as far as the observation [F.v] concerned, the causing reason can be attributed to the lower resolution in the x-direction, i.e. Δ_x=0.1 and Δ_z≈0.045[m].

4.2.4. One-dimensional one-sided power spectral density functions

Power spectral density functions are Fourier transform pairs with their corresponding autocorrelation functions for stationary processes (the *Wiener-Khinchin theorem*). Although this implies that both essentially possess the same influence on turbulence development, the former is a complementary tool that helps to draw conclusions from the same information inaccessible otherwise, such as how power and frequency contents are distributed over different spatial structures [78, p. 248] [114, p. 2-8]. In accordance with this, the *conditioned* and *representative-to-all* results for the *development phase* of the one-dimensional one-sided power spectral density functions (abbr. *psd*) were presented in this section via Figs. 11 and 16; in which Fig. 11 (DHIT) demonstrated the *adjustment phase* effects on the longitudinal *psd* components, and Fig. 16 (HST) the *evolvement phase* of the same components.

Two remarks were made for the first *adjustment-phase* node. [G.i] By comparison to the non-CFD results, a $\mathcal{O}$(-1)-times reduction was noted at the lowest wavenumber region for all benchmarks, methods and *psd* components. Nevertheless, the central and high wavenumber regions of the *psd*s were qualitatively found almost the same with their non-CFD counterparts. [G.ii] As regards model patterns, Klein model was observed possessing a premature drop starting from the central wavenumber range whereas the other models followed benchmark's and each other's pattern without any drop. Similarly, the drop was also found by [9, Fig. 9] for the same non-CFD benchmarks, and by [33, Fig. 6] for a CFD-DHIT study. Despite this, all the models were able to reconstruct the

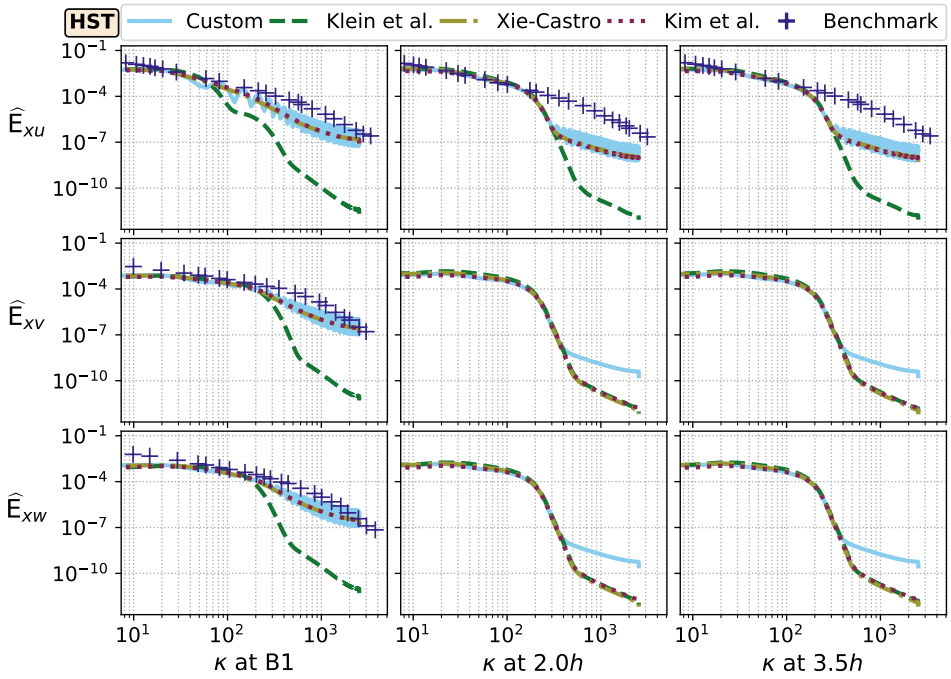

Figure 16: The one-dimensional sample power spectral density function results from the homogeneous shear turbulence computations (HST) [69] at three observation stations: the first block of nodes, i.e. B1 ($\approx 0h$), $2h$, and $3.5h$ longitudinally away from the inlet boundary, which correspond to $7.5h$, $9.5h$ and $11.0h$ benchmark stations in [69, Fig. 14]. The figure descriptors are the same with Fig. 11.

amplitude and trends of the benchmarks within $\mathcal{O}(\text{-}1)$ *bench-diff* range [cNp] with the exceptions of Klein model's drop, and Custom model's relatively high fluctuating tail. [G.*iii*] Moreover, the two remarks above remained unchanged in the second and third *adjustment-phase* nodes within the order of half-precision machine epsilon.

The findings suggest that the divergence-freeness enforcement and the N-S equation algorithm effects on *psd* are negligible within engineering accuracy. In addition, it can be inferred that the *adjustment phase* is limited to the first node. This alleged behaviour may help to optimise *psd* input with respect to first-node outcomes. Besides, the models were able to capture the most energetic wavenumbers in CFD (not necessarily structures themselves), which might be adequate for various engineering purposes. Nevertheless, the level of discrepancy rose for the least energetic wavenumbers. Lastly, the reason of the drop was analysed by [9, p. 455-457], and found to be due to the Gaussian-form *acorr* simplification of Klein's method in Eq. 11.

Along the *evolvement phase*, two new remarks were made. [H.*i*] The most significant observation

to emerge from the model pattern comparison across the benchmarks was that all methods steadily became indistinguishable along a course leading to Klein model's Gaussian-form trend as exemplified in Fig. 16 for HST. This behaviour was observed more apparent for transversal components as the longitudinal *psds* of $\widehat{\mathrm{E}}_{xu}$ proceeded with an exponential slope after following a Gaussian-like curvature for a certain range of wavenumber. [H.*ii*] Apart from this, the benchmark power levels at the low wavenumber region either remained captured or were slightly underpredicted while the underpredictions were amplified towards the tail for which this tendency was more dominant in the lateral *psd*s.

The observation [H.*i*] is in contradiction to that of [33, Fig. 6] who found that Klein method loses its initial *psd* drop downstream. Therein, the longitudinal *psd* development of Klein method was monitored by three different grid DHIT computations at three downstream stations which were exactly used in this study. To pinpoint the reasons for the disparity, the numerical settings were compared. In comparison to the DHIT settings reported in §3.1.2.1, the spatial resolutions in [33, Table 2] were ≈1.5 times coarser for their medium grid, and ≈1.2 times finer for their fine grid. Subsequently, the temporal resolutions in [33, Table 2] were ≈4 and ≈2 times coarser, respectively. The other key differences can be compared with §3.1.2.1 through a list of [33]'s settings as follows: a $10M$-side cubic computational domain with entirely cyclic boundary conditions, the constant-coefficient Smagorinsky sub-filter scale model, the first-order Euler temporal scheme, and the transversal length scales equated to the longitudinal counterparts. Apart from these, the remaining tools and settings were virtually the same in both studies. Considering the level of numerical fidelity is in favour of the current study, one would expect herein that the drop completely diminishes like in [33]. However, this study has been unable to reveal the reasons for the disagreement. A further study with more focus on the existence of the drop through isolated parameters is therefore suggested.

4.2.5. Wall shear stresses

The magnitude of longitudinal wall shear stress (abbr. *wss*) is a theoretically and practically important metric for wall-bounded flows by reason of the majority of momentum transfer and turbulence generation occurring through flow-wall interactions. Also, *wss* is usually being utilised as an indicator of the *adaptation length* in synthetic inflow turbulence studies of wall-bounded flows whilst its flow shaping effect was presumed to give tangible indications about flow states.

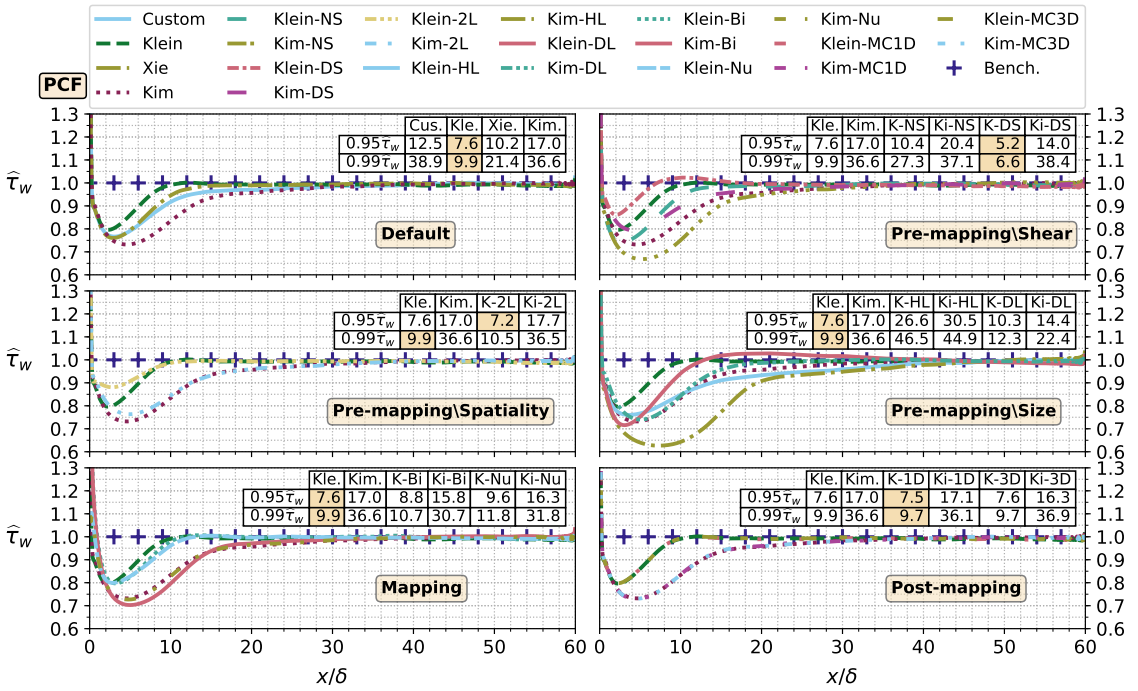

Figure 17: The longitudinal development of the sample wall shear stress vector's x-component, $\widehat{\tau}_w$, obtained from the bottom wall of smooth-wall plane channel flow [70] computations. $\widehat{\tau}_w$ fields were first time-averaged at each boundary node, and then spatial-averaged in the statistically homogeneous lateral direction. Each subplot represents a test group: *Default*-§4.2, *Pre-mapping/Shear*-§4.3.3, *Pre-mapping/Spatiality*-§4.3.2, *Pre-mapping/Size*-§4.3.1, *Mapping*-§4.4, and *Post-mapping*-§4.5. In the legend, the affixes denote: 'NS' no-shear, 'DS' double-shear, '2L' two length-scale sets, 'HL' halved length scales, 'DL' doubled length scales, 'Bi' bilinear mapping, 'Nu' non-uniform mapping, 'MC1D' and 'MC3D' one- and three-dimensional mass flux corrections, respectively. In each subplot, a table shows x/δ-distance where $\widehat{\tau}_w$ reaches the first time its 95% and 99%. Within each table, the shortest distance among the row-wise values is highlighted.

With DFM/FSM, *adaptation lengths* from 2-3 [13, p. 1112] to 20 [115, p. 69] characteristic-length is expected for *wss* depending on flow type and settings. Several studies attributed the *adaptation length* directly to the lack of phase information among modes of synthetic flow structures, [116, p. 3] [117, p. 2] to name a few. Yet these educated opinions seem not to adequately acknowledge counterexamples: For example, Xie method [2, Fig. 7] yielded ≈10 characteristic-length *adaptation length* for a plane channel flow in contrast to ≈18 characteristic-length from Kim method [17, Fig. 9a], both of which consisted almost the same spatiotemporally velocity field [17, Fig. 5].[29] Therefore, the causing mechanisms of the *adaptation length* arguably remain unclear.

Taking its significance into account, the *conditioned* longitudinal *wss* profiles of the models were

[29] Also, for the two computations, the same pseudo-random number generator was seeded with the same initializer, thereby resulting in the same random number sets to be used in both computations.

given and examined in this section via Fig. 17 (PCF), where *wss* results of the bottom wall were presented.

[J.*i*] As can be seen from the top-left subfigure in Fig. 17, the ranking of the methods that reached $\widehat{\tau}_w$=0.95 first (the benchmark value is $\widehat{\tau}_w$=1.00) was Klein, Xie, Custom and Kim methods at longitudinal distances of (7.6, 10.2, 12.5, 17.0)[δ], respectively, where δ is the half-channel height. When the criterion was increased to $\widehat{\tau}_w$=0.99, the ranking was somewhat changed as: Klein, Xie, Kim and Custom methods at distances of (9.9, 21.4, 36.6, 38.9)[δ]. [J.*ii*] Similarly, the ranking of the $\widehat{\tau}_w$ peaks from the closest to the farthest to the benchmark was Klein, Xie, Custom and Kim methods. Thereupon, Klein model peaked at $\approx 2\delta$ with $\widehat{\tau}_w \approx 0.8$, Custom and Xie models at $\approx 3\delta$ with $\widehat{\tau}_w \approx 0.75$, and Kim model at around ≈ 4-5δ with slightly lesser than $\widehat{\tau}_w$=0.75.

Considering this information, it can be deduced that Klein model yielded the shortest *adaptation length* for *wss*. It reached $\widehat{\tau}_{w,0.95}$ roughly $(2.6, 4.9, 9.4)[\delta]$ earlier than Xie, Custom and Kim methods. For $\widehat{\tau}_{w,0.99}$, the earliness increased to $(11.5, 29.0, 26.7)[\delta]$. Furthermore, Klein model can be seen possessing the fastest rate of *adaptation* since $\widehat{\tau}_w$ reached from 0.95 to 0.99 in $\approx 2.3\delta$ in opposition to the distances required for Xie, Kim and Custom models: $(11.2, 19.6, 26.4)[\delta]$, respectively.

However, Klein model's superiority in this regard is contrary to the implications deduced from *acorr* and *psd* observations in §4.2.3-§4.2.4 which have suggested that Klein model generally yields the highest *bench-diffs* in *acorrs* and *psds* along the *adjustment phases*, and mostly remains as is. Nonetheless, Klein method was also monitored that it produces the shortest *adaptation lengths* in term of the Reynolds stress tensor components, particularly the shear component, and its secondary associations, i.e. over-filter scale transport equation terms of kinetic energy (Fig. A.28), enstrophy (Fig. A.30), and mean total strain (Fig. A.32). Also, in these measures, the *adaptation lengths* had similar magnitudes. This finding, while preliminary, postulates that the *adaptation length* in terms of $\widehat{\tau}_w$ is predominantly determined by the Reynolds shear stresses rather than phase information or the level of benchmark resemblance in *acorrs*/*psds*. Notwithstanding its dependence, the *adaptation length* based on $\widehat{\tau}_w$ seems also more robust than that based on the Reynolds stress tensor, thus preferable as an *adaptation length* indicator.

4.3. Pre-mapping phase effects

As portrayed in §3.3, the *pre-mapping phase* effects on the *adjustment* and *evolvement phases* (Fig. 3) were explored in this section. To this end, two DFM/FSM stages deemed the most impor-

tant were regulated, i.e. the third and fourth stages displayed in Fig. 2. The stage-3 regulations were relevant to two-point correlation functions. Therein, (*i*) the size of input integral length scales, and (*ii*) the spatial variation of them were studied. The stage-4 regulations were related to one-point correlation tensor with which shear components were tested in isolation.

4.3.1. Effects of the size of integral length scales

In an investigation using the hybrid DFM-FSM into integral length-scale size effects, [2, p. 461-463] changed lateral scales within a plane channel flow (different from the current PCF) by factors of (1.3, 1.0, 0.9, 0.8), and probed the statistics of mean velocity and Reynolds stress tensor at x/δ=10 downstream, and *adaptation length* of $\widehat{\tau}_w$. The authors found out that the end-to-end variations were less than (10, 13, 4)% for $\sqrt{\overline{v'v'}}$, $\overline{u'v'}$ and $\widehat{\tau}_w$, respectively. Accordingly, it was concluded for these type of flows that the effects caused by lateral scale variations on these statistics are not considerable. This inertness was also corroborated by [10, p. 10][27, p. 43] for mean velocity.

As a continuation and extension of [2] in this particular, the current study carried out further tests, particularly filling the knowledge gaps concerned longitudinal-scale effects, and statistical developments at multiple stations. For this purpose, two new scenarios were prepared: The magnitude of all the nine members of the default length-scale set utilised in §4.2 was halved and doubled.

Amongst the statistics in Table 2, the mean velocity and all correlation functions measured at PCF benchmark stations (e.g. Fig. 13) within the *evolvement phase* remained virtually the same in the level of single-precision machine accuracy (not shown). Also, the correlation functions within first few nodes behaved in accord with expectations and in patterns similar to the observations from §4.2.3 (not shown).

On the other hand, regarding one-point second order correlation tensor (abbr. *the tensor*) along the *adjustment phase*, three observations were made (not shown). [K.*i*] First, in each model the double-scale resulted in positive $\mathcal{O}(1)$-level *default-diffs* [cNp] for the normal-components of *the tensor*, where the default case results were shown in Fig. 9. [K.*ii*] In contrary, the half-scale induced negative $\mathcal{O}(1)$-level *default-diffs*. [K.*iii*] Besides, for the $\overline{u'v'}$-component, the doubled length scales in Klein model prompted negative $\mathcal{O}(2)/\mathcal{O}(3)$-level *default-diffs*, and the halved length scales positive $\mathcal{O}(1)$-level *default-diffs*. In Kim model, the double-scale case behaved almost the same with Klein model; however, its half-scale case results remained similar to those of its default case.

According to these data, it can be inferred within the *adjustment phase* that the scaling factor

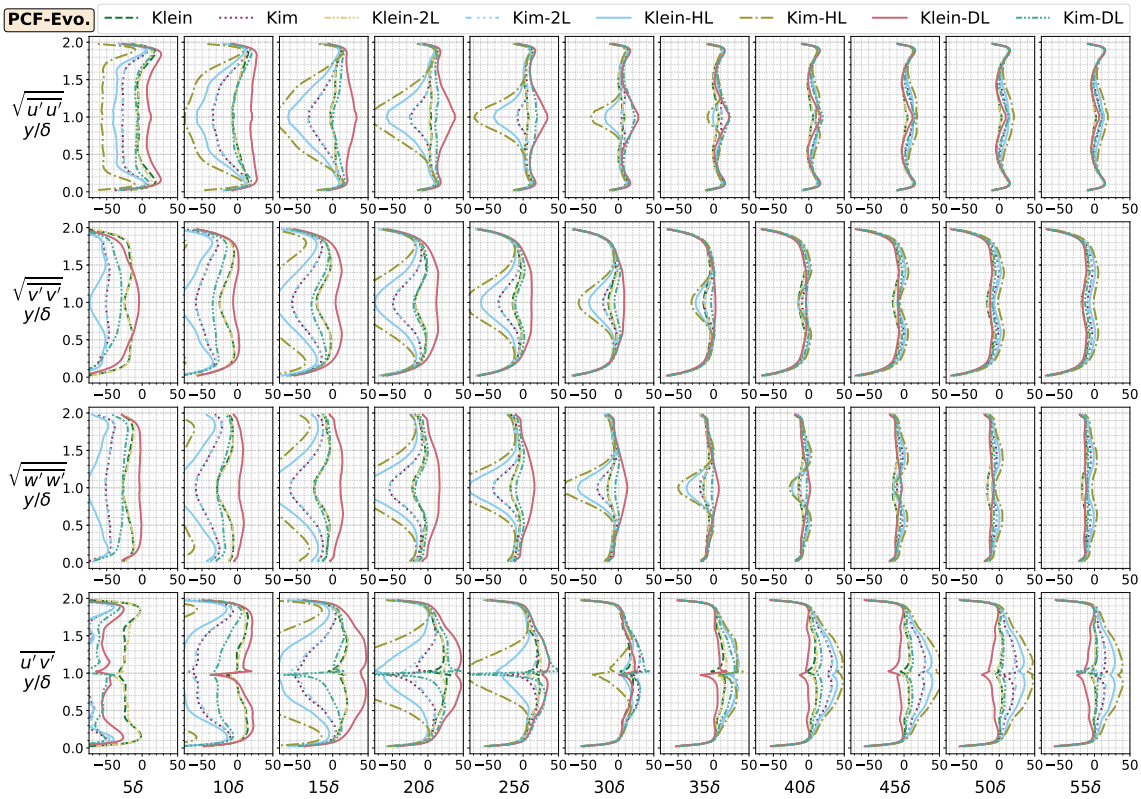

Figure 18: Effects of the length-scale size, and length-scale sets at different inlet zones on the one-point second-order symmetric correlation tensor components obtained from the smooth-wall plane channel flow (PCF) computations [70]. The results were given at the channel-height profiles along the longitudinal *evolvement phase* (Evo.), i.e. 11 equidistant stations from 5δ to 55δ away from the inlet in 5δ-distance steps, and represented the log percentage changes with respect to the benchmark, i.e. $\mathbb{L}\equiv 100\log_e(\bullet)$ centineper [cNp]. The absolute amplitudes were given in Fig. A.25. The remaining figure particulars and axes limits were provided in Figs. 10 and 17.

of the size of input integral length scales, i.e. C, determines the sign of *default-diffs* of *the tensor* components irrespective of DFM/FSM variants. More precisely, the sign of (C-1) will likely be the same with that of normal-component *default-diffs*, and the opposite with that of shear-component *default-diffs*. For example, a scaling factor smaller than unity could produce negative *default-diffs* in normal *tensor* components, hence an overall amplitude reduction. Nonetheless, the proportionality between the scaling factor and *default-diffs* seems not linear as the double-scale cases yielded larger absolute *default-diffs* than the half-scale cases. These findings were in line with the level and patterns of amplitudes reported by [2, Fig. 6] for the lateral length scale effects although the authors monitored x/δ=10, which was further downstream than the *adjustment phase*.

Within the *evolvement phase* of *the tensor* as demonstrated in Fig. 18, four other observations

were noted. [L.*i*] To start with at x/δ=10, the double-scale cases were all found to yield positive *default-diffs* for all *tensor* components with an absolute amplitude of 10-20[cNp], predominantly around the channel centre. [L.*ii*] In contrast, the half-scale triggered negative *default-diffs* for the same components somewhat larger than the doubled length scales. [L.*iii*] Throughout the *evolvement phase*, the absolute amplitudes of normal-component *default-diffs* in the double-scale Klein cases were initially increased, then decreased downstream while remaining positive. However, the shear-component *default-diffs*' sign fluctuated around plus/minus as their absolute amplitudes also alternated between increments and decrements downstream. The normal-component *default-diffs* of the double-scale Kim cases remained positive as well, yet without a ubiquitous pattern. For instance, the absolute amplitude of v-component *default-diffs* monotonically reduced downstream whereas that of u-component first increased, then decreased. For half-scale cases, all *default-diffs* were negative at first and switched to positive irrespective of DFM/FSM variant. Their absolute amplitudes were preliminarily decreased, and then were followed by increments. [L.*iv*] Moreover, both scale manipulations added an extra 10-20[δ] to the *adaptation lengths* of the *tensor* components, particularly around the channel centre, hence delayed *adaptation*.

Although the results at x/δ=10 indicated a direct link between (C-1) and the sign of *default-diffs* as observed in the *adjustment phase* and [2, Fig. 6], with the other observation stations in view, the counterexamples from the half-scale cases disconfirmed the supposed sign relation. Therefore, the sign link could only be presumed for the *adjustment phase*. In addition, no certain relation was identified between the magnitude of length-scale scaling factor and absolute amplitudes of *default-diffs* considering the reported decrement and increments above.

As regards wall shear stresses illustrated in Fig. 17, two points were detected. [M.*i*] The first is that both double-scale and half-scale nearly always increased $\widehat{\tau}_w$=0.95 and =0.99 *adaptation lengths*. As an example, the default Klein 0.95-*adaptation length* was increased by ≈1.4 times, and ≈3.5 times; 0.99-*adaptation length* by ≈1.2 times, and ≈4.7 times by the double-scale and half-scale, respectively. [M.*ii*] Additionally, the peaks of $\widehat{\tau}_w$ were raised by 10-20% in general.

Taken together, this study corroborates the literature findings regarding null effects of input length scales on the mean velocity and downstream correlation functions. However, unlike the DFM/FSM literature, amplitudes of the Reynolds stress tensor and wall shear stress with respect to benchmark, and corresponding *adaptation lengths* with respect to the default cases were found to be adversely influenced by input length scales to the extent described above. The dependencies

are hypothesised with the support of [L.*iii*] [M.*i*] [M.*ii*] that the isolated changes in the size of input length scales and *adaptation length* of a flow statistic are in a parabolic relation, i.e. the *adaptation length* reduces in parallel to the proximity of input length scales to optimal range of scales that other input flow properties/boundary conditions assume. Therefore, it is argued by contrast to the DFM/FSM literature presumptions that the size of input length scales is important to flow developments, and isolated changes in scales are discouraged in favour of a holistic changes of all input flow properties, if necessary.

4.3.2. Effects of the use of different correlation functions at inlet spatial zones

In the DFM/FSM literature, the dominant input convention for integral length/time scales is to use a single spatially-invariant set for the whole inlet boundary mostly due to the lack of further data and quantifications for multiple-set usage's possible costs and merits. Two potential problems of this convention were highlighted by [9, p. 457]: (*i*) length/time scales of a flow being modelled may in reality be spatiotemporally-variant over the inlet boundary, and (*ii*) a single time-scale set input into flows with spatial-variant inlet mean velocity by definition leads to uncontrolled spatial variation in length scales. To date, two studies provided insights into effects of the spatial variation in scales. First, [117, Fig. 6] compared effects on the longitudinal mean speed and three components of the Reynolds stress tensor caused by three inflow scenarios in a wall-modelled periodic hill flow: single, six and twelve scale sets, each of which contained three orthogonal scales. Although [117, p. 19-20, 23] qualitatively concluded that the spatial variation of scales improved the predictions of the aforementioned statistics, a quantitative analysis made herein for the data figures throughout the channel [117, Fig. 8-11] indicated that the improved *default-diffs* were overall below 5[cNp], and the outliers below ≈15[cNp]. In addition, a note of caution is due here for their results since the study's relatively coarse and unverified spatiotemporal resolution, and its use of a wall function in a flow where boundary-layer separation/reattachment occurs added unquantified sources of uncertainties. Second, [9, p. 457-461] examined effects of using twenty-four scale sets each of which contained nine scales through a non-CFD PCF, which used the same settings with the current study. The authors quantified considerable improvements in correlation and power spectral density functions whilst no Reynolds stress tensor component was affected within machine accuracy. Yet the authors also emphasised the need for a CFD study. Therefore, it is claimed that effects of spatial variation in scales are still inconclusive in the DFM/FSM CFD literature.

Unlike the aforementioned studies exploring effects of several sets at once, herein only *an* extra set of scales was incorporated to ease isolation of important factors, and follow the current duo-set practice in the DFM/FSM literature for wall-bounded flows, e.g. [2, Fig. 2] and [17, Fig. 4]. To that end, two inlet zones of 10% half-channel height from the top and bottom boundaries were allocated to a new set of benchmark scales belonging to y^+=40 (similar to [17, p. 64]). The remaining inlet zone (i.e. y=[0.1, 1.9][m]) kept its default set the same. Ultimately, the new computations were evaluated with Table 2 statistics.

[N.*i*] Inspection of the results revealed that the majority of Table 2 statistics appeared to be unaffected by the extra set addition up to the half-precision machine epsilon, e.g. the *evolvement phase* of *the tensor* shown in Fig. 18. The most apparent alterations occurred in the *adjustment phase* of *the tensor*, and in wall shear stress *adaptations* as depicted in Fig. 17. [N.*ii*] For the former, *default-diffs* were almost zero for all models and component profiles except at three points (not shown): $\sqrt{\overline{u'u'}}$ and $\overline{u'v'}$ *default-diffs* were ≈10 and $\mathcal{O}(2)$[cNp] at regions close to the walls, and $\sqrt{\overline{v'v'}}$ *default-diffs* were few centinepers across the channel height. In these three occasions, the *bench-diffs* were reduced, and the affected regions mainly corresponded to the regions where the new zone was defined. However, no new amplitude or pattern changes in *default-diffs* were observed, and all these improvements gradually vanished until the onset of the *evolvement phase*. [N.*iii*] Regarding $\widehat{\tau}_w$, for Klein and Kim models, $\widehat{\tau}_{w,0.95}$ was changed ≈(-0.4, 0.7)[δ], and $\widehat{\tau}_{w,0.99}$ ≈(0.6, -0.1)[δ], respectively, where the negativity meant an improvement. [N.*iv*] Additionally, all the $\widehat{\tau}_w$ peaks were reduced while the longitudinal location of the peaks was not relocated.

In the light of these observations, it could conceivably be hypothesised for wall-bounded flows that the effects of the spatial variation in input scales are not significant to engineering applications (neither improvement nor deterioration) since the effects are relatively small and are not preserved downstream. Therefore, it is postulated for wall-bounded flows that a single set of scales could be adequate for the fidelity that one wants to reach with more length scales available, which in practice difficult to obtain.

4.3.3. Effects of the shear stress and the wall boundary condition

In the default-setting wall-bounded computations (§4.2.2), the input Reynolds stress tensor components, especially $\overline{u'v'}$, were discovered deteriorating along the *adjustment phase*, and recovering within the *evolvement phase*. In addition to this, the *adaptation lengths* of *the tensor* components

and wall shear stress were found to be correlated to a certain degree. Nevertheless, this information did not shed on the main causes/contributors to the three behaviours above. Over and above this, there have been no controlled studies on this matter.

To close this knowledge gap, the causal roles of factors that were anticipated to be influential were inspected: (*i*) the shear component of *the tensor*, and (*ii*) no-slip velocity boundary condition. In line with this purpose, three new control scenarios were prepared: the $\overline{u'v'}$-input was zeroed and doubled, and the no-slip velocity boundary condition was changed to the slip condition. It should be noted that the doubled-$\overline{u'v'}$ alongside the current settings satisfies the *domain error* constraints for the *Lund transformation* stated in **??** 2.1.3.1, albeit unphysical.[30]

In consequence of the control scenarios, some of the Table 2 statistics of the default cases were found to be virtually unaltered along the *adjustment* and *evolvement phases* (not shown), prominently the *conditioned* results of mean velocity, correlation functions and one-point moments. At the same time, the Reynolds stress tensor and wall shear stress expectedly showed noticeable changes which were demonstrated in Figs. 17, 19 and 20.

As can be seen from Fig. 19 for the *adjustment phase* of *the tensor*, four remarks valid for both DFM and FSM can be listed. [O.*i*] First, the no-shear and double-shear cases had diametrically opposite effects on both $\sqrt{\overline{u'u'}}$ and $\sqrt{\overline{v'v'}}$. In detail for one side, the no-shear caused negative-$\mathcal{O}(1)$[cNp] *default-diffs* nearby walls and positive-$\mathcal{O}(1)$[cNp] around the channel centre for $\sqrt{\overline{u'u'}}$; and for $\sqrt{\overline{v'v'}}$, negative-$\mathcal{O}(1)$[cNp] *default-diffs* across the channel height. [O.*ii*] Nonetheless, neither of shear scenarios led to differences greater than $\mathcal{O}(-2)$[cNp] for $\sqrt{\overline{w'w'}}$, hence negligible in terms of engineering accuracy. [O.*iii*] For $\overline{u'v'}$, the double-shear yielded positive-$\mathcal{O}(2)$[cNp] *default-diffs* throughout the channel height, thus resulting in the same-order reduction of *bench-diffs*. Similar to the default case, an amplitude damping notable with respect to the benchmark occurred within the first two nodes, and thereafter the rate of damping died away. Furthermore, the no-shear expectedly yielded a null $\overline{u'v'}$ profile. [O.*iv*] Lastly, the slip-wall did not invoke any changes smaller than the single-precision machine epsilon for any *tensor* component.

The observation [O.*iv*] eliminates 'boundary condition effects' as one of the potential reasons why the input *tensor* components were distorted within the *adjustment phase*. This further strengthens the proposed reason discussed in §4.2.2, i.e. the divergence-freeness enforcement. Another implication that emerges from the observation [O.*iii*] is that the double-shear seems to

[30] For example, tripled-$\overline{u'v'}$ raises the *domain error*.

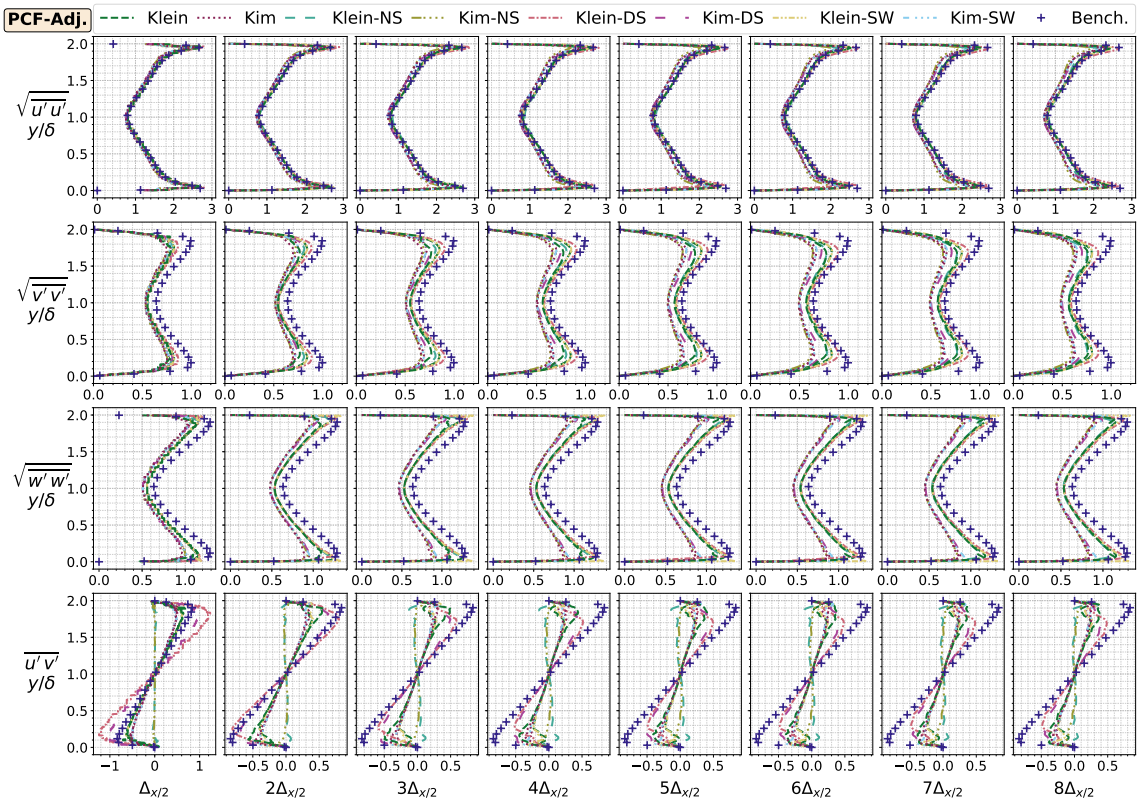

Figure 19: Effects of the shear stress and the wall boundary condition on the *adjustment phase* of the one-point second-order symmetric correlation tensor components obtained from the smooth-wall plane channel flow (PCF) computations [70]. The figure particulars were provided in Figs. 9 and 17 except the affix 'SW' which denotes slip-wall.

improve $\overline{u'v'}$ predictions within the *adjustment phase*. Although the rate and level of amplitude damping remained almost constant among the default and double-shear cases, the additional amplitude via the latter somewhat compensated the damping losses. Therefore, a higher-level resemblance with the benchmark happened for $\overline{u'v'}$ in the *adjustment phase* with the double-shear case. This amplitude amplification also seems to indirectly compensate losses in $\sqrt{\overline{u'u'}}$ and $\sqrt{\overline{v'v'}}$ as can be deduced from the observations [O.*ii*] and [O.*i*] where the lack of shear deteriorated these normal components.

The *evolvement phase* of *the tensor* was set out in Fig. 20, from which five observations were carried out. [P.*i*] In general, the double-shear cases provided somewhat shorter *adaptation lengths* for each *tensor* component profile in comparison to the default cases. An evidence of the premise can be seen in $\overline{u'v'}$ profiles in which the rate of change and *bench-diffs* of the double-shear Klein

model became almost zero starting from 25δ whilst its default case was $\mathcal{O}(1)$[cNp] away in ongoing development. [P.*ii*] Another important finding was that the no-shear cases produced the benchmark shear profile despite the lack of the $\overline{u'v'}$ input. For instance, the no-shear Klein model yielded profiles with $\approx$10[cNp] *default-diffs* at 10δ, and almost zero centineper at 20δ. [P.*iii*] In addition, a monotonic behaviour was found out between input and output amplitudes of *the tensor*: For each component and each model, the no-shear and double-shear profiles were diagonally opposite about the default profiles. As an example, negative $\mathcal{O}(-1)$[cNp] *default-diffs* transpired in the no-shear Kim model profiles until 25-30δ, and thereafter gradually became positive whereas the double-shear counterparts acted in a polar manner. [P.*iv*] Moreover, the slip-wall cases demonstrated that the input $\overline{u'v'}$ profiles were able to preserve up to 5δ without the turbulence maintenance effect of wall boundary conditions. After 5δ, commencing from the vicinity of walls, the input *tensor* profiles were gradually dissolved. [P.*v*] Finally, with regard to the model performances, Fig. 20 indicated that the double-shear Klein model nearly always generated the lowest *bench-diffs* while the no-shear Kim the highest. For example, the maximum amplitude differences between both at 40δ were found to be approximately 20, 15, 10-15 and 40[cNp] for the components in a usual order, respectively.

As regards $\widehat{\tau}_w$, two points can be highlighted from Fig. 17. First of all, the double-shear reduced the *adaptation lengths* in DFM whereas mixed responses were obtained for FSM: In Klein model, the *adaptation length* of $\widehat{\tau}_{w,95}$-$\widehat{\tau}_{w,99}$ was lowered by $(-2.4, -3.3)[\delta]$ while $(-3.0, 1.8)[\delta]$-change was observed in Kim model. Furthermore, the double-shear downscaled the $\widehat{\tau}_w$-peak of both models by $0.05\widehat{\tau}_w$. On the other hand, the no-shear brought about the opposite: the *adaptation length* of $\widehat{\tau}_{w,95}$-$\widehat{\tau}_{w,99}$ was increased by $(2.8, 17.4)[\delta]$ and by $(3.4, 0.5)[\delta]$ for Klein and Kim models, respectively, and their $\widehat{\tau}$-peaks raised by $0.05\widehat{\tau}_w$.

Three principal implications can be drawn from these observations: First, amplification of input $\overline{u'v'}$ amplitude profiles to a level that the *domain error* constraints (**??** 2.1.3.1) allow reduces *bench-diffs* of the Reynolds stress tensor components (except $\sqrt{\overline{w'w'}}$) within the *development phase*, and shortens their *adaptation lengths*. Second, the formation of the $\overline{u'v'}$-benchmark profile within no-shear cases suggests that particulars of an isolated flow quantity could be inherently dictated by the other specified flow properties/boundary conditions, which was also observed from another perspective in §4.3.1. Third, within the scope of current settings, the input $\overline{u'v'}$-benchmark profile preserved its main composure up to 5 characteristic lengths without re-energising effects of wall boundary conditions. Assuming the finding's extrapolation to similar-setting computations as few

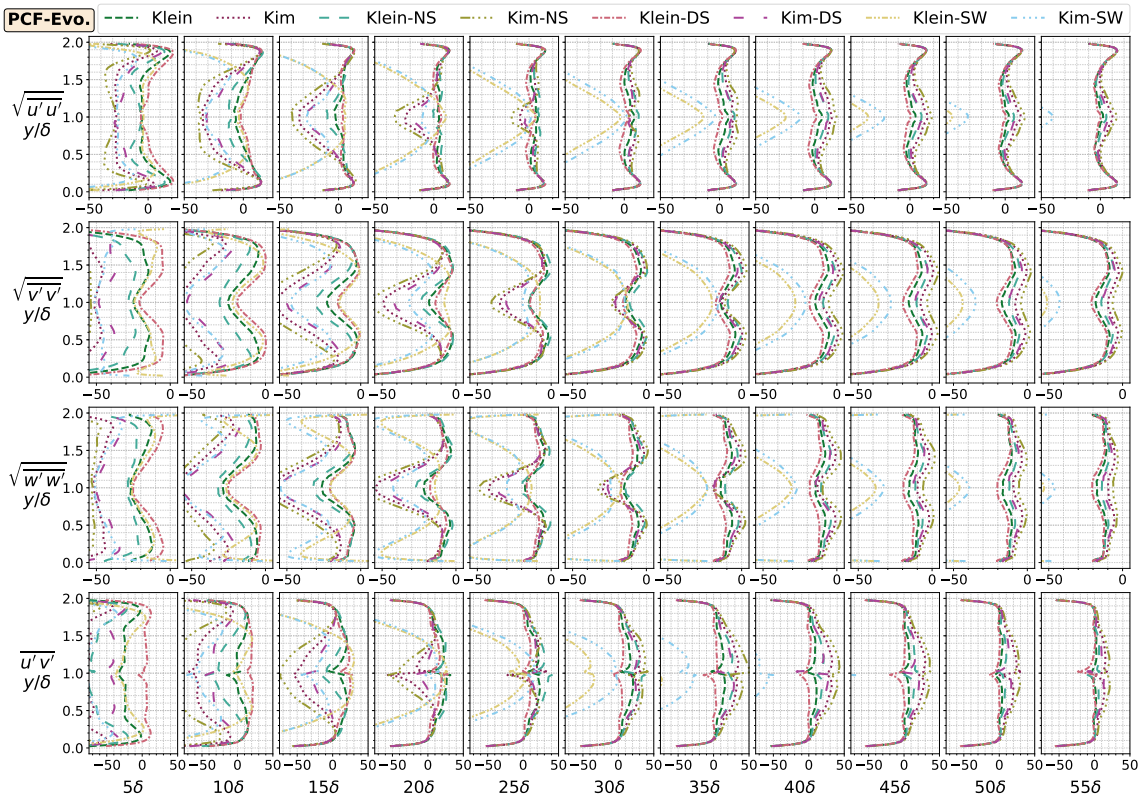

Figure 20: Effects of the shear stress and the wall boundary condition on the *evolvement phase* of the one-point second-order symmetric correlation tensor components obtained from the smooth-wall plane channel flow (PCF) computations [70]. The figure particulars were provided in Figs. 10, 17 and 18.

characteristic lengths, this observation may help to properly locate the field of interest within free-shear flow domains, e.g. turbine flows, to ensure its association with input shear.

4.4. Mapping phase effects

As outlined in sec. 1, it was hypothesised that quantifications of the information-transfer practices from the *pre-mapping phase* to the *post-mapping phase* (Fig. 3) are missing in the DFM/FSM literature, and techniques that can seamlessly generate synthetic time-series on non-uniform grids are absent.

To this end, two new seamless mapping techniques were introduced: §2.1.3.2 for DFM, and §2.1.3.3 for FSM. On top of this, two conventional mapping techniques were added into the test scheme: the two-dimensional nearest-neighbour projection (common), and the bilinear interpolation (occasional). The four techniques were assessed through the *adjustment* and *evolvement phases*

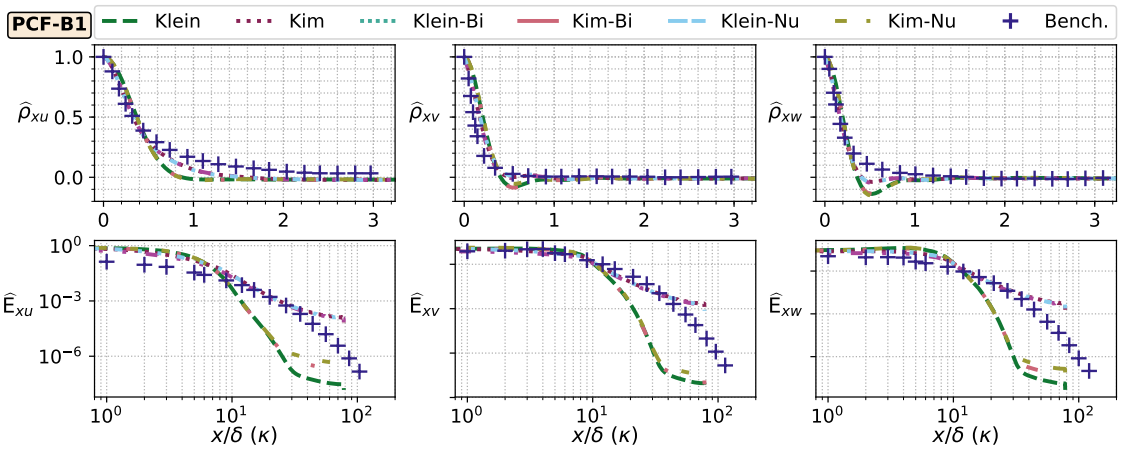

Figure 21: The *mapping phase* effects on the two-temporal-point longitudinal sample autocorrelation function (the top subplots) and one-dimensional sample power spectral density function (the bottom subplots) results obtained from the first block of nodes (B1) of the smooth-wall plane channel flow (PCF) computations [70]. The figure particulars were provided in Figs. 11 and 17.

thereafter.

Evaluations were conducted through Table 2 statistics. [R.*i*] Contrary to expectations, however, the studies did not find any significant-to-engineering-accuracy difference between the default and modified cases in any of the statistics apart from wall shear stresses depicted in Fig. 17. The changes in those statistics, particularly in *the tensor*, mainly occupied the *adjustment phase* and the outset of the *evolvement phase*, and were mostly in a degree less than $\mathcal{O}(\text{-}1)$[cNp] *default-diff*, albeit rarely few centinepers nearby walls. The lack of substantial differences was exemplified by Fig. 21 wherein the first *adjustment-phase* node results for autocorrelation and power spectral functions were briefly illustrated. [R.*ii*] In the case of $\widehat{\tau}_w$, it was observed that the bilinear and non-uniform Klein models postponed $\widehat{\tau}_{w,95}$ and $\widehat{\tau}_{w,99}$ by $(1.2, 2.0)$ and $(0.8, 1.9)[\delta]$, respectively, whereas the bilinear and non-uniform Kim models improved them by $(\text{-}1.2, \text{-}0.7)$ and $(\text{-}5.9, \text{-}4.8)[\delta]$ in turn. [R.*iii*] In addition, all the $\widehat{\tau}_w$ peak locations were qualitatively shifted downstream to a little extent, and their amplitudes virtually stayed the same within a $0.05\widehat{\tau}_w$ interval.

These observations suggested two implications: First, the mechanisms that underpin the *adaptation length* of $\widehat{\tau}_w$ appeared to be sensitive to the primary statistics' alterations that were previously deemed to be insignificant for engineering purposes. By contrast, this now-falsified proposition raises the importance of ensuring high-fidelity reconstruction of primary input statistics. Second, arguably, adequate isolated evidence was found to consider that distortive effects of information

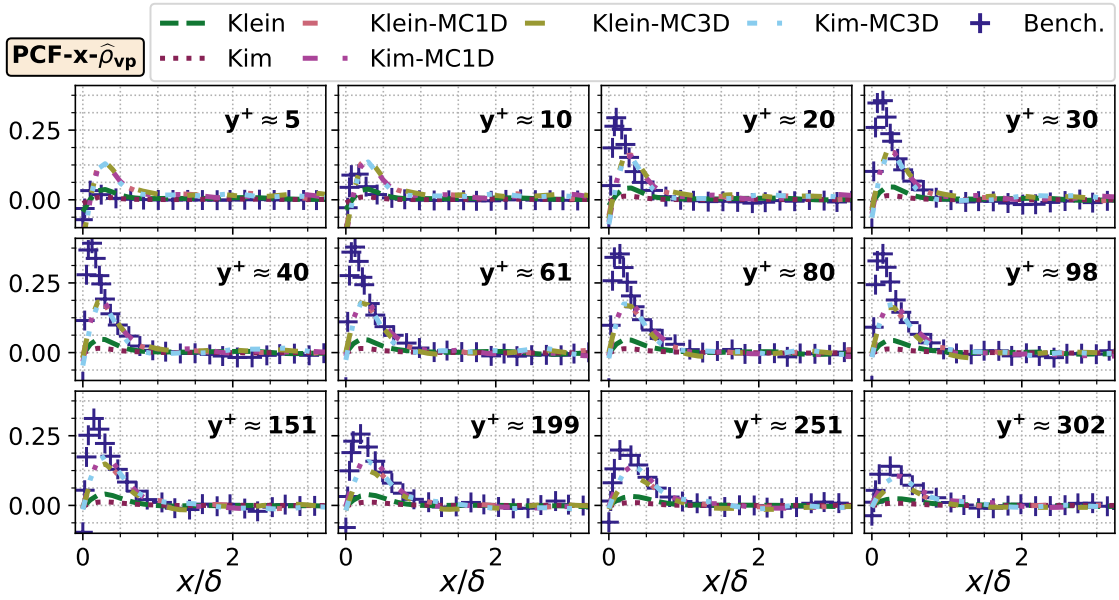

Figure 22: Effects of mass-influx corrections on the two-point sample crosscorrelation functions of $\widehat{\rho}_{\mathrm{vp}}$ obtained from the smooth-wall plane channel flow computations (PCF) [70]. All the figure particulars were given in Figs. 13 and 17.

transfer processes on input statistics are of secondary importance in proportion to the effects of *pre-mapping phase* manipulations. Although the seamless mappings were theoretically and practically obtained and information distortion was naturally prevented, their usage brought either slight improvement as in FSM or even some statistical degradation as in DFM. Therefore, the *mapping phase* manipulations may be neglected for the current scope of flows and similar numerical settings.

4.5. Post-mapping phase effects

As briefly discussed in sec. 1, mass influxes are not conserved in DFM/FSM. To date, the potential issue has received scant attention in the DFM/FSM literature: it was handled either by the omission of its presence or by heuristic corrections such as [17, Eq. 8]. Additionally, there remains a paucity of quantifications on its effects.

With this motivation, three mass-flux scenarios were investigated along the *development phase*: no correction, longitudinal correction, which was proposed in this study, and three-dimensional correction from [17, p. 57]. The corrections were formulated as: $\Phi_{\mathrm{initial}}\,\Phi^{-1}_{\mathrm{current}}\mathbf{u}_{nc}= c_{\mathrm{mass}}\mathbf{u}_{nc}=\mathbf{u}_c$ where $\Phi=D\sum_{i=0}^{f} u_f \|\mathbf{S}_f\|$ is the inlet-boundary total mass flux [$\mathrm{kg\,s^{-1}m^{-2}}$], D the constant fluid density [$\mathrm{kgm^{-3}}$], u_f the longitudinal flow speed at the boundary face f [$\mathrm{ms^{-1}}$], $\mathbf{S}_f$ the f-face area

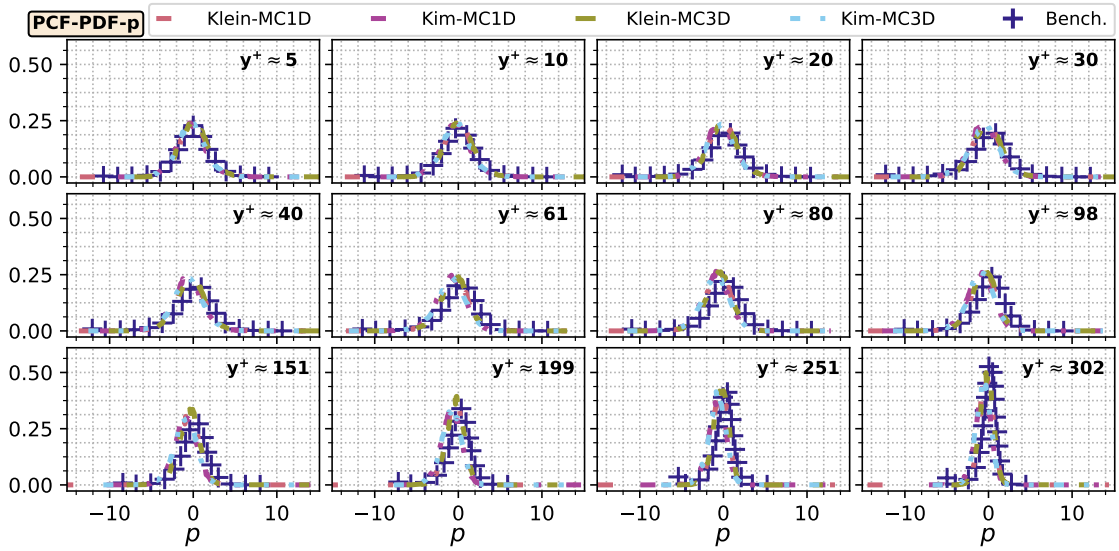

Figure 23: Effects of mass-influx corrections on the probability density functions of modified pressure, p, obtained from the smooth-wall plane channel flow computations (PCF) [70]. The samples were probed along channel heights at x_0=40[m] and z_0≈1.57[m], and the number of bins was 201. All the other figure particulars were given in Figs. 13 and 17.

vector [m^2], $\mathbf{u}_{nc}$ the boundary-mapped non-corrected synthetic velocity time-series, $\mathbf{u}_c$ the corrected time-series, c_{mass} the corrector scalar field [-], Φ_{initial} the initial-time Φ, and Φ_{current} the current-time Φ. The only difference between the corrections was that $\mathbf{u}_{nc/c}\equiv(u,v,w)$ for the three-dimensional approach, and $\mathbf{u}_{nc/c}\equiv(u,0,0)$ for the one-dimensional approach. The latter approach was put forth to avoid alleged inconsistency in the three-dimensional approach wherein c_{mass} is computed based only on u, yet is applied onto (u,v,w) including irrelevant lateral components.

In the light of explorations via Table 2 statistics, four main observations were noted. [S.i] Firstly, almost no difference larger than $\mathcal{O}$(-2)[cNp] *default-diff* was observed for any solely-velocity-based statistics at any stage of the *development phase*. This was exemplified by Fig. 17 wherein the $\widehat{\tau}_w$-amplitude alterations were at least an order of magnitude lower than the other phase results. Also, $\widehat{\tau}_w$-trajectories qualitatively remained unchanged even though in §4.4 $\widehat{\tau}_w$ was found susceptible to relatively small alterations in input statistics. [S.ii] However, the pressure-based statistics showed considerable differences between the uncorrected and corrected cases. In general, the no mass-flux correction resulted in several times/orders of magnitude centineper *bench-diffs* in pressure-based statistics, and considerably disparate trajectories with respect to the benchmark patterns. In contrast, both corrections reformed these spurious amplitude and pattern predictions towards the

benchmark. For example, from the data in Fig. 22 showing the cross-correlation functions of $\widehat{\rho}_{\mathrm{vp}}$ in the x-direction across the channel height, the benchmark patterns can be seen to be captured by both correction cases unlike their default counterparts. Moreover, Fig. 23 demonstrating the channel-height probability density functions of p at x=40δ is more revealing in terms of amplitude improvements by the corrections, through which the default case pressure fluctuations were reduced several orders of magnitude onto the benchmark results. [S.iii] Another interesting outcome was that the number of pressure iterations overall decreased by 1.25-1.5 times, which typically constitutes computationally the most expensive part of an incompressible CFD computation. [S.iv] Last but not least, no significant differences were detected between the three- and one-dimensional approaches.

These observations may support a premise that mass-flux corrections are notably beneficial for not only pressure predictions but also cost reductions. Furthermore, the one-dimensional correction is advisable over the literature three-dimensional approach considering the latter's inconsistent formulation and involvement of two extra multiplications per node per time-step, which becomes redundant due to the similar results obtained.

5. Conclusions

The main aim of this study was to conceptualise processes that time-series from digital-filter-based (DFM) and forward-stepwise-based (FSM) synthetic turbulence generation methods go through within CFD, and henceforth fill/identify knowledge/solution gaps to facilitate theoretical and practical advancement of DFM/FSM utilization in CFD applications.

For this purpose, excluding the non-CFD modelling part, DFM/FSM processes towards and within CFD were conceptualised into five consecutive phases as shown in Fig. 3. Thereafter, three test suites were designed with implicitly-filtered large eddy simulations (IFLES) of three building-block flows: decaying homogeneous isotropic turbulence [68], homogeneous shear turbulence [69] and smooth-wall plane channel flow [70]. Four DFM/FSM variants were chosen as representing the majority of capabilities, and were implemented into OpenFOAM®v1712 [39]: Bercin et al. [9] (DFM), Klein et al. [1] (DFM), Xie-Castro [2] (Hybrid DFM-FSM), and Kim et al. [21] (FSM). Finally, systematic explorations were carried out on the test suites through twelve statistics elaborated in Table 2.

Within the first test suite (§4.1), the quality of the computations and samples was evaluated. Therein, the fidelity of spatial/temporal resolutions was particularly investigated via six metrics from the literature: Pope's metric [64, p. 560], Celik et al.'s two single-grid metrics [65, Eq. 8a], Celik et al.'s two double-grid metrics [65, Eq. 15,16,18], and Lyapunov exponent [67]. Capabilities of the metrics were also discussed to provide a new understanding of their usage. In the second test suite (§4.2), the performance of the DFM/FSM variants using traditional settings was quantified and discussed at consecutive observation stations within the computational domains. In the last suite (§4.3-4.5), effects of viable DFM/FSM settings/sub-approaches were explored in isolation, and were compared with the second test-suite's traditional-setting cases.

Besides settings/sub-approaches available in the literature, three novel sub-approaches were proposed for aspects where appropriate solutions have been absent, and were added into the third-suite tests. A new technique for DFM (§2.1.3.2) and another for FSM (§2.1.3.3) were introduced to seamlessly generate synthetic time-series on non-uniform grids. Further, a one-dimensional longitudinal mass-flux correction technique was proposed (§4.5). Lastly, two new code practices were put forth (§3.2) for computational cost reductions.

In conclusion, sixty-two findings with various level of importance were made and labelled within the text. Nevertheless, eleven novel insights deemed the most significant were redelivered to the attention of beneficiaries. (The first test-suite): [i] In contrast to the counterarguments in the literature, Pope's LES-quality post-verification metric was quantified to be more robust, hence more advisable, than Celik et al.'s newer single-grid and double-grid metrics throughout the benchmarks.

(The second test-suite): [ii] Within the first three nodes, consistent occurrences of flow/model/component-independent downstream-affecting amplitude suppressions were observed for the input Reynolds stress tensor, particularly for the shear component, at a level of $\mathcal{O}(1)/\mathcal{O}(2)$ centineper, and the suppression was almost always lower in the highest-mean-speed direction. The divergence-freeness enforcement was then quantified to be their driving factor. [iii] Also, streamwise development of the Reynolds stress tensor amplitudes were found to follow an asymmetric quadratic pattern rather than monotonic as reported/presumed in the literature. [iv] Furthermore, Klein et al.'s model almost always provided the lowest level of amplitude differences with respect to the benchmarks and the shortest adaptation lengths for the Reynolds stress tensor components and wall shear stresses whereas Custom/Kim et al.'s models yielded the opposite even though the Lund transformation was identical in each model. [v] For the input autocorrelation and corresponding power

spectral density functions, a similar-scope amplitude suppression was also detected, yet the suppression was limited to the first node and vanished onwards. The causal role of the divergence-freeness enforcement in this suppression was ruled out by controlled tests, and the cause was speculated to be the first-time execution of the Navier-Stokes equation algorithms on synthetic time-series. [*vi*] Therein, in terms of patterns, Klein et al.'s method yielded Gaussian-form of correlation and power spectral density functions while the remaining methods prompted exponential-form for the correlations and Lorentzian-form for the spectra. [*vii*] Moreover, the model variations in all correlation and power spectral density functions faded away downstream, and these model outcomes converged to a common function, which mostly resembled Klein et al.'s form. The most likely reason of the convergence was then argued to be the domain/equation discretisations.

(The third test-suite): [*viii*] Investigations on length-scale size effects showed that a parabolic relation exists between amplitudes/adaptation lengths of the Reynolds stress tensor components/wall shear stresses and length scale sizes, that is for instance the adaptation length increases in parallel to the level of difference between input length scale sizes and optimal range of scale sizes that other input flow properties/boundary conditions impose. [*ix*] On the other hand, the use of multiple length-scale sets at different inlet zones and seamless non-uniform mapping were quantified to be relatively ineffective on flow statistics and be not long-lasting downstream. [*x*] Nonetheless, amplitude amplification of the shear component in the input Reynolds stress tensor to a degree that the domain error constraints permit was observed to downscale the aforementioned amplitude distortions of flow statistics within CFD, and shorten corresponding adaptation lengths. [*xi*] Lastly, mass-influx conservation corrections were revealed in detail to be considerably favourable for pressure predictions and computational cost reductions, albeit no impact on velocity-based statistics. The proposed one-dimensional mass-flux correction was also quantified to be advisable over the alternatives due to its consistent formulation and cheaper computational executions.

Taken all results into account, a best practice could be devised for similar flows: Klein et al.'s model using Xie-Castro model's exponential function simplification with the nearest-neighbour projection, the one-dimensional longitudinal mass-influx correction, the appropriately scaled-up input shear, and the code practices reported in §3.2 and [9, p. 449].

Arguably, further research could be required in the following areas: (*i*) additional isolated parameter-effect scenarios such as on normal components of the input Reynolds stress tensor or length scales in different directions, (*ii*) compressible flows, (*iii*) higher-Reynolds-number flows,

(*iv*) the applicability of fast Gaussian/exponential function convolution algorithms such as [118], and (*v*) modelling of inherent divergence-freeness in DFM/FSM.

6. Acknowledgement

The authors acknowledge the use of the IRIDIS 4/5 High Performance Computing Facility, associated support services at the University of Southampton, in the completion of this work. Bercin also acknowledges the Overseas Rayleigh Studentship from the Faculty of Engineering and the Environment at the University of Southampton. The authors also wish to thank ChengYue Wang from Beijing University of Aeronautics and Astronautics for graciously providing their divergence correction codes. Lastly, the authors also thank 'StackExchange' and 'Wikipedia' communities as well as Google LLC for their immense help.

References

[1] M. Klein, A. Sadiki, J. Janicka, A digital filter based generation of inflow data for spatially developing direct numerical or large eddy simulations, Journal of Computational Physics 186 (2) (2003) 652–665. doi:10.1016/S0021-9991(03)00090-1.

[2] Z. T. Xie, I. P. Castro, Efficient generation of inflow conditions for large eddy simulation of street-scale flows, Flow, Turbulence and Combustion 81 (3) (2008) 449–470. doi:10.1007/s10494-008-9151-5.

[3] G. R. Tabor, M. H. Baba-Ahmadi, Inlet conditions for large eddy simulation: A review, Computers and Fluids 39 (4) (2010) 553–567. doi:10.1016/j.compfluid.2009.10.007.

[4] N. S. Dhamankar, G. A. Blaisdell, A. S. Lyrintzis, Overview of turbulent inflow boundary conditions for large-eddy simulations, AIAA Journal (2017) 1–18doi:10.2514/1.J055528.

[5] X. Wu, Inflow turbulence generation methods, Annual Review of Fluid Mechanics 49 (1) (2017) 23–49. doi:10.1146/annurev-fluid-010816-060322.

[6] L. E. Borgman, Ocean wave simulation for engineering design, Technical report, Hydraulic Engineering Laboratory, Berkeley, California (1967).

[7] H. Nobach, Verarbeitung stochastisch abgetasteter signale, Ph.d. thesis, University of Rostock, Germany (1997).

[8] T. S. Lund, X. Wu, K. D. Squires, Generation of turbulent inflow data for spatially-developing boundary layer simulations, Journal of Computational Physics 140 (2) (1998) 233–258. doi:10.1006/jcph.1998.5882.

[9] K. M. Bercin, Z.-T. Xie, S. R. Turnock, Exploration of digital-filter and forward-stepwise synthetic turbulence generators and an improvement for their skewness-kurtosis, Computers & Fluids 172 (2018) 443–466. doi:10.1016/j.compfluid.2018.03.070.

[10] L. di Mare, M. Klein, W. P. Jones, J. Janicka, Synthetic turbulence inflow conditions for large-eddy simulation, Physics of Fluids 18 (2) (2006) 025107. doi:10.1063/1.2130744.

[11] L. di Mare, W. P. Jones, Algebraic and operator methods for generation of inflow data for LES and DNS, in: Fourth International Symposium on Turbulence and Shear Flow Phenomena (TSFP4), Williamsburg, Virginia, 2005, pp. 687–692.

[12] M. Fathali, M. Klein, T. Broeckhoven, C. Lacor, M. Baelmans, Generation of turbulent inflow and initial conditions based on multi-correlated random fields, International Journal for Numerical Methods in Fluids 57 (1) (2008) 93–117. doi:10.1002/fld.1627.

[13] J. Allegrini, J. Carmeliet, Evaluation of the filtered noise turbulent inflow generation method, Flow, Turbulence and Combustion 98 (4) (2017) 1087–1115. doi:10.1007/s10494-016-9798-2.

[14] A. Kempf, M. Klein, J. Janicka, Efficient generation of initial- and inflow-conditions for transient turbulent flows in arbitrary geometries, Flow, Turbulence and Combustion 74 (1) (2005) 67–84. doi:10.1007/s10494-005-3140-8.

[15] G. Fru, G. Janiga, D. Thévenin, Direct numerical simulation of highly turbulent premixed flames burning methane, in: H. Kuerten (Ed.), ERCOFTAC Series, Vol. 15, Springer-Verlag: Eindhoven, The Netherlands, 2011, pp. 327–332. doi:10.1007/978-94-007-2482-2_52.

[16] N. S. Dhamankar, C. S. Martha, Y. Situ, K. M. Aikens, G. A. Blaisdell, A. S. Lyrintzis, Z. Li, Digital filter-based turbulent inflow generation for jet aeroacoustics on non-uniform structured grids, in: 52nd Aerospace Sciences Meeting, no. January, American Institute of Aeronautics and Astronautics, Reston, Virginia, USA, 2014, pp. 1–35. doi:10.2514/6.2014-1401.

[17] Y. Kim, I. P. Castro, Z. T. Xie, Divergence-free turbulence inflow conditions for large-eddy simulations with incompressible flow solvers, Computers and Fluids 84 (2013) 56–68. doi:10.1016/j.compfluid.2013.06.001.

[18] R. Ewert, The simulation of slat noise applying stochastic sound sources based on solenoidal digital filters (SDF), in: Euromech Colloquium 467: Turbulent Flow and Noise Generation July 18-20, 2005, American Institute of Aeronautics and Astronautics, Reston, Virigina, 2005. doi:10.2514/6.2005-2862.

[19] A. Smirnov, S. Shi, I. Celik, Random flow generation technique for large eddy simulations and particle-dynamics modeling, Journal of Fluids Engineering 123 (2) (2001) 359. doi:10.1115/1.1369598.

[20] S. Lee, S. K. Lele, P. Moin, Simulation of spatially evolving turbulence and the applicability of Taylor's hypothesis in compressible flow, Physics of Fluids A 4 (7) (1992) 1521–1530. doi:10.1063/1.858425.

[21] Y. Kim, Z. T. Xie, I. P. Castro, A forward stepwise method of inflow generation for LES, in: AIP Conference Proceedings, Vol. 1376, American Institute of Physics, 2011, pp. 134–136. doi:10.1063/1.3651856.

[22] E. Touber, N. D. Sandham, Large-eddy simulation of low-frequency unsteadiness in a turbulent shock-induced separation bubble, Theoretical and Computational Fluid Dynamics 23 (2) (2009) 79–107. doi:10.1007/s00162-009-0103-z.

[23] S. Breuer, M. Schmidt, Extended synthetic turbulence inflow generator within a hybrid LES-URANS methodology for the prediction of non-equilibrium wall-bounded flows, Flow, Turbulence and Combustion 95 (4) (2015) 669–707. doi:10.1007/s10494-015-9639-8.

[24] K. Anupindi, R. D. Sandberg, Implementation and evaluation of an embedded LES-RANS solver, Flow, Turbulence and Combustion 98 (3) (2017) 697–724. doi:10.1007/s10494-016-9787-5.

[25] M. Ihme, Y. C. See, LES flamelet modeling of a three-stream MILD combustor: Analysis of flame sensitivity to scalar inflow conditions, Proceedings of the Combustion Institute 33 (1) (2011) 1309–1317. doi:10.1016/j.proci.2010.05.019.

[26] T. Okaze, A. Mochida, Cholesky decomposition-based generation of artificial inflow turbulence including scalar fluctuation, Computers and Fluids 159 (2017) 23–32. doi:10.1016/j.compfluid.2017.09.005.

[27] G. Lamberti, C. García-Sánchez, J. Sousa, C. Gorlé, Optimizing turbulent inflow conditions for large-eddy simulations of the atmospheric boundary layer, Journal of Wind Engineering and Industrial Aerodynamics 177 (2018) 32–44. doi:10.1016/j.jweia.2018.04.004.

[28] S. Schmidt, M. Breuer, Source term based synthetic turbulence inflow generator for eddy-resolving predictions of an airfoil flow including a laminar separation bubble, Computers and Fluids 146 (2017) 1–22. doi:10.1016/j.compfluid.2016.12.023.

[29] C. Huber, H. Gomaa, B. Weigand, Application of a novel turbulence generator to multiphase flow computations, in: High Performance Computing in Science and Engineering '10, Springer Berlin Heidelberg, Berlin, Heidelberg, 2011, pp. 273–286. doi:10.1007/978-3-642-15748-6_21.

[30] Z. A. Rana, B. Thornber, D. Drikakis, On the importance of generating accurate turbulent boundary condition for unsteady simulations, Journal of Turbulence 12 (35) (2011) 1–39. doi:10.1080/14685248.2011.613836.

[31] T. P. Lloyd, Large eddy simulations of inflow turbulence noise: Application to tidal turbines, Phd, University of Southampton (2013).

[32] T. P. Lloyd, S. R. Turnock, V. F. Humphrey, Assessing the influence of inflow turbulence on noise and performance of a tidal turbine using large eddy simulations, Renewable Energy 71 (2014) 742–754. doi:10.1016/j.renene.2014.06.011.

[33] D. Dietzel, D. Messig, F. Piscaglia, A. Montorfano, G. Olenik, O. T. Stein, A. Kronenburg, A. Onorati, C. Hasse, Evaluation of scale resolving turbulence generation methods for large eddy Simulation of turbulent flows, Computers and Fluids 93 (2014) 116–128. doi:10.1016/j.compfluid.2014.01.013.

[34] A. W. Abboud, S. T. Smith, Large eddy simulation of a coaxial jet with a synthetic turbulent inlet, International Journal of Heat and Fluid Flow 50 (2014) 240–253. doi:10.1016/j.ijheatfluidflow.2014.08.007.

[35] J. M. Vedovoto, A. d. S. Neto, L. F. F. da Silva, A. Mura, Influence of synthetic inlet turbulence on the prediction of low Mach number flows, Computers & Fluids 106 (2015) 135–153. doi:10.1016/j.compfluid.2014.09.046.

[36] M. R. Mankbadi, M. A. Vyas, J. R. DeBonis, N. J. Georgiadis, Evaluation of inflow turbulence methods in large-eddy simulations of a supersonic boundary layer, in: 2018 Fluid Dynamics Conference, American Institute of Aeronautics and Astronautics, Reston, Virginia, 2018. doi:10.2514/6.2018-3404.

[37] L. C. Berselli, T. Iliescu, W. J. Layton, Mathematics of large eddy simulation of turbulent flows, Scientific Computation, Springer-Verlag, Berlin/Heidelberg, 2006. doi:10.1007/b137408.

[38] C. Greenshields, Boundedness, conservation and steady-state (2013).
URL https://openfoam.org/release/2-2-0/numerics-boundedness/

[39] OpenCFD Limited, OpenFOAM: Programmer's guide (2018).
URL https://openfoam.com/

[40] P. Sagaut, Large eddy simulation for incompressible flows: An introduction, 3rd Edition, Scientific computation, Springer Berlin Heidelberg, 2006. doi:10.1007/b137536.

[41] U. Schumann, Subgrid scale model for finite difference simulations of turbulent flows in plane channels and annuli, Journal of Computational Physics 18 (4) (1975) 376–404. doi:10.1016/0021-9991(75)90093-5.

[42] F. F. Grinstein, L. G. Margolin, W. J. Rider, Implicit large eddy simulation: Computing turbulent fluid dynamics, Cambridge University Press, 2007.

[43] A. D. Beck, D. G. Flad, C. Tonhäuser, G. Gassner, C. Munz, On the influence of polynomial de-aliasing on subgrid scale models, Flow, Turbulence and Combustion 97 (2) (2016) 475–511. doi:10.1007/s10494-016-9704-y.

[44] M. Brio, G. M. Webb, A. R. Zakharian, Numerical time-dependent partial differential equations for scientists and engineers, Elsevier Inc., Amsterdam, The Netherlands, 2010. doi:10.1016/S0076-5392(10)21306-1.

[45] M. Baba-Ahmadi, G. Tabor, Inlet conditions for LES using mapping and feedback control, Computers & Fluids 38 (6) (2009) 1299–1311. doi:10.1016/j.compfluid.2009.02.001.

[46] F. M. Denaro, What does finite volume-based implicit filtering really resolve in large-eddy simulations?, Journal of Computational Physics 230 (10) (2011) 3849–3883. doi:10.1016/j.jcp.2011.02.011.

[47] S. T. Bose, P. Moin, D. You, Grid-independent large-eddy simulation using explicit filtering, Physics of Fluids 22 (10) (2010) 105103. doi:10.1063/1.3485774.

[48] M. Klein, An attempt to assess the quality of large eddy simulations in the context of implicit filtering, Flow, Turbulence and Combustion 75 (1-4) (2005) 131–147. doi:10.1007/s10494-005-8581-6.

[49] A. Leonard, Energy cascade in large-eddy simulations of turbulent fluid flows, in: Advances in Geophysics, Vol. 18, Charlottesville, Virginia, USA, 1975, pp. 237–248. doi:10.1016/S0065-2687(08)60464-1.

[50] E. de Villiers, The potential of large eddy simulation for the modeling of wall bounded flows, Phd, Imperial College of Science, Technology and Medicine (2006).
URL http://bit.ly/1unTPaB

[51] C. G. Speziale, Galilean invariance of subgrid-scale stress models in the large-eddy simulation of turbulence, Journal of Fluid Mechanics 156 (1985) 55. doi:10.1017/S0022112085001987.

[52] P. P. Sullivan, T. W. Horst, D. H. Lenschow, C. Moeng, J. C. Weil, Structure of subfilter-scale fluxes in the atmospheric surface layer with application to large-eddy simulation modelling, Journal of Fluid Mechanics 482 (2003) 101–139. doi:10.1017/S0022112003004099.

[53] J. Smagorinsky, General circulation experiments with the primitive equations, Monthly Weather Review 91 (3) (1963) 99–164.

[54] E. R. V. Driest, On turbulent flow near a wall, Journal of the Aeronautical Sciences (Institute of the Aeronautical Sciences) 23 (1956) 1007–1011. doi:10.2514/8.3713.

[55] C. Meneveau, T. S. Lund, W. H. Cabot, A Lagrangian dynamic subgrid-scale model of turbulence, Journal of Fluid Mechanics 319 (-1) (1996) 353. doi:10.1017/S0022112096007379.

[56] W. Rodi, G. Constantinescu, T. Stoesser, Large-eddy simulation in hydraulics, CRC Press, 2013.

[57] M. Matsumoto, T. Nishimura, Mersenne twister: a 623-dimensionally equidistributed uniform pseudo-random number generator, ACM Transactions on Modeling and Computer Simulation 8 (1) (1998) 3–30. doi:10.1145/272991.272995.

[58] G. Marsaglia, T. A. Bray, A convenient method for generating normal variables, SIAM Review 6 (3) (1964) 260–264. doi:10.1137/1006063.

[59] G. I. Taylor, The spectrum of turbulence, Proceedings of the Royal Society A: Mathematical, Physical and Engineering Sciences 164 (919) (1938) 476–490. arXiv:arXiv:1205.0516v2, doi:10.1098/rspa.1938.0032.

[60] J. Keiner, S. Kunis, D. Potts, Using NFFT 3 - A software library for various nonequispaced fast Fourier transforms, ACM Transactions on Mathematical Software 36 (4) (2009) 1–30. doi:10.1145/1555386.1555388.

[61] W. A. Woyczyński, A first course in statistics for signal analysis, 2nd Edition, Birkhäuser Boston, Boston, MA, USA, 2011. doi:10.1007/978-0-8176-8101-2.

[62] J. Keiner, S. Kunis, D. Potts, NFFT 3.0 - Tutorial (2017).
URL http://www.tu-chemnitz.de/âĹijpotts/nfft

[63] J. W. Cooley, J. W. Tukey, An algorithm for the machine calculation of complex Fourier series, Mathematics of Computation 19 (90) (1965) 297. doi:10.2307/2003354.

[64] S. B. Pope, Turbulent flows, Cambridge University Press, 2000.

[65] I. Celik, Z. N. Cehreli, I. Yavuz, Index of resolution quality for large eddy simulations, Journal of Fluids Engineering 127 (5) (2005) 949. doi:10.1115/1.1990201.

[66] I. Celik, M. Klein, J. Janicka, Assessment measures for engineering LES applications, Journal of Fluids Engineering 131 (3). doi:10.1115/1.3059703.

[67] G. Nastac, J. W. Labahn, L. Magri, M. Ihme, Lyapunov exponent as a metric for assessing the dynamic content and predictability of large-eddy simulations, Physical Review Fluids 2 (9). doi:10.1103/PhysRevFluids.2.094606.

[68] G. Comte-Bellot, S. Corrsin, Simple Eulerian time correlation of full-and narrow-band velocity signals in grid-generated, isotropic turbulence, Journal of Fluid Mechanics 48 (2) (1971) 273–337. doi:10.1017/S0022112071001599.

[69] S. Tavoularis, S. Corrsin, Experiments in nearly homogenous turbulent shear flow with a uniform mean temperature gradient. Part 1, Journal of Fluid Mechanics 104 (EM6) (1981) 311–347. doi:10.1017/S0022112081002930.

[70] R. D. Moser, J. Kim, N. N. Mansour, Direct numerical simulation of turbulent channel flow up to Reτ=590, Physics of Fluids 11 (4) (1999) 943–945. arXiv:1410.7809, doi:10.1063/1.869966.

[71] I. Celik, M. Klein, M. Freitag, J. Janicka, Assessment measures for URANS/DES/LES: An overview with applications, Journal of Turbulence 7 (48) (2006) 1–27. doi:10.1080/14685240600794379.

[72] P. L. O'Neill, D. Nicolaides, D. R. Honnery, J. Soria, Autocorrelation functions and the determination of integral length with reference to experimental and numerical data, in: 15th Australasian Fluid Mechanics Conference, Vol. 1, The University of Sydney, Sydney, Australia, 2004, pp. 1–4.

[73] V. Eswaran, S. B. Pope, Direct numerical simulations of the turbulent mixing of a passive scalar, Physics of Fluids 31 (3) (1988) 506. doi:10.1063/1.866832.

[74] H. G. Weller, G. Tabor, H. Jasak, C. Fureby, A tensorial approach to computational continuum mechanics using object-oriented techniques, Computers in Physics 12 (6) (1998) 620. doi:10.1063/1.168744.

[75] P. R. Spalart, Young-person's guide to detached-eddy simulation grids, Tech. rep., NASA Langley Research Center, Hampton, VA, USA (2001).

[76] M. Liefvendahl, C. Fureby, Grid requirements for LES of ship hydrodynamics in model and full scale, Ocean Engineering 143 (2017) 259–268. doi:10.1016/j.oceaneng.2017.07.055.

[77] U. Piomelli, Large eddy simulations in 2030 and beyond, Philosophical Transactions of the Royal Society A: Mathematical, Physical and Engineering Sciences 372 (2014) 1–13. doi:10.1098/rsta.2013.0320.

[78] H. Tennekes, J. L. Lumley, A first course in turbulence, MIT Press, Cambridge, MA, United States, 1972.

[79] J. S. Baggett, J. Jimenez, A. G. Kravchenko, Resolution requirements in large-eddy simulation of shear flows, in: Annual Research Briefs - 1997, Stanford, CA, USA, 1997, pp. 51–66.

[80] F. R. Menter, Best practice: Scale-resolving simulations in ANSYS CFD, Technical report (2015).

[81] L. Davidson, Large eddy simulations: How to evaluate resolution, International Journal of Heat and Fluid Flow 30 (5) (2009) 1016–1025. doi:10.1016/j.ijheatfluidflow.2009.06.006.

[82] D. Chapman, Computational aerodynamics development and outlook, AIAA Journal 17 (12) (1979) 1293–1313. doi:10.2514/3.61311.

[83] H. Choi, P. Moin, Grid-point requirements for large eddy simulation: Chapman's estimates revisited, Physics of Fluids 24 (011702). doi:10.1063/1.3676783.

[84] P. P. Sullivan, E. G. Patton, The effect of mesh resolution on convective boundary layer statistics and structures generated by large-eddy simulation, Journal of the Atmospheric Sciences 68 (10) (2011) 2395–2415. doi:10.1175/JAS-D-10-05010.1.

[85] J. Franke, C. Hirsch, A. G. Jensen, H. W. Krüs, M. Schatzmann, P. S. Westbury, S. D. Miles, J. A. Wisse, N. G. Wright, P. S. Westbury, J. A. Wisse, N. G. Wright, Recommendations on the use of CFD in wind engineering, in: J. P. A. J. van Beeck (Ed.), COST Action C14, Impact of Wind and Storm on City Life Built Environment. Proceedings of the International Conference on Urban Wind Engineering and Building Aerodynamics, 5âĂŞ7 May 2004, von Karman Institute, Sint-Genesius-Rode, Belgium, 2004, pp. 1–11.
URL http://bit.ly/2csTlhc

[86] R. M. Cummings, J. R. Forsythe, S. A. Morton, K. D. Squires, Computational challenges in high angle of attack flow prediction, Progress in Aerospace Sciences 39 (5) (2003) 369–384. doi:10.1016/S0376-0421(03)00041-1.

[87] P. Spalart, Trends in turbulence treatments, in: Fluids 2000 Conference and Exhibit, American Institute of Aeronautics and Astronautics, Reston, Virigina, 2000. doi:10.2514/6.2000-2306.

[88] A. Jackson, A comprehensive tour of snappyHexMesh (2012).
URL http://bit.ly/2cBilA5

[89] F. P. Karrholm, Numerical modelling of diesel spray injection, turbulence interaction and combustion, Phd thesis, Chalmers University of Technology (2008).
URL http://bit.ly/2cEQ5M1

[90] C. M. Rhie, W. L. Chow, Numerical study of the turbulent flow past an airfoil with trailing edge separation, AIAA Journal 21 (11) (1983) 1525–1532. doi:10.2514/3.8284.

[91] R. Courant, K. Friedrichs, H. Lewy, On the partial difference equations of mathematical physics, IBM Journal of Research and Development 11 (2) (1967) 215–234. doi:10.1147/rd.112.0215.

[92] R. I. Issa, Solution of the implicitly discretised fluid flow equations by operator-splitting, Journal of Computational Physics 62 (1) (1986) 40–65. arXiv:9809069v1, doi:10.1016/0021-9991(86)90099-9.

[93] H. Nilsson, How to implement your own application (2008).
URL http://bit.ly/2bH5P0f

[94] C. Fureby, F. F. Grinstein, Large eddy simulation of high-Reynolds-number free and wall-bounded flows, Journal of Computational Physics 181 (1) (2002) 68–97. doi:10.1006/jcph.2002.7119.

[95] L. Halpern, M. Schatzman, Artificial boundary conditions for incompressible viscous flows, SIAM Journal on Mathematical Analysis 20 (2) (1989) 308–353. doi:10.1137/0520021.

[96] N. Troldborg, Actuator line modeling of wind turbine wakes, Phd, Technical University of Denmark (2008).

[97] A. Bechmann, Large-eddy simulation of atmospheric flow over complex terrain, Phd thesis (2007).

[98] OpenCFD, Foundation course: Version 2.1.x (2012).

[99] E. Cuthill, J. McKee, Reducing the bandwidth of sparse symmetric matrices, in: Proceedings of the 1969 24th national conference of the ACM, ACM Press, New York, New York, USA, 1969, pp. 157–172. doi:10.1145/800195.805928.

[100] F. Pellegrini, PT-Scotch and libScotch 5.1 user's guide (2010).

[101] NIST-SEMATECH, NIST/SEMATECH e-handbook of statistical methods, National Institute of Standards and Technology, 2003.
URL http://www.itl.nist.gov/div898/handbook/

[102] R. D. Moser, DNS data for turbulent channel flow (2007).
URL http://bit.ly/2rJeQ3u

[103] P. D. Welch, The use of fast Fourier transform for the estimation of power spectra: A method based on time averaging over short, modified periodograms, IEEE Transactions on Audio and Electroacoustics 15 (2) (1967) 70–73. doi:10.1109/TAU.1967.1161901.

[104] J. C. R. Hunt, A. A. Wray, P. Moin, Eddies, streams, and convergence zones in turbulent flows, in: Studying Turbulence Using Numerical Simulation Databases, 2. Proceedings of the 1988 Summer Program, Stanford University, CA, United States, 1988, pp. 193–208.

[105] J. Jeong, F. Hussain, On the identification of a vortex, Journal of Fluid Mechanics 285 (1995) 69. doi:10.1017/S0022112095000462.

[106] L. Tornqvist, P. Vartia, Y. O. Vartia, How should relative changes be measured?, The American Statistician 39 (1) (1985) 43. doi:10.2307/2683905.

[107] T. Eiter, H. Mannila, Computing discrete Fréchet distance, Technical report, Technische Universität Wien, Wien (1994). doi:10.1.1.90.937.

[108] S. L. Seyler, A. Kumar, M. F. Thorpe, O. Beckstein, Path similarity analysis: A method for quantifying macromolecular pathways, PLoS Computational Biology 11 (10). arXiv:1505.04807, doi:10.1371/journal.pcbi.1004568.

[109] R. Murray, Writing for academic journals, 3rd Edition, Open University Press, 2013.

[110] L. F. Richardson, Weather prediction by numerical process, 1st Edition, Cambridge University Press, Cambridge, 1922.
URL https://archive.org/details/weatherpredictio00richrich

[111] C. M. de Silva, J. Philip, I. Marusic, Minimization of divergence error in volumetric velocity measurements and implications for turbulence statistics, Experiments in Fluids 54 (7) (2013) 1557. doi:10.1007/s00348-013-1557-8.
URL http://link.springer.com/10.1007/s00348-013-1557-8

[112] C. Y. Wang, Q. Gao, R. J. Wei, T. Li, J. J. Wang, Weighted divergence correction scheme and its fast implementation, Experiments in Fluids 58 (5) (2017) 44. doi:10.1007/s00348-017-2307-0.

[113] I. Azijli, R. P. Dwight, Solenoidal filtering of volumetric velocity measurements using Gaussian process regression, Experiments in Fluids 56 (11) (2015) 198. doi:10.1007/s00348-015-2067-7.

[114] I. P. Castro, Turbulence I: Physics & Measurement (2012).

[115] M. L. Shur, P. R. Spalart, M. K. Strelets, A. K. Travin, Synthetic turbulence generators for RANS-LES interfaces in zonal simulations of aerodynamic and aeroacoustic problems, Flow, Turbulence and Combustion 93 (1) (2014) 63–92. doi:10.1007/s10494-014-9534-8.

[116] G. D. Prisco, U. Piomelli, A. Keating, Improved turbulence generation techniques for hybrid RANS/LES calculations, Journal of Turbulence.

[117] I. Veloudis, Z. Yang, J. J. McGuirk, G. J. Page, A. Spencer, Novel implementation and assessment of a digital filter based approach for the generation of les inlet conditions, Flow, Turbulence and Combustion 79 (1) (2007) 1–24. doi:10.1007/s10494-006-9058-y.

[118] D. Potts, G. Steidl, A. Nieslony, Fast convolution with radial kernels at nonequispaced knots, Numerische Mathematik 98 (2) (2004) 329–351. doi:10.1007/s00211-004-0538-5.

Appendix A. Appendix

Appendix A.1. One-spatial-point second-order correlation tensor

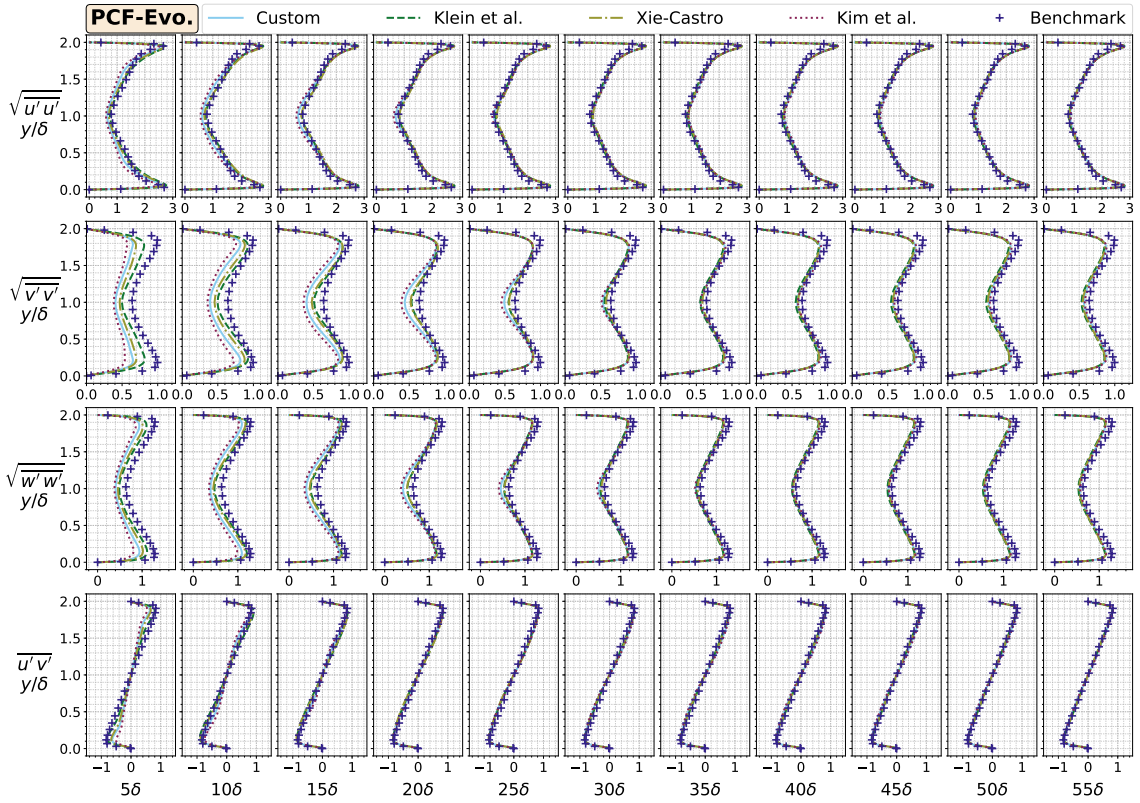

Figure A.24: The along-channel-height profiles of the one-point second-order symmetric correlation tensor components along the longitudinal *evolvement phase* (Evo.), i.e. 11 equidistant stations from 5δ to 55δ away from the inlet in 5δ-distance steps, obtained from the smooth-wall plane channel flow (PCF) computations [70]. The remaining figure particulars and axes limits are the same with Fig. 9.

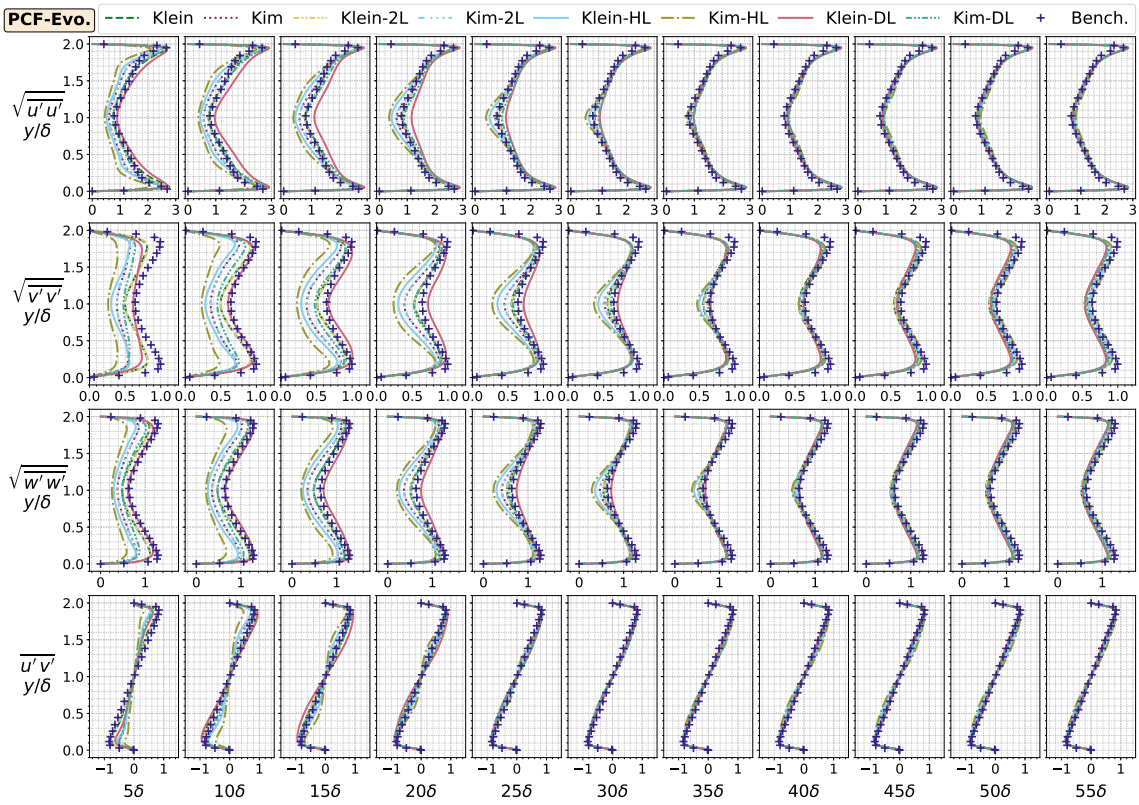
PCF-Evo.
Klein
Kim
Klein-2L
Kim-2L
Klein-HL
Kim-HL
Klein-DL
Kim-DL
Bench.
$\sqrt{\overline{u'u'}}$ y/δ
$\sqrt{\overline{v'v'}}$ y/δ
$\sqrt{\overline{w'w'}}$ y/δ
$\overline{u'v'}$ y/δ
5δ
10δ
15δ
20δ
25δ
30δ
35δ
40δ
45δ
50δ
55δ
Figure A.25: -

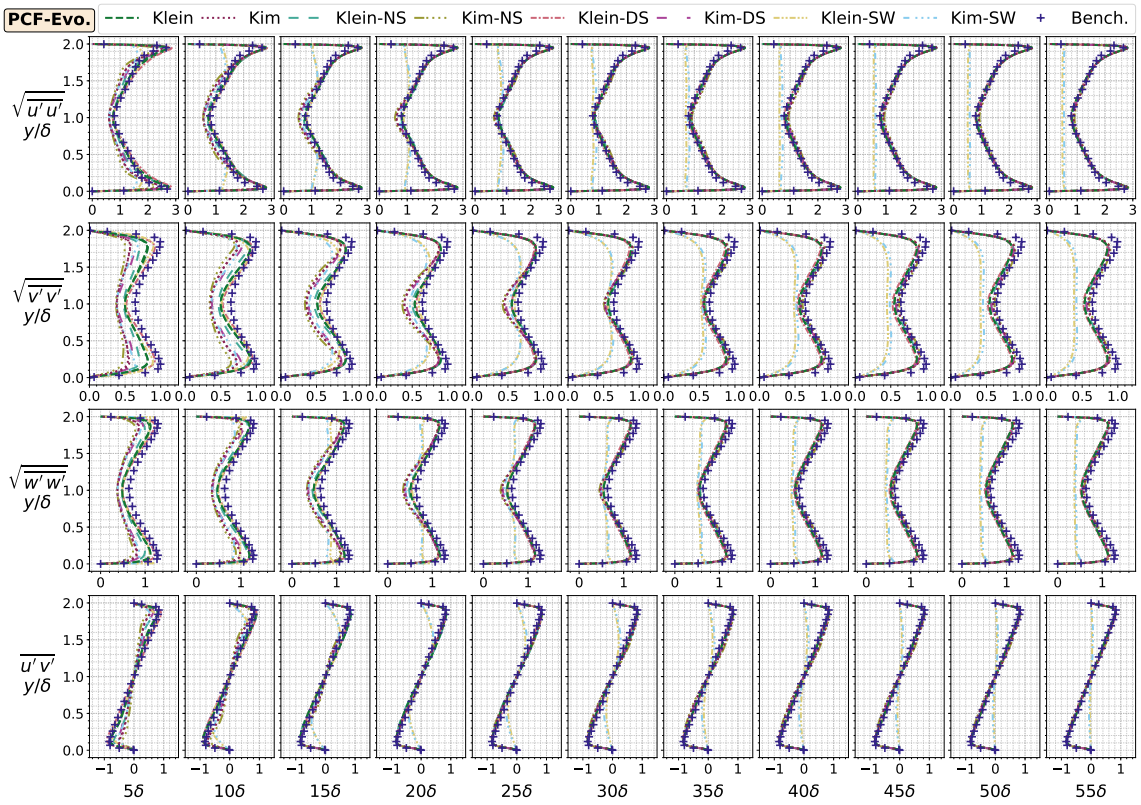
PCF-Evo.
Klein
Kim
Klein-NS
Kim-NS
Klein-DS
Kim-DS
Klein-SW
Kim-SW
Bench.
$\sqrt{\overline{u'u'}}$ y/δ
$\sqrt{\overline{v'v'}}$ y/δ
$\sqrt{\overline{w'w'}}$ y/δ
$\overline{u'v'}$ y/δ
5δ
10δ
15δ
20δ
25δ
30δ
35δ
40δ
45δ
50δ
55δ
Figure A.26: -

1740 *Appendix A.2. Over-filter scale kinetic energy transport equation*

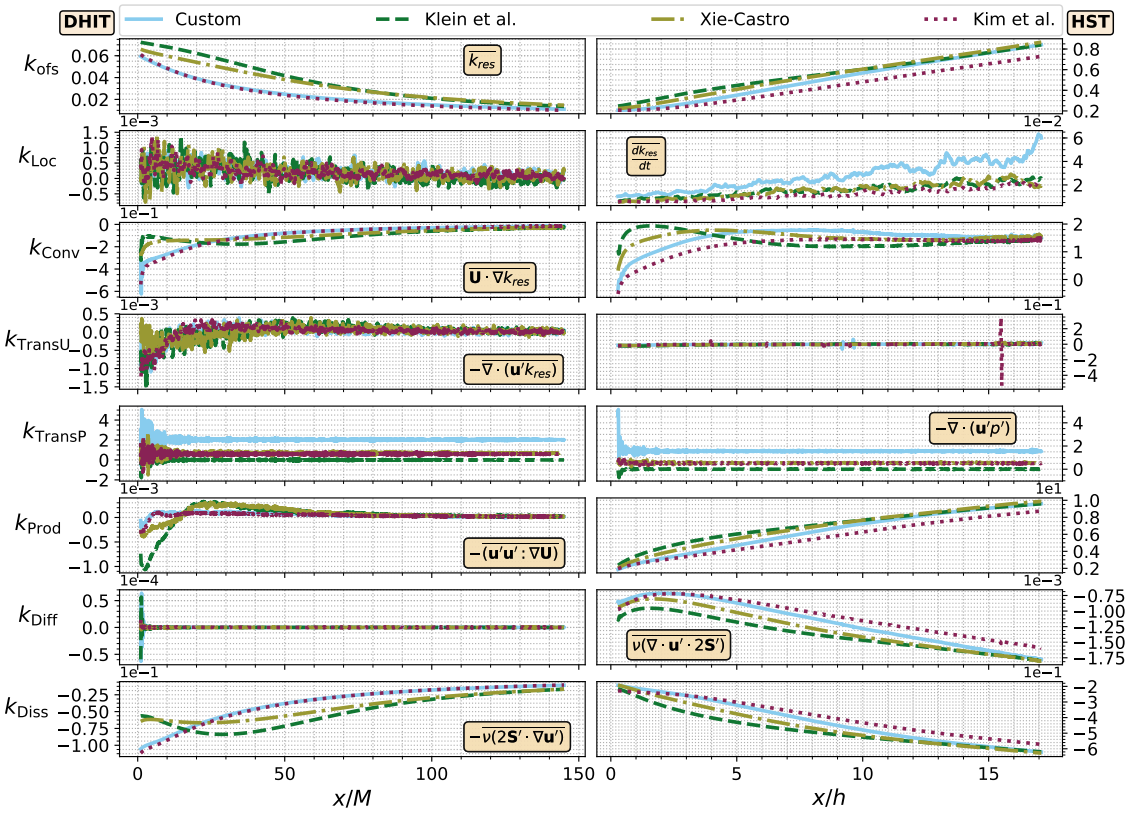

Figure A.27: -

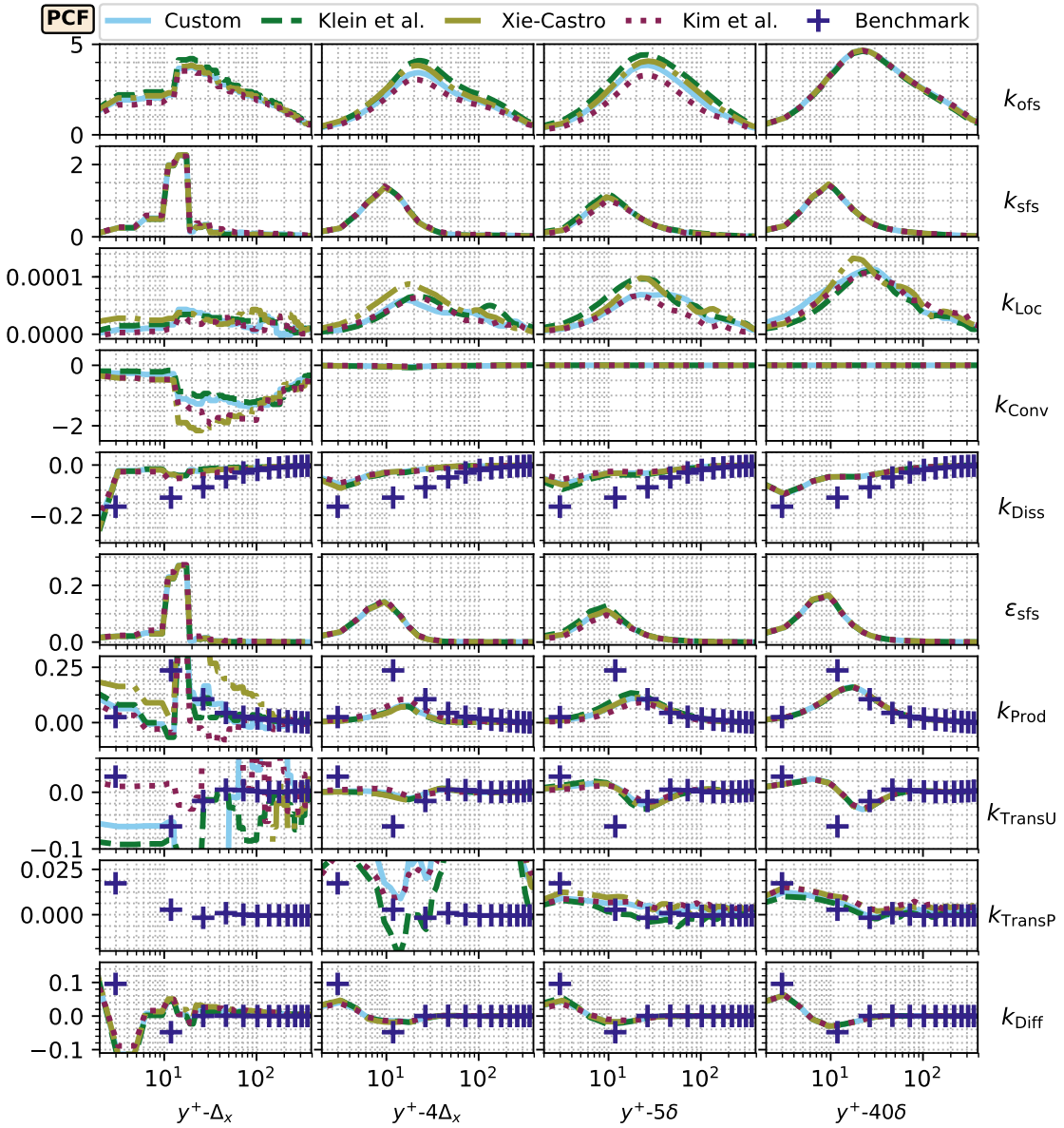
PCF
Custom
Klein et al.
Xie-Castro
Kim et al.
Benchmark
k_{ofs}
k_{sfs}
k_{Loc}
k_{Conv}
k_{Diss}
ε_{sfs}
k_{Prod}
k_{TransU}
k_{TransP}
k_{Diff}
y^+-Δ_x
y^+-$4\Delta_x$
y^+-5δ
y^+-40δ

Figure A.28: -

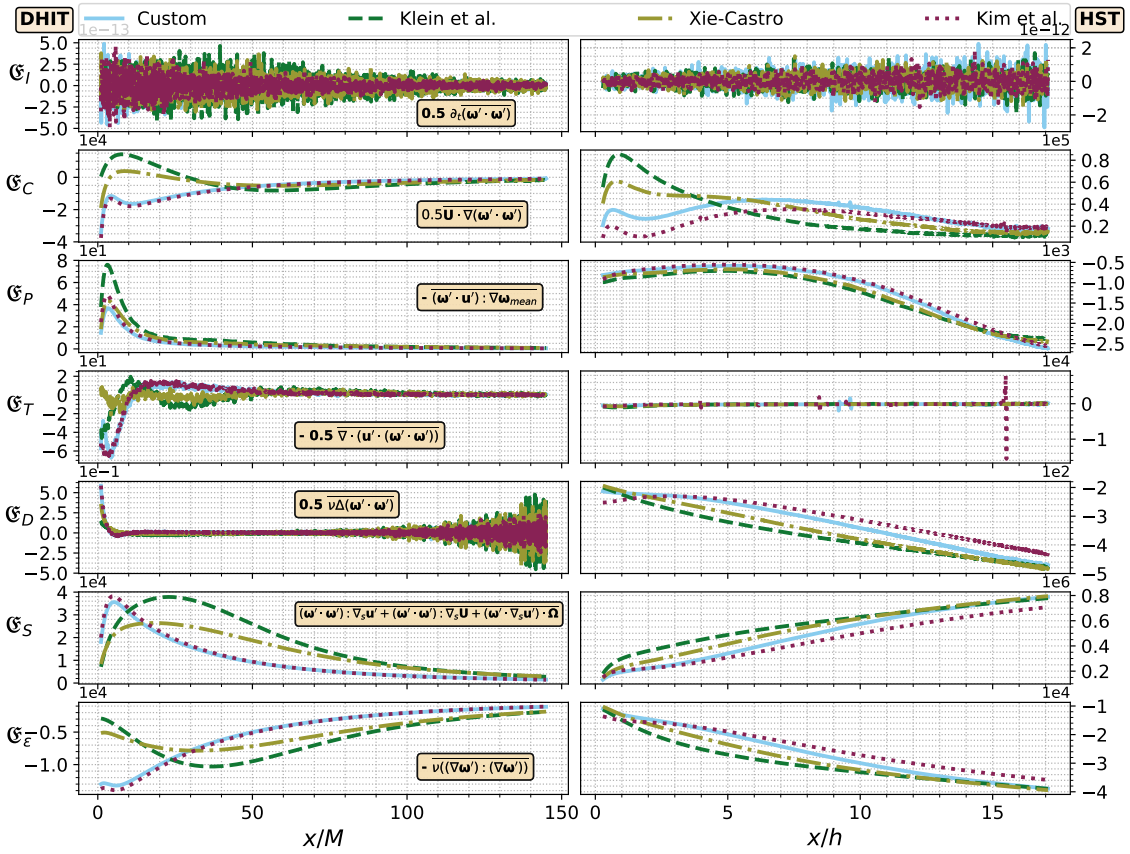
DHIT
HST
Custom
Klein et al.
Xie-Castro
Kim et al.
$\mathfrak{E}_I$
$\mathfrak{E}_C$
$\mathfrak{E}_P$
$\mathfrak{E}_T$
$\mathfrak{E}_D$
$\mathfrak{E}_S$
$\mathfrak{E}_\varepsilon$
$0.5\,\partial_t\overline{(\boldsymbol{\omega}'\cdot\boldsymbol{\omega}')}$
$0.5\overline{\mathbf{U}}\cdot\nabla\overline{(\boldsymbol{\omega}'\cdot\boldsymbol{\omega}')}$
$-\,\overline{(\boldsymbol{\omega}'\cdot\mathbf{u}')}:\nabla\boldsymbol{\omega}_{mean}$
$-\,0.5\,\overline{\nabla\cdot(\mathbf{u}'\cdot(\boldsymbol{\omega}'\cdot\boldsymbol{\omega}'))}$
$0.5\,\overline{\nu\Delta(\boldsymbol{\omega}'\cdot\boldsymbol{\omega}')}$
$\overline{(\boldsymbol{\omega}'\cdot\boldsymbol{\omega}'):\nabla_s\mathbf{u}'+(\boldsymbol{\omega}'\cdot\boldsymbol{\omega}'):\nabla_s\mathbf{U}+(\boldsymbol{\omega}'\cdot\nabla_s\mathbf{u}')\cdot\boldsymbol{\Omega}}$
$-\,\overline{\nu((\nabla\boldsymbol{\omega}'):(\nabla\boldsymbol{\omega}'))}$
1e−13
1e−12
1e4
1e5
1e1
1e3
1e−1
1e2
1e6
0
50
100
150
5
10
15
x/M
x/h

Figure A.29: -

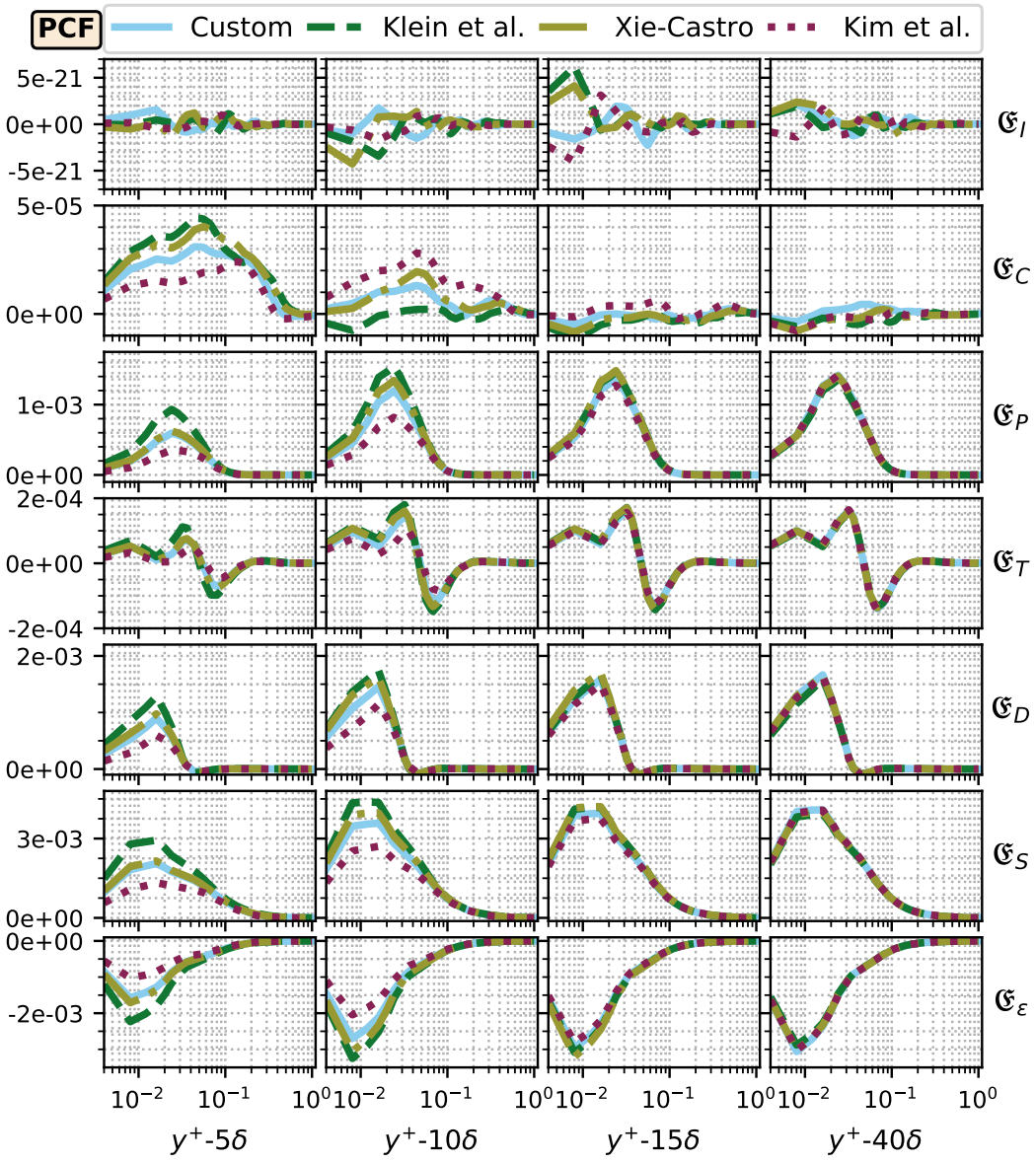
PCF
Custom
Klein et al.
Xie-Castro
Kim et al.
5e-21
0e+00
-5e-21
$\mathfrak{E}_I$
5e-05
0e+00
$\mathfrak{E}_C$
1e-03
0e+00
$\mathfrak{E}_P$
2e-04
0e+00
-2e-04
$\mathfrak{E}_T$
2e-03
0e+00
$\mathfrak{E}_D$
3e-03
0e+00
$\mathfrak{E}_S$
0e+00
-2e-03
$\mathfrak{E}_\varepsilon$
10^{-2}
10^{-1}
10^{0}
y^+-5δ
y^+-10δ
y^+-15δ
y^+-40δ

Figure A.30: -

Appendix A.4. Mean total strain transport equation

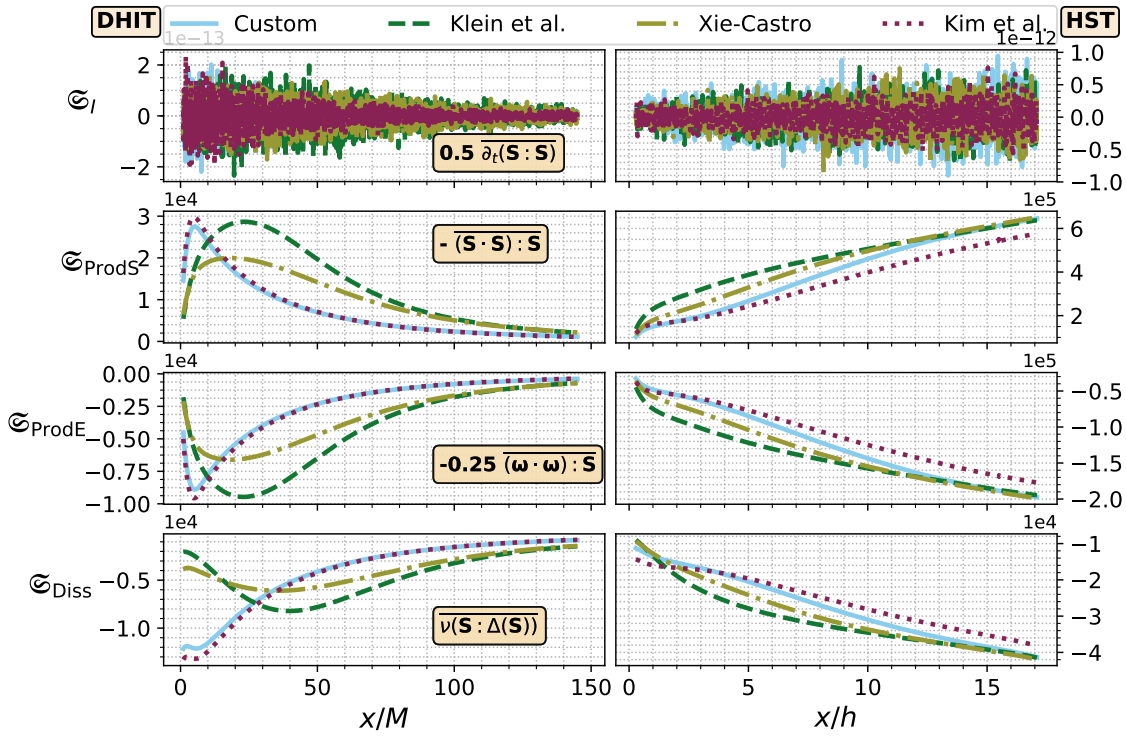

Figure A.31: -

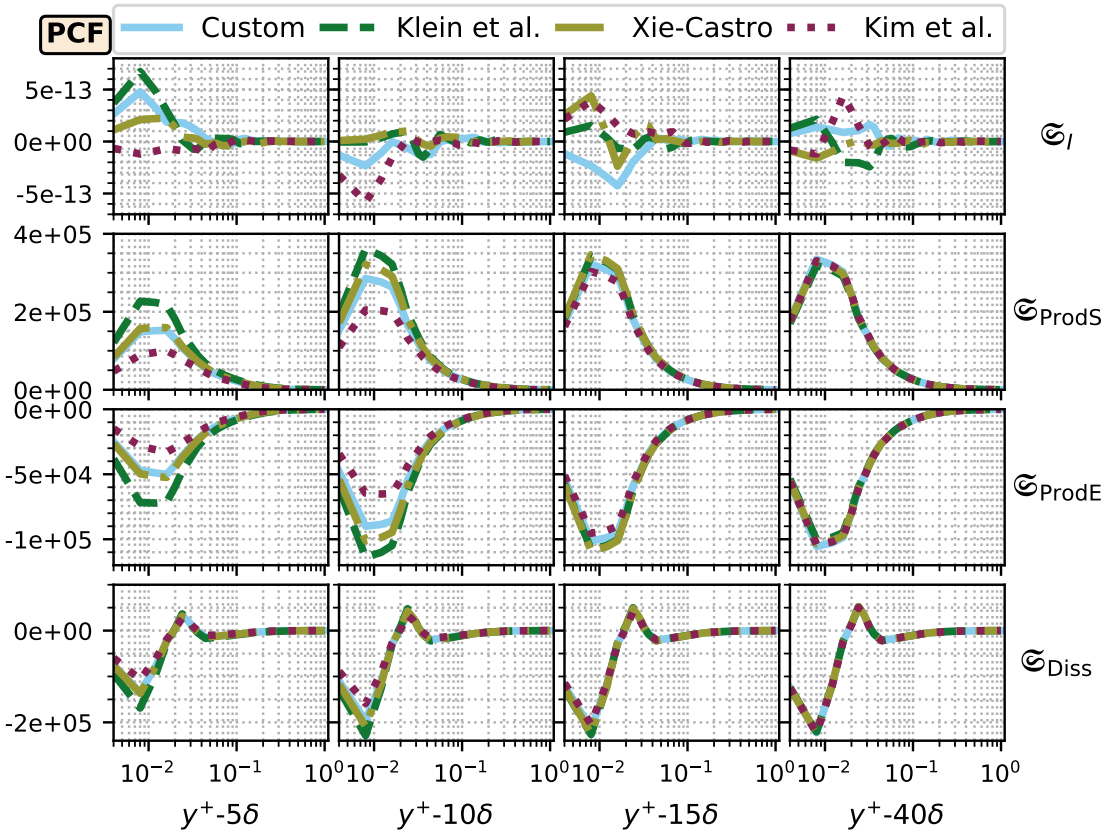
PCF
Custom
Klein et al.
Xie-Castro
Kim et al.
5e-13
0e+00
-5e-13
4e+05
2e+05
0e+00
0e+00
-5e+04
-1e+05
0e+00
-2e+05
$\mathfrak{S}_I$
$\mathfrak{S}_{ProdS}$
$\mathfrak{S}_{ProdE}$
$\mathfrak{S}_{Diss}$
10^{-2}
10^{-1}
10^{0}
y^+-5δ
y^+-10δ
y^+-15δ
y^+-40δ

Figure A.32: -

Appendix A.5. One-point skewness and kurtosis

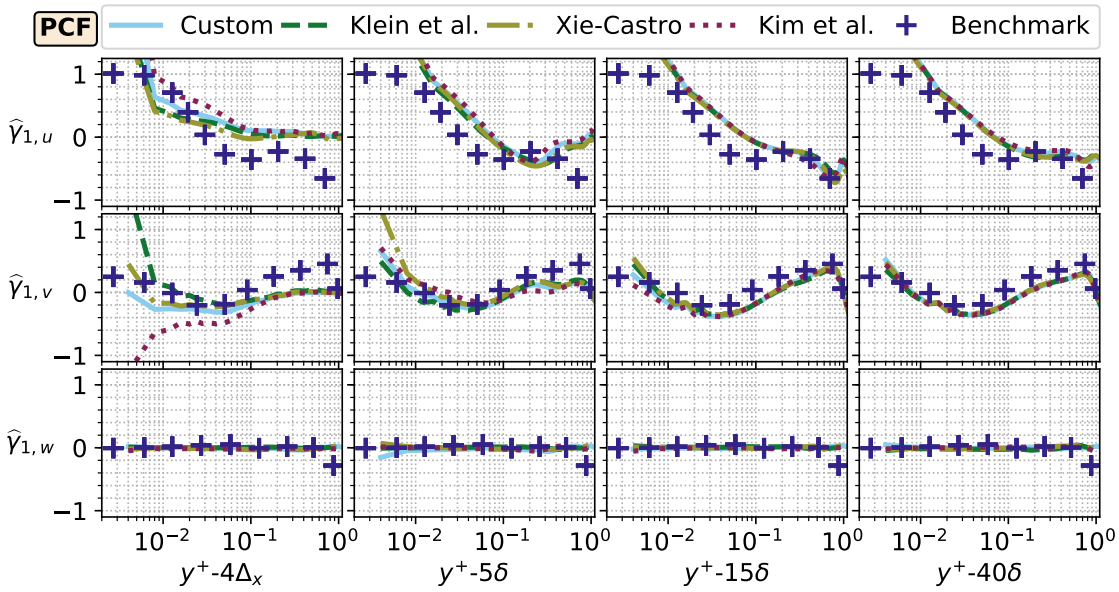

Figure A.33: -

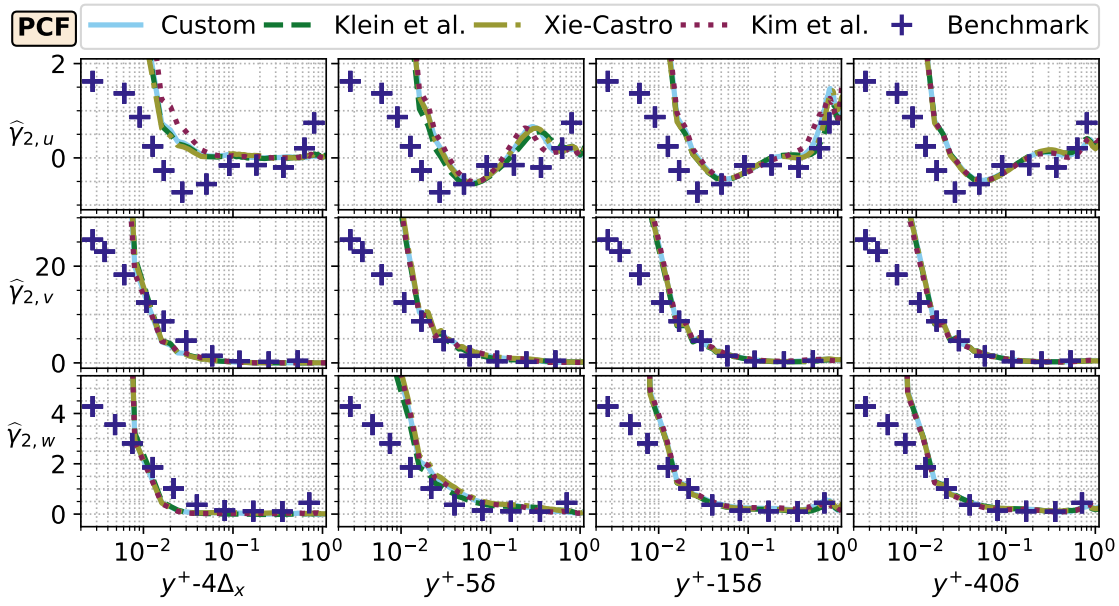

Figure A.34: -

Paper - III

LARGE EDDY SIMULATION AND ANALYTICAL WAKE MODEL INVESTIGATIONS ON HYDRODYNAMICS OF A MARINE TURBINE UNDER DECAYING HOMOGENEOUS ISOTROPIC TURBULENCE: FREESTREAM TURBULENCE INTENSITY EFFECTS

Large eddy simulation and analytical wake model investigations on hydrodynamics of a marine turbine under decaying homogeneous isotropic turbulence: Freestream turbulence intensity effects

Kutalmis M. Bercin*, Zheng-Tong Xie, Stephen R. Turnock

Faculty of Engineering and the Environment, University of Southampton, SO17 1BJ, Southampton, the UK

Abstract

A rigid model-scale experimental horizontal-axis marine turbine (so-called the *Southampton turbine*) was numerically investigated under decaying homogeneous isotropic turbulence in absence of its tower. Twelve controlled computations were carried out through wall-modelled and actuator-line-modelled large eddy simulations where the three-dimensional turbulence intensity, $I_{\mathbf{u}'_{\mathrm{rms}}}$, was the control variable. The first four computations excluded the blades, and examined the flow prediction effects of the *arbitrary mesh interface technique* (AMI) while *i*. stationary and *ii*. rotating, and *iii*. the presence of the turbine nacelle. The last eight computations explored the ways how three-dimensional turbulence intensity affects the turbine and its surrounding flow fields. Four turbulence intensities were tested, $I_{\mathbf{u}'_{\mathrm{rms}}}$=$\{0, 10, 20, 40\}$[%]. In addition, twelve analytical wake models from the wind and marine turbine literature were reviewed and assessed with respect to the wall-modelled computations under the same range of $I_{\mathbf{u}'_{\mathrm{rms}}}$. Among many, the prominent outcomes were as follows: [*i*] AMI-in-rotation adversely affected amplitude-based statistics by causing discontinuities on AMI-region boundaries, and differences between the inside and outside of the AMI-region. The effects were increased outwards from the AMI-region centre. [*ii*] However, AMI-in-rotation did not affect time-based statistics. [*iii*] Stationary AMI did not affect flow fields. Furthermore, irrespective of freestream $I_{\mathbf{u}'_{\mathrm{rms}}}$: [*iv*] Longitudinal mean speed fields (U-fields) began to be affected by the presence of the turbine nearly 4 rotor radii upstream of the turbine; [*v*] maxima of changes in U-fields occurred at around 2 rotor radii downstream of the turbine; [*vi*] U-fields became virtually indistinguishable commencing around 6 to 10 rotor radii downstream within the alignment of the turbine; however, were kept turbine signature by remaining different from U-freestream despite

* Corresponding author
Email address: Z.Xie@soton.ac.uk (Kutalmis M. Bercin*)

turbulence entrainment; [*vii*] wake recovery rates as a function of downstream distance followed a half-Gaussian-form. [*viii*] No significant deviations between the wall-modelled and actuator-line modelled computations occurred in terms of the statistics quantified. [*ix*] The coefficient of variation, skewness, kurtosis and maxima of longitudinal forces/moments were increasing functions of $I_{\mathbf{u}'_{\mathrm{rms}}}$ whilst the mean and minima were inversely varying with $I_{\mathbf{u}'_{\mathrm{rms}}}$. [*x*] An analytical model that was derived and calibrated specifically for a similar marine turbine was quantified to be superior to the other models in terms of wake profile and speed predictions, highlighting the importance of the similarity level between turbine-flow particulars at hand, and analytical model's derivation particulars.

Keywords: horizontal-axis marine turbine, wall-modelled large eddy simulation, actuator line model, synthetic turbulence, turbine hydrodynamics, turbulence intensity

1. Introduction

Horizontal-axis marine turbines (hereafter, HAMTs) are desired to provide maximal energy conversion in a subsea operation environment with as few scheduled maintenance appointments as possible. Yet the objective arguably appears difficult to accomplish due to knowledge gaps in understanding and modelling complex nature of flows and its interactions with HAMTs. A further complication is posed by HAMT plantations with which optimisation of a plant as a whole by tailoring individual turbine designs at specific locations becomes preferable over a mass design of turbines since various effects of neighbouring turbines, such as flow inductions and wakes, are introduced into the complexity. This additionally demands the consideration of interactions between turbines and turbine-induced flows to achieve the objective.

One of the determinants of such subsea environment deemed significant to HAMTs[1] is the level of kinetics of velocity fluctuation fields with respect to their mean fields. This is usually quantified by means of the longitudinal *turbulence intensity* ($I_{u'_{\mathrm{rms}}}$) and three-dimensional *turbulence intensity* ($I_{\mathbf{u}'_{\mathrm{rms}}}$)[2] which can be defined as the ratio between the root-mean-square of Reynolds-decomposed[3]

[1] Hereafter, all the literature review is limited to three-bladed HAMTs unless otherwise stated.

[2] In statistical terms, the *turbulence intensity* is the *coefficient of variation* of velocity fluctuation fields.

[3] Consider $\mathbf{u}(\mathbf{x},t)_{\{\mathbf{u}\in\mathbb{Q};\,\mathbf{u}=(u,v,w);\,t>0\}}$ as the instantaneous velocity field. Herein, the *Reynolds decomposition* using the averaging operator of the discrete *cumulative moving time average* is used on $\mathbf{u}(\mathbf{x},t)$: $\mathbf{u}(\mathbf{x},t)\equiv\overline{\mathbf{u}}(\mathbf{x})+\mathbf{u}'(\mathbf{x},t)\equiv\mathbf{U}+\mathbf{u}'$ where $\overline{\mathbf{u}}\equiv(\mathrm{N}\Delta_t)^{-1}\sum_{n=0}^{\mathrm{N}-1}\mathbf{u}(\mathbf{x},n\Delta_t)$ with Δ_t is the time-step size, N the number of time steps, and $\mathrm{N}\Delta_t$ the finite sample duration.

Table 1: Representative values of longitudinal turbulence intensity and maximum flow speed obtained from various measurement campaigns at fields presumed to be suitable for marine turbine operation. Additional field measurement campaigns can be found in [1, Table 1].

Region	Average longitudinal turbulence intensity [-]	Peak mean speed [ms^{-1}]	Height from seabed [m]
Sound of Islay, GB-SCT[2]	0.12-0.13	2.5	5.0
Puget Sound, US-WA[3]	0.10-0.11	2.0	4.6
Nodule Point, US-WA[4]	0.084-0.114	1.8	4.7
Admiralty Head, US-WA[4]	0.095-0.118	3.2	8.1
East River, US-NY[5]	0.15	2.0	4.25
Strangford Lough, NI[6]	0.17-0.40	2.1	3.4 (below surface)
East River, US-NY[7]	0.25-0.30	2.0	5.0
Falls of Lora, GB-SCT[8]	0.40	2.0	4.7
Kobe Strait, JP[9]	0.10-0.20	2.0	4.5-17.5

velocity fluctuation field (u'_{rms}, $\mathbf{u}'_{\mathrm{rms}}$),[4] and the Euclidean norm of the Reynolds-decomposed mean velocity field, (U, U_e)[5]: $I_{u'_{\mathrm{rms}}} \equiv u'_{\mathrm{rms}}/U$ and $I_{\mathbf{u}'_{\mathrm{rms}}} \equiv \mathbf{u}'_{\mathrm{rms}}/U_e$, respectively.

The majority of prospective energy conversion sites considered by the marine energy community belongs to diurnal/semidiurnal tides. Therein, turbulence intensities are generally observed comparable to those in the atmospheric boundary layer, and in high variation within a site and across sites in a site specific manner. For instance, Table 1 exemplified nine field measurement campaigns where the representative values of the time-averaged longitudinal turbulence intensity varied from 0.08 to 0.40. In addition to this, turbulence intensity's exponential-decay relation with mean speed [4, Fig. 6][9, Fig. 9][6, Fig. 13][6], and its log-law relation with height above seabed [11, p. 3191] increase the variability of turbulence intensity that a turbine may experience within its cut-in and cut-off speeds.

Various experimental and numerical studies have examined possible effects of freestream turbulence intensity levels on hydrodynamics, structural dynamics and energy conversion performances of HAMTs. In general, these studies monitored the effects in four aspects as elaborated below.

The first aspect is as regards time-averaged thrust and power coefficients of HAMTs, i.e. C_T and C_P. It was found out that three types of concluding remarks were reported in the literature: Negligible-arbitrary changes, losses or gains in the coefficients due to the $I_{\mathbf{u}'_{\mathrm{rms}}}$ augmentation. To

[4] $u'_{\mathrm{rms}}(\mathbf{x}) \equiv \sqrt{\overline{(u')^2}}$ and $\mathbf{u}'_{\mathrm{rms}}(\mathbf{x}) \equiv \sqrt{0.\dot{3}\,(\overline{(u')^2}+\overline{(v')^2}+\overline{(w')^2})}$. It should be highlighted that two different averaging operations exist within the *turbulence intensity*, i.e. the cumulative moving time average and the arithmetic average, unlike the *root-mean-square*'s actual formula involving only the arithmetic average.

[5] $U(\mathbf{x}) \equiv U$ and $U_e(\mathbf{x}) \equiv \|\mathbf{U}\|_2 \equiv \sqrt{U^2+V^2+W^2}$.

[6] For a contradicting observation that found no relation, see the measurements by [10, p. 15].

begin with, [12, p. 107] interpreted results from their k-ω-SST RANS and wall-resolved Lilly-Germano dynamic procedured Smagorinsky-model LES computations that time-averaged loadings were not affected through $I_{\mathbf{u}'_{\mathrm{rms}}}$=$\{1, 10, 20\}$[%] although [12, Table 4] illustrated general reductions of 2-6[%] and 0.2-0.6[%] for $\mathrm{C_T}$ and $\mathrm{C_P}$. Similarly, [13, p. 104, 115, Fig. 17] reported virtually no effect on the coefficients due to $I_{\mathbf{u}'_{\mathrm{rms}}}$=$\{3, 6, 9\}$[%] for a tip-speed-ratio (TSR) range of 1-10 in their k-ω-SST RANS computations. In favour of $\mathrm{C_T}$-$\mathrm{C_P}$-reduction observations, however, [14, p. 5, Fig. 6] observed from $I_{\mathbf{u}'_{\mathrm{rms}}}$=$\{8, 25\}$[%] flume-tank experiments that both coefficients were reduced by $\sim$9% within a TSR range of 9-15 while $\mathrm{C_P}$ remained almost unchanged and the $\mathrm{C_T}$-reduction persisted, albeit weaker, for TSR=$\{3, 6\}$. Likewise, [1, p. 739, Fig. 6] ($I_{\mathbf{u}'_{\mathrm{rms}}}$=$\{3, 15\}$[%]) and [15, p. 25, Table 6] ($I_{\mathbf{u}'_{\mathrm{rms}}}$=$\{6.8\text{-}25.2\}$[%]) identified coefficient reductions up to $\sim$10[%] in the same experimental facility. By contrast to these observations, [16, p. 128, Fig. 8] (the standard k-ϵ-RANS using an actuator disk model), [17, p. 4] (geometry-resolved k-ω-RANS; TSR=6; $I_{\mathbf{u}'_{\mathrm{rms}}}$=$\{1, 10\}$[%]), and [18, p. 7] (the blade element momentum theory using two synthetic inflow generators; TSR=2.5; $I_{\mathbf{u}'_{\mathrm{rms}}}$=$\{3, 5\}$[%]) stated that increments of $I_{\mathbf{u}'_{\mathrm{rms}}}$ resulted in increments of $\mathrm{C_T}$ less than $\sim$2[%]. Together, these studies indicate that no consensus exists regarding the effects of $I_{\mathbf{u}'_{\mathrm{rms}}}$ on $\mathrm{C_T}$-$\mathrm{C_P}$ in the literature since the experiments consistently showed an inverse relation and the computations yielded mixed patterns.

The second aspect is in respect of $\mathrm{C_T}$-$\mathrm{C_P}$ fluctuations. Unlike the first aspect, the aforementioned studies herein almost always corroborated each other in an assertion that $I_{\mathbf{u}'_{\mathrm{rms}}}$ and $\mathrm{C_T}$-$\mathrm{C_P}$ fluctuations are increasing functions of each other [14, p. 5][12, p. 107][1, p. 739][15, Table 6][18, p. 7]. For example, [1, p. 739] measured that the standard deviations of $\mathrm{C_T}$-$\mathrm{C_P}$ (i.e. $\sigma_{\mathrm{C_T}}$, $\sigma_{\mathrm{C_P}}$) were increased by $\sim$2.5 times with $I_{\mathbf{u}'_{\mathrm{rms}}}$=3[%] $\rightarrow$ 15[%]. Nevertheless, it was also reported that the dispersion level of $\mathrm{C_T}$-$\mathrm{C_P}$ fluctuations relative to the mean nearly always remained at least an order of magnitude lower than the mean values, e.g. in [12, Table 4] the difference was $\mathrm{C_T}\sim10^2\sigma_{\mathrm{C_T}}$ for the highest $I_{\mathbf{u}'_{\mathrm{rms}}}$.

The third aspect is relevant to the bending moments. Similar to the first aspect, the observations are somewhat in contradiction, thus making generalisations difficult. As an example, the presence of a direct proportionality between $I_{\mathbf{u}'_{\mathrm{rms}}}$ and bending moments was put forth by [19, Fig. 17] in view of the blade element momentum theory computations for $I_{\mathbf{u}'_{\mathrm{rms}}}$=$\{0\text{-}12\}$[%]. This monotonic relation was also confirmed by [20, p. 3] using the blade element theory with turbulence spectral models for $I_{\mathbf{u}'_{\mathrm{rms}}}$=$\{7.5, 15\}$[%]. However, [15, Table 6]'s experiments maintained an inverse proportionality for the moments whilst retaining the direct relation for their fluctuations. On the other hand, [21,

Table 2] reported almost no change for the mean moments, and a direct proportionality for their peaks and fluctuation ranges from immersed boundary method WALE-model LES computations for $I_{\mathbf{u}'_{\mathrm{rms}}}$=$\{0, 10, 20\}$[%].

The last aspect is as for wake characteristics. Several lines of evidence suggest that downstream signatures of a turbine within a flow field dissolve into freestream values in a shorter distance (i.e. wake recovery in terms of velocities and turbulence intensities) in parallel to augmentations of upstream $I_{\mathbf{u}'_{\mathrm{rms}}}$ [22, p. 218][1, p. 739][12, p. 108; Fig.15][14, p. 6][13, p. 115][23, p. 15]. Nonetheless, a note of caution was raised by [22, p. 225] that increments in $I_{\mathbf{u}'_{\mathrm{rms}}}$ may not always expedite wake recovery, particularly in case of low mean speeds.

Apart from the aforementioned conflicting remarks, the existing accounts are arguably unsatisfactory in three points. First, the investigations of turbulence intensity effects were not conducted through a complete isolation of the turbulence intensity from other turbulence characteristics. Yet realistic inflows were considered at the outset before testing fundamental inflows. For example, a mean-velocity wall-normal gradient was present in [15, p. 14]'s experiments, or [20, Table 1] tuned mean speed magnitude alongside the turbulence intensity in their quantifications; howbeit, such dual-alteration inherently makes turbulence intensity changes ambiguous since the turbulence intensity is by definition a function of mean speed. Therefore, studies wherein the only control variable is the turbulence intensity is debatebly needed, so that remarks directly linked to the turbulence intensity can be deduced without potential interactions with other turbulence notions. Second, the research to date predominantly focused on a range of turbulence intensities up to ∼10-15[%] by defining their maxima as normal or high levels. However, as can be seen from Table 1, field turbulence intensities were revealed to be highly varying within and throughout sites, and reaching up to ∼40[%] during operable use of HAMTs. For this reason, a broader range of turbulence intensities may need to be examined. Third, there remains a paucity of studies of turbulence intensity effects on aspects other than time-averaged wake profiles, and performance coefficients. Thereupon, quantitative analyses may need to be expanded towards various new subjects such as the components of turbulent kinetic energy budget, power spectral density functions, or higher moments of performance coefficients.

The main aim of this paper is therefore set to investigate interactions between the three-dimensional turbulence intensity in the most fundamental form of turbulence, and a typical model-scale rotor within a typical experimental-facility-sized channel in order to fill knowledge gaps or to

corroborate previously reported remarks within the realistic, yet complex, inflow-turbine interaction studies.

To this end, hydrodynamics of a rigid experimental HAMT (so-called the *Southampton turbine* [24]) without its tower under decaying homogeneous isotropic turbulence is explored through controlled studies involving wider range of statistics, and using wall-modelled & actuator-line-modelled implicitly-filtered large eddy simulations and twelve different analytical wake models, where the turbulence intensity ($I_{\mathbf{u}'_{\mathrm{rms}}}$=$\{0, 10, 20, 40\}$[%]) is retained to be the sole control variable.

The paper first introduces the flow and rotor models used, and their specific numerical settings (§2). Subsequently, the obtained results are illustrated and discussed (§3), and finally concluding remarks are presented to the attention of beneficiaries (§4).

2. Methodology

2.1. Flow modelling

2.1.1. Physical phenomena

The scope of physical phenomena was limited to Newtonian single-phase incompressible fluid flows, excluding any thermal, chemical, electromagnetic, scalar interactions, and any sea elements which may interrupt turbine operation (e.g. mould). Typical marine currents were presumed not to violate these assumptions. The set of governing equations of this scope is the pointwise conservation equations of volume and momentum shown in the following for an inertial frame of reference and a conservative external force field per unit mass [25]:

$$\nabla \cdot \overline{\mathbf{u}} = 0 \qquad \text{in} \quad \Omega \times (0, \mathrm{T}) \tag{1a}$$

$$\overline{\mathbf{u}}_t + \nabla \cdot (\overline{\mathbf{u}}\overline{\mathbf{u}}) = -\nabla\overline{\tilde{p}} + \nu\Delta\overline{\mathbf{u}} \qquad \text{in} \quad \Omega \times (0, \mathrm{T}) \tag{1b}$$

where $\overline{\{\cdot\}}$ is a linear operator (a spatial filter in the current scope), $\mathbf{u}(\mathbf{x}, t)_{\{\mathbf{u}\in\mathbb{Q};\, \mathbf{u}=(u_1,u_2,u_3);\, t>0\}}$ a velocity vector field [ms^{-1}], $\mathbf{u}_t \equiv \partial\mathbf{u}/\partial t$ [ms^{-2}], $\mathbf{uu}(\mathbf{x}, t)$ a dyadic field [$\mathrm{m}^2\mathrm{s}^{-2}$], $\tilde{p}(\mathbf{x}, t)$ a scalar kinematic pressure field[7] [$\mathrm{m}^2\mathrm{s}^{-2}$], ν the fluid kinematic viscosity [$\mathrm{m}^2\mathrm{s}$], Ω a finite-size fixed-in-space volume [m^3], and T an arbitrary instant of time [s]. The numerical modelling of Eq. 1 was performed

[7] The external conservative field term $\mathbf{f}$ is incorporated into the pressure gradient term: $-\nabla p+\mathbf{f}=-\nabla p-\nabla f=-\nabla p_f$, where f is a potential function, and p_f is conditioned with the uniform fluid density, ρ, as $\tilde{p}=p_f/\rho$.

with OpenFOAM®v1712 software [26] which discretizes the integral form of Eq. 1 via the *finite volume method*.

2.1.2. Turbulence modelling

Eq. 1 was computed via the implicitly-filtered large eddy simulation [27, p. 381] (hereafter, IFLES).[8] In IFLES, over-filter and sub-filter turbulence scales are split by means of spatiotemporal resolution and equation discretization schemes. Sub-filter scale *effects* on over-filter scales are then modelled.

The closure of Eq. 1 is obtained in five steps: Firstly, the unknown dyadic field $\overline{\mathbf{u}\mathbf{u}}$ is transformed into a more manageable form through the Reynolds and the Leonard decompositions [29, p. 44] in turn. Secondly, the transformed dyadic field is reduced into $(\overline{\mathbf{u}\mathbf{u}}\text{-}\overline{\mathbf{u}}\,\overline{\mathbf{u}})\approx\overline{\mathbf{u}'\mathbf{u}'}$ by omitting the transformed terms other than $\overline{\mathbf{u}'\mathbf{u}'}$. Thirdly, the unknown $\overline{\mathbf{u}'\mathbf{u}'}$ field is approximated as a function of known over-filter scales via the Boussinesq eddy-viscosity hypothesis: $\overline{\mathbf{u}'\mathbf{u}'}\approx\underline{\underline{\mathbf{B}}}\equiv(2/3)\,k_{\text{sfs}}\,\underline{\underline{\mathbf{I}}}\text{-}\nu_t\underline{\underline{\mathbf{S}}}_d$, where $\underline{\underline{\mathbf{B}}}$ is a symmetric tensor field [m^2s^{-2}], k_{sfs} a modelled sub-filter scale kinetic energy field per unit mass [m^2s^{-2}], $\underline{\underline{\mathbf{I}}}$ an identity tensor field [-], $\nu_{t\{\nu_t\geq 0\}}$ a scalar field of the modelled turbulent-viscosity of the flow [m^2s^{-1}], $\underline{\underline{\mathbf{S}}}_d=\{\underline{\underline{\mathbf{S}}}_t\text{-}3^{-1}\,\text{Tr}(\underline{\underline{\mathbf{S}}}_t)\underline{\underline{\mathbf{I}}}\}$ the deviatoric part of doubled strain rate tensor field [s^{-1}], i.e. $\underline{\underline{\mathbf{S}}}_t=2\underline{\underline{\mathbf{S}}}=2\{0.5(\nabla\mathbf{u}+(\nabla\mathbf{u})^\intercal)\}$ [s^{-1}], and $\text{Tr}(\cdot)\equiv\sum_{i=1}^{n}(\cdot)_{ii}$ the trace of a tensor. Lastly, k_{sfs} and inherently $\nu_t=f(k_{\text{sfs}})$ are modelled.

In this study, sub-grid scale effects were modelled into k_{sfs} with [30]'s localised dynamic k_{sfs} transport-equation model whose derivation can be found in [31], and code implementation is summarised below.[9] This model circumvents the local equilibrium assumption of algebraic eddy-viscosity models between sub-filter scale energy production and dissipation. As an implication, minimum grid requirements wherein this assumption holds can be relaxed, so that high Reynolds number flow computations could be performed on relatively coarser grids [31, p. 985]. Moreover, its dynamic procedure is based on the scale similarity hypothesis, which inherently resolves the prominent issues of Germano-type dynamic procedures [33] such as numerical instabilities and theoretical inconsistencies [31, p. 985-987].

The sub-filter scale model involves computing two coefficient fields from local flow, i.e. $C_{k\{C_k\in\mathbb{Q};\,C_k\geq 0\}}$

[8] For the definition of IFLES, the reader is referred to [28, p. 6-10].

[9] The initial sub-filter scale model that has been used was the Smagorinsky model with the Lagrangian-averaging dynamic procedure [32]. However, this model was found unstable for the wall-modelled computations. Therefore, it was replaced by [30]'s model.

and $C_{\epsilon\{C_\epsilon\in\mathbb{Q};\, C_\epsilon\geq 0\}}$, solving the k_{sfs} transport equation, and ultimately evaluating ν_t=$C_k\,\Delta\,k_{\mathrm{sfs}}^{0.5}$:

$$C_k = \frac{\overline{0.5(\underline{\underline{\mathfrak{L}}} \overset{s}{:} \underline{\underline{\mathfrak{M}}})}}{\overline{|\underline{\underline{\mathfrak{M}}}|^2}^{s} + \xi} \qquad C_\epsilon = \frac{\overline{\nu_{\mathrm{eff}}\,(|\overline{\underline{\underline{\mathfrak{D}}}}|^2}^{s} - |\overline{\underline{\underline{\mathfrak{D}}}}|^2)}}{(2\Delta)^{-1}\,\mathfrak{K}^{1.5}} \tag{2}$$

$$\frac{\mathrm{D}k_{\mathrm{sfs}}}{\mathrm{D}t} = \nabla^2(\nu_{\mathrm{eff}}\,k_{\mathrm{sfs}}) + G_{\mathrm{sfs}} - \epsilon_{\mathrm{sfs}} + S_k \tag{3}$$

where any negative values within C_k and C_ϵ are converted to zero; $\overline{\bullet}^{s} = (\sum_f \bullet_f\, A_f)\,(\sum_f A_f)^{-1}$ is the second (explicit) filter operator with its radius slightly smaller than 2Δ, $\bullet_f$ a field interpolated from cell centres to cell faces, A_f face area [m^2], $\Delta_{\{|\Delta|=\mathrm{N}\}} = m\sqrt[3]{V}$ characteristic grid-size field contributing to the effective (first) filter, N the number of nodes, m=1 a heuristic constant [-], $V_{\{V\geq 0\}}$ time-invariant computational cell volume field [m^3]; $\underline{\underline{\mathfrak{L}}}$, $\underline{\underline{\mathfrak{M}}}$ and $\underline{\underline{\mathfrak{D}}}$ symmetric tensor fields with $\underline{\underline{\mathfrak{L}}}$=$\mathrm{dev}[\overline{\mathbf{u}^2}^{s} - \overline{\mathbf{u}}^2]$ [ms^{-1}], $\underline{\underline{\mathfrak{M}}}$=$-2\Delta(\max[\mathfrak{K}, 0]\,\overline{\underline{\underline{\mathfrak{D}}}})^{0.5}}^{s}$ [$\mathrm{m}^5\mathrm{s}^{-2}$], and $\underline{\underline{\mathfrak{D}}}$=$\mathrm{dev}[\underline{\underline{\mathbf{S}}}]$ [s^{-1}], $\mathrm{dev}[\bullet]$ the deviatoric operator of a tensor, $\max[\bullet, \square]$ element-wise greater value finder operator, **:** the double inner product of two second-order tensors, ξ the smallest finite value of floating-point number, $\mathfrak{K}$=$0.5(\overline{|\mathbf{u}|^2} - |\overline{\mathbf{u}}|^2)$ a scalar field with $\mathfrak{K}$=$\max[\mathfrak{K}, \zeta]$ [$\mathrm{m}^4\mathrm{s}^{-2}$], ζ the machine epsilon, $\nu_{\mathrm{eff}} = \nu_{\mathrm{t}} + \nu_{\mathrm{lam}}$ the scalar field of effective kinematic viscosity [$\mathrm{m}^2\mathrm{s}^{-1}$], ν_{lam} the constant kinematic viscosity of the fluid; ϵ_{sfs}, G_{sfs}, and S_k=0 the dissipation, production, and source terms of k_{sfs} as ϵ_{sfs}=$C_\epsilon\,k_{\mathrm{sfs}}^{1.5}\,\Delta^{-1}$ [$\mathrm{m}^2\mathrm{s}^{-3}$], and G_{sfs}=$2\,\nu_t(\underline{\underline{\nabla\mathbf{u}}} : \underline{\underline{\mathfrak{D}}}) - (2/3)\,k_{\mathrm{sfs}}\,(\nabla\cdot\overline{\mathbf{u}})$ [$\mathrm{m}^2\mathrm{s}^{-3}$]. The term $\nabla\cdot\overline{\mathbf{u}}$ in the last expression is not removed despite the incompressibility assumption, because it remains non-zero in interim calculations.

2.1.3. Inflow modelling

IFLES requires spatiotemporal-variant inflow information that can evolve with designated particulars within its numerical domain. Such information was provided here by the hybrid digital-filter/forward-stepwise synthetic turbulence generator of [34] (hereafter, Xie-Castro method). Xie-Castro method was chosen as it satisfies four conditions deemed important in this study. First, capability-wise, Xie-Castro method is able to generate pseudo-stochastic and spatiotemporal-variant time-series containing statistics of two-spatial-point autocorrelations and one-spatial-point correlation tensor. More importantly, it allows the construction of statistics in an isolated and building-block fashion, e.g. a group of statistics can be turned off for a particular spatial direction. Confidence-wise, it has been successfully used for various types of flows, such as street-scale flows [35] and aerofoil flows [36], including flow types considered herein, i.e. canonical flows [28, 37].

Last but not least, Xie-Castro method provides a cheap-to-run and easy-to-code approach with high-fidelity in comparison to the other methods of the same class [28, 38].

Xie-Castro method creates spatiotemporal-variant Reynolds-decomposed fluctuation velocity fields in three consecutive steps: Firstly, a set of pseudo-random numbers, $\{\mathrm{r}\}_{\{|\mathrm{r}|=\mathrm{R};\ \mathrm{k,j}\in\mathbb{N}:\,1\leq\mathrm{k+j}\leq\mathrm{R}\}}$[10], obeying the probability distribution function of zero-mean ($\mathrm{R}^{-1}\sum_{\mathrm{k}=1}^{\mathrm{R}}\mathrm{r_k}=0$), unit-variance ($\mathrm{R}^{-1}\sum_{\mathrm{k}=1}^{\mathrm{R}}\mathrm{r_k^2}=1$), and independent ($\mathrm{R}^{-1}\sum_{\mathrm{k}=1}^{\mathrm{R}}\mathrm{r_k r_j}=0$ for $\mathrm{k}\neq\mathrm{j}$) Gaussian white-noise is generated. Secondly, two-spatial-point autocorrelation functions are incorporated into $\{\mathrm{r}\}$ through *i.* convolution summations for lateral directions (i.e. digital-filter method) and *ii.* autoregressive operations for streamwise direction (i.e. forward-stepwise method), which are given below for a single velocity component and dimension, respectively:

$$s_{\mathrm{k}}=\sum_{\mathrm{j}=-\mathrm{N}}^{\mathrm{N}}\mathrm{b_j r_{k+j}}\quad\text{with}\quad \mathrm{b}_i\approx\mathfrak{b}_i\left[\sum_{\mathrm{j}=-\mathrm{N}}^{\mathrm{N}}\mathfrak{b}_{\mathrm{j}}^2\right]^{-0.5}\quad\&\quad\mathfrak{b}_i=\exp\left(\frac{-c_1\,\pi\,|m_i|}{n}\right)\tag{4a}$$

$${}_2s^{\Psi}\left(y,z,t{+}\Delta_t\right)={}_2s^{\Psi}\left(y,z,t\right)\exp\left(\frac{-c_2\,\pi}{2}\,\frac{\Delta_t}{\mathrm{T}}\right)+{}_2s^{\psi}(y,z,t{+}\Delta_t)\left\{1-\exp\left(\frac{-c_2\,\pi\,\Delta_t}{\mathrm{T}}\right)\right\}^{0.5}\tag{4b}$$

where $\{s\}_{\{|s|=\mathrm{M}\,:\,s\in\mathbb{Q}\}}$ is a digital-filtered number set, $\{\mathrm{b}\}_{\{|\mathrm{b}|=2\mathrm{N}+1\,:\,\mathrm{b}\in\mathbb{Q}\}}$ a filter coefficient set, $\{\mathfrak{b}\}_{\{|\mathfrak{b}|=2\mathrm{N}+1\,:\,\mathfrak{b}\in\mathbb{Q}\}}$ an intermediate coefficient set, $\{\mathrm{N}\}_{\{\mathrm{N}\in\mathbb{N}^+\}}$ the filter support, $\mathrm{k}_{\{\mathrm{k}\in\mathbb{N}^0\}}$ the lag number, c_1 a constant with a suggested value of 1, n input integral length scale [grid-unit], $\{m\}_{\{m\in\mathbb{Q}\}}$ a number set containing rectilinear distances between arbitrary nodes and zero-lag [grid-unit], $\{{}_2s^{\Psi}\}$ a two-dimensional set belonging to an instant t and including transverse length-scales $\{\mathrm{L}_\alpha\}_{\{\alpha\in\{y,z\}\}}$, $\{{}_2s^{\psi}\}$ an auxiliary two-dimensional set created in the same way of $\{{}_2s^{\Psi}\}$, yet with a new pseudo-random number set, c_2 another constant with a value of 0.5 calibrated to the inflows of this study [38, p. 446], Δ_t the constant time-step size of the computation, and T streamwise Lagrangian time-scale calculated via Taylor's frozen turbulence hypothesis [39]. Lastly, one-spatial-point correlation tensor is embedded

[10] The set notation used is as follows: $\mathrm{r_k}\equiv\{\mathrm{r}\}[\mathrm{k}]$ where $\{\mathrm{r}\}$ is a set, and k is an index to the k^{th} member of the same set.

into $\{s\}$ by [40, p. 255]'s transformation:

$$\mathbf{u}'(\mathbf{x},t) = \underbrace{\begin{bmatrix} (R_{11})^{0.5} & 0 & 0 \\ R_{21}/A_{11} & (R_{22}\text{-}A_{21}^2)^{0.5} & 0 \\ R_{31}/A_{11} & (R_{32}\text{-}A_{21}A_{31})/A_{22} & (R_{33}\text{-}A_{31}^2\text{-}A_{32}^2)^{0.5} \end{bmatrix}}_{\underline{\underline{\mathbf{A}}}(\mathbf{x})} {}_2\mathbf{s}(\mathbf{x},t) \tag{5}$$

where $\underline{\underline{\mathbf{A}}}$ a second-order spatial-variant amplitude tensor[11], and $\{R_{ij}\}_{\{i,j\in[1,3]\}}$ (known) one-spatial-point correlation tensor members in units of variance (i.e. Reynolds stress tensor).

2.1.4. Analytical wake modelling

In order to identify implications of high-fidelity computations for engineering design applications, almost all (twelve) non-yawed horizontal-axis-turbine analytical wake models that wind/marine-energy industry software incorporated were evaluated: i.e. [41–52]. In view of their lengthiness, the models and their formulae were summarised in Appendix A.2.

2.2. Rotor modelling

Two approaches were used to model the rotor: the geometry-fitted wall-modelled approach (hereafter, AMI) and the actuator line model (hereafter, ALM). The two were chosen among the other concepts[12] since they were deemed to represent approximately the opposite polars of the model fidelity spectrum with which time-accurate rotor computations are possible. In the following, the modelling workflow were elaborated, and the utilised coordinate systems and aerofoil terminology were presented in Figs. 1 and 2.

2.2.1. Turbine benchmark

The benchmark turbine was from the hydrodynamic experiments of [24]. Two reasons contributed to the selection of this benchmark: its design paid regard to the model scaling constraints advised by the literature [54, p. 86], which presumably ensures sufficiently high Reynolds number flow over blades [54, p. 86] and minimum blockage correction [24, p. 409], and its rotor diameter to water depth ratio reportedly reflects full-scale operating prototypes [54, p. 86]. Therein, an upwind, towing-tank scale, clockwise-rotating, 0.8 [m] rotor-diameter tidal turbine with three

[11] $\underline{\underline{\mathbf{A}}}$ may also be temporal-variant; however, it is invariant in time for this study.
[12] The reader is referred to [53] for the other concepts and models.

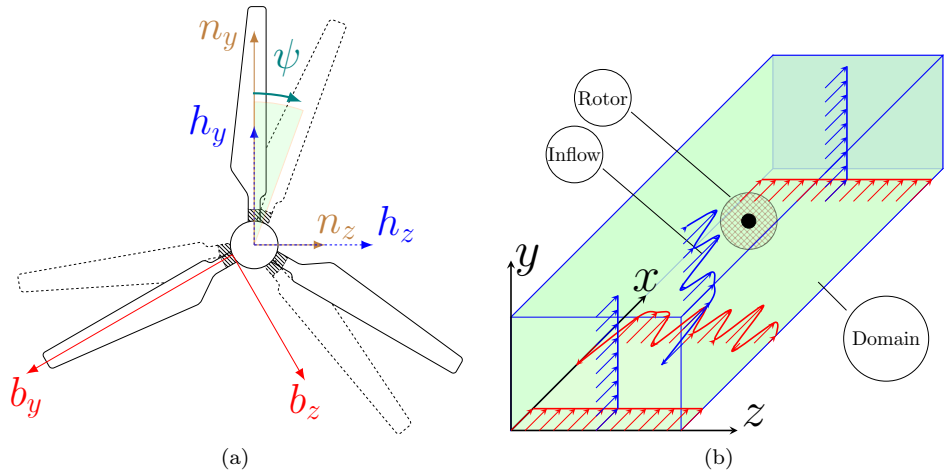

(a) (b)

Figure 1: (a) Three coordinate systems seen from upwind in an inertial frame of reference: $\mathscr{I}_{i\{i\in(n,h,b)\}}=(\mathscr{O}_i, \mathbf{e}_{xi}, \mathbf{e}_{yi}, \mathbf{e}_{zi})$ where the positive first direction of each axis is into the paper, and $\mathscr{O}$ their origin. n, h and b stand for the computational domain, hub and blades, respectively. $\mathscr{O}_n$ is fixed at the intersection of the inlet boundary and hub centreline at x=0[m], $\mathscr{O}_h$ at that of the twist axis and hub centreline at x=2.4[m], and $\mathscr{O}_b$ at that of the rotating blade-root plane and the twist axis that was assumed passing through 30% of any chord length (from the leading edge). ψ is the blade azimuth angle which is zero when the twist axis is upwards at a right-angle to the ground plane. ψ increases clockwise, which is also the rotor positive rotation direction. (b) A sketch of the computational domain. The black dot depicts the hub, and the cross-hatched disc the rotor plane. The axes indicate positive directions without their true origin.

"T6082-T6 aluminium alloy" [55] blades constructed by seventeen NACA 63-8xx aerofoils[13] was used [24, p. 409-410]. The experiment scenario [24, p. 418] corresponding to the spatiotemporally-uniform inflow of 1.5[ms^{-1}], 20° pitch angle, tip speed ratio of 6, and 0.55D deep tip immersion was selected because the operational particulars resemble to those of full-scale prototypes [54, p. 86] and a complementary numerical study [12] investigated the same scenario.

Previously, to the authors' knowledge, eight rotating-blade LES studies utilised this experimental turbine (e.g. no actuator disc), which were: uniform-inflow actuator line method without hub and tower [56], uniform-inflow immersed boundary method without tower (including a two-way loosely coupled fluid-structure interaction implementation) [57, 58], turbulent-inflow wall-modelled approach without tower [59–61], and turbulent inflow wall-resolved approach [12, 62].

Data-reference pairs of the benchmark scenario can be found as follows: *i*. operational conditions in Table 2, *ii*. spanwise distributions of chord length, structural twist angle, and aerofoil profiles [24, p. 410], *iii*. polar data (computed via) [63–65], *iv*. aerofoil coordinates (computed via) [63, 65], and *v*. dimensions of the experimental set-up and rig [66, p. 2,9] in Table 3.

[13] "xx" indicates the percentage ratio between the thickness and chord length of the blade sections.

Table 2: Primary operational conditions of the turbine benchmark [1][24, p. 418], [2][12, p. 97](computed).

Parameter	Value
Tip speed ratio[1]	6.0 [-]
Time-averaged uniform inflow speed[1]	1.5 [ms^{-1}]
Time-averaged rotational speed[2]	214.86 [rpm] $\approx$ 22.5 [$rad\,s^{-1}$]
Kinematic viscosity of water[2]	0.000001 [m^2s^{-1}]

2.2.2. Geometry-fitted wall-modelled approach

Herein, the rotor[14] modelling was carried out in five subsequent steps: the modellings of solid geometry, surface grid, surrounding volume mesh, rotation and wall grid. However, the turbine tower was excluded from consideration in order to isolate rotor effects on wake development from those of tower's non-streamlined structure. Another reason of this exclusion was that the channel asymmetry in the y-direction was intended to be isolated from the tower effects. For instance, [12, Fig. 103] found out an asymmetry in the downstream mean speed profiles of the same turbine, and attributed its reason to the tower-flow interactions. Yet another effective independent variable is the y-direction channel asymmetry which may interfere with the conclusion.[15]

For the solid modelling, initially, the planar coordinates of the seventeen NACA 6-series aerofoils [24, Table 1] were computed via the NACA456 software [65] that uses an algorithm from [63]. The coordinates were then refined by the QBlade software [67]; were scaled with the local chord lengths, and extended into the third dimension. As the sole simplification to ease the solid modelling, the sharp trailing edges of the aerofoil profiles were truncated by a maximum of 1.5% local chord lengths with presuming no effect on wake flow. In addition, there were two gaps within the experimental setup explanations [66]: i. No geometrical information was provided for the circular transition between the hub-blade junction at r/R=0.125 and the transition end at r/R=0.2; and ii. the coordinates of the blade twist axis were not defined. Therefore, the geometry of the circular transition was heuristically generated, and the blade twist axis was assumed to be passing 30% chord length away from the presumed leading edge point horizontally. The pitch angle direction is clockwise when you look from top of the tip surface to the root. The rest of the experimental setup particulars elaborated in [66] was conformed. Finally, the solid models were created in SolidWorks® 2017 software [68] according to [24, Table 1] through the profiles which were appropriately placed

[14] The term *rotor* refers to the blades and hub whereas the term *turbine* to the entire rig including the tower.
[15] In the following steps of this study, it was found out that Fig. 6 corroborated [12, Fig. 103]'s reasoning since the omission of the tower removed the flow asymmetry in the z-direction thereat.

in the spanwise direction, and were rotated about the blade twist axes.

The surface grids were generated in stereolithography format (i.e. STL) via the SALOME 8.4.0 software [69] based on the STEP-File format solid models while neither SolidWorks nor QBlade was found adequate for this purpose. Quadrangle and triangle mesh elements were respectively put to use on the blade planforms, and the remaining components (i.e. cylinder transition, hub) whilst the former element type was observed to facilitate iterations within the volume mesh generation by the preferred mesh generator. Furthermore, the grid was manually partitioned into sub-regions in order to enable mesh refinement level variation across the same blade. Considering error-free surface grids, especially in terms of watertightness and face-normal consistency, are central to the volume mesh generation, the STL quality quantification and if necessary repairs were made with the OpenFOAM® and MeshLab® software [70]. Subsequently, the *blockMesh* mesh generator [26] was used to discretize the computational domain into cubic elements.[16] On top of this, the *snappyHexMesh* mesh generator [26], which recursively splits a hexahedron into its octants based on prescribed refinement levels, was utilised to perform local surface-volume mesh refinements and morphing onto the surface grid in compliance with specified mesh metrics (e.g. maximum face skewness).

To model rotation, the computational domain was divided into two regions by dismantling a cylinder prism that surrounds the rotor longitudinally. The inner prism does constant-speed rigid-body rotation about the hub centreline and relative to the stationary outer region. Information across adjacent and non-conformal regions is conveyed via the *arbitrary mesh interface* method [71] of OpenFOAM® (AMI[17]). The AMI is a discrete-field interpolation algorithm wherein Galerkin projection is computed through a set of triangulated *supermesh*es corresponding to each local intersection of the regions [71, p. 90-95]. Elementally, the projection of a field from a donor region, q_D, onto a target region, q_T, begins with an intent to minimise L^2-norm of $\|q_D\text{-}q_T\|$ [71, Eq. 1]. Defining q in terms of its basis functions $\{\phi\}_{\{|\phi|=N\}}$, i.e. $q=\sum_{i\in N} q^i\phi^i$, results in a matrix equation whose solution yields desired q_T, i.e. $M_T\, q_T=M_{TD}\, q_D$ [71, Eq. 8], where the matrices are $M_T=f(\phi_T)$ and $M_{TD}=f(\phi_T\, \phi_D)$ [71, Eq. 9-10]. Herein, the computationally challenging part is the construction of M_{TD} due to its dependence on both regions. This is overcome by constructing a common grid

[16] It was observed that using cubic elements improves the subsequent mesh refinements and morphing phases in comparison to using other hexahedra types.

[17] In this study, the same abbreviation was put to use for the geometry-fitted wall-modelled approach computations that utilise the arbitrary mesh interface method.

for each intersection, and doing computations therein. In addition, the AMI is well-defined in discontinuous fields [71, p. 89], computationally scalable [71, p. 91, 99] in comparison with other options such as [72], and conditionally [71, p. 90] conservative since its local integration errors, i.e. $\int q_T \, dV = \int q_D \, dV$, are order of double-precision machine epsilon [71, p. 93]. Nonetheless, the AMI is 'not necessarily bounded' [73, p. 5] and not constrained with the incompressibility [71, p. 99]; thus, spurious fluctuations may occur in projected fields. The literature has, however, not treated effects of the AMI on flow predictions in much quantitative detail, particularly for turbulent structures. As a counter example, on the other hand, [74, p. 2] shared a qualitative observation that the AMI had no influence on flow visualizations from a number of uniform-inflow propeller computations. Similarly, [75, p. 121] and [60, p. 744] qualitatively analysed a turbulent-inflow tidal turbine computation, and concluded that the AMI did not alter the appearance of convecting turbulent structures. In addition to this, [62, p. 267] purported based upon their RANS-turbine computations that no qualitative changes were observed on velocity fields and gradients due to a sliding technique similar to the AMI.

The next key aspect was the wall modelling. Within wall-bounded flow regions, momentum-transfer-dominant scales are known to be order of viscous length scales whose size is inversely proportional to $\mathrm{Re_L}$.[18] As a consequence of [76, p. 3]'s node-number estimation for attached flows, i.e. $\mathrm{N_\Delta} \propto \mathrm{Re_L^{13/7}}$, the resolution of these scales becomes prohibitively expensive for turbine flows, wherein $\mathrm{Re_L} \approx \mathcal{O}(10^6\text{-}10^9)$ [77, p. 438]. Therefore, in this study, viscous and majority of the overlap layers were modelled rather than resolved. This brought three main questions to be addressed: *i*. near-wall grid resolution, *ii*. wall-flow model type, and *iii*. near-wall grid design strategy.

With respect to the near-wall grid resolution, minimum threshold recommendations may be found for canonical flows, and be projected onto the flows considered herein to avoid computation repetitions. Assuming the existence of the *log-layer* at sufficiently high $\mathrm{Re_L}$, the first wall-normal grid node was placed inside the presumed log-law region, whose lower limit reported in the literature was reviewed by [78, p. 377] as $30 < y^+ < 100$. A number of studies have postulated for the grid size within characteristic boundary layer thickness, δ: [79, p. 2] reasoned a grid with $\Delta_x \approx 0.08\delta, \Delta_z \approx 0.05\delta$ and Δ_y linearly varying from 0.02δ to 0.05δ within the outer layer. Further, [80, p. 20] offered $\mathrm{N}_{\Delta_x} \approx 10$; $\mathrm{N}_{\Delta_y} \approx 30\text{-}40$; $\mathrm{N}_{\Delta_z} \approx 20$ per δ, and similarly, [76, p. 2] put forward

[18] $\mathrm{Re_L} = \mathrm{U}_c \, \mathrm{L} \, \nu^{-1}$, where U_c is the characteristic flow speed [ms^{-1}], L the characteristic length scale [m], and ν the kinematic viscosity of the fluid [$\mathrm{m}^2\,\mathrm{s}^{-1}$]. $\mathrm{N_\Delta}$ stands for a given node number in a computational grid.

$N_{\Delta_x}\approx$10; $N_{\Delta_y}\approx$25; $N_{\Delta_z}\approx$10 in accompany with highlights from the literature that $N_{\Delta_x}\approx$5-32; $N_{\Delta_y}\approx$16-32; $N_{\Delta_z}\approx$15-32. Overall, [76, p. 2] asserted that $N_\Delta \propto Re_L$ for wall-modelled IFLES.

Menter et al.'s [81] wall model was adopted here owing to its automatic and gradual polynomial blending between the standard logarithmic law of the wall (y^+>30) and viscous sub-layer equation (y^+<5) as a function of local y^+. This treatment alleviates the sensitivity of the wall model to y^+-variations; hence, eases wall-grid design considerations within the same grid. The wall effect was incorporated through the turbulent kinematic viscosity, ν_t, as follows:

$$\nu_t = \max\left\{0,\ \frac{u_\tau^2}{\mathbf{n}_b \cdot (\nabla \mathbf{u})_b + \xi} - \nu_b\right\} \tag{6}$$

where $\mathbf{n}_b \cdot (\nabla \mathbf{u})_b$ is the velocity gradient normal to the boundary [s^{-1}], ξ the double-precision machine epsilon, ν_b the fluid kinematic viscosity on the boundary, and u_τ the friction velocity [ms^{-1}] [81, Eq. 17-18]:

$$u_\tau = (u_{\tau,\mathrm{vis}}^n + u_{\tau,\log}^n)^{n^{-1}} \qquad \text{with} \quad u_{\tau,\mathrm{vis}} = \frac{U}{y^+} \quad \& \quad u_{\tau,\log} = \frac{\kappa\, U}{\log(\mathrm{E}\, y^+)} \tag{7}$$

where $u_{\tau,\mathrm{vis}}$ and $u_{\tau,\log}$ are respectively the model contributions from the viscous sub-layer and logarithmic law equations, n=4 a model coefficient, U the magnitude of the planar first-wall-node velocity (i.e. its wall-normal component is zero) [ms^{-1}], κ=0.41 von Kármán's constant [82, p. 77], and E=9.8 a wall roughness parameter for smooth walls [82, p. 77]. The algorithm of the model implementation is shown in Appendix A.1.

2.2.3. Actuator line model

The actuator line model (ALM) is a reduced-order flow modelling approach for slender[19] bodies in which the governing equations of fluid dynamics and a force prediction method are two-way coupled (its first derivations: the vorticity-velocity form [83, p. 156-157], and pressure-velocity form [84, p. 46]). In the ALM, a body is simplified into a characteristic line (not necessarily straight) or a group of lines. The imaginary lines are then discretized into a set of *actuator points* in space wherein each point represents a line segment. The ALM became a well-received model in the wind-marine turbine discipline primarily due to three reasons: in comparison to a geometry-fitted approach, the ALM *i*. loosens spatial and temporal grid resolution constraints to a substantial extent, *ii*. renders

[19] *Slender* describes a body with its length is at least an order of magnitude longer than its remaining two dimensions.

quicker grid generation possible with minimised grid-quality issues and user expertise, and despite
295 the former two, *iii*. spatiotemporal-accurate flow entities (e.g. root-tip vortices, wake, induction regions [85, p. 8]) and rotor performance predictions were realised to an experimentally-validated level. The ALM consists of two main parts: flow and force modelling which are summarised below.

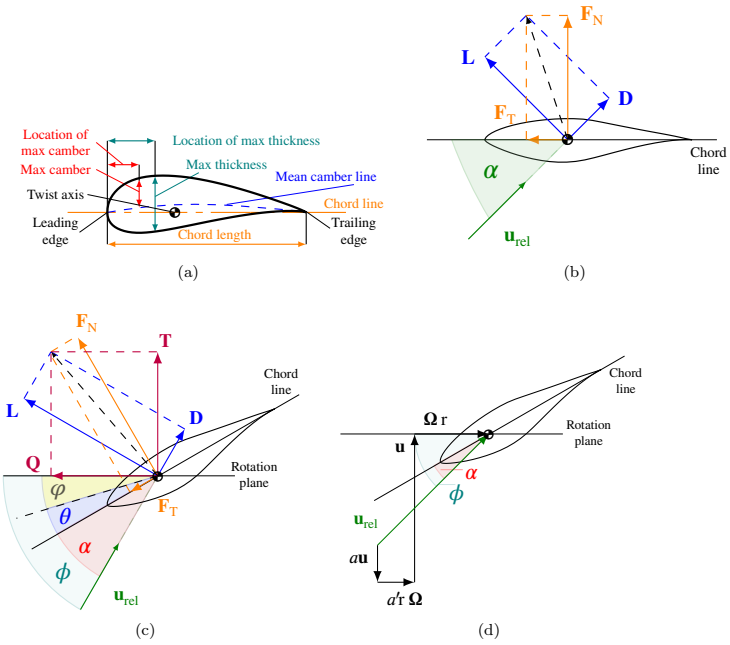

Figure 2: (a) Terminology for an aerofoil. All characteristic aerofoil centres, including those of structural twist, blade pitch, aerodynamics and mass, were assumed collinear, and dubbed as 'twist axis' along a blade. (b) A stationary blade-element cross-section illustrating forces acting upon the centre of pressure. **L** is the lift force, **D** drag force, $\mathbf{F}_\mathrm{N}$ normal-to-chord force, $\mathbf{F}_\mathrm{T}$ tangential-to-chord force, α angle of attack [rad], and u_rel relative velocity. (c) The rotating counter-part of (a). **T** is the normal-to-rotation-plane force, **Q** parallel-to-rotation-plane force, ϕ=ψ+θ+α flow angle, ψ global operational blade pitch angle, and θ local structural twist angle. (d) A velocity triangle for a rotating aerofoil showing flow induction effects. a and a' are axial and tangential induction factors [-], respectively, r spanwise location of the aerofoil, and $\mathbf{\Omega}$ rotational speed of the rotor [rad s^{-1}].

2.2.3.1. Actuator line model's flow modelling

For the fluid-part ALM equations, the prevailing pressure-velocity form was used in this study [84, p. 46] whereby Eq. 1 was re-expressed as follows:

$$\mathbf{u}_t + \nabla \cdot (\mathbf{uu}) = -\nabla p + \nu \Delta \mathbf{u} + \mathbf{f} \tag{8}$$

where $\nabla\tilde{p}$ was split back to the pressure gradient, ∇p, and the external force field term per unit mass, $\mathbf{f}$ [ms^{-2}], which is computed through a force prediction method.

In the context of the finite volume method, the spatial discretization of $\mathbf{f}$ for a single finite volume Ω with its centroid P can be performed through $\int_\Omega \mathbf{f}\mathrm{d}\Omega \approx \mathbf{f}_\mathrm{P}\Omega$ where $\mathbf{f}(\mathbf{x},t)\approx\mathbf{f}_\mathrm{P}(t)$. Further, within the preferred theoretical-level pressure-velocity coupling algorithm, i.e. PISO [86], the discretized term can be placed into the assembled explicit momentum equation as follows:

$$a_\mathrm{P}\mathbf{u}_\mathrm{P} = -\nabla p + s - \sum_{i=1}^{n} a_i\mathbf{u}_i + \mathrm{sgn}(m)\mathbf{f}_\mathrm{P}\Omega = -\nabla p + \mathbf{H}(\mathbf{u}) \tag{9}$$

where the left-hand side contributes to the diagonal part of the system of algebraic equations, and the right-hand side to the off-diagonal; P denotes the owner cell, n its neighbour cells, a_P and a_n known domain and equation discretization coefficients belong to the cells, s an agglomeration of source terms and boundary conditions, $\mathrm{sgn}(m)$ the sign function of $m_{\{m\in\{-1,1\}\}}$ with m=-1|1 energy extraction|supplement from|into the flow field, $\mathbf{H}(\mathbf{u})$ a function explicitly evaluating the off-diagonal part with the latest available values of $\mathbf{u}$. This common treatment, however, causes practical issues affecting flow field predictions in two subjects: *i*. how to input information from the force model, and *ii*. how to extract information from the flow model to be used in the force model.

For the first subject, the principal issue is that non-negligible spurious pressure-velocity fluctuations arise when sharp variations in $\mathbf{f}$, almost always present in the ALM, exist. Mencinger and Žun [87, p. 524] attributed its reason to the use of the practical-level pressure-velocity coupling method of the Rhie-Chow interpolation [88] in co-located grid arrangements, because the Rhie-Chow corrections applied to face velocity fields is by definition independent of $\mathbf{f}$, and do not ensure strong pressure-velocity coupling. Within the ALM scope, three solution approaches were proposed: *i*. the smearing function approach due to [89, p. 396], *ii*. the body-force modification of the Rhie-Chow interpolation due to [90, 91], and *iii*. the potential-flow routine [92]. In this study, the first was implemented due to its convenience.

The smearing function allows point forces to be fractionally dispersed across neighbouring points. Herein, the most commonly used form of the three-dimensional Gaussian function was used.[20] For

[20] It should be noted that, despite its wider preference, using the three-dimensional form Gaussian function has three drawbacks: *i*. the effective length of lines exceeds the actual line lengths because such distribution also spreads forces beyond the blade edges, *ii*. local forces of a zone are spread out neighbouring zones; thus, non-locality of forces increases, and *iii*. flow gradients are soothed, hence wake structures.

a single point, such form can be expressed as [84, p. 49]: $g(\mathbf{x})=\pi^{1.5}\sigma^{-3}\exp\left(-\{\|\mathbf{x}-\mathbf{x}_a\|\,\sigma^{-1}\}^2\right)$ where σ is the function support [m] that determines the weight of a point force at $\mathbf{x}_a$ on a node positioned at $\mathbf{x}$, and $d=\|\mathbf{x}-\mathbf{x}_a\|$ the straight line distance between the position vectors of an actuator point and a node [m]. In practise, the weightening becomes negligible after some d. The domain size of $g(\mathbf{x})$, therefore, can be truncated. To this end, the *full width at half maximum* was adopted, i.e. $d_{\max}=\sigma(2\ln w)^{0.5}$. Therein, $d_{\max}$ is the maximum d within which force distribution takes place, and w an independent variable with a default value that makes $d_{\max}\approx 4.8\sigma$, and accordingly ensures that the Gaussian function reduces well below its 1%. Ultimately, a distributed force field $\mathbf{f}_g$ is approximated through $\mathbf{f}_g=\mathbf{f}\star g+\epsilon_g$ independently for each actuator point, where $\{\star\}$ is the convolution summation operator, and ϵ_g an error term arising from $\mathbf{f}$'s discretization.

The function support σ is a free parameter; therefore, it needs to be constrained by an independent parameter from the numerical setup. Three support types are present in the literature: *i*. grid-based [84, p. 51], *ii*. chord-based [93, p. 1183], and *iii*. equivalent elliptical planform-based [94]. Among them, the first type was chosen owing to its easier implementation and the other types' not necessarily superior performance. The grid-based support is $\sigma=\epsilon_a\Delta$ where $\{\epsilon_a\}_{\{\epsilon_a\in\mathbb{R}\}}$ a time-invariant constant, and Δ a characteristic grid size within the field of actuator points.

The size of σ is an important factor in predictions of rotor performance and flow structures with the same grid. The main reason is that the predictions for rotor performance/flow structures and imposed body forces are functions of each other. Body forces are calculated depending on local flow field whereas the field itself develops in accordance with the imposed body forces; thus, leading to a complication in parameter-independent computations.[21] ϵ_a in the majority of studies was preferred within the range of $\epsilon_a=[1,4]$. Several studies [100, p. 25][96, p. 15][97, p. 1059] maintained that $(\epsilon_a)_{\min}=2$ is the advisable compromise, and the most common choice. Thus, this figure was employed in this study.

The second subject is the extraction of flow information for the force model, i.e. flow speed and angle of attack. Therein, preferences in three points affect the information: *i*. probe locations, *ii*. interpolation method to obtain flow speeds, and *iii*. estimation approach for angles of attack.

Relatively small transpositions of probes can cause non-negligible changes in force predictions

[21] In regard to rotor performance, power [95, p. 7] and thrust [85, p. 10] predictions were observed to be significantly depending upon ϵ_a, and both are in direct proportion without a sign of convergence [96, p. 21] [97, p. 1059]. For flow structures, some dependency on ϵ_a was also reported: Strength, spatial distribution [93, p. 1184] and phase differences [96, p. 30] of vortices were found to be influenced by ϵ_a whose increase reduces vorticity of flows [98, p. 205-206]. However, [99, p. 1, 9] demonstrated that ϵ_a is virtually ineffectual on mean wake deficit.

because of high flow gradients around actuator points, and exponential proportionality between flow speed and forces. Despite its importance, no probe location is present within the blade element theory (BET). Therefore, a universally-applicable location has been a matter of debate. Ideally, a probe should be located at the centre of the bound vortex, and the only induction at the probe location should stem from shed vortices in the wake. Otherwise, the true relative speed and angle of attack could not be attained. In this study, probes are located at actuator points presuming that they coincide with bound vortex centre whilst counter-symmetric induction about actuator points often exists [85, p. 8-9].

Normalised probe coordinate vectors are computed as follows: $\mathbf{z}{=}\mathbf{z}\,\|\mathbf{z}\|^{-1}$, $\mathbf{y}{=}(\mathbf{z}{\times}\mathbf{h})\,\|(\mathbf{z}{\times}\mathbf{h})\|^{-1}$, and $\mathbf{x}{=}(\mathbf{y}{\times}\mathbf{z})\,\|(\mathbf{y}{\times}\mathbf{z})\|^{-1}$ where $\mathbf{h}$ is the hub centreline vector towards downstream, $\mathbf{y}$ the vector along chord pointing from the leading edge to the trailing edge in opposite direction of the blade rotation, and $\mathbf{x}$ the vector along blade thickness pointing from the suction side to the pressure side towards downwind unless the rotor is pre-coned. Flow speeds are then extracted in three steps: inverse distance weighting interpolation of node velocities on probes ($\mathbf{u}_{\text{interp}}$), domain-to-line coordinate transformation of $\mathbf{u}_{\text{interp}}$ and reduction of velocities to one-dimensional flow speeds as: $u_1{=}\mathbf{x}\cdot\mathbf{u}_{\text{interp}}$, $u_2{=}\mathbf{y}\cdot\mathbf{u}_{\text{interp}}$, $u_3{=}\mathbf{z}\cdot\mathbf{u}_{\text{interp}}$. Finally, angle of attack α is approximated as depicted in Figs. 2c and 2d: $\alpha{=}\phi{-}\varphi{-}\theta$ where $\phi{=}\arctan(u_1\,(u_2{+}\omega r)^{-1})$ is the local flow angle [rad], ω rotational speed of the rotor [rad s^{-1}], $r{=}(y^2{+}z^2)^{0.5}$ spanwise location of the aerofoil, ψ global operational blade pitch angle, and θ local structural twist angle.

2.2.3.2. Actuator line model's force modelling

For the ALM force-part, the blade element theory (abbr. BET) [101, due to Drzewiecki, p. 169] was utilised.[22] It is a closed-form expression that predicts fluid forces on a stationary/rotating blade, and its derivation starts with the following assumptions and approximations: *i*. A blade can be non-uniformly broken down into a set of non-interacting blade elements, assuming the lack of interaction does not affect force estimations, *ii*. spanwise flow can be ignored; thus, resulting in a two-dimensional flow over a blade element, *iii*. any aerofoil cross-section possesses the same geometric, structural and fluid-dynamic properties within a blade element, *iv*. forces on a rotating blade element are the same with those on a stationary identical element for the same angle of

[22] Another method is the blade element momentum theory (abbr. BEMT), which is used to break mutual dependence between flow solutions and force computations (e.g. [102, p. 5]). The BEMT, however, brings arguably adverse issues, particularly for time-invariant inflow, such as the detachment of inflow information from the computational domain.

attack [103, p. 59], and *v.* an instantaneous equilibrium is present between flow field and forces although finite times of adjustment are actually needed for both.

For a stationary blade element shown in Fig. 2b, the magnitude of the resultant force on the element can be expressed in terms of its normal- and tangential-to-the-chord-line components:

$$\|\mathbf{F}_{\mathrm{N}}\| = \|\mathbf{L}\|\cos(\alpha) + \|\mathbf{D}\|\sin(\alpha) \qquad \|\mathbf{F}_{\mathrm{T}}\| = \|\mathbf{L}\|\sin(\alpha) - \|\mathbf{D}\|\cos(\alpha) \tag{10}$$

where $\mathbf{F}_{\mathrm{N}}$=$\mathbf{F}_{\mathrm{N}}(\mathbf{u}_{\mathrm{rel}}, \alpha, \mathrm{Ma}, \mathrm{Re})$ is the normal-to-chord force [N], $\mathbf{F}_{\mathrm{T}}$ the tangential-to-chord force, α the angle of attack [rad], $\mathbf{u}_{\mathrm{rel}}$ the relative velocity, $\mathbf{L}$ the lift force, $\mathbf{D}$ the drag force, and $\|\bullet\| = (\bullet_1^2 + \ldots + \bullet_n^2)^{0.5}$ the Euclidean norm.

For a blade element rotating about a fixed axis, $\mathbf{u}_{\mathrm{rel}}$ and flow angles are reconceptualized due to rotation as illustrated in Figs. 2c and 2d: $\|\mathbf{u}_{\mathrm{rel}}\| = \left(\{\|\mathbf{u}\|\,(1\text{-}a)\}^2 + \{\|\boldsymbol{\omega}\|\,r(1\text{+}a')\}^2\right)^{0.5}$ where $\mathbf{u}$ is the undisturbed flow velocity normal to the plane of rotation, $\boldsymbol{\omega}$ the rotational velocity of the blade element parallel to the plane of rotation, r the normal distance between the rotation axis and a representative point within the blade element, a the axial induction factor [-], and a' the tangential induction factor.

Eq. 10 remains the same; however, the resultant force may be further decomposed with respect to the plane of rotation:

$$\begin{aligned} \|\mathbf{T}\| &= \|\mathbf{F}_{\mathrm{N}}\|\cos(\theta) - \|\mathbf{F}_{\mathrm{T}}\|\sin(\theta) = \|\mathbf{L}\|\cos(\phi) + \|\mathbf{D}\|\sin(\phi) \\ \|\mathbf{Q}\| &= \|\mathbf{F}_{\mathrm{N}}\|\sin(\theta) + \|\mathbf{F}_{\mathrm{T}}\|\cos(\theta) = \|\mathbf{L}\|\sin(\phi) - \|\mathbf{D}\|\cos(\phi) \end{aligned} \tag{11}$$

where $\mathbf{T}$ is the force normal to the plane of rotation, $\mathbf{Q}$ the force parallel to the plane of rotation, ϕ=φ+θ+α the flow angle with φ the global operational pitch angle, and θ the local structural twist angle. Eq. 10 and 11 can be computed if a polar diagram, i.e. tuples of force coefficient-α[23], of the blade element is available through $\|\mathbf{L}\| = qA_bC_{\mathbf{L}}$ and $\|\mathbf{D}\| = qA_bC_{\mathbf{D}}$, where q=$0.5\rho\,\|\mathbf{u}_{\mathrm{rel}}\|^2$ the dynamic pressure [Nm^{-2}], A_b the planar area of the blade element [m^2], $C_{\mathbf{L}}$ the lift coefficient [-], and $C_{\mathbf{D}}$ the drag coefficient.

Assuming the BET assumptions hold, three factors further contribute to the error-uncertainty, F, of force predictions: $\|\mathbf{F}\| = \|\mathbf{F}_{\mathrm{BET}}\| + F_{\alpha} + F_{\mathbf{u}_{\mathrm{rel}}} + F_{\mathrm{polar}}$, wherein F_{α} and $F_{\mathbf{u}_{\mathrm{rel}}}$ emerge from the flow part (2.2.3.1), and $F_{\mathrm{polar}} = F_{\mathrm{quality}} + F_{\mathrm{compatibility}}$. There, F_{quality} arises from measurement

[23] Spatial integrations of aerofoil surface pressure and shear stress distributions as a function of α.

processes, and $F_{\text{compatibility}}$ from the level of match in conditions of between the flow and measurements/computations. With regard to F_{quality}, the most susceptible elements to F are: drag itself due to its similar order of magnitude to the level of confidence of data deduction/reduction methods, and post/deep stall regions because of its high sensitivity to time-variant flow environment.

Typically, the construction of a polar diagram involves: obtaining pre-stall polar dataset under envisaged operating conditions, and manipulating this dataset to regard the above susceptibles. To that end, the XFOIL software [104] with the built-in Kármán-Tsien compressibility correction[24] was utilised to acquire pre-stall polar datasets. Stall delay corrections on lift coefficients were then performed with [106]'s model for $r/\text{R}\leq 0.8$ and [107]'s model for $r/\text{R}>0.8$, and on drag coefficients with [108]'s model.[25] Moreover, the datasets were extrapolated onto (-180°)-(180°) spectrum by [109]'s polar extrapolation method. For the requirement of a tip-root correction for the BET-ALM, however, debates are ongoing. In principle, such correction should not be needed, because its raison d'être is expected to disappear with the finite-number blade representation of the ALM. Its use was, nevertheless, reported to lead to generally improved force predictions [99, p. 9][84, p. 53]. The reason why this happens is arguably that the ALM is in general deficient to model flow around the tip, and to resolve tip vortices. It is thought, therefore, that the justification of the use of tip corrections is only shifted from scientific to practical grounds for the ALM, because its effect is still desirable whereas the conditions of its derivation are violated. In the light of several tests among the available tip loss corrections in the literature (not reported), [110]'s and [101]'s methods were chosen to be used in tip and root regions, respectively.

The spatial resolution of the ALM involves: the number of actuator points per grid-size and nodes per an actuator-line length. Although both seem reciprocal, locally distinct requirements are present (e.g. for unevenly distributed points) to ensure smooth force distribution along a line, smooth force projection onto a computational grid, and fine resolution of vortices. As a minimum, [111, p. 6, 13] and [96, p. 46] recommended 0.75 actuator points per cell, and [97, p. 1050] 40 points per blade. For the second aspect, [112, p. 62] advised minimum 40 nodes per diameter, and likewise, [94, p.2] 30 to 60 nodes per line. In respect of temporal resolution, [100, p. 26] and [96] purported that rotor performance predictions are not influenced by Δ_t. These observations must be interpreted with

[24] Nguyen [105, p. 27] identified that the Kármán-Tsien method provides more accurate predictions than the more common Prandtl-Glauert compressibility correction.

[25] No appreciable change was observed because of the stall delay corrections for the current setup; thus, the non-corrected datasets were in use for the majority of computations.

Table 3: Dimensions of the towing tank set-up [1][24, p. 409, 410], [2][66, Fig. 2a] [3][66, p. 22, Fig. 15]. The values are given in meters [m], and if necessary, with rotor diameters [D].

Parameter	Value [m] - [D]
Tank section height[1]	1.8 - 2.25
Tank section width[1]	3.7 - 4.625
Tank length[1]	60.0 - 75.0
Rotor plane distance to the inlet[2]	2.4 - 3.0
Tower centreline distance to the inlet[2]	2.857
Hub particulars (length, radius, relative positions)[2]	-
Hub centreline height from the floor	0.96 - 1.2
Centred hub centreline distance to a side wall	1.85 - 2.3125
Hub distance to the inlet	2.269
Blade root diameter[3]	0.0241
AMI inlet to the inlet	2.26
AMI outlet to the inlet	2.505
AMI radius	0.45

caution because the relevant computations were performed with uniform inflow. For this reason, even a dramatic change in Δ_t will not alter force predictions whilst the inflow will always be the same.

2.3. The remaining numerical settings

In the pages that follow, the remaining numerical settings were presented to allow easy replication.

2.3.1. Computational domain models

The dimensions of the experimental facility and numerical domains were summarised in Table 3. In the domain models, the facility dimensions were imitated except its length, i.e. 75D. Instead, 13D from [12, p. 97] was used to reduce computational costs. This imitation violated four literature recommendations for a domain design as shown in Table 4. It is, however, argued that any detrimental effect due to the discrepancies is limited to the mapping between the experiments and modelled reality rather than the experiments and computations while the latter only approximates the experimental conditions. Therefore, no practical importance of the discrepancies was assumed for this study. In addition, the tower was left out owing to its influence on downstream flow field predictions, particularly for the mean velocity and turbulence intensity [113, p. 282].

Table 4: A comparison between the dimensions of the domain models and literature recommendations: [1][100, p. 25] [2][114, p. 5][117, p. 1751] [3][117, p. 1752][82, p. 283] [4][114, p. 5] [5][118, p. 231] [6][118, p. 231]. R is the characteristic size of a body, herein the rotor radius. The areal blockage ratio is equal to $\pi R^2/(h_y\, h_z)$, the lateral blockage ratio $h_z/(2R)$, and the vertical blockage ratio $h_y/(2R)$, where h_y and h_z are the height of width of the computational domain.

Parameter	Recommendation	Experiment & Computation
Min lateral distance to walls	[1]4.5 - [2]5R	1.1R
Min distance to the outlet	[3]10 - [4]15R	20R (Computation only)
Max areal blockage ratio	[5]3%	7.5%
Max lateral blockage ratio	[6]17%	21.6%
Max vertical blockage ratio	[6]17%	44.4%

2.3.2. Computational domain discretizations

The numerical domains were constructed in two main layers. First, a background grid was generated. Therein, the domain was divided into 27 sub-domains. The innermost block surrounded the rotor region with its size $\{h_x, h_y, h_z\}$=$\{10, 2.6, 2.6\}[R]$, and comprised of only cubic cells. In compliance with the suggestions reported in page 21, the grid size of the cubes was approximately $D/52$, where D=$2R$ is the rotor diameter. From this centre block, the remaining sub-domains' cells were stretched away with the maximum cell-to-cell expansion ratio of 1.005 in the x, and of 1.05 in the $\{y, z\}$ directions, whereby some of the literature suggestions were fulfilled such as 1.3 [114, p. 7], 1.25 [115, p. 379] [116, p. 10]. Second, the internal boundaries were embedded into the background grid without explicit local grid refinements as explained in §2.2.2.

The geometry and topology of the grids were checked and qualified through all mesh metrics available in OpenFOAM®v1712.[26] Prominently, for the grids without the turbine, maximum cell aspect ratio, maximum face skewness, mean and maximum face non-orthogonality were measured to be around 15.11, 3.96, 1.73, and 44.99, respectively. For the grids with the turbine, the magnitude of the four metrics became 15.11, 4.00, 4.97, and 45.00. While high aspect ratio populated the vicinity of the outlet boundary due to longitudinal grid stretching, high non-orthogonality and skewness regions mostly occupied AMI-nacelle intersections and blade trailing edges. Besides, the initial minimum, mean, and maximum of the AMI source-target face *weight-sums* were approximately 0.993-0.499, 1.237-1.235, 1.000-0.999, wherein the sum of the weights for each face is ideally unity, otherwise conservation errors raise [120]. Nevertheless, the *weight-sums* are time-variant due to rotor rotation, and null values might be encountered during computations. Accordingly, to avoid

[26] Refer to [119] for the definitions of the OpenFOAM® mesh metrics as they may differ from one software to another.

any AMI failure, the model switch that turns on the zero-gradient boundary condition for faces where the *weight-sums* below 0.01 was activated [120]. Ultimately, the spatial resolution in the geometry-fitted wall-modelled approach cases resulted in 7,004,897 cells whereof 1,171,311 cells were inside the arbitrary-mesh interface region, and 5,833,586 cells outside of it. On the other hand, in the actuator-line modelled cases, it yielded 5,767,740 cells. Representative illustrations of the numerical domains and rotor were given in Fig. 3.

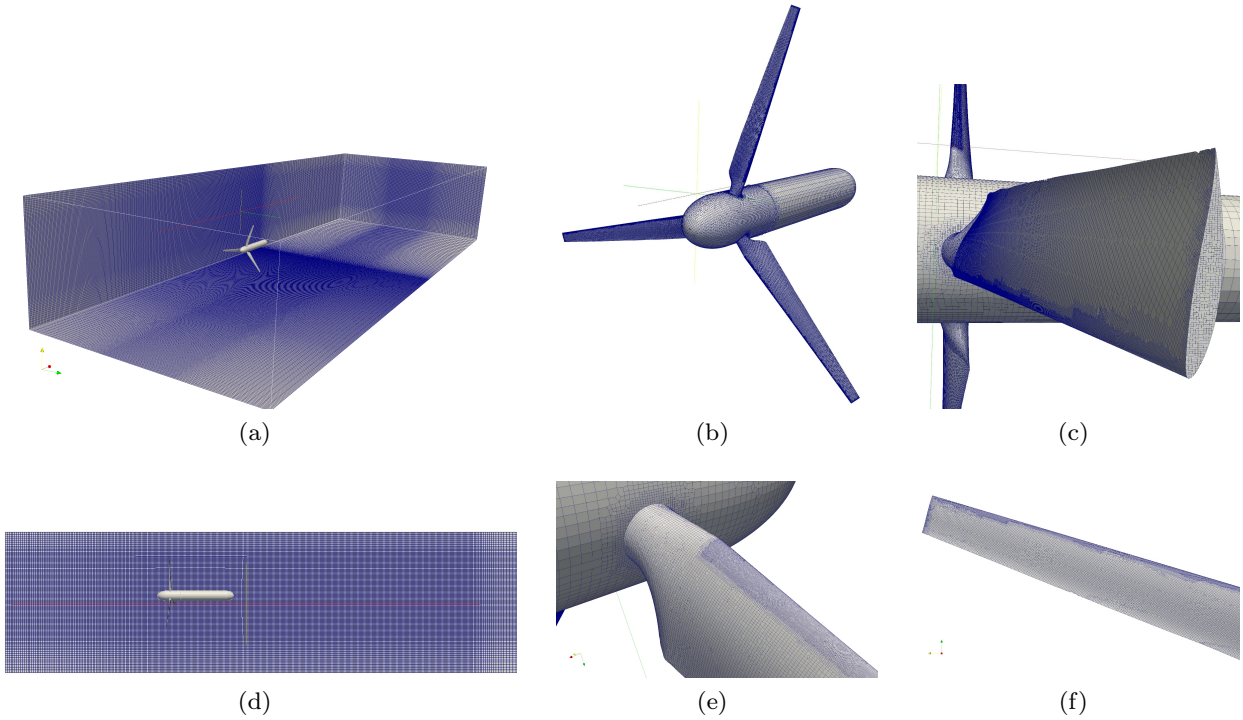

Figure 3: Various snapshots: (a) Isometric view of the numerical domain and its grid layout, (b) surface grid of the rotor, (c) blade tip detail, (d) side view of the partial numerical domain illustrating only the cubic-cell region, (e) blade root detail, and (f) blade planform detail.

In line with the spatial resolution, the temporal resolution was preset to 5×10^{-5}[s]. The durations of the initialisation and averaging phases were separately set to $\sim$7.02[s], which approximately corresponded to 25 full rotor rotations.

2.3.3. Equation discretizations, boundary conditions, solution algorithms & solvers

The central differencing scheme (CDS, Appendix A.5.1) was activated for all terms except the following: the second-order backward difference scheme (Appendix A.5.2) for the temporal derivatives and variables, a cell-based multidimensional-limited CDS (i.e. *cellMDLimited* 0.25) [121, p. 87-88] for the velocity gradient, a total variation diminishing scheme (i.e. *limitedLinear* 0.1 Appendix A.5.3) for the divergence and convection terms of turbulent kinetic energy, and a normalized variable diagram scheme (i.e. *GammaV* 0.2 Appendix A.5.4) for the velocity convection. In addition, the integration of surface integrals were held by the Gauss quadrature method, and the linear interpolation was used to obtain flow quantities required at cell faces from adjoining cell centroids while assuming spatial uniformity of the quantity across the common face. Also, the surface normal gradients and Laplacian terms were explicitly corrected for the mesh non-orthogonality. Nonetheless, to ensure the initial diagonal dominance within the system of algebraic equations, all the computations were initiated by using the most diffusive numerical scheme alternatives for a duration of one-half rotor rotation, and subsequently the above schemes were switched on. In these computations, the boundary conditions summarised in Table 5 were adopted.

Table 5: The boundary conditions employed for velocity $\mathbf{u}$, kinematic pressure $\tilde{p}$, turbulent kinematic viscosity ν_t, and turbulent kinetic energy k, at each geometric boundary.

Boundaries	**Boundary conditions**			
	$\mathbf{u}$	p	ν_t	k
Inlet	Dirichlet	Zero Neumann	Calculated	Dirichlet
Outlet	Convective	Zero Dirichlet	Calculated	Convective
Sides	Symmetry	Symmetry	Calculated	Symmetry
Blades and nacelle	No-slip	Zero Neumann	Menter's wall function	Zero Dirichlet

[a] A *boundary* is a topological element of a computational domain whereas a *boundary condition* is a set of mathematical operations computed at the boundary.

On top of these settings, the theoretical-level pressure-velocity coupling algorithm PISO [86] was selected with four momentum correctors. Finally, the numerical solution of the linear system of algebraic equations was carried out by means of the following linear solvers: *Stable biconjugate gradient method* preconditioned with the *diagonal-based incomplete LU preconditioner* for the turbulent kinetic energy (tolerance=10^{-6}, relative tolerance=0), an iterative solver using the *Gauss-Seidel smoother* for the velocity (tolerance=10^{-8}, relative tolerance=0), and *geometric agglomerated algebraic multigrid solver* with the same smoother for the pressure (tolerance=10^{-6}, relative

tolerance=0-10^{-3}). For parallel computations, the numerical domain and fields were decomposed by the *scotch* partitioning method [122].

3. Results & Discussion

In this study, twelve computations were conducted in total, and were elaborated in the following sections. In addition to Table 2, the spatiotemporally-invariant input set that these computations commonly used consisted of: The mean longitudinal flow speed U_o=1.5[ms^{-1}], longitudinal-transverse integral length scales L_{long}=L_{trans}=0.2[m]=0.5[R], and one-point normal-anisotropic correlations $\{\sqrt{\overline{(u'_{ii})^2}}\}_{\{i\in(1,2,3)\}}$=$\{(0.00)_{0\%}, (0.15)_{10\%}, (0.30)_{20\%}, (0.60)_{40\%}\}$[ms^{-1}]-$\{\sqrt{\overline{(u'_{ij})^2}}\}_{\{i\neq j\}}$=0.0 for four different three-dimensional turbulence intensity values studied here, $I_{\mathbf{u}'_{\text{rms}}} \equiv 100(1/3(\overline{u'u'}+\overline{v'v'}+\overline{w'w'}))^{0.5}/(U^2+V^2+W^2)^{0.5}=\{0, 10, 20, 40\}$[%].

3.1. Confidence assessments of the numerical solutions

In this section, the quality of all computations was assessed in six aspects: (*i*) spatiotemporal resolution, (*ii*) numerical stability, (*iii*) statistical convergence of numerical fields and probe samples, (*iv*) evolvement of input statistics, (*v*) integrated and local parameters of turbine performance, and (*vi*) near wake flow modelling.

(*i*) First, the spatiotemporal resolutions were evaluated through two statistical LES-quality post-verification metrics while grid-independency in IFLES was argued to be theoretically unattainable [28, p. 7]: Pope's metric [123, p. 560], and Celik et al.'s metric [124, Eq. 8a][27] both of which were quantified to be robust and effective relative to their alternatives [28, p. 29-33]. The first three statistical moments of the metric fields obtained for each numerical case were set out in Table 6. Data from Table 6 shows that the sample means of all numerical cases were around 10[cNp] higher than the recommended metric qualifiers (i.e. a metric magnitude of 0.8 and above claims adequate resolution). Also, the level of variations within the metric fields was quantified to be an order to two orders of magnitude smaller than the mean levels.[28] Moreover, the sample skewness of all cases was found to be negative and around $\mathcal{O}(1)$. The negativity here implies that below-mean quality locations were present more frequently than above-mean quality regions within the computations.

[27] The explicit expressions of the metrics can be found in [28, p. 16-17].

[28] *Variance* was wrapped by scalings of the unbiased standard deviation and mean (resulting in *the coefficient of variation*) to ease commentations on the extent of variability with respect to the mean.

Table 6: The quality of the computations according to two statistical LES-quality metrics: Pope's metric [123, p. 560], and Celik et al.'s metric [124, Eq. 8a] both of which deem the metric value of 0.8 and above as an indication of adequate spatiotemporal resolution in LES. Below, the sample mean, coefficient of variation, and skewness of the metric fields, i.e. $\hat{\mu}_1$, $\sqrt{\hat{\mu}_2}/\hat{\mu}_1$, and $\hat{\gamma}_1$, that were time-averaged for one longitudinal-mean-speed domain-pass-through (twenty-five full rotor rotations) were shown. From left to right, the three numerical case groups involved domains without the turbine, with the geometry-fitted wall-modelled turbine and with the actuator-line modelled turbine. Therein, 'A' was completely empty, 'B' & 'C' consisted of non-rotating and rotating arbitrary mesh interfaces, respectively, and the percentages indicated the turbulence intensity. The results were rounded to three decimal places.

LES-quality metrics ↓	Cases →	Domains Without Turbine			Geometry-Modelled Turbine			Actuator-Line Modelled Turbine		
		A	B	C	10%	20%	40%	10%	20%	40%
Γ_{Pope}	$\hat{\mu}_1$	0.930	0.934	0.930	0.970	0.941	0.892	0.971	0.930	0.873
	$\sqrt{\hat{\mu}_2}/\hat{\mu}_1$	0.061	0.059	0.064	0.040	0.058	0.073	0.033	0.059	0.075
	$\hat{\gamma}_1$	-0.851	-0.910	-0.976	-4.190	-1.263	-0.112	-1.885	-0.809	0.136
Γ_{Celik}	$\hat{\mu}_1$	0.952	0.952	0.952	0.952	0.952	0.951	0.952	0.952	0.951
	$\sqrt{\hat{\mu}_2}/\hat{\mu}_1$	0.000	0.000	0.001	0.000	0.001	0.001	0.000	0.001	0.000
	$\hat{\gamma}_1$	-2.331	-4.608	-13.455	-6.391	-13.604	-5.324	-3.275	-8.775	-13.924

These results indicate according to the two metrics that the level of spatiotemporal resolution of all the numerical cases qualified as adequate. Although the skewness of the fields hinted the existence of low-quality regions, the variance showed that the resolution was almost completely homogeneous, which further implies the low-quality regions were considerably localised. Regarding the wall-flow modelling, y^+ measurements of all cases and blades revealed that the turbulence intensity does not notably alter the median and mean of y^+ fields, which were respectively quantified as around 30-37 and 49-55 alongside the minimum and maximum outliers of 1 and 340. Therefore, the obtained y^+ fields mostly fulfilled the requirements of Menter's wall function being used here.

(*ii*) The time-marching of the computations was monitored via the time-averaged and maximum Courant numbers, Co_{mean} and Co_{max}. In the computations, the rotor tip Courant number of 0.03 was aimed at the outset, so that the rotating arbitrary mesh interface cells or actuator points could be restricted to translate a neighbouring cell at most. For the domains without the turbine, AMI, and ALM cases with the same time-step size, Co_{mean} was found commonly around 0.003-0.004, and $\text{Co}_{\text{max}}\approx(0.15\text{-}0.16, 6.8\text{-}7.2, 0.018\text{-}0.019)$, respectively. These figures convey three points: First, except the AMI-Co_{max}, the conventional Courant-number thresholds were sufficiently obeyed. Second, although the building-block assumption of PISO was locally violated by the AMI-Co_{max}, the computations remained numerically robust likely due to the use of the blended numerical schemes and relatively-small & highly-localised grid deficiencies. Third, unanticipatedly, the mere presence of the arbitrary mesh interfaces increased Co_{max} at least an order of magnitude, which may demand

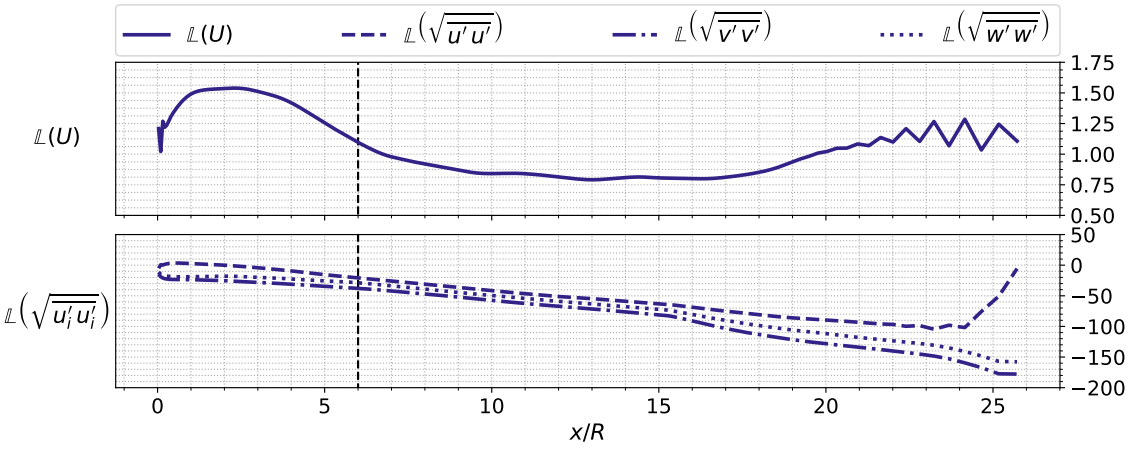

Figure 4: The longitudinal evolvement of the spatiotemporally-invariant streamwise mean speed (the top subplot) and normal components of the Reynolds stress tensor (the bottom subplot) through an empty domain. The domain belongs to the inflow scenario of $I_{\mathbf{u}'_{\text{rms}}}$=20[%]; however, the rotor, hub and AMI were removed. The vertical axes show the log percentage change of a given variable with respect to its input value, i.e. $\mathbb{L}\equiv 100\ln(x_{\text{new}}/x_{\text{bench}})$[centineper]. The inputs were U=1.5[ms^{-1}], and $\sqrt{\overline{u_i'u_i'}}\equiv\{\sqrt{\overline{u'u'}}, \sqrt{\overline{v'v'}}, \sqrt{\overline{w'w'}}\}$=0.3[ms^{-1}]. The results were obtained by the cumulative moving average along time at each node followed by spatial averages in the statistically homogeneous lateral and vertical directions. The horizontal axes represent the domain length, x, normalised by the rotor radius, R=0.4[m]. The dashed vertical line stands for the rotor-plane location.

for a development either in the Courant number computation through an interface or in the AMI method itself.

(*iii*) Regarding the convergence of statistics, the synthetic time-series generator being used here, the hybrid DFM-FSM [34], was previously quantified to yield statistically weak stationary and ergodic time-series [38, p. 457]; thus, flow fields were assumed to be stationary and ergodic in this study. As a potential drawback herein, the number of domain pass-throughs of the computations was considerably lower than a typical IFLES of free-shear flows. The sole reason of this shortening was the prohibitive additional computational cost appeared due to four factors: the constraint of the blade-tip Courant number which is more restrictive than the flow Courant numbers, the rigid body rotation, arbitrary mesh interface interpolations, and more importantly, increased number of pressure iterations per time-step (e.g. in comparison to a finer-grid computation of decaying homogeneous isotropic turbulence from [38], the number of pressure iterations was more than doubled). Nevertheless, the statistics investigated herein were mostly limited to the first- and second-order normal moments which are expected to converge relatively quickly unlike the cross-components of the Reynolds stress tensor. In addition to this, the number of domain pass-throughs

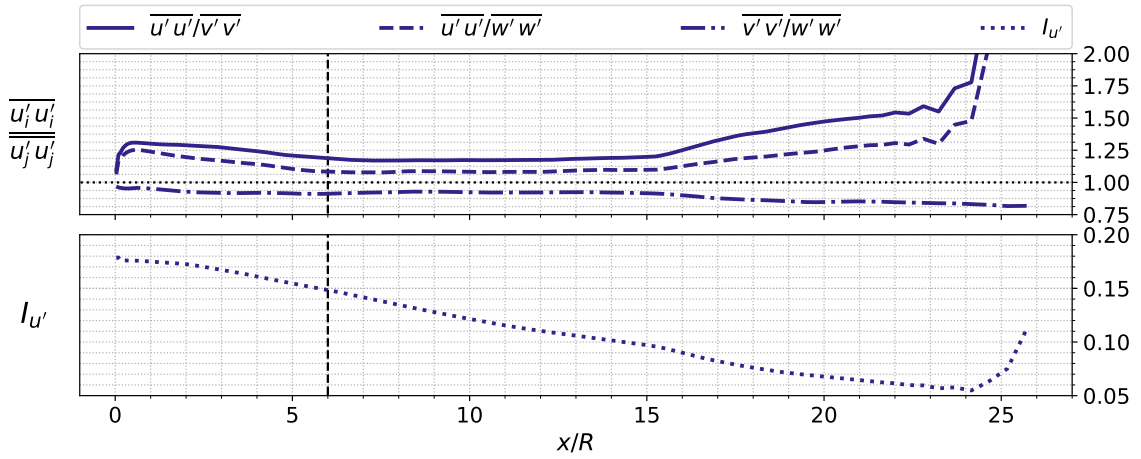

Figure 5: The longitudinal evolvement of the Reynolds stress tensor isotropy (the top subplot) and turbulence intensity (the bottom subplot) through the empty domain. The figure particulars are the same with Fig. 4 except the following. The vertical axes illustrate the non-dimensional variables, and the horizontal dotted line in the top subplot signify the complete isotropy. The turbulence intensity was defined and inputted as: $I_{\mathbf{u}'}\equiv(1/3(\overline{u'u'}+\overline{v'v'}+\overline{w'w'}))^{0.5}/(U^2+V^2+W^2)^{0.5}$=0.20.

and full-rotations of the current computations was kept higher than the same-turbine computations from the literature, i.e. 10-12 [12, p. 100], 4-12 [60, p. 743, 746] full-rotations for initialisations and averagings/samplings, respectively, in contrast to 25-25 full-rotations of this study. In light of these two points, the first two sample moments of probed velocity time-series were monitored, and they were found to be qualitatively converged (not shown). Therefore, the approximate convergence of the flow fields was postulated in this study.

(*iv*) The evaluation of the target flow characteristics at the field of interest was carried out by means of the AMI computation with $I_{\mathbf{u}'_{\mathrm{rms}}}$=20[%] (AMI-20), wherein the arbitrary mesh interface, rotor, and hub were removed, and the other settings were kept the same. For support of the premises below, Figs. 4 and 5 presented the longitudinal evolvement of the streamwise mean flow speed, normal components of the Reynolds stress tensor, turbulence isotropy, and turbulence intensity, respectively, within the empty domain. As can be seen from Fig. 5, the mean speed was realised ∼1.1[cNp] higher than the input at the rotor location, and within a range of 1.5-0.75[cNp] throughout the domain. Moreover, the normal Reynolds stresses were observed in linear decay downstream. The reduction occurred at the rotor plane was roughly 20, 30, and 40[cNp] for $\sqrt{\overline{u'u'}}, \sqrt{\overline{v'v'}}, \sqrt{\overline{w'w'}}$, respectively, and the rate of decay qualitatively remained constant between $x/R\approx3$ and $x/R\approx16$ engulfing the rotor plane. The deviations from the perfect isotropy shown

Table 7: Time-averaged thrust coefficient ($\overline{\mathrm{C_T}}$) and power coefficient ($\overline{\mathrm{C_P}}$) predictions from the spatiotemporal-invariant inflow cases. 'Exp.' refers to the benchmark experiment [24, Fig. 8], 'Afgan et al.' another IFLES study using the same turbine (including the tower as well) [12, Table 4], 'AMI' the arbitrary-mesh-interface method, and 'ALM' the actuator-line method. 'Corrected' indicates the tunnel blockage correction from [24, p. 424-425][66, p. 28-29] which was used to correct the experimental results [24, p. 416] and 'Afgan et al.' results [12, p. 98]. The coefficients were defined as: $\overline{\mathrm{C_T}}$=$\overline{F_x}$/($0.5U_o^2A$), and $\overline{\mathrm{C_P}}$=($\overline{M_x}\Omega$)/($0.5U_o^3A$) where F_x the longitudinal force component exerted on blades and hub per unit density [$\mathrm{m^4s^{-2}}$], U_o=1.5[$\mathrm{ms^{-1}}$] the inflow speed, A≈0.503[$\mathrm{m^2}$] the projected rotor area, M_x the torque component about the hub centreline exerted on blades per unit density [$\mathrm{m^5s^{-2}}$], and Ω≈22.5[$\mathrm{rads^{-1}}$]. The numerical results were presented as the log percentage change with respect to the 'Exp.' ($\mathbb{L}\equiv 100\ln(x_{\mathrm{new}}/x_{\mathrm{bench}})$[centineper]) and the coefficient magnitudes were given in the parentheses.

	Exp.[a]	Afgan et al.[b]	AMI	AMI-Corrected	ALM	ALM-Corrected
$\overline{\mathrm{C_T}}$	0.801	-2.53 (0.781)	-2.66 (0.780)	-5.52 (0.758)	3.32 (0.828)	-5.52 (0.758)
$\overline{\mathrm{C_P}}$	0.443	-2.05 (0.434)	4.20 (0.462)	-0.23 (0.442)	21.45 (0.549)	8.02 (0.480)

[a] *WebPlotDigitizer* [125] was used to digitise the experimental data from [24, Fig. 8].
[b] Afgan et al. [12, Table 4] inadvertently reported the experiment coefficients for the pitch-angle-25° [66, p. 33] cases instead of the pitch-angle-20°.

in Fig. 5 were roughly within -6.5 to 17[cNp] at the rotor plane, and remained nearly similar from the inlet up to x/R≈15-16. Lastly, the aforementioned linear decay pattern also transpired for the turbulence intensity which reduced to ∼15[%] from 20[%] till the rotor. The level of these metamorphoses of synthetic inflow[29] up to x/R=16 was arguably acceptable for engineering purposes. Also, the almost constant rate of changes in these statistics with respect to the longitudinal distance till x/R=16 suggests that turbulence is statistically developed in the scope of these metrics, and the effective statistics experienced by the rotor could be somewhat corrected. Accordingly, the input verifications were assumed with the presumption of these level and pattern of changes applicable for all scenarios of this study.

(v) Furthermore, the time-averaged thrust coefficients and power coefficients of all cases were quantified, and compared with the experiment. As an example, the results from the spatiotemporally-invariant inflow computations were presented in Table 7 since the experiment was limited to uniform inflow. The comparison showed that both coefficients from the AMI and ALM cases deviated from the experiment and [12]'s IFLES within ±5.5[cNp] and ±8.0[cNp] ranges, respectively, with the experiment's tunnel blockage correction. Therefore, the verification of the computations in terms of the integrated performance parameters was assumed, and speculatively was extrapolated to other inflow cases. As regards local performance parameters, the chordwise distributions of the time-averaged pressure coefficients were compared with those of the structured-grid wall-resolved IFLES

[29] The metamorphoses are due to natural processes and CFD-synthetic inflow interactions. The readers are referred to [28] for their systematic quantifications and analyses.

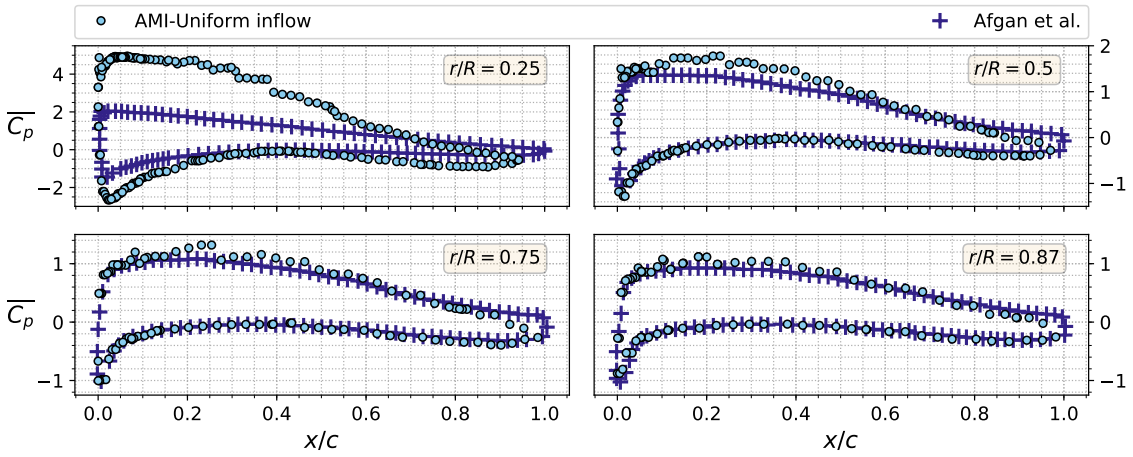

Figure 6: Chordwise distributions of the time-averaged pressure coefficients, $\overline{C_p}$, at four different spanwise stations of a blade, $\{r/R\}$=$\{0.25, 0.5, 0.75, 0.87\}$. 'AMI-Uniform inflow' labels the spatiotemporally-invariant laminar inflow AMI computation, and 'Afgan et al.' another IFLES study of the same rotor (additionally including the tower) with the same inflow settings [12, Fig. 4b, TSR=6]. The vertical axes show $\overline{C_p}$=-$\bar{\tilde{p}}\{0.5(U_o^2$-$\Omega^2 r^2)\}$ where $\bar{\tilde{p}}$ is the time-averaged kinematic gauge pressure field on the blade boundary [m^2s^{-2}], U_o=1.5[ms^{-1}] the mean streamwise inflow speed, $\Omega\approx$22.5[$rads^{-1}$] the rotational speed of the rotor, and r the spanwise distance of the station to the hub centreline [m]. The horizontal axes depict chordwise length of the suction and pressure sides of the aerofoil, x, normalised by the local chord length, c. *WebPlotDigitizer* [125] was used to digitise unavailable 'Afgan et al.' data from the plots.

from [12, Fig. 4b] in Fig. 6 at four spanwise locations. A significant discrepancy was observed at r/R=0.25 section while observing resemblance adequate for engineering purposes at the remaining three sections. The exact reason of the discrepancy could not be revealed. However, three model differences at this particular region were speculated to play a role: the wall boundary conditions, the near-wall grid arrangements, and the heuristic geometry design for the blade transition and twist axis due to the lack of geometrical information highlighted in [§2.2.2, p. 12]. The alleviation of the discrepancy could not be obtained within the current setup; nevertheless, on top of its arguable ineffectiveness for the global performance parameters, its prospective impact was investigated for wake predictions. With this objective, time-averaged longitudinal speed profiles at the immediate aft of the rotor, where the rotor's signature on flow field is expected to be predominant, were computed and illustrated in Fig. 7 through a comparison with [12, Fig. 8]. Therein, the impact of Fig. 6 difference was seen to be limited to y/D=z/D=$\pm$0.1, and the rest of the profiles was observed resembling each other (except the omitted tower's wake). Hence, it was assumed that the discrepancies were ineffective and the computations were verified in terms of $\overline{C_p}$ and near wake predictions.

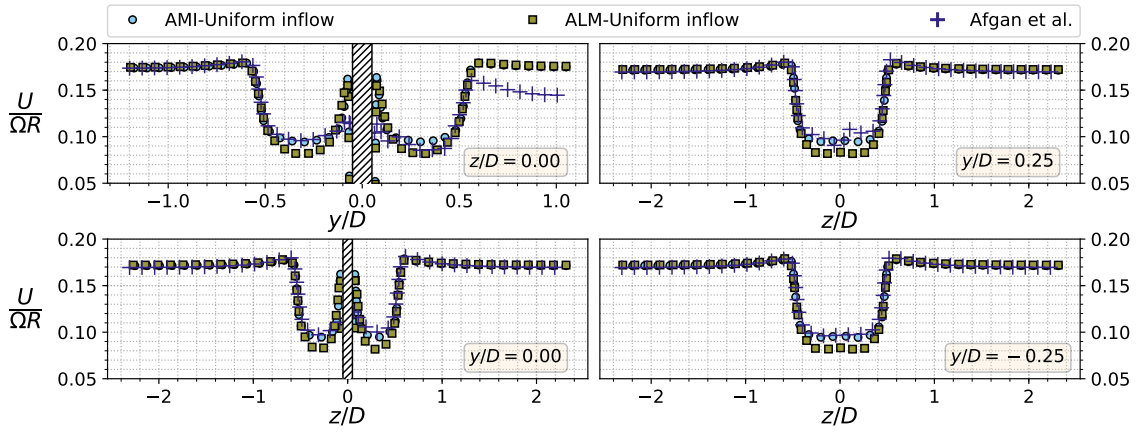

Figure 7: Time-averaged profiles of the streamwise flow speed, U, along four different lines orthogonal to the longitudinal direction at x/D=0.4. 'AMI-Uniform inflow' and 'ALM-Uniform inflow' represent the spatiotemporally-invariant laminar inflow computations of arbitrary-mesh-interface (AMI) and actuator-line (ALM) methods, and 'Afgan et al.' another IFLES study of the same rotor (additionally including the tower) with the same inflow settings [12, Fig. 8, TSR=6]. The vertical axes demonstrate the flow speed U normalised by Ω=22.5[rads^{-1}] the rotor rotational speed, and R=0.4[m] blade radius. The horizontal axes depict the lateral z and vertical y positions normalised by D=0.8[m] the rotor diameter. The black vertical rectangles in the left subplots stand for the hub boundary.

3.2. Effects of the arbitrary mesh interface technique and the nacelle boundary on turbine flows

As mentioned earlier in page 13, surprisingly, probable effects of the arbitrary mesh interface technique (AMI) on turbulent flows have not been quantified and closely examined. Although any effect has been plausibly presumed to be inconsiderable in the literature, a line of evidence needs to be established since the technique's unquantified impact may corrupt numerical predictions. Therefore, in this section, AMI effects were explored under $I_{\mathbf{u}'_{\mathrm{rms}}}$=20[%] turbulent inflow by means of three scenarios all of which were empty channels involving: *i*. no AMI, *ii*. non-rotating AMI, and *iii*. rotating AMI. Furthermore, another scenario containing only the nacelle of the turbine was introduced for the sake of completeness in investigating non-rotor elements' effects.

To that end, various statistics were quantified along approximately eight-hundred profiles distributed evenly in the three directions. Common-to-all results were discussed below, and among them, three representative-to-all figures were presented by Figs. 8–10.

In Fig. 8, an example from the longitudinal profiles was exhibited for the time-averaged velocity components and normal Reynolds stress tensor components. To start with, the only-nacelle case was found ineffectual on flow statistics along any of the longitudinal and lateral profiles (Fig. 9), except near wall and near wake regions. Its composed effects in comparison to the empty case could

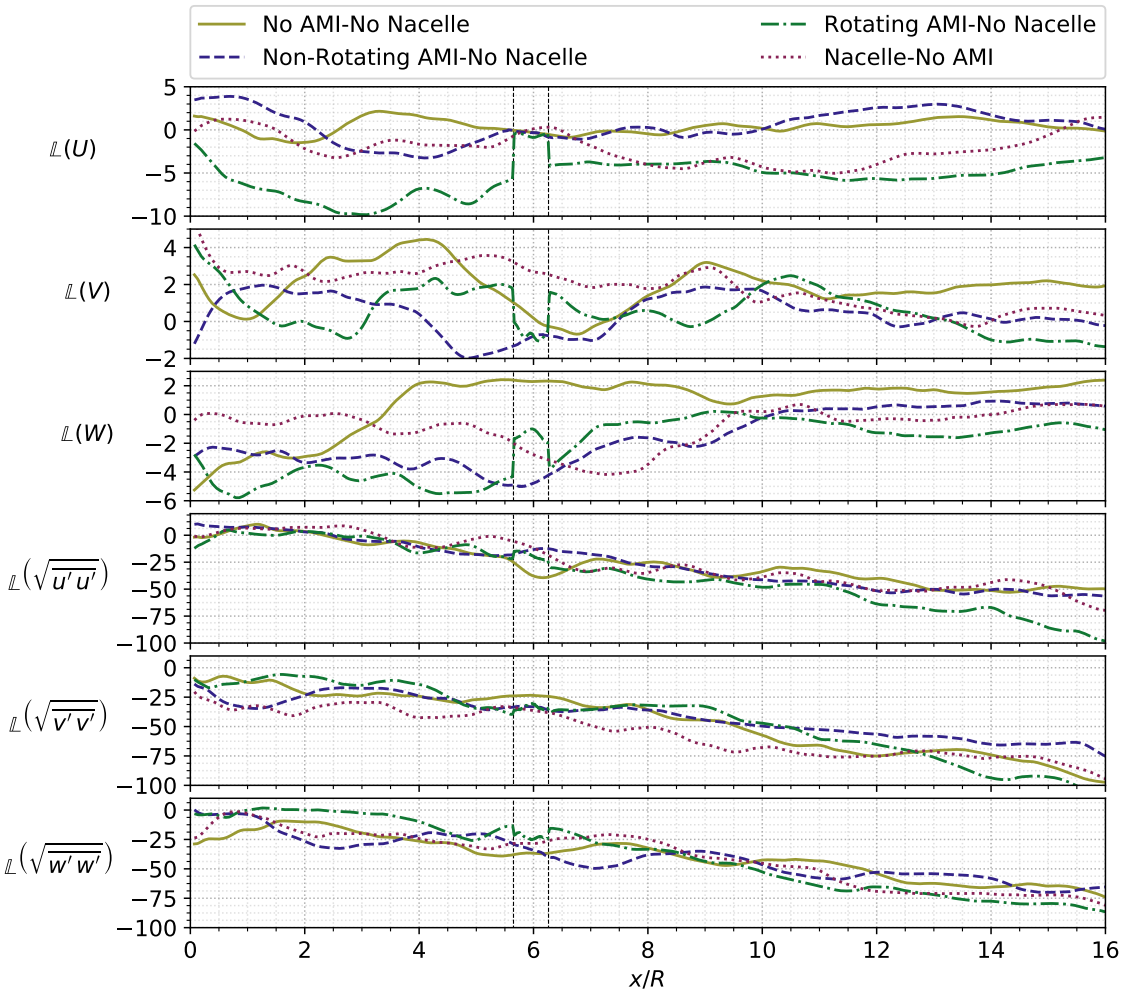

Figure 8: Effects of the stationary and rotating arbitrary mesh interfaces (AMI), and the nacelle on the longitudinal profiles of the time-averaged velocity components and normal Reynolds stress tensor components under $I_{\mathbf{u}'_{\text{rms}}}$=20[%]. $\{y, z\}$ positions of the profiles are $\{0.425, 0.000\}$[m], and the AMI cylinder's radius 0.45[m]. No blade was present within the computations. No spatial averaging was performed since no statistically homogeneous direction exists; thus, the fields are spatial-variant. The vertical axis of a subplot is the log percentage change of a component with respect to its input value, i.e. $\mathbb{L} \equiv 100 \log_e(x_{\text{result}}/x_{\text{input}})$[centineper]. The two vertical dashed lines stands for the x/R coordinates of the AMI inlet and outlet. The horizontal axis represents the longitudinal coordinate of the computational domain, x, non-dimensionalised by the rotor radius, R=0.4[m]. To avoid the logarithmic singularity in V and W since their input were zero, their values were shifted by U_o.

reasonably be deemed inconsiderable and spatially very local to the surroundings of the nacelle. Likewise, for the non-rotating AMI case, all flow statistics were observed continuous through the AMI region. Nevertheless, a closer look also revealed relatively tiny excursions across the interface

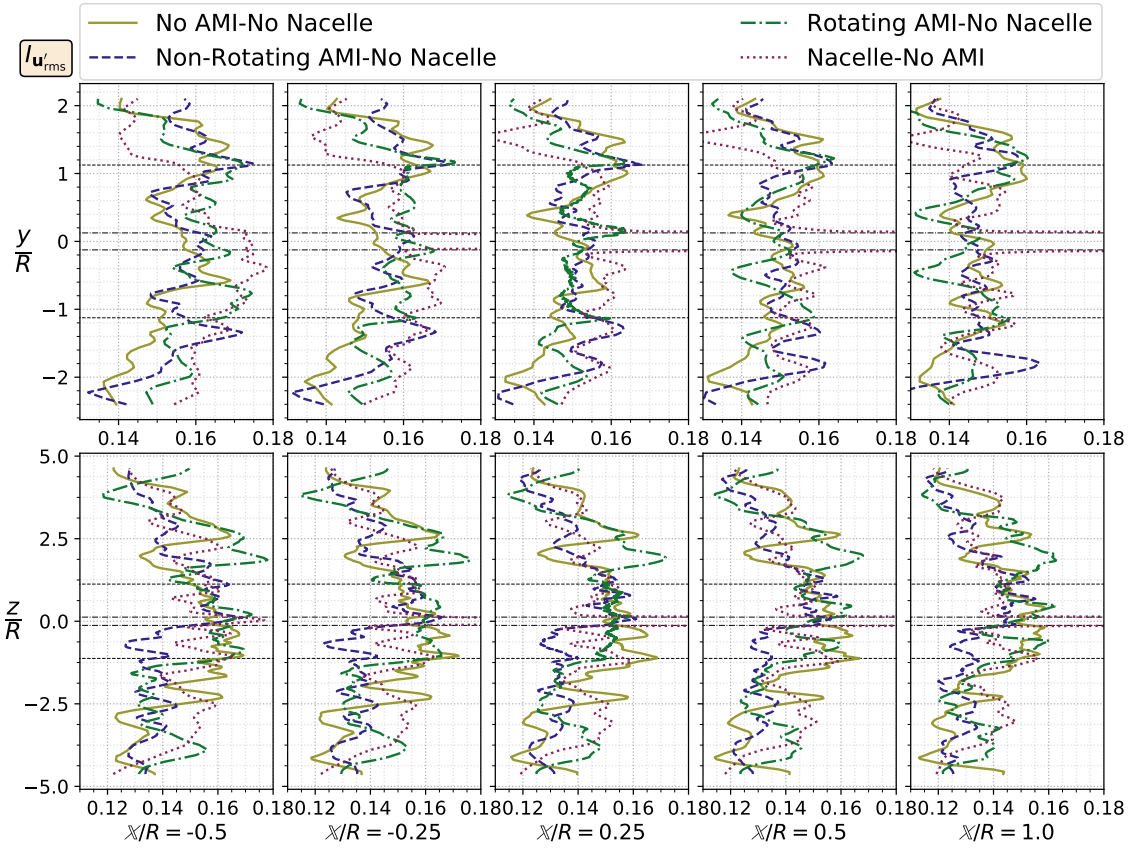

Figure 9: Effects of the stationary and rotating arbitrary mesh interfaces (AMI), and the nacelle on the vertical y and lateral z profiles of the time-averaged three-dimensional turbulence intensity $I_{\mathbf{u}'_{\mathrm{rms}}}$ under $I_{\mathbf{u}'_{\mathrm{rms}}}$=20[%]. No blade was present within the computations, no spatial averaging was performed, and the profiles pass through the hub centreline. The vertical axes show the y and z coordinates normalised by the rotor radius, R=0.4[m]. The horizontal axes stand for $(x\text{-}x_{\mathrm{rotor}})/R \equiv \mathbb{X}/R$ where x_{rotor}=2.4[m] is the rotor plane distance to the inlet, and thus $\mathbb{X}_{\mathrm{rotor}}/R$=0.0. The horizontal dashed line illustrates the lateral coordinates of the AMI edges, and the dash-dot line those of the nacelle. Horizontally, the AMI is present between $\mathbb{X}/R$=[-0.35, 0.2625], and the nacelle between $\mathbb{X}/R$=[-0.3275, 1.555].

sides, which could legitimately be attributed to the post-processing interpolation practice.

However, four patterns were observed in the rotating AMI case. First, what stands out in Fig. 8, which represents the maxima among all the computed longitudinal profiles, was the stepwise increments and decrements of the statistics on the interfaces. Quantitatively, the amplitude changes in $\{A\} \equiv \{U, V, W, \sqrt{\overline{u'u'}}, \sqrt{\overline{v'v'}}, \sqrt{\overline{w'w'}}\}$ at the AMI inlet were $\{A\} \approx \{6, -4, 7, 6, 6, -10\}$[cNp], and at the AMI outlet were $\{A\} \approx \{-3, 4, -3, -6, -5, 10\}$[cNp]. Consequently, the longitudinal profiles appeared as discontinuous functions with discontinuities reside on the interfaces. Second, the statistics

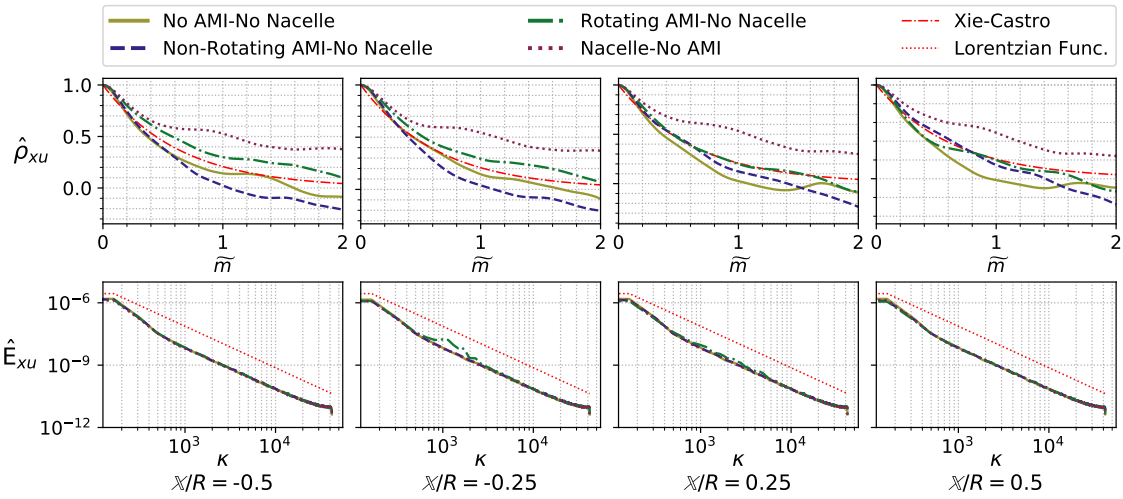

Figure 10: Effects of the stationary and rotating arbitrary mesh interfaces (AMI), and the nacelle on the two-temporal-point longitudinal sample autocorrelation function, $\widehat{\rho}_{xu}$[-], (the top subplots) and one-dimensional sample power spectral density function, $\widehat{\mathrm{E}}_{xu}$[m^{3}s^{-2}], (the bottom subplots). The time-series were probed at $\{y, z\}$=$\{0.0, 0.2\}[m]$ and $(x\text{-}x_{\mathrm{rotor}})/R \equiv \mathbb{X}/R$ positions where x_{rotor}=2.4[m] is the rotor plane distance to the inlet, and thus $\mathbb{X}_{\mathrm{rotor}}/R$=0.0. The horizontal axes of the top subplots represent the normalised spatial lag, $\tilde{m} \equiv (U\Delta_t m)/R$ where U=1.5[ms^{-1}] is the longitudinal mean flow speed, Δ_t=0.00005[s] the time-step, and R=0.4[m] the rotor radius. Those of the bottom subplots show the spatial wavenumber $\kappa \equiv (2\pi f)/(U\Delta_t)$[m^{-1}].

became more fluctuating per unit distance within the AMI region, albeit no amplitude increase, in comparison to the rest of the flow field. The third result to emerge from the longitudinal profiles was that the amplitude of the stepwise changes was generally in increase from the hub centreline to the AMI circular cross sections (not shown). Last, these observations in the longitudinal direction were also made for the derived statistics such as the turbulent kinetic energy budget components (not shown). Nonetheless, none of these observations seem to affect the flow field outside the AMI region since the observations could not be repeated for the profiles passing by the sides of the AMI region, and for its upstream/downstream.

Possible effects were also inspected in terms of the time-averaged three-dimensional turbulence intensity, $I_{\mathbf{u}'_{\mathrm{rms}}}$. In Fig. 9, a representative set of results was demonstrated along the vertical and lateral directions within the AMI neighbourhood. Similar to Fig. 8 observations, the only-nacelle and non-rotating AMI cases were found to be ineffectual on $I_{\mathbf{u}'_{\mathrm{rms}}}$. For the rotating AMI case, however, two remarks which are only valid within the AMI region were made in confirmation of Fig. 8 findings. Firstly, $I_{\mathbf{u}'_{\mathrm{rms}}}$-discontinuities were detected on the interfaces, and secondly, the spatial frequency of $I_{\mathbf{u}'_{\mathrm{rms}}}$ profiles was increased alongside amplitude suppressions.

In addition to the above amplitude-domain statistics, potential effects were also monitored in terms of time-frequency characteristics. In Fig. 10, the sample autocorrelation functions, $\widehat{\rho}_{xu}$, and power spectral density functions, $\widehat{\mathrm{E}}_{xu}$, were exemplified for the AMI neighbourhood. Inspections consisting the time-series of approximately five-hundred probes throughout the domain revealed that almost no significant and structured differences between the cases were evident. The sole exception occurred within the rotating AMI region as a form of overshoots in $\widehat{\mathrm{E}}_{xu}$. As exemplified in Fig. 10, these 'kicks' were triggered in the midst of the inertial-subrange spatial frequencies, and mostly with relatively small amplitude. The frequency of the overshoots nearly corresponded to a quarter of the rotational speed at the probe location; therefore, these might not be directly linked to the rotation.

The results imply for a flow field that the AMI rotation is somewhat influential inside an AMI region and on its boundaries, particularly toward AMI edges, whilst the non-rotating AMI causes virtually no effect. Also, the influence seems to be limited with the amplitude statistics, and does not affect time-frequency characteristics. A possible explanation for this might be that the AMI rotation somehow causes traction on the incoming flow. The existence of such traction was supported by the consistency between the direction of the amplitude changes in Fig. 8 (i.e. the top part of the AMI, $\{y, z\}$=$\{0.425, 0.0\}$[m]), and the rotational direction of the rotor. For instance, through the AMI inlet, the changes in U and W were positive, and in V were negative with respect to the coordinate systems shown in Fig. 1. Considering the rotor rotates in the clockwise direction seen from upwind, the rotation may generate a rigid-body-like vortex effect which could actuate similar effects on approaching flow in the same directions (e.g. an induction of U into the AMI due to a formed vorticity rotating clockwise). Through the AMI outlet, on the other hand, the directions of the amplitude changes were reversed. From an observer point of view inside the AMI, however, the stationary downstream domain rotates in the counterclockwise direction. This condition may be speculated to be the reason of the direction reversals. Although these remarks were observed to be valid in the majority of profiles, various counterexamples where the directions of the rotor and amplitude changes appear inconsistent were also identified. In consequence, despite the AMI rotation's effects were quantified in a tangible way, the generalisation of the remarks regarding its causal role is considered to be premature, and further controlled studies need to be carried out.

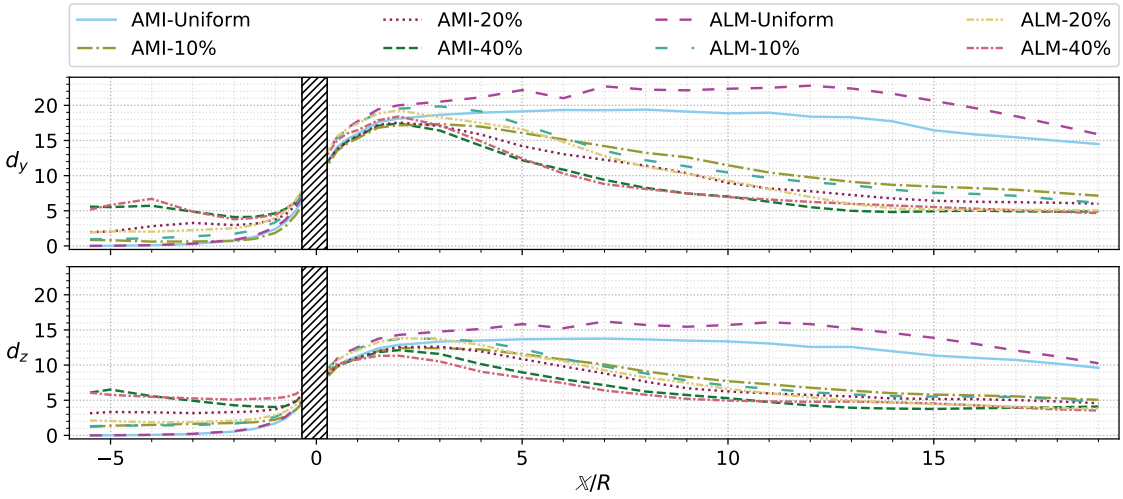

Figure 11: Effects of the three-dimensional turbulence intensity on the time-averaged U field sampled along the whole-domain vertical y (the top subplot) and lateral z directions (the bottom subplot) at numerous x cross sections. The $U(y)$ and $U(z)$ profiles pass through the nacelle centreline. The vertical axes show the Euclidean distance of the $U(y)$ and $U(z)$ profiles at each $\mathbb{X}/R$ station with respect to the input flow speed, U_o=1.5[ms^{-1}], i.e. $\{d_i\}_{\{i\in\{y,z\}\}}=(\sum_{j=1}^{n}(U_j\text{-}U_o)^2)^{0.5}$ where n=200 is the number of probes uniformly distributed in a single y or z profile. The levels of Euclidean distances for the z-direction are overall lower than those in the y-direction since the numerical domain is larger in the z-direction, and therefore the contribution of the freestream inflow speed is higher there. The horizontal axes demonstrate $(x\text{-}x_{\text{rotor}})/R\equiv\mathbb{X}/R$ where R=0.4[m] is the rotor radius, and x_{rotor}=2.4[m] the rotor plane distance to the inlet, hence $\mathbb{X}_{\text{rotor}}/R$=0.0. The hatched rectangles indicate the presence of the AMI region wherein the rotor resides. Note that the parts of the domain within $0.5R$ from the inlet and outlet were omitted in the presentation.

3.3. Effects of three-dimensional turbulence intensity

Based on the three knowledge gaps identified in page 5 regarding interactions between inflow turbulence intensity[30] and HAMTs, analyses were attempted to address these gaps: *i*. by the isolation of turbulence intensity as the sole control variable, *ii*. by considering a wider range of turbulence intensity encompassing the field measurements illustrated in Table 1, and *iii*. by a scope of statistics broader than previously considered.

For this purpose, in this section, wall-modelled and actuator-line-modelled IFLES computations with the settings elaborated in §2 were conducted under decaying homogeneous isotropic turbulence which involved four different inflow turbulence intensities, i.e. $I_{\mathbf{u}'_{\text{rms}}}=\{0,10,20,40\}$[%]. Representative results were presented by Figs. 11–A.22 and Table 8.

To start with, in Fig. 11, the effects of $I_{\mathbf{u}'_{\text{rms}}}$ on the time-averaged $U(\mathbf{x})$ fields were demonstrated.

[30] Henceforth, the term 'turbulence intensity' only refers to the three-dimensional turbulence intensity, $I_{\mathbf{u}'_{\text{rms}}}$.

Therein, the Euclidean distances[31] of $U_{\{y,z\}}$ profiles with respect to the input U_o were computed for each x cross section, i.e. $d_{\{y,z\}}$.

From the figure, in upstream of the rotor, two prominent observations were made. Firstly, the approaching flow field began to sense the presence of the rotor at around $4R$ upstream as can be seen most apparently from the uniform inflow cases. The observation somewhat accords with that of [126] who found the same parameter more than $6R$ in their model-scale wind turbine experiments with 3% areal blockage ratio [126, p. 694] (in this study, 7.5%), and $4R$ in their actuator-line computations [126, p. 694]. Secondly, in front of the rotor, the Euclidean distances of all cases developed into a similar range irrespective of their $I_{\mathbf{u}'_{\mathrm{rms}}}$ content. This development of incoming U field occurred in a nonlinear fashion towards the rotor. For example, the $d_{\{y,z\}}$-difference between the AMI-Uniform and AMI-40 was nearly 5-6 whereas it was reduced to $\sim$1 at the AMI inlet. It may be, therefore, possible to conceptualise that the rotor acts as a unit that assimilates various incoming mean flow fields into a kindred field independent of their normal Reynolds stresses characteristics.

In downstream shown in Fig. 11, three other observations were noted. The first is a peak in $d_{\{y,z\}}$ that emerged around $2R$ in all cases. The rotor signature on the flow field seems to be predominant over $I_{\mathbf{u}'_{\mathrm{rms}}}$ up to $2R$ since the rates and amplitudes of changes in U were similar in all cases. The second is that, after $2R$, the downstream development of $d_{\{y,z\}}$ predicted by each case started to differentiate as a function of the corresponding $I_{\mathbf{u}'_{\mathrm{rms}}}$: the increments in $I_{\mathbf{u}'_{\mathrm{rms}}}$ led to higher wake recovery rates, which was frequently observed in the literature. The last is that, in the non-zero $I_{\mathbf{u}'_{\mathrm{rms}}}$ cases, the rate of U-recovery gradually declined, and levelled off. As a consequence, even at $19R$ downstream, the amplitude of $d_{\{y,z\}}$ of all the non-zero $I_{\mathbf{u}'_{\mathrm{rms}}}$ cases remained above that of the $I_{\mathbf{u}'_{\mathrm{rms}}}$=40[%] inlet values. The implication of this is that the rotor signature on the longitudinal flow speed field is able to persist far downstream despite energetic turbulence entrainment.

As regards patterns between AMI and ALM, it was observed in Fig. 11 that the levels of $d_{\{y,z\}}$ were in general higher for ALM at $2R$, and were in a faster decay. Both indicates higher level of axial flow induction and more energetic turbulence entrainment mechanisms generated by ALM for the same rotor. To allow further inspection of these mechanisms, time-averaged over-filter scale fields of kinetic energy, kinetic energy production and enstrophy production were visualised on the z-normal hub centreline plane in Figs. 12–14. Among them, enstrophy is mostly generated by

[31] It should be highlighted that the Euclidean distance does not show the direction of changes. Instead, it shows the total absolute difference of a quantity with respect to a given input.

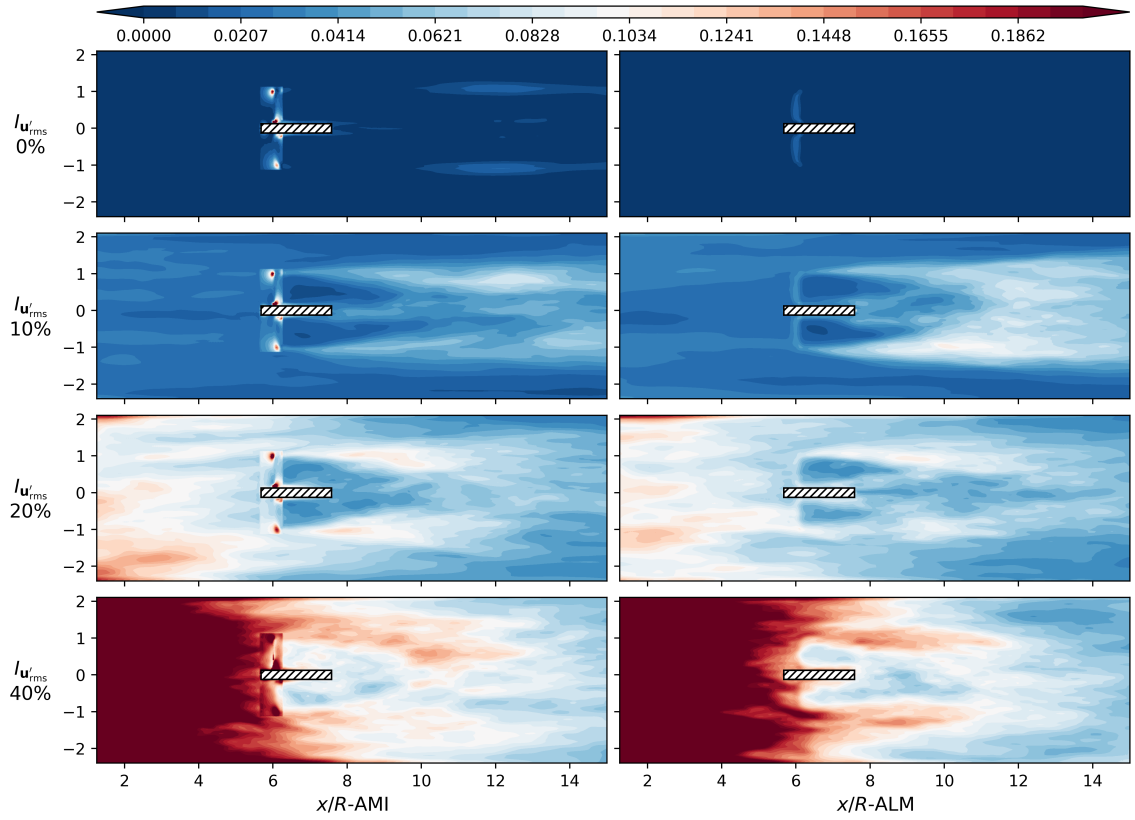

Figure 12: Contour plots of the time-averaged over-filter scale kinetic energy fields, $k_{\mathrm{ofs}}[\mathrm{m^2s^{-3}}]$, on the z-normal hub centreline plane. The left subplots belong to the geometry-fitted wall-modelled approach computations (AMI), and the right subplots the actuator-line modelled computations (ALM). Each row shows the input three-dimensional turbulence intensity, $I_{\mathbf{u}'_{\mathrm{rms}}}$. The vertical axes represent the numerical domain height y normalised by the rotor radius, R=0.4[m], and the horizontal axes the normalised longitudinal distances, x/R. The colorbar of each subplot is the same.

vortex stretching [127, p. 348], and its production may indicate regions where vortex stretching is dominant. On the other hand, vortex stretching indicates the energy cascade wherein strain gradients of mean velocity stretch vortex structures in parallel and antiparallel manners, usually resulting in net vortex stretching. A stretched vortex elongates in length, yet shrinks its diameter to preserve its mass. The conservation of angular momentum concurrently forces the vortex to spin faster, thus energising its neighbourhood mostly at smaller scales through traction. Considering this chain of relations, one could expect higher enstrophy production results in higher levels of mean flow energy transfer to heat dissipation. As can be seen in Fig. 14, for example, the enstrophy production within the wakes of the ALM cases was qualitatively higher and more chaotic than that of the AMI

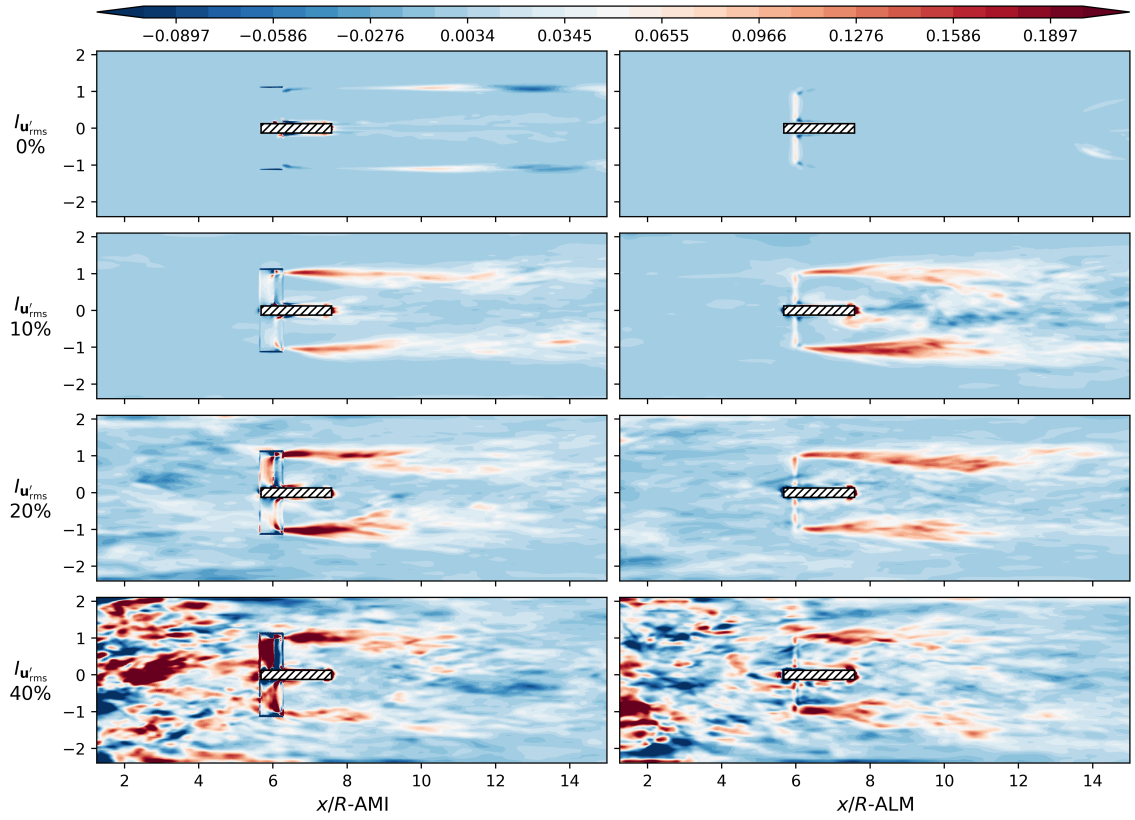

Figure 13: Contour plots of the time-averaged over-filter scale kinetic energy production fields, $k_{\mathrm{Prod}} = -\{\overline{(\mathbf{u}')^2}\}:\nabla U$ [$\mathrm{m^2 s^{-3}}$], on the z-normal hub centreline plane. The remaining figure particulars were summarised in Fig. 12.

cases. Accordingly, the deeper wake deficits and faster recovery rates observed in the ALM cases could be linked to the enstrophy production mechanism. Furthermore, it is postulated that the higher enstrophy production stemmed from ALM's force exertion in amounts similar to AMI, yet within a smaller space, likely caused an augmentation in velocity gradients around actuator points. In view of enstrophy production's dependency on vorticity (hence velocity) gradients, it could be thought that ALM manifested its effect through this way.

To reveal the direction of the changes (i.e. increments/decrements) in Fig. 11, the $\{y, z\}$ profiles of U at various x cross sections were set out in Figs. 15–17 for the upstream, immediate aft, and downstream of the rotor, respectively.

In the upstream stations of Fig. 15, the U-profiles of the non-zero $I_{\mathbf{u}'_{\mathrm{rms}}}$ cases gradually lost

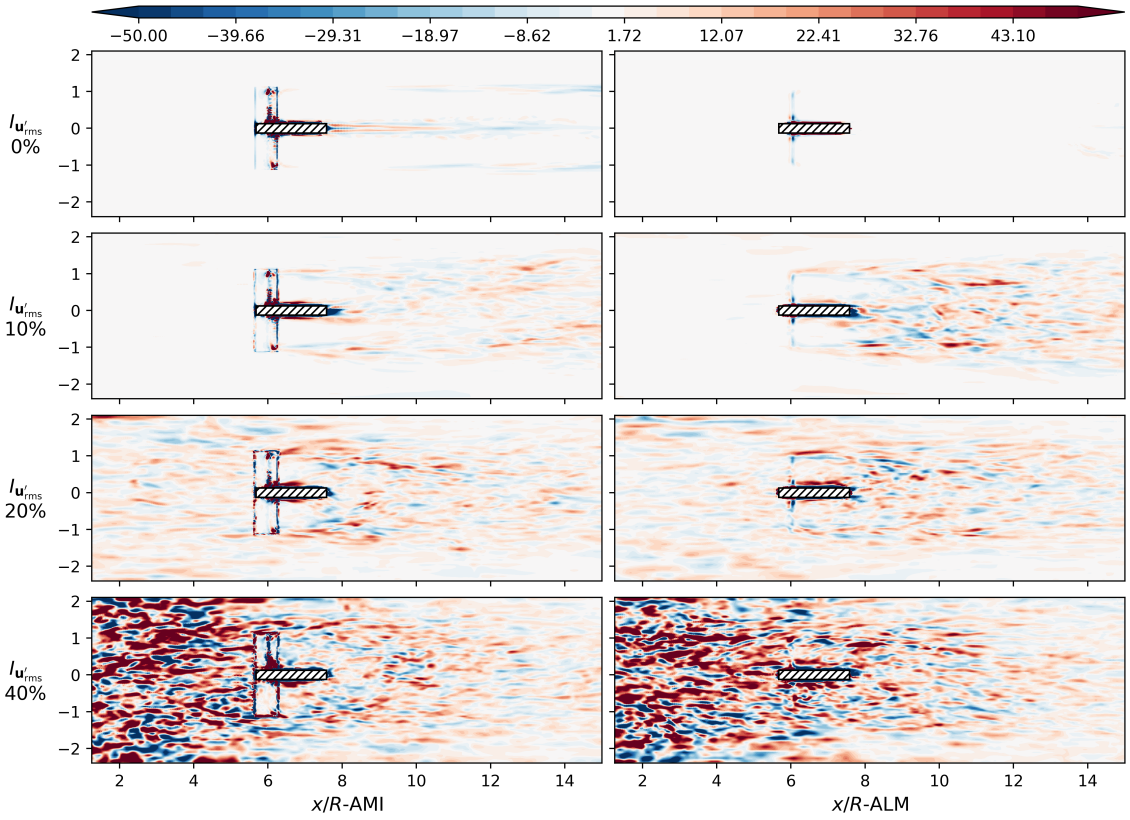

Figure 14: Contour plots of the time-averaged over-filter scale enstrophy production fields, $\mathfrak{E}_{\mathrm{Prod}} = -\{(\boldsymbol{\omega}' \cdot \mathbf{u}') : \nabla\Omega\}$ [s^{-2}] where $\boldsymbol{\omega}' = \nabla \times \mathbf{u}'$ is the over-filter scale vorticity [s^{-1}], and Ω the time-averaged vorticity. The remaining figure particulars were summarised in Fig. 12.

their fluctuation features and virtually converged to a common form towards the rotor by slowing down (previously observed in Fig. 11). At -0.5R, the common form was in a Gaussian shape with its maximum velocity deficit was around 15-25[cNp]. Also, its lateral size roughly exceeded the alignment of the rotor diameter by nearly 1R in the z-direction and by 0.5-0.75R in the y-direction (likely due to the domain constraint). Nonetheless, the signatures of $I_{\mathbf{u}'_{\mathrm{rms}}}$ remained apparent at the sides of the U-profiles. Lastly, the AMI-ALM comparison exhibited no considerable/structural differences except that ALM-Uniform yielded slightly deeper U-reduction at -0.5R (previously observed in Fig. 11).

Although the predictions for the immediate aft region are likely not of importance to downstream turbines, some model developments may utilise the findings. With this motivation, six general

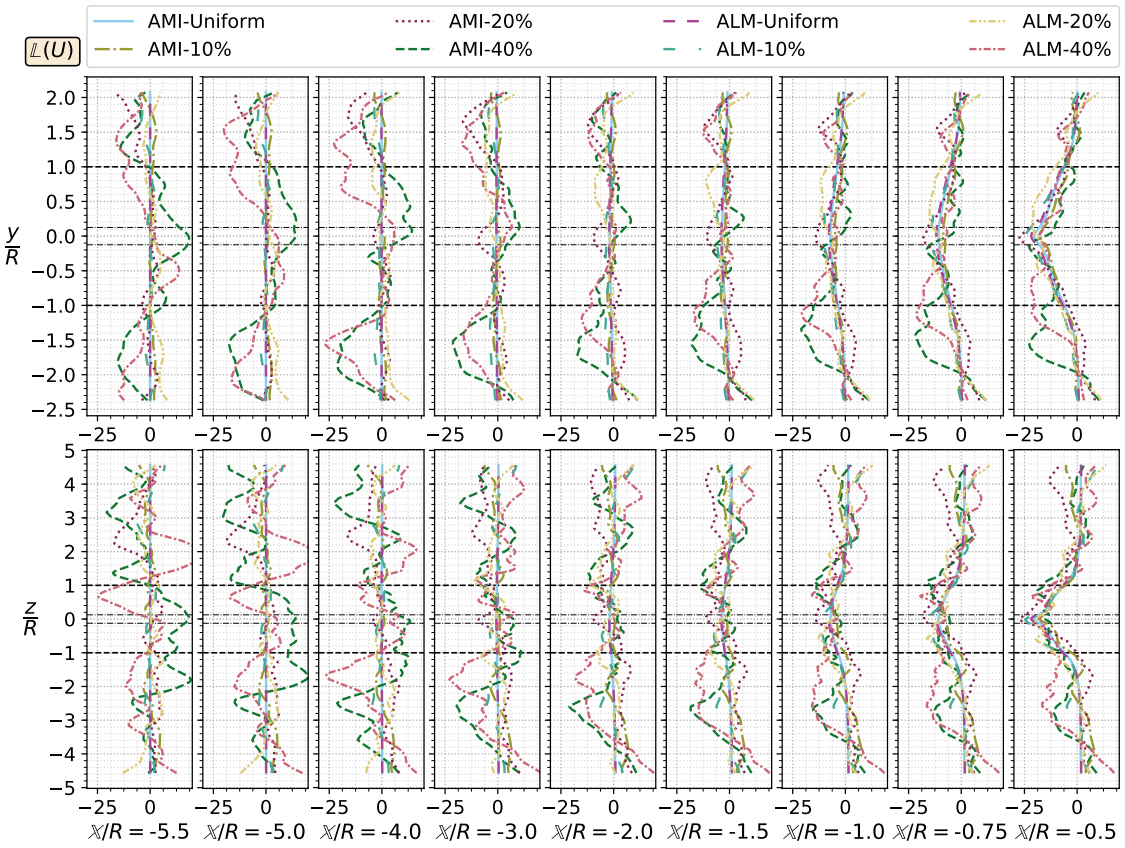

Figure 15: Effects of the three-dimensional turbulence intensity on the time-averaged U-profiles along the vertical y and lateral z directions, upstream of the rotor. The profiles pass through the hub centreline, and are shown in the units of the log percentage change of U with respect to U_o=1.5[ms^{-1}], i.e. $\mathbb{L}\equiv 100\log_e(U/U_o)$ centineper. The horizontal dashed line shows the lateral coordinates of rotor tip, and the dash-dot line those of the nacelle. The remaining figure particulars are given in Fig. 11.

patterns were identified in Fig. 16: Firstly, a double-Gaussian form with its maxima approximately at the mid-blade radius was observed in all cases for the speed deficit shape. Secondly, the form possessed qualitatively-some asymmetry in the ALM cases whereas a higher degree of symmetry appeared in the AMI cases. Thirdly, on the question of the amplitudes of the speed deficits, the deficits were found nearly the same for all the AMI cases at $0.5R$ with a $\sim$-50[cNp] peak. For the ALM cases at $0.5R$, on the other hand, the deficits were $\sim$-10[cNp] deeper, and were somewhat in variation with $I_{\mathbf{u}'_{\mathrm{rms}}}$. Towards $2R$, these peaks were deepened by $\sim$-5[cNp] per $0.5R$ for each case. When the flow completely left the nacelle at $2R$, the peaks were shifted toward the nacelle centreline and $I_{\mathbf{u}'_{\mathrm{rms}}}$ manifested its effects in a nonlinear manner thereat. As an example, the centreline deficit

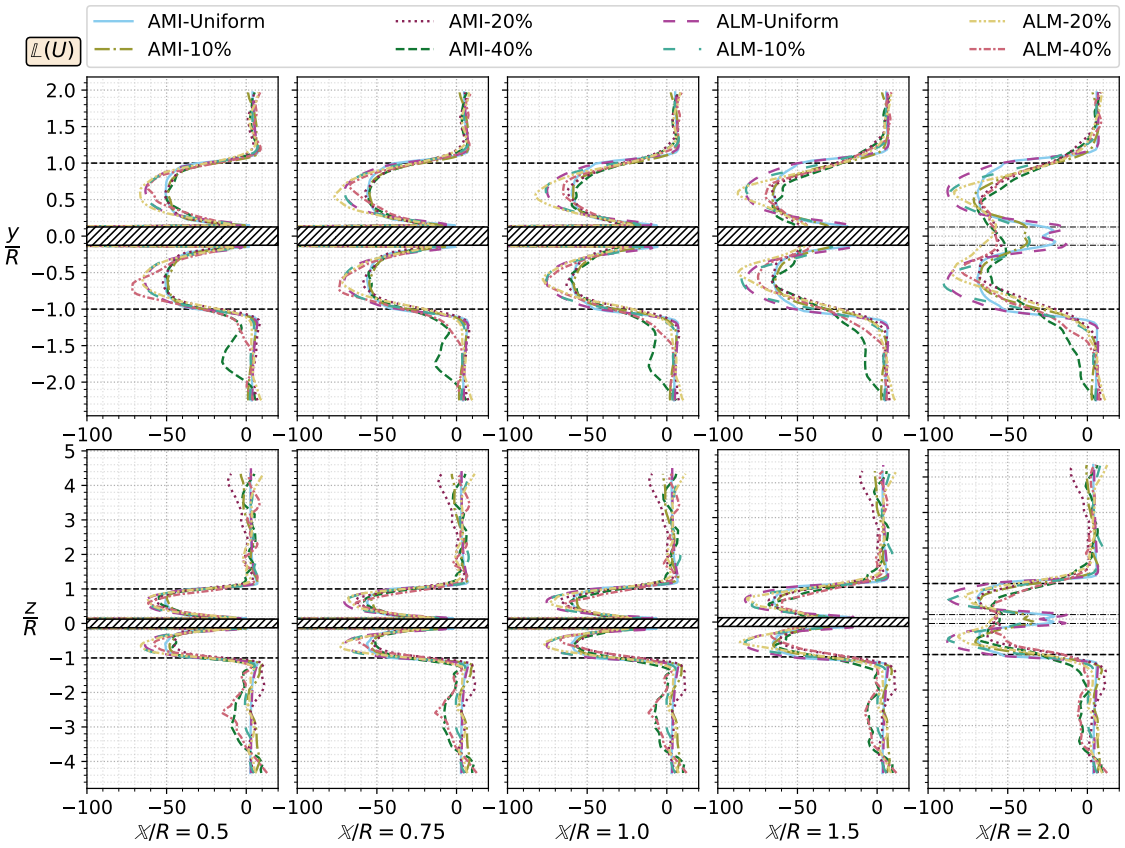

Figure 16: Effects of the three-dimensional turbulence intensity on the time-averaged U-profiles along the vertical y and lateral z directions in the immediate aft of the rotor. The hatched rectangles indicate the presence of the nacelle. The remaining figure particulars are given in Fig. 11.

was decreased from ∼-20-(-40)[cNp] to -40[cNp] through the addition of $I_{\mathbf{u}'_{\text{rms}}}$=10[%] on the uniform inflow cases whereas both $I_{\mathbf{u}'_{\text{rms}}}$=20[%] and $I_{\mathbf{u}'_{\text{rms}}}$=40[%] cases produced -50-(-60)[cNp] despite the doubling of $I_{\mathbf{u}'_{\text{rms}}}$.

Further downstream, Fig. 17 showed the U-$\{y, z\}$ profiles at between $3R$ and $13R$ with intervals of R. In the non-zero $I_{\mathbf{u}'_{\text{rms}}}$ cases, the double-Gaussian form convected from the immediate wake was dissolved by 3-4R while this form was preserved in the uniform inflow cases till $11R$. At $3R$, the maxima of the U deviations with respect to the input U_o were ranged between ∼-40-(-90)[cNp] for the non-zero $I_{\mathbf{u}'_{\text{rms}}}$ cases, and were declined to ∼-20-25[cNp] at $13R$. Furthermore, the rate of recovery considerably slackened and subsequently levelled out in the non-zero $I_{\mathbf{u}'_{\text{rms}}}$ cases after reaching -20[cNp] with respect to the input U_o. A curious finding stemmed from these observations

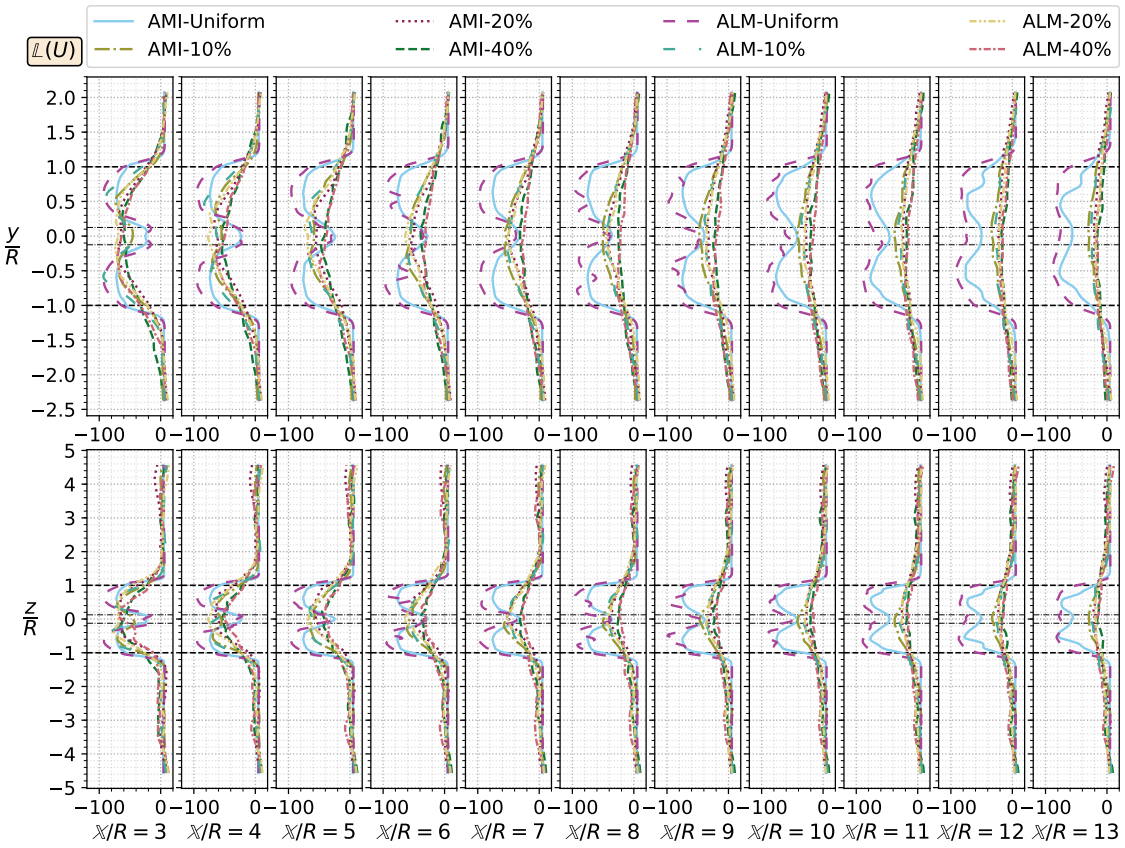

Figure 17: Effects of the three-dimensional turbulence intensity on the time-averaged U-profiles along the vertical y and lateral z directions, downstream of the rotor. The remaining figure particulars are given in Fig. 11.

was that the wake recovery rate varied with the downstream distance obeying a half-Gaussian function to a certain extent. This can be exemplified by the AMI-20 and AMI-40 cases. For the former, the peak speed deficit at the stations of $\{3, 5, 7, 9, 11, 13\}[R]$ was approximately negative $\{60, 60, 50, 40, 20, 20\}$[cNp], respectively, and for the latter negative $\{60, 40, 30, 20, 20, 20\}$[cNp]. As can be deduced from a projection of these patterns, the peak deficits remained at a constant level before they fell quickly, and consecutively levelled off again. It can thus be suggested within the current scope that the wake recovery rate with respect to the downstream distance approximately follows a half-Gaussian-form. Last but not least, the ALM cases were detected to be generally recovering faster than the AMI cases from this perspective as well in addition to the aforementioned similar observations. For instance, the peak U-deviations at $3R$ were nearly 90[cNp] and 65[cNp]

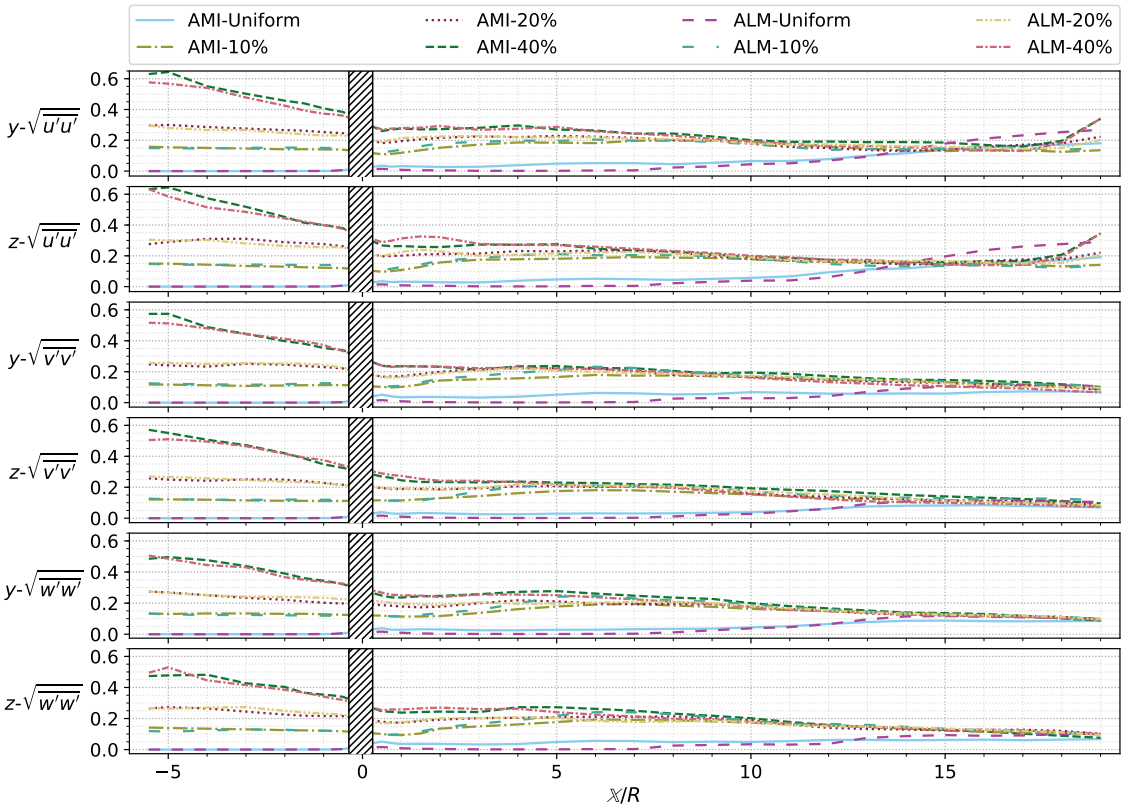

Figure 18: Longitudinal profiles of the normal components of the time-averaged Reynolds stress tensor. The results were first sampled in the vertical y and lateral z direction within $-R \leq \{y, z\} \leq R$ at various x cross sections, and were subsequently arithmetic-averaged. The remaining figure particulars were given in Fig. 11.

for the ALM-10 and AMI-10 cases in turn. However, the ALM-10's peak U-deviation reached the level of the AMI-10 at $5R$ and continued to yield lower deviations in the remaining downstream.

With regard to velocity fluctuations, Fig. 18 compared $I_{\mathbf{u}'_{\mathrm{rms}}}$ effects on the longitudinal profiles of the time-averaged Reynolds stress tensor's normal components. Three prominent behaviours were identified in this figure. First, immediate decreases were observed in the normal components at the first node, which were more distinct in the lateral components. This behaviour was identified as an inherent feature of the current version of the inflow model being utilised (§2.1.3), and was quantitatively elaborated in [28] with its reasons. Second, the rotor was observed to act as a filter that changes the decay rates of the normal components, and shapes them in a way that the evolvement of the components unifies downstream. The evidence can be seen in the figure that all

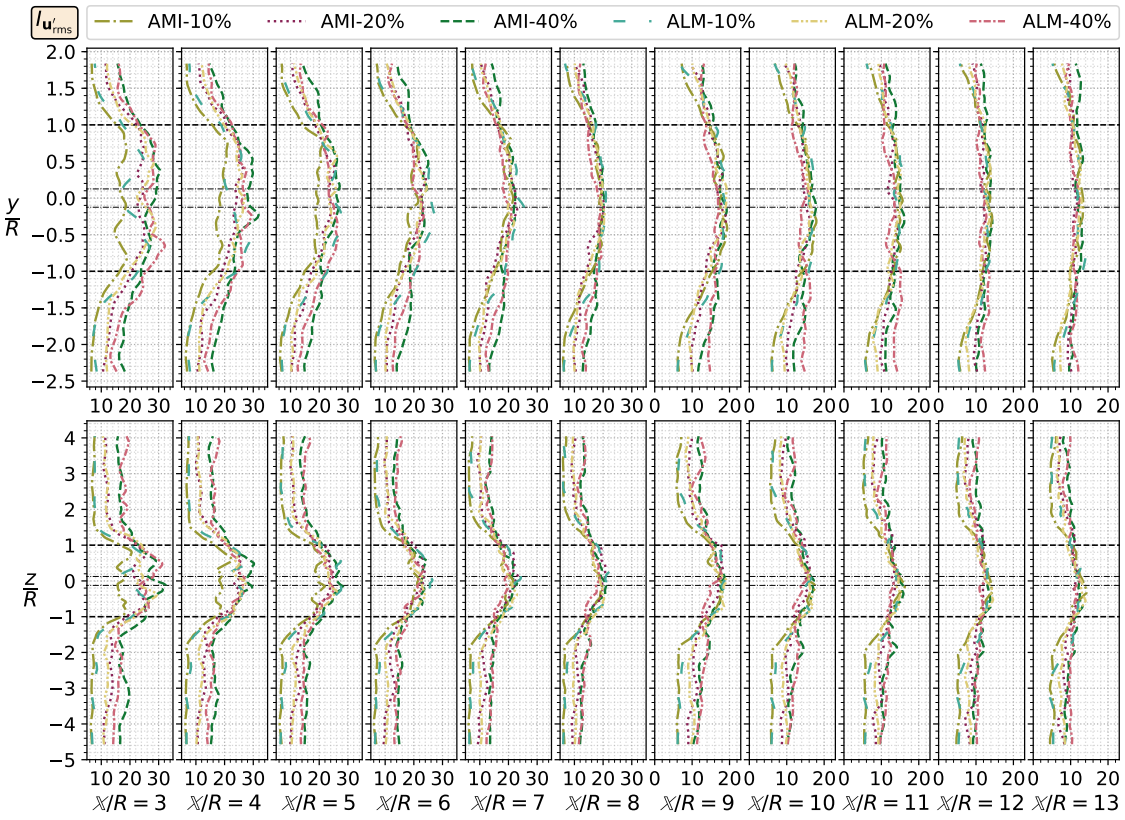

Figure 19: Effects of the interactions between the turbine and different upstream (three-dimensional) turbulence intensities on the downstream time-averaged turbulence intensity profiles, $I_{\mathbf{u}'_{\mathrm{rms}}}[\%]$, along the vertical y and lateral z directions. The x-limits of the subplots of $\mathbb{X}/R \geq 9$ are zoomed in to ease the parsing of the details therein. The remaining figure particulars are given in Fig. 11.

the normal components in all cases roughly converged into a band between 0.15–0.25[ms^{-1}] until $5R$, and the band was further narrowed to a range of 0.05[ms^{-1}] at $10R$ independently from the input $I_{\mathbf{u}'_{\mathrm{rms}}}$. Moreover, as can be seen from the adjacent neighbourhood of the rotor in Fig. 18, the rotor also reduced the amplitude of the normal components in proportion to their incoming amplitudes, i.e. higher the initial amplitude, higher the dampening effect within the immediate aft of the rotor. Lastly, no significant difference in either amplitude or pattern was found between the AMI and ALM cases of the same $I_{\mathbf{u}'_{\mathrm{rms}}}$.

In examination of the above, $\{y, z\}$ profiles of $I_{\mathbf{u}'_{\mathrm{rms}}}$ along the downstream of the rotor were illustrated in Fig. 19. Most of the remarks related to the longitudinal speed deficits shown in Fig. 11 were found to be valid for $I_{\mathbf{u}'_{\mathrm{rms}}}$ as well. First of all, the profile patterns of $I_{\mathbf{u}'_{\mathrm{rms}}}$ were monitored

Table 8: The total force and moment components in and about the axial direction exerted on the blades, i.e. F_x[m^{4}s^{-2}] and M_x[m^{5}s^{-2}], obtained from the geometry-fitted wall-modelled approach computations (AMI) with four different input three-dimensional turbulent intensities, $I_{\mathbf{u}'_{\mathrm{rms}}}$. $\hat{\mu}_1$ is the sample mean, $\sqrt{\hat{\mu}_2}/\mu_1$ the sample coefficient of variation, $\hat{\mu}_2$ the biased sample standard deviation, $\hat{\gamma}_1$ the biased sample skewness, and $\hat{\gamma}_2$ Fisher's biased sample kurtosis. The results were rounded to three decimal places.

	$I_{\mathbf{u}'_{\mathrm{rms}}}$	$\hat{\mu}_1$	$\sqrt{\hat{\mu}_2}/\hat{\mu}_1$	Min	Max	$\hat{\gamma}_1$	$\hat{\gamma}_2$
F_x	0%	0.437	0.000	0.437	0.438	-0.001	0.045
	10%	0.442	0.087	0.099	0.601	-0.022	-0.273
	20%	0.436	0.169	-0.380	0.725	0.062	-0.147
	40%	0.430	0.282	-0.420	2.434	0.193	0.567
M_x	0%	0.0174	0.000	0.017	0.018	0.349	4.446
	10%	0.0180	0.141	0.010	0.026	0.079	-0.613
	20%	0.0181	0.271	0.000	0.034	0.278	-0.592
	40%	0.0182	0.400	-0.009	0.06	0.733	0.432

to be somewhat corresponding to the speed deficits, albeit possessing smoother trajectories in general. However, an exception was also observed within these similarities: The $I_{\mathbf{u}'_{\mathrm{rms}}}$ profiles were generally asymmetric in the y-direction to some degree due to the lower $I_{\mathbf{u}'_{\mathrm{rms}}}$ levels along the bottom side of the rotor unlike the speed deficit profiles. This result could be explained by the fact that the nacelle centreline was located closer to the top boundary, and the blockage ratio of the upper side is higher than that of the lower side of the domain. Slightly different effects of the asymmetric positioning of the rotor on U and $I_{\mathbf{u}'_{\mathrm{rms}}}$ imply that uneven side blockage ratios may have more impact upon turbulent fluctuations than the mean flow. In terms of amplitude levels, $I_{\mathbf{u}'_{\mathrm{rms}}}$ of all cases approximately converged onto the same level within the alignment of the rotor diameter qualitatively at around 7-8R and convected downstream in unison. Nevertheless, outside of this alignment the $I_{\mathbf{u}'_{\mathrm{rms}}}$ profiles stayed different within a range of $\sim$8[cNp]. Additionally, $I_{\mathbf{u}'_{\mathrm{rms}}}$ within the alignment was observed to remain higher with respect to $I_{\mathbf{u}'_{\mathrm{rms}}}$ convecting through the sides. According to this observation, it can be inferred that the rotor signature on turbulence intensities is also able to preserve itself downstream in addition to the similar observation made for U in Fig. 11. By way of illustration, Figs. 13 and 14 exemplified in the same vein that over-filter scale kinetic energy and enstrophy production regions generated by the blade tips stretching downstream distances an order of magnitude farther than the blade radius; implying the underlying mechanisms why the rotor signature could remain in defiance of high freestream $I_{\mathbf{u}'_{\mathrm{rms}}}$. Lastly, as far as the differences between the AMI and ALM cases are concerned, no particular pattern significant in regard to engineering purposes was detected for $I_{\mathbf{u}'_{\mathrm{rms}}}$ downstream evolvement except that the

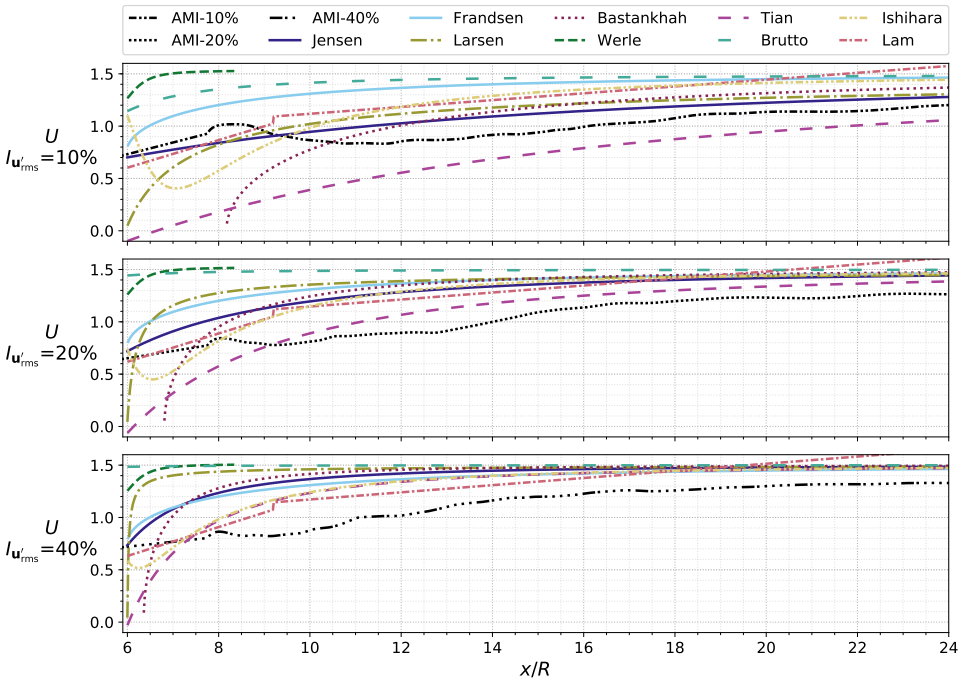

Figure 20: Time-averaged longitudinal U-profile predictions of the geometry-fitted wall-modelled arbitrary-mesh-interface approach (AMI) and nine analytical wake models (§ Appendix A.2) along the hub centreline downstream of the rotor. The vertical axis of each subplot represents U-magnitude belonging to a case with different three-dimensional turbulence intensity, $I_{\mathbf{u}'_{\mathrm{rms}}}$=$\{10, 20, 40\}$[%]. The horizontal axes demonstrate the rotor-radius-normalised longitudinal distance x starting from the rotor plane, where R=0.4[m].

ALM-10's $I_{\mathbf{u}'_{\mathrm{rms}}}$-profile around the centreline was consistently higher than the AMI-10's $I_{\mathbf{u}'_{\mathrm{rms}}}$-profile until $8R$.

In the case of rotor performance, effects of $I_{\mathbf{u}'_{\mathrm{rms}}}$ on longitudinal forces and moments of the rotor were investigated through six descriptive statistics, and the obtained results were summarised in Table 8. What can be seen in this table is the consistent relations between $I_{\mathbf{u}'_{\mathrm{rms}}}$ and the statistical moments. As regards trends between forces/moments and $I_{\mathbf{u}'_{\mathrm{rms}}}$ excluding the laminar inflow case, it was found out that the sample coefficient of variation, skewness, kurtosis, and maxima of total forces/moments were increasing functions of $I_{\mathbf{u}'_{\mathrm{rms}}}$ while their sample mean[32] and minima were decreasing with increasing $I_{\mathbf{u}'_{\mathrm{rms}}}$. These relations were, however, somewhat nonlinear with monotonically decreasing rate of change. For example, from $I_{\mathbf{u}'_{\mathrm{rms}}}$=10[%] to $I_{\mathbf{u}'_{\mathrm{rms}}}$=20[%] $\sqrt{\hat{\mu}_2}/\mu_1$ was increased by ∼64[cNp] whilst from $I_{\mathbf{u}'_{\mathrm{rms}}}$=20[%] to $I_{\mathbf{u}'_{\mathrm{rms}}}$=40[%] the increase was contended

[32] Except the sample mean of moments which scantly increased with $I_{\mathbf{u}'_{\mathrm{rms}}}$.

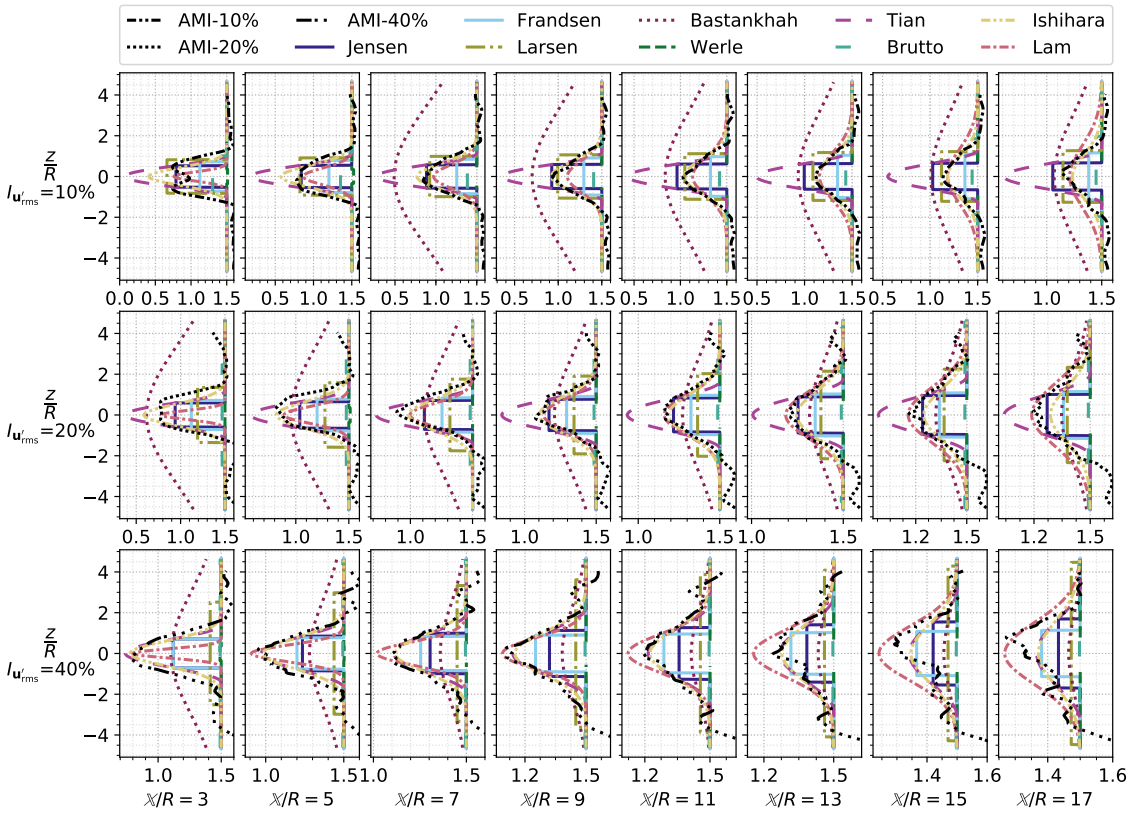

Figure 21: Time-averaged lateral-z-direction U profiles at eight x cross-sections from the geometry-fitted wall-modelled arbitrary-mesh-interface approach (AMI) and nine analytical wake models (§ Appendix A.2). The profiles pass through the hub centreline. Each row demonstrates a three-dimensional turbulence intensity, $I_{\mathbf{u}'_{\mathrm{rms}}}$={10, 20, 40}[%]. The horizontal axes show $(x\text{-}x_{\mathrm{rotor}})/R \equiv \mathbb{X}/R$ where x_{rotor}=2.4[m] is the rotor plane distance to the inlet, and R=0.4[m].

with ∼51[cNp]. Closer inspection of the table also showed that although decrements occurred in $\hat{\mu}_1$ with increasing $I_{\mathbf{u}'_{\mathrm{rms}}}$, the level of decrements could be deemed inconsiderable relative to the mean itself. As an example, from $I_{\mathbf{u}'_{\mathrm{rms}}}$=10[%] to $I_{\mathbf{u}'_{\mathrm{rms}}}$=40[%], the decrement in $\hat{\mu}_1$ was ≈-2.8[cNp]. This almost constancy in $\hat{\mu}_1$ could be related to the unifying effect of the rotor on longitudinal mean speed profiles with different $I_{\mathbf{u}'_{\mathrm{rms}}}$, previously observed in Fig. 11 at immediate upstream and downstream. The observations for $\hat{\mu}_1$, $\sqrt{\hat{\mu}_2}/\hat{\mu}_1$, minima and maxima are in general in line with the literature moderately overviewed in §1. Nonetheless, to the authors' knowledge, no comparable data was found in the literature for skewness and kurtosis. Assuming the validity of the information obtained herein for $\hat{\gamma}_1$ and $\hat{\gamma}_2$, the positiveness in $\hat{\gamma}_1$ with an increasing trend indicates that above-

mean force/moment fluctuations occurred more frequently than the below-mean fluctuations in parallel to the increments in $I_{\mathbf{u}'_{\mathrm{rms}}}$. An important implication of this is that sudden, brief and strong excursions such as gusts that a turbine may experience become more likely to happen in higher $I_{\mathbf{u}'_{\mathrm{rms}}}$ inflows. Moreover, the trend in forces/moments from platykurtic to leptokurtic distribution with increasing $I_{\mathbf{u}'_{\mathrm{rms}}}$, i.e. $\hat{\gamma}_2{<}0 \rightarrow \hat{\gamma}_2{>}0$, meant that flow excursions began to accumulate at distinct spatial and temporal locations throughout flow field leaving more space for lulls. In consequence, however, fluctuation slicings of the rotor became more abrupt with higher $I_{\mathbf{u}'_{\mathrm{rms}}}$, hence potential adverse effects on rotor structure.

Finally, the time-averaged longitudinal flow speed results from the downstream of the AMI cases were compared with twelve analytical wake models in order to assess certain aspects of engineering design tools via high-fidelity research tools under $I_{\mathbf{u}'_{\mathrm{rms}}}$ variation. The analytical models comprised the majority of the models being reported in the wind and marine turbine literature, and were computed with their default settings although calibration of the models for a certain case is the proper approach in practical applications. Consequently, preliminary computations revealed at the outset that the models from [49], [48], and [51] were found to be incompatible with the current turbine setup and conditions; therefore, they were left out from the following analyses. The remaining nine models were computed using $I_{\mathbf{u}'_{\mathrm{rms}}}{=}\{10, 20, 40\}[\%]$, and their predictions for the time-averaged longitudinal U-profiles and lateral-z-direction U-profiles were respectively presented in Figs. 20 and 21 alongside the corresponding AMI cases.

In Fig. 20, seven generic observations were made. First of all, Werle's model [43] within R immediately saturated to the freestream speed in all scenarios. Second, till $10R$, the models half-an-half overpredicted and underpredicted the AMI-10 whilst the increments of $I_{\mathbf{u}'_{\mathrm{rms}}}$ directed them to do more overpredictions. Third, within 6-$10R$ range, the first three models yielded the closest outcome to the AMI cases were realised as: $\{\text{Lam, Jensen, Larsen}\}_{I_{\mathbf{u}'_{\mathrm{rms}}}=10\%}$, $\{\text{Lam, Ishihara, Jensen}\}_{I_{\mathbf{u}'_{\mathrm{rms}}}=20\%}$, and $\{\text{Lam, Ishihara, Tian}\}_{I_{\mathbf{u}'_{\mathrm{rms}}}=40\%}$, respectively. After $10R$, all the models almost always made overpredictions, and produced similar rate of change of U. From this downstream location, the list of the models for the closest prediction became: $\{\text{Jensen, Bastankhah, Larsen}\}_{I_{\mathbf{u}'_{\mathrm{rms}}}=10\%}$, $\{\text{Tian, Lam, Frandsen}\}_{I_{\mathbf{u}'_{\mathrm{rms}}}=20\%}$, and $\{\text{Lam, Ishihara, Tian}\}_{I_{\mathbf{u}'_{\mathrm{rms}}}=40\%}$, respectively. Lastly, Lam et al.'s model [47] exceeded the freestream speed as can be seen between $22R$ and $24R$ far downstream.

The U-profile prediction capabilities of the models in the lateral direction were shown in Fig. 21. The figure revealed that Lam et al.'s model, Tian et al.'s model and particularly Ishihara-Qian's

model yielded considerably high level of resemblance with the AMI profiles in terms of shape and amplitude levels in each x cross sections for each $I_{\mathbf{u}'_{\mathrm{rms}}}$ input. In contrast, the remaining models either could not predict the maximum speed of the deficits or the profile trajectories. As an example, Frandsen, Larsen and Jensen models generated step profiles rather than a bell-curve.

Overall, these results indicated that Lam et al.'s model [47] performed relatively superior. This result may be explained by the fact that Lam et al.'s model was derived and calibrated based on a model-scale HAMT experiment [47, Table 1]. This finding, while preliminary, highlights the importance of the resemblance between the turbine-flow particulars at hand, and the analytical model's derivation particulars. In addition, it can be deduced that Tian et al.'s model [46] performed relatively well in the $I_{\mathbf{u}'_{\mathrm{rms}}}$=$\{20, 40\}$[%] cases, and Ishihara-Qian's model [52] for the lateral wake profile predictions. Considering both models used wind turbines in their derivations, yet performed decently for the marine turbine herein, it can be inferred that wake deficit behaviour for wind and marine turbines is likely very similar.

4. Conclusions

The main aim of this study was to explore interactions between a typical model-scale marine turbine and three-dimensional turbulence intensity in isolation by minimising other aspects of turbulence.

For this purpose, a rigid experimental horizontal axis marine turbine [24] was numerically investigated under decaying homogeneous isotropic turbulence in absence of its tower. Twelve controlled computations were carried out via wall-modelled & actuator-line-modelled implicitly-filtered large eddy simulations wherein the turbulence intensity was the control variable. Initially, with the four of the computations in which the rotor was excluded, the effects of the *arbitrary mesh interface technique* [71] and the presence of a nacelle on flow field predictions were examined (§3.2). The remaining eight computations focused on the examination of the way the three-dimensional turbulence intensity, $I_{\mathbf{u}'_{\mathrm{rms}}}$, affects the rotor and flow fields (§3.3). Therein, four turbulence intensities were considered: $I_{\mathbf{u}'_{\mathrm{rms}}}$=$\{0, 10, 20, 40\}$[%]. Lastly, twelve analytical wake models were reviewed and evaluated in comparison to the wall-modelled computations under the same range of turbulence intensities (§3.3).

Ultimately, this study has identified the following prominent pockets of knowledge:

- The arbitrary mesh interface technique (AMI) adversely affected AMI-traversing flow field's amplitude-based statistics such as mean velocity, Reynolds stress tensor, and turbulence intensity when the AMI was in rotation.
  - The rotating AMI caused flow field discontinuities on the AMI boundaries.
  - The flow field within the AMI region was differed in comparison with its surrounding to some extent, e.g. fluctuations per distance were increased within the AMI region.
  - The adverse effects were increased outwards from the AMI centre.
  - The rotating AMI did not adversely affect time-based statistics such as power spectral density functions.
  - The non-rotating AMI did not alter the flow field.
- Longitudinal mean speed field, U-field, started to be affected by the presence of the rotor approximately $4R$ upstream of the rotor.
- Maximum deviation of U-fields with respect to the freestream U_o occurred at around $2R$ downstream of the rotor irrespective of the freestream $I_{\mathbf{u}'_{\text{rms}}}$.
- Wake recovery rates in terms of wake $I_{\mathbf{u}'_{\text{rms}}}$ and wake U-field were increasing functions of freestream $I_{\mathbf{u}'_{\text{rms}}}$.
- Wake recovery rates with respect to downstream distance varied in a half-Gaussian-form irrespective of the freestream $I_{\mathbf{u}'_{\text{rms}}}$, i.e. a consecutive pattern of gradual-steep-gradual rate of change.
- Incoming U-fields with different $I_{\mathbf{u}'_{\text{rms}}}$ lost their fluctuation features towards the rotor and became indistinguishable immediately in front of it.
- Incoming U-fields with different $I_{\mathbf{u}'_{\text{rms}}}$ also became indistinguishable starting at around 6–$10R$ downstream and within the alignment of the rotor, yet almost always remained different from freestream despite turbulence entrainment.
- The effects of the rotor on each normal component of the Reynolds stress tensor were in the same manner. The rotor altered the decay rate of the components, and reduced their amplitudes in proportion to the freestream $I_{\mathbf{u}'_{\text{rms}}}$.
- Almost no significant differences were found between the wall-modelled and actuator-line modelled computations in terms of the statistics quantified in this study. An exception was that ALM with the settings being used herein usually generated more chaotic wake flow.
- The coefficient of variation, skewness, kurtosis and maxima of longitudinal forces/moments

acting on the rotor blades were quantified to be increasing functions of $I_{\mathbf{u}'_{\mathrm{rms}}}$ whereas the mean and minima were found to be inversely varying with $I_{\mathbf{u}'_{\mathrm{rms}}}$.

- The analytical wake models of Lam et al. [47], Tian et al. [46], and Ishihara-Qian [52] were quantified to be superior to the other models studied in terms of U-profile shape and amplitude predictions.

Further work needs to be carried out in the following three subjects to establish whether the concluding remarks drawn in this study are generalizable: isolated effects of *i*. the longitudinal, lateral and vertical turbulence intensities, *ii*. the integral length scales, and *iii*. cross components of the Reynolds stress tensor.

5. Acknowledgement

The authors acknowledge the use of the IRIDIS 4/5 High Performance Computing Facility, associated support services at the University of Southampton, in the completion of this work. Bercin also acknowledges the Overseas Rayleigh Studentship from the Faculty of Engineering and the Environment at the University of Southampton. The authors also wish to thank Dr. Imran Afgan from the University of Manchester for graciously providing the raw data from one of his journal papers. Lastly, the authors also thank 'StackExchange' and 'Wikipedia' communities as well as Google LLC for their immense help.

References

[1] P. Mycek, B. Gaurier, G. Germain, G. Pinon, E. Rivoalen, Experimental study of the turbulence intensity effects on marine current turbines behaviour. Part I: One single turbine, Renewable Energy 66 (2014) 729–746. doi:10.1016/j.renene.2013.12.036.

[2] I. A. Milne, R. N. Sharma, R. G. J. Flay, S. Bickerton, Characteristics of the turbulence in the flow at a tidal stream power site, Philosophical Transactions of the Royal Society A: Mathematical, Physical and Engineering Sciences 371 (1985). doi:10.1098/rsta.2012.0196.

[3] J. Thomson, B. Polagye, M. Richmond, V. Durgesh, Quantifying turbulence for tidal power applications, in: OCEANS 2010 MTS/IEEE SEATTLE, IEEE, 2010, pp. 1–8. doi:10.1109/OCEANS.2010.5664600.

[4] J. Thomson, B. Polagye, V. Durgesh, M. C. Richmond, Measurements of turbulence at two tidal energy sites in Puget Sound, WA, IEEE Journal of Oceanic Engineering 37 (3) (2012) 363–374. doi:10.1109/JOE.2012.2191656.

[5] B. Gunawan, V. S. Neary, J. Colby, Tidal energy site resource assessment in the East River tidal strait, near Roosevelt Island, New York, New York, Renewable Energy 71 (2014) 509–517. doi:10.1016/j.renene.2014.06.002.

[6] P. Jeffcoate, R. Starzmann, B. Elsaesser, S. Scholl, S. Bischoff, Field measurements of a full scale tidal turbine, International Journal of Marine Energy 12 (2015) 3–20. doi:10.1016/j.ijome.2015.04.002.

[7] Y. Li, J. A. Colby, N. Kelley, R. Thresher, B. Jonkman, S. Hughes, Inflow measurement in a tidal strait for deploying tidal current turbines: Lessons, opportunities and challenges, in: 29th International Conference on Ocean, Offshore and Arctic Engineering: Volume 3, ASME, 2010, pp. 569–576. doi:10.1115/OMAE2010-20911.

[8] R. Starzmann, I. Goebel, P. Jeffcoate, Field performance testing of a floating tidal energy platform - Part 1: Power performance, in: Proc. 4th Asian Wave and Tidal Energy Conference, Taipei, Taiwan, 2018.

[9] P. G. Novo, Y. Kyozuka, Field measurement and numerical study of tidal current turbulence intensity in the Kobe Strait of the Goto Islands, Nagasaki Prefecture, Journal of Marine Science and Technology 22 (2) (2017) 335–350. doi:10.1007/s00773-016-0414-x.

[10] M. Guerra, R. Cienfuegos, J. Thomson, L. Suarez, Tidal energy resource characterization in Chacao Channel, Chile, International Journal of Marine Energy 20 (2017) 1–16. doi:10.1016/j.ijome.2017.11.002.

[11] R. Mathis, I. Marusic, O. Cabrit, N. L. Jones, G. N. Ivey, Modeling bed shear-stress fluctuations in a shallow tidal channel, Journal of Geophysical Research: Oceans 119 (5) (2014) 3185–3199. doi:10.1002/2013JC009718.

[12] I. Afgan, J. McNaughton, S. Rolfo, D. D. Apsley, T. Stallard, P. Stansby, Turbulent flow and loading on a tidal stream turbine by LES and RANS, International Journal of Heat and Fluid Flow 43 (2013) 96–108. doi:10.1016/j.ijheatfluidflow.2013.03.010.

[13] W. Tian, J. H. VanZwieten, P. Pyakurel, Y. Li, Influences of yaw angle and turbulence intensity on the performance of a 20 kW in-stream hydrokinetic turbine, Energy 111 (2016) 104–116. doi:10.1016/j.energy.2016.05.012.

[14] F. Maganga, G. Germain, J. King, G. Pinon, E. Rivoalen, Experimental characterisation of flow effects on marine current turbine behaviour and on its wake properties, IET Renewable Power Generation 4 (6) (2010) 498. doi:10.1049/iet-rpg.2009.0205.

[15] T. Blackmore, L. E. Myers, A. S. Bahaj, Effects of turbulence on tidal turbines: Implications to performance, blade loads, and condition monitoring, International Journal of Marine Energy 14 (2016) 1–26. doi:10.1016/j.ijome.2016.04.017.

[16] T. Nishino, R. H. J. Willden, Effects of 3-D channel blockage and turbulent wake mixing on the limit of power extraction by tidal turbines, International Journal of Heat and Fluid Flow 37 (2012) 123–135. doi:10.1016/j.ijheatfluidflow.2012.05.002.

[17] J. McNaughton, S. Rolfo, D. Apsley, T. Stallard, P. Stansby, CFD power and load prediction on a 1MW tidal stream turbine with typical velocity profiles from the EMEC test site, in: Proceedings of the 10th European Wave and Tidal Energy Conference, Aalborg, Denmark, 2013.

[18] M. Togneri, I. Masters, C. Carlier, C. C. Bex, G. Pinon, Comparison of synthetic turbulence approaches for two numerical tidal turbine models, in: Proceedings of the 12th European Wave and Tidal Energy Conference, Cork, Ireland, 2017.

[19] G. N. McCann, Tidal current turbine fatigue loading sensitivity to waves and turbulence-a parametric study, in: Proceedings of the 7th European Wave and Tidal Energy Conference, Porto, Portugal, 2007.

[20] I. A. Milne, R. N. Sharma, R. G. J. Flay, S. Bickerton, The role of onset turbulence on tidal turbine blade loads, in: Proc. 17th Australasian Fluid Mechanics Conference, Auckland, NZ, 2010.

[21] P. Ouro, M. Harrold, T. Stoesser, P. Bromley, Hydrodynamic loadings on a horizontal axis tidal turbine prototype, Journal of Fluids and Structures 71 (2017) 78–95. doi:10.1016/j.jfluidstructs.2017.03.009.

[22] L. E. Myers, A. S. Bahaj, Experimental analysis of the flow field around horizontal axis tidal turbines by use of scale mesh disk rotor simulators, Ocean Engineering 37 (2-3) (2010) 218–227. doi:10.1016/j.oceaneng.2009.11.004.

[23] T. Blackmore, W. M. J. Batten, A. S. Bahaj, Influence of turbulence on the wake of a marine current turbine simulator, Proceedings of the Royal Society A: Mathematical, Physical and Engineering Sciences 470 (2170) (2014) 20140331–20140331. doi:10.1098/rspa.2014.0331.

[24] A. S. Bahaj, A. F. Molland, J. R. Chaplin, W. M. J. Batten, Power and thrust measurements of marine current turbines under various hydrodynamic flow conditions in a cavitation tunnel and a towing tank, Renewable Energy 32 (3) (2007) 407–426. doi:10.1016/j.renene.2006.01.012.

[25] L. C. Berselli, T. Iliescu, W. J. Layton, Mathematics of large eddy simulation of turbulent flows, Scientific Computation, Springer-Verlag, Berlin/Heidelberg, 2006. doi:10.1007/b137408.

[26] OpenCFD Limited, OpenFOAM: Programmer's guide (2018).
URL https://openfoam.com/

[27] U. Schumann, Subgrid scale model for finite difference simulations of turbulent flows in plane channels and annuli, Journal of Computational Physics 18 (4) (1975) 376–404. doi:10.1016/0021-9991(75)90093-5.

[28] K. M. Bercin, Z.-T. Xie, S. R. Turnock, Evaluation of digital-filter and forward-stepwise synthetic turbulence generators with large eddy simulation of three canonical flows, and various model enhancements.

[29] P. Sagaut, Large eddy simulation for incompressible flows: An introduction, 3rd Edition, Scientific computation, Springer Berlin Heidelberg, 2006. doi:10.1007/b137536.

[30] W.-W. Kim, S. Menon, A new dynamic one-equation subgrid-scale model for large eddy simulations, in: 33rd Aerospace Sciences Meeting and Exhibit, American Institute of Aeronautics and Astronautics, Reston, Virigina, 1995. doi:10.2514/6.1995-356.

[31] W.-W. Kim, S. Menon, An unsteady incompressible Navier-Stokes solver for large eddy simulation of turbulent flows, International Journal for Numerical Methods in Fluids 31 (6) (1999) 983–1017. doi:10.1002/(SICI)1097-0363(19991130)31:6<983::AID-FLD908>3.0.CO;2-Q.

[32] C. Meneveau, T. S. Lund, W. H. Cabot, A Lagrangian dynamic subgrid-scale model of turbulence, Journal of Fluid Mechanics 319 (-1) (1996) 353. doi:10.1017/S0022112096007379.

[33] M. Germano, A proposal for a redefinition of the turbulent stresses in the filtered NavierâĂŞStokes equations, Physics of Fluids 29 (7) (1986) 2323. doi:10.1063/1.865568.

[34] Z.-T. Xie, I. P. Castro, Efficient generation of inflow conditions for large eddy simulation of street-scale flows, Flow, Turbulence and Combustion 81 (3) (2008) 449–470. doi:10.1007/s10494-008-9151-5.

[35] Z.-T. Xie, I. P. Castro, Large-eddy simulation for flow and dispersion in urban streets, Atmospheric Environment 43 (13) (2009) 2174–2185. doi:10.1016/j.atmosenv.2009.01.016.

[36] Y. Kim, Z.-T. Xie, Modelling the effect of freestream turbulence on dynamic stall of wind turbine blades, Computers & Fluids 129 (2016) 53–66. doi:10.1016/j.compfluid.2016.02.004.

[37] Y. Kim, I. P. Castro, Z.-T. Xie, Divergence-free turbulence inflow conditions for large-eddy simulations with incompressible flow solvers, Computers and Fluids 84 (2013) 56–68. doi:10.1016/j.compfluid.2013.06.001.

[38] K. M. Bercin, Z.-T. Xie, S. R. Turnock, Exploration of digital-filter and forward-stepwise synthetic turbulence generators and an improvement for their skewness-kurtosis, Computers & Fluids 172 (2018) 443–466. doi:10.1016/j.compfluid.2018.03.070.

[39] G. I. Taylor, The spectrum of turbulence, Proceedings of the Royal Society A: Mathematical, Physical and Engineering Sciences 164 (919) (1938) 476–490. arXiv:arXiv:1205.0516v2, doi:10.1098/rspa.1938.0032.

[40] T. S. Lund, X. Wu, K. D. Squires, Generation of turbulent inflow data for spatially-developing boundary layer simulations, Journal of Computational Physics 140 (2) (1998) 233–258. doi:10.1006/jcph.1998.5882.

[41] N. O. Jensen, A note on wind generator interaction, Technical, Risø DTU National Laboratory for Sustainable Energy (1983).

[42] S. Frandsen, R. Barthelmie, S. Pryor, O. Rathmann, S. Larsen, J. Højstrup, M. Thøgersen, Analytical modelling of wind speed deficit in large offshore wind farms, Wind Energy 9 (1-2) (2006) 39–53. doi:10.1002/we.189.

[43] M. J. Werle, A new analytical model for wind turbine wakes, Technical, Wilbraham, MA (2008).

[44] G. C. Larsen, A simple stationary semi-analytical wake model, Technical, Technical University of Denmark (2009).

[45] M. Bastankhah, F. Porté-Agel, A new analytical model for wind-turbine wakes, Renewable Energy 70 (2014) 116–123. doi:10.1016/j.renene.2014.01.002.

[46] L. Tian, W. Zhu, W. Shen, N. Zhao, Z. Shen, Development and validation of a new two-dimensional wake model for wind turbine wakes, Journal of Wind Engineering and Industrial Aerodynamics 137 (2015) 90–99. doi:10.1016/j.jweia.2014.12.001.

[47] W.-H. Lam, L. Chen, R. Hashim, Analytical wake model of tidal current turbine, Energy 79 (2015) 512–521. doi:10.1016/j.energy.2014.11.047.

[48] A. Keane, P. E. O. Aguirre, H. Ferchland, P. Clive, D. Gallacher, An analytical model for a full wind turbine wake, Journal of Physics: Conference Series 753. doi:10.1088/1742-6596/753/3/032039.

[49] G. Xiaoxia, Y. Hongxing, L. Lin, Optimization of wind turbine layout position in a wind farm using a newly-developed two-dimensional wake model, Applied Energy 174 (2016) 192–200. doi:10.1016/j.apenergy.2016.04.098.

[50] O. A. L. Brutto, V. T. Nguyen, S. S. Guillou, J. Thiébot, H. Gualous, Tidal farm analysis using an analytical model for the flow velocity prediction in the wake of a tidal turbine with small diameter to depth ratio, Renewable Energy 99 (2016) 347–359. doi:10.1016/j.renene.2016.07.020.

[51] P. Pyakurel, W. Tian, J. H. VanZwieten, M. Dhanak, Characterization of the mean flow field in the far wake region behind ocean current turbines, Journal of Ocean Engineering and Marine Energy 3 (2) (2017) 113–123. doi:10.1007/s40722-017-0075-9.

[52] T. Ishihara, G.-W. Qian, A new Gaussian-based analytical wake model for wind turbines considering ambient turbulence intensities and thrust coefficient effects, Journal of Wind Engineering and Industrial Aerodynamics 177 (2018) 275–292. doi:10.1016/j.jweia.2018.04.010.

[53] B. Sanderse, S. P. Van Der Pijl, B. Koren, Review of computational fluid dynamics for wind turbine wake aerodynamics, Wind Energy 14 (7) (2011) 799–819. doi:10.1002/we.458.

[54] A. Bahaj, L. Myers, Shaping array design of marine current energy converters through scaled experimental analysis, Energy 59 (2013) 83–94. doi:10.1016/j.energy.2013.07.023.

[55] Metals4u Ltd, 6082/ 6082T Aluminium (2016).
URL http://bit.ly/2ci7dHf

[56] F. Baratchi, T. L. Jeans, A. G. Gerber, Actuator line simulation of a tidal turbine in straight and yawed flows, International Journal of Marine Energy 19 (2017) 235–255. doi:10.1016/j.ijome.2017.08.003.

[57] X. Bai, E. J. Avital, A. Munjiza, J. J. R. Williams, Numerical simulation of a three blade marine current turbine, in: M. Piasecki (Ed.), 11th International Conference on Hydroinformatics HIC 2014, New York City, USA, 2014.

[58] X. Bai, E. Avital, A. Munjiza, J. Williams, Numerical simulation of a marine current turbine in free surface flow, Renewable Energy 63 (2014) 715–723. doi:10.1016/j.renene.2013.09.042.

[59] Q. Guo, L. J. Zhou, Y. X. Xiao, Z. W. Wang, Flow field characteristics analysis of a horizontal axis marine current turbine by large eddy simulation, IOP Conference Series: Materials Science and Engineering 52 (5) (2013) 052017. doi:10.1088/1757-899X/52/5/052017.

[60] T. P. Lloyd, S. R. Turnock, V. F. Humphrey, Assessing the influence of inflow turbulence on noise and performance of a tidal turbine using large eddy simulations, Renewable Energy 71 (2014) 742–754. doi:10.1016/j.renene.2014.06.011.

[61] J. Banks, K. M. Bercin, T. P. Lloyd, S. R. Turnock, Fluid structure interaction analyses of tidal turbines, in: 16th Numerical Towing Tanks Symposium 16th Numerical Towing Tanks Symposium, Germany. 02 - 04 Sep 2013, 2013.
URL https://eprints.soton.ac.uk/359259/

[62] J. McNaughton, I. Afgan, D. D. Apsley, S. Rolfo, T. Stallard, P. K. Stansby, A simple sliding-mesh interface procedure and its application to the CFD simulation of a tidal-stream turbine, International Journal for Numerical Methods in Fluids 74 (4) (2014) 250–269. doi:10.1002/fld.3849.

[63] R. Carmichael, Algorithm for calculating coordinates of cambered NACA airfoils at specified chord locations, in: 1st AIAA, Aircraft, Technology Integration, and Operations Forum, American Institute of Aeronautics and Astronautics, Reston, Virigina, 2001. doi:10.2514/6.2001-5235.

[64] A. F. Molland, A. S. Bahaj, J. R. Chaplin, W. M. J. Batten, Measurements and predictions of forces, pressures and cavitation on 2-D sections suitable for marine current turbines, Proceedings of the Institution of Mechanical Engineers, Part M: Journal of Engineering for the Maritime Environment 218 (2) (2004) 127–138. doi:10.1243/1475090041651412.

[65] R. Carmichael, NACA456 Program (2017).
URL http://www.pdas.com/

[66] A. S. Bahaj, W. M. J. Batten, A. F. Molland, J. R. Chaplin, Experimental investigation into the hydrodynamic performance of marine current turbines, Tech. rep., University of Southampton, Southampton, the United Kingdom (2005).

[67] D. Marten, J. Wendler, G. Pechlivanoglou, C. N. Nayeri, C. O. Paschereit, QBlade: An open source tool for design and simulation of horizontal and vertical axis wind turbines, International Journal of Emerging Technology and Advanced Engineering 3 (3) (2013) 264–269.

[68] Dassault Systèmes SolidWorks Corporation, SolidWorks 2017 (2017).
URL https://www.solidworks.com/

[69] OPEN CASCADE, SALOME 8.4.0 (2017).
URL http://www.salome-platform.org

[70] ISTI, CNR, MeshLab (2017).
URL http://www.meshlab.net

[71] P. E. Farrell, J. R. Maddison, Conservative interpolation between volume meshes by local Galerkin projection, Computer Methods in Applied Mechanics and Engineering 200 (1-4) (2011) 89–100. doi:10.1016/j.cma.2010.07.015.

[72] P. E. Farrell, M. D. Piggott, C. C. Pain, G. J. Gorman, C. R. Wilson, Conservative interpolation between unstructured meshes via supermesh construction, Computer Methods in Applied Mechanics and Engineering 198 (33-36) (2009) 2632–2642. doi:10.1016/j.cma.2009.03.004.

[73] H. R. Hiester, M. D. Piggott, P. A. Allison, The impact of mesh adaptivity on the gravity current front speed in a two-dimensional lock-exchange, Ocean Modelling 38 (1-2) (2011) 1–21. doi:10.1016/j.ocemod.2011.01.003.

[74] R. E. Bensow, Simulation of unsteady propeller loads using OpenFOAM, in: Proceedings of the 16th Numerical Towing Tank Symposium, 2-4 September, Mülheim, 2013.

[75] T. P. Lloyd, Large eddy simulations of inflow turbulence noise: Application to tidal turbines, Phd, University of Southampton (2013).

[76] H. Choi, P. Moin, Grid-point requirements for large eddy simulation: Chapman's estimates revisited, Physics of Fluids 24 (011702). doi:10.1063/1.3676783.

[77] U. Piomelli, Wall-layer models for large-eddy simulations, Progress in Aerospace Sciences 44 (6) (2008) 437–446. doi:10.1016/j.paerosci.2008.06.001.

[78] R. Örlü, J. H. M. Fransson, P. Henrik Alfredsson, On near wall measurements of wall bounded flows - The necessity of an accurate determination of the wall position, Progress in Aerospace Sciences 46 (8) (2010) 353–387. doi:10.1016/j.paerosci.2010.04.002.

[79] J. Larsson, S. Kawai, J. Bodart, I. Bermejo-Moreno, Large eddy simulation with modeled wall-stress: recent progress and future directions, Mechanical Engineering Reviews 3 (1) (2016) 15–00418–15–00418. doi:10.1299/mer.15-00418.

[80] F. R. Menter, Best practice: Scale-resolving simulations in ANSYS CFD, Technical report (2015).

[81] F. Menter, J. C. Ferreira, T. Esch, B. Konno, The SST turbulance model with improved wall treatment for heat transfer predictions in gas turbines, in: Proc. Int. Gas Turbine Congress, Tokyo, Nov. 2âĂŞ7. IGTC2003-TS-059, 2003, pp. 2–7.

[82] H. K. Versteeg, W. Malalasekera, An introduction to computational fluid dynamics: The finite volume method, 2nd Edition, Pearson Education Ltd, 2007.

[83] J. N. Sørensen, W. Z. Shen, Computation of wind turbine wakes using combined Navier-Stokes/actuator-line methodology, in: E. L. Petersen (Ed.), 1999 European Wind Energy Conference: Wind Energy for the Next Millennium, Nice, France, 1999, pp. 156 – 159.
URL http://bit.ly/1DR9srh

[84] R. Mikkelsen, Actuator disc methods applied to wind turbines, Phd, Technical University of Denmark (2003).

[85] M. J. Churchfield, S. Lee, J. Michalakes, P. J. Moriarty, A numerical study of the effects of atmospheric and wake turbulence on wind turbine dynamics, Journal of Turbulence 13 (14) (2012) 1–32. doi:10.1080/14685248.2012.668191.

[86] R. I. Issa, Solution of the implicitly discretised fluid flow equations by operator-splitting, Journal of Computational Physics 62 (1) (1986) 40–65. arXiv:9809069v1, doi:10.1016/0021-9991(86)90099-9.

[87] J. Mencinger, I. Žun, On the finite volume discretization of discontinuous body force field on collocated grid: Application to VOF method, Journal of Computational Physics 221 (2) (2007) 524–538. doi:10.1016/j.jcp.2006.06.021.

[88] C. M. Rhie, W. L. Chow, Numerical study of the turbulent flow past an airfoil with trailing edge separation, AIAA Journal 21 (11) (1983) 1525–1532. doi:10.2514/3.8284.

[89] J. N. Sørensen, W. Z. Shen, Numerical modeling of wind turbine wakes, Journal of Fluids Engineering 124 (2) (2002) 393. doi:10.1115/1.1471361.

[90] P.-E. Réthoré, N. N. Sørensen, A discrete force allocation algorithm for modelling wind turbines in computational fluid dynamics, Wind Energy 15 (7) (2012) 915–926. doi:10.1002/we.525.

[91] N. Troldborg, N. N. Sørensen, P.-E. Réthoré, M. P. van der Laan, A consistent method for finite volume discretization of body forces on collocated grids applied to flow through an actuator disk, Computers & Fluids 119 (2015) 197–203. doi:10.1016/j.compfluid.2015.06.028.

[92] J. Schluntz, R. H. J. Willden, An actuator line method with novel blade flow field coupling based on potential flow equivalence, Wind Energy 18 (8) (2015) 1469–1485. doi:10.1002/we.1770.

[93] M. Shives, C. Crawford, Mesh and load distribution requirements for actuator line CFD simulations, Wind Energy 16 (8) (2012) 1183–1196. doi:10.1002/we.1546.

[94] P. K. Jha, M. J. Churchfield, P. J. Moriarty, S. Schmitz, Guidelines for volume force distributions within actuator line modeling of wind turbines on large-eddy simulation-type grids, Journal of Solar Energy Engineering 136 (3). doi:10.1115/1.4026252.

[95] M. J. Churchfield, J. Laursen, A. Loeven, S. Lee, P. J. Moriarty, A comparison between wind turbine aerodynamics model output when using generic versus actual turbine characterization as input, in: 51st AIAA Aerospace Sciences Meeting including the New Horizons Forum and Aerospace Exposition 2013, American Institute for Aeronautics and Astronautics, Grapevine, Texas, 2013.

[96] L. A. Martínez-Tossas, S. Leonardi, Wind turbine modeling for computational fluid dynamics, Technical, National Renewable Energy Laboratory (NREL), Golden, CO, USA (2013). doi:10.2172/1089598.

[97] L. A. Martínez-Tossas, M. J. Churchfield, S. Leonardi, Large eddy simulations of the flow past wind turbines: Actuator line and disk modeling, Wind Energy 18 (6) (2015) 1047–1060. doi:10.1002/we.1747.

[98] S. Ivanell, R. Mikkelsen, J. N. Sørensen, D. Henningson, Validation of methods using EllipSys3D, Technical (2008).

[99] M. Draper, G. Usera, Evaluation of the actuator line model with coarse resolutions, Journal of Physics: Conference Series 625. doi:10.1088/1742-6596/625/1/012021.

[100] N. Troldborg, Actuator line modeling of wind turbine wakes, Phd, Technical University of Denmark (2008).

[101] H. Glauert, Airplane propellers, in: Aerodynamic Theory, Springer Berlin Heidelberg, Berlin, Heidelberg, 1935, pp. 169–360. doi:10.1007/978-3-642-91487-4_3.

[102] S. Xie, C. Archer, Self-similarity and turbulence characteristics of wind turbine wakes via large-eddy simulation, Wind Energy 18 (10) (2015) 1815–1838. doi:10.1002/we.1792.

[103] T. Burton, N. Jenkins, D. Sharpe, E. Bossanyi, Wind energy handbook, 2nd Edition, John Wiley & Sons, Ltd, Chichester, The United Kingdom, 2011. doi:10.1002/9781119992714.

[104] M. Drela, XFOIL: An analysis and design system for low Reynolds number airfoils, in: Low Reynolds number aerodynamics, Vol. 54, 1989, pp. 1–12. doi:10.1007/978-3-642-84010-4_1.

[105] L. C. Nguyen, The NASA aircraft noise prediction program improved propeller analysis system, Technical report (1991).

[106] H. Snel, R. Houwink, J. Bosschers, W. J. Piers, G. J. W. v. Bussel, A. Bruining, Sectional prediction of 3-D effects for stalled flow on rotating blades and comparison with measurements, Technical, ECN (1993).

[107] C. Lindenburg, Investigation into rotor blade aerodynamics, Technical, ECN, Petten, Netherlands (2003).
URL http://bit.ly/2cPgsmU

[108] A. J. Eggers, R. Digumarthi, Approximate scaling of rotational effects on mean aerodynamic moments and power generated by CER blades operating in deep-stalled flow, in: 11th ASME Wind Energy Symposium, 1992, pp. 33–43.

[109] B. Montgomerie, Methods for root effects, tip effects and extending the angle of attack range to +-100 degree, with application to aerodynamics for blades on wind turbines and propellers, Technical, Swedish Defence Research Agency, Stockholm (2004).

[110] S. Goldstein, On the vortex theory of screw propellers, Proceedings of the Royal Society A: Mathematical, Physical and Engineering Sciences 123 (792) (1929) 440–465. doi:10.1098/rspa.1929.0078.

[111] L. Martinez, S. Leonardi, M. Churchfield, P. Moriarty, A comparison of actuator disk and actuator line wind turbine models and best practices for their use, in: 50th AIAA Aerospace Sciences Meeting including the New Horizons Forum and Aerospace Exposition, American Institute of Aeronautics and Astronautics, Reston, Virgina, 2012. doi:10.2514/6.2012-900.

[112] M. J. Churchfield, S. Lee, P. Moriarty, Overview of the simulator for offshore wind farm application SOWFA (2012).
URL http://bit.ly/2cOosU3

[113] M. Shives, C. Crawford, Adapted two-equation turbulence closures for actuator disk RANS simulations of wind & tidal turbine wakes, Renewable Energy 92 (2016) 273–292. doi:10.1016/j.renene.2016.02.026.

[114] J. Franke, C. Hirsch, A. G. Jensen, H. W. Krüs, M. Schatzmann, P. S. Westbury, S. D. Miles, J. A. Wisse, N. G. Wright, P. S. Westbury, J. A. Wisse, N. G. Wright, Recommendations on the use of CFD in wind engineering, in: J. P. A. J. van Beeck (Ed.), COST Action C14, Impact of Wind and Storm on City Life Built Environment. Proceedings of the International Conference on Urban Wind Engineering and Building Aerodynamics, 5âĂŞ7 May 2004, von Karman Institute, Sint-Genesius-Rode, Belgium, 2004, pp. 1–11.
URL http://bit.ly/2csTlhc

[115] R. M. Cummings, J. R. Forsythe, S. A. Morton, K. D. Squires, Computational challenges in high angle of attack flow prediction, Progress in Aerospace Sciences 39 (5) (2003) 369–384. doi:10.1016/S0376-0421(03)00041-1.

[116] P. Spalart, Trends in turbulence treatments, in: Fluids 2000 Conference and Exhibit, American Institute of Aeronautics and Astronautics, Reston, Virigina, 2000. doi:10.2514/6.2000-2306.

[117] Y. Tominaga, A. Mochida, R. Yoshie, H. Kataoka, T. Nozu, M. Yoshikawa, T. Shirasawa, AIJ guidelines for practical applications of CFD to pedestrian wind environment around buildings, Journal of Wind Engineering and Industrial Aerodynamics 96 (10-11) (2008) 1749–1761. doi:10.1016/j.jweia.2008.02.058.

[118] B. Blocken, Computational fluid dynamics for urban physics: Importance, scales, possibilities, limitations and ten tips and tricks towards accurate and reliable simulations, Building and Environment 91 (2015) 219–245. doi:10.1016/j.buildenv.2015.02.015.

[119] A. Jackson, A comprehensive tour of snappyHexMesh (2012).
URL http://bit.ly/2cBilA5

[120] C. J. Greenshields, OpenFOAM 2.3.0: Arbitrary mesh interface: Non-conforming AMI patches (2014).
URL https://openfoam.org/release/2-3-0/non-conforming-ami/

[121] Y. Liu, O. Hinrichsen, CFD modeling of bubbling fluidized beds using OpenFOAM®: Model validation and comparison of TVD differencing schemes, Computers & Chemical Engineering 69 (2014) 75–88. doi:10.1016/j.compchemeng.2014.07.002.

[122] F. Pellegrini, PT-Scotch and libScotch 5.1 user's guide (2010).

[123] S. B. Pope, Turbulent flows, Cambridge University Press, 2000.

[124] I. Celik, Z. N. Cehreli, I. Yavuz, Index of resolution quality for large eddy simulations, Journal of Fluids Engineering 127 (5) (2005) 949. doi:10.1115/1.1990201.

[125] A. Rohatgi, WebPlotDigitizer (2018).
URL https://automeris.io/WebPlotDigitizer

[126] D. Medici, S. Ivanell, J. Å. Dahlberg, P. H. Alfredsson, The upstream flow of a wind turbine: blockage effect, Wind Energy 14 (5) (2011) 691–697. doi:10.1002/we.451.

[127] W.-H. Cai, F.-C. Li, H.-N. Zhang, DNS study of decaying homogeneous isotropic turbulence with polymer additives, Journal of Fluid Mechanics 665 (2010) 334–356. doi:10.1017/S0022112010003939.

[128] I. Katic, J. Højstrup, N. O. Jensen, A simple model for cluster efficiency, in: W. Palz, E. Sesto (Eds.), EWEC'86, Rome: A. Raguzzi, 1986.

[129] M. L. Thøgersen, T. Sørensen, P. Nielsen, A. Grötzner, S. Chun, WindPRO/PARK: Introduction to wind turbine wake modelling and wake generated turbulence, Tech. rep. (2011).
URL https://bit.ly/2MW7i9r

[130] A. Peña, P.-E. Réthoré, M. P. van der Laan, On the application of the Jensen wake model using a turbulence-dependent wake decay coefficient: the Sexbierum case, Wind Energy 19 (4) (2016) 763–776. doi:10.1002/we.1863.

[131] A. Niayifar, F. Porté-Agel, Analytical modeling of wind farms: A new approach for power prediction, Energies 9 (9) (2016) 741. doi:10.3390/en9090741.

[132] S. Frandsen, L. Chacon, A. Crespo, P. Enevoldsen, R. Gomez-Elvira, J. Hernandez, J. Hojstrup, F. Manuel, K. Thomsen, P. Sorensen, Measurements on and modelling of offshore wind farms, Tech. rep., Risø National Laboratory (1996).

[133] A. F. Molland, S. R. Turnock, D. A. Hudson, Numerical methods for propeller analysis, in: Ship Resistance and Propulsion, Cambridge University Press, Cambridge, 2011, pp. 337–368. doi:10.1017/CBO9780511974113.018.

[134] W. Z. Shen, R. Mikkelsen, J. N. Sørensen, C. Bak, Tip loss corrections for wind turbine computations, Wind Energy 8 (4) (2005) 457–475. doi:10.1002/we.153.

[135] F. Moukalled, L. Mangani, M. Darwish, The finite volume method in computational fluid dynamics, Vol. 113 of Fluid Mechanics and Its Applications, Springer International Publishing, 2016. doi:10.1007/978-3-319-16874-6.

[136] S. Ghosal, An analysis of numerical errors in large-eddy simulations of turbulence, Journal of Computational Physics 125 (1) (1996) 187–206. doi:10.1006/jcph.1996.0088.

[137] N. J. Georgiadis, D. Rizzetta, C. Fureby, Large-eddy simulation: Current capabilities, recommended practices, and future research, AIAA Journal 48 (July) (2010) 1772–1784. doi:10.2514/1.J050232.

[138] OpenCFD Limited, Advanced course: Version 2.1.x (2012).

[139] P. K. Sweby, High resolution schemes using flux limiters for hyperbolic conservation laws, SIAM Journal on Numerical Analysis 21 (5) (1984) 995–1011. doi:10.1137/0721062.

[140] H. Jasak, Error analysis and estimation for the finite volume method with applications to fluid flows, Phd thesis, Imperial College (1996).
URL http://bit.ly/1pXhegn

Appendix A. Appendix

Appendix A.1. Menter et al.'s wall model algorithm

Input: ν_t, ν_b, $(\nabla_{\mathbf{n}}\mathbf{u})_b$, y, U, N_b
Output: $u_{\tau,\text{final}}$
for $i = 0, \ldots, N_b$ **do**
  $u_\tau = (((\nu_t)_i + (\nu_b)_i)\,|(\nabla_{\mathbf{n}}\mathbf{u})_b|_i)^{0.5}$
  if $|u_\tau > \xi|$ **then**
    ϵ=GREAT
    j=0
    while j<10 and ϵ>0.001 **do**
      $y^+ = \frac{y_i\, u_\tau}{(\nu_b)_i}$
      $u_{\tau,\text{vis}} = \frac{U_i}{y^+}$
      $u_{\tau,\log} = \frac{\kappa\, U_i}{\log(\mathrm{E}\, y^+)}$
      $u_{\tau,\text{new}} = (u^n_{\tau,\text{vis}} + u^n_{\tau,\log})^{n^{-1}}$
      $\epsilon = \frac{|u_\tau - u_{\tau,\text{new}}|}{u_\tau + \xi}$
      $u_\tau = 0.5\,(u_\tau + u_{\tau,\text{new}})$
    end
  end
  $(u_{\tau,\text{final}})_i = u_\tau$
end

Algorithm 1: Menter et al.'s [81] wall model algorithm [26]. u_τ is the friction velocity [ms^{-1}], N_b number of grid faces on the corresponding boundary, ν_t turbulent kinematic viscosity on the boundary [m^{2}s^{-1}], ν_b fluid kinematic viscosity on the boundary, $(\nabla_{\mathbf{n}}\mathbf{u})_b$ velocity gradient normal to the boundary [s^{-1}], ξ the smallest floating-point value, GREAT inverse of the machine epsilon, ϵ an error parameter, y wall-normal distance of the first off-the-wall node [m], $u_{\tau,\text{vis}}$ and $u_{\tau,\log}$ respectively the model contributions from the viscous sub-layer and logarithmic law equations, n=4 a model coefficient, U magnitude of the planar velocity of first off-the-wall node (i.e. the wall-normal component is converted to zero) [ms^{-1}], κ=0.41 von Kármán's constant, and E=9.8 a wall roughness parameter for smooth walls.

Appendix A.2. Analytical wake models

In the pages that follow, twelve non-yawed horizontal-axis-turbine analytical wake models from the literature were chronologically presented: i.e. [41–52]. The models were viewed as black boxes; hence, only their explicit formulae were presented alongside with the fundamental theory and major building-block assumptions that their derivations are based upon. All the models share the following notations and assumptions: x represents the horizontal distance to the rotor plane, r the radial

distance to the hub centreline, u_w the longitudinal (i.e. no lateral component) wake speed, u_f the longitudinal mean freestream speed, C_T the rotor thrust coefficient, D the rotor diameter, D_w the wake diameter, R the rotor radius, R_w the wake radius, $A \equiv \pi R^2$ the rotor area, and $I_a \equiv u_{rms}\, u_f^{-1}$ the ambient turbulence intensity [-] with $u_{rms} \equiv (3^{-1}(\overline{u_x'^2}+\overline{u_y'^2}+\overline{u_z'^2}))^{0.5}$ the root-mean-square of fluctuations. As common assumptions in the models, the predicted flow dynamics is time-invariant, and inflow is longitudinally and radially-uniform.

Appendix A.2.1. Jensen's model

The basis [41]: Mass conservation [45, p. 117] rather than momentum conservation as stated in [41, p. 5].

Prominent assumptions: [41, Fig. 1], *i*. Constant wake speed in the radial direction, *ii*. linear and free wake expansion [41, p. 5, 8], *iii*. no near-wake region [41, p. 5], and *iv*. immediate wake diameter is equal to D [128, p. 408].

Governing equations [41, Eq. 2, Fig. 1]:

$$u_w(x) = u_f \left\{ 1\text{-}2a \left(\frac{R}{R+\beta x} \right)^2 \right\} \quad \text{and} \quad R_w(x) = R+\beta x \tag{A.1}$$

where a is the axial induction factor [-] presumed to be equal to $0.5(1\text{-}(1\text{-}C_T)^{0.5})$ [128, p. 408], and β the wake-decay constant whose value was variously estimated as, for instance, 0.04-0.075 [129, p. A-3] or $0.4\sigma_{u_{hub}}/u_{hub}$ [130, Eq. 6], and u_{hub} the hub height instantaneous longitudinal inflow speed.

Appendix A.2.2. Frandsen's model

The basis [42]: Mass and momentum conservation in a cylinder control volume [42, p. 40-41, Eq. 1].

Prominent assumptions: *i*. Axisymmetric, self-similar, and immediately expanding wake [42, p. 41, 42].

Governing equations [42, Eq. 11, 13]:

$$u_w(x) = u_f \left\{ 0.5 + 0.5(1\text{-}2A\, A_w^{-1} C_T)^{0.5} \right\} \quad \text{and} \quad D_w(x) = D(\beta^{k/2}+\alpha x D^{-1})^{1/k} \tag{A.2}$$

where $A_w(x)=0.25\pi D_w^2$ is the wake cross-section area, β a parameter governing the initial wake

expansion rate as β=0.5(1+(1-C_T)$^{0.5}$)(1-C_T)$^{-0.5}$ [42, Eq. 10], k a factor for the wake expansion order - by default k=2 [42, p. 43], and α a constant to be evaluated experimentally [42, p. 43], yet can be estimated as α=$\beta^{k/2}$[(1+2$\alpha_n x$D^{-1})^k-1]Dx^{-1} with α_n≈0.05 [42, Eq. 15].

Appendix A.2.3. Werle's model

The basis [43]: Biot-Savart law, Prandtl's turbulent shear layer model, and Prandtl-Swain's axisymmetric wake analysis for near-, intermediate-, and far-wake regions, which are interlinked, respectively.

Prominent assumptions: *i*. Axisymmetric wake [43, p. 6], and *ii*. distinct assumptions-derivations valid for near-, intermediate- and far-wake regions.

Governing equations [43, Eq. 11a, 11b, 12a, 12b]:

$$u_w = \begin{cases} 1+0.5(1-u_\infty)\left\{1+2x(1+4x^2)^{-0.5}\right\} & \text{if } x<x_m \\ 1-(1-u_m)\left\{(x-x_m)(2-2u_m)^{1.5}C_T^{-0.5}+1\right\}^{-2/3} & \text{if } x>x_m \end{cases} \tag{A.3}$$

$$D_w = \begin{cases} D\left\{0.5(1+u_\infty)u_w^{-1}\right\}^{0.5} & \text{if } x<x_m \\ D_m\left\{C_T(x-x_m)(D_m D^{-1})^{-3}+1\right\}^{1/3} & \text{if } x>x_m \end{cases} \tag{A.4}$$

where $\{\cdot\}_m$ is a subscript that denotes the downstream location, x_m, where the near-wake sub-model is coupled with the far-wake sub-model, x_m=x_i+k_mD$_\infty$(1+u_∞)D^{-1}(1-u_∞)$^{-1}$ the location of the coupling [43, Eq. 10], x_i the outset location of the intermediate wake region assumed to be 2.0 [43, p. 6], k_m a model variable [43, p. 6] with a possible value 0.1, D$_\infty$=D$\left\{0.5(1+u_\infty)u_\infty^{-1}\right\}^{0.5}$ the wake diameter at the downstream infinity [43, Eq. 2b], u_∞=(1-C_T)$^{0.5}$ the non-dimensional flow speed at the downstream infinity [43, Eq. 4a], u_m=1+0.5(1-u_∞)$\left\{1+2x_m(1+4x_m^2)^{-0.5}\right\}$ the centreline flow speed at the location m [43, Eq. 11c], and D$_m$=D$\left(0.5(1+u_\infty)u_m^{-1}\right)^{0.5}$ [43, Eq. 12c].

Appendix A.2.4. Larsen's model

The basis [44]: Incompressible, homogeneous, thin shear layer approximated Navier-Stokes equations [44, p. 7-8].

Prominent assumptions: *i*. Axisymmetric [44, p. 7] and self-similar [44, p. 8] wake, *ii*. empirical boundary conditions [44, p. 8-9], *iii*. the model is a summation of a first-order and second-order approximations; however, the latter contribution is neglected with a justification that it is not of

importance for power farm computations.

Governing equations [44, Eq. 11, 3]:

$$u_w(x,r) = -u_f\, 9^{-1} \left\{ \mathrm{C_T} A (x+x_o)^{-2} \right\}^{1/3} \left[r^{1.5} \left\{ 3c_1^2 \mathrm{C_T} A (x+x_o) \right\}^{-0.5} - (35(2\pi)^{-1})^{3/10} (3c_1^2)^{-0.2} \right]^2 \quad \text{(A.5)}$$

$$\mathrm{R}_w(x) = \left\{ 105 c_1^2 (2\pi)^{-1} \right\}^{0.2} \left\{ \mathrm{C_T} A (x+x_o) \right\}^{1/3} \quad \text{(A.6)}$$

where x_o is a parameter defined as x_o=9.6D$\{(2\mathrm{R}_{9.6}(k\mathrm{D})^{-1})^3-1\}^{-1}$ [44, Eq. 5], c_1 another parameter as c_1=$(0.5k\mathrm{D})^{2.5}\{105(2\pi)^{-1}\}^{-0.5}(\mathrm{C_T} A x_o)^{-5/6}$ [44, Eq. 6], k=$(0.5(m+1))^{0.5}$ [44, Eq. 7], m=$(1-\mathrm{C_T})^{-0.5}$ [44, Eq. 8], and $\mathrm{R}_{9.6}$ the 9.6D downstream wake radius which was empirically approximated as:

$$\mathrm{R}_{9.6} = a_1 \exp(a_2 \mathrm{C_T^2} + a_3 \mathrm{C_T} + a_4)(b_1 I_a + 1)\mathrm{D} \quad \text{(A.7)}$$

with a_1=0.435449861, a_2=0.797853685, a_3=-0.124807893, a_4=0.136821858, and b_1=15.6298 [44, Eq. 10].

Appendix A.2.5. Bastankhah-Porté-Agel's model

The basis [45]: Mass and momentum conservation [45, p. 118].

Prominent assumptions: *i*. Gaussian-form wake in the radial direction [45, p. 118], *ii*. linear wake expansion [45, p. 118], and *iii*. axisymmetric, self-similar wake [45, p. 118].

Governing equations [45, Eq. 23]:

$$\begin{aligned} u_w(x,y,z) = u_f - u_f \left(1 - \left\{ 1 - 0.125 \mathrm{C_T} (k^* x \mathrm{D}^{-1} + 0.2\beta^{0.5})^{-2} \right\}^{0.5} \right) \\ \exp\left(-0.5 (k^* x \mathrm{D}^{-1} + 0.2\beta^{0.5})^{-2} \left\{ (z-z_h)^2 \mathrm{D}^{-2} + y^2 \mathrm{D}^{-2} \right\} \right) \end{aligned} \quad \text{(A.8)}$$

where k^* signifies the wake growth rate for which a relation was given by [131, Eq. 15] as k^*=0.3837 I_a +0.003678 for 0.065<I_a<0.15, β=0.5 $\left\{1+(1-\mathrm{C_T})^{0.5}\right\}$ $(1-\mathrm{C_T})^{-0.5}$ [45, Eq. 6], and z_h the hub height [45, p. 118].

Appendix A.2.6. Tian et al.'s model

The basis [46]: Jensen's model [46, p. 91].

Prominent assumptions: *i*. Cosine-form wake in the radial direction [46, p. 91], and *ii*. a heuristic relation between the wake turbulence intensity and x, $\mathrm{C_T}$, I_a [46, p. 92].

Governing equations [46, Eq. 10]:

$$u_w(x,r) = (u_f - u_\mathrm{J})\cos[\pi\, r\, \mathrm{R}_\mathrm{J}^{-1} + \pi] + u_\mathrm{J} \tag{A.9}$$

where u_J and $\mathrm{R}_\mathrm{J}^{-1}$ are respectively the wake deficit speed and diameter from the original Jensen's model computed by a new expression for its β_J as $\beta_\mathrm{new}=(k_n\, \mathrm{C_T}\, \mathrm{D}\, x^{-1}+I_a)\beta_\mathrm{J} I_a^{-1}$ [46, Eq. 14, 15], and k_n a constant $k_n \leq 0.4$ [132, p. 7].

Appendix A.2.7. Lam et al.'s model

The basis [47]: Ship propeller jet theory and axial momentum theory [47, p. 512].

Prominent assumptions: *i*. Gaussian-form wake in the radial direction [47, p. 515], and *ii*. the final form of the model heavily rely on measurements from *a* particular turbine.

Governing equations [47, Table 4]:

$$u_{w,\min}(x) = \begin{cases} u_e(0.0106x\mathrm{D}^{-1}+1.0351) & \text{if } x\mathrm{D}^{-1}\leq 4 \text{ and } I_a=3\% \\ u_e(0.1505x\mathrm{D}^{-1}+0.8597) & \text{if } x\mathrm{D}^{-1}\leq 4 \text{ and } I_a=15\% \\ u_e(0.1123x\mathrm{D}^{-1}+0.5826) & \text{if } x\mathrm{D}^{-1}>4 \text{ and } I_a=3\% \\ u_e(0.0372x\mathrm{D}^{-1}+1.4085) & \text{if } x\mathrm{D}^{-1}>4 \text{ and } I_a=15\% \end{cases} \tag{A.10}$$

where $u_e=u_f(1-\mathrm{C_T})^{0.5}$ [47, Table 4] is the *efflux speed*, which is the minimum speed of lee flow adjacent to the rotor [47, p. 513]. The radial distribution of the wake deficit, $u_w(x,r)$, is defined as $u_w=u_f-(u_f-u_{w,\min})\exp(\mathfrak{A})$ with $\mathfrak{A}(x,r)$:

$$\mathfrak{A}(x,r) = \begin{cases} -0.5\left\{(r-\mathrm{R_{mo}})\,(0.5\mathrm{R_{mo}}+0.065(x-\mathrm{R}))^{-1}\right\}^2 & \text{if } 1.2\mathrm{D}<x\leq 3.0\mathrm{D} \text{ and } I_a=3\% \\ -0.5\left\{r\,(0.5\mathrm{R_{mo}}+0.095(x-\mathrm{R}))^{-1}\right\}^2 & \text{if } 1.2\mathrm{D}<x\leq 3.0\mathrm{D} \text{ and } I_a=15\% \\ -0.5\left\{r\,(0.065(x-\mathrm{R}))^{-1}\right\}^2 & \text{if } x>3.0\mathrm{D} \text{ and } I_a=3\% \\ -0.5\left\{r\,(0.095(x-\mathrm{R}))^{-1}\right\}^2 & \text{if } x>3.0\mathrm{D} \text{ and } I_a=15\% \end{cases} \tag{A.11}$$

where $\mathrm{R_{mo}}=0.067(\mathrm{R}-\mathrm{R}_h)$ the radial location of the efflux speed [47, Table 4], and R_h the hub radius.

Appendix A.2.8. Lo Brutto et al.'s model

The basis [50]: Jensen's model [50, p. 347].

Prominent assumptions: *i*. Exponential-form wake expansion [50, p. 356], *ii*. Gaussian-form wake in the radial direction [50, p. 357]

Governing equations [50, Eq. 9]:

$$\mathrm{R}_w(x) = \mathrm{R}\, c\, \{5.58(1 - \exp[-0.051 x\, \mathrm{D}^{-1}]) + 1.2\} \tag{A.12}$$

with $c(I_a) = -15.542 I_a^2 + 21.361 I_a + 0.2184$ [50, Eq. 11].

Appendix A.2.9. Xiaoxia et al.'s model

The basis [49]: Jensen's and Tian et al.'s models.

Prominent assumptions: *i*. Gaussian-form wake in the radial direction [49, p. 193].

Governing equations [49, Eq. 12]:

$$u_w(x, r) = u_f - 5.16\, (u_f - u_\mathrm{J})\, (2\pi)^{-0.5} \exp[-0.5\, r^2\, (\mathrm{R}_w/2.58)^{-2}] \tag{A.13}$$

where the notations stated for Tian et al.'s model Appendix A.2.6 can be directly used except $\beta_\mathrm{new} = (k_n\, \mathrm{C_T}\, (x\mathrm{D}^{-1})^{-0.5} + I_a^{0.5})^2 \beta_\mathrm{J} I_a^{-1}$.

Appendix A.2.10. Keane et al.'s model

The basis [48]: Mass and momentum conservation with respect to the actuator disk theory, Jensen's and Bastankhah-Porté-Agel's models [48, p. 1].

Prominent assumptions: *i*. Double-Gaussian-form wake in the radial direction [48, p. 1].

Governing equations [48, Eq. 22, 15, 5, 13]:

$$u_w(x, r) = u_f\, \{1 - c\, F(x)\, f(r, \sigma(x))\} \tag{A.14a}$$

$$F(x) = \lambda + (\lambda^2 - 0.5 \psi \mathrm{C_T} \mathrm{D}^2)^{0.5}\, (2\psi)^{-1} \tag{A.14b}$$

$$f(r, \sigma(x)) = 0.5\{\exp(E_+) + \exp(E_-)\} \tag{A.14c}$$

$$\lambda = 2\sigma^2 \exp(-0.5\tau^2) + (2\pi)^{0.5} a\sigma\{\mathrm{erfc}\, (\tau 2^{-0.5}) - 1\} \tag{A.14d}$$

$$\psi = \sigma^2 \exp(-\tau^2) + 0.5\pi^{0.5} a\sigma\{\mathrm{erfc}\, (x) - 1\} \tag{A.14e}$$

where $\tau = \mathrm{R}_o \sigma^{-1}$ [48, Eq. 13] with $\mathrm{R}_o = 0.75\mathrm{R}$ [48, p. 7], $\sigma = k^* x^{1/3} + \epsilon$ [48, Eq. 16], $E_\pm = -0.5\sigma^{-2}(r \pm \mathrm{R})^2$ [48, Eq. 5], and c, a, k^* and ϵ constants that can be estimated by using [48, Tab. 1] according to the

specific operational-environmental conditions.

Appendix A.2.11. Pyakurel et al.'s model

The basis [51]: Jensen's and Ainslie's models [51, p. 122].

Prominent assumptions: *i*. Gaussian-form wake in the radial direction [51, p. 115].

Governing equations [51, Eq. 5, 6, 8]:

$$u(w,r) = u_f - u_f u_w^* \exp\{-3.56(0.5r\mathrm{R}^{-1}b^{-1})^2\} \tag{A.15a}$$

$$b = \{0.445\mathrm{C_T}{u_w^*}^{-1}(1-0.5u_w^*)^{-1}\}^{0.5} \tag{A.15b}$$

where u_w^* is $u_w(x)$ of Jensen's model A.1.

Appendix A.2.12. Ishihara-Qian model

The basis [52]: Mass and momentum conservation [52, p. 289-291].

Prominent assumptions: *i*. Gaussian-form wake in the radial direction [52, p. 283], and *ii*. axisymmetric, self-similar wake [52, p. 282].

Governing equations [52, Tab. 2]:

$$u_w(x,y,z) = u_f - u_f \left\{a + bx\mathrm{D}^{-1} + c(1+x\mathrm{D}^{-1})^{-2}\right\}^{-2} \exp\left(-0.5r^2\sigma^{-2}\right) \tag{A.16}$$

where a, b, and c are placeholders for the sub-expressions [52, Tab. 2]: a=$0.93\mathrm{C_T}^{-0.75}\, I_a^{0.17}$, b=$0.42\mathrm{C_T}^{0.6}\, I_a^{0.2}$, and c=$0.15\mathrm{C_T}^{-0.25}\, I_a^{-0.7}$; $\sigma(x)$=k^*x+$\epsilon_\mathrm{m}\mathrm{D}$ the representative wake width, k^*=$0.11\mathrm{C_T}^{1.07}\, I_a^{0.20}$ the wake growth rate, and ϵ_m=$0.23\mathrm{C_T}^{-0.25}\, I_a^{0.17}$ a model parameter.

Appendix A.3. Actuator line model pseudo-algorithm

Input: Polar data, rotor operational data, blade geometric data and computation settings.
Initialise **u**, p and cell-search sub-regions;
Initialize actuator points and find surrounding cells;
while Run time < Computation end time **do**
  Obtain **u** and p at actuator points;
  Compute forces by the BET;
  Rotate actuator points, and find new surrounding cells;
  Project force fields onto the flow field;
  PISO;
  Output desired information;
  Advance in time;
end

Algorithm 2: The implemented actuator line model pseudo-algorithm.

Appendix A.4. Tip-root correction methods

The tip and root corrections are applied by multiplying their factors with lift and drag forces.

Appendix A.4.1. Goldstein-Wellicome's tip loss correction

Goldstein-Wellicome's tip loss correction can be read in [133, p. 346]:

$$F_{\text{tip}} = \begin{cases} 1.0 & \text{if } \tan(\phi) < 0.001 \quad \text{or} \quad g > 85.0 \\ \frac{2}{\pi}\cos^{-1}\left\{\frac{\cosh(r\mathrm{R}^{-1}g)}{\cosh(g)}\right\} & \text{if } \tan(\phi) \geq 0.001 \quad \text{and} \quad g \leq 85.0 \end{cases} \tag{A.17}$$

where F_{tip} is the tip loss correction factor, ϕ the flow angle, r the section radius, R the blade radius, g=$\mathrm{N}_b\mathrm{R}(2r\tan(\phi))^{-1}$-0.5 a parameter, and N_b the number of blades.

Appendix A.4.2. Prandtl-Glauert's root loss correction

Prandtl-Glauert's tip loss correction was fetched from [134, Eq. 1], and modified for root sections:

$$F_{\text{hub}} = \frac{2}{\pi}\cos^{-1}\left\{\exp\left(-\frac{\mathrm{N}_b(r-\mathrm{R}_{\text{hub}})}{2r\sin\phi}\right)\right\} \tag{A.18}$$

where F_{hub} is the hub loss correction factor, and R_{hub} the hub radius.

Appendix A.5. Numerical schemes

Appendix A.5.1. Central differencing scheme

The central differencing scheme (abbr. the CDS) is spatially second-order accurate in terms of Taylor series truncation error under certain conditions. A broad assessment of the scheme can be found in [82, p. 145]. For unstructured grids, the CDS is [135, p. 275-276]: ϕ_f=$d_\mathrm{P}\,\phi_\mathrm{P}$+(1-$d_\mathrm{P}$)$\,\phi_\mathrm{N}$ where d_P is a geometric weighting factor: d_P=$\|\mathbf{r}_\mathrm{N}$-$\mathbf{r}_f\|\,(\|\mathbf{r}_\mathrm{N}$-$\mathbf{r}_\mathrm{P}\|)^{-1}$, $\mathbf{r}$ the position vector of the centroid of an owner (i.e. $\bullet_\mathrm{P}$) or neighbour cell (i.e. $\bullet_\mathrm{N}$), or of a face (i.e. $\bullet_f$).

The CDS was chosen primarily in view of its highest spatial accuracy possible. Two issues, however, appeared to be considered: *i*. the CDS is second-order accurate if and only if the line connecting centroids of adjoining cells intersects the common face centre [135, p. 276], and *ii*. truncation errors due to the second-order schemes (i.e. negative numerical diffusion) may happen to be order of sub-filter scale terms [136, p. 201-202]. Mesh-orthogonality and -skewness issues cause the former. For the latter low level production of numerical diffusion due to the CDS can alleviate impacts of high diffusion due to sub-filter scale models.

Appendix A.5.2. Backward difference scheme

DeBonis and Scott [137, p. 1777] showed that low-order temporal discretizations in IFLES reduce merits of high-level spatial resolutions and schemes. Therefore, the second-order backward difference scheme was identified "ideal" for OpenFOAM®-IFLES [138, p. 33]. For $\mathbf{u}$, it is defined as [26, p. 41]:

$$\int_\Omega \partial\mathbf{u}_t \,\mathrm{d}\Omega \approx \frac{3\,(\mathbf{u}_\mathrm{P}\,\Omega)^n - 4\,(\mathbf{u}_\mathrm{P}\,\Omega)^o + (\mathbf{u}_\mathrm{P}\,\Omega)^{oo}}{2\Delta_t} \tag{A.19}$$

where $n, o,$ and oo denote current, previous and previous-to-the-last time-step, respectively. Moreover, temporal discretizations of spatial elements are done by [26, p. 44]:

$$\int_t^{t+\Delta t} \mathbf{u}_\mathbf{q}\,\mathrm{d}t \approx \frac{3\mathbf{u}_\mathbf{q}^n - 4\mathbf{u}_\mathbf{q}^o + \mathbf{u}_\mathbf{q}^{oo}}{2\Delta_t} \tag{A.20}$$

where $\mathbf{u}_\mathbf{q}$ is the spatial solution.

Appendix A.5.3. Total variation diminishing scheme

The CDS can be blended with the upwind differencing scheme (abbr. UDS), to trade off the spatial accuracy for numerical stability as follows: ϕ_f=$\{1\text{-}\psi(r)\}(\phi_f)_\mathrm{UDS}$+$\psi(r)(\phi_f)_\mathrm{CDS}$ where ϕ_f

is the convective volumetric face flux, $\psi(\bullet)$ the limiter function, r the ratio of consecutive flux gradients [139, Eq. 3.7], i.e. between the upwind-side gradient to the downwind-side [140, Eq. 3.67].

The *limitedLinear* is an upwind-biased *total variation diminishing* scheme (abbr. TVD[33]) with:

$$\psi(r) = \max\left\{0, \min\left(\frac{2}{\max[\kappa, \xi]}r, 1\right)\right\} \tag{A.21}$$

where $\{\kappa\}_{\{\kappa\in[0,1]\}}$ is a model parameter with κ=0 the CDS is recovered, and ξ the machine epsilon. Although it is a widely held presumption that Eq. A.21 is the Sweby function, e.g. [75, p. 45], the coded form is different from the original [139, Eq. 3.17], i.e. $\psi(r)$= max(0, min(αr, 1), min(α, r)) with $\{\alpha\}_{\{\alpha\in[1,2]\}}$.

Appendix A.5.4. Normalized variable diagram scheme

The *GammaV* scheme is based on the "normalized variable diagram" (hereafter, NVD) approach that prohibits unphysical oscillations by bounding flux of each node between that of their neighbouring nodes [140, p. 101]. Its expression reads: γ= min{max($\tilde{\phi}\beta_m^{-1}$, 0), 1} where the TVD-limiter $\psi(r)$ is redefined as a "blending factor" γ [140, p. 108], $\tilde{\phi}$ the "normalized variable" expressed in [140, p. 109], $\{\beta_m\}_{\{\beta_m\in[0.1,0.5]\}}$= max(0.5$\Gamma$, ξ) a constant, ξ the machine epsilon, and $\{\Gamma\}_{\{\Gamma\in[0.2,1.0]\}}$ an input parameter wherein numerical stability increases towards 1.0. Justifications for the requirement of the scheme and reasoning behind its derivation can be found in [140, p. 98-111].

[33] Refer to [82, p. 165-176] for more detailed information.

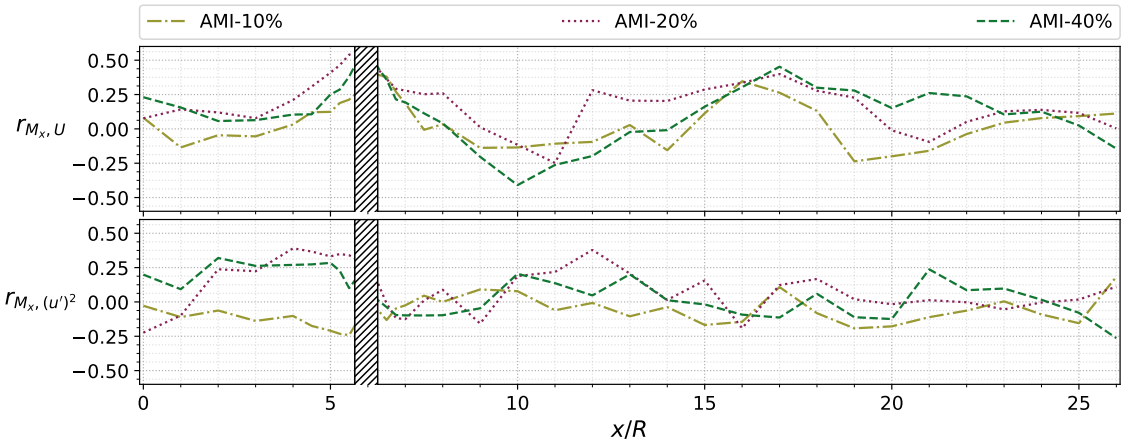

Figure A.22: Along x-direction Pearson correlation coefficients between the total out-of-plane blade bending moment, $M_x(t)$, (no blockage correction) and the longitudinal mean flow speed, $U(t)$ (top subplot)/the longitudinal flow speed fluctuations, $(u'(t))^2$ (bottom subplot) obtained from the three-dimensional turbulence intensity computations of the geometry-fitted wall-modelled arbitrary-mesh-interface approach (AMI), $I_{\mathbf{u}'_{\mathrm{rms}}}$=$\{10, 20, 40\}$[%]. Thirty-four probes were evenly placed along the x-direction at $\{y, z\}$=$\{0.0, 0.1\}$[m] to obtain the time-series. The vertical axes show the Pearson correlation coefficient, and the horizontal axis the x-distance normalised by the rotor radius, R=0.4[m].

Appendix

Efficient method for analysing fluid-structure interaction of horizontal axis tidal turbine blades

Kutalmis Bercin*, Thomas Lloyd, Zheng-Tong Xie, Stephen R. Turnock
Faculty of Engineering and the Environment
University of Southampton
Southampton SO17 1BJ, UK
E-mail: kb8e10@soton.ac.uk*, T.P.Lloyd@soton.ac.uk, Z.Xie@soton.ac.uk, srt@soton.ac.uk

***Abstract*—An open-source computational framework for the fluid-structure interaction of tidal turbine blades has been developed to be used in the preliminary design cycle. The main purpose of the framework is to assess the maxima of blade deflections under dynamic extreme inflow conditions. The framework is composed of a computational fluid dynamics library coupled with blade element momentum theory and time-accurate Euler-Bernoulli beam theory. The paper explores: (i) effect of computational grid density on wake development predictions, (ii) effect of buoyancy force on blade deflections, (iii) quasi-steady inflow and (iv) a stepwise tidal-gust effects on the deflection level of different types of blades. It is revealed that (i) tuned flexibility of a blade may contribute performance increase, (ii) buoyancy force makes edgewise loading of a rotating blade less severe (iii) the level of static and dynamic flapwise deflection of tip of a blade is likely the highest as the dynamic edgewise oscillation frequency is higher than those of others and (iv) blade deformation changes wake structures.**

***Index Terms*—Fluid-structure interaction, blade element momentum theory, Euler-Bernoulli beam theory, horizontal axis tidal turbine blade, tidal-gust**

I. Introduction

Horizontal axis marine current turbines (i.e. HAMCT) are required to provide reliable electrical energy production in a subsea operation environment with as few scheduled maintenance appointments as possible. Failures related to turbine blades will have a significant impact on their overall cost-effectiveness. The use of composite blades for such machines offers mass and cost savings [1], [2]. However, the turbulent nature of the tidal flow will result in a dynamic interaction of the hydrodynamic blade loading and its structural response with implications for the assessment of through life fatigue loading. There is an economic drive to increase blade diameter to either extract energy from lower current sites or to reduce the number of components in an array. The coupling of a stochastic flow regime with significant flapwise and twist deformations of the blade also requires rapid time domain solutions to deal with the inherent non-linearities.

The HAMCT blade modelling methods are essentially made of three components: hydrodynamics of the flow regime around and through the machine; structural dynamics of the blades and the interaction of these two mechanisms. The modelling approaches to treat these can be categorized into a number of main classes. The study of hydrodynamics of the flow regime can be carried out with four primary methods:

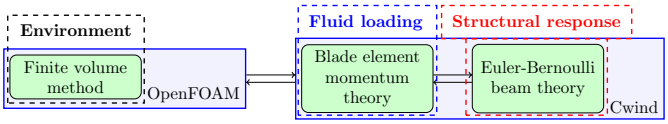

Fig. 1. Schematic of the fluid-structure interaction method

blade element momentum theory (i.e. BEMT) [3], lifting line [4], surface panel (i.e. boundary element) [5] and finite volume methods [6]. Apart from hydrodynamics modelling, the solid mechanics can be modelled with three approaches: modal decomposition, multi-body system and finite element methods [2], respectively.

In this study, BEMT and a modal decomposition method are combined with a finite volume method as shown with the computational tools used in Fig. 1. These concepts are briefly presented in the section II. In the following methodology section, the description of the coupling techniques between these methods is introduced. In the section IV, the verification and validation studies of the implementations are demonstrated. In the section V, a group of case studies, in which a $20m$-rotor-diameter tidal turbine considered with three different blades in terms of their flexibility, are carried out for: (i) BEMT-structure model coupling, (ii) BEMT-finite volume method coupling and (iii) BEMT-finite volume method-structure model coupling. Section VI shows results and discussions. Finally, some conclusions are drawn in the section VII.

II. Theory

A. Blade Element Momentum Theory

BEMT is used to estimate the forces exerted on a specified blade geometry. The theory combines momentum theory (i.e. the actuator disk theory) and blade element analysis. The former represents the blade swept area as an infinitely thin disc which alters the axial and tangential momentum of fluid particles passing through. The latter divides the blade into a number of non-interacting sections and estimates forces generated by using its aerodynamic force coefficients for its relative velocity inflow. Normal and tangential force equations are obtained for each theory and these equations are equated in an iterative manner with respect to the axial and tangential induction factors, which are non-dimensional representations of the local induced normal and tangential velocities at the disk region. Ultimately, local non-dimensional power coefficient

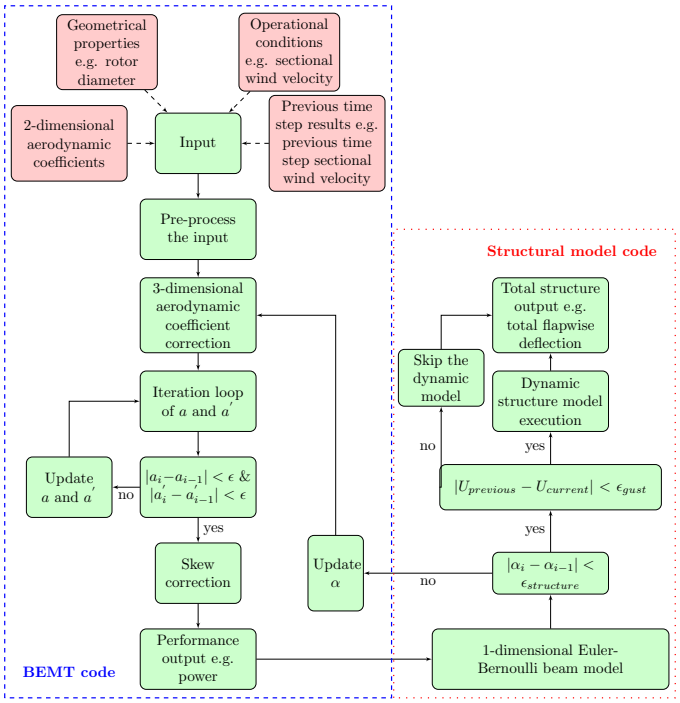

Fig. 2. The algorithm of Cwind C++, which is composed of BEMT and structural model codes. a and a' are axial and tangential induction factors, respectively; α is the effective angle of attack; ϵ is the convergence criteria and U is the instantaneous sectional wind speed.

(i.e. C_p) and thrust coefficient (i.e. C_t), which depict the performance of an isolated rotor, are acquired as follows:

$$\delta C_p = \delta P / 0.5 \rho U_o^3 A \quad (1)$$

$$\delta C_t = \delta T / 0.5 \rho U_o^2 A \quad (2)$$

where δP is the sectional power [W], δT is the sectional thrust [N], ρ is the reference fluid density $[kgm^{-3}]$, A is the projected area of the relevant blade element $[m^2]$ and U_o is the sectional undisturbed velocity magnitude normal to the rotor disc $[ms^{-1}]$.

Such methods have been used by [7] to investigate the possible differences between the loading prediction capabilities of a sectional BEMT model and a finite element model that maps pressure distribution over an identical wind turbine blade showing negligible difference with respect to the deflection results.

1) The BEMT Code: The modified BEMT code was Cwind, developed by [8]. It was integrated into the tidal turbine applications and compared with a surface panel method resulting in good agreement [9] and was validated against experiments [3]. In the original code, the loading is computed by the sectional blade element consideration using tabulated 2-dimensional aerofoil data. A Glauert correction for the turbulent wake state and Goldstein momentum averaging factor for tip loss, as is asserted by [10] supplies more realistic approach than that of Prandtl tip loss correction, are included. Cwind was re-written in C++ with a few additional functionalities such as: Lanzafame and Messina's tangential induction factor [11], Snel et al.'s 3-dimensional tabulated data correction [12], Lindenburg's 3-dimensional tabulated data correction near the tip [13], Snel and Schepers' yaw misalignment correction [14], active-passive blade part functionality and quadratic interpolation for the tabulated data. The resulting algorithm is shown in Fig. 2.

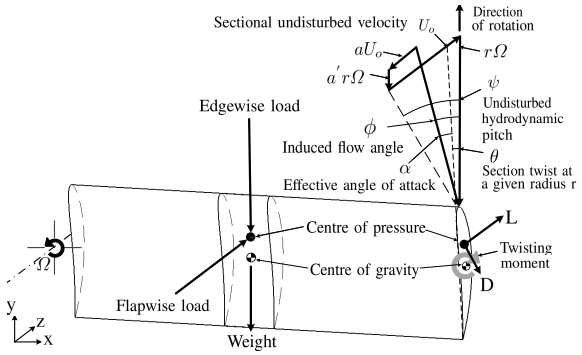

Fig. 3. Sketch of aerodynamic parameters on a typical rotating turbine blade segment

B. Structural Modelling

It is Baumgart's [15] assertion that slender solid body modelling, such as for a tidal turbine blade, with a beam model captures the essential features in comparison to a more complex solid or shell - finite element model. In addition, as is claimed in [16], as far as the mechanical features of a three-dimensional blade can be extracted, a one-dimensional beam model can cope with the most structural examinations in a prompt way. Thus, a beam model is likely to be convenient whilst a slender beam can be adequately modelled in a computationally effective way. On account of these claims and for sake of isolation of the each parameter investigated herein, the structure of the blade was modelled as a homogeneous, isotropic material, uniform cantilever box beam. As is purported in [17] that a reasonable presentation of slender bodies can be achieved with using such simplification at the early design stages.

BEMT provides aerodynamic loading at discrete locations along the blade span that are located at the centre of each segment. A linear structure is considered for simplicity; therefore, each load's deformative effect is computed separately and then summed using superposition. In addition, the model accommodates the time varying sectional flapwise (i.e. out-of-plane), edgewise (i.e. in-plane) and torsional deflection approximations by using a dynamic structure model whose results are mapped onto the results of a static structure model.

1) Static Structure Modelling: Euler-Bernoulli beam theory assumptions are adopted whilst there is no distinguishable difference in results appears compared to the Timoshenko beam theory [18] for slender beams. The time scale of inflow to the rotor disc is assumed an order of magnitude higher than that of rotor rotation ensuring that the static deflections occur in a quasi-steady manner.

Flapwise and edgewise static deformations are computed with:

$$v(x) = -Fx^2(3s - x)/6EI \qquad 0 \le x \le s \quad (3)$$

$$v(x) = -Fs^2(3x - s)/6EI \qquad s < x \le x_{tip} \quad (4)$$

where x is the location where the deflection is monitored on the beam neutral axis $[m]$, s is the location where point loads is applied $[m]$, $v(x)$ is the amount of deflection in the same plane and direction with those of the applied load $[m]$, as is shown in Fig. 3, F is the normal force to the blade element section centre parallel to the oncoming flow velocity for a flapwise deflection case and is tangential to the same centre in parallel to the angular velocity of the rotating blade element for edgewise deflection case [N], E is Young's modulus of the blade element material [Nm^{-2}], I is the area moment of inertia of the blade element's cross section whose value depends on the axis about where bending occurs $[m^4]$.

Torsional deflections are computed:

$$\gamma(x) = Mx/GJ \qquad 0 \leq x \leq s \tag{5}$$

$$\gamma(x) = \gamma(s) \qquad s < x \leq x_{tip} \tag{6}$$

where $\gamma(x)$ is the angle of twist relative to the undeformed configuration $[rad]$, M is the twisting moment [Nm], G is the shear modulus of the material [Nm^{-2}] and J is the polar moment of inertia of the relevant section $[m^4]$.

2) Dynamic Structure Modelling: The modal decomposition method is used in order to reduce the computational cost. With this method, as its stages of the application is given in [19], [20], the infinite number of natural frequencies and vibration modes of the continuous media of the structure is minimized. The orthogonality condition of the method ensures that the mode shapes are uncoupled and independent [20]. A number of vibration modes will dominate for low frequency responses in terms of their contribution to the deformation; therefore, linear summation of those prominent modes would give a reasonable picture of the actual dynamic deflection. According to [21], there is no precise rule for the determination of the number of modes. In this study, the first 10 modes are considered.

Dynamic Euler-Bernoulli beam equation is:

$$EI\frac{\partial^4 w(x,t)}{\partial x^4} + \rho A\frac{\partial^2 w(x,t)}{\partial t^2} = q(x,t) \tag{7}$$

where $w(x,t)$ is the in-plane deflection at any location on the beam at any time $[m]$ and $q(x,t)$ is the corresponding arbitrary in-plane loading [Nm^{-1}]. The in-plane deflection [19], [20] :

$$w(x,t) = \sum_{i=1}^{\infty} \phi_i(x)a_i(t) \approx \sum_{i=1}^{N} \phi_i(x)a_i(t) \tag{8}$$

where $\phi_i(x)$ is the mode shape [-], $a_i(t)$ is the generalized coordinate which is a function of time $[m]$, N is the number of modes considered and i is the rank of the mode. The reduced form of the modal equation for a cantilever beam with Euler-Bernoulli beam assumptions:

$$\ddot{a}_i(t) + 2\zeta_i\omega_i\dot{a}_i(t) + \omega_i^2 a_i(t) = \frac{F_i(t)}{M_i} \tag{9}$$

where ω_i is the natural frequency of the beam corresponding to the mode shape $[rads^{-1}]$, ζ_i is the damping ratio [-] as $\zeta_i = \lambda_i/2M_i\omega_i$, λ_i is the generalized damping $[kgs^{-1}]$, M_i is the generalized stiffness $[kg]$ and F_i is the generalized force [N]. The reason why the modal equation is reduced into that form is the fact that the damping ratio slowly varies according to the mode [19]. Accordingly, general estimation of damping ratio can be used for a specific system (e.g. heavily damped system).

Moreover, rotation of blades causes a tensile load exerted axially outward from the hub centreline. Such augmentation contributes to increasing natural frequencies of the modelled beam [22]. The modification of the natural frequencies due to tensile load can be presumed with the following approximate equation for a uniform cantilever beam:

$$\frac{f_i|_{P\neq 0}}{f_i|_{P=0}} = \left(1 + \frac{P_a}{|P_b|}\frac{(k_1L)^2}{(k_iL)^2}\right)^{1/2} \tag{10}$$

where $|P_b| = \pi^2 EI/4L^2$ is the buckling load for a cantilever beam [N], P_a is the axial load [N], $f_i|_{P=0}$ is the natural frequency without the axial load [Hz] and $f_i|_{P\neq 0}$ is with the axial load [Hz]. Note that k_1L and k_iL are determined without the axial load.

Finally, the time history of the dynamic response of the structure can be obtained by using convolution integral which sums the successive unit impulse responses.

$$w(x,t) = \sum_{i=1}^{N} \phi_i(x) \int_0^L F_i(\tau)h_i(t-\tau)d\tau \tag{11}$$

where τ is the instance when the corresponding force is exerted on the structure $[s]$ and $h_i(t)$ is the response function of the beam to a unit impulse $[skg^{-1}rad^{-1}]$.

C. Finite Volume Method

Incompressible Reynolds averaged Navier-Stokes (RANS) equations were implemented in order to estimate the relevant single-phased and Newtonian flow field's time averaged mean flow parameters. The RANS equations were computed with the open-source code OpenFOAM 2.1 [23]. Unsteady RANS equations are:

$$\frac{\partial U_i}{\partial x_i} = 0 \tag{12}$$

$$\frac{\partial U_i}{\partial t} + \frac{\partial U_i U_j}{\partial x_j} = -\frac{1}{\rho}\frac{\partial P}{\partial x_i} - \frac{\partial \overline{u_i' u_j'}}{\partial x_j} + \frac{\partial}{\partial x_j}\left\{\nu\left(\frac{\partial U_i}{\partial x_j} + \frac{\partial U_j}{\partial x_i}\right)\right\} + f_i \tag{13}$$

where U_i and u_i' are the mean and the fluctuating velocity components $[ms^{-1}]$, P is the mean pressure [Nm^{-2}], ν is the kinematic viscosity $[m^2s^{-1}]$, f_i is the momentum source term $[ms^{-2}]$ and i, j are the index variables.

III. Methodology

A. BEMT - Structure Model Coupling

As is shown in Fig. 3, the BEMT code provides two forces, namely thrust and tangential force exerted on the centre of pressure of the relevant aerofoil, and one moment, namely twisting moment, about the centre of twist due to the twisting effect of thrust and tangential force. There are

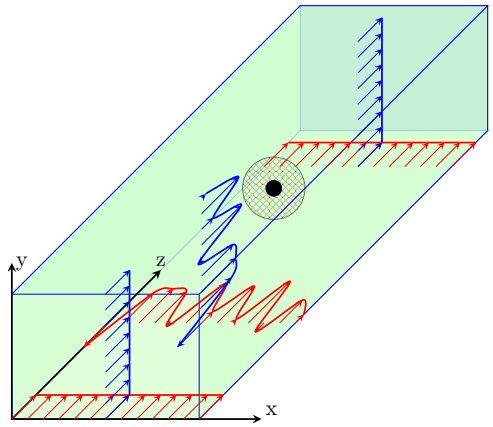

Fig. 4. A sketch of the computational domain. The solid black dot shows the hub, the dark green cross-hatch circle represents the rotor disc, red and blue vectors in the z-direction depict the velocity profile at the relevant plane. Note that the profiles just in front of the domain present an arbitrary gust occurrence.

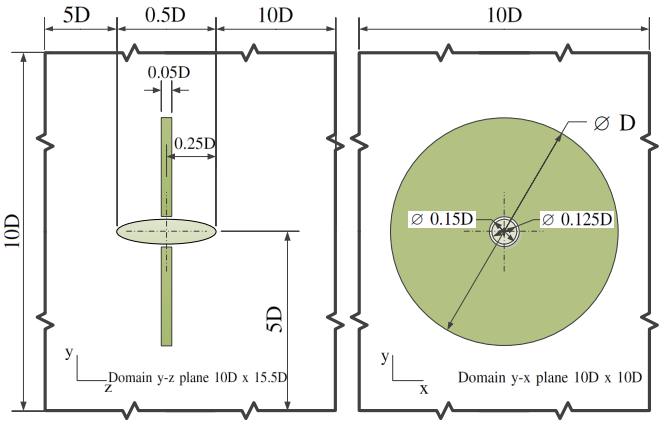

Fig. 5. A side and front view of the computational domain from left to right. The green region represents the hub. The dark green region shows the volume where the momentum sources are applied. The narrow space between both regions is for the passive part of the blade through which fluid can pass with a drag penalty depends on the drag coefficient for a prescribed geometry.

several assumptions which facilitate the process that should be noted. Firstly, the centre of pressure is assumed to be at a fixed location, which is the quarter-chord point behind the leading edge, for small angles of attack and it remains at this fixed point whereas the angle of attack changes. Secondly, the location of the centre of twist of the aerofoil section is assumed to be identical to the location of the centre of gravity of the same section. Although it is true for a symmetric and homogeneous aerofoil, this fact may turn into an assumption for a cambered aerofoil, which is considered herein. Thirdly, tangential force contribution to the twisting moment is neglected as it is an order of lower in magnitude compared to thrust. In addition, twisting moment is the product of thrust and the moment arm that is the right distance between the centre of pressure and the centre of gravity. Further, the orientation of area moments of inertia are assumed constant even though this alters instantaneously when angle of attack changes. Additionally, the change of the angle of attack, thus the loading regime on the blade depends solely on the torsional deflection. The flapwise and edgewise deflections are assumed not to affect the angle of attack.

Thrust induces the flapwise deflection of the beam. In addition, tangential force with the additional time-dependent force components tangent to the rotation of the centre of gravity induce the edgewise deflection of the beam. These additional forces are due to the blade section's self-weight and the buoyancy force. Lastly, twisting moment induces the torsional deflection of the beam cross-section. Flapwise, edgewise and torsional deflections are obtained independently from each other; consequently, it is presumed that there is no coupling among these deflections.

For the dynamic deflection analysis, on the other hand, a simple criteria is set in the BEMT code. Any inflow change whose time scale is smaller than that of rotor rotation and magnitude of velocity is 50% less or higher than that of quasi-steady inflow anywhere on the rotor disc, e.g. a pocket of gust, triggers the dynamic structure modelling code. The differences occur in thrust, tangential force and twisting moment in comparison to those of quasi-steady inflow are multiplied by the duration of the change. The continuous duration is divided into very small short durations. With evaluating the obtained continuous loading as successive unit impulses with very short durations, the dynamic model produces time-dependent deflection future histories of flapwise, edgewise and torsional vibration depending on the specified damping ratio.

B. BEMT - Finite Volume Method Coupling

Similar to [24] and [25], as can be seen in Fig. 4 and 5, a part of RANS computational domain which has identical circular area of the actual rotor area is selected as an inner domain by flagging the cell centres with a single cell thickness in the stream-wise direction. The identified inner domain is sub-divided radially into a number of annuli that has the same number of blade elements in the BEMT code. The BEMT code estimates the forces. Then the forces are transferred to the RANS simulation via the momentum source terms, f_i, localized to the cell centres of the inner domain. Hence, the inner domain becomes a time-varying source of momentum depending on the blade forces. The estimated forces vary radially; however, are uniform circumferentially. Note that although actuator disk has zero thickness in the BEMT, this identified zone has thickness due to the finite volume of the selected cells contain the flagged cell centres. Estimated thrust for each blade element is connected with the axial momentum source term of the counterpart annulus, f_{ix} $[ms^{-2}]$:

$$f_{ix} = \frac{\delta T}{\rho\, V} = \frac{1/2\,\rho\, U_o^2\, A\, \delta C_t}{\rho\, A\, L} \tag{14}$$

where V is the relevant annulus volume of the inner domain $[m^3]$ and L is the thickness of the annulus volume in the stream-wise direction $[m]$. Estimated tangential force for each blade element is connected with the tangential source term of the counterpart annulus, $f_{i\theta}$ $[ms^{-2}]$:

$$f_{i\theta} = \frac{\delta Q}{\rho\, r\, V} = \frac{1/2\,\rho\, U_o^3\, A\, \delta C_p}{\rho\, r\, \Omega\, A\, L} \tag{15}$$

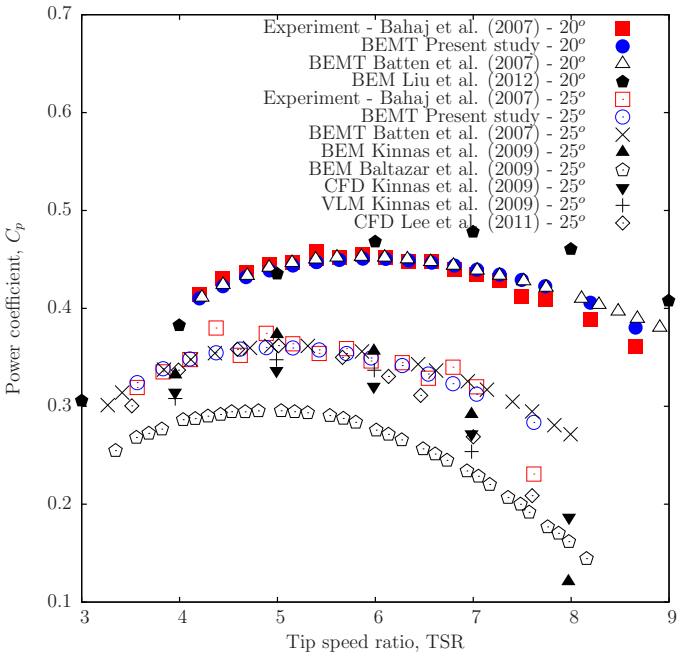

Fig. 6. Power coefficient estimations on a typical range of tip speed ratios

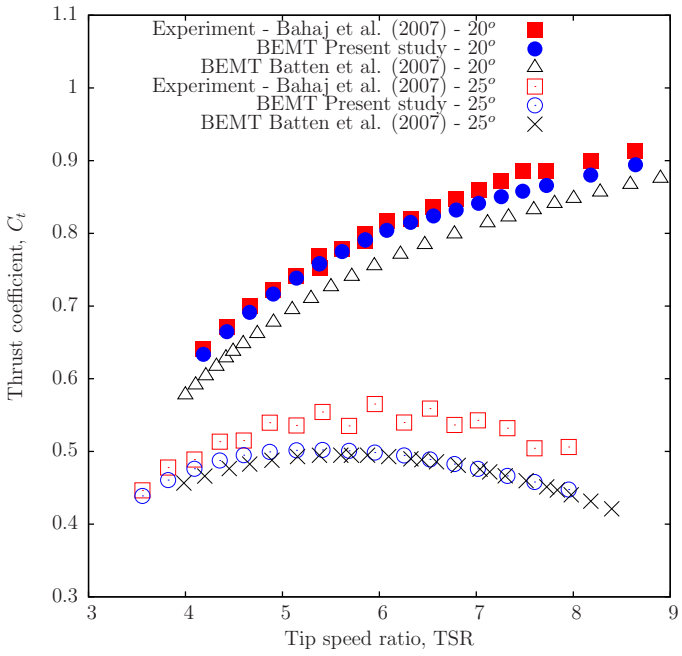

Fig. 7. Thrust coefficient estimations on a typical range of tip speed ratios

where δQ is the estimated torque acts on the relevant annulus [Nm], r is the distance from the hub centreline to the relevant annulus's cell centre on the rotor plane [m] and Ω is the constant angular velocity of the rotor [$rads^{-1}$].

On the other hand, the undisturbed velocity magnitudes required by the BEMT code are determined from the inlet section of the inner domain annuli instantaneously. The oncoming stream-wise speed at the virtual disc is extracted for each cell centres, where the momentum sources are implemented, at each time step of the RANS simulation. Afterwards, the extracted velocity magnitudes are circumferentially averaged for each annulus. The obtained single velocity magnitude is the disturbed velocity magnitude due to the fact that the implemented momentum sources change instantaneously the upstream velocity field. Therefore, an empirical correction is demanded in order to transform the disturbed velocity magnitude into an undisturbed velocity magnitude. The disturbed velocity magnitudes for each annulus are corrected by the axial induction factor from the previous time step.

IV. Validation & Verification

A. The BEMT Code Verification & Validation

The new C++ version of Cwind was verified against the original code. Fig. 6 and 7 show the variation in C_p and C_t predictions for the following set of data: the experiment [26], BEMT [27], boundary element method [28], [29], vortex lattice method [30] and finite volume method [31]. Two dataset of C_p and C_t in zero yaw condition are considered: 20^o hub pitch angle - 1.73 ms^{-1} & 25^o hub pitch angle - 1.54 ms^{-1} uniform inflow speed. The geometrical and operational features of [26] are input. The horizontal axis of both figures presents the tip speed ratio (i.e. TSR), which equals to $0.5\Omega D/U_{hub}$. As is depicted in Fig. 6, the C_p estimations are in good agreement for TSR between 4 - 7.5; however, TSR $>$ 7.5 the code overpredicts the experimental results. As is shown in Fig. 7, the C_t predictions have reasonable agreement with the experiment for 20^o hub pitch; nevertheless, the code underestimates the experimental results of 25^o hub pitch in almost all of the TSR range.

B. The Structure Model Code Validation

Static and dynamic structural codes were compared against the commercial finite element code, ANSYS Mechanical APDL version 13.0. The BEAM4 3-dimensional elastic beam element was used in the validation process of all types of deflections. Identical results are obtained, except a discrepancy occurs in the torsional vibration validation where the modal decomposition method deals with high frequency responses less adequately in comparison to the low frequency responses due to the fact that the domination of the number of initial modes no longer exists [32].

V. The Case Study

A. The HAMCT Geometrical and Operational Properties

The geometrical properties of HAMCT of [26] given in [27] are scaled by a factor of 25 to give a turbine diameter of 20m. The material of the blade is taken to be T6082-T6 aluminum alloy as used in the experiment [33]. Plus, seawater properties are considered [34]. It is [26]'s interpretation that the 20^o hub pitch angle setting with TSR between 5-7 provides the most efficient performance for the relevant rotor. Therefore, the operational setting of 20^o hub pitch and TSR of 5.63, which ensures constant 1.73 ms^{-1} inflow velocity of the experiment, was studied.

B. The Modelled Blade Structure

In order to examine the effects of flexibility of a blade on the structure deflection, three cantilever box beams are

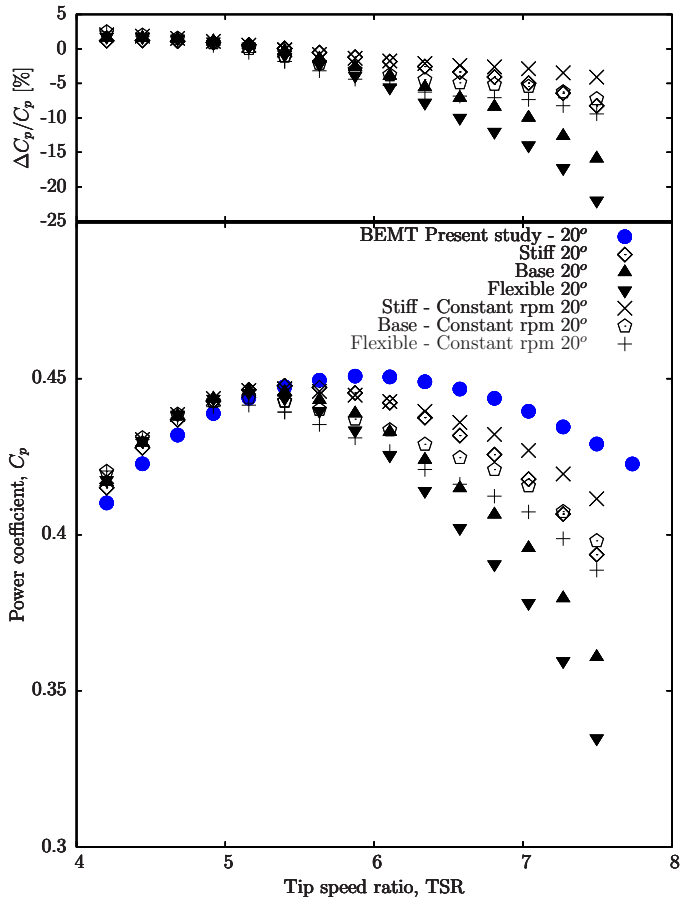

Fig. 8. Power coefficient results of the case studies

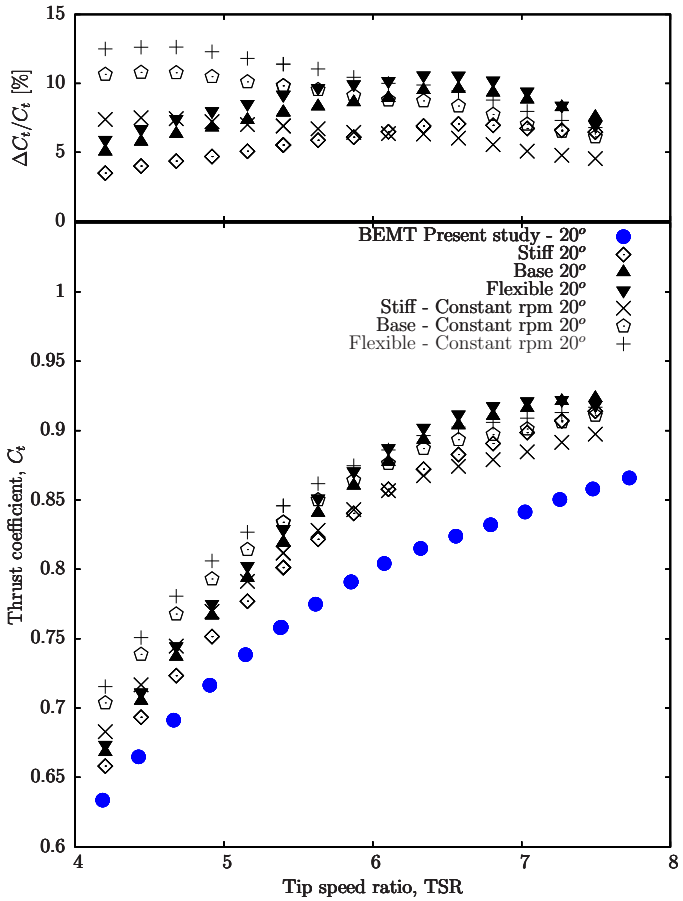

Fig. 9. Thrust coefficient results of the case studies

modelled. Those beams are labelled as 'stiff', 'base' and 'flexible'. Differences in flexibility is ensured by virtue of changing the geometrical properties of the modelled beam. Initially, the experimental blade's root section (i.e. NACA63-824) is uniformly extended to obtain the 'stiff' beam whilst the actual geometrical characteristics of the blade root are determined from XFOIL 6.97 [35]. Also, thickness of the beam is adjusted to $0.05m$. Further, the area moment of inertia parameters of the 'stiff' beam are all scaled down to 70% for the 'base' (i.e. corresponds to approximately 18% sectional area reduction) and 60% for the 'flexible' beam (i.e. corresponds to approximately 24% sectional area reduction). The other properties are kept the same.

Damping estimations of the system due to fluid and structure damping effects are lumped into a single parameter: damping ratio, ζ and three typical values are prescribed in order to identify its relative impact. For a lightly, typically and heavily damped system, ζ is designated as 0.001, 0.01 and 0.1, respectively [19].

C. The Modelled Gust

Steady-state inflow through the rotor disc is projected as constant, uniform and equal to $1.73ms^{-1}$ of the relevant experiment. Dynamic flow, however, is designated as a pocket of stream-wise disturbance encompassing the whole rotor disc. This gust is assumed to be uniform radially and is superimposed on the steady flow. The characteristic length scale of the gust is assumed to be equal to the rotor radius in the stream-wise direction and its velocity scale is 150% of that of the steady flow (i.e. $2.595m/s$) in parallel to the indications of the tidal field measurements [36], for the extreme tidal flow circumstances. Approximately 3.85 s of time scale of the gust, therefore, is ascertained from the above estimations. Hence, such a period does not give a chance to the turbine blades to adjust themselves; thus, resulting in resisting this temporary hydrodynamic loading increase with an unchanged configuration. All case studies below consider a single identical step-wise gust occurrence for a finite duration. A representation of a typical gust occurrence is shown in Fig. 4.

D. The Finite Volume Numerical Setting

1) Computational Domain Description: A succinct set of dimensions of the Cartesian computational domain is given in Fig. 5. The flow is towards the positive z-direction.

2) Discretization: A combination of structured and unstructured mesh is generated. Unstructured tetrahedral and hexahedral elements are used for a cylinder with the radius of passive blade along the domain in the stream-wise direction. The rest of the domain is constructed with hexahedral elements. The finite volume method with SIMPLE algorithm is used to solve partial differential equations for the incompressible and

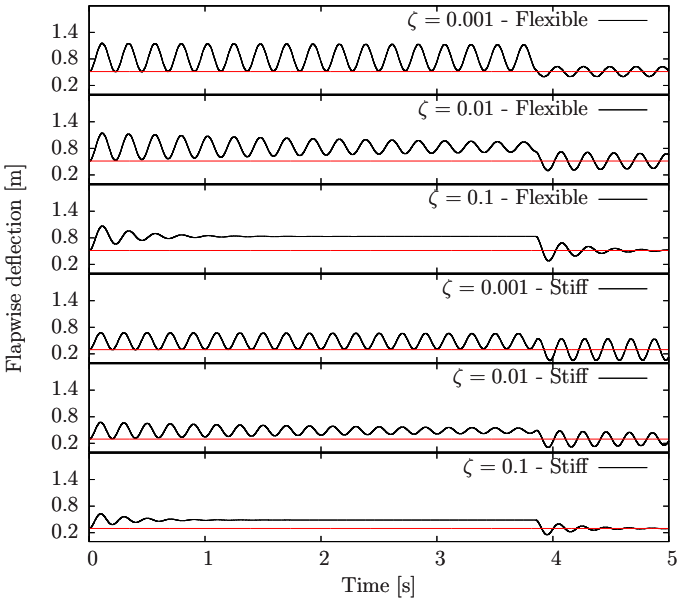

Fig. 10. Flapwise deflection of the blades at the tip point at TSR 5.63

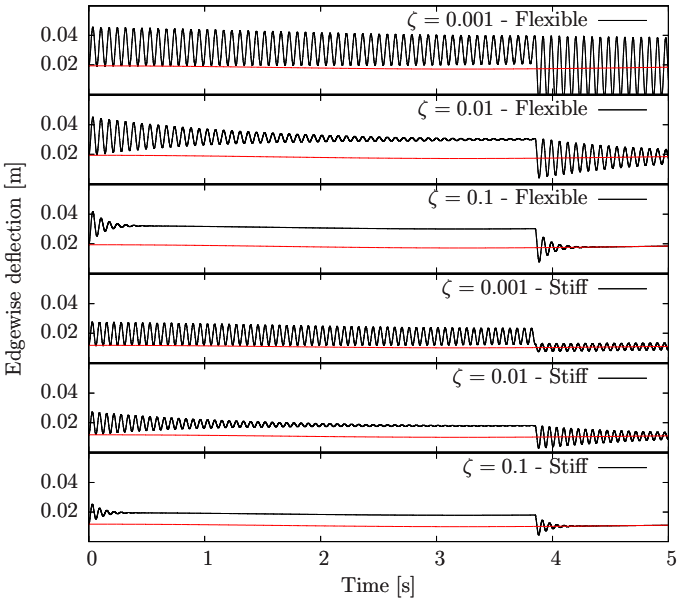

Fig. 11. Edgewise deflection of the blades at the tip point at TSR 5.63

turbulent flow.

3) Boundary Conditions: Constant uniform velocity inlet condition is applied upstream of the rotor disc plane with $1.73ms^{-1}$ in order to repeat the constant flow velocity condition of the experiment. Zero gradient pressure outlet condition is deployed at the downstream. A slip wall condition is applied to the lateral domain faces as well as the hub region in order to block flow through whilst avoiding the wall boundary layer resolution. Submersion depth effect is neglected because as is claimed by [37] it has marginal effect on turbine wake.

4) Turbulence Model and Turbulence Properties: k - ω SST turbulence model is used in order to model the flow around the rotor disk as [37] claims that the model performs better compared to the other eddy-viscosity models for similar studies. The ambient turbulence intensity is set down to 1%. Turbulence length scale is estimated to be 5% of the size of the computational domain inlet in the stream-wise direction.

VI. Results - Discussion

A. BEMT - Structure Model Coupling

1) Steady-state Case: With the help of the steady-state structure model, the effects of two factors on the performance parameters are attempted to be investigated briefly: the relative flexibility of blades and constant rpm operation.

Fig. 8 and 9 plot the resulting C_p and C_t as a function of TSRs from 4 to 8, respectively. The relevant isolated BEMT code results are also arranged as a reference point in the same figures. Additionally, at the top of each plot, the relative change of the parameter in question as compared to the reference result is depicted in units of percentage. The plots demonstrate that the performance at each TSR has changed.

Firstly, taking the relative flexibility of blades into account, as shown in Fig. 8, the C_p remained at the reference level with a minimal increase inversely proportional to the flexibility until TSR of 5.3 for the three modelled cases. In contrast, TSR 5.3 to 8, there is a gradual decline in C_p comparison to the reference and is directly proportional to the flexibility of the blade. Fig. 8, however, depicts a steady increase in C_t for the entire TSR range for all modelled blades whilst the increase levels off and in general it changes in proportion to the resilience of the blade up to TSR 7.5.

With this configuration, the blockage effect of blades increases with flexibility due to the decline in twist angle. Although lift-drag ratio is increased accordingly owing to the increase in effective angle of attack, C_p is decreased for TSR>5.3. The reasoning behind it is that the twisting angle is higher than the change of angle of attack; thus, resulting in smaller induced velocity angle. In turn, lift contribution to the rotation falls off whilst thrust goes up.

Secondly, the default operational setting, which is variable rotor rotation speed with constant inflow speed, is changed to another setting, which is fixed rotor rotation speed with variable inflow speed, by keeping TSR identical. As can be seen from Fig. 8 and 9, the trends of C_p and C_t remain the same with the first case study with regard to the reference. Nevertheless, the level of C_p is lower than that of the first case up to around TSR 6.10 where the inflow speeds of both cases get equal each other. After this point, C_p becomes higher compared to that of the first case for the rest of the TSR range. In a similar fashion, the degree of C_t is higher than that of the first case until TSR 6.10 whereas it is lower for the remaining range of TSR.

This difference signifies the importance of the inflow speed. For instance, from TSR 6.10 to higher TSRs, thrust, which is accounted for the torsional deflection, is decreasing due to the descending inflow speed. Torsional deflection decline, therefore, is triggered and this leads to higher induced flow angles.

2) Tidal-gust Effect on the Structure Response: By means of the dynamic structure model, the effects of two factors on

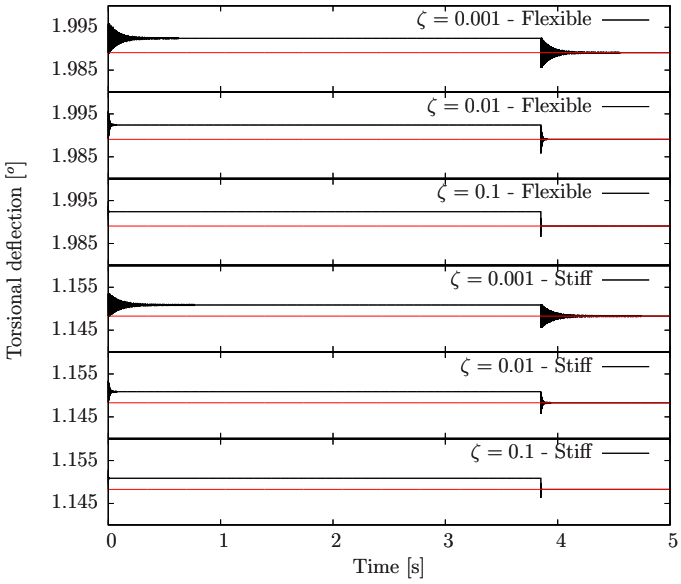

Fig. 12. Torsional deflection of the blades at the tip point at TSR 5.63

the level of deformation of the modelled blades are tried to be studied in brief: the relative flexibility of blades and the damping ratio.

Fig. 10, 11 and 12 present the estimated time-dependent flapwise, edgewise and torsional deflections of the tip point of the blade according to time from when step-wise tidal-gust response starts at 0 s and ends at 3.85 s, in turn. The response is monitored for 5 s. Between 3.85 s and 5 s, the blade freely vibrates with damping according to the blade properties and the position of the blade tip at the end of tidal-gust occurrence. Each figure has six stacked sub-figures. From top to bottom inside any of the figures, first three sub-figures illustrate the modelled flexible blade response and the last three sub-figures show the modelled stiffer blade response. Within any pile of three sub-figures, from top to bottom, the specified damping ratios are 0.001, 0.01 and 0.1, which increase ten-fold at each case. The horizontal axis represents the time that the deflection monitored in units of second and the vertical axes of the figures of flapwise and edgewise deflections represent deflection in units of meters and of the figure of torsional deflection presents deflection in units of degrees as against the unstrained blade configuration. Note that the horizontal axis of the figures is composed of six identical ranged sub horizontal axes. Lastly, in all figures, the red dashed line displays the static deflection and the black line indicates the total deflection that is the instantaneous summation of the dynamic and static deflections.

First, on account of the relative flexibility of blades, Fig. 10, 11 and 12 show that increase in flexibility contributes to higher maxima of the deflections by comparison with those of stiffer blade at any instant. Furthermore, the figures illustrate that the amplitudes of the dynamic response are higher to some extent for the cases corresponding to the flexible blades. Also note that the oscillation frequency of edgewise deflection is noticeably higher than that of flapwise deflection. Besides, the response frequency of stiffer blade is minimally higher.

The reason why the difference in response frequency is

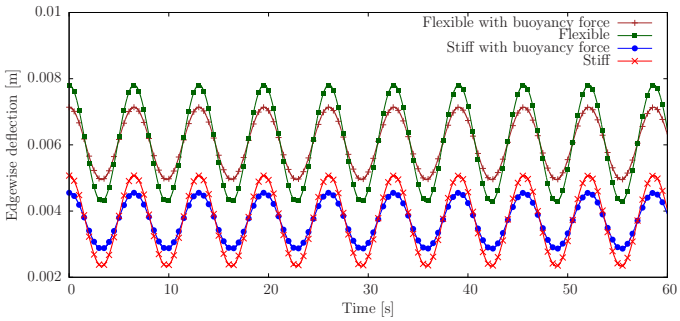

Fig. 13. Buoyancy effect on the static edgewise deflection at TSR 5.63

marginal is that the order of magnitude of increase in stiffness of blade is balanced by the almost same magnitude of decrease in mass of the flexible blade. On the other side, the higher maxima likely means for upwind turbines that flexible blades are more prone to the possibility of accidental strike to the tower due to a tidal-gust whilst the clearance between the tip of the blade and the tower is reduced. Moreover, edgewise oscillation may pose a more serious crack problem to the blade in parallel to the experience from wind turbines [38].

Second, taking the damping ratio on board, Fig. 10, 11 and 12 demonstrate that the increase in the damping ratio comparatively results in narrower amplitude range and lesser maxima of the deflections.

This highlights the significance of damping for a tidal turbine operating in turbulent tidal conditions as an appropriate artificial damping may significantly reduce the risks due to the oscillation for even the flexible tidal turbine blade.

3) Buoyancy Force Effect: Fig. 13 summarizes the buoyancy force effect on the static edgewise deflection of rotating flexible and stiffer blades at the design TSR 5.63 for a minute. The horizontal axis presents the monitoring time in units of seconds and the vertical axis shows the static edgewise deflection in units of meters. The graph implies that the buoyancy force due to the surrounding fluid reduces the amplitude range of oscillation cycles.

B. BEMT - Steady-state Finite Volume Method Coupling

1) Grid Effect: In order to investigate the effect of number of cells on the numerical results, two computational domains with different grid density are prepared. The initial domain contains 1.3M cells in total. The number of grid points are increased 30% in all directions in order to generate the second domain which contains 2.6M cells. The number of blade sections for the BEMT is 9 as is found that the number of sections do not affect far downstream velocity profile. Fig. 14 shows the axial wake velocity results obtained from both domains. The horizontal axis presents the axial flow speed in the streamwise direction non-dimensionalized by the axial far upstream flow speed and the vertical axis represents the distance from the hub centreline, non-dimensionalized by the rotor radius. The curves depict the axial wake profiles extracted from far upstream and downstream locations at 1D, 3D, 5D and 7D distant from the rotor plane. The mesh dependency effect appears small except in the local vicinity immediately behind

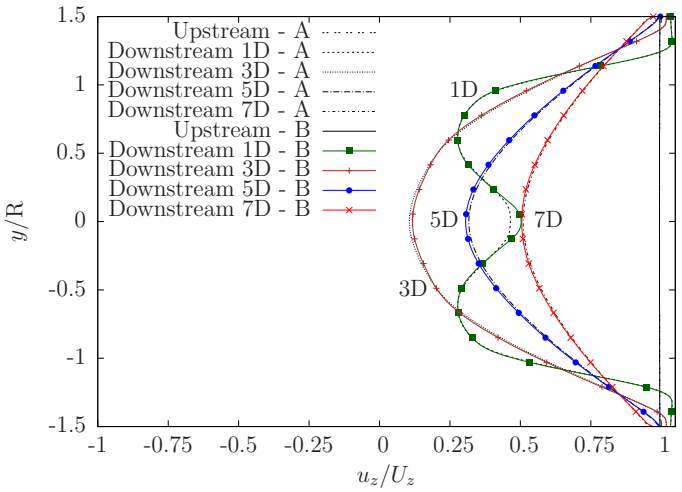

Fig. 14. Grid density effect on the axial wake velocity profile at TSR 5.63. D indicates the rotor diameter. A and B depict 1.3 and 2.6 million-cell-domains, respectively.

the hub. The near wake structure and its eventual transition to a Gaussian far wake (>3D) is as expected, [39], [40].

2) Verification of BEMT - Finite Volume Method Coupling: Table I summarizes the differences between the isolated BEMT code (i.e. A) and the BEMT code - steady-state RANS coupling (i.e. B) in terms of performance parameters. In the view of results, the empirical correction estimation in order for obtaining the undisturbed velocity magnitudes has produced similar inlet velocity magnitudes to that of the isolated BEMT code.

C. BEMT- Steady-state Finite Volume Method - Static Structure Model Coupling

Fig. 15 illustrates the axial wake velocity profiles obtained from the BEMT - steady-state RANS coupling with (i.e. B) and without (i.e. A) the static structure model. The number of blade sections for the BEMT is 9. The plot properties are identical to that of Fig. 14. In the light of the assumption that either flapwise or edgewise deflection does not affect the blade loading, one may conclude that the deflected blade structure remains in the actuator disk plane in order not to violate the fundamental BEMT assumptions. The graph indicates that the two peaks in the 1D and the single peak in the 3D are more prominent with the structure deflection. The single peaks at the 5D and 7D downstream, however, depict a slight drop in peak height.

The near wake length is decreased as 1D-B in Fig.15 indicates an earlier joining of two peaks. Besides, the lowered wake velocity is shown with 3D-B in Fig.15. This reduction is in-line with the C_t rise due to the structure deflection, similar to [37]'s statement. Finally, the small drop in peak height of 5D-B and 7D-B implies that the wake recovery is faster.

VII. Conclusions

In conclusion, a numerical fluid-structure interaction approach is proposed for tidal turbine blade assessment under severe conditions in the earlier stages of the design. Apart from its fundamental purpose of modelling the maxima of blade deflections accurately, it is aimed to obtain a method which is less demanding of computational resources. To this end, the developed method implements a flow solution using OpenFOAM 2.1 coupled via axial and tangential momentum sources with a C++ BEMT code to rapidly deduce a strip wise sectional loading for the instantaneous inflow conditions on each blade. Within the code a time-accurate Euler-Bernoulli beam theory is used to predict the deformation and twist of the blades. A group of numerical case studies are carried out with an experimental tidal turbine that is scaled up to $20m$ diameter. It is revealed for this configuration that: (i) the level of flexibility likely affects the maximum deflection of blades and performance of rotor depending on the configuration, (ii) edgewise loading of a rotating blade becomes less violent with buoyancy forces, (iii) a tidal-gust may considerably increase especially the flapwise deformation and edgewise oscillations of blades and (iv) blade deformation contributes to a different wake development. In the near future, the focus will be on the (i) investigation of tidal turbine blade response under more realistic turbulent inflow conditions by using [41] and (ii) to develop the method into a fully-unsteady manner.

TABLE I
Verification of BEMT - RANS coupling at TSR 5.63

Parameters	A	B	Difference [%]
Power coefficient	0.449493	0.449491	4.45E-4
Thrust coefficient	0.776121	0.776125	-5.20E-4
Gross power [kW]	374.649	374.647	5.34E-4
Thrust [N]	374804	374806	5.34E-4

VIII. Acknowledgements

Bercin gratefully acknowledges the Research Studentship from the Faculty of Engineering and the Environment, University of Southampton and the partial financial support from EPSRC project "Passive adaptive composites" funded through EP/009876/1, and Arup and Partners Ltd.. The computations were performed on Iridis3 cluster, University of Southampton.

References

[1] R. F. Nicholls-Lee and S. R. Turnock, "Enhancing performance of a horizontal axis tidal turbine using adaptive blades," in *OCEANS 2007 - Europe*, USA, 2007, pp. 1–6.

[2] R. F. Nicholls-Lee, S. R. Turnock, and S. W. Boyd, "Application of bend-twist coupled blades for horizontal axis tidal turbines," *Renewable Energy*, vol. 50, pp. 541 – 550, 2013.

[3] W. Batten, A. Bahaj, A. Molland, and J. Chaplin, "The prediction of the hydrodynamic performance of marine current turbines," *Renewable Energy*, vol. 33, no. 6, pp. 1085 – 1096, 2008.

[4] J. A. C. Falcão de Campos, "Hydrodynamic power optimization of a horizontal axis marine current turbine with lifting line theory," in *Proceedings of the 17th International Offshore and Polar Engineering Conference*, vol. 1, 2007, pp. 307–313.

[5] J. Baltazar and J. A. C. Falcão de Campos, "Hydrodynamic analysis of a horizontal axis marine current turbine with a boundary element method," *Journal of Offshore Mechanics and Arctic Engineering*, vol. 133, no. 4, pp. 041 304/1–10, 2011.

[6] J. McNaughton, I. Afgan, D. D. Apsley, S. Rolfo, T. Stallard, and P. K. Stansby, "CFD simulation of a 3-Bladed horizontal axis tidal stream turbine using RANS and LES," Oxford Tidal Energy Workshop, 2012.

[7] T. J. Knill, "The application of aeroelastic analysis output load distributions to finite element models of wind," *Wind Engineering*, vol. 29, no. 2, pp. 153–168, 2005.

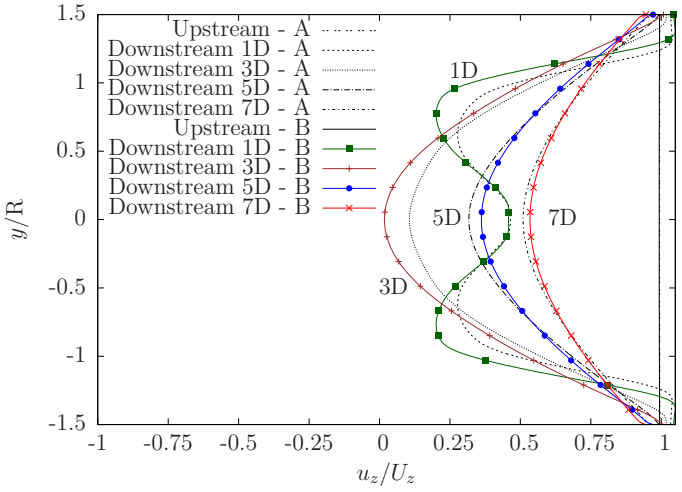

Fig. 15. The BEMT - steady-state RANS - static structure model coupling axial wake velocity profiles at TSR 5.63. D indicates the rotor diameter. A and B depict 1.3 and 2.6 million-cell-domains, respectively.

[8] M. Barnsley and J. Wellicome, "Dynamic models of wind turbines aerodynamic model development," the Commission of the European Communities Directorate, Tech. Rep. JOUR 0110, 1993.

[9] S. R. Turnock, "Predictions of hydrodynamic performance of horizontal axis tidal turbines," Wolfson Unit for Marine Technology and Industrial Aerodynamics., Tech. Rep. 1878, 2006.

[10] W. Z. Shen, R. Mikkelsen, J. N. Sørensen, and C. Bak, "Tip loss corrections for wind turbine computations," *Wind Energy*, vol. 8, no. 4, pp. 457 – 475, 2005.

[11] R. Lanzafame and M. Messina, "Fluid dynamics wind turbine design: Critical analysis, optimization and application of BEM theory," *Renewable Energy*, vol. 32, no. 14, pp. 2291 – 2305, 2007.

[12] H. Snel, R. Houwink, and J. Bosschers, "Sectional prediction of lift coefficients on rotating wind turbine blades in stall," ECN, Tech. Rep. ECN-C–93-052, 1994.

[13] C. Lindenburg, "Investigation into rotor blade aerodynamics," ECN, Tech. Rep. ECN-C-03-025, 2003.

[14] H. Snel and J. Schepers, "Joint investigation of dynamic inflow effects and implementation of an engineering method," ECN, Tech. Rep. ECN-C–94-107, 1995.

[15] A. Baumgart, "A mathematical model for wind turbine blades," *Journal of Sound and Vibration*, vol. 251, no. 1, pp. 1 – 12, 2002.

[16] D. J. Malcolm and D. L. Laird, "Modeling of blades as equivalent beams for aeroelastic analysis," in *2003 ASME Wind Energy Symposium AIAA/ASME*, Reno, USA, 2003, pp. 293–303.

[17] E. C. Smith and I. Chopra, "Formulation and evaluation of an analytical model for composite box-beams," *Journal of the American Helicopter Society*, vol. 36, no. 3, pp. 23–35, 1991.

[18] L. Majkut, "Free and forced vibrations of Timoshenko beams described by single difference equation," *Journal of Theoretical and Applies Mechanics*, vol. 47, no. 1, pp. 193–210, 2009.

[19] J. L. Guyader, *Vibration in continuous media*. ISTE, 2006.

[20] J. M. Jonkman, "Modeling of the UAE wind turbine for refinement of FAST AD," National Renewable Energy Laboratory, Tech. Rep. NREL/TP-500-34755, 2003.

[21] P. H. Madsen, S. T. Frandsen, W. E. Holley, and J. C. Hansen, "Dynamics and fatigue damage of wind turbine rotors during steady operation," Danmarks Tekniske Universitet, Risø Nationallaboratoriet for Bæredygtig Energi, Tech. Rep. Risø-R-512, July 1984.

[22] R. D. Blevins, *Formulas for natural frequency and mode shape*. New York: Van Nostrand Reinhold, 1979.

[23] OpenCFD, *OpenFOAM user guide version 2.1.1 edition*, Reading, 2012.

[24] S. R. Turnock, A. B. Phillips, J. Banks, and R. Nicholls-Lee, "Modelling tidal current turbine wakes using a coupled rans-bemt approach as a tool for analysing power capture of arrays of turbines," *Ocean Engineering*, vol. 38, no. 11, pp. 1300–1307, 2011.

[25] E. Paterson, "Propeller dynamics/body force model," http://bit.ly/11A6cxv, 2010.

[26] A. Bahaj, A. Molland, J. Chaplin, and W. Batten, "Power and thrust measurements of marine current turbines under various hydrodynamic flow conditions in a cavitation tunnel and a towing tank," *Renewable energy*, vol. 32, no. 3, pp. 407–426, 2007.

[27] W. Batten, A. Bahaj, A. Molland, and J. Chaplin, "Experimentally validated numerical method for the hydrodynamic design of horizontal axis tidal turbines," *Ocean Engineering*, vol. 34, no. 7, pp. 1013 – 1020, 2007.

[28] P. Liu and B. Veitch, "Design and optimization for strength and integrity of tidal turbine rotor blades," *Energy*, vol. 46, no. 1, pp. 393 – 404, 2012.

[29] J. Baltazar and J. A. C. Falcão de Campos, "Unsteady analysis of a horizontal axis marine current turbine in yawed inflow conditions with a panel method," in *First International Symposium on Marine Propulsors, smp09*, K. Koushan and S. Steen, Eds., Trondheim, Norway, 2009.

[30] J. H. Lee, D. H. Kim, S. H. Rhee, I. R. Do, B. C. Shin, and M. C. Kim, "Computational and experimental analysis for horizontal axis marine current turbine design," in *Second International Symposium on Marine Propulsors smp11*, Hamburg, Germany, 2011.

[31] S. A. Kinnas and W. Xu, "Analysis of tidal turbines with various numerical methods," in *1st Annual MREC Technical Conference, Massachusetts, USA*, 2009.

[32] A. Blanc, "Validation of vibro-acoustic numerical models," Ph.D. dissertation, Purdue University, 2007.

[33] Aalco, "Aluminium Alloy 6082 - T6 T651," http://bit.ly/103bCjR, 2013.

[34] 26th ITTC Specialist Committee on Uncertainty Analysis, "ITTC recommended procedures - fresh water and seawater properties," International Towing Tank Conference, Tech. Rep. 7.5-02-01-03, 2011.

[35] M. Drela, "XFOIL: An analysis and design system for low Reynolds number airfoils," in *Low Reynolds number aerodynamics*, T. J. Mueller, Ed., Dame, USA, 1989.

[36] G. S. Bir, M. J. Lawson, and Y. Li, "Structural design of a horizontal-axis tidal current turbine composite blade," in *Proceedings of the International Conference on Offshore Mechanics and Arctic Engineering - OMAE*, Rotterdam, the Netherlands, 2011.

[37] M. E. Harrison, W. M. J. Batten, L. E. Myers, and A. Bahaj, "Comparison between CFD simulations and experiments for predicting the far wake of horizontal axis tidal turbines," *Renewable Power Generation, IET*, vol. 4, no. 6, pp. 613–627, 2009.

[38] T. Moeller, "Blade cracks signal new stress problem, preventative investment needed on turbines with large LM blades," http://bit.ly/15tDjJ4, 1997.

[39] M. Magnusson and A. S. Smedman, "Air flow behind wind turbines," *Journal of Wind Engineering and Industrial Aerodynamics*, vol. 80, no. 12, pp. 169 – 189, 1999.

[40] U. Högström, D. Asimakopoulos, H. Kambezidis, C. Helmis, and A. Smedman, "A field study of the wake behind a 2 MW wind turbine," *Atmospheric Environment*, vol. 22, no. 4, pp. 803 – 820, 1988.

[41] Z. T. Xie and I. P. Castro, "Efficient generation of inflow conditions for large eddy simulation of street-scale flows," *Flow, Turbulence and Combustion*, vol. 81, no. 3, pp. 449–470, 2008.

OPENFOAM-EXPLORATION OF DIGITAL-FILTER-BASED SYNTHETIC TURBULENCE GENERATION METHODS AND AN IMPROVEMENT TO THEIR NON-GAUSSIAN CAPABILITIES

KUTALMIS M. BERCIN[1], ZHENG-TONG XIE[1], STEPHEN R. TURNOCK[2]
[1]*Aerodynamics and Flight Mechanics, University of Southampton, Southampton, UK, K.Bercin@soton.ac.uk*
[2]*Fluid Structure Interactions, University of Southampton, Southampton, UK*

Keywords: *inflow turbulence, synthetic turbulence, inlet conditions, random flow generation, non-Gaussian turbulence*

Introduction

Turbulent flow regimes are the norm in nature; thus, significant to consider in engineering applications. Yet, their modelling poses substantial ongoing challenges. A physical model concept progressively adopted at many levels of industry and academia is Large Eddy Simulation (LES). LES approximations are, however, known to be deterministically and to a lesser extent statistically sensitive to spatiotemporal characteristics of inflow boundary conditions. Theoretical or practical and stochastic or statistical delineation of these conditions in space and time is, on the other hand, proved to be challenging mainly due to the complex nature of turbulence; hence, resulting in various methods. One important category of such methods is the *digital-filter-based synthetic turbulence generation methods* (hereafter, DFM), originally proposed by [1].

DFM transforms a random signal into a stochastically and statistically new signal involving a set of *target* statistics (predominantly consisting of $i.$ first & second-order one-spatial-point correlations and $ii.$ two-spatial/temporal-point autocorrelation functions). The transformation is performed by a train of arithmetic operations, which is often called a *discrete filter operator*, or briefly a *filter*. Attributes and order of the operations in the filter are arranged by the target statistics, so that the *realized* statistics of the new signal may match the *target*.

DFM has been preferred across a broad range of LES applications in the literature (more than a-thousand papers to date) due to, in comparison to the other concepts, the easiness of its code implementation and its relatively low computational cost for a satisfactory level of fidelity in synthetic turbulence realizations.

Although DFM was frequently utilised and various physical insights were acquired through LES depending upon DFM, the relevant literature arguably lacks systematic evaluations of fundamental capabilities of DFMs, and clear-cut conclusions/recommendations regarding inner parameters/mechanisms of DFMs. Instead, most method proposal papers either used flows more complex than 'building-block' flows to assess their methods (e.g. no homogeneous isotropic/shear turbulence study was carried out for the DFM variant of [2]) or the set of basic validation measures presented in these papers was not extensive (e.g. [1] did not provide any results for power spectral density function). The former complicates the quantitative examination of cause and effect (or input-output) relations between model components and their outcomes; thus, hampering attempts to theoretical capability-oriented improvements. The latter's lack of structured knowledge, on the other hand, obscures comparative decision-making for the most appropriate DFM variant to the problem at hand. Furthermore, the output of DFM is limited to the Gaussian probability distribution function. By contrast, the frequency of occurrence of various turbulence characteristics tends to follow non-Gaussian distributions. For instance, [3] reviewed the literature that kurtosis (i.e. the fourth standardized central moment) is approximately 2.85 (rather than 3.0) for velocity fluctuations in homogeneous isotropic turbulence. Even more pronouncedly, [4] reported for Re_τ = 395 plane channel flow that skewness (i.e. the third standardized central moment) and kurtosis vary across from -0.8 to 0.4, and from 2.1 to 38.0, respectively.

The aims of this research study are, therefore, $i.$ to systematically explore patterns in parameters-mechanisms of DFM to fill the aforementioned knowledge gaps, and $ii.$ to add non-parametric non-Gaussian turbulence realization generation capability into DFM. To this end, DFM is summarized in Sec. §2, the objectives of the research are elaborated in Sec. §3, a sample of results is presented in Sec. §4, and concluding remarks alongside incomplete challenges are listed in Sec. §5. It should be highlighted at this point that the suite of our DFM implementations of the current study is being implemented into OpenFOAM+ community repository.

Theory

The mathematical essence of virtually all DFMs is three-fold. The first is the construction of $\{u_i'(x_i,t) \in \mathbb{Q}^n\}_{n\in\{2,3\}\ \&\ \{i\in\mathbb{N}:1\le i\le n\}}$ as follows:

$$\underbrace{\begin{bmatrix} u' \\ v' \\ w' \end{bmatrix}}_{u_i'(x_i,t)} = \underbrace{\begin{bmatrix} a_{11} & a_{12} & a_{13} \\ a_{21} & a_{22} & a_{23} \\ a_{31} & a_{32} & a_{33} \end{bmatrix}}_{a_{ij}(x_i)} \underbrace{\begin{bmatrix} s^u & s^v & s^w \end{bmatrix}^{\mathsf{T}}}_{s^i(x_i,t)} \tag{1}$$

where u_i' is spatio-temporal-variant Reynolds-decomposed fluctuation velocity field, a_{ij} spatial-variant amplitude tensor, which complements one-point correlations into u_i', and s^i spatio-temporal-variant filter-applied random number field, which incorporates two-point correlations into u_i'.

The second stage is the construction of a_{ij} through [5]'s transformation as:

$$a_{ij} = \begin{bmatrix} (R_{11})^{0.5} & 0 & 0 \\ R_{21}/a_{11} & (R_{22} - a_{21}^2)^{0.5} & 0 \\ R_{31}/a_{11} & (R_{32} - a_{21}a_{31})/a_{22} & (R_{33} - a_{31}^2 - a_{32}^2)^{0.5} \end{bmatrix} \tag{2}$$

where R_{ij} is the known one-point correlation tensor.

The last stage is the construction of s^i, where filtering is conducted. For a one-dimensional field of discrete points:

$$s_{\mathrm{k}} \equiv \mathrm{F_N}\left(\mathrm{r_k}\right) = \sum_{\mathrm{j=-N}}^{\mathrm{N}} \mathrm{b_j r_{k+j}} \tag{3}$$

where $\{\mathrm{r}\}_{\{\mathrm{k,j}\in\mathbb{N}\,:\,1\leq\mathrm{k+j}\leq\mathrm{R}\}}$ is a set of R random numbers obeying the amplitude distribution of zero-mean ($\mathrm{R^{-1}}\sum_{\mathrm{k=1}}^{\mathrm{R}} \mathrm{r_k} = 0$), unit-variance ($\mathrm{R^{-1}}\sum_{\mathrm{k=1}}^{\mathrm{R}} \mathrm{r_k^2} = 1$), independent ($\mathrm{R^{-1}}\sum_{\mathrm{k=1}}^{\mathrm{R}} \mathrm{r_k r_j} = 0$ for $\mathrm{k} \neq \mathrm{j}\,\&\,\mathrm{k} = \mathrm{j} \pm c$) Gaussian white-noise, $\{\mathrm{b}\}_{\{\mathrm{j}\in\mathbb{N}\,:\,\text{-}\mathrm{N}\leq\mathrm{j}\leq\mathrm{N}\}}$ a set of $(2\mathrm{N}+1)$ unknown filter coefficients, $\{s\}_{\{\mathrm{k}\in\mathbb{N}\,:\,1\leq\mathrm{k}\leq\mathrm{M}\}}$ a set of M digital-filtered numbers, $\mathrm{F_N}$ a linear, non-recursive, discrete filter operator performing the convolution summation on two finite sequences, and N the support of the filter. Herein, the aim of DFM is to compute the set b according to the expected values $\{\mathbf{E}[f_m(s)]\}_{\{m\in\mathbb{N}\,:\,m\geq 1\}}$ of various, known statistical measures $f_m(s)$ (e.g. autocorrelation function of u_i'), so that unknown s can be computed with the help of known a_{ij} and r. Based upon this essence, DFMs diversify primarily due to the different explicit/implicit expressions proposed for the relation between known $\mathbf{E}[f_m(s)]$ and unknown b, and sometimes for a_{ij}. To the author's knowledge, eight research studies contributed model developments in DFM: [1, 6, 2, 7, 8], and [9, 10, 11, 12], in which the former five put forth major changes, and the latter four propounded adjunct; nevertheless, still important alterations.

For a non-Gaussian velocity field ${}^g u_i'$, a generic analytic expression g_i was sought which changes the first four standardized central moments of u_i' to the desired values while keeping the other incorporated statistics the same such that: ${}^g u_i'(x_i,t) = u_i'(x_i,t)g_i(x_i)$. For this purpose, three approaches were proposed and tested: i. non-Gaussian random number set input-based approach, ii. deterministic deconvolution-based approach, and iii. probability mass function transformation-based approach.

Methodology

Four DFM were implemented into OpenFOAM suite and tested through a test-bed. The methods sorted by descending computational cost are: i. di Mare et al. [6], ii. Klein et al. [1], iii. Xie-Castro [2] and iv. Kim et al. [7]. The chosen methods represent the majority of DFM capabilities and varieties. The test-bed involves three 'building-block' flows: i. homogeneous isotropic turbulence (the case of M = 0.0508) [13], ii. homogeneous shear turbulence (the case of h = 0.305) [14], and iii. plane channel flow (the case of Re_τ=395) [4], each of which focuses on an isolated aspect of turbulent flows. OpenFOAMv1612+ was used with the physical model of incompressible *implicitly filtered* LES (IFLES). Sub-filter scales were modelled with Smagorinsky model (C_e = 1.048, C_k = 0.02107) corrected by van Driest damping function near the walls. Computational domain models replicated the physical domain of each benchmark scenario, and domain discretization was made with unstructured rectangular cuboids. Pre-assessment for the spatial resolutions ensured that maximum Courant number remains below the unity. Due to the inability of separating discretization errors and IFLES modelling uncertainty errors, grid-independency is not possible for IFLES. Post-assessment of spatial resolution is therefore performed by *one-point* and *two-point grid estimator*s. Finite volume method was utilised for equation discretization. Numerical integration of all spatial derivatives-variables, and node-to-face interpolations were held through second-order central difference scheme. Backward differencing scheme of second order was used for numerical integration of temporal derivatives-variables. The system of algebraic governing equations were then solved on a co-located grid arrangement. Pressure-velocity decoupling at the practical and theoretical level were respectively removed by a variant of Rhie-Chow momentum interpolation method and PISO algorithm. The inner mechanism of DFM was divided into four consecutive building-block stages, so that the effects of each stage on statistics are isolated: i. random number generation, ii. incorporation of two-point spatiotemporal correlations through digital filtering, iii. incorporation of one-point correlations through [5]'s transformation, and iv. non-Gaussian transformation. To quantify-compare the level of fidelity of each DFM's flow reconstruction, the following statistical measures (mostly of the benchmark databases) were used: profiles of i. standardized central moments, ii. second-order one-spatial-point correlation tensor, iii. two-spatial/temporal-point correlation functions, iv. one-dimensional one-sided power spectral density functions, v. one-spatial-point probability mass functions (*pmf*), vi. *pmf*s of velocity differences across various distances and vii. entrance length.

Sample Results and Discussion

As an example illustration from the obtained results, one-dimensional one-sided power spectral density functions are presented in Fig. 1. What stands out in the figure is a sharp and flow-type-independent drop in the energy spectrum created by [1] towards higher wavenumbers although the energy across large turbulence length scales match those observed in the test-bed flows. In contrast, the other methods' reconstructions are overall in better agreement with those in benchmarks across the whole range of wavenumbers. The result may be explained by one of the major differences between the methods that [1] uses Gaussian-shape form for input correlation functions whereas [2, 7] use an exponential form, and [6] an exact

form. In order to test this postulation, [1]'s form was converted into an exponential one. It was then found that the drop disappears (not reported). This finding supports and suggests the view that exponential form of correlation functions is more appropriate choice for turbulence correlations than Gaussian. Considering [1] is the most cited member of any DFM, any insights utilised [1] must therefore be re-interpreted with caution.

Moreover, non-Gaussianity studies showed that i. the first two proposed approaches were proved to be ineffective, and ii. the third approach was found to be promising. Although a feasible method was mostly developed, it is still significant to examine how the first two sound methods did perform.

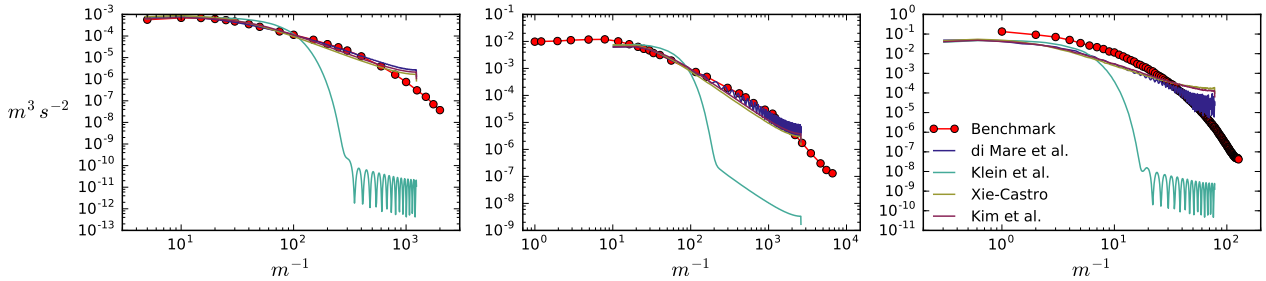

Figure 1: Estimated one-dimensional one-sided power spectral density functions obtained from four DFM for the building-block flows: from left to right, homogeneous isotropic turbulence, homogeneous shear turbulence and plane channel flow. Synthetic turbulence was generated on a discrete plane domain containing 2^{14} nodes. For each node, a time series consisting of 4×10^4 temporal points were created. Next, for each time-series, the power spectral density was estimated, and the estimations were spatially averaged in homogeneous directions. In the estimation, Welch's method with Hann window using 50% overlap was used (length of each segment was set 512 temporal points).

Future Work

The following remains incomplete to reach the two aims of the study: i. prospective simulations of the test scenarios need to be completed, and ii. the method-yielding-promising-results for non-Gaussian functionality needs to undergo a formalization, and more extensive-various tests.

Acknowledgments

The authors acknowledge the use of the IRIDIS High Performance Computing Facility, associated support services at the University of Southampton, in the completion of this work, and thank all those involved in the organisation of OFW12 and to all the contributors that will enrich this event. Bercin also acknowledges the international research studentship from the Faculty of Engineering and the Environment at the University of Southampton.

References

[1] M. Klein, A. Sadiki, and J. Janicka, "A digital filter based generation of inflow data for spatially developing direct numerical or large eddy simulations," *Journal of Computational Physics*, vol. 186, no. 2, pp. 652–665, 2003.

[2] Z. Xie and I. P. Castro, "Efficient generation of inflow conditions for large eddy simulation of street-scale flows," *Flow, Turbulence and Combustion*, vol. 81, no. 3, pp. 449–470, 2008.

[3] J. Jimenez, "Turbulent velocity fluctuations need not be Gaussian," *Journal of Fluid Mechanics*, vol. 376, 1998.

[4] R. D. Moser, J. Kim, and N. N. Mansour, "Direct numerical simulation of turbulent channel flow up to Reτ=590," *Physics of Fluids*, vol. 11, no. 4, pp. 943–945, 1999.

[5] T. S. Lund, X. Wu, and K. D. Squires, "On the generation of turbulent inflow conditions for boundary layer simulations," *Journal of Computational Physics*, vol. 140, no. 2, pp. 233–258, 1998.

[6] L. di Mare, M. Klein, W. P. Jones, and J. Janicka, "Synthetic turbulence inflow conditions for large-eddy simulation," *Physics of Fluids*, vol. 18, no. 2, p. 025107, 2006.

[7] Y. Kim, Z. T. Xie, and I. P. Castro, "A Forward Stepwise Method of Inflow Generation for LES," in *Proceedings of the Sixth International Conference on Fluid Mechanics*. American Institute of Physics, 2011, pp. 134–136.

[8] M. Fathali, M. Klein, T. Broeckhoven, C. Lacor, and M. Baelmans, "Generation of turbulent inflow and initial conditions based on multi-correlated random fields," *International Journal for Numerical Methods in Fluids*, vol. 57, no. 1, pp. 93–117, 2008.

[9] I. Veloudis, Z. Yang, J. J. McGuirk, G. J. Page, and A. Spencer, "Novel implementation and assessment of a digital filter based approach for the generation of les inlet conditions," *Flow, Turbulence and Combustion*, vol. 79, no. 1, pp. 1–24, 2007.

[10] A. M. Kempf, S. Wysocki, and M. Pettit, "An efficient, parallel low-storage implementation of Klein's turbulence generator for LES and DNS," *Computers and Fluids*, vol. 60, pp. 58–60, 2012.

[11] Y. Kim, I. P. Castro, and Z. Xie, "Divergence-free turbulence inflow conditions for large-eddy simulations with incompressible flow solvers," *Computers and Fluids*, vol. 84, pp. 56–68, 2013.

[12] N. S. Dhamankar, C. S. Martha, K. M. Aikens, and G. A. Blaisdell, "Digital Filter-based Turbulent Inflow Generation for Jet Aeroacoustics on Non-Uniform Structured Grids," in *52nd Aerospace Sciences Meeting*, no. January. Reston, Virginia, USA: American Institute of Aeronautics and Astronautics, 2014, pp. 1–35.

[13] G. Comte-Bellot and S. Corrsin, "Simple Eulerian time correlation of full-and narrow-band velocity signals in grid-generated, isotropic' turbulence," *Journal of Fluid Mechanics*, vol. 48, no. 02, p. 273, 1971.

[14] S. Tavoularis and S. Corrsin, "Experiments in nearly homogeneous turbulent shear flow with a uniform mean temperature gradient. Part 2. The fine structure," *Journal of Fluid Mechanics*, vol. 104, pp. 349–367, 1981.

AN EVALUATION OF DIGITAL-FILTER BASED SYNTHETIC TURBULENCE GENERATION METHODS AND IMPROVEMENTS TO THEIR QUANTIFIED DEFICIENCIES

Kutalmis Bercin[1], Zheng-Tong Xie[1] & Stephen R. Turnock[2]
[1]*Aerodynamics and Flight Mechanics, University of Southampton, Southampton, UK*
[2]*Fluid Structure Interactions, University of Southampton, Southampton, UK*

As emphasized by [4], the governing equations for turbulent flows are extremely sensitive to inlet boundary conditions. Lorenz [4] showed, for example, that an alteration in the streamwise velocity component initial condition merely at a level of $\mathcal{O}\left(10^{-6}\right)$ yields diverse instantaneous realizations in turbulent convection mechanisms. Large eddy simulation (LES) is also subject to such sensitivity because of the direct computation of the governing equations for time-dependent large-scale turbulent motions. Inlet boundary conditions for LES, therefore, must be carefully modelled. Yet, theoretical and practical inlet turbulence generation is proved to be difficult mainly due to the complex nature of turbulence; hence, resulting in various methods.

One important category of such methods is the *digital-filter based synthetic turbulence generation methods*, originally proposed by [3], (hereafter, DFMs) refer to which accept a set of *target* statistics and a discrete random signal as input, and transform them mostly through mathematical techniques into a new deterministically and statistically different signal representing the fluctuating component of a Reynolds decomposed turbulence parameter, $\phi'(\mathbf{x}, t)$. The transformation is performed by a train of arithmetic operations, which as a whole is often called a *discrete filter operator* (*filter*). Attributes and sequence of operations are arranged by the *target* statistics, so that the *realized* statistics of the new signal may match the *target*. The major advantage of DFMs in comparison to the other methods is the easiness of their code implementations and their relatively low computational cost for a similar level of fidelity for the generated turbulence realizations.

Despite the use of DFMs across a broad range of LES applications in the literature, the relevant literature arguably lacks systematic and complete conclusions/recommendations regarding inner parameters/mechanisms of DFMs. For instance, quantitative examinations for their modelling assumptions, input-output relations, best numerical implementation/usage practices, and extensive comparative analyses across their variants are, in general, either unavailable or unorganized. Lack of knowledge on such issues may, however, hamper theoretical and practical improvements for DFMs, and their correct usage.

The aim of this research study is, thus, to systematically explore patterns in parameters/mechanisms of DFMs to fill these knowledge gaps, and to propose and evaluate possible improvements. For this purpose, the objective is set to investigate each building-block assumption of DFMs in a consecutive order, examine outcome realizations to reveal capabilities and deficiencies of the method, and search for new extensions/inversions to remedy the quantified deficiencies.

Three methods representing general capabilities of DFMs are tested with and without LES: i. [3], ii. [2]'s forward stepwise method (FSM), and iii. [5]'s hybrid FSM-DFM. Their common point is that their applicability to most LES cases is possible unlike, for example, [1] is limited to homogeneous shear flows in practice. Additionally, the test beds of the methods involve: i. homogeneous isotropic turbulence, ii. homogeneous shear flow, iii. channel flow, and iv. backward facing step flow, each of which helps to focus one isolated aspect of turbulent flows.

Initial quantifications showed two principal deficiencies in outcomes of DFMs: i. they are limited to Gaussian distributions, and ii. they lose energy near cut-off scales. In addition, initial work suggested that DFMs may provide more sophistication at a lower computational cost. For the first time, accordingly, a new method was proposed in order to improve DFMs to produce non-parametric non-Gaussian turbulence processes. Furthermore, two new methods for DFMs' inner computations were developed, one reduced the floating-point operations per time-step (FLOPT) from $\mathcal{O}\{N^6\}$[1] to $\mathcal{O}\{N^3(3N)\}$, and the other reduced the FLOPT from $\mathcal{O}\{N^6\}$ to $\mathcal{O}\{N^3 log_3(N)\}$ for a typical LES computation.

In the final work, the characteristics/quantifications of DFMs' parameters/assumptions/mechanisms, arguably in the largest scale in the literature to date, and, the methods-yielding-promising-results, which will undergo formalization and more extensive tests, will be presented.

References

[1] M. Fathali, J. Meyers, G. Rubio, S. Smirnov, and M. Baelmans. Sensitivity analysis of initial condition parameters on the transitional temporal turbulent mixing layer. *Journal of Turbulence*, **9**:N12, 2008.

[2] Y. Kim, Z. T. Xie, and I. P. Castro. A forward stepwise method of inflow generation for les. *Proceedings of the Sixth International Conference on Fluid Mechanics*, pages 134–136, 2011.

[3] M. Klein, A. Sadiki, and J. Janicka. A digital filter based generation of inflow data for spatially developing direct numerical or large eddy simulations. *Journal of Computational Physics*, **186**:652–665, 2003.

[4] S. B. Pope. *Turbulent Flows*. Cambridge University Press, 2000.

[5] Z. Xie and I. P. Castro. Efficient generation of inflow conditions for large eddy simulation of street-scale flows. *Flow, Turbulence and Combustion*, **81**:449–470, 2008.

[1] N is the number of grid points along a coordinate axis.

Paper-II: Supplementary Document - I

List of Tables

Table 1: The sample mean (i.e. $\widehat{\mu}_1$) and corresponding coefficient of variation (i.e. $\{\bullet\}_{\text{CV}}$) of time-averaged spatial-variant fields of five IFLES-quality post-metrics (i.e. Γ_{Pope}, Γ_{ν}, $\Gamma_{\text{Celik-I}}$, $\Gamma_{\text{Celik-II}}$, and $\Gamma_{\text{Celik-III}}$) obtained from the decaying homogeneous isotropic turbulence (DHIT), homogeneous shear turbulence (HST), and plane channel flow with smooth walls (PCF) computations of the four digital-filter-based and forward-stepwise-based synthetic time-series generators.

Method $\downarrow$ $\widehat{\mu}_{1_{\text{CV}}}$ $\rightarrow$		Γ_{Pope}	Γ_{ν}	$\Gamma_{\text{Celik-I}}$	$\Gamma_{\text{Celik-II}}$	$\Gamma_{\text{Celik-III}}$
DHIT	Custom	$0.977_{0.41}$	$1.764_{18.07}$	$0.937_{0.46}$	$0.937_{2.21}$	$0.936_{2.12}$
	Klein et al.	$0.980_{0.44}$	$1.822_{16.59}$	$0.936_{0.36}$	$0.939_{1.45}$	$0.939_{1.31}$
	Xie-Castro	$0.985_{0.30}$	$1.730_{36.99}$	$0.937_{0.30}$	$0.932_{1.43}$	$0.932_{1.22}$
	Kim et al.	$0.975_{0.48}$	$1.772_{26.89}$	$0.937_{0.50}$	$0.933_{2.83}$	$0.932_{2.63}$
HST	Custom	$0.947_{0.77}$	$7.306_{37.04}$	$0.875_{1.52}$	$1.089_{51.96}$	$0.878_{63.75}$
	Klein et al.	$0.953_{0.71}$	$8.003_{46.91}$	$0.870_{1.60}$	$1.050_{24.39}$	$0.904_{26.82}$
	Xie-Castro	$0.953_{0.66}$	$7.837_{22.04}$	$0.871_{1.57}$	$1.014_{21.98}$	$0.924_{22.72}$
	Kim et al.	$0.947_{0.87}$	$7.579_{111.34}$	$0.873_{1.40}$	$1.070_{89.28}$	$0.906_{105.22}$
PCF	Custom	$0.929_{8.67}$	$1.230_{10.70}$	$0.947_{0.29}$		
	Klein et al.	$0.930_{8.66}$	$1.231_{10.87}$	$0.947_{0.29}$		
	Xie-Castro	$0.930_{8.69}$	$1.230_{10.81}$	$0.947_{0.29}$		
	Kim et al.	$0.928_{8.76}$	$1.229_{10.65}$	$0.947_{0.29}$		

Table 2: Seven descriptive statistics of the time-averaged $\Gamma_{\text{Pope}}(\mathbf{x})$ spatial-variant fields: from the leftmost to the rightmost column, the estimations of mean, standard deviation, skewness, kurtosis, maximum, median and minimum.

Benchmark	Method	$\widehat{\mu}_1$	$\sqrt{\widehat{\mu}_2}$	$\widehat{\gamma}_1$	$\widehat{\gamma}_2$	Max	Med	Min
DHIT	Custom	0.977	0.004	-1.931	16.266	0.987	0.978	0.684
	Klein et al.	0.980	0.004	1.802	17.682	0.999	0.979	0.556
	Xie-Castro	0.985	0.003	1.548	17.274	0.997	0.984	0.738
	Kim et al.	0.975	0.005	-2.782	31.398	0.986	0.977	0.504
HST	Custom	0.947	0.007	-0.355	0.252	0.976	0.947	0.847
	Klein et al.	0.953	0.007	0.317	1.029	0.980	0.952	0.933
	Xie-Castro	0.953	0.006	0.049	0.235	0.978	0.953	0.933
	Kim et al.	0.947	0.008	-0.624	0.025	0.971	0.949	0.802
PCF	Custom	0.929	0.080	-2.573	6.120	0.980	0.961	0.458
	Klein et al.	0.930	0.080	-2.562	6.021	0.988	0.961	0.480
	Xie-Castro	0.930	0.081	-2.557	6.024	0.987	0.962	0.475
	Kim et al.	0.928	0.081	-2.582	6.231	0.976	0.960	0.445

Table 3: Seven descriptive statistics of the time-averaged $\Gamma_\nu(\mathbf{x})$ spatial-variant fields: from the leftmost to the rightmost column, the estimations of mean, standard deviation, skewness, kurtosis, maximum, median and minimum.

Benchmark	Method	$\widehat{\mu}_1$	$\sqrt{\widehat{\mu}_2}$	$\widehat{\gamma}_1$	$\widehat{\gamma}_2$	Max	Med	Min
DHIT	Custom	1.764	0.319	488.543	752365.327	535.32	1.674	1.378
	Klein et al.	1.822	0.302	455.518	424499.612	365.488	1.807	1.291
	Xie-Castro	1.730	0.640	1683.659	3370998.906	1469.935	1.717	1.407
	Kim et al.	1.772	0.477	1033.414	1717421.129	902.502	1.669	1.363
HST	Custom	7.306	2.706	710.047	1032664.268	4360.736	7.246	3.115
	Klein et al.	8.003	3.754	853.124	1215278.736	6191.585	8.205	3.281
	Xie-Castro	7.837	1.755	1.046	218.996	354.276	7.854	3.352
	Kim et al.	7.579	8.438	1700.926	3456797.376	18410.885	7.412	3.89
PCF	Custom	1.230	0.132	1.486	2.031	1.844	1.194	1.011
	Klein et al.	1.231	0.133	1.516	2.085	1.850	1.195	1.012
	Xie-Castro	1.230	0.133	1.487	2.003	1.850	1.194	1.011
	Kim et al.	1.229	0.131	1.449	1.943	1.837	1.194	1.011

Table 4: Seven descriptive statistics of the time-averaged $\Gamma_{\text{Celik-I}}(\mathbf{x})$ spatial-variant fields: from the leftmost to the rightmost column, the estimations of mean, standard deviation, skewness, kurtosis, maximum, median and minimum.

Benchmark	Method	$\widehat{\mu}_1$	$\sqrt{\widehat{\mu}_2}$	$\widehat{\gamma}_1$	$\widehat{\gamma}_2$	Max	Med	Min
DHIT	Custom	0.937	0.004	-1.485	48.807	0.944	0.938	0.417
	Klein et al.	0.936	0.003	-2.992	232.38	0.946	0.936	0.467
	Xie-Castro	0.937	0.003	-6.357	884.612	0.943	0.938	0.295
	Kim et al.	0.937	0.005	-1.765	73.668	0.944	0.938	0.352
HST	Custom	0.875	0.013	-0.125	7.693	0.916	0.875	0.191
	Klein et al.	0.870	0.014	0.217	10.214	0.914	0.868	0.164
	Xie-Castro	0.871	0.014	0.324	-0.527	0.913	0.870	0.471
	Kim et al.	0.873	0.012	-0.439	20.659	0.907	0.874	0.099
PCF	Custom	0.947	0.003	-1.339	1.664	0.952	0.948	0.935
	Klein et al.	0.947	0.003	-1.370	1.711	0.952	0.948	0.935
	Xie-Castro	0.947	0.003	-1.341	1.630	0.952	0.948	0.935
	Kim et al.	0.947	0.003	-1.30	1.578	0.952	0.948	0.935

Table 5: Seven descriptive statistics of the time-averaged $\Gamma_{\text{Celik-II}}(\mathbf{x})$ spatial-variant fields: from the leftmost to the rightmost column, the estimations of mean, standard deviation, skewness, kurtosis, maximum, median and minimum.

Benchmark	Method	$\widehat{\mu}_1$	$\sqrt{\widehat{\mu}_2}$	$\widehat{\gamma}_1$	$\widehat{\gamma}_2$	Max	Med	Min
DHIT	Custom	0.937	0.021	0.673	1.654	1.163	0.932	0.739
	Klein et al.	0.939	0.014	1.704	15.438	1.246	0.938	0.773
	Xie-Castro	0.932	0.013	2.989	24.561	1.188	0.93	0.81
	Kim et al.	0.933	0.026	0.777	1.348	1.167	0.927	0.787
HST	Custom	1.089	0.566	-65.586	350468.792	496.023	1.066	-549.239
	Klein et al.	1.05	0.256	-1159.041	2224036.659	18.697	1.055	-503.639
	Xie-Castro	1.014	0.223	609.624	1425706.669	380.388	1.007	-230.211
	Kim et al.	1.07	0.956	-601.424	2498816.151	1363.767	1.057	-1807.874

Table 6: Seven descriptive statistics of the time-averaged $\Gamma_{\text{Celik-III}}(\mathbf{x})$ spatial-variant fields: from the leftmost to the rightmost column, the estimations of mean, standard deviation, skewness, kurtosis, maximum, median and minimum.

Benchmark	Method	$\widehat{\mu}_1$	$\sqrt{\widehat{\mu}_2}$	$\widehat{\gamma}_1$	$\widehat{\gamma}_2$	Max	Med	Min
DHIT	Custom	0.936	0.020	0.347	0.240	1.000	0.932	0.739
	Klein et al.	0.939	0.012	0.193	3.855	1.000	0.938	0.754
	Xie-Castro	0.932	0.011	0.917	6.626	1.000	0.930	0.810
	Kim et al.	0.932	0.025	0.355	-0.126	1.000	0.927	0.787
HST	Custom	0.878	0.560	67.918	365975.095	551.239	0.922	-494.023
	Klein et al.	0.904	0.243	1363.489	2761521.425	505.639	0.922	-16.697
	Xie-Castro	0.924	0.210	-729.373	1812852.472	232.211	0.931	-378.388
	Kim et al.	0.906	0.954	605.306	2519999.512	1809.874	0.933	-1361.767